Measurement of multi-differential cross sections for the production of top quark pairs plus additional jets in pp collisions at $\sqrt{s} = 13\,\mathbf{TeV}$.

Dissertation

zur Erlangung des Doktorgrades

an der Fakultät für Mathematik,

Informatik und Naturwissenschaften

Fachbereich Physik

der Universität Hamburg

vorgelegt von

Rafael Eduardo Sosa Ricardo

aus

Holguin, Kuba

Hamburg

2021

Hiermit erkläre ich an Eides statt, dass ich die vorliegende Dissertationsschrift selbst verfasst und keine anderen als die angegebenen Quellen und Hilfsmittel benutzt habe.

I hereby declare, on oath, that I have written the present dissertation by my own and have not used other than the acknowledged resources and aids.

Hamburg, den 10. November 2021 Rafael Eduardo Sosa Ricardo

Gutachter der Dissertation:	PD Dr. Dr. Olaf Behnke Prof. Dr. Elisabetta Gallo
Zusammensetzung der Prüfungskommission:	Prof. Dr. Caren Hagner Prof. Dr. Elisabetta Gallo Dr. Maria Aldaya Prof. Dr. Gudrid Moortgat-Pick PD Dr. Olaf Behnke
Vorsitzender der Prüfungskommission:	Prof. Dr. Caren Hagner
Datum der Disputation:	13.12.2021
Vorsitzender des Fach-Promotionsausschusses Physik:	Prof. Dr. Wolfgang Hansen
Leiter des Fachbereichs Physik:	Prof. Dr. Günter H. W. Sigl
Dekan der Fakultät MIN:	Prof. Dr. Heinrich Graener

ABSTRACT

This thesis presents measurements of multi-differential top quark pair ($t\bar{t}$) production cross sections in pp collisions at the LHC with a centre-of-mass energy of 13 TeV using events containing two opposite-sign leptons. The analyzed dataset was recorded with the CMS detector in the years 2016, 2017 and 2018, and corresponds to an integrated luminosity of $137\,\text{fb}^{-1}$.

Precision double- and triple-differential cross sections are measured as a function of observables describing the kinematic properties of the top quark, top antiquark, and $t\bar{t}$ system, for both parton and particle level definitions of these objects. Furthermore, single- and double-differential cross sections as functions of these observables are extracted in the presence of additional jets in the event. The set of results contains also the single differential cross section of the number of additional jets for different ranges of minimum p_T of the jets. Studies are also presented as function of the kinematics of the leading and sub-leading extra jets and the combined $t\bar{t}$ plus leading extra jet system. The obtained unfolded cross sections are compared to MC predictions based on Next-to-Leading order QCD matched to parton showers, and also to different beyond-NLO theory predictions.

A study is performed on the possibility of using the double differential measurement as function of the top quark transverse momentum and $t\bar{t}$ invariant mass as a two-dimensional reweighting of the $t\bar{t}$ signal simulations at generator level, to improve the simulation. The effects of the application of such correction on different top and $t\bar{t}$ system observables are analyzed.

ZUSAMMENFASSUNG

In dieser Doktorarbeit werden Messungen multi-differenzieller Wirkungsquerschnitte für die Top-Quark Paarproduktion ($t\bar{t}$) in *pp* Kollisionen am LHC bei einer Schwerpunktsenergie von 13 TeV vorgestellt, unter Benutzung von Ereignissen mit zwei gegenätzlich geladenen Leptonen im Endzustand. Die analysierten Daten wurden mit dem CMS Detekor in den Jahren 2016, 2017 und 2018 aufgenommen und entsprechen einer integrierten Luminosität von $137\,\mathrm{fb}^{-1}$.

Präzise zwei- und dreifach differenzielle Wirkungsquerschnitte werden gemessen als Funktion von kinematischen Observablen des Top-Quarks, des Top-Antiquarks und des $t\bar{t}$ Systems, sowohl für "Parton und Particle Level"Definitionen dieser Objekte. Darüberhinaus werden ein- und zweifach differenzielle Wirkungsquerschnitte als Funktion derselben Variablen studiert, in Abhängigkeit von der Multiplizität zusätzlicher "Jetsïn den Ereignissen. Einfach differenzielle Wirkungsquerschnitte der Multiplizität solcher Ëxtra-Jets"werden auch vorgestellt, als Funktion des minimalen Transversalimpulses dieser Jets. Weiterhin werden Studien durchgeführt als Funktion der Kinematik des führenden (höchster Transversalimpuls) und nächst-führenden Jets und des kombinierten Systems bestehend aus dem $t\bar{t}$ System und dem führenden Jet. Die erzielten entfalteten Wirkungsquerschnitte werden mit Monte Carlo Vorhersagen verglichen die QCD Matrix Elemente der nächst-führenden Ordnung mit Parton Schauern verbinden, sowie auch mit Rechnungen die noch höhere Ordnungen der Störungstheorie beinhalten.

Eine Studie wird vorgestellt welche die Möglichkeit untersucht die gemessenen doppelt differenziellen Messungen als Funktion der Masse des $t\bar{t}$ Systems und des Transversalimpulses des Top-Quark für eine zweidimensionale Umgewichtung der $t\bar{t}$ Signal-MC Simulation auf Generatorniveau zu verwenden um die Simulation zu verbessern. Die Effekte der Anwendung einer solchen Korrektur auf verschiedene kinematischen Spektren des Top-Quarks und des $t\bar{t}$ Systems werden studiert.

CONTENTS

1 Introduction **1**

2 The Standard Model of particle physics and the top quark **3**
2.1 The Standard Model of particle physics 4
2.1.1 Fermions 4
2.1.2 Fundamental interactions and force mediators 6
2.2 The top quark 10
2.2.1 Top quark production 11
2.2.2 Top quark pair decay 13
2.2.3 Extra jets in the $t\bar{t}$ system 14

3 Experimental Setup **17**
3.1 The Large Hadron Collider 17
3.2 The Compact Muon Solenoid 18
3.2.1 The coordinate system and remarks on the measured observables . . . 19
3.2.2 The solenoid magnet 21
3.2.3 Tracking detectors 21
3.2.4 Electromagnetic and Hadron Calorimeters 22
3.2.5 The muon system 23
3.2.6 Event triggering and data acquisition systems 24
3.2.7 Luminosity measurements at CMS 25

4 Event Simulation **29**
4.1 Matrix element calculation 30
4.2 Parton shower simulation 31
4.3 Hadronization process 31
4.4 Matching matrix element to parton shower 32
4.5 Underlying event model 33

4.6 Colour reconnection model . . . 33
4.7 Monte Carlo Generators . . . 34
4.8 Simulation of the detector response . . . 36

5 Event Reconstruction **37**
5.1 Track and vertex reconstruction . . . 37
5.1.1 Track reconstruction and vertex reconstruction . . . 38
5.2 Objects reconstruction . . . 40
5.2.1 Muon reconstruction . . . 41
5.2.2 Electron reconstruction . . . 41
5.2.3 Leptons: used triggers and isolation criteria . . . 42
5.2.4 Jet reconstruction. Identification of jets originating from b quarks . . . 43
5.2.5 Missing transverse energy . . . 45

6 Event Selection **47**
6.1 Data sample . . . 48
6.2 $t\bar{t}$ event selection . . . 48
6.3 Background sources . . . 49
6.3.1 Background estimation . . . 51
6.4 Event yields and control distributions . . . 52

7 Reconstruction of the top-pair kinematics **65**
7.1 Description of the methods . . . 65
7.1.1 Full kinematic reconstruction . . . 66
7.1.2 Loose kinematic reconstruction . . . 68
7.2 Performance of the kinematic reconstruction . . . 69
7.3 Control distributions . . . 69

8 Cross Section Measurement **73**
8.1 Background subtraction . . . 74
8.2 Unfolding of the experimental results . . . 74
8.2.1 TUnfold minimization . . . 75
8.3 Multi-differential $t\bar{t}$ production cross sections . . . 77
8.3.1 Cross section definition . . . 77
8.3.2 Combination of the results from different years and channels . . . 77
8.3.3 Phase space definition . . . 78
8.3.4 Efficiency, purity and stability . . . 81

9 Systematic Uncertainties **83**
9.1 Systematic uncertainties . . . 83
9.1.1 Experimental uncertainties . . . 84
9.1.2 Background uncertainties . . . 85
9.1.3 Model uncertainties . . . 86
9.2 Treatment for Run II combination . . . 88
9.3 Determination of the total systematic uncertainty . . . 90
9.4 Summary . . . 90

10 Results **95**
10.1 Multi-differential cross sections 95
10.2 Unfolded cross sections results and comparison to MC models 96
10.2.1 Kinematic properties of the top quark, top antiquark and $t\bar{t}$ system . 98
10.2.2 $t\bar{t}$ production in the presence of additional jets 107
10.2.3 $t\bar{t}$ plus additional jets: studies with leading and sub-leading extra jets 116
10.3 Comparison of 2D $t\bar{t}$ system cross sections to the latest beyond-NLO fixed order QCD calculations 120
10.4 Top p_T reweighting at generator level using $[M(t\bar{t}),p_{\mathrm{T}}(t)]$ unfolded cross section 126
10.5 Summary of the results 132

11 Conclusions and Outlook **135**
11.1 Summary 135
11.2 Outlook 136

A Contribution to the measurement of the integrated luminosity in the CMS detector **139**
A.1 Cross detector stability uncertainty 139
A.1.1 Behavior and stability comparison of luminometers in 2016. 140
A.1.2 Best/second luminometer method. Integrated Luminosity for 2016. . . 141
A.1.3 Cross detector stability uncertainty in 2016. 142
A.1.4 Cross detector stability uncertainty in 2015. 142
A.2 Linearity uncertainty 143
A.2.1 Fill-by-fill linearity studies. 144
A.2.2 Linearity uncertainty for 2015 and 2016. 145

B Control distributions for individual years **153**

C Full set of cross sections results **163**
C.1 Cross sections 163
C.2 Cross sections values 191
C.3 Tables with χ^2 values for the comparison of results with MC models. 269

Bibliography **275**

CHAPTER

1

INTRODUCTION

Since its prediction in 1973 by Kobayashi and Maskawa, the top quark has played a crucial role in testing the validity and properties of the standard model (SM), which is a very successful theory that describes the elementary particles and their interaction. The search for the top quark, the heaviest known elementary particle, lasted more than two decades until finally, in March 1995, when its discovery was announced at the Fermi National Accelerator Laboratory (Fermilab) [1]. Its large mass, which is around the same as for an atom of gold, makes it the only quark that decays before hadronizing, providing a unique opportunity to investigate the properties of a bare quark. The heavy mass of the top quark is in the SM directly related to its large Yukawa coupling to the Higgs boson and in many Beyond SM models the top quark plays an essential role in the electroweak symmetry breaking mechanism.

The Large Hadron Collider (LHC) at CERN is the world's largest particle accelerator ever built. With a center-of-mass energy that has been increasing from 7 TeV in 2011 and 8 TeV in 2012 to 13 TeV in 2015, it has become a genuine top quark factory giving a unique opportunity to perform detailed studies of its properties. The top quarks are predominantly produced in pairs (a top quark and a top anti-quark), commonly known as $\mathrm{t\bar{t}}$ production. The measurements of the $\mathrm{t\bar{t}}$ process play a crucial role in testing the validity of the SM and searching for new phenomena. Each of the top quarks decays almost exclusively to a W boson and a b-quark, and therefore, the final decay of the $\mathrm{t\bar{t}}$ system depends only on the decay channels of the two W bosons.

This work presents measurements of multi-differential top quark pair ($\mathrm{t\bar{t}}$) production cross sections in pp collisions at a center-of-mass energy of 13 TeV, using events containing two opposite-sign leptons. For this purpose, the dataset recorded with the CMS detector in 2016, 2017, and 2018 was used. The amount of analyzed data corresponds to an integrated luminosity of $137\,\mathrm{fb}^{-1}$. The kinematic spectra of the $\mathrm{t\bar{t}}$ system, the top quark (t) and top anti-quark ($\bar{t}$), and additional jets in the event are studied. The multi-differential $\mathrm{t\bar{t}}$ production cross sections allow studying the $\mathrm{t\bar{t}}$ production dynamics in great detail by giving not only the information of the distribution for one observable but simultaneously as function of two

or more variables providing also access to their correlations. The measurements in this work are excellent for testing the current understanding and precision of perturbative QCD. The additional jets provide a second hard kinematic scale in the events that competes with the $t\bar{t}$ invariant mass, giving raise to a multi-scale situation that is known to provide a challenge for the perturbative expansion [2]. The cross section measurements are performed at the parton level of the top and top anti-quark in the full kinematic phase space and at particle level in a fiducial phase space. All results are compared to several SM based predictions from Monte Carlo (MC) generators based on Next-to-Leading order QCD matched to parton showers and also to different beyond-NLO theory predictions.

Similar differential dileptonic top-quark production analyses have been performed within CMS using the 2012 [3] and 2016 [4–6] datasets. This work follows many of the analysis procedures from [4] (e.g., event selection, particle and parton level definitions) and [6] (e.g., cross-section unfolding procedure, top quark kinematic reconstruction). In this analysis, besides including the complete set of measurements from [6], new cross-sections are presented that are mainly focused on the correlation between the number of extra jets in the event and other top and $t\bar{t}$ kinematic observables. New two-dimensional (2D) and three-dimensional (3D) combinations of top and $t\bar{t}$ systems observables are also included, as well as new observables constructed from the combination of the $t\bar{t}$ system and the extra jet with the highest transverse momentum ($t\bar{t}$ plus leading extra jet system).

The thesis is organized as follows. In **Chapter 2** a brief overview of the standard model of particle physics is provided, giving special attention to the top quark physics. Topics like the elementary particles and fundamental interactions and the production and decay mechanisms of top quarks are described in this chapter. The experimental setup of the LHC accelerator and the Compact Muon Solenoid experiment are detailed in **Chapter 3**. In **Chapter 4** an overview of the simulation models and techniques exploited for the simulation of pp collisions are presented, emphasizing relevant aspects for $t\bar{t}$ processes, as well as introducing the simulation programs used for the production of the MC calculations used in this work. In **Chapter 5** a description of the reconstruction of the collision events collected by the CMS detector is provided. Also, the reconstruction algorithms of the relevant final state objects, like jets and leptons, are discussed. The further event selection and the respective selection criteria is described in **Chapter 6**. The two methods used for the reconstruction of the $t\bar{t}$ system kinematics from the detector information are presented in **Chapter 7**.

After the reconstruction of the $t\bar{t}$ event kinematics, the multi-differential $t\bar{t}$ production cross sections extraction procedure is described in **Chapter 8**. This chapter explains topics like background subtraction, the procedure for correcting the data for detector effects and the evaluation of the differential cross sections. In **Chapter 9** the different systematic uncertainties sources are described, and the assessment of the resulting systematic uncertainties in the measured cross sections is discussed. The treatment for the correlations of the different uncertainty sources among the different years and their final combination is also described in this chapter. The cross section results and the comparison to different NLO MC models and beyond-NLO theory predictions are presented in **Chapter 10**.

Finally, a summary of the thesis and an outlook are provided in **Chapter 11**.

CHAPTER

2

THE STANDARD MODEL OF PARTICLE PHYSICS AND THE TOP QUARK

Contents

2.1 The Standard Model of particle physics 4
2.1.1 Fermions 4
2.1.2 Fundamental interactions and force mediators 6
2.2 The top quark 10
2.2.1 Top quark production 11
2.2.2 Top quark pair decay 13
2.2.3 Extra jets in the $t\bar{t}$ system 14

Since ancient times the question about what are the constituents of matter has been present as one of the mysteries to be solved in order to satisfy our urge for understanding everything that surrounds us. It was around 460-370 B.C. that it was suggested by Democritus that the matter was composed of small indivisible particles. He called these particles *atomos*, which stands for indivisible in Greek. Around 1800, Dalton used this name again and postulated that all substances are made of atoms which are the smallest and indivisible particles of matter [7], but what it was thought to be the indivisible "atom" resulted to be made of other particles. The discovery of the "true" elementary particles (see Section 2.1.1) has been a big priority for the scientific community together with the need of a theory capable of describing all the fundamental forces in the universe (see Section 2.1.2). All these efforts resulted in the formulation of the Standard Model of particle physics, also referred as the Standard Model (SM).

In this chapter, an overall description of the SM is given with a focus on the top quark physics and other relevant aspects for this thesis. An overview of the elementary particles and their interaction as described by the SM is provided in Section 2.1, while some important aspects of the top quark physics are discussed in Section 2.2.

2.1 The Standard Model of particle physics

The properties of the elementary particles and their interactions is described by the SM [8–15], a gauge quantum field theory (QFT) based on a $SU(3) \times SU(2) \times U(1)$ symmetry group [16, 17] which is the pillar of modern particle physics.
The late 1960s and early 70s can be named as the birth period of the Standard Model, which was followed in the late 1970s and early 80s by the experimental verification of many of its predictions [18, 19]. The Electroweak Theory [15], first proposed by Steven Weinberg and Abdus Salam in 1967, unify the description of the electromagnetism and the weak interaction. Only a few years later, in 1973, the Quantum Chromodynamics [20] was formulated with the goal of the description of the strong interaction, which confines quarks (see Section 2.1.1) into hadron particles such as the proton and neutron [21]. However, it wasn't until 1974 that the SM was presented in full for the first time by John Iliopoulos [19]. In the following sections, a summary of the SM elementary particles and their interactions is given.

2.1.1 Fermions

It has been always of great interest to know which are the elementary constituents of the universe. Starting with the discovery of the electron by Thomson in 1897 [22], several particles were discovered, with no evidence until today, of having an internal structure. These "indivisible" particles represent the building blocks of the matter in the universe[1].
The elementary particles are grouped in the SM according to their spin into fermions (spin 1/2), vector bosons (spin 1), and scalar bosons (spin 0). Only one scalar boson has been discovered: the Higgs boson. Its experimental observation in 2012 completed the confirmation of all the elementary particles of the SM. In Figure 2.1 a summary of the SM particles and their properties is shown.

There are 12 **fermions** among the SM elementary particles: 6 quarks (q), 3 electrically charged leptons (l) and 3 electrically neutral leptons (ν_l). Fermions are described with the Dirac equation [25], having solutions with positive energy states, representing the particles with the properties shown in Figure 2.1, and also with negative energy states giving raise to the so called antiparticles. Every fermion shown in Figure 2.1 has an antiparticle, a mirror particle with the same mass and spin but with opposite physical charges, like the electric charge. If "a" (e.g. t) is a particle, then usually its antiparticle is denoted as "$\bar{a}$" (e.g. $\bar{t}$) and named using the "anti-" prefix (e.g. anti-top)[2].
As shown in Figure 2.1, the **quarks** can have an electric charge[3] of $-1/3$, which is the case for the down (d), strange (s) and bottom (b) quarks, also referred as "down-type" quarks; or a charge of $2/3$ for the up (u), charm (c) and top (t) quarks, known as "up-type" quarks.

[1] This affirmation excludes dark matter since its structure is still unknown [23].

[2] For historical reasons the antiparticle of the electron (e) is usually named as positron (e^+).

[3] In this work, the electric charge of elementary particles is given in units of the electric charge carried by an electron, known as the elementary charge (e_{charge}) and equal to $1.602 \cdot 10^{-19}$ coulombs.

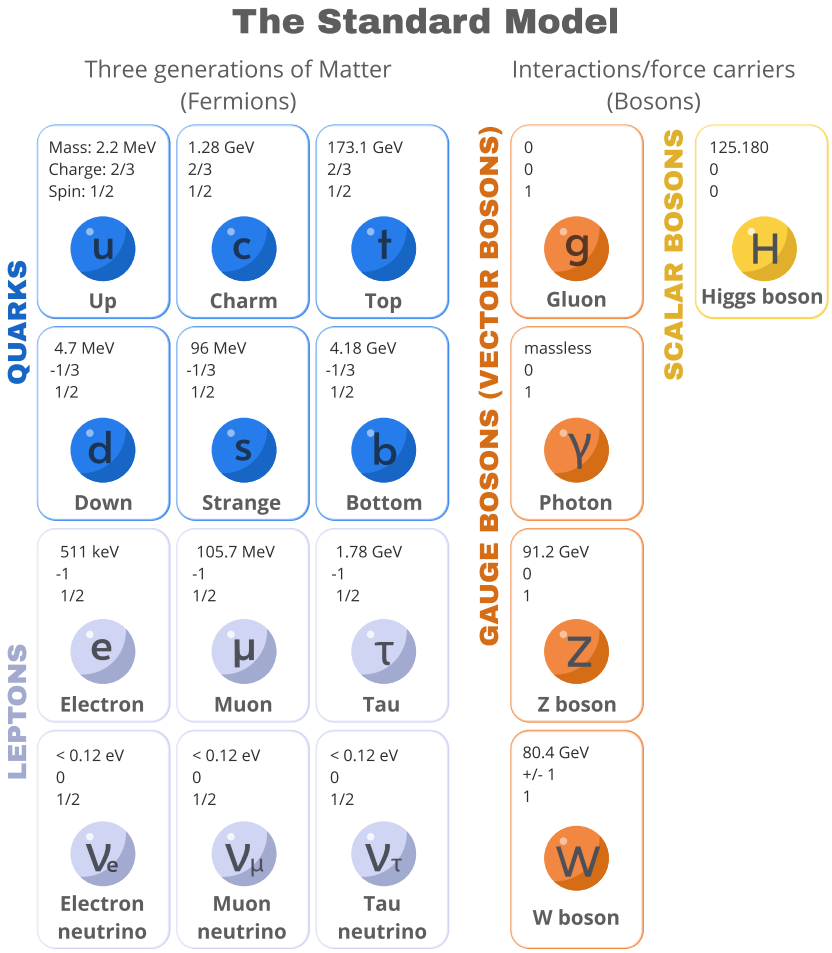

Figure 2.1: The Standard Model of Elementary Particle Physics with three generations of matter fermions, gauge bosons (vector bosons) and a Higgs boson (scalar boson). The properties of the particles are also shown in each box. Modified figure from [24].

Another type of charge called color is a characteristic property of quarks and is given by one of three conventional states: red, green and blue. The antiquarks carry an "anti-colour" version of these charges. The quarks are always observed in bound states called *hadrons*, with the exception of the top quark (see Section 2.2).
The other fermion particles present in the SM are the **leptons**: the electron (e), muon (μ) and tau (τ), electrically charged particles and their respective neutrinos (ν_e, ν_μ and ν_τ) with neutral electric charge. A charged lepton and its respective neutrino represent a "family" with a corresponding lepton flavor number. For example, an electron and an electron neutrino have a lepton flavor number l_e. The total lepton number, defined as $L = n_l - n_{\bar{l}}$ is preserved in all interactions. The lepton flavor, on the other way, is only approximately conserved, and is notably not conserved in the neutrino oscillation process [26].
Fermions can be classified into three generations, corresponding to the columns in Figure 2.1. Each generation contains one up-type and down-type quark, as well as one charged and neutral lepton. The mass for the same type of lepton increases with the generation. For

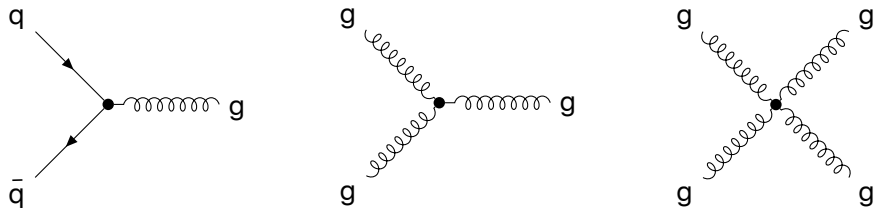

Figure 2.2: Interaction vertices of quantum chromodynamics (QCD): quark-gluon coupling (left) and gluon self-couplings (middle and right). Individual diagrams taken from [29].

example, the first generation contains the lightest charged lepton and the lightest up-type quark, while the third generation contains the heaviest ones. High precision experiments at the CERN LEP collider have found that the number of different types of neutrinos is three [27], that is compatible with the number of fermion generations in the SM.

2.1.2 Fundamental interactions and force mediators

The elementary particles and the fundamental forces of the SM are the strong, the electromagnetic, and the weak interactions. These interactions are described in the SM through the exchange of mediator bosons, shown in the last two columns of Figure 2.1. The strong and electroweak interactions between fermions are mediated by gauge bosons. The existence of these force mediators arises from the gauge fields of the respective symmetry group. The mediator of the electromagnetic interaction is the photon (γ), the charged- and neutral-current weak interactions are mediated by the $W^{\pm}$ and Z bosons, respectively, and the gluon (g) is the strong interaction mediator. The Higgs boson (H) mediates a scalar field interaction responsible for generating the mass of all elementary particles through the mechanism of spontaneous symmetry breaking.

The quantum chromodynamics (QCD) [20], with the symmetry group SU(3), describes the **strong interaction** between particles carrying a colour charge: the six quarks (see Section 2.1.1) and eight linearly-independent color gluon states, which correspond to the "eight types" or "eight colors" of gluons. While quarks (anti-quarks) carry a color (anti-color), the gluon itself carries colour and anti-colour charges simultaneously. The combinations of a color and its corresponding anti-color, as well as the combinations of all the colors or all anti-colors, result in “colorless” states. Gluons couple to quarks with the same flavour and different colours and, as a consequence of the SU(3) symmetry group, trilinear and quartic self-interaction vertices are possible for gluons. The Feynman diagrams shown in Figure 2.2 represent the quark-gluon couplings and gluon self-couplings. One of the main experimental confirmations of the QCD theory was the discovery of the gluon at the DESY PETRA storage ring [28].

The strength of the strong interaction is described by the strong coupling constant α_s which has a dependance on the energy scale Q as shown in Figure 2.3. The value of α_s rapidly increases with the decrease of Q, meaning that the interaction between the quarks becomes stronger while they are further separated from each other in terms of distance. This phenomenon is known as colour confinement and leads to that particles carrying colour charge cannot be directly observed as bare states. One could think that with enough energy it

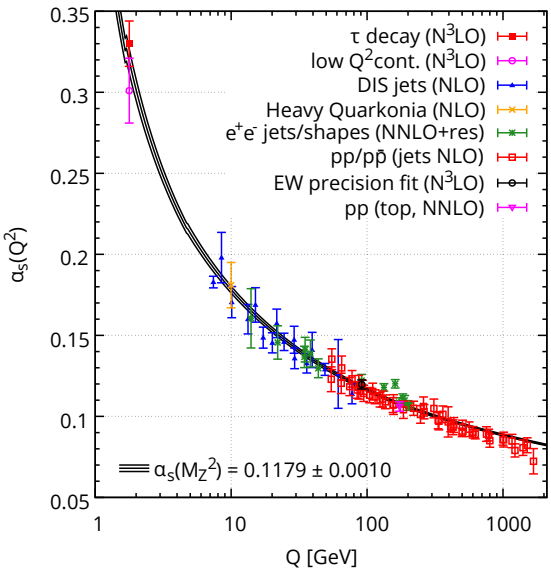

Figure 2.3: Summary of measurements of α_s as a function of the respective energy scale Q. The plot includes results from different degrees of QCD perturbation theory used in the extraction of α_s (NLO: next-to-leading order; NNLO: next-to-next-to leading order; N3LO: next-to-NNLO; NNLO+res: NNLO matched to a resummed calculation) [30].

should be possible to separate a quark from its bound state but the reality is that before that could happen, a quark-antiquark pair production out of the vacuum occurs since the gluon field would reach the needed critical energy. This sequential quark pair production is called hadronization, which results in the formation of colourless bound states composed of quarks, known as hadrons (more information about the hadronization process is given in Section 4.3). The classification of a hadron is done according to its *valence quarks* which determine the quantum numbers of the hadron. When it is said that a hadron has a certain quark structure, for example "u, u, d", this refers to the valence quarks. However, since the quarks interact via gluons which can interact among themselves and split into a virtual quark-antiquark pair, the structure of hadrons contain also virtual quarks (sea quarks) and gluons. The sea quarks and gluons do not contribute to the quantum numbers of hadrons. Particles like protons and neutrons are classified as *baryons*, which are hadrons made of three valence quarks; and *mesons*, consisting of a quark and antiquark valence pair. The proton is the only known stable baryon and all known mesons are unstable.

The other important feature observed in Figure 2.3, is that α_s gets smaller with increasing the Q value. This implies that at high energies, which is equivalent to short-distance interactions, the coupling becomes weaker. This behavior is known as *asymptotic freedom* and allows to treat the quarks in this kinematic regime as if they were approximately free particles [31,32] and the description of their interactions can be approximated using a perturbative expansion in terms of α_s. The accuracy of the perturbative QCD calculations (pQCD) with the lowest order in α_s, is the so-called leading-order (LO) accuracy, e.g. $\mathcal{O}(\alpha_s)$. Similarly, next-to-leading order (NLO) accuracy denotes calculations that additionally include contributions with the second lowest order in α_s, e.g. $\mathcal{O}(\alpha_s^2)$. The **electromagnetic interaction** is described by the Quantum electrodynamics (QED) theory [33,34]. As shown in Figure 2.4,

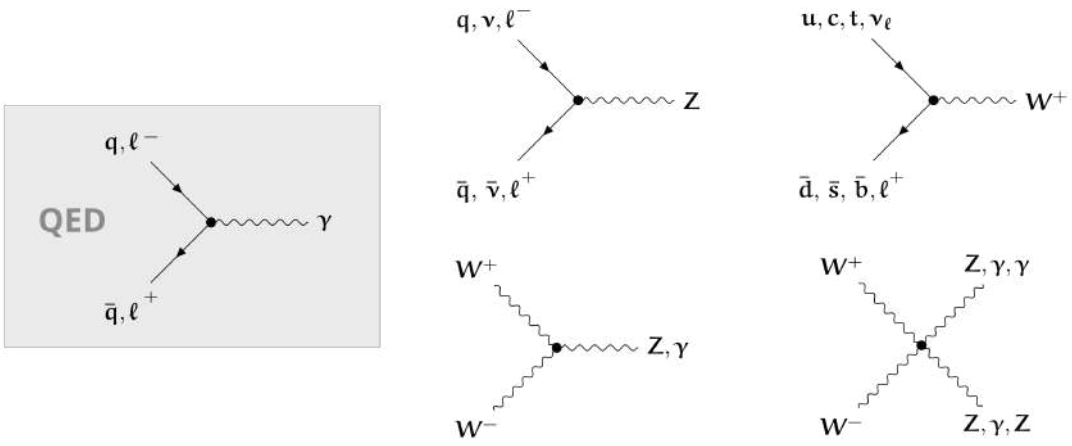

Figure 2.4: Interaction vertex of quantum electro-dynamics (QED) on the left and interaction vertices of the weak interaction on the right. Individual diagrams taken from [29].

the electromagnetic interaction between the electrically charged fermions is mediated by the photon: a massless vector boson without electric charge (see Figure 2.1). Since the strength of the electromagnetic interaction $\alpha_{em} \approx 1/137$ is significantly smaller than unity[4], QED processes can be accurately described using perturbative expansions.

The **weak interaction** is the only of the fundamental forces that involves all fermions, being the β-decay its most known example. The inclusion of the word "weak" in its name comes from the fact that its strength is many orders of magnitude smaller than the one for the electromagnetic and strong interaction. The weak isospin (I_3) charge is the quantum number related to the weak interaction and its force mediators are the $W^{\pm}$ boson and the Z bosons (see Figure 2.1). The interaction vertex of the $W^{\pm}$ and Z bosons with the fermions, photons and also between each other are presented in Figure 2.4. While the charged weak interaction is related to the $W^{\pm}$ bosons, the Z boson mediates the neutral weak interaction and couples to fermions and anti-fermions of the same flavour. The $W^{\pm}$ bosons only mediate interactions between leptons of the same generation, while the interaction between quarks of the same and of different generation (flavour mixing) is possible and is described by the Cabibbo-Kobayashi-Maskawa (CKM) matrix [35–37].
From the diagrams in Figure 2.4 one can easily see the similarities and strong relation between the weak and the electromagnetic interactions, which were unified into the **electroweak interaction**, which is described by the electroweak theory, a spontaneously broken gauge theory based on the non-Abelian $SU(2)_L \times U(1)_Y$ symmetry group of weak left–handed isospin and hypercharge. The hypercharge is defined as $Y = (2Q - I_3)$, where Q is the electric charge and I_3 the isospin. The fields W^1_μ and W^2_μ coupled to left-handed[5] fermions, and W^3_μ to the neutrinos, are introduced by the $SU(2)_L$ group; and the field B_μ, which can couple to neutrinos, is introduced by the $U(1)_Y$ symmetry. In this theory the $W^{\pm}$ bosons are expressed

[4]The value of α_{em} increases with smaller momentum transfer or larger distance. The provided value belongs to zero momentum transfer conditions.

[5]While the helicity of a particle depends on the spin orientation with respect to its direction of motion: is right-handed (left-handed) if the direction of its spin is the same (opposite) as the direction of its motion; the chirality is more abstract and its states are different components of the Dirac spinor [38]. The parity transformation change the chirality and for massless particles chirality is the same as helicity.

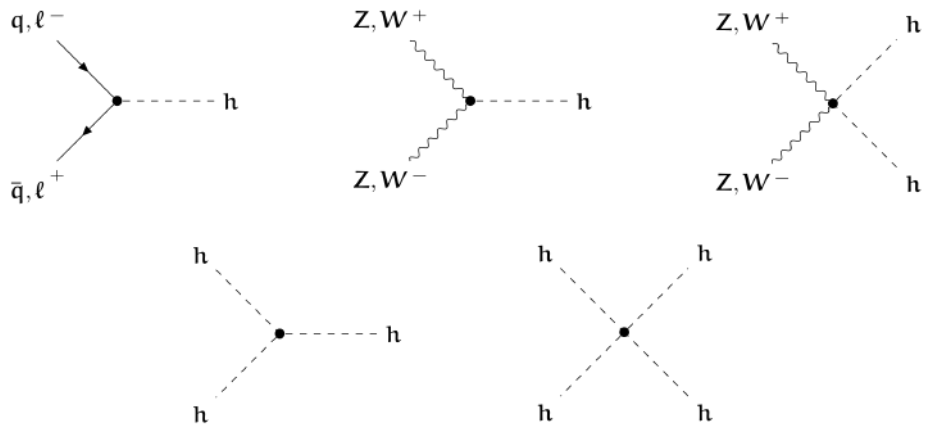

Figure 2.5: Interaction vertices of the Higgs boson. Individual diagrams taken from [29].

as a linear combination of W_μ^1 and W_μ^2, while the γ and Z arise from mixed states of W_μ^3 and B_μ. The veracity of the electroweak theory, also known as Glashow-Weinberg-Salam (GWS) model [8, 14, 15], has been extensively tested by several experiments (e.g. CERN LEP [27]) showing a remarkable agreement between its prediction and the experimental data.
The GWS model predicts massless $W^\pm$ and Z bosons, but it has been experimentally measured with a very good precision that the masses of these particles are 80.4 GeV and 91.2 GeV [30], respectively. In order to explain the non-zero masses of the W and Z bosons, the Brout-Englert-Higgs (BEH) mechanism [39], also known as the **Higgs mechanism**, was formulated in 1964 and published almost simultaneously by three independent groups (Robert Brout & François Englert, Peter Higgs and Gerald Guralnik et al.) expanding the SM with an additional self-interacting quantum field (the Higgs field) that pervades the whole space of our universe. Formulated as a complex doublet of the $SU(2)$ symmetry, the Higgs field is described by a symmetric potential with a set of equivalent minimum vacuum states located around its center characterized by a nonzero vacuum expectation value $\nu \approx 246\,\text{GeV}$ [30]. The shape of this potential is very similar to a mexican hat, this is the reason why is commonly known as the Mexican-hat potential. The existence of the Higgs field leads to the spontaneous breaking of the electroweak symmetry. The Higgs boson (H) is the visible manifestation of the Higgs field which gives mass to particles when they interact with it through the Higgs mechanism. H is a scalar boson with no electric charge and no colour charge which couples to all massive particles with interaction strengths proportional to the masses of the particles (see Figure 2.5). Its interaction with fermions is described by the Yukawa couplings which introduce mass terms proportional to the Yukawa coupling constant y_f, specific to each fermion [40].

The SM has been tested by a huge number of experiments and all its predicted particles have been discovered. However, there are some **important questions that can't be answered by the SM** [29]. For example, it doesn't describe gravity, which phenomena are explained by classical non-quantum field theory, the general relativity [41, 42]. Up to now, gravity hasn't been successfully combined with the SM and also there is no explanation yet about why the weak force is 10^{24} times stronger than gravity (hierarchy problem). Attempts to formulate a QFT of gravity are known as quantum gravity [43, 44]. The formulation of a

quantum gravity theory predicts the existence of a spin 2 and zero mass gravity gauge boson (graviton) and up to now, there has been no experimental proof of its existence. Furthermore, such a theory is found to be non-renormalizable, i.e. comes with unsolvable infinites in its calculations [44]. A theory capable of describing all the fundamental forces, the "theory of everything", is one of the major goals of modern physics. Besides the formulation of a quantum gravity theory, the other important step would be the unification of the electro-weak and strong interactions, also known as "grand unified theory" (GUT) [45,46]. A step further, would be the unification of the fourth fundamental force, the "theory of everything" [46,47]. The SM can't also explain the existence of dark matter [48,49] and dark energy [50], which accounts for gravitational interactions required to explain observations at galactic scales. Many theories have been developed as extensions of the SM leading to new elementary particles that could explain dark matter [51]. The fact that the SM predicts equal production of matter and antimatter, it is also in contradiction with astrophysical observations [52]. The theoretical explanation of the spontaneous conversion of neutrino flavours into each other, known as neutrino oscillations [26, 53], requires a nonzero mass for the neutrinos. This contradicts the SM which predicts a zero mass for the neutrinos. The other opened question related to the neutrino nonzero mass (currently constraint to $m_\nu < 0.12\,\text{eV}$ [54]), is why there are huge mass differences for the elementary particles (e.g. $m_\nu \ll m_t$).
Many theoretical models have been developed focused on the explanation of the one or more of these open questions. For example, the supersymmetry principle (SUSY), which is based on making the SM Lagrangian symmetric with respect to exchange of the force and matter terms, or what is analogous, symmetric for fermions and bosons [55]. SUSY could be the answer to some of the issues of the SM. For example, the Minimal Supersymmetric Standard Model (MSSM) [56] would solve the hierarchy problem, and one of its predicted new particles could serve as a dark matter candidate. Another important theory is the SM effective field theory (SMEFT) [57,58], which extends the SM with all possible higher order couplings between the SM fields; and the string theory [59, 60], a candidate for a theory of everything which provides an unified description of gravity and particle physics where the point-like particles are replaced by multi-dimensional objects called strings. Many experiments have looked for evidence of predictions made by these theories, like new particles, but up to now none of them has been verified by any experimental observation.

2.2 The top quark

From all the described SM fundamental particles the top quark is the most relevant for this work. It was discovered in 1995 by the CDF and D0 Collaborations at the Fermilab Tevatron, using $p\bar{p}$ collisions at $\sqrt{s} = 1.8\,\text{TeV}$ [1, 61]. The top quark is the heaviest known elementary particle with a pole mass[6] of $172.5 \pm 0.7\,\text{GeV}$ [30] that results in a lifetime smaller than its hadronization time. This means that top quarks decay before forming bound states which provides the possibility to study the properties of an unconfined quark. For example, its invariant mass can be directly measured from the invariant mass of its decay products. This section describes the top quark production and decay processes.

[6]The pole mass of an elementary particle corresponds to the rest mass as defined in the special theory of relativity [17, 62].

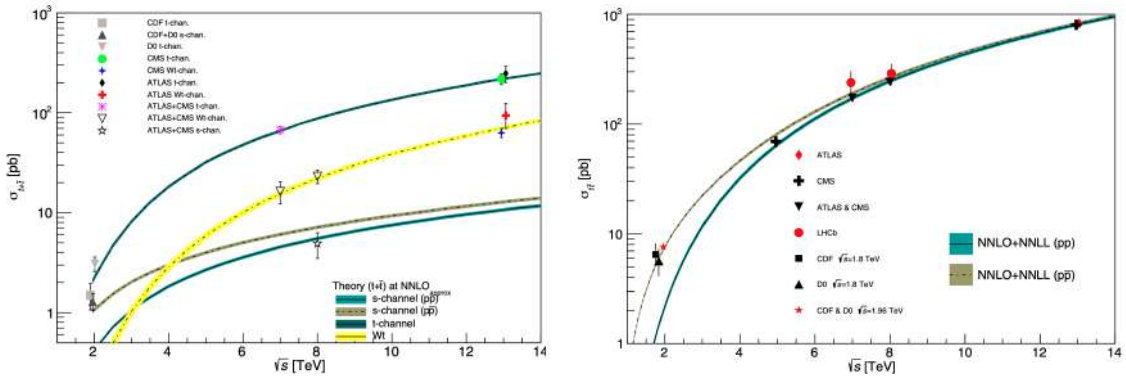

Figure 2.6: Measured and predicted single top (left) and $t\bar{t}$ (right) production cross sections from Tevatron energies in $p\bar{p}$ collisions to LHC energies in pp collisions. Taken from [30].

2.2.1 Top quark production

The top quarks can be produced as single top quarks or in pairs and the corresponding cross sections, as shown in Figure 2.6, depend on the center-of-mass energy of the experiment in which they are produced. It can be also observed in these plots that the LHC (see Chapter 3) is an excellent top production factory with a cross section almost an order of magnitude larger than at the Tevatron [63].

The **production of single top quarks** occurs via the weak interaction, specifically through a Wtb vertex. In Figure 2.7, Feynman diagrams at LO are shown for the different channels of the single top production: the t- and s- channels via the exchange of the virtual W boson; and the tW-channel where the top quark is produced in association with a real W boson. The single top quark production is directly sensitive to the element $|V_{tb}|$ of the CKM matrix. The most abundant process is the single top quark production in the t-channel. The inclusive cross sections of the single top channels and their contributions as background processes are further discussed in Section 6.3.

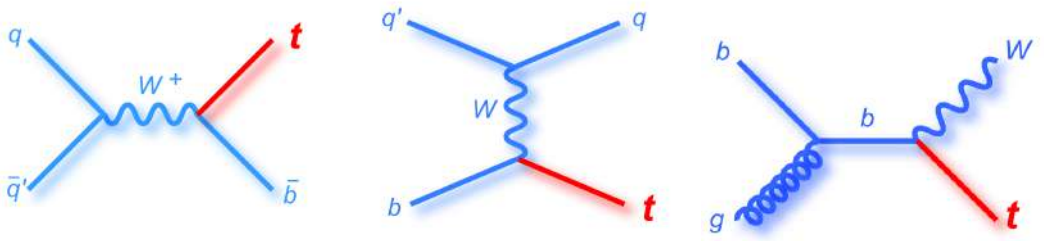

Figure 2.7: Examples of LO Feynman diagrams for the single top quark production in the s-channel (left), t-channel (middle) and tW-channel (right). Taken from [64].

In pp collisions, top quarks are mainly produced in quark-antiquark ($t\bar{t}$) pairs, known as $t\bar{t}$ **production** or top quark pair production. The top-quark pair production occurs predominantly by means of the strong interaction via the gg-fusion ($gg \to t\bar{t}$) or the $q\bar{q}$-annihilation ($q\bar{q} \to t\bar{t}$). In the case of pp collisions at 13 TeV, which are the experimental conditions of this analysis, the gg-fusion is predominant ($\sim 90\%$ of cases). The corresponding LO Feynman diagrams are presented for the mentioned channels in Figure 2.9. The $t\bar{t}$

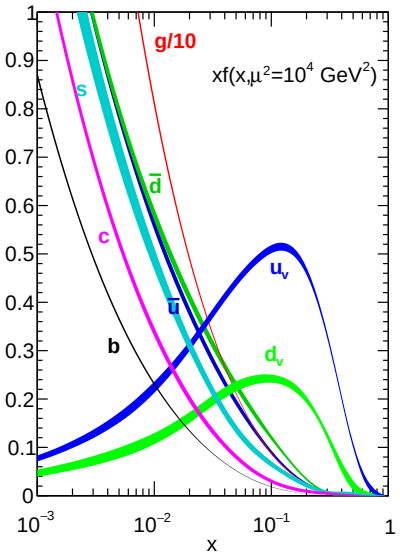

Figure 2.8: Proton PDFs evaluated at a scale of 100 GeV [67].

production process, in particular for the pp collisions at the LHC conditions, can be precisely described by perturbative QCD calculations. The inclusive $\mathrm{t\bar{t}}$ production cross section in a proton-proton interaction can be factorized as follows:

$$\sigma_{\mathrm{t\bar{t}}}(s, m_t) = \sum_{i,j=q,\bar{q},g} \int dx_i dx_j f_i(x_i, \mu_F^2) f_j(x_j, \mu_F^2) \cdot \hat{\sigma}_{ij\to \mathrm{t\bar{t}}}(\hat{s}, m_t, \mu_F, \mu_R, \alpha_s) \tag{2.1}$$

The sum is running over all quarks and gluons contributing to the process. The squared center-of-mass energy for the pp collision is referred to as s, the mass of the top quark is denoted by m_t, x is the parton momentum fractions with respect to the proton momenta and $\hat{s} = s \cdot x_i \cdot x_j$ is the partonic center-of-mass energy. The function $f_{i(j)}(x_{i(j)}, \mu_F^2)$, known as the parton distribution function (PDF), describes the soft interaction inside the protons giving the probability to find a parton with longitudinal momentum fraction x inside a proton. The proton PDFs are a priori not calculable in perturbation theory and need to be extracted from experimental measurements like from the deep-inelastic scattering in electron-proton collisions data collected at the DESY Hadron-Electron Ring Accelerator (HERA) [65]. Figure 2.8 (right) shows the NNPDF3.1 proton PDFs set computed with a next-to-next-to-leading order (NNLO) accuracy for a factorization scale (μ_F) of 100 GeV [66]. It can be observed that the largest PDF density belongs to the gluons, which are also more probable to be found at lower values of x. The factorization scale is the scale used to split the long distance PDFs and the short distance hard scattering cross sections [30, 68]. Collinear gluon emissions with a p_{T} below μ_F are absorbed in the PDFs, if not, they are treated in the hard scattering. The evolution of PDFs with μ_F is predictable and is described by the so-called DGLAP equations [69]. A second scale in the process is the renormalization scale μ_R, corresponding to the scale at which is a renormalized parameter is redefined, e.g., the strong coupling $\alpha_s(\mu)$. The renormalization procedure absorbs ultraviolet divergences that occur in higher order loop diagrams (e.g. a gluon splitting into two gluons that reunite again to a single gluon) and

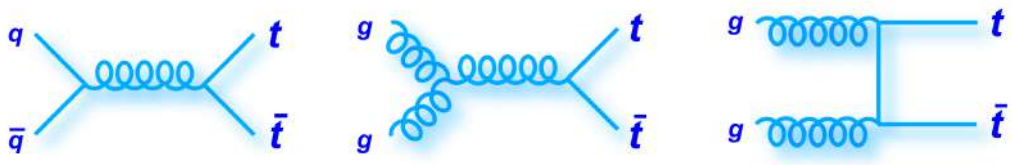

Figure 2.9: Examples of LO Feynman diagrams for the top quark pair ($t\bar{t}$) production in the $q\bar{q}$-annihilation (left) and the gg-fusion (middle, right). Taken from [5].

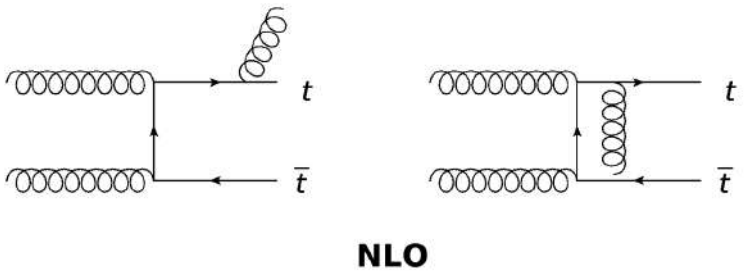

Figure 2.10: Examples of $t\bar{t}$ production diagrams via the gg-fusion at next-to-leading order (NNLO) for the first real emission correction (middle) and for the first virtual correction (right).

express the theory in terms of finite renormalized parameters.

In perturbation theory, the cross section factorization formula can be expressed as $\sigma \sim \sum_i c_i \alpha_s^i$, where c_i are calculable coefficients and the smallest i defines the leading order. The order of α_s is directly proportional to the number of vertices involving a gluon in the respective Feynman Diagram of a hard scattering process. The leading order (LO) process for top pair production, as shown in Figure 2.9, are of order α_s^2 or $\mathcal{O}(\alpha_s^2)$. A next to leading order (NLO) processes with a real gluon emission is shown in Figure 2.10 and present an $\mathcal{O}(\alpha_s^3)$ order with respect to α_s. Available calculations for inclusive ttbar productions have reached next-to-next-to-leading (NNLO) accuracy, that is $\mathcal{O}(\alpha_s^4)$ and include Feynman diagrams with two hard gluon emissions or up to two loops with virtual gluons.

The total $t\bar{t}$ production cross section, at NNLO with next-to-next-to-leading-logarithmic (NNLL) precision, is predicted to be $831.76 \pm^{19.77}_{29.20} \pm 35.06(\mathrm{PDF} + \alpha_s)$ [5]. Besides of gathering information about various top properties, e.g. mass or spin of the t-quark, the experimental measurement of this cross sections provides a test of perturbative QCD and can provide constraints on the proton PDFs (in particular about the gluon density) and α_s. Furthermore, a deviation from the QCD predictions may point to some processes beyond the SM.

2.2.2 Top quark pair decay

The top quark decays before hadronizing via charged-current weak interaction almost exclusively via the decay channel represented by the process $t \to Wb$. The branching ratio for this channel (B_{bW}) can be calculated in terms of the elements of the unitary CKM matrix. The SM prediction, computed in terms of the measured CKM matrix elements is $B_{bW} = 0.998$ [30]. From the experimental side, in a CMS measurement it was determined that B_{bW} is larger than 0.955 at 95% confidence level [70]. Neglecting other decay chan-

nels than $t \to Wb$, the final states of a the top quark pair decay (see Figure 2.11) can be distinguished as:

- In the **full hadronic channel** both W bosons decay into $q\bar{q}$ pairs: $\mathrm{t\bar{t}} \to (\mathrm{W^+} \to \mathrm{q\bar{q}'})\mathrm{b}\ (\mathrm{W^-} \to \mathrm{q''\bar{q}'''})\mathrm{\bar{b}}$. This decay channel has the largest branching ratio (BR) of about 0.454, but also has the largest contamination from background processes.

- The **lepton+jets channel** corresponds to cases where one W boson decay into a charged lepton and a neutrino, and the other decays hadronically: $\mathrm{t\bar{t}} \to (\mathrm{W^+} \to \mathrm{l^+}\nu_\mathrm{l})\mathrm{b}\ (\mathrm{W^-} \to \mathrm{q\bar{q}'})\mathrm{\bar{b}}$. This channel has a moderate contamination by background processes while its $BR \approx 0.441$ is rather large.

- In the **dileptonic channel** both W bosons decay into charged leptons and their corresponding neutrinos: $\mathrm{t\bar{t}} \to (\mathrm{W^+} \to \mathrm{l^+}\nu_\mathrm{l})\mathrm{b}\ (\mathrm{W^-} \to \mathrm{l^-}\bar{\nu}_\mathrm{l})\mathrm{\bar{b}}$. This channel has the lowest $BR \approx 0.107$ among the decay modes, but is also affected by lowest backgrounds since the two high momentum charged leptons provide a clear signature in the LHC collisions, making this channel widely used in physics analyses.

To simplify the reconstruction of event kinematics and the event selection, and to reduce combinatorial backgrounds, the $\mathrm{t\bar{t}}$ events with decays via τ leptons are usually excluded from the experimental analyses with lepton+jets or dilepton final states. This results in a reduction of the BRs whose values are reduced to 0.288 and 0.0455 for the lepton+jets and the dilepton channel, respectively [5].
This analysis is dedicated to the study of $\mathrm{t\bar{t}}$ production in the dileptonic channel where decays via τ leptons are not included in the signal definition (see Chapter 6) and are, instead, classified as background.

2.2.3 Extra jets in the $\mathrm{t\bar{t}}$ system

As shown in Figure 2.12, QCD extra radiation, i.e. gluons, can be emitted from partons taking part in the hard interaction (see more in Section 4.2). The decay products of this extra radiation, after its energy falls below a certain scale, get combined into a collimated stream of hadrons, known as "jet" [71] (see Section 5.2.4 for information about jet reconstruction). This translates into extra jets additional to the ones related to the $\mathrm{t\bar{t}}$ decay products. The study of extra jet production, which is dominated by gluon radiation, is one of the key topics of this thesis.

The production of extra jets provides a direct probe of the next orders of the QCD perturbation series and its presence lead to a multi-scale situation which is known to provide a challenge for the perturbative QCD expansion [2]. The origin of this issue is the additional kinematic scale that emerges as a result of the extra jets which competes with the $\mathrm{t\bar{t}}$ invariant mass giving raise to a multi-scale situation. In this work, not only the top, top anti-quark and the $\mathrm{t\bar{t}}$ systems is studied, but also observables related to the $\mathrm{t\bar{t}}$ plus extra extra jets combined system are measured. In Figure 2.12, the different systems used for the observables definition are shown.

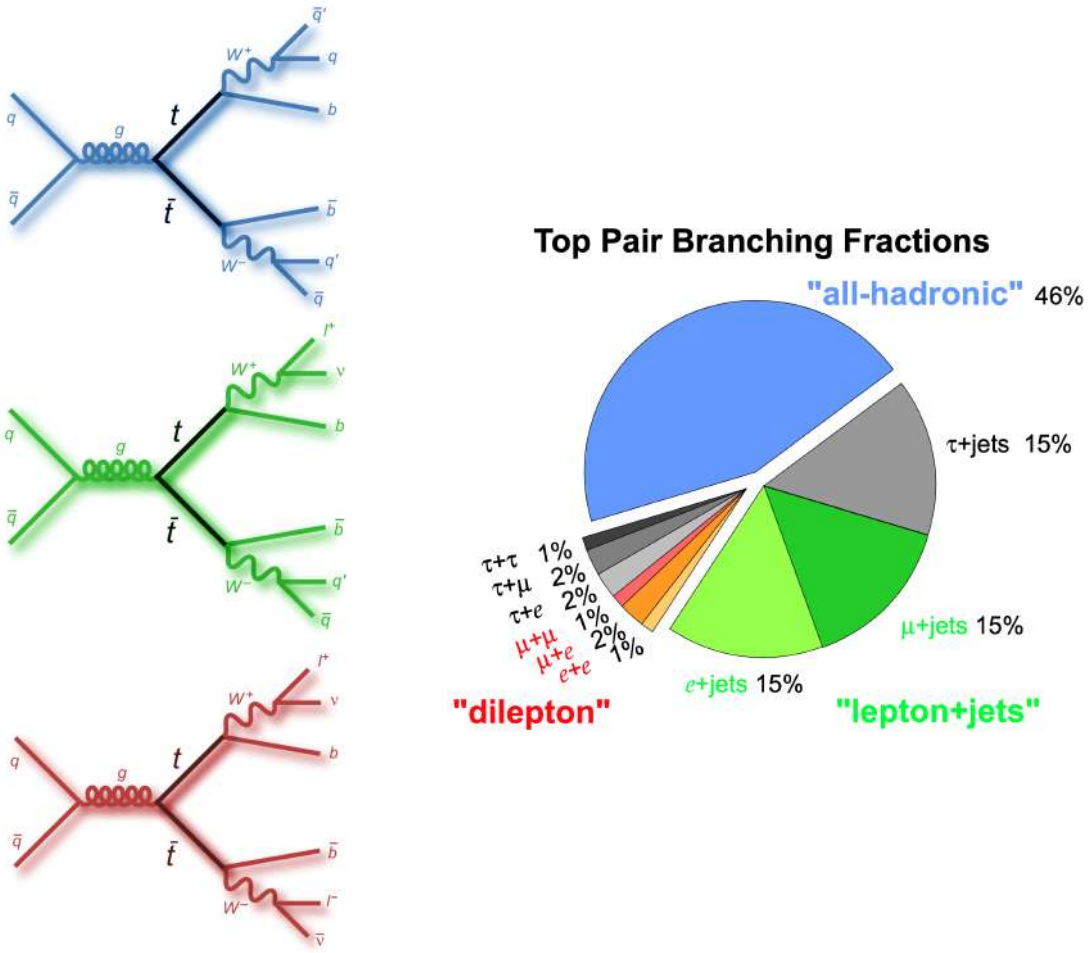

Figure 2.11: Summary of the different $t\bar{t}$ decay channels. On the left, examples of LO Feynman diagrams for the decays corresponding to the all-hadronic (upper), lepton+jets (middle) and dilepton (bottom) channels. On the right, the distribution of the corresponding branching ratios (numbers are approximate) of each decay channel. Taken from [5].

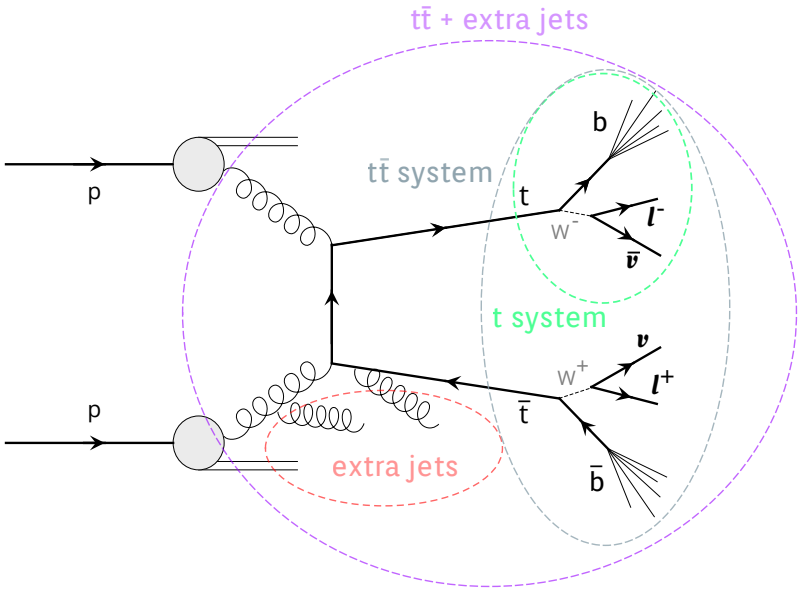

Figure 2.12: Diagram of the $t\bar{t}$ + additional jets system. Inspired on figure from [3].

CHAPTER

3

EXPERIMENTAL SETUP

Contents

3.1 The Large Hadron Collider 17
3.2 The Compact Muon Solenoid 18
3.2.1 The coordinate system and remarks on the measured observables . . 19
3.2.2 The solenoid magnet 21
3.2.3 Tracking detectors 21
3.2.4 Electromagnetic and Hadron Calorimeters 22
3.2.5 The muon system 23
3.2.6 Event triggering and data acquisition systems 24
3.2.7 Luminosity measurements at CMS 25

3.1 The Large Hadron Collider

The world's largest and most powerful particle accelerator, the Large Hadron Collider (LHC) [72], is located at CERN in Switzerland and France. It is a circular hadron accelerator and collider with a circumference of 27 km, designed to accelerate and collide proton beams at a center-of-mass energy of up to 14 TeV. The LHC can also be used to collide heavy ions, or protons and heavy ions, but for this thesis, only data from proton-proton collisions are used. A schematic representation of the CERN accelerator complex is given in Figure 3.1. After passing through a sequential system of smaller particle accelerators , two beams containing proton bunches are injected with an energy of 540 GeV into the LHC ring, where they are further accelerated through a system of superconducting radiofrequency cavities. These proton bunches collide every 25 ns at four interaction points, where the CMS [73] , ALICE [74] , ATLAS [75] and LHCb [76] experiments are located (Figure 3.1). After many

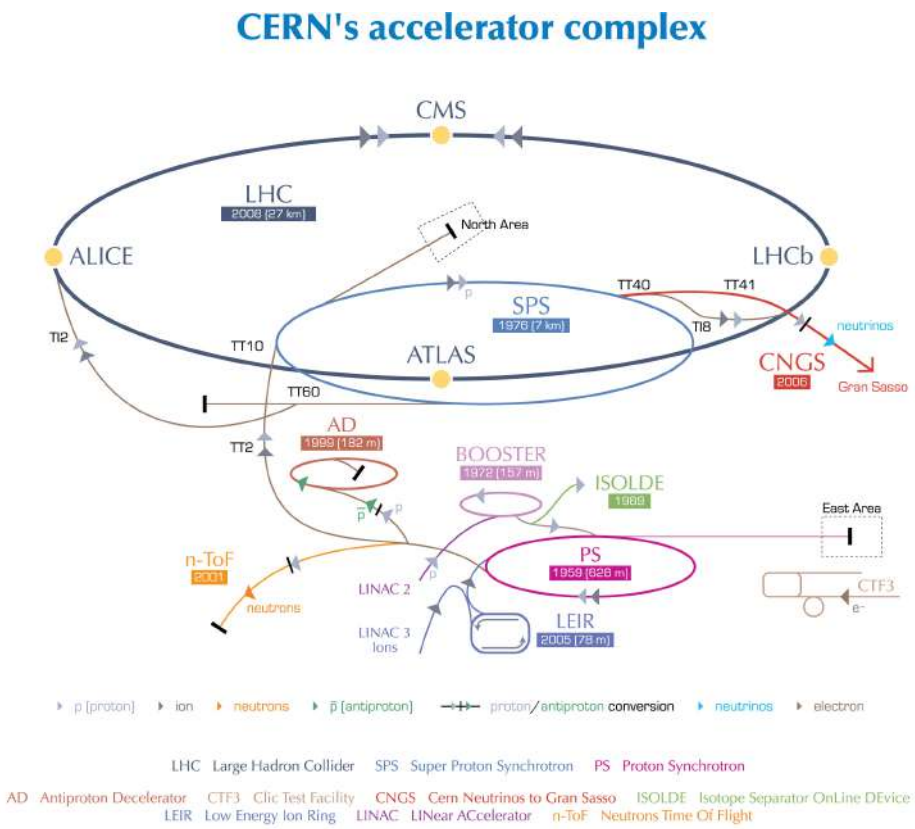

Figure 3.1: The accelerator complex at the CERN laboratory in Geneva [77]

hours of producing collisions for the experiments, the beams are finally dumped. The period of time from injection to beam dump is defined as a "fill" and represents the smallest unit of recorded data with a common beam setup.

The collected data by the LHC experiments can be divided into two main periods: "Run 1" from 2009 to 2013, where proton-proton collisions were produced with a center-of-mass energy of 7 (in 2009-2011) and 8 TeV (in 2012), and "Run 2" from 2015 to 2018. For this last period, the energy of the pp was increased to $\sqrt{s} = 13$ TeV and also heavy-ion collisions were produced. Alternating in between the data-takings, the accelerator and the experiments are shut down for needed upgrades and maintenance. The first long shut down (2.5 years) happend between the end of "Run 1" and the start of "Run 2", and currently, a 4 years shut down is taking place from the end of 2018 until the planned beginning of the next data-taking period "Run 3" (2022-2024), aiming to reach a center-of-mass energy of 14 TeV. Another shut down is planned to start in 2024 for the preparation of the High-Luminosity LHC (HL-LHC) project [78, 79], with a major upgrade for the accelerator and also the experiments. The HL-LHC run will start in 2027 and is expected to reach around 10 times higher luminosity (see Section 3.2.7) values in comparison to previous runs.

3.2 The Compact Muon Solenoid

The Compact Muon Solenoid is a multi-purpose experiment located underground (about 100 m deep) at the interaction point 5 (IP5) of the LHC ring (see Figure 3.1). It follows

a cylindrical design along the beam axis, where its components are placed as barrel-like layers and also endcap disks perpendicular to the beam pipe as shown in Figure 3.2. This configuration allows detecting the particles coming from the interactions, produced in the center of the detector, over nearly the full solid angle. The design is highly focused on the optimization of the precision for the spatial information near the interaction point to be able to discriminate between particles that originated in the pp interaction point from the ones coming from subsequent decays (secondary vertices), like from beauty and charm flavoured hadrons. As indicated in the detector name, the precision for muon reconstruction is also one of the key points considered for the detector design. The main parts of the detector can be divided into a silicon tracker, an electromagnetic calorimeter (ECAL), a hadron calorimeter (HCAL), a superconducting solenoid of 6 m of internal diameter which is capable of producing a 3.8 T magnetic field, and the muon systems. All these elements form a structure with an overall diameter of 15 m, 28 m of length and 14000 tons of total weight (see Figure 3.2). These dimensions can be taken as "compact" if one compare them to the ATLAS experiment, another LHC multi-purpose detector, which is around two times bigger with 25 m of diameter and 46 m of length [75].

3.2.1 The coordinate system and remarks on the measured observables

The right-handed Cartesian coordinate system adopted in the CMS experiment is shown in Figure 3.3. The z-axis is chosen alongside the beam line, the x-axis points directly to the center of the LHC ring and the y-axis upwards. The azimuthal angle ϕ is defined from the positive x-axis in the (x, y) plane, also known as the transverse plane; while the polar angle θ is measured from the positive z-axis.The distance from the interaction point is defined as $r = \sqrt{x^2 + y^2}$.

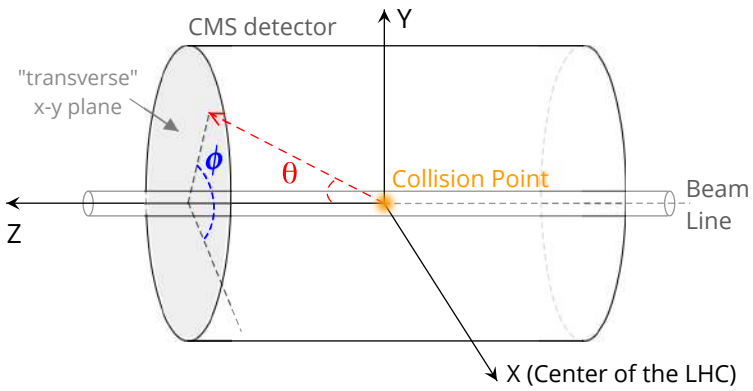

Figure 3.3: Coordinates system used in the CMS experiment.

The energy E and the projections (p_x, p_y, p_z) of the 3-vector momentum $\vec{p}$ into the respective coordinate axis constitute the 4-momentum vector (E, p_x, p_y, p_z) which characterize a measured physics object. For a given particle the rapidity y and pseudo rapidity η are defined as:

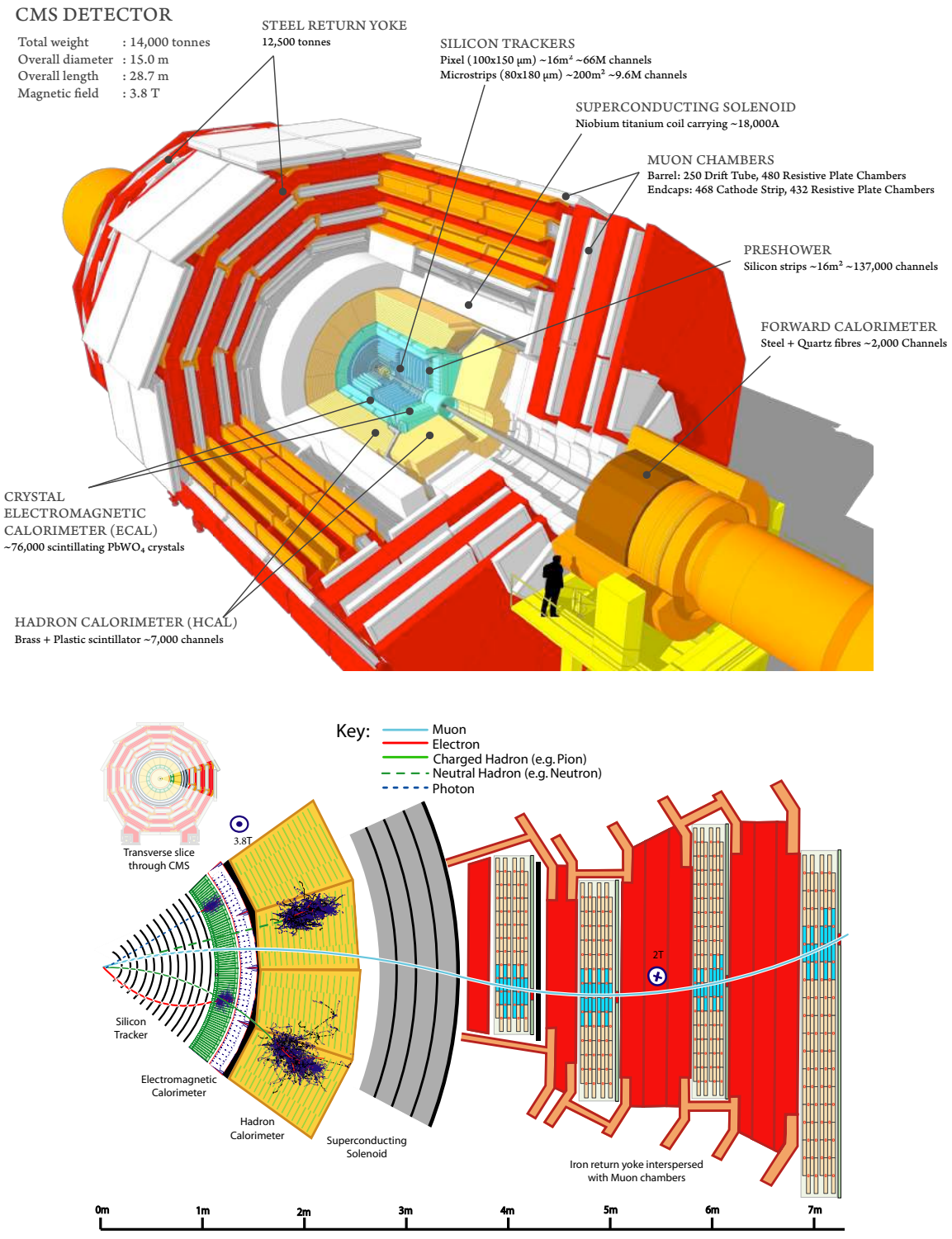

Figure 3.2: A schematic representation of the CMS detector and its components. A 3D view on the top [80], and a transverse slice of the detector including the specific particle interactions with the different parts of the detector on the bottom [81].

$$y = \frac{1}{2} \ln \frac{E + p_z}{E - p_z} \tag{3.1}$$

$$\eta = \frac{1}{2} \ln \frac{|\vec{p}| + p_z}{|\vec{p}| - p_z} = -\ln \left[\tan \left(\frac{\theta}{2} \right) \right] \tag{3.2}$$

For particles with a mass much smaller than $|\vec{p}|$, the relation holds that $\eta \approx y$. These observables are very useful since the difference for two particles in its rapidities ($\Delta y = y_1 - y_2$) or pseudorapidities ($\Delta\eta = \eta_1 - \eta_2$) is invariant with respect to a Lorentz boost along the beam axis.

The momentum and energy transverse to the beam direction, are computed from the x and y components and denoted as p_T and E_T respectively. Particles "invisibles" for the detector (mostly neutrinos) lead to a difference between the total real energy and the measured energy by the detector. Taking into account that the initial transverse momentum is equal to zero, one can compute the imbalance of the momentum measured in the transverse direction, known as missing transverse energy. This quantity can be used for reconstructing information about these "invisible" particles and is commonly named missing E_T, also denoted as E_T^{miss} or MET. The vector of missing transverse energy $\vec{E}_T^{miss}$ is defined as the negative vector sum of the transverse momenta of all reconstructed particles i in the event:

$$\vec{E}_T^{miss} = -\sum_i \vec{p}_T(i) \tag{3.3}$$

3.2.2 The solenoid magnet

One of the CMS key elements for the reconstruction of charged particles is its superconducting (niobium-titanium) solenoid. With a length of 13 m and 6 m of inner diameter it is capable of producing a magnetic field of 3.8 T, which is saturated in the surrounding of the solenoid using a steel flux return yoke (shown in red in Figure 3.2) where the magnetic field is 2 T. The trajectories (tracks) of charged particles bent in the magnetic field are used for the determination of their momenta and also the charge sign.

3.2.3 Tracking detectors

The tracking system is made of segmented silicon pixel and silicon strip detectors (Figure 3.4) and is located inside the solenoid and represents the innermost part of the detector. Its main goal is to provide precise measurements of the trajectories of charged particles. Originally, with 66 million sensors of 150x100 μm^2, **the silicon pixel detector** consisted of three barrel layers at radii of 4.4, 7.3 and 10.2 cm; and two endcaps of pixel modules. During the LHC shutdown between 2016 and 2017 data takings the whole system was rebuild adding also one layer in the barrel and one endcap disk per side were added to the pixel detector. To improve precision in the interaction vertices reconstruction, the innermost layer and the endcaps were placed even closer to the interaction point [83,84]. **The silicon strip tracker**, with 9.6 million strip sensors with strip spacings between 80 and 180 μm, consists of inner and outer barrels with four and six concentric layers respectively, three tracker inner disks on each side, and a tracker endcap which extends the coverage up to $|\eta| = 2.5$ with nine disks on each side.

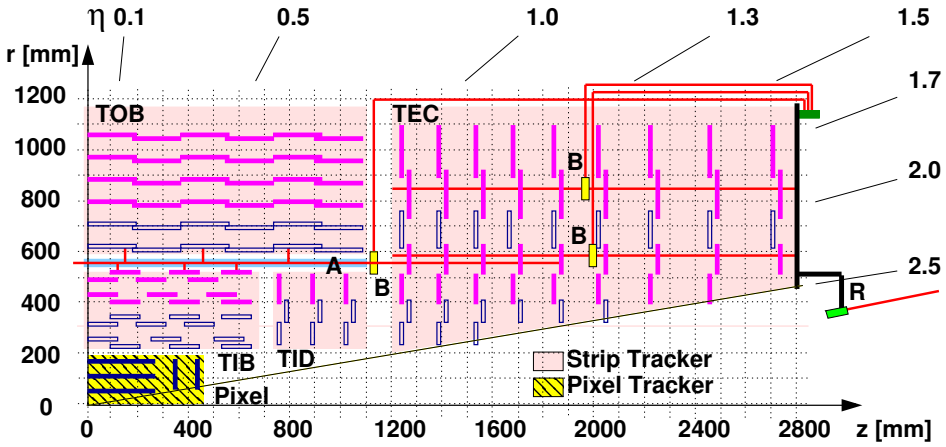

Figure 3.4: Substructures of the CMS silicon tracker: inner barrel (TIB), outer barrel (TOB), inner disks (TID) and endcaps (TEC) are shown for a quarter of the CMS silicon tracker in an $r - z$ view [82].

3.2.4 Electromagnetic and Hadron Calorimeters

Calorimeters are one of the most important detectors in experimental particle physics. By forcing the particles passing through it to create particle showers and therefore to deposit all of their energy within the detector, they can collect and measure this energy. Typically, calorimeters are formed by layers of an "absorbing" high density material (like lead for example) and an "active" medium (solid lead-glass, liquid argon, etc) which generates signal like ionization charges or light that can be detected by sensors. A "sampling calorimeter" consists of a metallic absorber sandwiched with an active material, while in an "homogeneous calorimeter" the entire volume is sensitive and contributes to the signal. The measurement of the particles energy is not the only goal of the calorimeters, the determination of the particles identity and its position and direction must be also taken into account for the design. A transverse segmented arrangement is a key factor for reconstructing information about the particles position and direction, while a longitudinal segmentation is more relevant for the particles identification by facilitating the analysis of the showers patterns [30].

The CMS calorimeter system can be separated into two subsystems:

- **The electromagnetic calorimeter (ECAL)**, is an homogeneous and fine-grained calorimeter, made of lead tungstate crystals located surrounding the tracker system (see Figure 3.2). Its design (Figure 3.5), allows the CMS ECAL to measure the energy of particles having the electromagnetic force as its main interaction and absorb more than 98% of the energy deposited by electrons and photons with energies up to 1 TeV [85, 86]. The crystals, forming the 8 super-modules in the barrel section covering the $|\eta| < 1.479$ range, have a transverse size of $2.2\,\mathrm{x}\,2.2\,\mathrm{cm}^2$. For the endcap modules, located over the $1.479 < |\eta| < 3.0$ pseudorapidity, crystals where chosen with a size of $2.9\,\mathrm{x}\,2.9\,\mathrm{cm}^2$. With the goal of enhancing the electromagnetic shower, a preshower detector is placed before the endcap crystals in the range $1.653 < |\eta| < 2.6$. The preshower improves the distinction between prompt high-energetic photons emerging

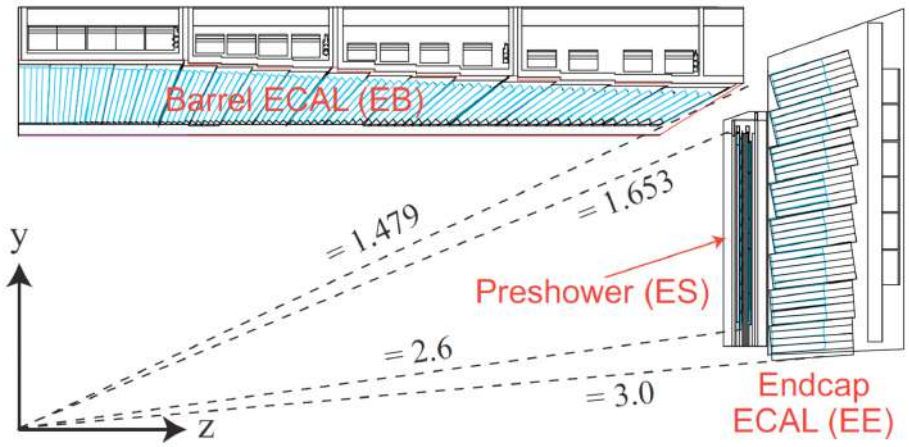

Figure 3.5: Geometric view of one quarter of the CMS electromagnetic calorimeter (ECAL), presenting the arrangement of barrel super-modules, endcaps and the preshower in front [85].

directly from the pp collisions, and low-energetic photons from π^0 decays.

- **The hadron calorimeter (HCAL)**, as shown in Figure 3.2 is located between the ECAL and the solenoid. It is a sampling calorimeter with brass radiators and scintillator sensors. The barrel (HB)($|\eta| < 1.3$) and the endcap (HE)($1.3 < |\eta| < 3.0$) parts are complemented with an outer calorimeter (HO)($0 < |\eta| < 1.26$) located in front of the muon chambers just inside the steel yoke (see Figure 3.6). While the HB and HO calorimeters use alternating layers of brass absorbers and plastic scintillators, the HO uses the magnet coil and the steel from the return yoke. The pseudorapidity range is further extended up to $|\eta| = 5.2$ with the forward hadron calorimeter (HF) located surrounding the beamline, as shown in Figures 3.2 and 3.6 [87]. Due to the intensive radiation conditions in the forward regions, the HF calorimeter uses steel as an absorber, and quartz fibers as sensitive material to be as resistant as possible to radiation damage. The transverse size (in the $\eta - \phi$ plane) of the read-out towers used in the HCAL are $0.087 \,\mathrm{x}\, 0.087$ for $|\eta| < 1.6$ and $0.17 \,\mathrm{x}\, 0.17$ for $|\eta| > 1.6$; while a $0.175 \,\mathrm{x}\, 0.175$ size is used in the HF calorimeter. Its design allows the HCAL to measure the deposited energy by strongly-interacting particles, being essential for jets detection and the determination of E_T^{miss} [88]. The resolution for the measurement of jets energy is almost constant across the HCAL, being about 12% for jets of 100 GeV in the transverse plane.

3.2.5 The muon system

The muon system is composed of three different kinds of gaseous detectors and it is designed to optimize the muons detection as well as the determination of its trajectories. The spatial resolution is around $100\,\mu$m and in combination with the tracker information, a relative momentum resolution of $1\% - 3\%$ for $20\,\mathrm{GeV} \lesssim p_T^{muon} \lesssim 100\,\mathrm{GeV}$ is achieved. As shown in Figure 3.2, the system parts are intercalated with the flux-return yokes covering the $|\eta| < 2.4$ region. The drift tube stations (DTs) and the cathode strip chambers (CSCs) are placed in the barrel and endcap regions respectively. The resistive plate chambers (RPCs) are used

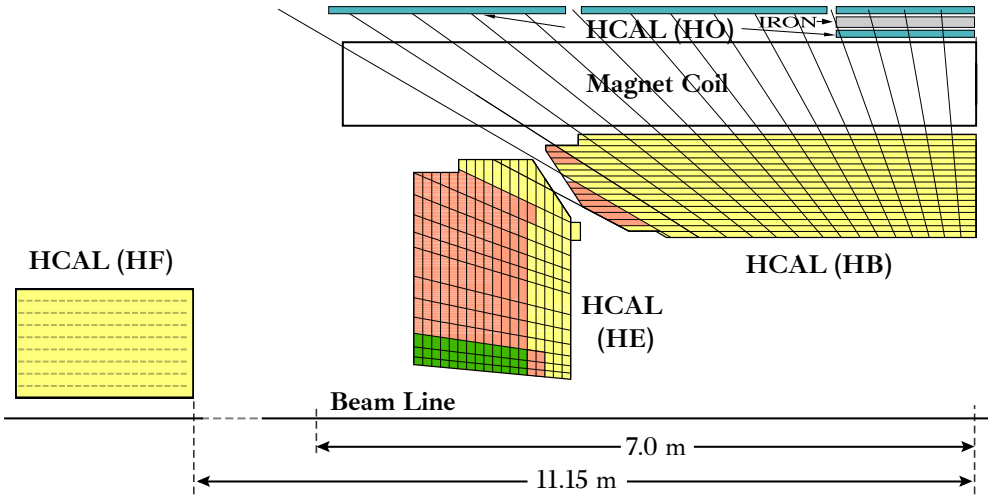

Figure 3.6: Schematic view of the CMS hadron calorimeter (HCAL) in the $r - z$ plane, divided into its subcomponents: HCAL barrel (HB), endcap (HE), outer (HO) and forward (HF) [89].

mainly for the purpose of the trigger system (see Section 3.2.6) due to its fast response of around 1 ns, and they are placed, as shown in Figure 3.7, next to the DTs and CSCs chambers.

3.2.6 Event triggering and data acquisition systems

As described in Section 3.1, the proton bunches collide every 25 ns in the LHC interaction points, corresponding to a bunch crossing frequency of 40 MHz. The CMS infrastructure, mostly due to technical limitations in its maximum data storage capacity and speed, is only able to handle an event rate up to 1 kHz that can be processed by the offline computing systems. This means that a reduction of the information to be stored for further analysis is needed. Given that the events of particular interest for the experiment are those that originated in collisions with hard parton interactions, which represent only a small fraction of the produced events, the task of the trigger is to filter these events based on their high energetic signatures in the detector.
The **level-1 trigger (L1)** is based on custom hardware processors that use all muon systems and the calorimeters to decide (with a latency of 4 μs) whether to keep the data from a particular bunch crossing, based on a fast basic identification of measured particles [88]. After a reduction of the event rate to about 100 kHz by the L1 trigger, the events are further processed by the **high-level trigger (HLT)**. Using measurements from all subdetectors, the software-based HLT trigger performs an event reconstruction, close to the offline reconstruction (see Chapter 5), and decides whether to keep an event for the offline analysis. A trigger path is defined as the complete sequence of L1 and HLT selection criteria, including any prescale of the number of selected events. Depending on the trigger paths, the event rate can be reduced to $100 - 1000$ Hz [90].

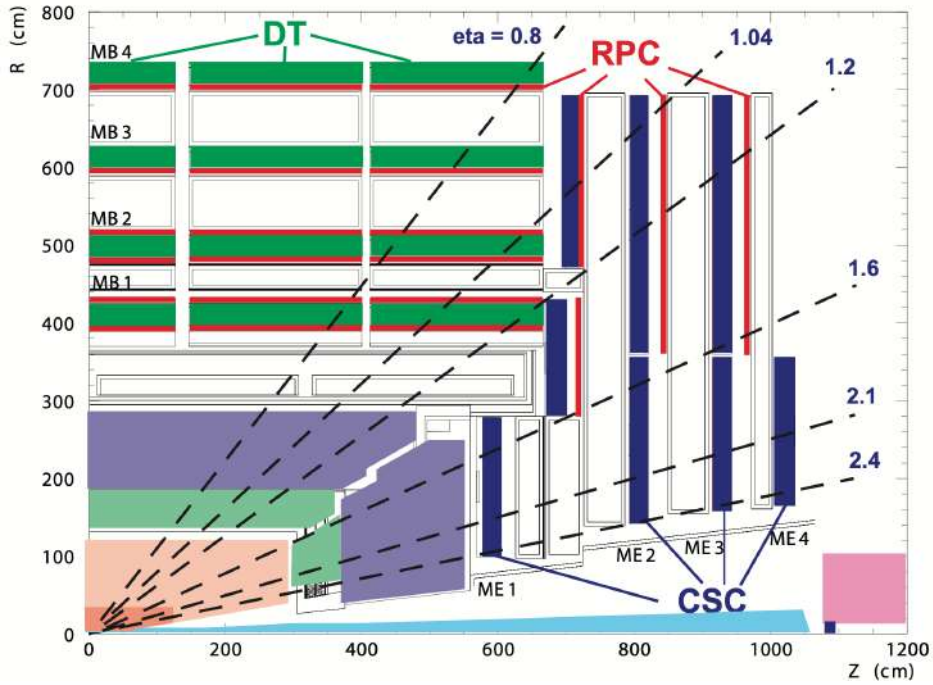

Figure 3.7: Layout of one quarter of the CMS muon system for initial low luminosity running. [88].

3.2.7 Luminosity measurements at CMS

The luminosity [29, 91, 92] is one of the most important accelerator properties for each collider experiment. In the LHC, the instantaneous luminosity ($\mathcal{L}$) is related to the number of protons in a coincidence area per unit of time. Its integration over a period of time ($L = \int \mathcal{L} dt$) is known as the integrated luminosity (L). This magnitude relates the cross-section (σ) and the total number of events of a given process through the relation $N_{events} = \sigma \cdot L$. The integrated luminosity plays a key role in the normalization of the event statistics, and also, the bunch-by-bunch luminosity measurement is important for accelerator diagnostics and optimization.

In general, the luminosity of a collider can be estimated from machine parameters [92]. For two colliding bunches with N_1 and N_2 numbers of particles, the luminosity can be obtained from:

$$L = \frac{N_1 N_2 f n_b}{A_{eff}} \tag{3.4}$$

where n_b is the number of colliding bunches and f the revolution frequency in the collider. These values, together with N_1 and N_2, are obtained from measurements of the LHC machine. The luminous region parameter (A_{eff}) is related to the effective area of the colliding bunches and it can be obtained following the procedure proposed by Simon van der Meer in 1968 using simple beam separation scans (VdM scans) to estimate the beam overlap area [93].

In the CMS experiment, as well as in the other LHC experiments like ATLAS and LHCb, different parts of the detector and also dedicated sub-detectors are used for the measurement of the instantaneous luminosity. The availability of more than one "luminometer" is beneficial

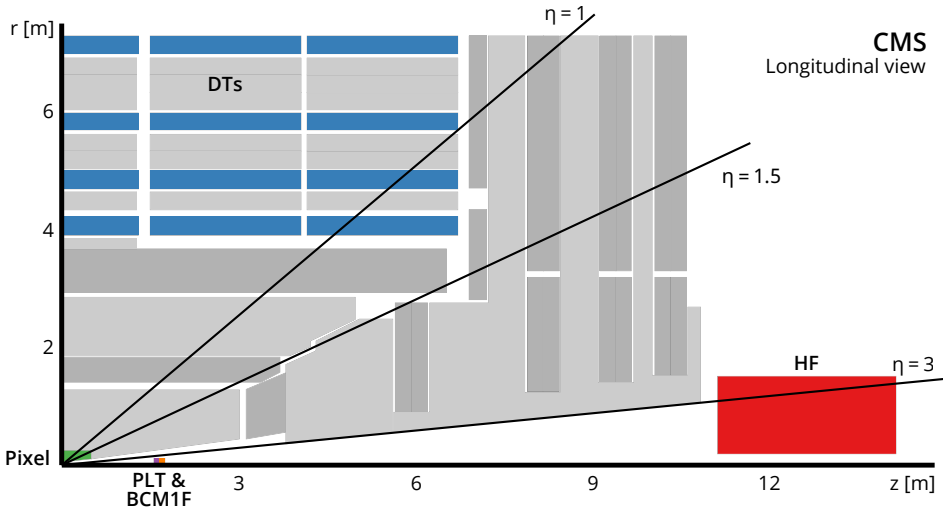

Figure 3.8: Schematic cross section through the CMS detector (one quarter) in the $r - z$ plane showing the main luminometers used in the Run 2 data taking period: silicon pixel detector, PLT, BCM1F, DTs and HF. The two RAMSES monitors used as a luminometer in Run 2 are located directly behind the HF. The center of the detector, corresponding to the approximate position of the *pp* collision point, is located at the origin. Taken from [91]

not only to guarantee uninterrupted luminosity measurement but also for cross-checks of the measurement methods leading to the reduction of the uncertainty of the total integrated luminosity. The Pixel Luminosity Telescope (PLT) and the Fast Beam Conditions Monitor (BCM1F) are fast readout dedicated systems for measuring luminosity [91,92] used for online[1] and high precision measurements used in physics. Also, some CMS subsystems are used as luminometers: The pixel cluster counting (PCC) method uses the mean number of pixel clusters in the silicon pixel detector exploiting the vast number of pixels in the inner part of the CMS tracking system, the two outer rings in η of the hadron calorimeter system are used for the HF occupancy method (HFOC), and the luminosity measurement based on the DT muon detector is based on the muons rate in the CMS barrel [91]. The Radiation Monitoring System for the Environment and Safety (RAMSES), a radiation monitoring subsystem of CERN, is also used for the luminosity measurement, being especially useful for detector linearity studies [91]. The approximate location of the mentioned luminometers is shown in Figure 3.8.

During the VdM scans, the two beams are moved with respect to each other in steps in the x and then in the y plane scanning the colliding bunches against each other in the plane transverse to the beam axis; and the rate R is measured by the luminometers. These scans are used to calibrate the absolute scale of the rate measurement of the mentioned luminosity detectors[2]. The "visible cross section" (σ_{vis}), which represent, the absolute scale of the rate measurement for a given luminosity detector, is independent of the beam conditions and incorporates acceptance and efficiency of the detection method used in the specific detector

[1] Online measurements are referred to ones measured in real-time during the experiment operations.

[2] Only PLT, BCM1F, PCC and HFOC luminometers have a dedicated calibration using the VdM scans. The other detectors (DT, RAMSES) are cross-calibrated (the rate is normalized) to one of the independently calibrated luminometers (e.g., PCC).

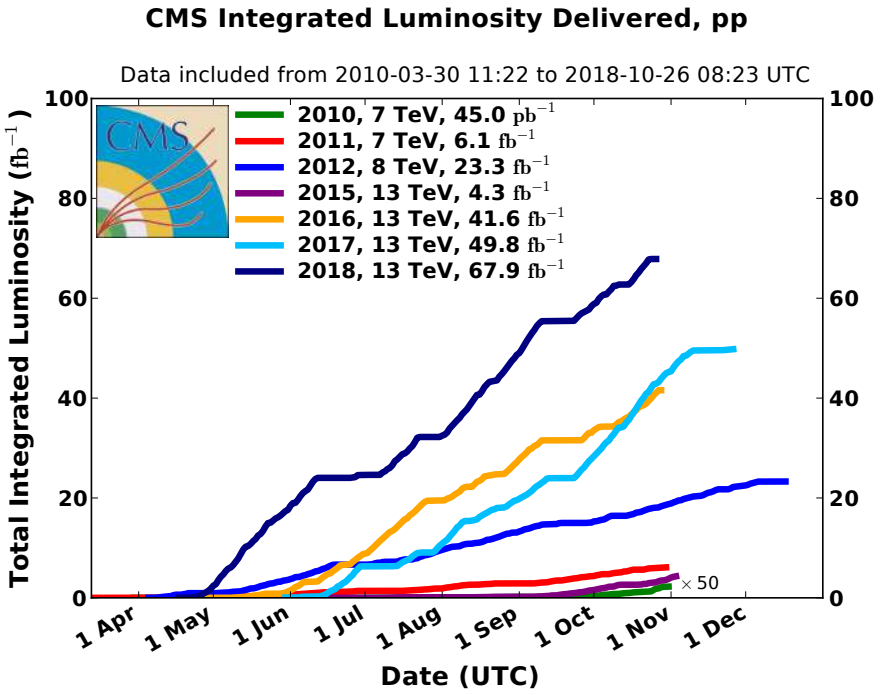

Figure 3.9: Integrated luminosity of proton-proton collisions for different data-taking periods at $\sqrt{s} = 7$, 8, and 13 TeV. Taken from [95]

[29, 94]. It can be obtained from the rate measurements via:

$$\sigma_{vis} = \frac{2\pi\Sigma_x\Sigma_y}{N_1 N_2 f n_b} \cdot R_{peak} \tag{3.5}$$

where R_{peak} is the average maximum rate of the x and y scan directions. The Σ_x and Σ_x parameters describe the effective widths of the beam overlap area along two orthogonal directions and are obtained by fitting the measured rates as a function of the beam separation. After determining the value of σ_{vis}, the measured count rate is used to measure the luminosity ($L = R/\sigma_{vis}$). To obtain the integrated luminosity of the dataset, the integral over the whole data-taking period is taken. In Figure 3.9, the integrated luminosity of proton-proton collisions for different data-taking periods is shown. It is assumed that σ_{vis} remains constant over the whole data-taking. Besides the integrated luminosity uncertainties related to the detector calibration (e.g., beam-beam effects, VdM scan fit consistency) also other uncertainties sources arise accounting from changes of the detector response at different pileup ("linearity") and over time ("stability") [29, 91]. The CMS experiment can measure the integrated luminosity with a relative precision of $1.2 - 2.5\%$. Recently, the measurements published in the "Precision luminosity measurement in proton-proton collisions at $\sqrt{s} = 13$ TeV in 2015 and 2016 at CMS" [91] paper, achieved an impressive relative precision of 1.2% (1.5%) for the 2016 (2015) dataset; making it one of the most precise luminosity measurements at bunched-beam hadron colliders. The estimation of the cross-detector stability and linearity uncertainties are key for achieving such precision. Studies about these uncertainties are presented in Appendix A.

CHAPTER

4

EVENT SIMULATION

Contents

4.1	**Matrix element calculation**	**30**
4.2	**Parton shower simulation**	**31**
4.3	**Hadronization process**	**31**
4.4	**Matching matrix element to parton shower**	**32**
4.5	**Underlying event model**	**33**
4.6	**Colour reconnection model**	**33**
4.7	**Monte Carlo Generators**	**34**
4.8	**Simulation of the detector response**	**36**

The pp collision processes and their subsequent development in time which involves particles production and their interactions with the detector is extremely complicated to be described in every aspect in a fully analytical way. Here comes into play the Monte-Carlo (MC) simulations, which are extremely important in particle physics experiments. The simulation of an event makes use of various generator programs implementing the MC method [96], relying on random sampling to perform relevant numerical calculations. These programs can be used to predict not only the signal but also the background processes event yields and to simulate the detector response including acceptance, efficiency and smearing effects.

The simulation of the signal process of this analysis ($pp \to t\bar{t} \to \bar{l}\nu b\, l\bar{\nu}\bar{b}$), including the subsequent decays and interactions, can be subdivided into different relevant steps as shown in Figure 4.1. First, the collision and production of partons are simulated using the factorization approach with PDFs and hard scattering as explained in Section 2.2, followed by the incorporation of the parton showering tools for the description of the electromagnetic and QCD radiation of the initial and the final step particles. While partonic scattering is calculated in perturbation theory using numerical methods, the parton showers are programs designed to

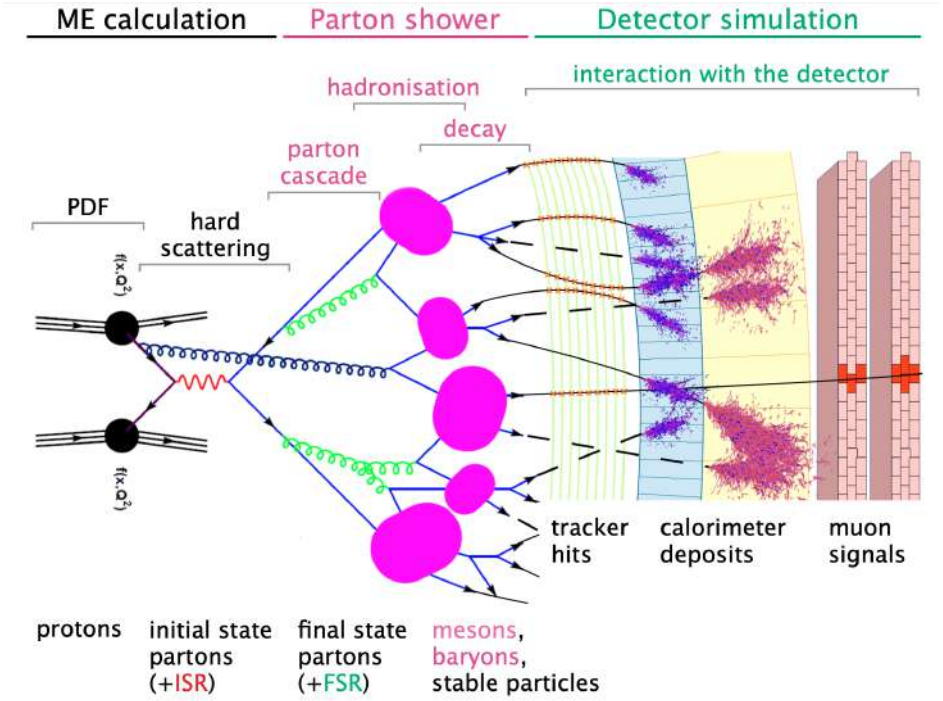

Figure 4.1: Schematic representation of the MC simulation of a hadron-hadron collision. From [97]

approximate higher-order terms with a simplified perturbative approach. Further steps of the event, such as multiple parton interactions, the hadronization, and hadron decays, involve soft processes and can only be described with phenomenological models. Finally, a model of the detector is used in the simulation of the interaction of the generated particles with the detector materials and the detector response.

All relevant simulation steps are further described in the following sections.

4.1 Matrix element calculation

The matrix element (ME) of the hard scattering process is calculated in perturbation theory at a fixed order of α_s describing the interacting partons from the protons. For the case of this analysis, the interacting partons can be two gluons or a quark-antiquark pair as described for the top quark pair production in Chapter 2. The initial momenta of partons in the hard scattering are randomly assigned from the proton PDFs. These initial state partons produce, as a result of their interaction, the outgoing partons corresponding to the final state of the hard scattering.
The ME generators included in this analysis (more details in Section 4.7) produce predictions at NLO accuracy, which includes either the first real emission correction or the first virtual (one-loop) correction.

4.2 Parton shower simulation

Due to their restriction to a fixed order of perturbation, the hard scattering models are unable to describe the higher-order effects of the event. An approximate solution of the emission of additional radiation by the partons present in the initial and final states, known as parton shower, is simulated by different generator programs relying on a probabilistic approach to determine the occurrence of additional emissions. The radiation can be originated from QCD or QED emissions: $q \to qg$, $q \to q\gamma$, $g \to gg$, $g \to q\bar{q}$, $\gamma \to q\bar{q}$, and also $l \to l\gamma$ and $\gamma \to l\bar{l}$.
The evolution of the showering is conditioned by the Sudakov form factor [98] which gives the probability of no emission for a parton between two evolution scales μ_1 and μ_2, where $\mu_1 > \mu_2$. The ordering by the energy-dependent scale μ is a key component of the PS models. One way, known as transverse-momentum-ordered parton shower, is to define the scale as $\mu = p_T^2$ where p_T is the transverse momentum of the radiating parton [99]. A different approach is the angular-ordered parton shower, where μ is computed using the energy of the radiating parton and the angle between two radiated partons [100]. The starting scale t_{max}, usually chosen according to the scale of the hard process, is introduced into the Sudakov form factor as the input scale $\mu_1 = \mu_{max}$ to obtain the scale μ_2 of the new emission and the corresponding emission is generated. All these processes will iteratively continue as long as they are energetically allowed. This happens at energies of the order of 1 GeV or as equal to Λ_{QCD}, where the partons start clustering into hadrons and below which the perturbation theory is no longer applicable [98].
As mentioned before, the radiation can be emitted by partons in the initial or final states. Therefore, the parton shower is usually divided into the initial state radiation (ISR) and the final state radiation (ISR). The FSR is described by a sequential splitting of the colored objects with energy decreasing after each splitting and repeated until some defined evolution criterion is reached. For ISR a similar procedure is used, but in this case inverting the "direction" of the process such that the emitted shower objects, collapse back to the initial partons.

4.3 Hadronization process

As a direct consequence of the colour confinement, at the Q_{had} scale where the event starts to enter into the non-perturbative regime ($\alpha_s \approx 1$), the resulting partons after the showering process start forming hadrons, which can further decay into other hadrons. This process is called hadronization and its description is performed using phenomenological models:

- **The string hadronization model** exploits the feature that the potential of the colour and anticolour dipole grows linearly with the separation of the color charges, up to distances of about a femtometer. This is called linear confinement and is a feature of the string model of elementary particle physics [101].
  The Lund model [102, 103] is one of the most used generator string models. Neglecting the Coulomb interaction, the color potential between the quarks is described as $V(r) = kr$. This is analogous to a string, in this case with tension $k \sim 1\,\mathrm{GeV/fm} \sim 0.2\mathrm{GeV}^2$. As shown in Figure 4.2(a), during the quark separation in space, the "string" bonding the quarks starts to experience more and more tension till it breaks, resulting, if is

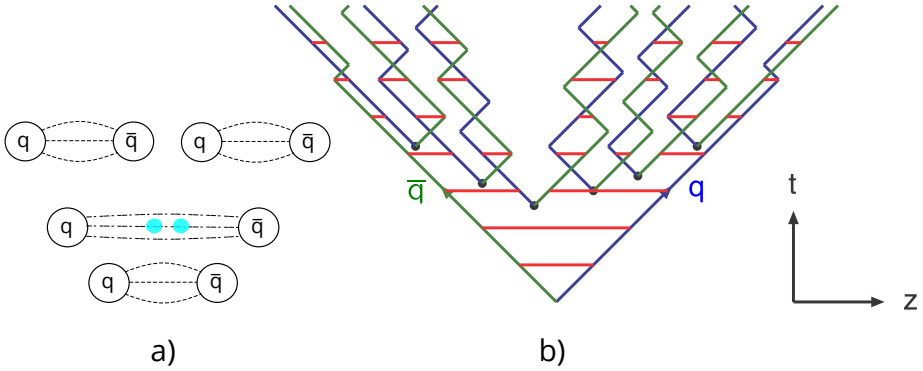

Figure 4.2: (a) The schematic evolution of the colour string connecting the quark pair in the Lund string model. A string breaks to produce a new quark pair out of the QCD vacuum. (b) The motion and breakup of a string system, with the two transverse degrees of freedom suppressed (diagonal lines are (anti-)quarks, horizontal ones snapshots of the string field). Taken from [104].

energetically allowed, in the creation of a new meson (quark-antiquark pair). Also, Baryons (at least 3 valence quarks) can be produced, but in this case, the string breaking produces a pair of diquarks. The hadron production continues as long as any of the strings have enough energy to create another hadron.

- **The cluster hadronization model** [104] is based on the preconfinement property of parton showers [105], which states that the clusters (color-singlet parton subsystems) occur with universal mass distribution depending only on its formation scale Q_0 and the colour structure of showers is assigned already during their evolution. The hadronization process starts by forcing all gluons resulting from the parton shower process into $q\bar{q}$ pairs. Then, the initial clusters formed out of the quark pairs connected by the colour, are forced to decay into clusters of lighter invariant masses. An illustration of the cluster hadronization in comparison to string hadronization is shown in Figure 4.3.

4.4 Matching matrix element to parton shower

Events like $gg \to t\bar{t} + 1jet$ can be generated as a result of the ME calculation (with at least a NLO accuracy in this case), but also by the PS. To avoid double counting of real emissions, a matching between the matrix element calculation and the parton shower is required. While the ME calculation describes the hard interaction including large angle radiation, the parton showers on the other hand, can accurately reproduce soft collinear radiation. This means that one simple way of avoiding double counting would be to remove the hardest emissions from the parton shower. When ME and PS simulations are performed together using the same event generator this effect is handled internally by the generator itself. If different softwares are used for ME and PS, a dedicated matching algorithm is needed.
For the simulation of signal $t\bar{t}$ events presented in this work, the following approaches are used:

- The Powheg method [107, 108] is one of the most used matching algorithms, where

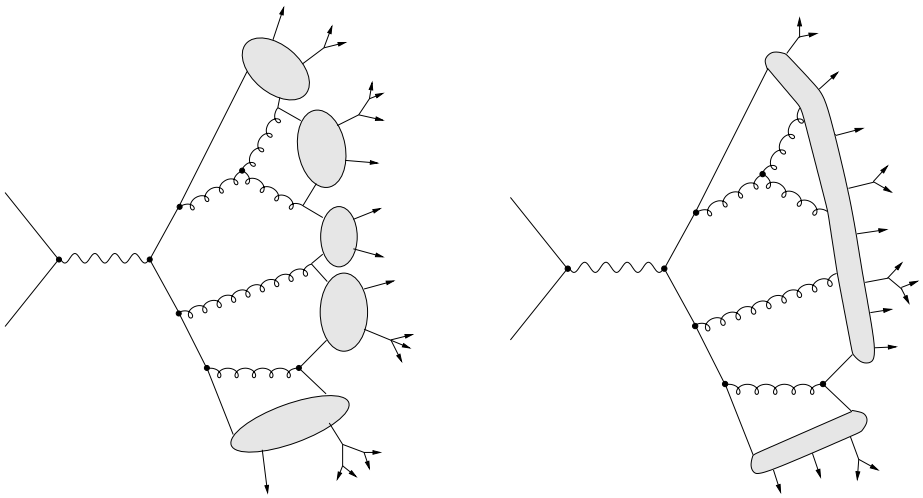

Figure 4.3: Representation of cluster (left) and string (right) hadronization models. Taken from [106].

suitable corrections are introduced into the Sudakov form factor, which plays an essential role for the generation of parton showers. The matching procedure is designed to preserve, at the same time, the NLO accuracy of the matrix element and also the leading-logarithmic resummation properties of the parton shower. The freely adjustable parameter h_{damp} is the scale at which the matching is performed which is known as resummation scale [109] and its value is constrained using data [110].

- The FxFx algorithm [111] is used to patch together NLO hard matrix elements for $t\bar{t}$ processes with up to two extra jets, and parton showers that are independently generated but vetoed if they significantly alter the partonic jet topology of an event.

4.5 Underlying event model

So far, different aspects of the simulation of partonic hard interactions and their subsequent development in time have been discussed. But also multiple parton-parton interactions (MPI) can occur in the events. The soft QCD processes resulting from these interactions is known as underlying event (UE) and is simulated by using phenomenological models. The simulation is governed by free phenomenological parameters usually tuned to experimental data [110]. The MPI are the result of the collisions between the beam particles and also from the hadronization of beam-beam remnants (BBR), which include hadrons originating from partons that do not participate in the hard interactions [112]. The main impact of MPI on the experiment is coming from soft interactions which can affect, for example, the missing E_T distribution in the events and can enhance the jet activity. This means that the jet activity by the PS simulation may be affected by the involved UE model.

4.6 Colour reconnection model

As a direct consequence of the colour confinement in QCD, all partons in the event are required to be connected in terms of the colour-flow, leading to a neutral overall colour. The

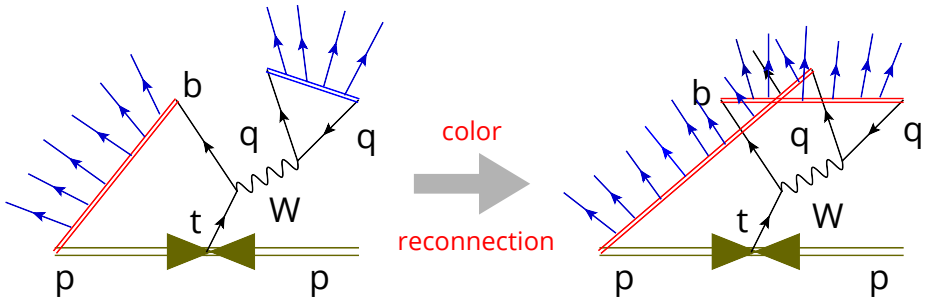

Figure 4.4: A schematic example of the colour reconnection process for the Lund string hadronization model for the decay of the top quark in the hadronic channel. The colour structure of the system before (left) and after (right) the colour reconnection. The red-coloured and green-coloured strings represent the colour structure while blue arrows indicated the directions of the hadrons production. Figure taken from [116], modified.

color reconnection (CR) models aim to correct the colour-flow configuration to achieve a more accurate description of the experimental data [113]. The CR is modeled by phenomenological algorithms which make non-perturbative rearrangements in the colour-flow among the partons by changing the colour connections between them. An illustration of the colour reconnection process is shown in Figure 4.4. The p_T distribution and multiplicity of the jet activity in the event are highly influenced by the described effect.
One of the colour reconnection models relevant for this analysis is the MPI-based scheme, which allows the reconnection of colour flows between two different MPI-systems which are merged according to a probability governed by the p_T-scales of both systems [114]. The merging is performed iteratively over all MPI-systems available in the event in such a way that it minimizes the total length of strings inside the resulting MPI-system.
The other model present in the simulations for this analysis is known as the plain colour reconnection model (PCR) [115]. It starts by selecting random quarks which are part of a cluster (A). Then a colour reconnection is considered with all other clusters (B) that exist at that time. If at least one reconnection possibility fulfill certain conditions related to the new clusters that would emerge from it (C and D), the color reconnection which results in the smallest sum of cluster masses ($m_C + m_D$) is selected and the clusters A and B are replaced by the newly formed clusters C and D. Then a different quark is selected and the process is repeated.

4.7 Monte Carlo Generators

For the event simulation in this thesis, a set of general-purpose Monte Carlo (GPMC) generators was selected to obtain full simulations of the high-energy collisions from different models and be able to compare their performance in the description of the experimental data. For all simulations, the NNPDF3.1NLO PDFs sets [67, 117] were exploited, and the value of the top quark mass parameter is fixed to $m_t^{MC} = 172.5\,GeV$.

- **Pythia8** is a general-purpose event generator where pp, γp and e^+e^- collisions can

be modeled. It can produce, with LO QCD accuracy, hundreds of hardcoded hard subprocesses, which are not limited to the Standard Model, but also include some exotic beyond Standard Model processes [118]. For the parton showering the parton emissions are ordered by the transverse momentum of the radiating parton ($Q^2 = p_T^{\text{parton}}$) and for the hadronization, the Lund string model is used. For the colour reconnection, the MPI-based scheme has been chosen. In this analysis, PYTHIA is mainly used for the simulation of parton showering, hadronization, and MPIs. Except for the case of the diboson background processes which is fully simulated using PYTHIA. The version 8.230 of the program [119] is used with the CP5 tune [120] for the UE modeling.

- **Herwig** [121] is also a general-purpose event generator, producing LO matrix element computations supplemented by parton showers. It can model hadron-hadron, lepton-lepton, and hadron-lepton collisions including Standard Model QCD, electroweak and elementary beyond the standard model processes. The partons are ordered by the scale $Q^2 \sim 1 - \cos(\theta)$ for the parton showering, where θ is the angle between the parent and the emitted partons. This feature and the use of the cluster model for the hadronization are the main differences with PYTHIA regarding the simulation of parton showering and hadronization. For the colour reconnection, the PCR model has been taken. The HERWIG simulations presented in this analysis use the CH3 tune [122] for the optimized set of parameters of the underlying-event model.

- **MG5_aMC@NLO(FxFx)** [123] offers an automated computation of tree-level LO and NLO matrix elements with up to several additional partons, like $t\bar{t}+1jet$, $t\bar{t}+2jet$, etc. The matching to the parton shower simulation is performed using the FxFx NLO-merging approach [124]. The MadSpin package [125] is used to model the decays of narrow resonances but also taking care of preserving spin correlation effects. This generator provides some events with negative weights. However, the fraction of these events is very small. As for POWHEG, it has to be interfaced for the showering with other general-purpose generators.

- The Positive Weight Hardest Emission Generator **Powheg** (v.2) [96, 126] is capable of modeling the hard interaction in various types of collisions ($p\bar{p}$, pp, e^+e^-) with NLO accuracy. It has been widely used for the modeling of different processes, like for example, heavy-flavour production [127], e^+e^- annihilation into hadrons [128] and into top pairs [129], and single-top production [130]. It has been used also as the reference ME generator in previous dileptonic $t\bar{t}$ decay analyses [4, 6]. This generator takes directly into account spin correlations in the decay products of top quarks, and unlike MC@NLO, produces always events with positive weight. The POWHEG method does not have parton showering included, it has to be interfaced with a complementary generator for a full event description. For the presented simulations, the h_{damp} value, which regulates the damping of real emissions in the NLO calculation when matching to the parton shower, is set to $1.581\, m^{MC}$.

The nominal $t\bar{t}$ MC samples are generated using POWHEG, for the ME calculations of the hard process, interfaced with PYTHIA8 which takes care of the parton showering, hadronization, and MPI. From this point, this will be denoted as POWHEG + PYTHIA8 ('POW+PYT') and referred to as the "reference MC simulation". The $t\bar{t}$ simulation is normalized to

a cross section of $\sigma_{t\bar{t}} = 831.76\ ^{+19.77}_{-29.20}\ (\text{scale}) \pm 35.06(\text{PDF} + \alpha_s)\,\text{pb}$ calculated with the TOP++ (version 2.0) program [131] at NNLO including resummation of next-to-next-to-leading-logarithm (NNLL) soft-gluon terms [132–137], and assuming a top quark pole mass $m_{\text{pole}} = 172.5\,\text{GeV}$. The results will be also compared to the other two combinations of the previously described generators, which will be referred to as MG5_aMC@NLO(FxFx) + Pythia8 ('FXFX+PYT') and Powheg + Herwig7 ('POW+HER'). A summary of the generators configurations and features is presented in Table 4.1.

MC generator	ME (matching)	PS ordering	Hadronization	CR	Tune
'POW+PYT'	NLO (Powheg)	$Q^2 = p_T^{\text{parton}}$	Lund string	MPI-based	CP5
'FXFX+PYT'	NLO (FxFx)	$Q^2 = p_T^{\text{parton}}$	Lund string	MPI-based	CP5
'POW+HER'	NLO (Powheg)	$Q^2 \sim 1 - \cos(\theta)$	cluster	PCR	CH3

Table 4.1: The table shows the configuration of the different generators regarding the main features described in this chapter.

4.8 Simulation of the detector response

The simulation of the interaction between the final state particles resulting from the hard interaction, PS and hadronization with the CMS detector is simulated using GEometry ANd Tracking (Geant4) [138], version 10.0X. Geant4 is a toolkit designed for an accurate simulation of the passage of particles through matter relying on MC methods, geometrical and composition information of the detector parts. It also needs parametrizations of the interaction of different particles with particular materials which are derived using experimental data. The software also includes the storage of events and tracks, making possible the visualization of the modeled detector and particle trajectories. Not only the detector response is simulated, but also the emulation of the CMS triggering system is performed to get a more accurate description of the real effects of the detector in the recorded data.

CHAPTER

5

EVENT RECONSTRUCTION

Contents

5.1 Track and vertex reconstruction 37
5.1.1 Track reconstruction and vertex reconstruction 38
5.2 Objects reconstruction 40
5.2.1 Muon reconstruction 41
5.2.2 Electron reconstruction 41
5.2.3 Leptons: used triggers and isolation criteria 42
5.2.4 Jet reconstruction. Identification of jets originating from b quarks . 43
5.2.5 Missing transverse energy 45

The goal of the event reconstruction is the translation of the information collected by the detector into relevant properties of the particles resulting from the proton-proton interactions; like their identity, momentum and trajectory. In this chapter, the reconstruction algorithms of the relevant objects for this analysis, as well as their related corrections, are discussed. Also scale factors ($SF = \epsilon_{data}/\epsilon_{MC}$) are used where necessary to optimize the description of the data by the simulation. The scaling factors are generally applied as event weights to the simulation, unless stated differently. All the corrections and scale factors mentioned in this chapter are derived and applied independently for each year in order to match the varying detector performance and data taking conditions.

5.1 Track and vertex reconstruction

The estimate of the point in space where a particle originated is called **vertex**, and can be associated with the collision point or a secondary interaction, while the set of information about the trajectory and momentum of a charged particle, is called a **track**. Vertices and

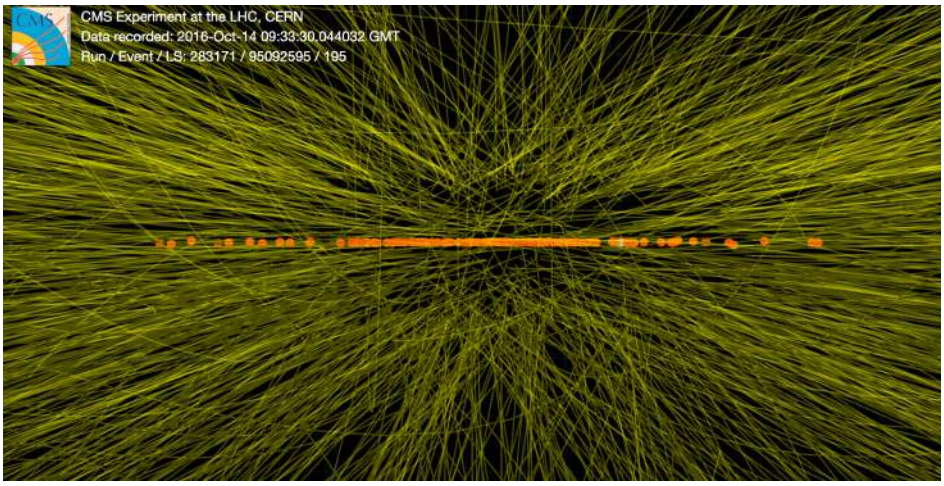

Figure 5.1: A recorded collision by the CMS detector during the 2016 data taking [139]. The lines correspond to the reconstructed tracks and the dots represent the reconstructed pp interaction vertices.

tracks are fundamental for particles reconstruction and provide an essential input to the Particle Flow algorithm. In Figure 5.1, it is illustrated how reconstructed tracks and vertices look in a collision recorded by the CMS detector.

5.1.1 Track reconstruction and vertex reconstruction

The reconstruction of the **tracks**, in the CMS experiment, is performed using the information of the hits of charged particles in the pixel and strip tracker detectors. Knowing the sensor positions with accurate precision is essential for this procedure. The estimation of the sensor positions, minimizing the residuals between hit position and reconstructed tracks using cosmic-ray data and collision data, is known as alignment [140]. The track reconstruction can be separated into the reconstruction of the hits in the tracker system, and the determination and selection of the tracks using the information from the hits.
The reconstruction of the hits starts with the local reconstruction consisting of clustering signals above given thresholds in the tracker sensors. The neighboring pixels or strips which produce signals compatible in time are grouped into clusters that are projected onto orthogonal axes in a local coordinate system. Then, based on the geometry of the sensors and taking into account the Lorentz drift of the collected charge in the magnetic field, an initial estimate of the hit position is obtained by the charge weighted average of the strip or pixel positions. A further hit reconstruction is performed using templates that take into account the irradiation status of the sensors. The pixel and strip hits are reconstructed with efficiency above 99.5% (excluding non-operative modules). Depending on the particle incidence angle and the width of the clusters, the hit position resolution is estimated to be in the range of $20 - 50\,\mu$m for the pixel, and $10 - 50\,\mu$m for the strip detector [141].
After reconstructing the hits, the trajectory of a particle can be determined by fitting a sequence of selected hits. This process starts by looking for all possible 3 points combinations,

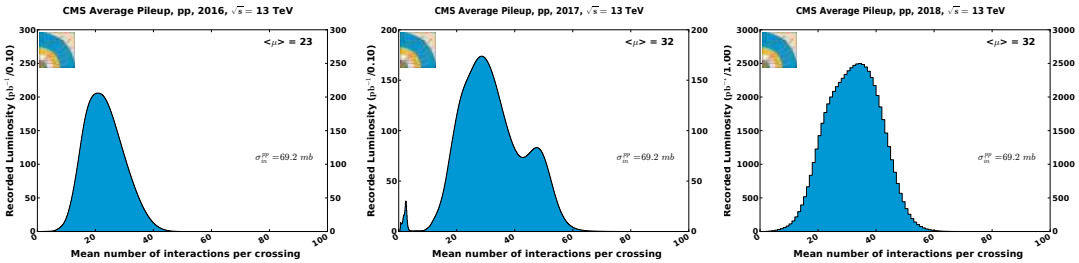

Figure 5.2: Mean number of interactions per bunch crossing for the 2016 (left), 2016 (middle) and 2018 (right) *pp* run at 13 TeV. For the determination of these distributions the CMS recommended value of 69.2 mb was used as the minimum bias cross section. Taken from [95].

coming from 3 pixel hits or 2 strip hits and the beam spot center[1], which are required to be compatible with a helical trajectory assuming a quasi-uniform magnetic field. Also a minimum p_T value and a beam spot impact parameter below some maximum value is required. Here the impact parameter is the minimum distance of the track to a certain vertex, or beam spot in this case, in the transverse plane. These initial (seed) track candidates, determined using only the hits from the first tracker system layers, are extrapolated into the expected path through the other layers searching for the best hit coincidences for each layer using a χ^2 approach, based on the Kalman filter method [142]. A track is not accepted if no hit is found in a 3 sigma region around the seed trajectory for more than one layer. The selected hits of the accepted seed tracks are refitted, but in this case without the constraints set on the seeding step. To optimize the track-finding efficiency, while keeping under control the fraction of fake tracks (i.e. those formed from unrelated hits), the tracks need to pass a track selection which sets physical and quality constraints based on a good resulting χ^2 of the fit, and a reasonable value of the track impact parameter with respect to the beam spot. This track finding process is iterated up to 6 times, having the tightest requirements on the seed tracks in the first iteration. For each subsequent iterations, the requirements become softer (lower p_T cut or allowing larger displacement from the interaction vertex) and they only use available hits not previously selected as part of another final track. The efficiency of reconstructing tracks with $p_T > 1\,\text{GeV}$ is larger than 99% for isolated muons over the entire pseudorapidity range of the tracker, while depending on the track pseudorapidity, efficiencies for electrons and pions vary between 80 and 99%. Using the track curvature and the known information from the magnetic field, the transverse momentum of the particle can be computed. The resolution on the track p_T is below 1% for central muons with p_T between 1 and 10 GeV and in general depends significantly on the p_T and η of the particles [141].

The *pp* interaction **vertices** are reconstructed using selected tracks with certain requirements like being produced in the primary interaction region, a certain minimum number of associated hits, and a track fit $\chi^2/dof \leqslant 20$, where dof stand for the number of degrees of freedom. These "high-quality" tracks, are clustered considering their z-axis position and the distance to the beam spot center [143]. Each resulting cluster, with at least two associated tracks, is fitted using an adaptive vertex fitter [144], having the vertex position as an output. The **primary vertex (PV)** is defined as the one with the highest sum of squared transverse

[1]The beam spot is defined as the 3-dimensional profile of the LHC luminous region where the collisions between the bunches occur. Its center (beam spot center) is computed as the average value of the *pp* interaction points over many events.

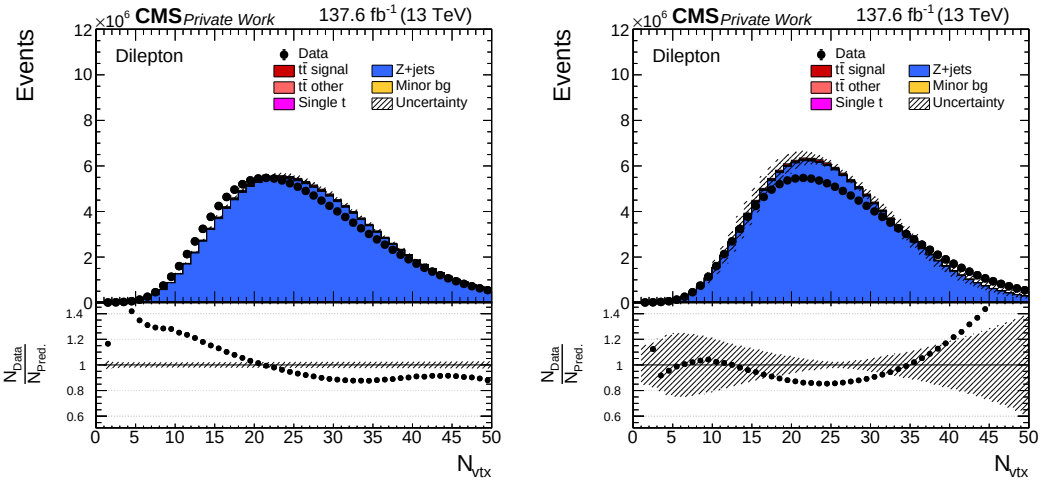

Figure 5.3: Reconstructed distribution of the number of *pp* vertices per event. The left (right) plot shows the distribution before (after) the application of the reweighting of the simulation according to the true-level pile-up profile in data. The distributions are obtained after the lepton-pair requirement of the event selection (see 6.2). The hatched area indicates the shape systematic uncertainties on the $t\bar{t}$ signal and backgrounds (see Chapter 9).

momenta (p_T^2) of associated tracks, while the other interaction vertices are referred to as pileup (PU) vertices which correspond to multiple *pp* interactions within a bunch crossing. The mean number of interactions per bunch crossing for the 2016 data-taking period was 23, while for 2017 and 2018 this values was 32 [95]. Vertices can be reconstructed with an efficiency close to 100% if they have more than two associated tracks and about 98% for vertices with only two tracks. For the vertex position, the achieved resolution is between 10 and 100 μm, depending not only on the number of associated tracks but also on the average p_T of the tracks [141].
At least one "good" primary vertex is required for accepting an event. The number of tracks associated to these vertices has to be larger than four and they should be positioned in the center of the detector: $|z| < 24\,\text{cm}$ and $|r| < 2\,\text{cm}$.
Due to differences in the reconstructed vertices in data and simulation, the true-level $N_{vertices}$ distribution in the MC simulation is reweighted event-by-event to make it match the data distribution. The also called "pileup correction" is determined using the instantaneous luminosity per bunch crossing, the integrated luminosity of the data taking period and the total *pp* inelastic cross section. In Figure 5.3, the reconstructed distribution of the number of *pp* vertices per event is shown before and after the application of the correction.

5.2 Objects reconstruction

The Particle Flow (PF) algorithm [81, 145] is used in this analysis for reconstructing and identifying, in an iterative process, the particles and jets arising from the LHC proton-proton collisions (see Figure 5.4). For this goal, the information collected from the different detector subsystems is used. The algorithm starts by reconstructing the muons, following by the charged hadrons after blinding the muon signals in the detector. The next step is

Figure 5.4: Schematic showing the essence of the Particle Flow algorithm [146].

the electron reconstruction, and afterwards, all the remaining signals are assigned to neutral hadrons and photons. The E_T^{miss} is then determined after all particles are reconstructed by using all available information.

5.2.1 Muon reconstruction

The muon system, as described in Section 3.2.5, is one of the strongest points in the design of the CMS detector. The identification of muons is rather straightforward, since they are the only particles expected to be detected in the muon system (see Figure 3.2). According to the sub-detector systems used for their reconstruction they can be grouped into *standalone*, *tracker* or *global* muons. For the *standalone* case, only the information coming from the muon system is used. On the contrary, for *tracker* muons, the tracks are reconstructed using only the tracking detector hits, but with the requirement of having at least one compatible hit in the muon system. For the reconstruction of *global* muons, the hits from the tracker and the muon system are fitted simultaneously [147].
Reconstruction and selection efficiencies for the muon candidates can be calculated using the tag-and-probe data-driven method [148, 149]. This algorithm relies on the use of muon pairs stemming from the decay of a Z-boson resonance, where the events are selected requiring a muon candidate, referred to as "tag", passing a single muon trigger and tight selection requirements, while the other muon candidate, referred to as "probe", is used to measure the corresponding efficiency. The combined efficiency of the muon reconstruction and selection is about 94%. The simulation is corrected by dedicated scale factors, which are data-to-MC ratios of efficiencies in bins of the p_T and $|\eta|$ of the muon candidate, and they are centrally provided by the CMS Collaboration.

5.2.2 Electron reconstruction

The PF algorithm uses the information from tracking system tracks and clusters from the ECAL for the electron reconstruction. The ECAL clusters are combined into groups (superclusters) of one or more associated clusters. The transverse energy of a supercluster has to be equal or higher than 4 GeV. Then a *tracker driven seeding* is performed by matching tracks with $p_t < 5\,\text{GeV}$ to compatibles ECAL superclusters. For tracks with $p_t \geqslant 5\,\text{GeV}$, *ECAL*

driven seeds are formed by fitting the ECAL superclusters to the tracks. Assuming that the tracks are associated with an electron, all the seeds are fitted using a Gaussian Sum Fitter (GSM) [150], taking into account the energy losses by the bremsstrahlung radiation of the electrons. In the last step, the fitted tracks are filtered by a multivariate analysis (MVA) for the tracker seeds [151], and by imposing restrictions on the GSM matching in η and ϕ for ECAL seeds [152]. The track candidates that passed the preselection process are assigned to electrons.
The electron reconstruction and selection efficiencies are computed, as for muons, using the tag-and-probe method, obtaining a combined electron efficiency of around 65%. The simulation is corrected for differences in efficiencies compared to the data, using differential scale factors determined as a function of the electron candidate p_T and the η of an associated supercluster.

5.2.3 Leptons: used triggers and isolation criteria

For the analysis described in this thesis, The events have to be accepted by selected HLT (see Section 3.2.6) **lepton triggers**, which require one or two leptons (e or μ) with transverse momenta above predefined thresholds. The dielectron (dimuon) trigger requires the presence of two electrons (muons) with a minimum transverse momentum of 23 GeV (17 GeV) and 12 GeV (8 GeV) for the leading[2] and sub-leading lepton, respectively. In the case of the $e\mu$-trigger, the requirements are an electron with 23 GeV and a muon with 8 GeV, or a muon with 23 GeV and an electron with 12 GeV. In order to mitigate the fact that the dilepton triggers are not 100% efficient, single lepton triggers are also introduced. The single-electron (single-muon) trigger requires an electron (muon) with 27 GeV (24 GeV). The events are selected using a logical "OR" operation[3] between the dilepton and single lepton triggers making it possible to recover approximately 10% of dilepton events that were not triggered by the dilepton triggers. The same trigger selection is applied on the data and the simulated event samples.
Scale factor corrections were applied in order to take into account that triggers may have different efficiencies for the data and MC. The efficiencies are measured in data and simulation as a function of $|\eta|$ of the two leading leptons in the event. The method for the efficiencies determination [148, 153] is based on the use of unprescaled monitor triggers which are uncorrelated to the lepton triggers. The efficiency is computed as the ratio between the number of events which were selected simultaneously by the tested and the monitor trigger, over the number of events selected by the monitor trigger only. The obtained scale factors ($SF_{trigger}$) are then used to correct, double differentially in bins of the two leptons pseudorapidities, the MC simulation to the observed efficiency in data.

The **lepton isolation** requirement is another important ingredient to ensure the quality of the measurements by removing contributions from leptons originating from QCD events. As in previous works [3, 5, 6], all muons in the event are required to fulfill the condition $I^{\mu}_{rel} \leq 0.15$. The relative isolation (I_{rel}) is defined as the sum of transverse energy deposits

[2] The leading and sub-leading terms are referred to the particle with the highest and second-highest p_T, respectively. It is usually used in the scope of a defined type of particles like for example leptons or jets (e.g. leading jet, leading lepton, etc).

[3] The operation of logical OR implies that the event is accepted if one or more trigger paths are fired

from charged and neutral hadrons and photons, relative to the lepton p_T, inside a cone with $\Delta R < 0.4$ around the muon track. For the electrons, the isolation is computed as the p_{T} sum of all neutral hadron, charged hadron, and photon candidates in a cone of $\Delta R < 0.3$ from the electron, divided by the p_{T} of the electron candidate. A maximum value of I_{rel} is allowed, in a range of 5-10%, depending on the p_{T} and η of the electron candidate. The efficiencies for the lepton isolation are also computed in data and simulation using a tag and probe method and in bins of lepton p_T and η separately for electrons and for muons.

5.2.4 Jet reconstruction. Identification of jets originating from b quarks

Generally jets can be reconstructed using two different strategies: *sequential clustering* and *cone algorithms*. Cone algorithms are the fastest and simplest, but they don't ensure collinear and infrared safety [4], while the sequential clustering procedures can. A sequential clustering algorithm, named anti-k_T [154], is used in CMS for the jet reconstruction. The process starts by defining the distances between two objects, particles or pseudojets, i and j in the detector (d_{ij}) and between the beam direction and the object i (d_{iB}) as:

$$d_{ij} = \min\left({p_T}_i^{-2}, {p_T}_j^{-2}\right)\frac{\Delta R_{ij}^2}{R^2} \tag{5.1}$$

$$d_{iB} = {p_T}_i^{-2} \tag{5.2}$$

By the setting of the R parameter, which in CMS is chosen as 0.4, one can control the "size" of the reconstructed jets. Then, looking at all i and j combinations, one takes the one with minimum d_{ij}. If this d_{ij} is smaller than all of the d_{iB} values, the two objects i and j are merged. Otherwise, the jet i with the minimum d_{iB} value is taken as a final jet. These output jets have a circular shape in the (y, ϕ) plane and their momentum is quantified as the vectorial sum of all particle momenta clustered in the jet. The particles used as input objects for the jet reconstruction are the charged and neutral hadrons, photons, electrons, and muons; as previously identified by the PF algorithm [155].
The reconstructed jets require calibration of their energies and momenta to account for the non-linear and non-uniform responses of the calorimeter and other inefficiencies in the jet reconstruction. The jet energy scale (JES) and the jet energy resolution (JER) corrections [148] are applied to mitigate these effects. The JES correction deals with the additional energy in the jet which does not occur from a hard process but rather from the detector noise or pileup, the detector response to hadrons, and residual differences between data and MC simulation as a function of the jet pseudorapidity η and transverse momentum p_T. The jet energy scale is corrected using a correction factor obtained via a b-jet energy regression based on a Deep Neural Network estimator [156]. The jet energy resolution (JER) in the data is worse than in the simulation, that is why the jet 4-momenta in the simulation are smeared to describe the data. For the case of JES, the correction depends on jet properties, e.g. p_T, η and flavour; while for JER, is applied in bins of $|\eta_{jet}|$ after the JES correction.

The identification of jets originating from b quarks, also called b-jets, is known as **b-tagging**. For this analysis, it is an essential input for the reconstruction of the $t\bar{t}$ system.

[4] Collinear and infrared safety means insensitive to soft and collinear gluon emission, and collinear gluon splitting.

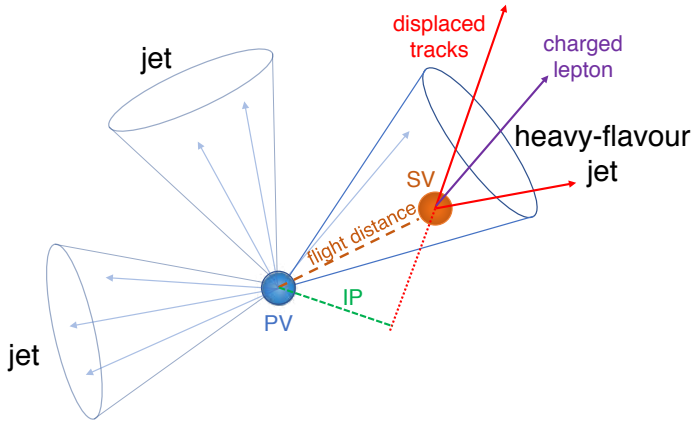

Figure 5.5: Sketch of a heavy-flavour jet with a secondary vertex (SV) from the decay of a b or c hadron resulting in charged-particle tracks (including possibly a soft lepton) that are displaced with respect to the primary interaction vertex (PV) [157].

Having a lifetime of about 1.5 ps, the beauty hadrons can travel from the PV up to a few cms before decaying. As shown in Figure 5.5, the point in space where the beauty hadrons decay occurs, determined by tracks displaced from the PV, is named as "secondary vertex" (SV). The inclusive vertex finder (IVF) algorithm is used in CMS for the reconstruction of SVs by making use of all available tracks in the event independently of the jet clustering. The impact parameter (IP), defined as the distance of the closest approach of each track to the primary vertex, is an essential variable for the distinction between SVs and PVs. Tracks originating from SVs are expected to have mainly positive IP[5], while the IP values of tracks originating from the PV are symmetrically distributed around zero. Another important quantity is the flight distance (FD), which as shown in Figure 5.5, is the distance between a SV and the PV. Also, to take the detector resolution into account, the IP significance (IP/σ_{IP}) and the FD significance (FD/σ_{FD}) are introduced, where σ_{IP} and σ_{FD} are the uncertainties for IP and FD respectively. Another useful discriminating variables are the number of reconstructed SVs and their corrected mass[6].
The described variables, with information of up to six tracks, are used as inputs to the DeepCSV algorithm [157], which is based on a deep neural network architecture that improves the performance of the classification with respect to older taggers like CSVv2 [157, 158]. It is a multclassifier, trained to distinguish between five exclusive jet flavour categories defined according to the jet content: one b hadron (b), exactly two b hadrons (bb), exactly one c hadron and no b hadrons (c), exactly two c hadrons and no b hadrons (cc), or none of the above ($udsg$). The DeepCSV training is performed in all vertex categories simultaneously, and the best b tagging performance can be obtained by using the quantity $P(b) + P(bb)$ as binary classifier; here $P(f)$ is the probability for a jet to belong to the flavour category (f) [157]. There are three different operating points defined as the values of the discriminator cut, for which the rate of "light flavoured jet" (l-jet)[7] misidentification as a b jet is 10% (loose), 1% (medium)

[5]If the angle between the jet direction and the IP is smaller than $\pi/2$, the IP sign is taken as positive, otherwise a negative sign is assigned.

[6]The estimated mass is corrected for the effect of particles that were not detected or associated with the secondary vertex.

[7]Light jets are jets from gluons, u, d and s quarks

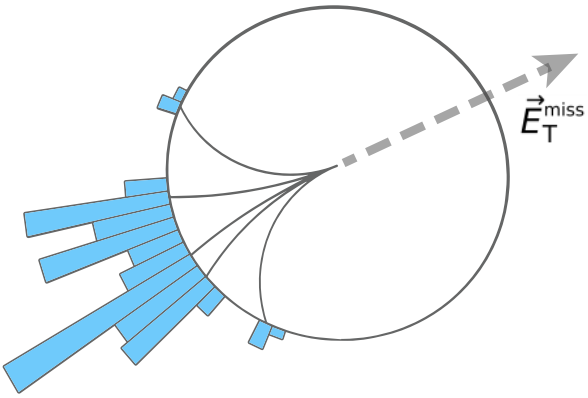

Figure 5.6: Illustration of how missing transverse energy ($\vec{E}_T^{miss}$) can be reconstructed by computing the imbalance of the transverse momentum. The blue columns, represent the associated energy deposited by visible particles (solid curved lines show the track of charge particles) in the calorimeter. Modified figure from [159].

or 0.1% (tight). For the b-jet identification in this analysis, the DeepCSV algorithm is used with the loose working point resulting in a b-tagging efficiency of $\sim 80-90\%$ for jets with $p_T > 30\,\text{GeV}$, a mistagging efficiency of $\sim 1\%$ for jets originating from gluons, as well as u, d, or s quarks, and $\sim 30\text{˘}40\%$ for jets originating from c quarks. The tagging efficiency of b-jets, as well as the mistag rates of c-jets and l-jets, is different between the data and simulation. This is corrected by the application of scale factors measured using samples containing only multijet events [157]. These scale factors depend on the p_T, $|\eta|$ and flavour of the jets.

5.2.5 Missing transverse energy

Another ingredient for the reconstruction of the di-leptonic $t\bar{t}$ system is the missing transverse energy (see Section 3.2.1), which in this case, contains essential information about the kinematic properties of the neutrinos coming from the leptonic W-decays in the event. The reconstruction of $\vec{E}_T^{miss}$, as shown in Figure 5.6, is computed using the information of all the reconstructed particles in the event as previously defined in Equation 3.3. The determination of the $\vec{E}_T^{miss}$ distributions is highly affected by the effect of PU on observables of clustered hadrons. In this analysis, the pileup-per-particle-identification (PUPPI) [160] algorithm is used for the correction of this effect by giving weights to particles based on the probability that they come from pileup or the primary vertex (PV). The jet energy corrections, b-jet energy regression and lepton energy scale corrections are propagated to the E_T^{miss}.

Since the collisions have a rotational symmetry with respect to the beam axis, the true distribution of the missing transverse energy is uniform in terms of the ϕ-direction. But, due to different detector effects like anisotropic response and imperfect detector alignment, the reconstructed distribution possesses a sinusoidal-like modulation [161, 162]. In order to mitigate these effects and reduce the modulation, a correction is applied via a shift of the $\vec{E}_T^{miss}$ components in the x and y directions. This correction is applied event-by-event

separately in the data and simulation.

CHAPTER

6

EVENT SELECTION

Contents

6.1 Data sample **48**

6.2 $t\bar{t}$ **event selection** **48**

6.3 Background sources **49**

6.3.1 Background estimation 51

6.4 Event yields and control distributions **52**

This work is focused on reconstructing the $t\bar{t}$ pair in the dilepton decay channel ($t\bar{t} \rightarrow W^+bW^-\bar{b} \rightarrow \nu l^+ b\, \bar{\nu} l^- \bar{b}$). These events produce a detector signature with two isolated and opposite charged leptons, at least two high energetic jets originating from b quarks and the presence of significant missing transverse energy from neutrinos which pass undetected through the detector. Only the processes with direct decays of both W bosons into an electron or a muon, and the corresponding neutrino, are considered as signal ($t\bar{t}$*-signal*). The τ channel from the W decay ($W \rightarrow \tau\nu_{tau}$), with an electron or muon originating from the subsequent decay of the τ lepton, is not taken as signal in this analysis. The inclusion of these events would complicate the reconstruction of the $t\bar{t}$ event kinematics. Thus, $t\bar{t}$ decays involving at least one intermediate τ lepton decaying leptonically and all other non dileptonic $t\bar{t}$ decay channels are treated as background and denoted as $t\bar{t}$*-other*.
This chapter gives an overview of the event selection used in this analysis describing its different steps and requirements. The resulting control distributions, containing the event yields from the data and simulated signal, and backgrounds processes, are presented and discussed.

6.1 Data sample

This analysis uses data recorded by the CMS detector for pp collisions at $\sqrt{s} = 13\,\text{TeV}$ in the Run-II period, which corresponds to an integrated luminosity of 137.7 fb^{-1} [163–166]. In Table 6.1, the luminosity values for the individual years are shown. Only data-taking periods in which the detector was fully operational are used. These "good" for physics analysis periods are selected by the CMS Collaboration using data quality monitoring [167] and offline certification procedures. During these collisions, considering the total $t\bar{t}$ production cross section and the dileptonic decay branching ratios, approximately one million $t\bar{t}$ dileptonic events were produced.

Dataset	Integrated luminosity
2016	36.3 $\text{fb}^{-1}\pm$ 1.2%
2017	41.5 $\text{fb}^{-1}\pm$ 2.3%
2018	59.7 $\text{fb}^{-1}\pm$ 2.5%
Run-II	137.7 $\text{fb}^{-1}\pm$ 1.8%

Table 6.1: Integrated luminosity values for the years 2016, 2017, 2018 and for the full Run-II period. Values are taken from [164] for 2016, [165] for 2017 and [166] for 2018. All information about the luminosity measurement is summarized by the CMS collaboration in Ref. [163].

6.2 $\mathrm{t\bar{t}}$ event selection

The analysis follows the event selection strategy from other previous CMS measurements [4, 6], which, complemented with all the object reconstruction and corrections mentioned in Chapter 5, can be summarized into the following steps which are applied consecutively in the analysis:

- **Triggering:** Events are required to pass the trigger requirements previously summarized in Section 5.2.3.

- **Lepton pair selection (= 2 leptons):** Exactly two isolated leptons of opposite charge with $p_T > 25(20)\,\text{GeV}$ for the leading (trailing) candidate and $|\eta| < 2.4$ are required for each event. Depending on lepton flavours of the resulting lepton pair, events are classified into e^+e^-, $e^\pm\mu^\mp$ and $\mu^+\mu^-$ channels. The dilepton channel is referred to as the combination of all the events coming from these three different channels.
  To reduce the contamination from low-mass DY processes and events associated with decays of heavy flavour resonances, all events with a lepton pair invariant mass $m_{l\bar{l}} \leq 20\,\text{GeV}$ are rejected. Furthermore, events in the e^+e^- and $\mu^+\mu^-$ channels are excluded if the lepton pair mass is inside a region of $\pm 15\,\text{GeV}$ around the nominal mass of the Z resonance ($76\,\text{GeV} < m_{l\bar{l}} < 106\,\text{GeV}$). This cut, called in the following Z-veto cut, aims to further suppress Drell-Yan processes.

- **Jets selection ($\geq$ 2 jets):** Events which contain at least two jets with $p_T > 30\,\text{GeV}$ and $|\eta| < 2.4$ are accepted. Only jets with with an angular distance of $\Delta R(l,j) > 0.4$ with respect to each selected lepton are accepted[1].

- **Missing transverse energy:** Since DY events do not have neutrinos in the final state, they are not expected to possess a large missing transverse energy. Therefore, events in the e^+e^- and $\mu^+\mu^-$ channels are only accepted if $E_T^{miss} > 40\,\text{GeV}$, leading to a further reduction of the DY background.

- **b-jets selection ($\geq$ 1 b-jets):** A selected event has to contain at least one jet, tagged as originating from a b-quark with b-tagging probability according to the DeepCSV "loose cut" criterion (Section 5.2.4). By requiring at least one b-tagged jet and not at least two, it is possible to recover b-jets not selected by the b-tagging algorithm, using the kinematic reconstruction procedure described in Chapter 7. Taking into account that the efficiency of the used b-tagging algorithm is $\sim 80-90\%$, if at least two b-jets would be required, around 27%[2] of the signal events would be lost due to b-tagging inefficiencies; while only a 2%[3] would be lost due to this effect with the "at least one b-jets" requirement.

- **Kinematic reconstruction:** Events are only selected if they have a physical solution for the top-quark pair kinematic reconstruction (see Section 7.1).

- **Extra jets selection:** The extra jets, by definition in this analysis, are the jets produced during the $t\bar{t}$ process excluding selected lepton and b-jets coming from the top and antitop quarks decays. The extra jets, besides all the cuts already mentioned for the jet selection, are required to have a $p_T > 40\,\text{GeV}$ and an angular separation of $\Delta R(b,j) > 0.8$; where b refers to the b-jets identified, in the kinematic reconstruction, as originating from the top and anti-top quark decays. This last cut is aiming at reducing the possible contamination coming from gluon radiation emitted by these b-jets. It has been estimated that this effect is reduced to less than $\sim 1\%$ by using the mentioned cuts. It is important to mention that if no jet in the event fulfill the requirements, this event is not excluded as in the other selection steps, in this case it means just that a $t\bar{t}$ event was successfully reconstructed but it has no extra jets.

All the selection steps are performed following the mentioned order and they dramatically reduce the fraction of background events, while retaining a large fraction of good quality signal events.

6.3 Background sources

Events that have two identified leptons and two jets in the final state can arise also from other physics processes different from the defined signal in this analysis. The resulting events from these processes will be referred to, from now on, as *background*. Background sources whose contributions are negligible compared to the signal are not taken into account. The

[1] $\Delta R(l,j) \equiv \sqrt{(\Delta\phi(l,j))^2 + (\Delta\eta(l,j))^2} = \sqrt{(\phi_l - \phi_j)^2 + (\eta_l - \eta_j)^2}$

[2] if at least two b-jets are required: $N_{\text{lost}} \sim 1 - \epsilon_{btag}^2 \approx 27\%$ taking $\epsilon_{btag} \approx 85\%$.

[3] if at least one b-jets are required: $N_{\text{lost}} \sim (1 - \epsilon_{btag})^2 \approx 2\%$ taking $\epsilon_{btag} \approx 85\%$.

background simulations are normalized according to their theoretical cross sections from approximate fixed order calculations.

- $t\bar{t}$***-other*****:** includes other $t\bar{t}$ event topologies that are not classified as signal, and it is dominated by the already mentioned dileptonic channel via at least one intermediate τ lepton. This category also contains events from the $l + jets$ or all-hadronic decay modes (as introduced in Chapter 2) which can be misidentified as dileptonic events.

- $t\bar{t} + Z$ $(t\bar{t} + W)$**:** is a process where the top-quark pair is produced in association with a Z (W) boson. For the $t\bar{t} + Z$ events where the Z boson decays leptonically (hadronically), a cross section of 0.2529 pb (0.5297 pb) was used. For the $t\bar{t} + W$ process, the leptonic (hadronic) W decay channels are normalized to a cross section of 0.2043 pb (0.4062 pb). All mentioned cross sections were computed internally by the CMS collaboration with NLO accuracy using MC samples from the MG5_aMC@NLO(FxFx) + Pythia8 generator. Both contributions are combined into a single category named as $t\bar{t} + Z/W$.

- ***Single top*****:** A single top is produced through an electroweak interaction which, when produced in association with a W boson, can lead to a final state with two leptons, where the W boson can be mistreated as it were produced from the top decay. The tW simulation samples are normalized according to a theoretical cross section of 35.85 pb. The s and t production channels are also considered. A cross section value of 136.02 pb (80.95 pb) was taken for the single top (antitop) t-channel, and 10.32 pb for the s-channel. These values were computed using approximate-NNLO calculations [168,169]. In the following, the contribution from all mentioned single top channels is denoted as *single t*. The tW process represents, with respect to the other channels, the biggest contribution for the signal final state.

- ***Diboson*****:** refers to WW, WZ and ZZ diboson production. These events can also have a dileptonic final state which may be picked as a $t\bar{t}$ candidate.
  The WZ and ZZ simulated samples are normalized with cross sections of 47.1 pb and 16.5 pb, respectively, computed using MCFM [170] NLO predictions. The WW events are normalized to a cross section of 118.7 pb, obtained with the NNLO QCD calculations [171].

- $Z + jets$**:** refers to Drell-Yan (DY) processes, $Z/\gamma^* \to \tau\tau$ and $Z/\gamma^* \to ee/\mu\mu$, which leads to a dileptonic final state signature which could be misidentified as $t\bar{t}$ signal. At higher orders, jets originate from this process arising from initial state radiation (ISR). Since the rate of production is much larger for $Z+jets$ than for $t\bar{t}$, this is one of the most important background sources and requires a careful estimation (see Section 6.3.1). As explained in Section 6.2, its corresponding contribution can be strongly suppressed with the selection requirements related to the mass of the lepton pair system.
  The used simulation samples include $Z + jets \to (e^+e^-,\ \mu^+\mu^-$ or $\tau^+\tau^-)$ processes divided into two mass regions at generator level: $10\,\text{GeV} < m_{l\bar{l}} < 50\,\text{GeV}$ and $m_{l\bar{l}} >= 50\,\text{GeV}$. The events are normalized with the cross sections of 22635.1 pb (from NNLO FEWZ 3.1) and 6077.22 pb (NNLO FEWZ 3.1.rc) respectively for the mentioned low and high mass regions [172–174].

Year	e^+e^-	$\mu^+\mu^-$	$\mu^\pm e^\mp$
2016	0.92	0.88	0.89
2017	0.94	1.02	0.98
2018	1.05	1.04	1.05
Run 2	0.97	0.99	0.98

Table 6.2: Data-driven Z+jets background scale factors (Drell-Yan SFs) for the $\mu^+\mu^-$ and e^+e^- channels after the "$E_{\mathrm{T}}^{\mathrm{miss}}$" selection requirement for all years and full Run 2.

- $W + jets$**:** events are classified according to the decay modes of the W boson produced from an *up quark* and a *down anti-quark* from two different protons. Even if only one charged lepton can be present after the leptonic decay of a W boson, this process could be wrongly included as a signal-like event due to non-prompt leptons from b and c jets, leptons from inflight decays of kaons and pions in hadronic jets, or fake leptons from hadronic jets. The used sample, corresponding to the lepton (either e, μ or τ) plus neutrino channels, is normalized to a cross section of 61526.7 pb obtained with FEWZ v.3.1 at NNLO accuracy [172–174].

6.3.1 Background estimation

Even after the noticeable reduction of the contribution of background processes to the final event sample, a considerable amount of background events are still present and their total contributions are estimated using simulation-based and data-driven techniques.
The background contributions from *single* t, $t\bar{t} + Z/W$, *diboson* and $W + jets$ are estimated directly from the MC samples (see Table 6.3) and their event rates are normalized, based on the cross section of the respective process, and the integrated luminosity of the data sample. For the case of the Z+$jets$ processes, the largest background is in the e^+e^- and $\mu^+\mu^-$ channels and their total contribution rates are extracted from data, while their distribution shapes are estimated from the simulated samples (see Figure 6.1). The normalization is obtained from a binned template fit to the data, using the *TFractionFitter* class implemented in ROOT [175] following the method described in [176]. The event fractions of $Z + jets$ processes, together with the sum of all other contributions, are fitted to the $m_{l\bar{l}}$ data distributions within the Z peak signal region $76\,\mathrm{GeV} < m_{l\bar{l}} < 106\,\mathrm{GeV}$. This region is orthogonal to the signal region of our analysis since it is excluded in the event selection as explained in Section 6.2 and it is broad enough to still separate Z contribution (peaking) from the others (approximately flat). Independent normalization scale factors are fitted for the template distributions obtained from MC simulations in the e^+e^- (SF_{ee}) and $\mu^+\mu^-$ ($SF_{\mu\mu}$) channels. The scale factor for the $e^\pm\mu^\mp$ channel, is calculated as the geometric mean of them: $SF_{\mu e} = \sqrt{SF_{ee} \times SF_{\mu\mu}}$. These values, in the following named as Drell-Yan scale factors, used to scale the Drell-Yan component after the full event selection, are computed after the E_T^{miss} selection requirement (see "missing transverse energy" step in Section 6.2). As can be observed in Table 6.2, the obtained Drell-Yan SFs agree within a few percent with unity.

Sample	ME generator	σ [pb]
$t\bar{t}$-*signal* / $t\bar{t}$-*other* (dileptonic)	POWHEG	831.76×0.10706
$t\bar{t}$-*other* (semileptonic)	POWHEG	831.76×0.44113
$t\bar{t}$-*other* (hadronic)	POWHEG	831.76×0.45441
single top/antitop: tW	POWHEG	35.85
single top/antitop: s-channel	MG5_aMC@NLO	10.32
single top/antitop: t-channel	POWHEG	top: 136.02, antitop: 80.95
$Z + jets$ ($10\,\text{GeV} < m_{l\bar{l}} < 50\,\text{GeV}$)	MG5_aMC@NLO(MLM)	22635.1
$Z + jets$ ($m_{l\bar{l}} >= 50\,\text{GeV}$)	MG5_aMC@NLO(FxFx)	6077.22
$W + jets$ ($W \to l\nu$)	MG5_aMC@NLO(MLM)	61526.7
diboson: WW	PYTHIA8	118.7
diboson: WZ	PYTHIA8	47.1
diboson: ZZ	PYTHIA8	16.5
$t\bar{t} + W$ ($W \to l\nu$)	MG5_aMC@NLO(FxFx)	0.2043
$t\bar{t} + W$ ($W \to q\bar{q}$)	MG5_aMC@NLO(FxFx)	0.4062
$t\bar{t} + Z$ ($Z \to l\bar{l}$, $Z \to \nu\bar{\nu}$)	MG5_aMC@NLO	0.2529
$t\bar{t} + Z$ ($Z \to q\bar{q}$)	MG5_aMC@NLO	0.5297

Table 6.3: Summary of background simulation samples. PYTHIA8 is used for the simulation of the PS and hadronization for all background sources. The used ME generator is indicated for each sample. The dileptonic, semi-leptonic and hadronic branching ratios are taken from [30].

6.4 Event yields and control distributions

The event yields are then combined from the different channels and years, and compared to the data in control distributions. In Table 6.4, the number of observed events in data and its comparison to the expected number of signal and background is presented for each subsequent selection requirement and all individual channels, including the combined dilepton channel.

In this section, several kinematic distributions in data and MC are presented corresponding to different steps of the event selection. For Figure 6.3 and all subsequent ones, the rates in $Z + jets$ simulations are scaled by the normalization scale factors (see Section 6.3.1), leading to an improved agreement between data and simulated distributions. The hatched area shown in the plots represents the shape-dependent systematic uncertainties on the $t\bar{t}$ signal and backgrounds, further described in Chapter 9.

The following selection of plots has the goal of showing examples of how the different cuts and corrections affect some of the most important distributions for this analysis. In the plots, the "Minor bg" category is referred to background sources with a relatively small contribution:

$\mu^+\mu^-$ sample	2 leptons	2 jets	E_T^{miss}	b-tag	kin. fit	loose. kin. fit
$t\bar{t}$ signal	444855.9	355495.3	298368.2	282649.9	253742.1	270402.6
$t\bar{t}$ other	79962.5	63990.1	52861.7	49395.8	45740.4	47084.6
$t\bar{t}$ + Z/W	1340.1	1272.0	1093.8	1042.1	849.6	921.4
Single top	51821.6	23943.4	20183.8	17946.9	12569.9	14020.2
diboson	70605.2	9496.5	5915.2	2125.0	1221.5	1364.8
W+jets	7964.7	1487.6	1284.1	621.8	360.5	364.4
Z+jets	7423415.1	590204.4	227674.6	82410.8	52847.3	56849.7
Sum MC	8079965.1	1045889.2	607381.3	436192.3	367331.3	391007.6
Data	8089847.0	1019665.0	601963.0	428294.0	360945.0	381792.0
$\mu^\pm e^\mp$ sample	2 leptons	2 jets	E_T^{miss}	b-tag	kin. fit	loose. kin. fit
$t\bar{t}$ signal	807429.9	646894.4	646894.4	613361.4	563073.5	588473.3
$t\bar{t}$ other	143899.9	115370.0	115370.0	108215.4	101679.7	103698.6
$t\bar{t}$ + Z/W	2191.6	2071.6	2071.6	1958.6	1676.9	1774.9
Single top	93452.7	43161.4	43161.4	38445.7	28163.3	30528.2
diboson	110821.1	9591.8	9591.8	3183.9	1998.2	2161.2
W+jets	22723.9	3299.5	3299.5	947.8	676.9	696.7
Z+jets	281184.0	25594.6	25594.6	8942.2	7136.2	7282.5
Sum MC	1461703.1	845983.3	845983.3	775055.0	704404.8	734615.4
Data	1424701.0	803181.0	803181.0	730465.0	663856.0	689489.0
e^+e^- sample	2 leptons	2 jets	E_T^{miss}	b-tag	kin. fit	loose. kin. fit
$t\bar{t}$ signal	229181.8	183585.9	151039.8	143001.8	129703.4	136411.9
$t\bar{t}$ other	37047.0	29710.4	24440.2	23026.2	21516.4	22069.8
$t\bar{t}$ + Z/W	730.3	693.4	578.1	548.4	444.6	480.6
Single top	26264.2	12375.5	10192.1	9131.2	6331.5	6951.6
diboson	35380.7	4947.9	2741.8	1029.3	581.9	651.8
W+jets	7465.3	899.7	623.8	231.5	114.7	116.2
Z+jets	3284703.0	271230.6	80952.9	29045.8	19274.4	20836.9
Sum MC	3620772.3	503443.4	270568.7	206014.0	177966.9	187518.8
Data	3436947.0	472229.0	258627.0	193868.0	167443.0	174818.0
combined sample	2 leptons	2 jets	E_T^{miss}	b-tag	kin. fit	loose. kin. fit
$t\bar{t}$ signal	1481467.6	1185975.6	1096302.3	1039013.1	946519.0	995287.8
$t\bar{t}$ other	260909.4	209070.4	192671.9	180637.4	168936.5	172853.0
$t\bar{t}$ + Z/W	4262.0	4037.1	3743.5	3549.0	2971.1	3176.9
Single top	171538.5	79480.2	73537.2	65523.8	47064.8	51500.0
diboson	216807.0	24036.2	18248.9	6338.2	3801.6	4177.8
W+jets	38153.8	5686.8	5207.4	1801.1	1152.2	1177.3
Z+jets	10989302.1	887550.6	334195.3	120384.8	79261.8	84973.0
Sum MC	13162440.4	2395837.0	1723906.6	1417247.4	1249706.8	1313145.8
Data	12951495.0	2295075.0	1663771.0	1352627.0	1192244.0	1246099.0

Table 6.4: Event yields corresponding to an integrated luminosity of 137.7 $fb^{-1}$of the collected data at 13 TeV compared with the estimated signal and background simulated event rates. The values are given for the different channels after each consecutive selection step.

$t\bar{t}+Z/W$, $W+jets$ and *Diboson* (WW, WZ and ZZ). The invariant mass of the dilepton system is shown in Figure 6.1 for the e^+e^-, $\mu^+\mu^-$, $e^\pm\mu^\mp$ and combined dilepton decay channels after the trigger and lepton pair selection criteria. In these plots, it can be observed, as a direct effect from the requirement of the presence of a lepton pair, that the $W+jets$ background (contained in the "Minor bg" in the plots) shows only a small contribution to the total event yield. One example of the effect in the $Z+jets$ background reduction of the Z-veto cut is shown in Figure 6.2, where it can be seen how the region with at least 2 jets is mostly dominated by the $\mathrm{t\bar{t}}$ signal events. The described jet selection requirements, including the $N_{jets} \geq 2$ cut, starts to be present in Figure 6.3 where the E_T^{miss} distributions are shown for the e^+e^- and $\mu^+\mu^-$ channels. One important conclusion from these plots is that the region with $E_T^{miss} < 40\,\mathrm{GeV}$ is dominated by the $Z+jets$ events. After excluding the events within this E_T^{miss} region from the e^+e^- and $\mu^+\mu^-$ channels, in Figures 6.4 and 6.5 the distributions for the pseudorapidity of the selected jets and lepton candidates are shown, respectively. In these distributions, the large reduction of $Z+jets$ background contribution can be observed. The presence of at least one b-tagged jet is required for each event starting with Figure 6.6 and for all the following ones. These remaining Figures 6.6-6.10 show the distribution of the physics objects which serve as inputs to the kinematic reconstruction of the $\mathrm{t\bar{t}}$ system, discussed in Chapter 7. In more detail, the distributions corresponding to the p_T of the selected b-jet (Figure 6.7) and lepton candidates (Figure 6.8), and the E_T^{miss} (Figure 6.10); are examples of kinematic spectra of observables that are direct inputs for the top kinematic reconstruction procedures. In overall a good agreement is observed between the POWHEG + PYTHIA8 reference MC and the data. This is also observed for control distributions for the individual years which are presented in Appendix B.

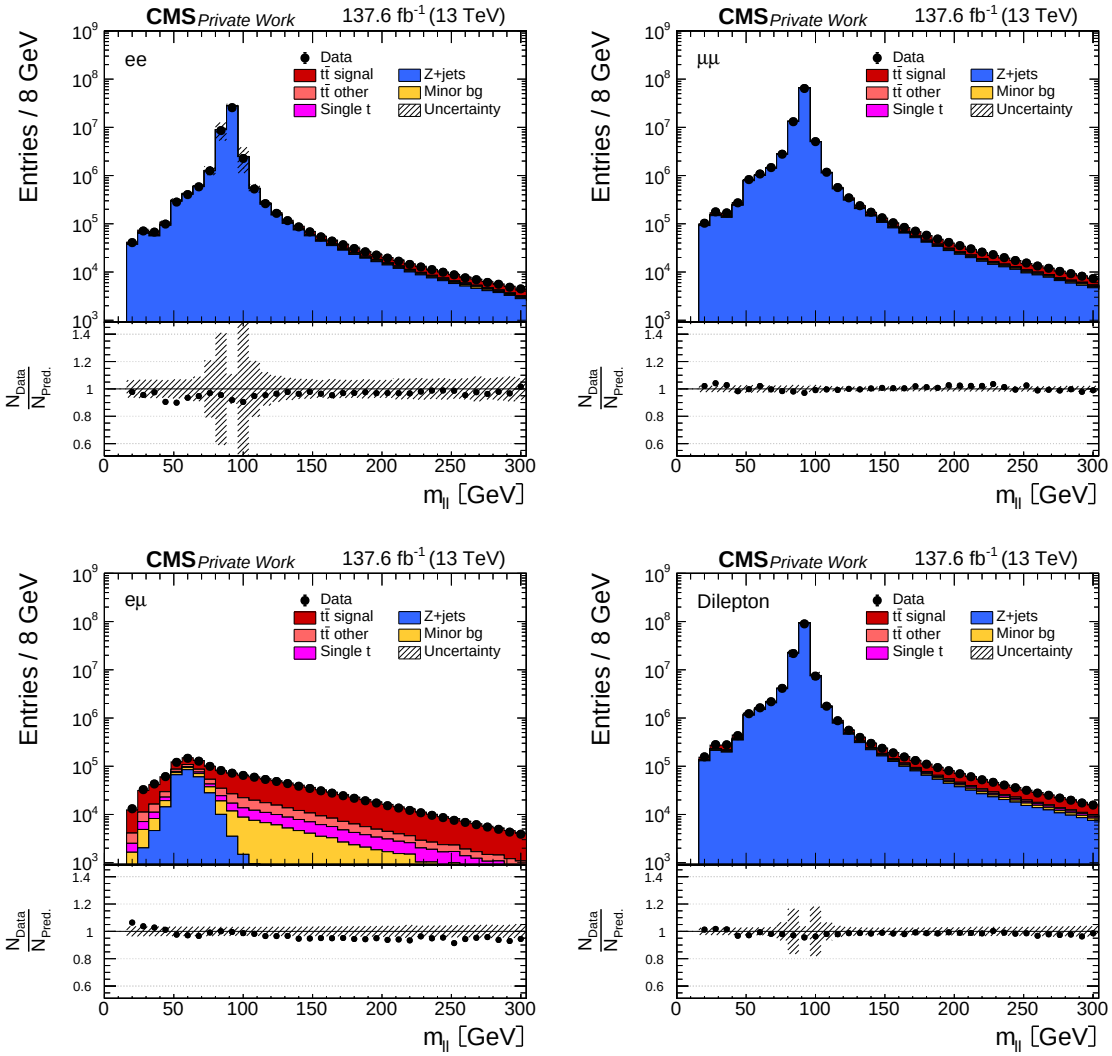

Figure 6.1: Distributions of the invariant mass of the dilepton system. The trigger and lepton pair selection (except the Z-veto cut) requirements have been applied to the events. The scale factors accounting for the trigger and lepton selection efficiencies, described in Sections 5.2.1-5.2.3, are used. The distributions are shown for the different e^+e^- (upper left), $\mu^+\mu^-$ (upper right) and $e^\pm\mu^\mp$ (lower left) channels, and their combination named as Dilepton (lower right). The hatched area represents the shape systematic uncertainties on the $t\bar{t}$ signal and backgrounds (see Chapter 9). The Minor bg category is referred to background sources with a relatively small contribution: $t\bar{t} + Z/W$, $W + jets$ and *Diboson* (WW, WZ and ZZ).

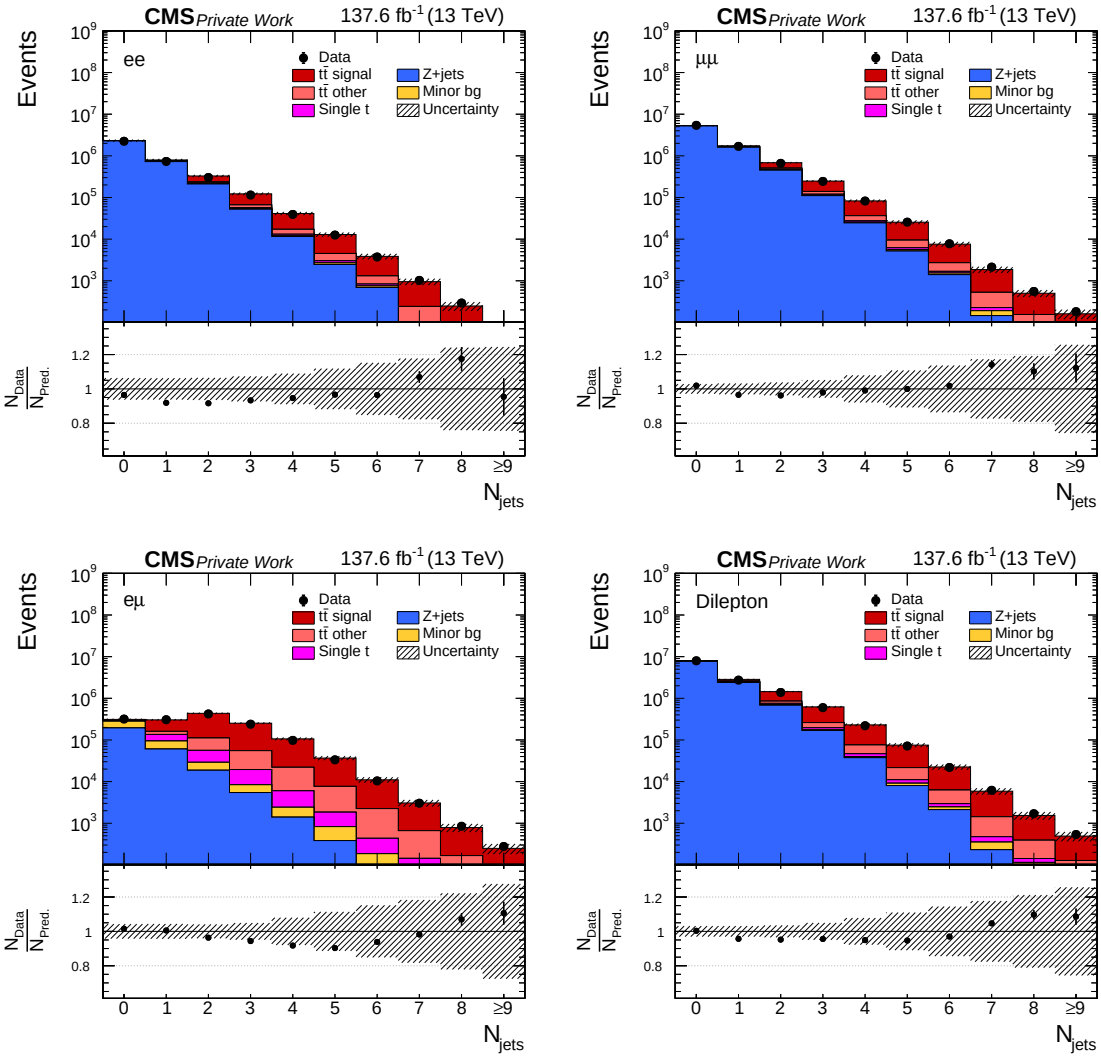

Figure 6.2: Control distributions of the number of jets per event after the Z-veto requirement, including all previous requirements. The distributions are shown for the different e^+e^- (upper left), $\mu^+\mu^-$ (upper right) and $e^\pm\mu^\mp$ (lower left) channels, and for their combination named as Dilepton (lower right). The hatched area represents the shape systematic uncertainties on the $\mathrm{t\bar{t}}$ signal and backgrounds (see Chapter 9).

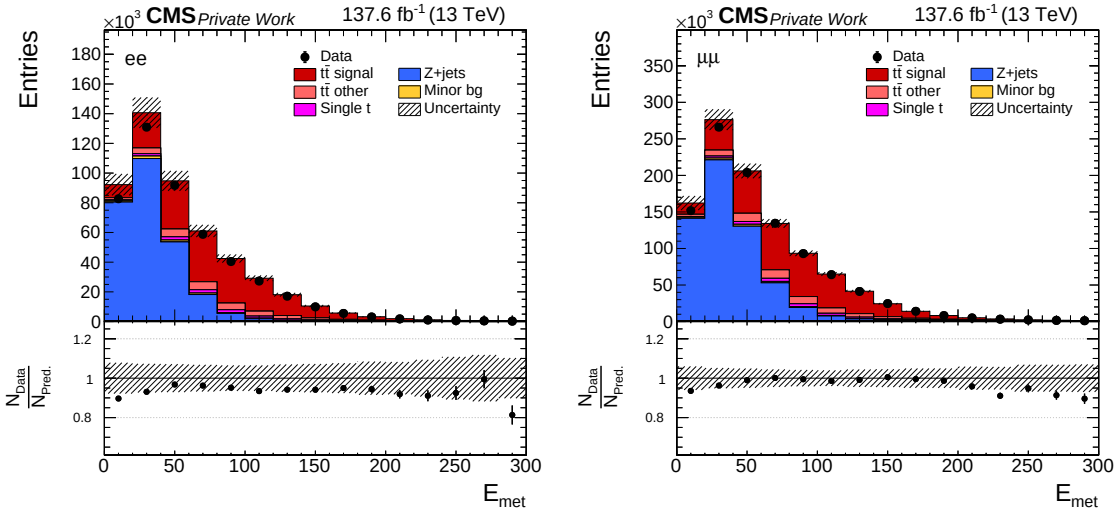

Figure 6.3: Control distributions of the missing transverse energy (E_T^{miss}) in the e^+e^- (left) and $\mu^+\mu^-$ (right) channels after the jets selection (≥ 2) step (see Section 6.2), including all previous steps requirements. DY scale factors are applied. The hatched area represents the shape systematic uncertainties on the $\bar{\text{t}}\text{t}$ signal and backgrounds (see Chapter 9).

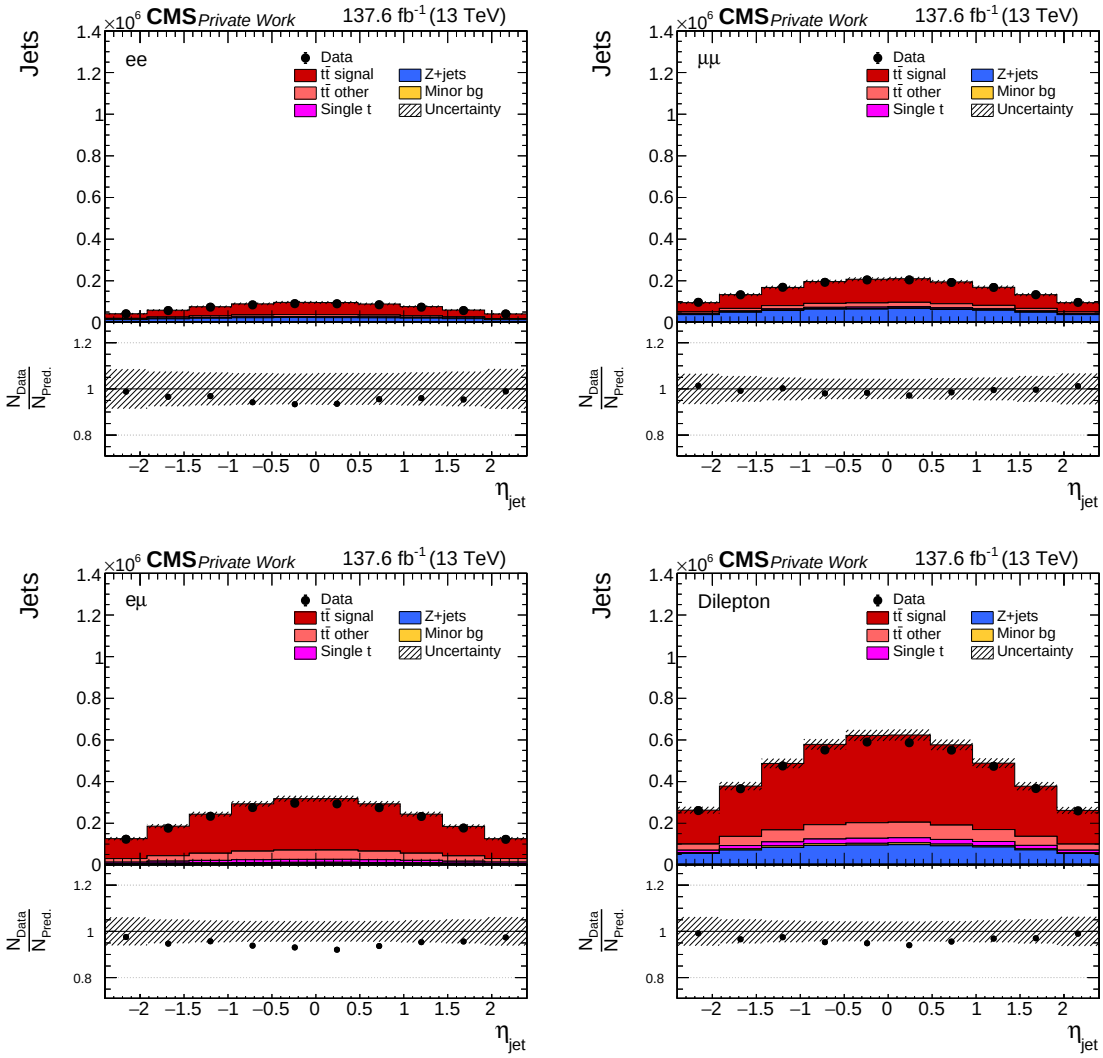

Figure 6.4: Control distributions of the pseudorapidity of jets after the lepton pair and jet-related selection requirements. In the e^+e^- and $\mu^+\mu^-$ channels, events satisfying the $E_T^{miss} > 40\,\text{GeV}$ condition are excluded. This plot also include all steps previous to the missing transverse energy requirement as described in Section 6.2. DY scale factors are applied. The hatched area represents the shape systematic uncertainties on the $\text{t}\bar{\text{t}}$ signal and backgrounds (see Chapter 9).

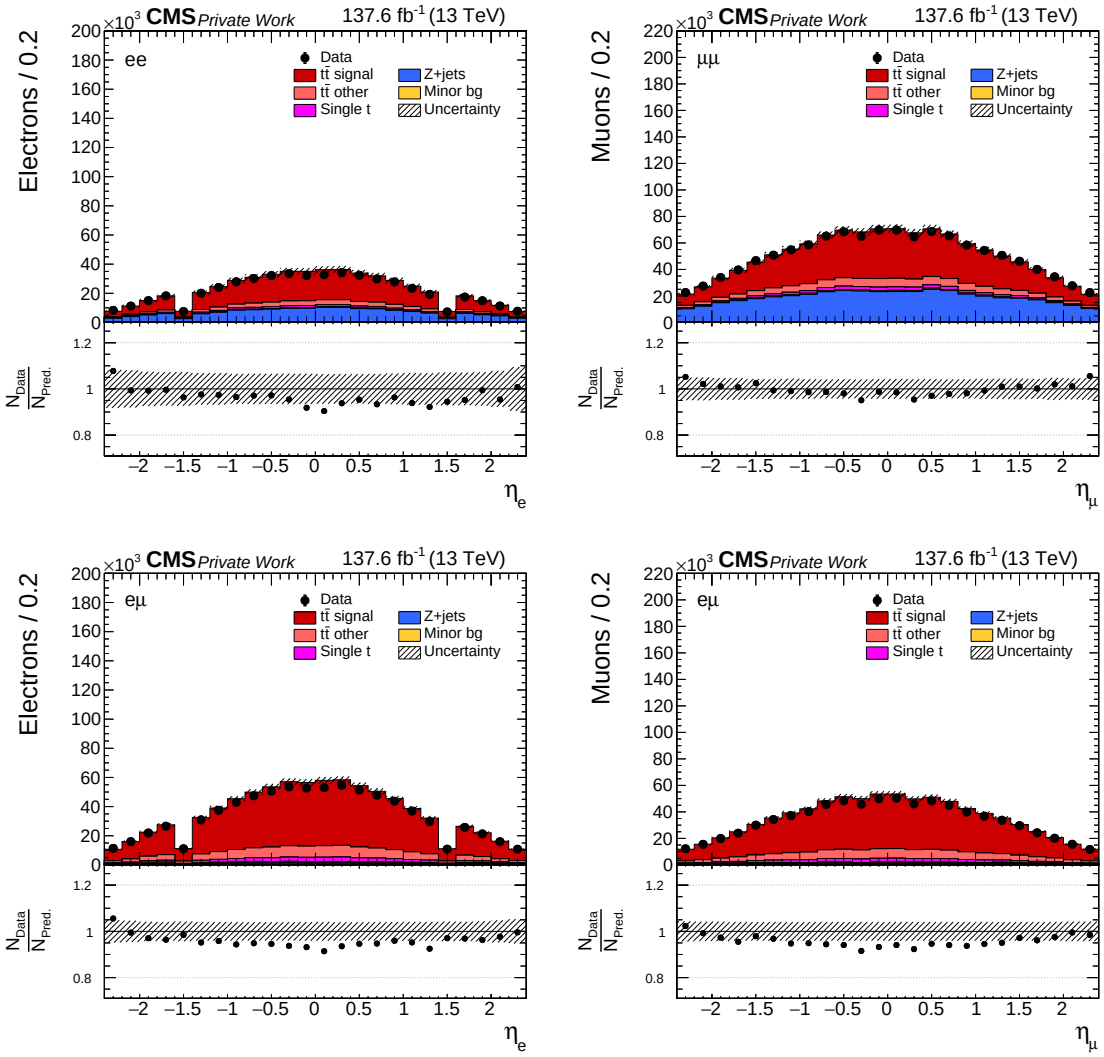

Figure 6.5: Control distributions of the pseudorapidity of electrons (left) and muons (right) in the e^+e^- (top left), $\mu^+\mu^-$ (top right), and $e^\pm\mu^\mp$ (bottom left and right) channels after the lepton pair and jet-related selection requirements. In the e^+e^- and $\mu^+\mu^-$ channels, events satisfying the $E_T^{miss} > 40\,\text{GeV}$ condition are excluded. This plot also include all steps previous to the missing transverse energy requirement as described in Section 6.2.

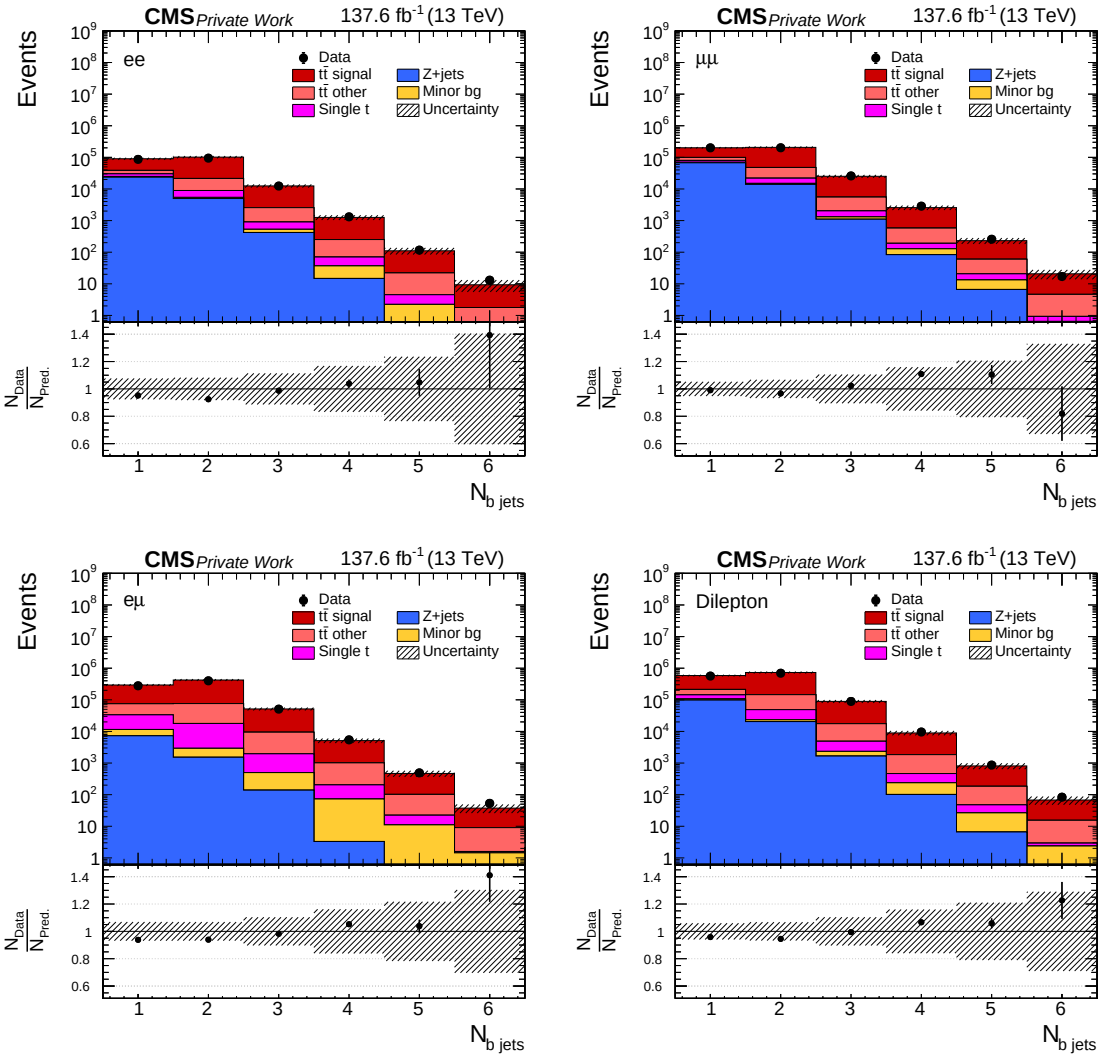

Figure 6.6: Control distributions of the multiplicity of b-jets after the requirement of at least one b-tagged jet, including also all previous steps as described in Section 6.2. DY scale factors are applied. The distributions are shown for the different e^+e^- (upper left), $\mu^+\mu^-$ (upper right) and $e^\pm\mu^\mp$ (lower left) channels, and its combination named as Dilepton (lower right). The hatched area represents the shape systematic uncertainties on the $\mathrm{t\bar{t}}$ signal and backgrounds (see Chapter 9).

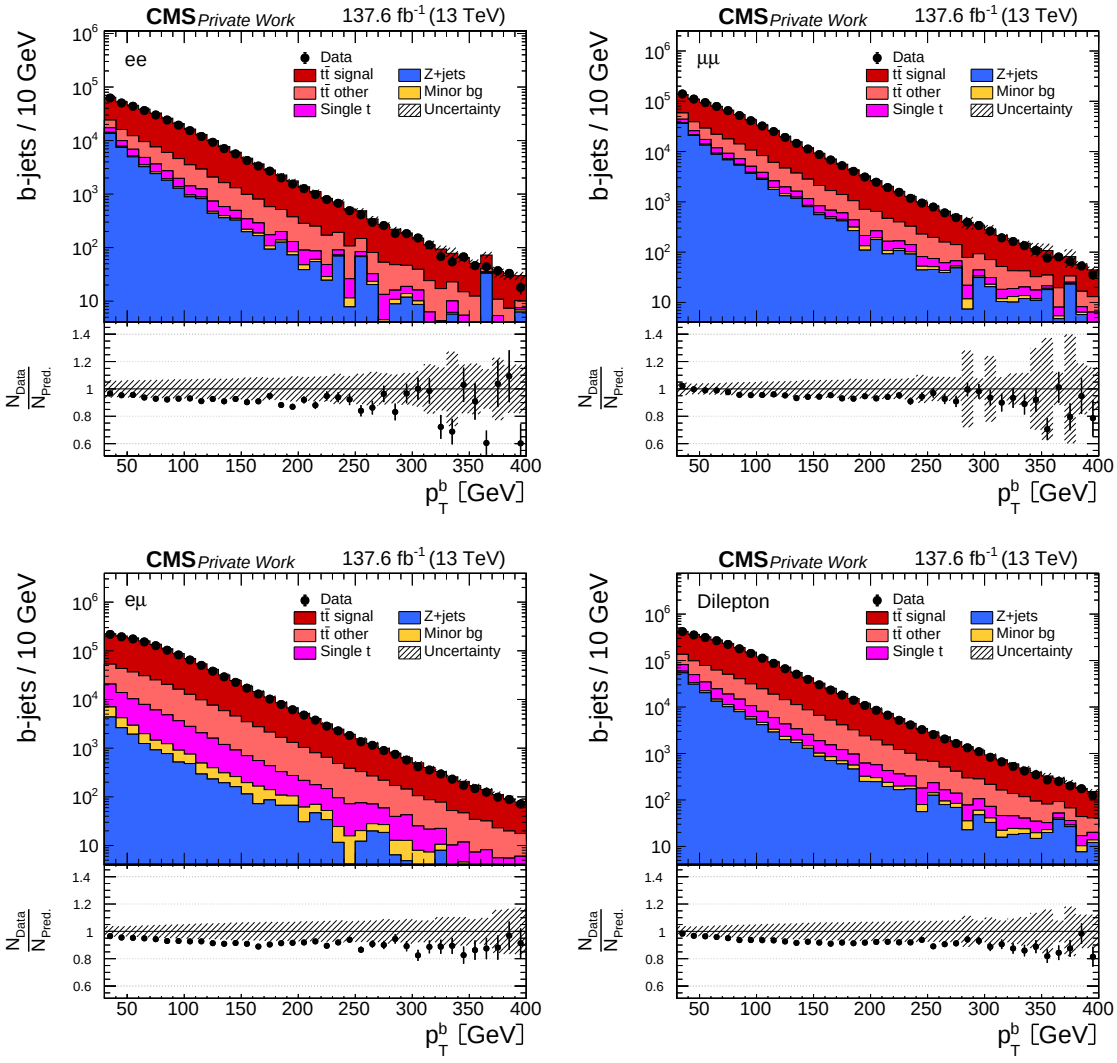

Figure 6.7: Control distributions of the transverse momentum of b-jets after the requirement of at least one b-tagged jet, including also all previous steps as described in Section 6.2. DY scale factors are applied. The distributions are shown for the different e^+e^- (upper left), $\mu^+\mu^-$ (upper right) and $e^\pm\mu^\mp$ (lower left) channels, and its combination named as Dilepton (lower right). The hatched area represents the shape systematic uncertainties on the $\mathrm{t\bar{t}}$ signal and backgrounds (see Chapter 9). This distribution is used as an input to the top-quark pair kinematic reconstruction.

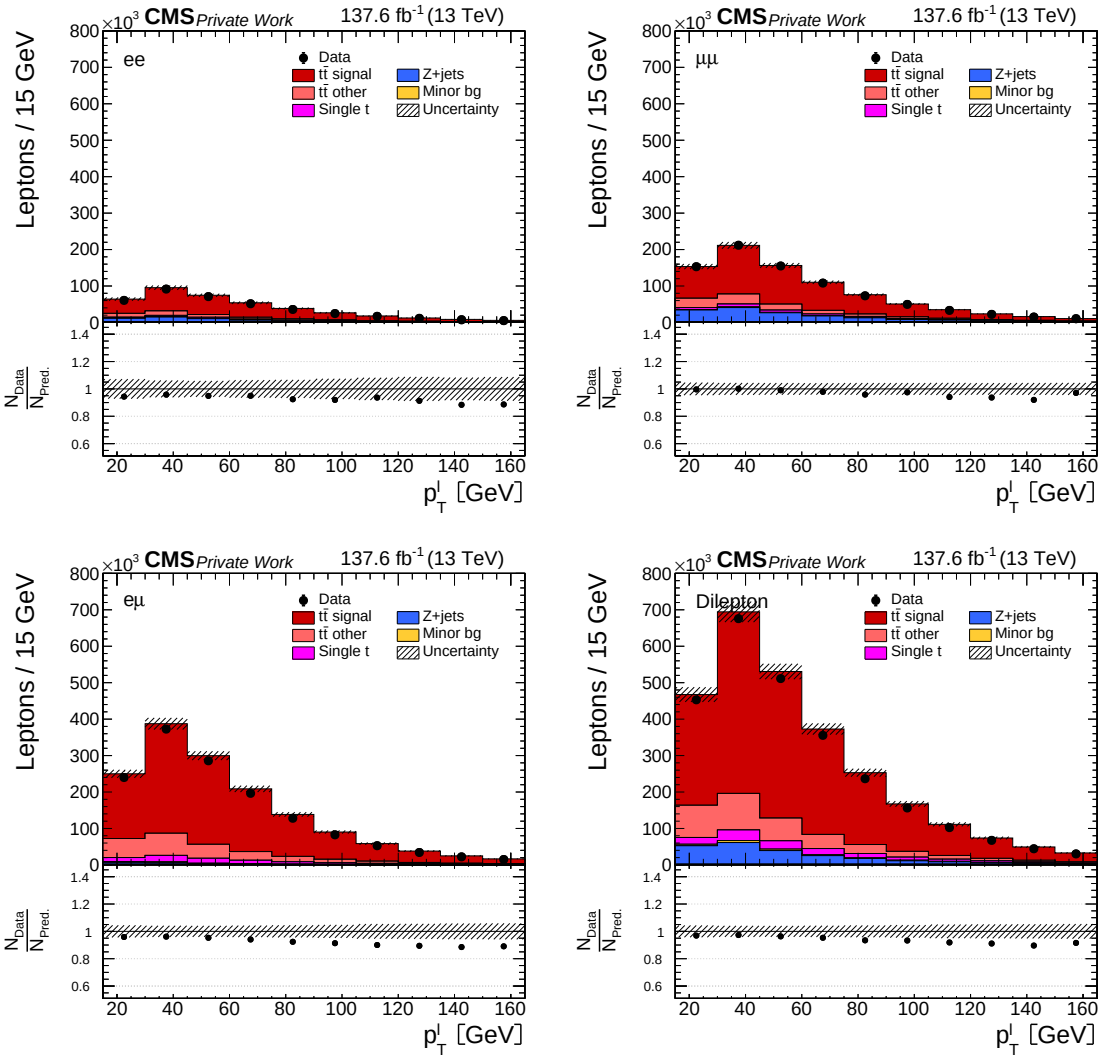

Figure 6.8: Control distributions of the transverse momentum of leptons after the requirement of at least one b-tagged jet, including also all previous steps as described in Section 6.2. DY scale factors are applied. The distributions are shown for the different e^+e^- (upper left), $\mu^+\mu^-$ (upper right) and $e^\pm\mu^\mp$ (lower left) channels, and its combination named as Dilepton (lower right). The hatched area represents the shape systematic uncertainties on the $\mathrm{t\bar{t}}$ signal and backgrounds (see Chapter 9). This distribution is used as an input to the top-quark pair kinematic reconstruction.

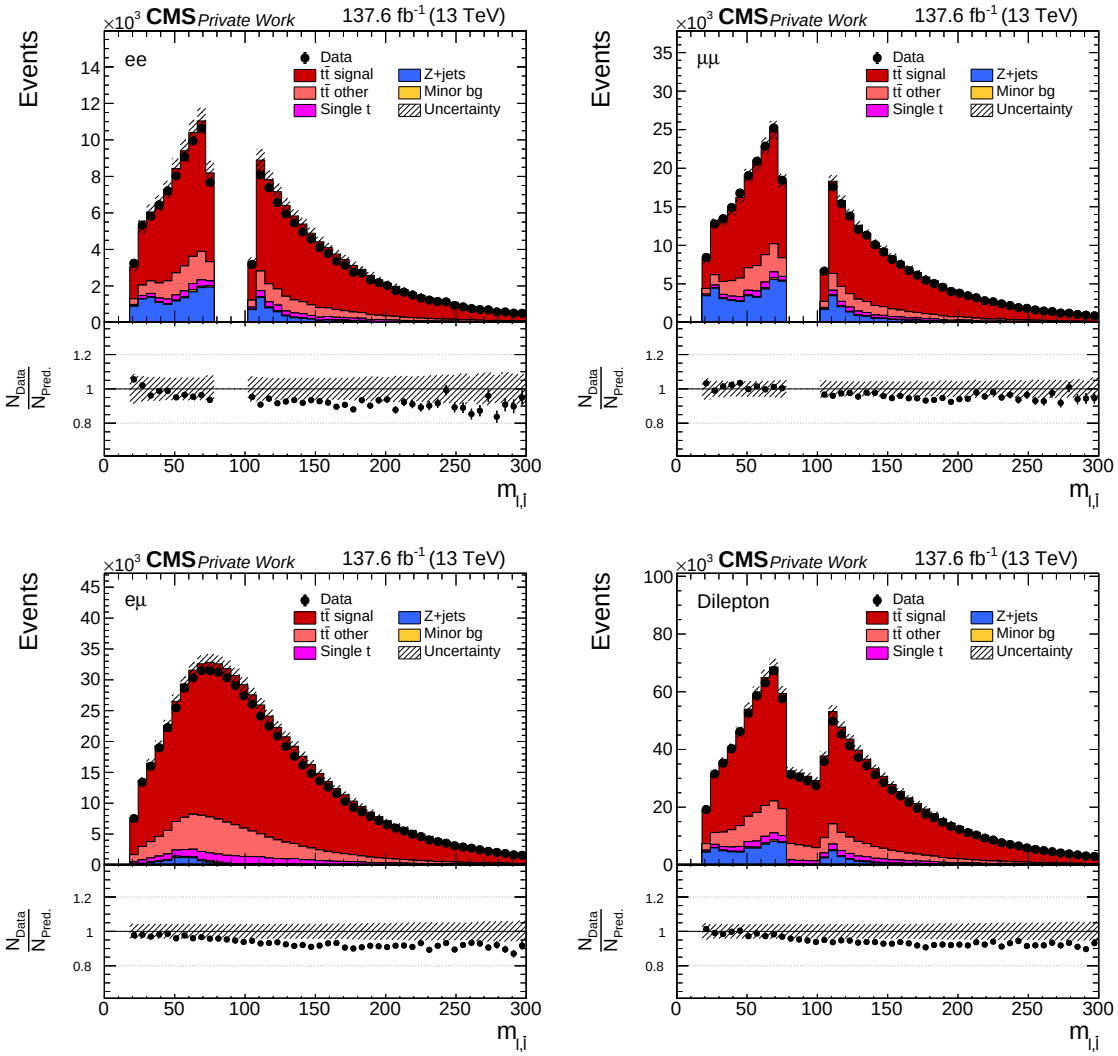

Figure 6.9: Control distributions of the invariant mass of the dilepton system after the requirement of at least one b-tagged jet, including also all previous steps as described in Section 6.2. DY scale factors are applied. The distributions are shown for the different e^+e^- (upper left), $\mu^+\mu^-$ (upper right) and $e^\pm\mu^\mp$ (lower left) channels, and its combination named as Dilepton (lower right). The hatched area represents the shape systematic uncertainties on the $t\bar{t}$ signal and backgrounds (see Chapter 9).

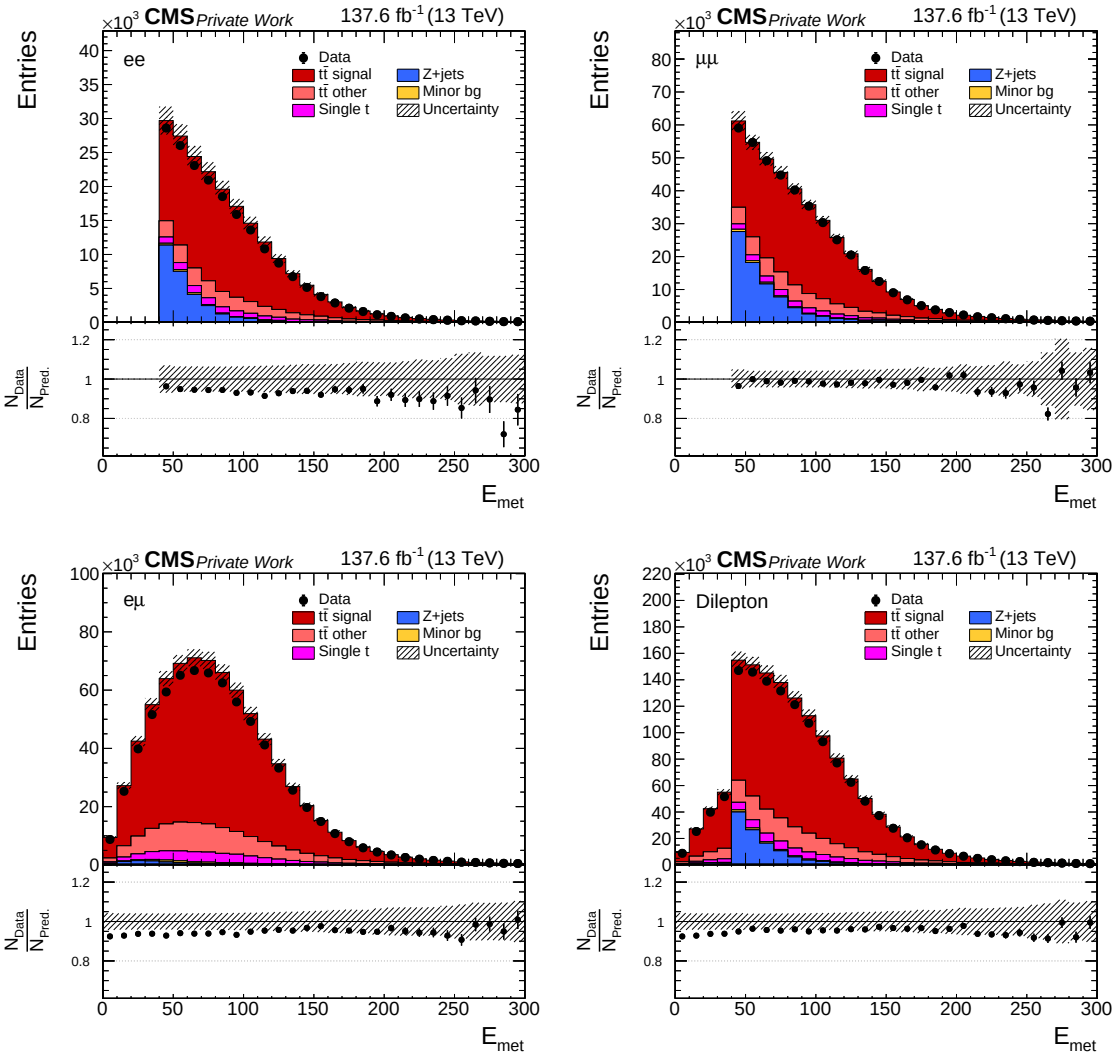

Figure 6.10: Control distributions of the missing transverse energy in the event after the requirement of at least one b-tagged jet, including also all previous steps as described in Section 6.2. DY scale factors are applied. The distributions are shown for the different e^+e^- (upper left), $\mu^+\mu^-$ (upper right) and $e^\pm\mu^\mp$ (lower left) channels, and its combination named as Dilepton (lower right). The hatched area represents the shape systematic uncertainties on the $t\bar{t}$ signal and backgrounds (see Chapter 9). This distribution is used as an input to the top-quark pair kinematic reconstruction.

CHAPTER

7

RECONSTRUCTION OF THE TOP-PAIR KINEMATICS

Contents

7.1 Description of the methods 65

7.1.1 Full kinematic reconstruction 66

7.1.2 Loose kinematic reconstruction 68

7.2 Performance of the kinematic reconstruction 69

7.3 Control distributions 69

Due to their high mass, top quarks decay before their hadronization, but the full final state kinematics of the $t\bar{t}$ system can be reconstructed from the decay products. Since the two neutrinos resulting from the leptonic W boson decay are not detected, some extra assumptions are needed for the reconstruction of the top quarks kinematics, in addition to the measured experimental information.
This chapter describes the two methods used for the kinematic reconstruction: *full* and *loose*, as well as their performance and resulting control distributions. The *full* method reconstructs the individual information of each quark, the t and $\bar{t}$, but it requires the constraint of the top quark mass. The *loose* approach doesn't fix the m_t value but it is only able to reconstruct the combined $t\bar{t}$ system kinematics.

7.1 Description of the methods

This section describes the relevant aspects for the kinematic reconstruction methods used in this analysis.

7.1.1 Full kinematic reconstruction

The *full* reconstruction method (*full KR*) [3,177] makes use of the exact solution of the $t\bar{t}$ kinematics in the dilepton channel obtained using the algebraic method described in [178,179]. Some differential $t\bar{t}$ cross section measurements from the CMS Collaboration have used this method in analysis of data recorded at 8 TeV, e.g. [177,180] and 13 TeV, e.g. [4,6].
In the previous chapters, it has been described how the b-jets and leptons coming from the $t\bar{t}$ decays are reconstructed and identified. The only missing ingredient so far are the neutrinos, which since they aren't detected, contribute to the measured E_T^{miss}-vector in the event. In order to be able to reconstruct the information about their 4-momenta $\nu \equiv (E_\nu, p_{\nu_x}, p_{\nu_y}, p_{\nu_z})$ and $\bar{\nu} \equiv (E_{\bar{\nu}}, p_{\bar{\nu}_x}, p_{\bar{\nu}_y}, p_{\bar{\nu}_z})$, the following kinematic constraints are imposed:

1. Top and antitop quarks masses, m_t and $m_{\bar{t}}$, are constrained to the same value of 172.5 TeV [30].
2. The W boson masses ($m_{W^\pm}$) are assumed to be the same and equal to 80.4 TeV [30].
3. The whole missing transverse energy of the event is assumed to originate entirely from the two neutrinos.

These assumptions lead to the following system of equations, which describe the kinematics of $t\bar{t}$ dilepton events by making use of the conservation of energies and momenta, in the $t\bar{t}$ decay:

$$E_\nu^2 = m_\nu^2 + \sum_{i=x,y,z} p_{\nu_i}^2 \tag{7.1}$$

$$E_{\bar{\nu}}^2 = m_{\bar{\nu}}^2 + \sum_{i=x,y,z} p_{\bar{\nu}_i}^2 \tag{7.2}$$

$$E_x^{miss} = p_{\nu_x} + p_{\bar{\nu}_x} \tag{7.3}$$

$$E_y^{miss} = p_{\nu_y} + p_{\bar{\nu}_y} \tag{7.4}$$

$$m_{W^+}^2 = (E_{l^+} + E_\nu)^2 - \sum_{i=x,y,z} (p_{l_i^+} + p_{\nu_i})^2 \tag{7.5}$$

$$m_{W^-}^2 = (E_{l^-} + E_{\bar{\nu}})^2 - \sum_{i=x,y,z} (p_{l_i^-} + p_{\bar{\nu}_i})^2 \tag{7.6}$$

$$m_t^2 = (E_{l^+} + E_\nu + E_b)^2 - \sum_{i=x,y,z} (p_{l_i^+} + p_{\nu_i} + p_{b_i})^2 \tag{7.7}$$

$$m_{\bar{t}}^2 = (E_{l^-} + E_{\bar{\nu}} + E_{\bar{b}})^2 - \sum_{i=x,y,z} (p_{l_i^-} + p_{\bar{\nu}_i} + p_{\bar{b}_i})^2 \tag{7.8}$$

Here the $E_{l^\pm}$ and $p_{l^\pm_{x,y,z}}$ correspond to the lepton (l^-) and antilepton (l^+) energy and momentum components respectively; while $E_b(E_{\bar{b}})$ and $p_{b_{x,y,z}}(p_{\bar{b}_{x,y,z}})$ represent the $b(\bar{b})$-jet energy and the individual momentum components; the $E_{x,y}^{miss}$ are the two components of the missing transverse energy; and the $p_{\nu_{x,y,z}}(p_{\bar{\nu}_{x,y,z}})$ are the neutrino (antineutrino) momenta components.
Assuming that the masses of the neutrino and antineutrino are equal to zero ($m_\nu = m_{\bar{\nu}} = 0$), the energies E_ν and $E_{\bar{\nu}}$, are determined from their momenta as shown in Equations

7.1 and 7.2. The remaining six unknowns (components of the neutrino and antineutrino momenta) form part of a system of six equations (Equations 7.3-7.8), from which a fourth order polynomial equation for the neutrino momentum component p_{ν_x} can be derived:

$$0 = h_0 p_{\nu_x}^4 + h_1 p_{\nu_x}^3 + h_2 p_{\nu_x}^2 + h_3 p_{\nu_x} + h_4 \tag{7.9}$$

The coefficients h_i depend on the measured values of E_T^{miss} and the four-momenta of the leptons, antileptons, b- and $\bar{b}$-jets [179]. The lepton masses are neglected for simplification and the masses of b-jets are taken as 4.8 GeV, which is the same value used for the mass of the b-quark in the reference $t\bar{t}$ simulation.
The Equation 7.9 is expected to have either two or four real solutions [179]. Due to computing accuracy issues which create indistinguishable solutions, in some very rare cases a total of one or three solutions can be obtained. Two and four solutions per event are observed in $\sim 80\%$ and $\sim 20\%$ of the cases[1] respectively. Only $\sim 0.1\%$ are found to have one or three solutions [179]. In order to handle the ambiguity coming from the multiple solutions, the one with the smallest invariant mass of the $t\bar{t}$ system is chosen. This mass-dependent criterion gives the best overall performance in a wide kinematic range [3].
In a considerable number of events, a real solution can't be found for Equation 7.9 for the corresponding input values of particle momenta and E_T^{miss} measured in the event. In order to recover these cases where experimental effects [2] shift the input values preventing finding a solution, the relevant input observables are smeared according to their detector resolutions. For each event, 100 smearing iterations are performed [3]. In each iteration, the input values of energies and directions of the reconstructed leptons and jets are randomly smeared around the nominal values within their resolution.
Since for each event two leptons and at least two jets are present, several permutations of the lepton-jet pairs to reconstruct the top quarks are possible[3]. For example, for an event with two jets (j_1 and j_2), the leptons (l_1 and l_2) and jets could be combined as ($l_1 j_1$, $l_2 j_2$) or ($l_1 j_2$, $l_2 j_1$). The lepton-jet permutation with the highest number of b-tagged jets, with a physical solution, is chosen over the others and it is required that at least one of the two jets is b-tagged. It can happen that multiple combinations of the same rank in terms of b-tagged jets are present in the same event. In these cases, for every smearing attempt (with index i) a total weight is computed as the product of individual weights for the top quark and antiquark decay chains: $w(lb)_i = w_{m_{l^+b}} \cdot w_{m_{l^-\bar{b}}}$. If no solution is found $w(lb)_i$ it is set to zero for the respective iteration. The weights $w_{m_{l^+b}}$ and $w_{m_{l^-\bar{b}}}$ are based on the expected true spectrum of the invariant mass of the lepton and b-jet system. The chosen lepton-jet permutation is the one with the largest sum of the individual weights of each smearing iteration: $w(lb)_\Sigma = \sum_i w(lb)_i$. In the following steps of the analysis, every jet forming part of an accepted permutation is considered as a b-(anti)quark jet from the corresponding top (anti)quark decay, even if it wasn't previously b-tagged by the b-tagging algorithm.
As the final step of the reconstruction. the top/anti-top quark 4-momentum is evaluated. For the energy the relation $E = \sqrt{m_t^2 + |\vec{p}_{(t/\bar{t})}|^2}$ with $m_t = 172.5$ GeV is used. Here $\vec{p}_{(t/\bar{t})}$ is

[1] These numbers are obtained using the $t\bar{t}$ signal simulation
[2] Mostly due to imperfections in the detector response
[3] The number of these possible permutations increases with the jet multiplicity as $N_{jets}!/(N_{jets} - N_{leptons})!$

obtained from:

$$\vec{p}_{(t/\bar{t})} = \frac{1}{w(lb)_{\Sigma}} \sum_{i}^{100} w(lb)_i \cdot \vec{p}_{(t/\bar{t})_i}, \tag{7.10}$$

where i represents the i-th smearing iteration. Events with no solution after smearing are rejected.

7.1.2 Loose kinematic reconstruction

The reconstructed value of $m_{\mathrm{t\bar{t}}}$ from the full kinematic reconstruction method is highly sensitive to the value set to constrain the top quark mass. The *loose* kinematic reconstruction (*loose KR*) [6], described in this section, is used to reconstruct the $\mathrm{t\bar{t}}$ kinematic variables without using the top quark mass constraint and taking as input the reconstructed lepton pair, two jets and E_T^{miss}.
The first step in this method is to chose which jets will be taken as the input b-quark candidates. The selection of the two jets is performed following the next steps by first selecting only jets with $M_{lb} < 180\,\mathrm{GeV}$. The M_{lb} value is computed by selecting for each of two possible lepton and jet assignments, the maximum M_{lb} of the two decay "legs", corresponding to the top quark and top antiquark. Then, the minimum value of this observable over the two possible jet-lepton assignments is taken.
Following the basic logic of the event topology studied in this analysis, combinations with 2 b-tagged jets are prefered over combinations with 1 b-tagged jet. In the cases where multiple combinations with the same number of b-tagged jets are available, jets with the higher p_T are chosen. In this case there is no ambiguity for the b-jets like in the *full* method, where one needs to associate the top and anti-top quarks with their decay products $l\bar{b}$ and $\bar{l}b$.
The whole missing transverse energy of the event is assumed to originate entirely from the two neutrinos from the $\mathrm{t\bar{t}}$ decay, this means that the transverse momentum of the $\nu\bar{\nu}$ system is computed directly from E_T^{miss}. The longitudinal momentum of the $\nu\bar{\nu}$ system is estimated from the longitudinal momentum and the energy of the lepton pair. The conditions $M(\nu\bar{\nu}) \geq 0$ and $M(W^+W^-) \geq 2M_W$ are imposed on the invariant masses of the neutrino pair and the W bosons respectively[4].
The algorithm can be summarized in the following steps which are executed for each event:

1. Two jets are selected from the input jet collection (more information at the beginning of this section) and $M_{lb} < 180\,\mathrm{GeV}$ is required for both lepton-b pairs.

2. The transverse momenta of $\nu\bar{\nu}$ is computed as $p(\nu\bar{\nu})_{x,y} = E_T^{miss}$.

3. If $p_T(\nu\bar{\nu}) < E(l\bar{l})$, then $p(\nu\bar{\nu})_z = p(l\bar{l})_z$. Otherwise $p(\nu\bar{\nu})_z = 0$.

4. If $|p(\nu\bar{\nu})| < E(l\bar{l})$, then $E(\nu\bar{\nu}) = E(l\bar{l})$. Otherwise $E(\nu\bar{\nu}) = |p(\nu\bar{\nu})|$.

5. The 4-momentum of the $l\bar{l}\nu\bar{\nu}$ system is computed from the leptons and the $\nu\bar{\nu}$ energy and momentum determined in the previous steps: $l\bar{l}\nu\bar{\nu} = l + \bar{l} + \nu\bar{\nu}$.

6. If $M(l\bar{l}\nu\bar{\nu}) < 2M_W$ where $M_W = 80.4\,\mathrm{GeV}$, then $l\bar{l}\nu\bar{\nu}$ is parametrized in terms of p_x, p_y, y, M. Here M is set to $M(l\bar{l}\nu\bar{\nu}) = 2M_W$.

[4]These requirements have only a minor effect on the performance of the reconstruction.

7. Finally, the 4-momentum of the $t\bar{t}$ system is calculated as $t\bar{t} = l\bar{l}\nu\bar{\nu} + b + \bar{b}$.

As can be seen from the final step, this method only reconstructs the $t\bar{t}$ system, but not the top quark and antiquark kinematics separately. This is directly related to the fact that, only the information of the $\nu\bar{\nu}$ system is extracted, without reconstructing the individual kinematics of ν and $\bar{\nu}$. Therfore, only $t\bar{t}$ kinematic variables can be measured, but not individual top or anti-top quark observables. For example, it is possible to use this method for $p_{\mathrm{T}}(t\bar{t})$ and $y(t\bar{t})$, but not for $p_{\mathrm{T}}(t)$ or $y(t)$.

7.2 Performance of the kinematic reconstruction

As stated in Section 6.2, only events with a valid solution of the kinematic reconstruction are accepted. A very good estimator of the performance of the kinematic reconstruction is to check which part of the total number of input events can be solved by the method. The efficiency of the kinematic reconstruction can be defined as $\epsilon_{kin.reco} = N_{solved}/N_{input}$ and its value in data ($\epsilon^{data}_{kin.reco}$) and MC ($\epsilon^{MC}_{kin.reco}$) are about 90% for the different ee, $e\mu$ and $\mu\mu$ channels[5]. In order to correct for possible differences between $\epsilon^{data}_{kin.reco}$ and $\epsilon^{MC}_{kin.reco}$, a uniform scale factor $SF_{kin.reco.} = \epsilon^{data}_{kin.reco}/\epsilon^{MC}_{kin.reco}$ is a computed and applied for each channel. The obtained values for $SF_{kin.reco.}$ are very close to unity[6], showing a good agreement between simulation and data.

Figure 7.1 shows the mean and RMS of the distribution of the difference between the values of the reconstructed observable at detector level and the true values at generator level, for the $p_{\mathrm{T}}(t)$, $y(t)$, $M(t\bar{t})$, $p_{\mathrm{T}}(t\bar{t})$ and $y(t\bar{t})$ observables. Values for both *full KR* and *loose KR* methods are shown for the $t\bar{t}$ system observables, while only *full KR* values are shown for the individual top quark observables ($p_{\mathrm{T}}(t)$ and $y(t)$) due to, as explained before, that the *loose KR* is unable to reconstruct the information of the individual top quarks. The mean and RMS values, reflect not only the genuine resolution of the algorithm, but also the possible usage of wrong input jets and/or wrong jet to lepton assignment. From the $t\bar{t}$ observables plots one can conclude that similar results are obtained for the full and loose algorithms. As studied in [6], the $M(lb) < 180\,\mathrm{GeV}$ cut has a big impact on the resolution of the *loose KR* making it very similar to the resolution of the *full KR*. In general, both methods show a good performance in the kinematic ranges used in this analysis and showing comparable $t\bar{t}$ kinematic resolutions and reconstruction efficiency.

7.3 Control distributions

The event kinematic reconstruction methods described in this chapters are used for the determination of the kinematics of top quarks and $t\bar{t}$ system. Figure 7.2 shows the control distributions of the kinematic quantities of the top quark system. The distribution of the transverse momentum of the top quark (left plot) shows a good agreement between experimental data and simulation at small p_{T}. However, the ratio between the data and the MC shows a clear negative slope as function of $p_{\mathrm{T}}(t)$, indicating a too hard momentum spectrum

[5] This value has been estimated using the $t\bar{t}$ signal simulation

[6] The values for the $SF_{kin.reco.}$, for the *full* and *loose* KR methods, are between 0.9835 and 1.0070 for the different channels and years

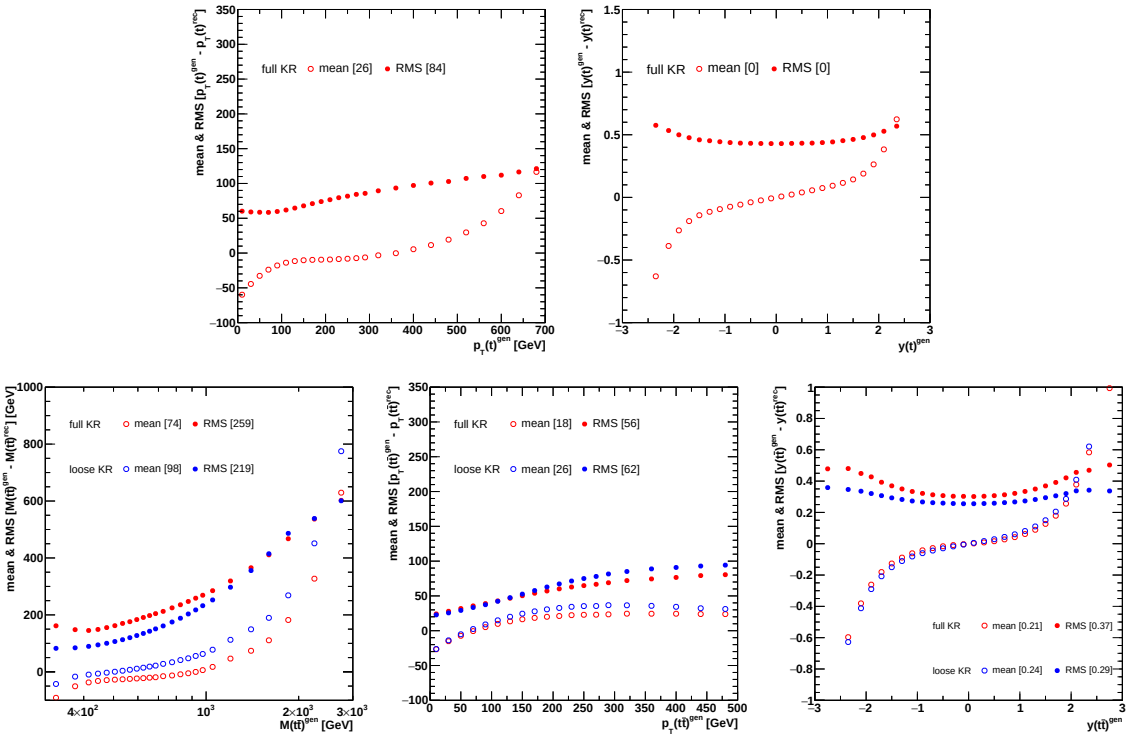

Figure 7.1: The mean and RMS of the distribution of the difference between the reconstructed (detector) and true (generator) values of kinematic observables. The two plots on the top, show the performance for $p_{\mathrm{T}}(t)$ (left) and $y(t)$ (right) using the *full* kinematic reconstruction algorithm. In the bottom, the values are shown for the *full* and *loose* kinematic reconstruction algorithms for $M(\mathrm{t\bar{t}})$ (left), $p_{\mathrm{T}}(\mathrm{t\bar{t}})$ (middle) and $M(\mathrm{t\bar{t}})$ (right) observables. The average values of the mean and RMS are given in brackets.

in the $\mathrm{t\bar{t}}$ MC. This effect has been observed in previous $\mathrm{t\bar{t}}$ production cross section measurements at 7 TeV [181], 8 TeV [3] and 13 TeV [4, 6, 182, 183], and its origin it is still not fully understood. From now on, this feature will be referred as "the p_T-slope problem", and it will be one of the goals of this work to look for its possible correlation with other observables. The other distribution shown in Figure 7.2 (right plot), is the rapidity of the top quark, which is in general well described by the simulation, except in the central region where the simulation is a bit higher than data.

In Figure 7.3 the control distributions of the kinematic variables of the $\mathrm{t\bar{t}}$ system are presented for the *full* (plots on the left) and *loose* (plots on the right) kinematic reconstruction algorithms. The transverse momentum is overall well described by the simulation. The invariant mass of the $\mathrm{t\bar{t}}$ system is reasonably well described by the simulation for the complete mass range. A slight excess in the simulation is observed in central rapidity $y(\mathrm{t\bar{t}})$, but otherwise the data are well described by the simulation. These plots show that the distributions obtained using the two kinematic reconstruction methods are in general very similar. One of the few differences is observed in the total number of reconstructed events, being slightly higher for the *loose KR* method, which can also be observed in Table 6.4.
In general, all distributions show a reasonably good description of the experimental data by

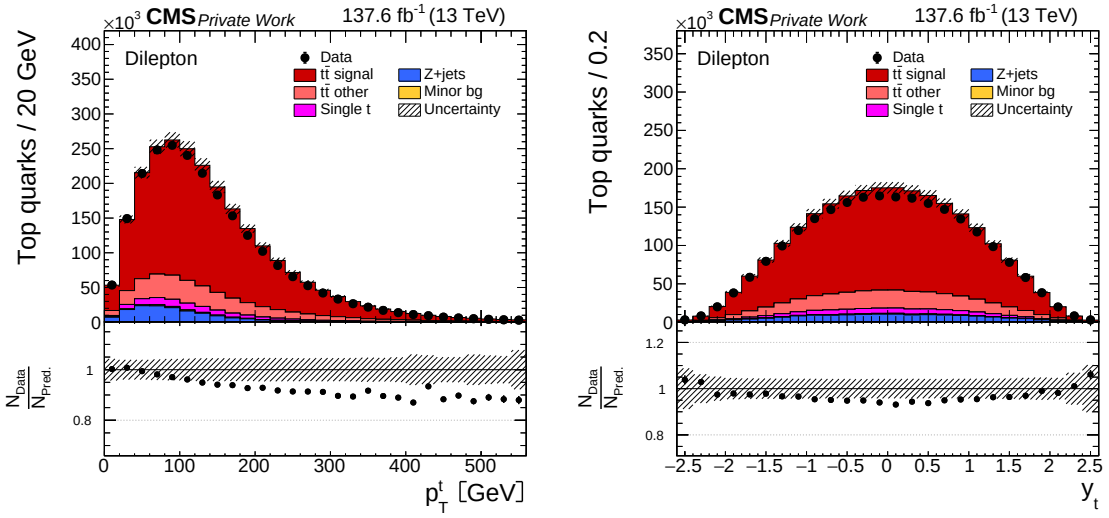

Figure 7.2: Distribution of transverse momentum (left) and rapidity (right) of the reconstructed top quark and antiquark. Events include all selection requirements described in Section 6.2.

the simulation. This is very important since the MC simulations are used for describing and subtracting the contributions from background sources (see Section 8.1), and for correcting detector effects (see unfolding in Section 8.2) in the signal events.

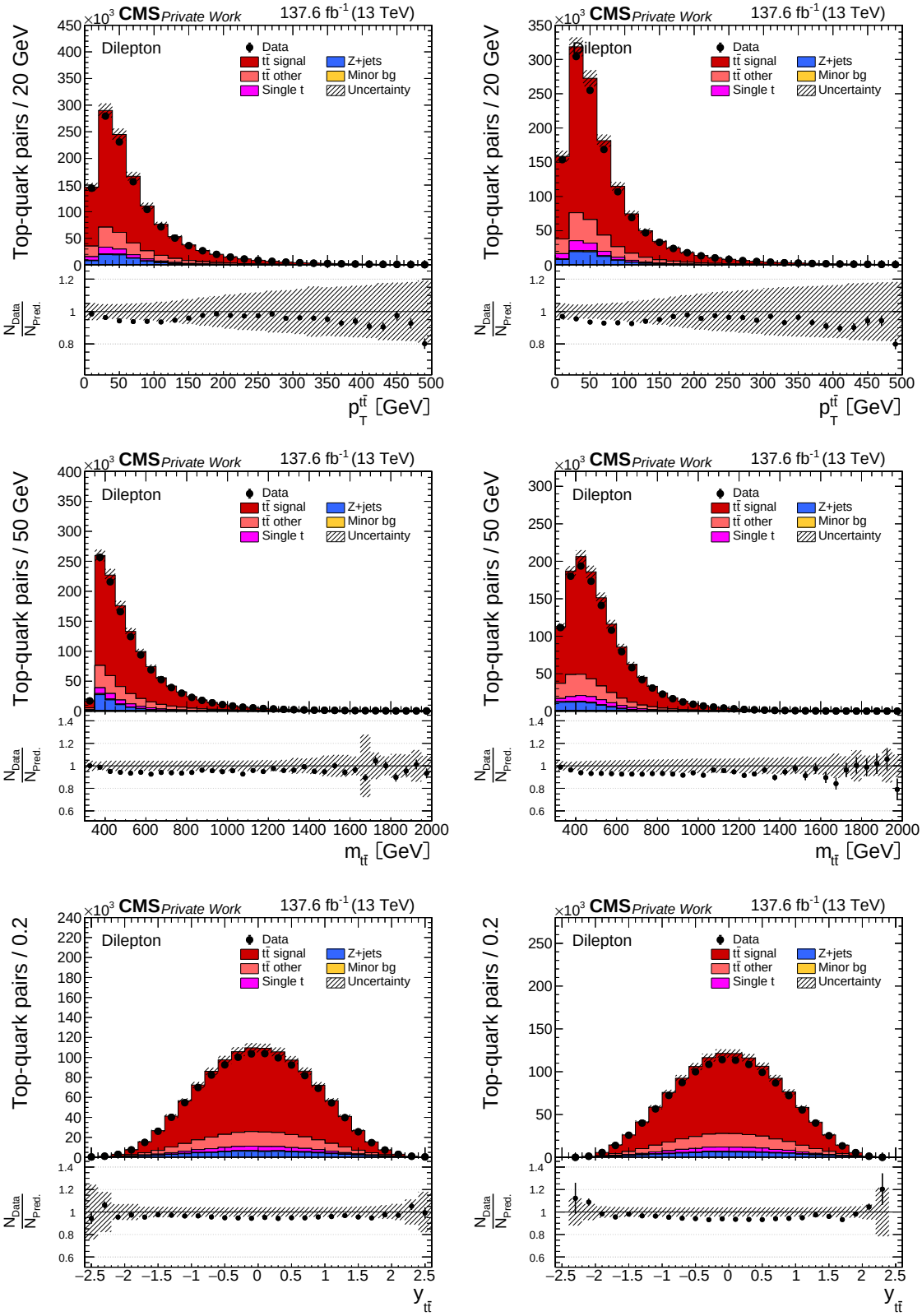

Figure 7.3: Transverse momentum (top), invariant mass (middle) and rapidity (bottom) of the reconstructed $\mathrm{t\bar{t}}$ system. Results are shown for *full* (left) and *loose* (right) kinematic reconstruction. Events include all selection requirements described in Section 6.2.

CHAPTER

8

CROSS SECTION MEASUREMENT

Contents

8.1 Background subtraction 74
8.2 Unfolding of the experimental results 74
8.2.1 TUnfold minimization 75
8.3 Multi-differential $t\bar{t}$ production cross sections 77
8.3.1 Cross section definition 77
8.3.2 Combination of the results from different years and channels 77
8.3.3 Phase space definition 78
8.3.4 Efficiency, purity and stability 81

This work aims at the measurement of multi-differential $t\bar{t}$ production cross sections describing the production rate in certain kinematic ranges of up to three observables simultaneously. The events can be separated into different groups defined by different ranges of the observables (e.g. events with $50\,\text{GeV} \geq p_{\text{T}}(t\bar{t}) \geq 80\,\text{GeV}$ and $N_j = 1$), which are used for a measurement of the production cross section in the associated differential bin. A double-differential (2D) cross section, measured in bins of an observable O_1 (e.g. $p_{\text{T}}(t\bar{t})$) which is also measured in bins of another observable O_2 (e.g. N_{jet}), will be denoted in the following as $[O_2, O_1]$ (e.g. $[N_{\text{jet}}, p_{\text{T}}(t\bar{t})]$). For the case of triple-differential (3D) cross sections a similar notation $[O_3, O_2, O_1]$ is used, where O_3 is a third observable. The procedures explained in this chapter, like unfolding (Section 8.2) and cross section determination (Section 8.3), will be explained following a one-dimensional notation, but they are equivalent for the case of the 2D or 3D cross sections since in this work the multi-dimensional binnings are "projected" into a one-dimensional scheme.
Measurements of absolute and normalized cross sections will be presented. The absolute differential cross sections contain information about the $t\bar{t}$ signal production rate and also the associated shape as a function of the measured observable. For the case of normalized cross

sections, only the shape dependence is present but it has the advantage of a better precision since it is less affected by normalization effects like the uncertainty on the total integrated luminosity. In this chapter, the procedure for the measurement of multi-differential cross sections is presented, while the full list of measurements, as well as their results, is presented in Chapter 10.

8.1 Background subtraction

The reconstructed signal event rates (N_i^{sig}), for a given bin i, can be computed by subtracting the background contributions from the total reconstructed events (N_i^{data}) which passed the selection criteria (see Sections 6.2 and 7.1):

$$N_i^{sig} = (N_i^{data} - N_i^{\text{non-t}\bar{\text{t}}\,\text{BG}}) \cdot f_{sig}, \quad 1 \leq i \leq n \tag{8.1}$$

In this equation, N_i^{BG} is the estimated number of background events coming from non-$\text{t}\bar{\text{t}}$ background sources (introduced in Section 6.3) after the full event selection. The term ($N_i^{data} - N_i^{BG}$) denotes the number of $\text{t}\bar{\text{t}}$ events. To obtain the desired number of $\text{t}\bar{\text{t}}$ signal events, this term is then multiplied by the factor f_{sig}, which is the fraction of $\text{t}\bar{\text{t}}$ signal events ($N_{\text{t}\bar{\text{t}}}^{MC\,signal}$) over the total $\text{t}\bar{\text{t}}$ events ($N_{\text{t}\bar{\text{t}}}^{MC\,signal} + N_{\text{t}\bar{\text{t}}}^{MC\,other}$) estimated using the simulation samples. The usage of this factor makes the result independent from the normalization of the $\text{t}\bar{\text{t}}$ simulation sample.

8.2 Unfolding of the experimental results

The obtained signal yields ("detector level") distributions are distorted from the "truth" distributions due to detector effects, statistical fluctuations, and other effects like background events being wrongly reconstructed as signal. Since the event properties are measured only with finite precision and limited efficiency, some events may be reconstructed in the wrong bin or even not reconstructed at all. In order to obtain cross section measurements, the data unfolding procedure described in reference [184] is used. In this process, as shown in Figure 8.1, the information about the truth content of the bins is extracted for a given measurement. The whole problem can be mathematically described as:

$$M_i^{sig} = \sum_{j=1}^{m} A_{ij} M_j^{unf} \quad 1 \leq i \leq n,\ 1 \leq j \leq m \tag{8.2}$$

Here the M_j^{unf} in m bins represents the true distribution, independent of the detector effects; while M_i^{sig} in n bins is the expected number of signal events at detector level, which can be different to the observed N_i^{sig} due to statistical fluctuations.
The term A_{ij} is the element of the response matrix A, which represents the probability to find an event produced in bin j to be measured in bin i. The response matrix contains information about migrations among bins as well as the detector efficiency and acceptance. It is computed using the reference $\text{t}\bar{\text{t}}$ signal simulation (see Section 4.7) for each measured observable and separately for both definitions of the reference phase space (see Section 8.3.3):

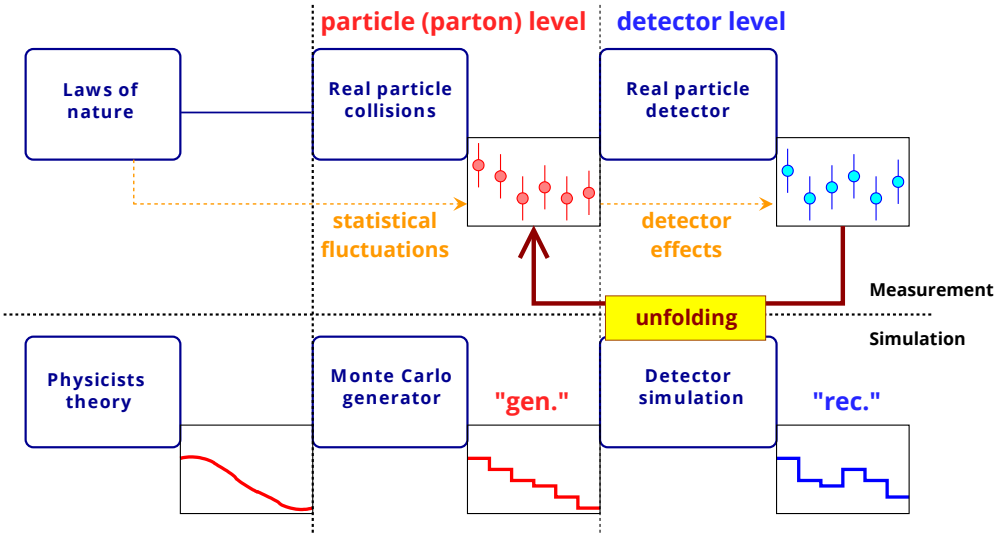

Figure 8.1: Sketch describing the logic of the unfolding process. The label gen.(rec.) is referred to the generator (reconstructed) level in simulation. The parton and particle levels, are phase space definitions further discussed in Section 8.3.3. Modified figure from [185].

$$A_{ij} = \frac{N_{ij}^{MC,rec\wedge gen}}{N_i^{gen}} \tag{8.3}$$

Here the number $N_{ij}^{MC,rec\wedge gen}$ corresponds to the number of generated events in truth bin j and reconstructed at detector level in bin i, while N_i^{gen} is the total number of generated events in truth bin j, including events which are not reconstructed in any of the bins i. An example of the migration matrix for the $[M(\mathrm{t\bar{t}}),y(t)]$ cross section is shown in Figure 8.2, separately for parton and particle level.

8.2.1 TUnfold minimization

The TUnfold algorithm [186] was used for the unfolding in this analysis. The chosen method is based on least square minimization plus Tikhonov regularization [187]. The regularization reduces the effect of the statistical fluctuations present in N_i^{sig} on the high-frequency content of the estimated value of the truth distribution M_j^{unf} computed by the unfolding algorithm, referred to as $\hat{M}_j^{unf}$ in the following.
The used configuration from the TUnfold package is based on the minimization of:

$$\chi^2_{\mathrm{TUnfold}} = \chi^2_A + \tau^2\chi^2_L, \tag{8.4}$$

where:

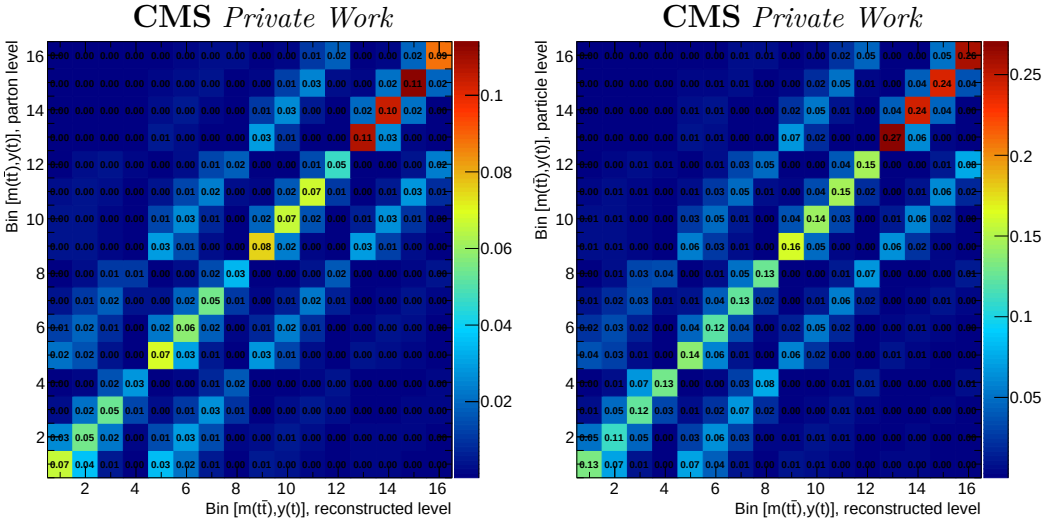

Figure 8.2: The response matrices for the $[M(\mathrm{t\bar{t}}),y(t)]$ cross section defined at parton (left) and particle (right) levels. The matrix is obtained from the POWHEG + PYTHIA8 $\mathrm{t\bar{t}}$ signal sample. The complete binning information for this cross section can be found in Table C.29.

$$\chi^2_A = (\mathbf{N}^{\mathrm{sig}} - \mathbf{A}\mathbf{M}^{\mathrm{unf}})^{\mathrm{T}}\, \mathbf{Cov}^{-1}_{\mathbf{N}^{\mathrm{sig}}\mathbf{N}^{\mathrm{sig}}}\, (\mathbf{N}^{\mathrm{sig}} - \mathbf{A}\mathbf{M}^{\mathrm{unf}}) \tag{8.5}$$

$$\chi^2_L = (\mathbf{M}^{\mathrm{unf}} - \mathbf{M}^{\mathrm{bias}})^{\mathrm{T}} (\mathbf{L}^{\mathrm{T}}\mathbf{L}) (\mathbf{M}^{\mathrm{unf}} - \mathbf{M}^{\mathrm{bias}}) \tag{8.6}$$

The term χ^2_A is the usual least square minimization, while the χ^2_L is responsible for the regularization. The vectors $\mathbf{N}^{\mathrm{sig}}$, $\mathbf{M}^{\mathrm{unf}}$ and the matrix $\mathbf{A}$ were described in the previous section and $\mathbf{Cov}_{\mathbf{N}^{\mathrm{sig}}\mathbf{N}^{\mathrm{sig}}}$ denotes the covariance matrix of $\mathbf{N}^{\mathrm{sig}}$. In this work, $\mathbf{Cov}_{\mathbf{N}^{\mathrm{sig}}\mathbf{N}^{\mathrm{sig}}}$ is a diagonal matrix with entries set equal to the event yields $\mathbf{N}^{\mathrm{data}}_i$ according to Poisson statistics.

The factor τ^2 is known as the regularization strength and $\mathbf{M}^{\mathrm{bias}}$ is the bias vector taken from the $\mathrm{t\bar{t}}$ signal simulation at generator level. The matrix $\mathbf{L}$ represents the so-called regularization conditions, which in this work are defined as the second derivative[1] of $\hat{\mathbf{M}}^{\mathrm{unf}}$. The case $\tau = 0$ corresponds to the case where no regularization is applied, whereas for very large τ values the result is strongly biased towards $\mathbf{M}^{\mathrm{bias}}$. This means that it is essential to choose the optimal regularization strength, which in this analysis is determined using the minimization of the average global correlation coefficient[2] method [184]. In this procedure, the unfolding is repeated[3] for different choices of the regularization parameter and the average over all the bins of the global correlation coefficient is recorded. The regularization parameter is chosen as the one corresponding to the minimum average value. For all unfolded cross sections in this work, the contribution of the regularization term $(\tau^2\chi^2_L)$ to $\chi^2_{\mathrm{TUnfold}}$ is always less than

[1] The chosen $\mathbf{L}$ corresponds to the initialization of a matrix with three non-zero elements per row ($L_{i,i} = 1$; $L_{i,i+1} = -2$ per row and $L_{i,i+2} = 1$) and $m - 2$ rows.

[2] The average global correlation coefficient is a measure of the level of bin-to-bin correlations in the unfolded covariance matrix $\mathbf{Cov}_{\mathbf{M}^{\mathrm{sig}}\mathbf{M}^{\mathrm{sig}}}$.

[3] 50 iterations are used in this analysis

1%.
The problem described in this section can be summarized as the finding of $\hat{\mathbf{M}}^{\text{unf}}$ and its covariance matrix $\mathbf{Cov}_{\hat{\mathbf{M}}^{\text{unf}}\hat{\mathbf{M}}^{\text{unf}}}$, taking $\mathbf{N}^{\text{sig}}$, $\mathbf{Cov}_{\mathbf{N}^{\text{sig}}\mathbf{N}^{\text{sig}}}$, response matrix $\mathbf{A}$ and $\mathbf{M}^{\text{bias}}$ as inputs.

8.3 Multi-differential $t\bar{t}$ production cross sections

In this section, it is explained how the differential cross sections are computed from the unfolded event yield distributions. The phase space definition and different estimators for the quality of the chosen binning schemes are also discussed.

8.3.1 Cross section definition

After performing the unfolding of the measured distributions, the absolute differential cross section in bin i for a variable X can be computed as:

$$\left(\frac{d\sigma}{dX}\right)_i = \frac{1}{\Delta x_i} \cdot \frac{N_i^{unf}}{BR \cdot L} \tag{8.7}$$

Here N_i^{unf} is the observed number of signal events in a bin i with width Δx_i. This value is the output from the unfolding process, which means that the detector efficiency and acceptance, and also the migrations between bins have been corrected. The terms L and BR are the integrated luminosity and the dilepton branching ratio respectively.
The normalized differential cross sections can be obtained dividing Equation 8.7 by the total $t\bar{t}$ production cross section[4] corresponding to the visible range of the observable X, leading to the following expression:

$$\left(\frac{1}{\sigma}\frac{d\sigma}{dX}\right)_i = \frac{1}{\Delta x_i} \cdot \frac{N_i^{unf}}{\sum_i N_i^{unf}} \tag{8.8}$$

From this equation one can see that the normalized differential cross sections are independent of the total rate of the input distribution, since any component affecting only the total normalization of the distribution of any observable X cancels out. This directly translates into a better precision compared to absolute cross sections. It also means that only shape comparisons between the measured and theoretically predicted differential distributions can be performed for the the normalized cross sections.

8.3.2 Combination of the results from different years and channels

For the production of the combined (dilepton) channel results using the full Run-II data, after the $t\bar{t}$ event selection and kinematic reconstruction, all needed inputs for the normalized and absolute differential cross section measurements are obtained by combining the event yields of the individual decay channels in each year. The differential measurement is performed over these combined distributions. This means that first, all data from the different years and channels are combined and then the unfolding procedure is performed over this combined data. This is possible due to the similar detector conditions during the three years,

[4]The total $t\bar{t}$ production cross section for a given X is defined as: $\sigma_X^{\Sigma} = (\sum_i N_i^{unf})/(BR \cdot L)$

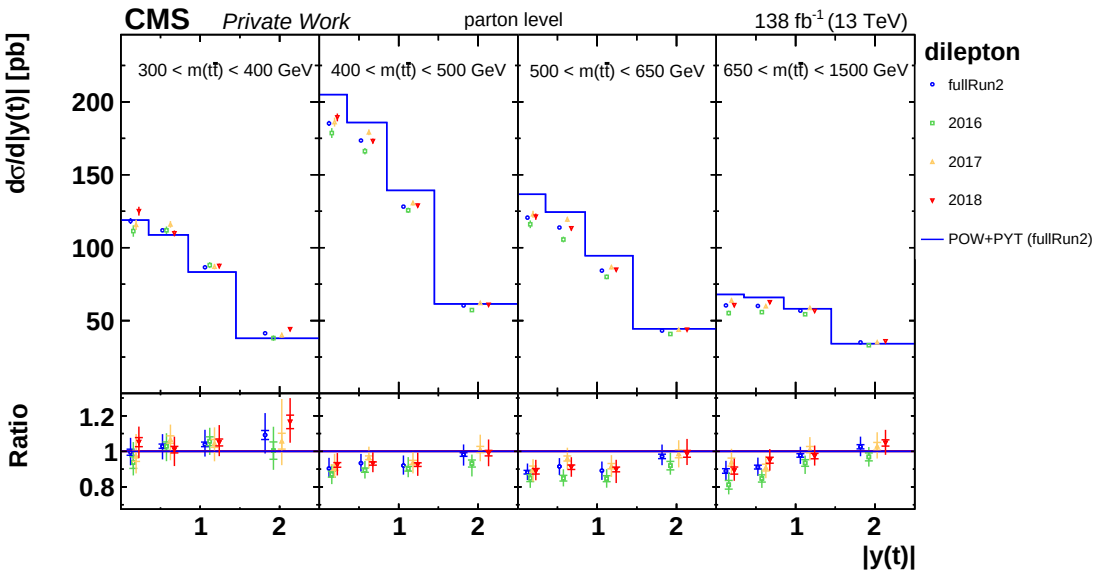

Figure 8.3: Results for the unfolded $[M(\mathrm{t\bar{t}}),y(t)]$ absolute cross section, at parton level, for the different years, including the combined full Run-II results (data points). The predicted distributions by the reference simulation (POW+PYT) are also shown (lines). The ratios presented in the bottom part of the plot are computed relative to the 'POW+PYT' prediction. The inner vertical bars on the data points represent the statistical uncertainties and the full bars include also the systematic uncertainties added in quadrature. More information about the uncertainties can be found in Chapter 9.

making the response matrices and therefore the quality of unfolded cross section results comparable across the different years. This is also the case for the different channels, where results of similar precision are obtained for the individual cross sections of the ee, $e\mu$, and $\mu\mu$ channels.
Figures 8.3 and 8.4 ilustrate the previous statements by showing the comparisons of the $[M(\mathrm{t\bar{t}}),y(t)]$ absolute parton level cross section between different years and channels, respectively. The details about the uncertainties shown in these plots are discussed in Chapter 9. These exemplary plots show a good consistency of results across years and channels. A This is also the case for the other measurements of this analysis.

8.3.3 Phase space definition

For every computation of a certain cross section, the definition of the associated phase space is needed. A phase space depends on the definition of the physics objects and their decay products, and also on imposed conditions on their kinematics, like p_T and η.
The event selection requirements (Section 6.2) define the *detector phase space*, also referred to as detector level. The *full phase space* at generator level, on the other hand, is not limited by any kinematic requirements. The *fiducial phase space* is contained within the *full phase space*, but is restricted to the region that follows closely the CMS detector acceptance and the kinematic selection cuts applied in the analysis for final state objects such as leptons and jets. Two different definitions of top quarks and top antiquarks are used in this analysis:

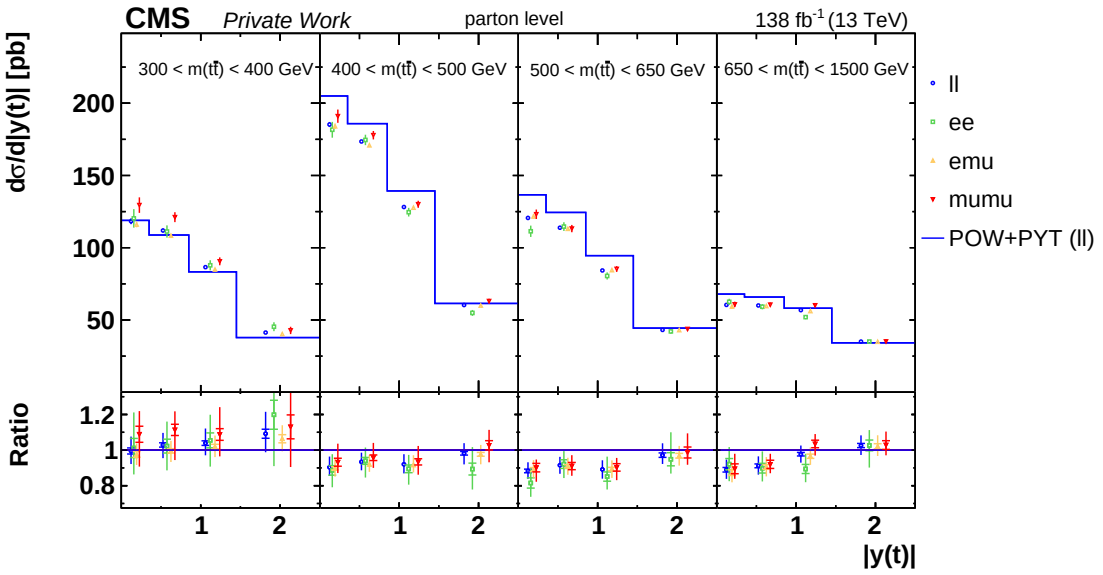

Figure 8.4: Results for the unfolded $[M(t\bar{t}),y(t)]$ absolute cross section (data points), at parton level, for the different channels, including the combined dileptonic channel (ll). See description about plotted lines, ratios and vertical bars from Figure 8.3.

parton level and the particle level.

At **parton level**, the cross sections are defined with respect to top quarks or antiquarks at parton level before their decay and after QCD radiation. This definition imitates the model assumptions of the bare top quark that are universally used in fixed order theoretical calculations, making it possible to validate theoretical models of the MC or fixed-order predictions. The used definition is the same as in [6] where normalized multi-differential cross sections were measured in this phase space using 2016 CMS data. Parton level cross sections can also be used for fitting or extraction of PDF sets and other SM parameters. For example, in the CMS-TOP-18-004 paper [6] a simultaneous fit of PDFs, α_s and m_t^{pole} was performed at NLO precision using $[N_{\text{jet}},M(t\bar{t}),y(t\bar{t})]$ unfolded results at parton level. For the phase space extrapolation, the reference POWHEG + PYTHIA8 $t\bar{t}$ simulation is used. The parton level top quarks are taken from the Pythia8 status code "62" [188], being consistent with the recommendations provided by the LHCTopWG working group [189] commonly used in the ATLAS and CMS analyses. The parton level cross sections, compared to the particle level result, have usually larger systematic uncertainties due to the phase space extrapolation that introduce a strong dependence on the modeling uncertainties (see Section 9.1.3) of the reference MC generator used in the unfolding procedure (POWHEG + PYTHIA8).

For the particle-level results, the definition of the particle-level objects and the kinematic reconstruction procedure employed to estimate the kinematic properties of the particle-level top quarks are given in Ref. [4] and are summarized below: The **particle level** definition is constructed out of the stable particles with a mean lifetime $> 0.3 \times 10^{-10}s$. The used definition is the same as in reference [4]. In this case, the top quarks are defined at generator level reconstructing them using the final state particles just before their propagation through the detector simulation. The physics objects are defined as following [5, 190]:

- All simulated **electrons** and **muons**, including those from tau lepton decays but

not originating from the decay of a hadron, are corrected ("dressed")[5] for effects of bremsstrahlung by adding the momentum of a photon to that of the closest lepton if their separation in $\eta - \phi$ space is 0.1. Leptons are required to have $p_{\mathrm{T}} > 20\,\mathrm{GeV}$ and $|\eta| < 2.4$.

- **Neutrinos** originating from non-hadronic decays (i.e. prompt neutrinos) are used.

- **Jets** are clustered using the anti-kt jet algorithm with a distance parameter of 0.4. All stable particles, with the exception of the dressed leptons and prompt neutrinos, are clustered. Jets with $p_{\mathrm{T}} > 30\,\mathrm{GeV}$ and $|\eta| < 2.4$ are selected if there is no electron or muon, as defined above, within a distance of 0.4.

- **b-jets** are defined as those jets that contain a b-hadron using the ghost-matching technique [191,192]. In this method, as a result of the short lifetime of b hadrons only their decay products are considered for the jet clustering. However, to allow their association with a jet, the b hadrons are also included with their momenta scaled down to a negligible value. This preserves the information of their directions, but removes their impact on the jet clustering.

- The following additional event-level requirements are applied to define the fiducial phase-space region in which the particle-level cross sections are measured: it is required that the W bosons produced from decays of the top quark and anti-quark in a $\mathrm{t\bar{t}}$ event themselves decay to an electron or muon; events where these W bosons decay to tau leptons are rejected; exactly two selected leptons candidates with opposite charges, a dilepton invariant mass greater than 20 GeV, and at least two b jets are required.

- The top quark reconstruction at particle level then proceeds as follows: prompt neutrinos are combined with the dressed leptons to form W boson candidates by minimizing the difference to the nominal W mass of 80.4 GeV. Subsequently, the W boson candidates are combined with b jets to form particle-level top quark candidates by minimizing the difference to the nominal top quark mass of 172.5 GeV. For each event, the permutation of leptons, neutrinos, and b jets that minimizes these mass differences, is taken.

Due to the finite detector resolution it can happen that events that are at the generator level outside the fiducial phase-space region are measured at detector level inside the accepted region. These events are subtracted, before the unfolding, by a fractional correction of the observed number of events after subtracting all other backgrounds. The fraction is applied separately for each detector-level bin and defined as the number of the events in the $\mathrm{t\bar{t}}$ signal simulation that pass both the detector and particle level selection cuts, divided by the number of all events fulfilling the detector level requirements.
Extra jets are defined for both parton and particle level definitions of the top and top-antiquark using the remaining reconstructed jets in the event after requiring $p_T > 40\,\mathrm{GeV}$, $|\eta| < 2.4$, and a spatial separation (ΔR) against the selected leptons and b-jets higher than 0.4 and 0.8, respectively. In this way the extra jets objects have a consistent definition among parton, particle and detector level. The motivation of these cuts is explained in Section 6.2. In the case of the differential cross sections measured as a function of the multiplicity of

[5] A dressed lepton is the system formed of a charged lepton and nearby photons.

additional jets in the event, e.g. $[N_{\mathrm{jet}},p_{\mathrm{T}}(t)]$, the top quark and antiquark are measured either at the parton level in the full phase space or at the particle level in a fiducial phase space, as described above, while the additional jets are always measured at the particle level. Specifically for the measurements of the top quark and top antiquark at parton level, two more differences in the definition of the extra jets are introduced (following Ref. [6]): the neutrinos from decays of hadrons are excluded in the clustering of these jets, and the charged leptons and b quarks used in the jet isolation are taken directly after W boson and top quark decays, respectively.

8.3.4 Efficiency, purity and stability

The quality of the reconstruction in the different bins can be characterized by the following quantities:

- The efficiency (ϵ) is an estimator of the effects of the detector acceptance and the reconstruction efficiency. For a given bin i it can be computed as:

$$\epsilon_i = \frac{N^{reco} \cup N_i^{gen}}{N_i^{gen\,tot}} \tag{8.9}$$

  where N_i^{gentot} is the total number of the generated events in bin i, and the term $N^{reco} \cup N_i^{gen}$ represents the number, of all reconstructed events (N^{reco}), that were generated in bin i (N_i^{gen}).

- The purity (p) describes migrations into a certain bin. It can be obtained dividing the number of the events which were generated (N_i^{gen}) and reconstructed (N_i^{reco}) in the same bin i, by the total number of the reconstructed events in this bin (N_i^{reco}):

$$p_i = \frac{N_i^{gen} \cup N_i^{reco}}{N_i^{reco}} \tag{8.10}$$

  If the purity value for a certain bin is high (low), this means that there is a small (big) portion of the events migrating into the bin from other generator bins. These migrations from bin to bin are caused by detector resolution and reconstruction effects.

- The stability (s) quantifies the migrations out of the bin, which means that the higher the stability is, the less events migrate to other bins. It can be computed as the fraction of the number of events generated (N_i^{gen}) and reconstructed (N_i^{reco}) in the same bin, and the number of the generated events inside this bin N_i^{gen} that were reconstructed in any detector level bin ($N_{\forall_i}^{reco}$):

$$s_i = \frac{N_i^{gen} \cup N_i^{reco}}{N_i^{gen} \cup N_{\forall_i}^{reco}} \tag{8.11}$$

All of these quantities are determined from the reference $\mathrm{t\bar{t}}$ simulation. As an example, the efficiency, purity, and stability are shown in Figure 8.5 for the $[M(\mathrm{t\bar{t}}),y(t)]$ cross section bins at parton and particle level. In this analysis, all the multi-differential cross sections present in CMS-TOP-18-004 [6] (only parton level and 2016 CMS data were used) are measured not

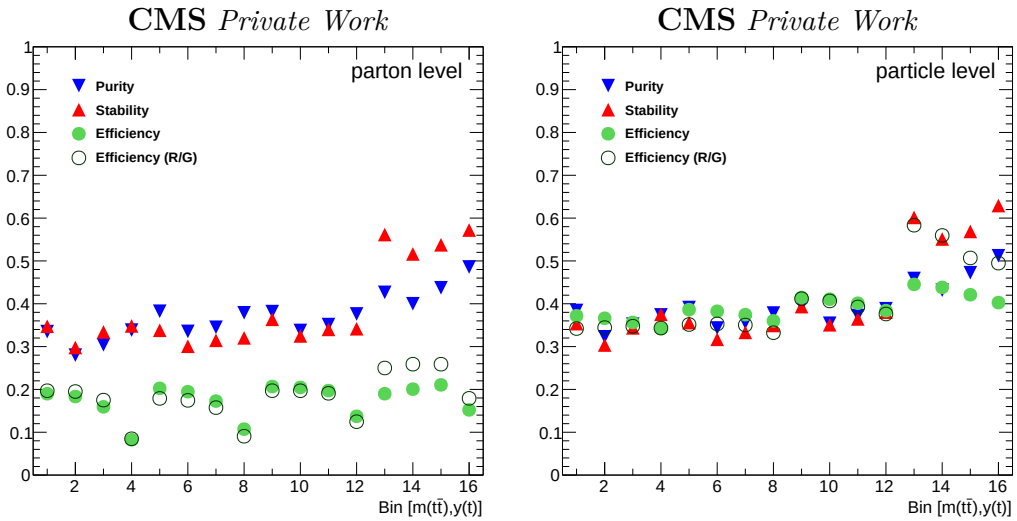

Figure 8.5: The purity (blue triangles) and stability (red triangles), as well as the product of the detector efficiency (green circles) and the efficiency R/G (black line circles) as a function of the bin number. The efficiency R/G is just the ratio of the number of reconstructed and generated events in the bin. The values are shown for the $[M(\mathrm{t\bar{t}}),y(t)]$ cross section at parton (left) and particle (right) levels.

.

only at parton, but also at particle level. For all cross sections, including the ones measured for the first time (e.g. $[N_{\mathrm{jet}},M(\mathrm{t\bar{t}})]$), it has been checked that the purities and stabilities are, in all bins, above $\sim 20\%$ for 2D and $\sim 15\%$ for 3D. If this would have not been taken into account for the binning scheme, the bins could have too small ranges leading to critically small purities and stabilities. This would lead to a strong anti-correlations of the unfolded cross section results for neighboring bins and therefore, result in a significant dependency on the applied regularization [3, 5].

CHAPTER

9

SYSTEMATIC UNCERTAINTIES

Contents

9.1 Systematic uncertainties 83
9.1.1 Experimental uncertainties 84
9.1.2 Background uncertainties 85
9.1.3 Model uncertainties 86
9.2 Treatment for Run II combination 88
9.3 Determination of the total systematic uncertainty 90
9.4 Summary 90

The precision of the measured cross sections is limited by different uncertainties sources. It is very important to estimate these uncertainties to know the expected spread of the measurements around their true values, which facilitates comparisons to other experimental results and theoretical models. The value for a given uncertainty is computed by repeating the unfolding process, varying the uncertainty related assumptions or corrections. Then, the shifted result is compared to the nominal[1] cross section values. The systematic variations are applied on the MC only.

9.1 Systematic uncertainties

While the statistical uncertainties come from the Poisson event counts in the data, the systematic uncertainties arise from imperfections in the modeling of the performance of the detector (experimental uncertainties), the intrinsic limitations present in the signal simulation

[1]The nominal result refers to the resulting cross section using all default values and corrections as described in previous chapters.

(model uncertainties) and the uncertainties on the normalization of the background processes (background uncertainties). In this section, an overview of the systematic uncertainties assessment performed in this analysis is presented. The definition and treatment follows for most of the systematics sources the procedures from previous $t\bar{t}$ differential analyses [4–6].

9.1.1 Experimental uncertainties

The experimental uncertainties are linked to the variations of the correction factors connected with some specific reconstruction procedure:

- The **trigger efficiency** uncertainty is obtained by varying the trigger scale factors (Section 5.2.3) within their uncertainties. This variation mostly leads to a change in the total events rate.
  Only during the 2016 and 2017 data-taking periods, a specific inefficiency affected the ECAL L1 trigger called pre-firing. This effect, produced by a gradual shift in the timing of the trigger inputs, was located in the forward endcap region ($|\eta| > 2.4$). Since the effect is not described by the simulation, it is corrected in this analysis by the application of event weights computed as the product of the non prefiring probability of all objects present in the event. The weights are applied to all 2016 and 2017 MC samples involved in the analysis. The correction is relevant in events with high-p_T jets with $2.4 < |\eta| < 3.0$. This region is excluded for the event selection in this analysis, however, in order to avoid underestimation of any possible effect of this issue on the object reconstruction, a systematic uncertainty is assigned and computed by shifting all prefiring probabilities by $\pm 1\sigma$. The resulting uncertainty has a very low impact on the measured cross sections ($\sim 0.1\%$).

- For the computation of the different **lepton efficiency** uncertainties, the scale factors are varied individually for the electron (see Section 5.2.2) and muon (see Section 5.2.1) flavour cases. These variations are independently computed for identification, isolation and reconstruction components of the scale factors.

- The **jet energy scale (JES)** (described in Section 5.2.4) uncertainty is determined by the independent variation of the different JES sub-corrections [193]. In this work, a version with a reduced set of seven different sources, from the original set of twenty-six separate sources, is used. This set, obtained by merging several common sources, is helpful since it preserves the main effects of systematic uncertainties but reduces the amount of statistical fluctuations, that are present in the signal and background MC samples and are added up when doing the separate variations.

- The **jet energy resolution (JER)** uncertainty is computed from the variation of the JER in the simulated samples by $\pm 1\sigma$ in different η regions [193]. This correction has been previously described in Section 5.2.4.

- The **unclustered** E_T^{miss} uncertainty is obtained varying the deposited energy by the charged and neutral hadrons and photons. The variations are performed according to the energy resolutions and propagated through the different analysis components for the estimation of the corresponding impact on the measurement. More information about E_T^{miss} can be found in Section 5.2.5.

- For the estimation of the **b-tagging efficiency** uncertainty the values of b-tagging scale factors (see Section 5.2.4) are varied per bin within their estimated uncertainties and subsequently propagated to the corresponding event weights in the MC simulations. The uncertainty on the b-tagging scale factors takes into account a variation that is fully correlated between beauty and charm jets and also another independent variation which is applied for light flavor jets. Apart from the statistical uncertainty, the measurement of the b-tagging is also affected by several sources of systematic effects [157]. The components with the higher impact are independently computed. This selection of five correction sub-sources, besides the statistical component, includes pile-up, JES, light-flavour SFs, and other specific physics modeling and method specific parameters.

- For the estimation of the **pile-up** uncertainty, the central value of the total pp inelastic cross section ($\sigma_{pp}^{MB} = 69.2\,\text{mb}$ [194]) used for the pile-up reweighting (see Section 5.2.5) is varied within its uncertainty of $\pm 4.6\%$ [194].

- The uncertainties on the **integrated luminosities** of the 2016, 2017, and 2018 data samples are shown in Table 6.1. The variation in the normalization is applied on the MC simulated samples for each year according to its respective uncertainty and then combined before the unfolding procedure. This uncertainty mostly affects the total normalization of the differential measurements and its effect is largely reduced for the normalized cross section results.

As described in most of the previous cases, the uncertainties related to a specific correction are determined by varying the central scale factor or correction within their uncertainties, which are provided by dedicated physics objects calibration research groups of the CMS collaboration. In some cases, like for b-tagging, the variations are provided subdivided in different components which is useful for the proper handling of the correlation of the sources along the different years (see Section 9.2).

9.1.2 Background uncertainties

The background normalization uncertainty can be subdivided according to the treatment of the different backgrounds: Drell-Yan (DY) and the other sources. For each case the uncertainty is computed by repeating the unfolding process after applying an up or down variation of the respective background contributions.

The uncertainty of the $Z+$jets background normalization is assessed by repeating template fits to $m(l\bar{l})$ distributions, described in Section 6.2, in different steps of the event selection. The first varied scenario is after the *missing transverse energy* selection step, the next one is after the *b-jets selection* and the last one is done after the *kinematic reconstruction* step. See Section 6.2 for the description of the different selection steps. The size of the variation for the determination of DY background uncertainty, was chosen as the maximal deviation among the scaling factors (see Section 6.3.1) computed at the different selection steps for a given channel and year. This maximal deviation was found to be about 20%. Therefore, a symmetric $\pm 20\%$ variation was used for the estimation of the DY background normalization uncertainty.
For the case of the remaining background sources, excluding DY, a conservative variation

of ±30% is applied following [4–6]. These two sub-sources, DY and other contributions, are computed independently. This means that for the computation of the DY normalization uncertainty the non-DY contributions stay unchanged. The opposite happens when computing the uncertainty of the non-DY sources, in this case the normalization of the DY contribution is not changed while the other sources are varied simultaneously. The total background normalization uncertainty is obtained by adding these sources in quadrature.

9.1.3 Model uncertainties

The model uncertainties are estimated by repeating the measurements after applying variations on different assumptions used in the modeling of the $t\bar{t}$ signal events. These variations are applied by repeating the full analysis replacing the reference POWHEG + PYTHIA8 $t\bar{t}$ signal sample by either dedicated simulated samples, or via the reweighting of the reference simulation with the respective weights in the reference nominal sample. A summary of all the uncertainties taken into account in this analysis is presented in this section.

- As described in Section 4.7, the **top quark mass (m_t)** was taken as 172.5 GeV in the nominal $t\bar{t}$ MC sample. To account for the experimental uncertainty of the top-quark mass, the cross section process was repeated using two additional $t\bar{t}$ signal samples, with $m_t = 169.5\,\text{GeV}$ and $m_t = 175.5\,\text{GeV}$, as alternative signal samples, and evaluating the resulting differences with respect to the nominal unfolded cross sections. The obtained uncertainties are linearly scaled down by the factor of 3 to achieve a variations of $\pm 1\,\text{GeV}$ in the m_t value.

- The uncertainty coming from the **parton distribution functions (PDFs)** is estimated by varying the $t\bar{t}$ signal simulation using 100 eigenvectors of the NNPDF3.1 error PDF sets [67]. The total contribution is obtained by adding in quadrature the resulting differences from each eigenvector with respect to the nominal cross section measurement. In addition, the value of the strong coupling constant, taken as $\alpha_S = 0.118$ in the nominal $t\bar{t}$ simulation, is varied by ±0.001 and its effect on the measurement result is computed [67].

- The **renormalization (μ_R) and factorization (μ_F) scales**, play a very important roll in the matrix element calculation of the hard process. The total uncertainty coming from these parameters, is determined as an envelope[2] out of the following variations included as weights in the reference $t\bar{t}$ sample:

  - factorization scale variation: μ_R fixed, varied μ_F by a factor of 2 (0.5) for up (down).
  - renormalization scale variation: μ_F fixed, varied μ_R by a factor of 2 (0.5) for up (down).
  - combined variation: varied simultaneously μ_R and μ_F by a factor of 2 (0.5) for up (down).

- The **Parton shower (ISR, FSR)** uncertainties are computed separately by varying the respective scales, α_S^{ISR} and α_S^{FSR}, up(down) by factors of 2(0.5) chosen according

[2] Estimation of the uncertainty as an envelope: for each measurement bin, the maximum up- and downwards variations of the measured cross sections are taken as the final uncertainty.

to the PS tuning uncertainties [120]. These variations, are included as weights in the reference $t\bar{t}$ sample.

- The matching of the matrix element to parton shower (**ME-PS matching**) uncertainty is determined using two dedicated $t\bar{t}$ MC samples with the h_{damp} parameter varied as $h_{damp} = 1.379^{+0.926}_{-0.5052} m_t$ [120].

- The **Underlying event tune** depends on several parameters, which are simultaneously varied up and down within their uncertainties [120]. Dedicated POWHEG + PYTHIA8 $t\bar{t}$ signal samples containing these variations are used for the estimation of the uncertainty [120].

- As described in Section 4.6, the default **colour reconnection (CR)** model in the reference POWHEG + PYTHIA8 simulation is the MPI-based scheme (see Section 3.6), where only top quarks are considered in the CR, meaning that, the CR is not performed among the top quark decay products. For the estimation of the uncertainty for the colour reconnection, dedicated samples were produced with three more CR schemes:

  - MPI-based with ERD (early resonance decays) switched on: allows the early resonance decays of the top quarks and corresponding W-bosons. In this case, the top quark decay products also participate in the CR process.
  - Gluon-move: incorporate the reconnection of the top quark decay products with the rest of the event [195]. In this case the gluons are allowed to participate multiple times in the reconnection.
  - QCD-inspired: the full QCD colour calculation is used in the colour reconnection process. The used sample for this systematic source also has ERD enabled.

  The envelope of the three variations with respect to the nominal measurement is taken as the uncertainty coming from the CR method.

- The **b-fragmentation** is referred to as the momentum transfer from the b-quark to the B-hadron and is described in the reference $t\bar{t}$ simulation using a Bowler-Lund function [196]. The impact from the up ($+0.224$) and down (-0.157) variations of the Bowler-Lund parameter (0.855) [197] was computed by reweighting the relevant transfer function at the generator level in the reference $t\bar{t}$ sample. The uncertainty resulting from the application of a different fragmentation function, the Peterson function [198], is also estimated. The total uncertainty is then computed as an envelope from the mentioned variations.

- The **B semi-leptonic decay branching ratio** uncertainty accounts for the dependency of the detector energy response for b-jets with the multiplicity of the undetectable neutrinos emerging from the $B \to l\nu$ decay. Weights containing the up/down variations of the branching ratio of the semi-leptonic B hadron decay are used for the reweighting of the nominal $t\bar{t}$ sample for the computation of the uncertainty. The up/down variations are performed according to the branching ratio uncertainty [30].

- The used **decay branching ratios** for the $W \to l\nu$ process are taken as $br_{(W\to e\nu)} = 0.1071$, $br_{(W\to \mu\nu)} = 0.1063$, and $br_{(W\to \tau\nu)} = 0.1138$ [30]. An uncertainty of 1.5%,

coming from the precision of these values [30], is propagated only to the absolute cross section measurements since it cancels out for the normalized measurements.

9.2 Treatment for Run II combination

For some systematic sources a correlation exists between the uncertainties in the different years where the data were collected. Some of these sources are fully or partially correlated while others are completely uncorrelated among the different years. In Table 9.1, the assumed correlation of the systematics (previously described in this chapter) for the different pairs of years is shown. Since the same theory models and variations are used for all periods, a full correlation is assumed for all theoretical uncertainties. For experimental uncertainties we use either uncorrelated, partial or full correlations. A value of 100% for a year pair means that the uncertainty is fully correlated in the respective years, while 0% stands for fully uncorrelated. For the cases of JES and b-tagging, since the different sub-sources had different correlations, each of these sub-sources was evaluated using their respective correlation.

The fully correlated sources are treated by varying the event yields of the MC simulated samples simultaneously for all years. For example, the top quark mass up (down) uncertainty variation is measured by combining the events resulting from varying up (down) the top quark mass the samples for the samples of all three years. For the uncorrelated sources, the first step is to obtain independent unfolded results by varying only the samples of one year and use the nominal simulation for the other years. Then the overall uncertainty from this source variation can be obtained by summing in quadrature the difference of these results with respect to the ones using the nominal simulation. One example of an uncorrelated source is JER, which is computed by first producing three independently unfolded measurements: varying 2016 and use nominal for the other years, varying 2017 and use nominal for the other years, and varying 2018 and use nominal for the other years. Then the differences of these results with the one obtained from the nominal simulation are added in quadrature.
The first step for computing the contribution from partially correlated sources is the determination of their correlated and uncorrelated components. This is done as if they were fully correlated or fully uncorrelated sources following the previously explained procedures for these cases. The resulting systematic uncertainty from the correlated and uncorrelated components are rescaled by a factor of $\sqrt{\rho}$ and $\sqrt{1-\rho}$ respectively, where ρ is the level of correlation, taken from the values shown in Table 9.1 (e.g. $30\% \rightarrow \rho = 0.30$).
The treatment described above for the determination of the full Run-II uncertainty, can be summarized for a given variation of a systematic source (e.g. up variation of the integrated luminosity) with the equation[3]:

$$\mathrm{Unc}^2_{\text{Run-II}} = \rho \cdot \mathrm{Unc}^2_{\text{corr}} + (1-\rho) \cdot \mathrm{Unc}^2_{\text{uncorr}} \tag{9.1}$$

Here $\mathrm{Unc}_{\text{corr}}$ and $\mathrm{Unc}_{\text{uncorr}}$ stands for the correlated and uncorrelated components which are determined by:

$$\mathrm{Unc}^2_{\text{uncorr}} = (\mathrm{Unf}_{var16} - \mathrm{Unf}_{nom})^2 + (\mathrm{Unf}_{var17} - \mathrm{Unf}_{nom})^2 + (\mathrm{Unf}_{var18} - \mathrm{Unf}_{nom})^2 \tag{9.2}$$

[3]This relation is only valid if the correlation coefficient (ρ) is the same across all the years.

Systematic source	16-17	16-18	17-18
Trigger efficiency	0%	0%	0%
L1 ECAL prefiring	100%	-	-
Electron efficiencies	100%	100%	100%
Muon efficiencies	100%	100%	100%
Background sources (DY, TW and others)	100%	100%	100%
Jet energy scale (JES)	treatment by source		
Jet energy resolution (JER)	0%	0%	0%
Pile-up	100%	100%	100%
b-tagging	treatment by source		
Unclustered met	0%	0%	0%
Top quark mass	100%	100%	100%
ME μ_R and μ_F scales	100%	100%	100%
PS (α_S^{FSR} and α_S^{FSR})	100%	100%	100%
ME-PS matching	100%	100%	100%
Underlying event tune	100%	100%	100%
PDF (α_S and replicas)	100%	100%	100%
Colour reconnection	100%	100%	100%
b-fragmentation	100%	100%	100%
B semi-leptonic BR	100%	100%	100%
$\mathcal{BR}\left(t\bar{t} \to \ell\ell + X\right)$	100%	100%	100%
Luminosity	30%	30%	30%

Table 9.1: Summary of the assumed correlations among years for all systematic uncertainties (left column) previously described in Sections 9.1.1, 9.1.2 and 9.1.3. For the cases of JES and b-tagging the different sub-sources had different correlations, so each sub-source was evaluated separately.

$$\mathrm{Unc}_{\mathrm{corr}} = \mathrm{Unf}_{var16,var17,var18} - \mathrm{Unf}_{nom} \tag{9.3}$$

The term Unf_{nom} is the nominal unfolded result, while Unf_{var16}, Unf_{var17} and Unf_{var18} stands for the unfolded cross sections using the simulation varied only in 2016, 2017 and 2018 respectively, and using the nominal simulation for the other years. Finally, the quantity $\mathrm{Unf}_{var16,var17,var18}$ is obtained by using the simulations containing the variation in all three years at the same time.

9.3 Determination of the total systematic uncertainty

The total systematic uncertainty is estimated from the different experimental and model variations perviously described. The effect of the variations can result, for a given bin, in a higher or lower value compared to the nominal measurement. The deviations resulting in a higher value are summed up in quadrature, and the same for the lower ones. This is done after the determination of the needed envelopes (e.g the envelopes containing the coulour reconnection sources). If a systematic uncertainty leads to two cross section variations of the same sign, the largest one is taken and the opposite variation is set to zero. The total uncertainty in a bin, is computed by adding in quadrature, separately for up and down variations, the overall systematic uncertainty and the statistical uncertainty which is obtained from the unfolding χ^2 fit performed with TUnfold [186].

9.4 Summary

A few examples of the contributions from the different uncertainties sources are shown in Figures 9.1-9.3. It can be observed in Figure 9.1, where the normalized and absolute $[M(\mathrm{t\bar{t}}),y(t)]$ parton level cross section are presented, that the total uncertainties are smaller for absolute cross sections in comparison with the normalized results. This is expected since, as discussed in the previous section, some normalization related systematics, like the luminosity uncertainty, cancel out in the normalized measurements. Figure 9.2 also shows the uncertainties breakdown for the normalized and absolute $[M(\mathrm{t\bar{t}}),y(t)]$ cross section, but for the measurements at particle level. Comparing the Figures 9.1 and 9.2, one can conclude that the shape and total contribution of the uncertainties are almost the same for parton and particle level results. Two more examples for normalized parton level $[N_{\mathrm{jet}},p_{\mathrm{T}}(t)]$ and $[p_{\mathrm{T}}(\mathrm{t\bar{t}}),M(\mathrm{t\bar{t}}),y(\mathrm{t\bar{t}})]$ cross sections are shown in Figure 9.3.
As can be observed in the previously described plots, the measurements in this work are dominated by the systematics uncertainties, with the highest contribution coming from the experimental sources. The statistical uncertainty has a very low impact in most of the bins. The experimental uncertainties are dominated for all the cross sections by the *JES* and *lepton efficiency*, with always *JES* being the dominant source in this group. The background uncertainties also contribute significantly to the total uncertainty, in particular in specific phase space regions such as low mass and momentum. For the absolute cross sections, the "luminosity" uncertainty also becomes significant. From the side of the theory sources, *colour reconnection* has a considerable impact in all the measurements. For the t, $\bar{t}$ and $\mathrm{t\bar{t}}$ system cross sections, depending on the cross section, theory sources like m_t, μ_R, μ_F and/or *ME-PS matching* can cause a significant contribution. In the $\mathrm{t\bar{t}}$ plus additional jets measurements,

the *ISR* uncertainty has a considerable impact.
The overall uncertainty for the different measurements in this work (up to $\sim 20\%$), has been reduced by a factor of ~ 2 with respect to previous similar works [6]. This improvement comes from different ingredients of this analysis like a better estimation for the DY background process contribution, the use of a reduced set of JES sources and exploiting of MC simulated samples with largely higher statistics for nominal and alternative $\mathrm{t\bar{t}}$ samples used in the unfolding procedure and for assessing the systematic uncertainties, respectively. The usage of improved procedures in the reconstruction and correction of observables used in the analysis (e.g. PUPPI for E_T^{miss} reconstruction, DeepCSV b-tagging), and the application of refined calibrations determined separately for each year (see Chapter 5) played an important roll.

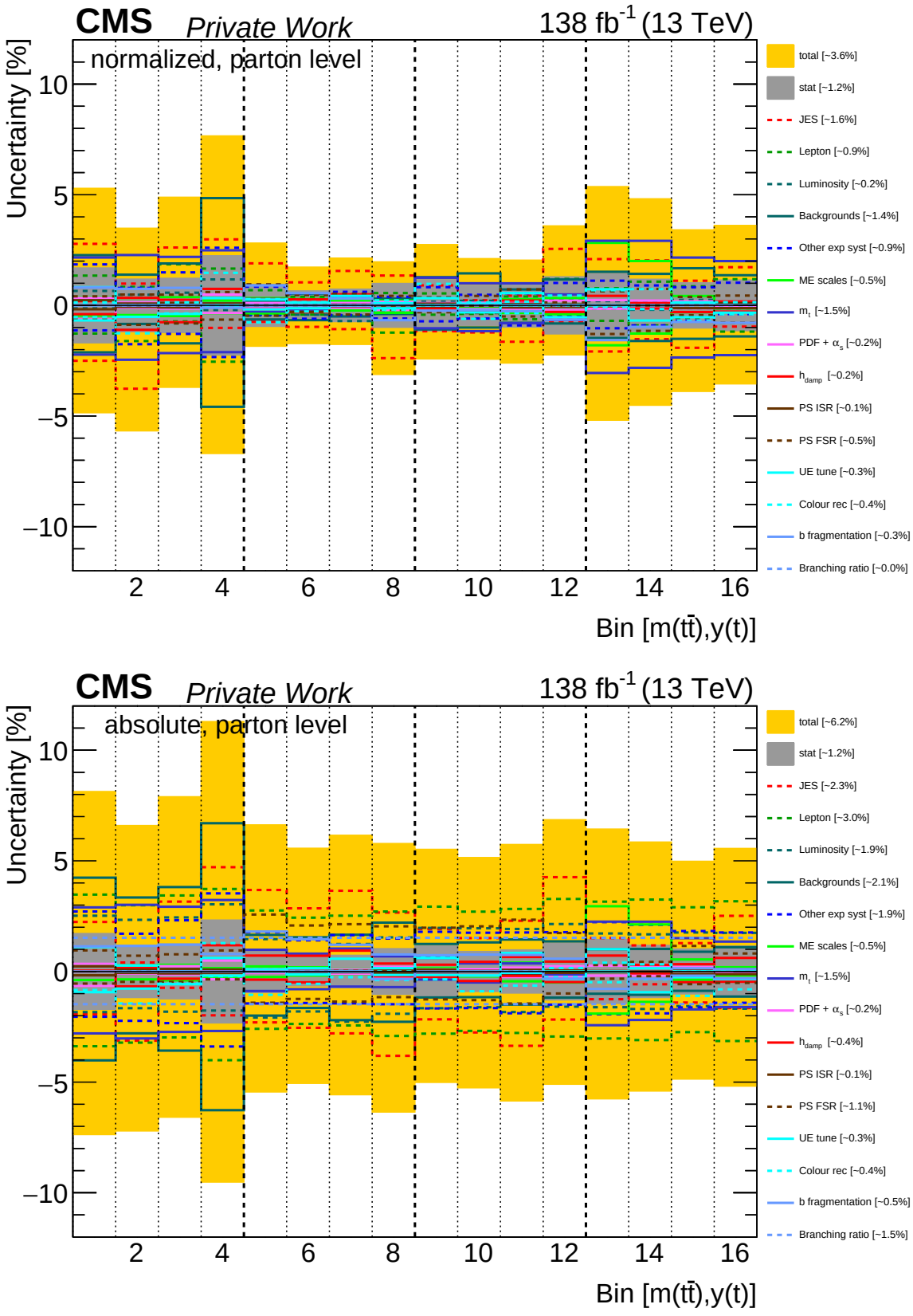

Figure 9.1: Uncertainties contribution breakdown for the normalized (top) and absolute (bottom) $[M(\mathrm{t\bar{t}}),y(t)]$ parton level cross section for each bin. Thicker vertical lines are delimiters for the $M(\mathrm{t\bar{t}})$ bins. Complete binning information in Table C.29.

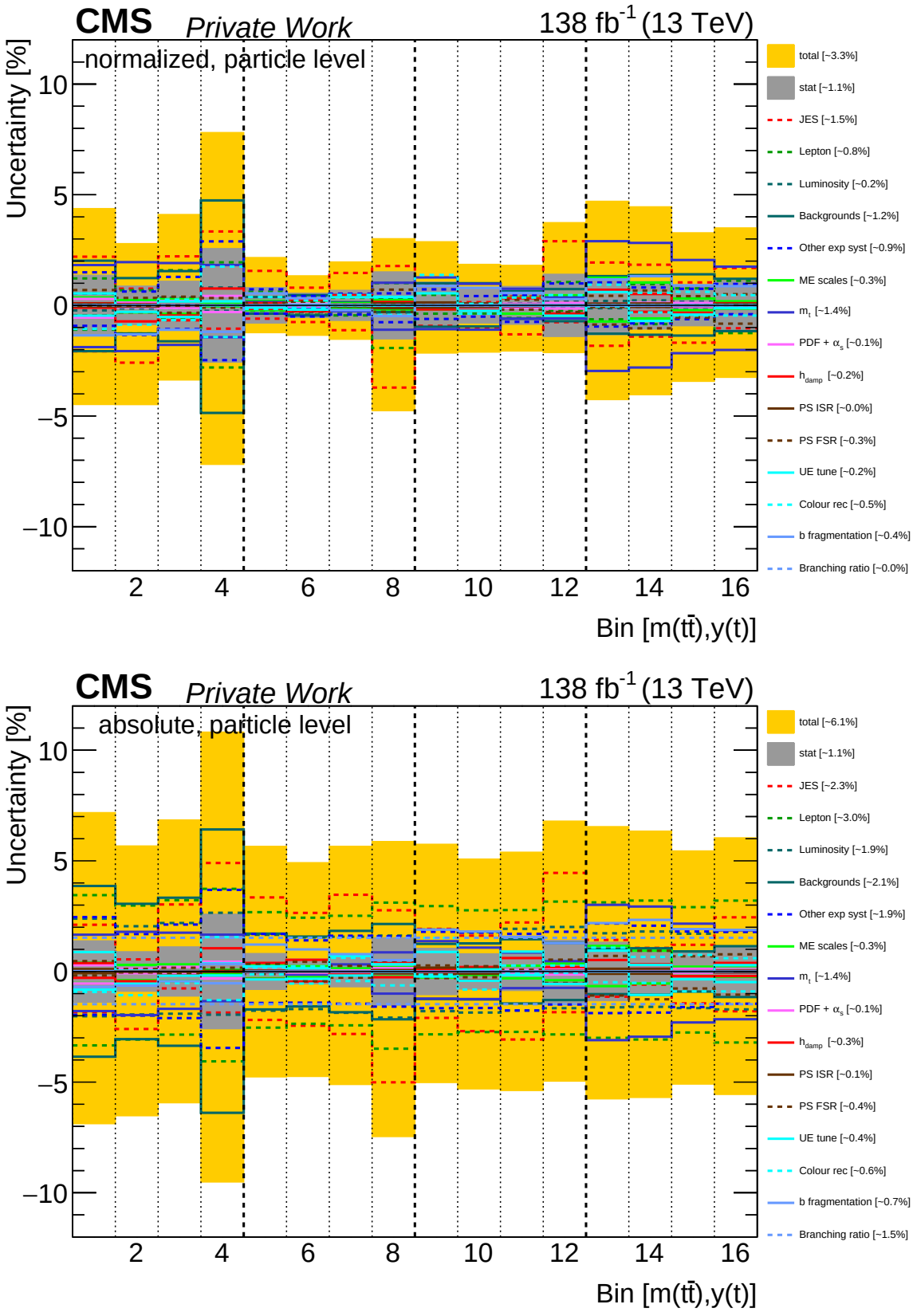

Figure 9.2: Uncertainties contribution breakdown for the normalized (top) and absolute (bottom) $[M(\mathrm{t\bar{t}}),y(t)]$ particle level cross section for each bin. Thicker vertical lines are delimiters for the $M(\mathrm{t\bar{t}})$ bins. Complete binning information in Table C.29.

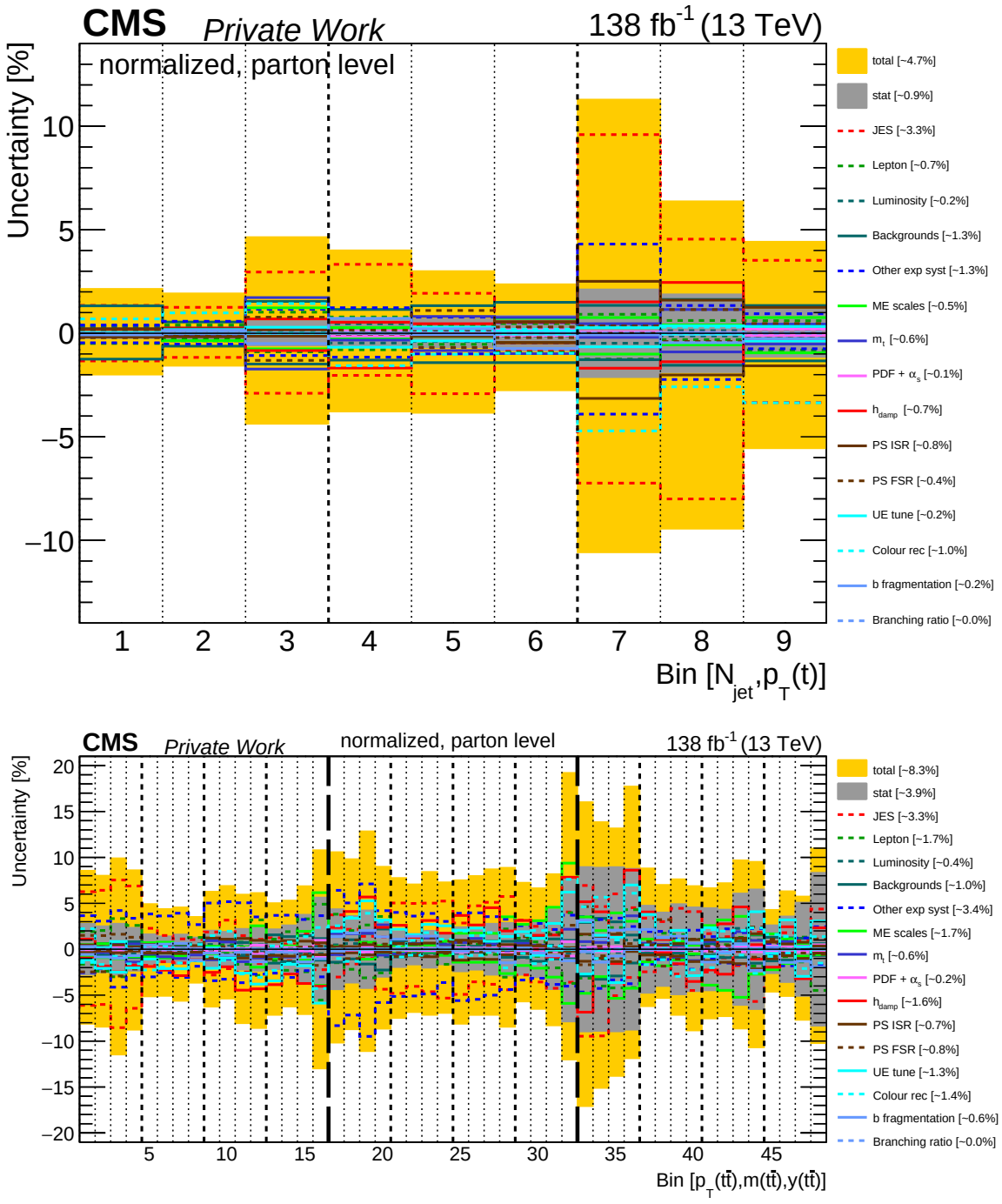

Figure 9.3: Uncertainties contribution breakdown for the normalized parton level cross sections $[N_{\text{jet}},p_{\text{T}}(t)]$ (top) and $[p_{\text{T}}(t),M(\text{t}\bar{\text{t}}),y(\text{t}\bar{\text{t}})]$ (bottom) for each bin. Thicker vertical lines are delimiters for the multidimensional bins. Complete binning information in Tables C.57 and C.25.

CHAPTER

10

RESULTS

Contents

10.1 Multi-differential cross sections 95

10.2 Unfolded cross sections results and comparison to MC models . 96

10.2.1 Kinematic properties of the top quark, top antiquark and $t\bar{t}$ system 98

10.2.2 $t\bar{t}$ production in the presence of additional jets 107

10.2.3 $t\bar{t}$ plus additional jets: studies with leading and sub-leading extra jets 116

10.3 Comparison of 2D $t\bar{t}$ system cross sections to the latest beyond-NLO fixed order QCD calculations 120

10.4 Top p_T reweighting at generator level using $[M(t\bar{t}),p_T(t)]$ unfolded cross section 126

10.5 Summary of the results 132

10.1 Multi-differential cross sections

The normalized and absolute multi-differential[1] cross sections are measured in the full phase space at parton level and in the fiducial phase space at particle level (see Section 8.3.3). The measurements can be grouped into:

- Precision 2D and 3D cross sections as a function of observables describing the kinematic properties of the top quark, top antiquark, and $t\bar{t}$ system (see Figure 2.12). The list of corresponding observables measured at parton and particle level is given in Table 10.1.

[1]For presentation purposes, all measured multi-differential cross sections are reported as single-differential ones in different ranges of the other observable(s), i.e., the cross sections are divided by the bin width of one of the variables only. More details in Section 8.3.

Observables	*Figure*	*Remarks/Motivation*
Correlation of $p_{\mathrm{T}}(t)$ with other top and $\mathrm{t\bar{t}}$ observables		
$[y(t),p_{\mathrm{T}}(t)]$	10.1, 10.2	Complete top kinematics
$[M(\mathrm{t\bar{t}}),p_{\mathrm{T}}(t)]$	10.3	Test of QCD dynamics
$[p_{\mathrm{T}}(t),p_{\mathrm{T}}(\mathrm{t\bar{t}})]$		correlation of t and $\mathrm{t\bar{t}}$ kinematics
Complete set of 2D $\mathrm{t\bar{t}}$ combinations		
$[M(\mathrm{t\bar{t}}),y(\mathrm{t\bar{t}})]$	10.4	Prime combination for extraction of gluon PDF
$[y(\mathrm{t\bar{t}}),p_{\mathrm{T}}(\mathrm{t\bar{t}})]$		Correlation of gluon radiation with $\mathrm{t\bar{t}}$ rapidity
$[M(\mathrm{t\bar{t}}),p_{\mathrm{T}}(\mathrm{t\bar{t}})]$		Gluon radiation vs. $\sqrt{\hat{s}}$
$[M(\mathrm{t\bar{t}}),y(t)]$	10.6	Test of QCD dynamics
$[M(\mathrm{t\bar{t}}),\Delta\eta(t,\bar{t})\ ]$		$p_{\mathrm{T}}(t)$ problem
$[M(\mathrm{t\bar{t}}),\Delta\phi(t,\bar{t})\ ]$		Gluon radiation vs. $\sqrt{\hat{s}}$
3D Combinations of $\mathrm{t\bar{t}}$ system observables		
$[p_{\mathrm{T}}(\mathrm{t\bar{t}}),M(\mathrm{t\bar{t}}),y(\mathrm{t\bar{t}})]$	10.5	Complete $\mathrm{t\bar{t}}$ kinematics

Table 10.1: The set of observables, describing the kinematic properties of the top quark, top antiquark and $\mathrm{t\bar{t}}$ system, that is used for the multi-differential cross section measurements at parton and particle levels. This set of observables can be of particular interest for comparisons with modern fixed-order predictions within the standard model, as well as for studying various physics aspects, like those listed in the table. The quatity $\hat{s} = M(\mathrm{t\bar{t}})^2$ denotes the $\mathrm{t\bar{t}}$ center of mass energy. References are given to the respective figure showing the measured cross section and its comparison to different MC models (see Section 10.2). The highlighted observables are measured for the first time as part of this work.

- Cross sections as a function of observables of the top quark, top antiquark, and the $\mathrm{t\bar{t}}$ system in the presence of additional jets (see Figure 2.12). The list of corresponding observables is given in Table 10.2.

For the cross section notation in this work, when the variables $y(t)$, $y(\mathrm{t\bar{t}})$ and $\Delta\eta(t,\bar{t})$ are mentioned, what is actually used is the absolute values of these observables. This was chosen in order to simplify the notation. The *full KR* method is used for all cross sections with the exception of the $M(\mathrm{t\bar{t}})$ related measurements, where the application of the *loose KR* method is possible (e.g. $[M(\mathrm{t\bar{t}}),y(\mathrm{t\bar{t}})]$). For the N_{jet} related cross sections, like for example $[N_{\mathrm{jet}},M(\mathrm{t\bar{t}})]$, a $p_T > 40\,\mathrm{GeV}$ and $\Delta R_{iso} = 0.8$ is required for the extra jets as described in Section 6.2. A set of N_{jet} cross sections for different minimum p_T and ΔR_{iso} are also measured.

10.2 Unfolded cross sections results and comparison to MC models

As described in Chapter 4, the different MC event generators take different approaches for the simulation of the same process, like for parton showering or colour reconnection,

Observables	*Figure*	*Remarks/Motivation*
Additional jet multiplicity in $t\bar{t}$ events		
N_{jet}	10.7, 10.8	Study jet multiplicity for different minimum jet p_T
How $t\bar{t}$ dynamics is correlated with additional jets		
$[N_{\text{jet}},p_{\text{T}}(t)]$	10.9	How higher order radiation affects these observables
$[N_{\text{jet}},y(t)]$	10.10	
$[N_{\text{jet}},\Delta\eta(t,\bar{t})]$		
$[N_{\text{jet}},M(t\bar{t})]$	10.11	Study jet production as function of $\hat{s}$
$[N_{\text{jet}},y(t\bar{t})]$		How higher order radiation affects $y(t\bar{t})$
$[N_{\text{jet}},p_{\text{T}}(t\bar{t})]$		Recoil of $t\bar{t}$-system against additional jets
$[N_{\text{jet}}^{0,1,2+},M(t\bar{t}),y(t\bar{t})]$	10.12	Sensitive to m_t, α_s and PDFs
$[N_{\text{jet}}^{0,1,2+},M(t\bar{t}),y(t\bar{t})]$	10.13	
$[N_{\text{jet}}^{0,1,2,3+},M(t\bar{t}),y(t\bar{t})]$		
$t\bar{t}$ + leading additional jet		
$p_{\text{T}}(\text{ej}_1)$, $p_{\text{T}}(\text{ej}_2)$	10.14	Exploring leading and sub-leading jets kinematics.
$\eta(\text{ej}_1)$, $\eta(\text{ej}_2)$		
$M(t\bar{t}+\text{ej}_1)$	10.15	Sensitive to top quark mass
$p_{\text{T}}(t\bar{t}+\text{ej}_1)$		Test of perturbative QCD
$M(t\bar{t}+\text{ej}_1)/\text{M}(t\bar{t})$	10.16	Sensitive to soft gluon resummation
$p_{\text{T}}(\text{ej}_1)/M(t\bar{t})$		Test of perturbative QCD
$\Delta\eta(t,ej_1)/\Delta\eta(t,\bar{t})$		Are the leading extra jets emitted between the two top quarks?

Table 10.2: The set of observables used for probing the $t\bar{t}$ production in the presence of additional jets. Different combinations of observables are used to perform differential measurements as a function of one or several dimensions. This set of observables can be of particular interest for comparisons with modern fixed-order predictions based on the standard model, as well as for studying various physics aspects, like those listed in the table. The leading additional jet (ej_1) is the additional jet with the higher p_{T} in the event. The reference to the respective figure showing the resulting cross section and its comparison to different MC models (see Section 10.2) is also given. The highlighted observables are measured for the first time as part of this work. Some of the N_{jet} combinations has been already measured for other decay channels (e.g. in the lepton plus jets channel [199]) but not for the dileptonic channel.

leading to differences in the description of the observables distributions. In Figs. 10.1–10.16, the measured cross sections are compared to three different MC simulations: POWHEG + PYTHIA8 , MG5_aMC@NLO(FxFx) + PYTHIA8 and POWHEG + HERWIG7 (for more information see Section 4.7), referred to in the plots as 'POW+PYT', 'FXFX+PYT' and 'POW+HER', respectively. For each comparison, a χ^2 value is reported which is calculated taking into account the statistical and systematic data uncertainties as follows:

$$\chi^2 = \mathbf{R}_{N-1}^T \mathbf{Cov}_{N-1}^{-1} \mathbf{R}_{N-1}, \tag{10.1}$$

where $\mathbf{R}_{N-1}$ is the column vector of the residuals calculated as the difference of the measured cross sections and the corresponding predictions, discarding one of the N bins, and $\mathbf{Cov}_{N-1}$ is the $(N-1) \times (N-1)$ sub-matrix obtained from the full covariance matrix by discarding the corresponding row and column. The obtained matrix $\mathbf{Cov}_{N-1}$ is invertible, while the original covariance matrix **Cov** is singular. This a consequence from the loss of one degree of freedom for normalized cross sections[2], as can be deduced from Eq. (8.7). The covariance matrix **Cov** is calculated as:

$$\mathbf{Cov} = \mathbf{Cov}^{\text{unf}} + \mathbf{Cov}^{\text{syst}}, \tag{10.2}$$

where $\mathbf{Cov}^{\text{unf}}$ and $\mathbf{Cov}^{\text{syst}}$ are the covariance matrices accounting for the statistical uncertainties obtained from the unfolding, and the systematic uncertainties, respectively.
The systematic covariance matrix $\mathbf{Cov}^{\text{syst}}$, for $1 \leqslant i, j \leqslant N$, is computed as:

$$\mathbf{Cov}_{ij}^{\text{syst}} = \sum_{k,l} \frac{1}{N_k} C_{j,k} C_{i,k} \tag{10.3}$$

where $C_{i,k,l}$ stands for the signed systematic uncertainty from variation l of source k in the ith bin, and N_k is the number of variations for source k. The sums run over all sources of the systematic uncertainties and all corresponding variations. Most of the systematic uncertainty sources in this analysis consist of up and down variations (e.g. m_t) and thus have $N_k = 2$, whilst several model uncertainties (the model of color reconnection and the b quark fragmentation function) consist of more than two variations which is accounted for in Eq. 10.3.

All obtained χ^2 values of MC model to data comparisons, together with the corresponding numbers of degrees of freedom, are listed in Appendix C in Tables C.111-C.115. The χ^2 values of each MC model are also included in the cross sections plots presented in the following subsections.

10.2.1 Kinematic properties of the top quark, top antiquark and $\mathrm{t\bar{t}}$ system

The $[y(t), p_{\mathrm{T}}(t)]$ cross section gives a complete description of the relevant top quark kinematic. Since this is the first measurement presented in this work, an overall description of the comparison plots style and structure is provided in Figure 10.1, where the absolute and normalized parton level $[y(t), p_{\mathrm{T}}(t)]$ cross sections results are shown. From the comparison to the different MC models, it can be seen that the data distribution is softer than that of the predictions over the entire $|y(t)|$ range. The 'POW+HER' MC model gives the overall best

[2]The discarded bin is usually the first one.

description but exhibits a stronger positive $p_{\mathrm{T}}(t)$ slope with respect to the data in the lowest and highest $|y(t)|$ ranges. The worst description is given by 'FXFX+PYT' which clearly provides too hard $p_{\mathrm{T}}(t)$ spectra. 'POW+PYT' gives a better description but also shows a positive p_{T} slope for all different $y(t)$ bins. Similar results are obtained for normalized and absolute measurements at parton and particle level (see Figure 10.2). This is also the case for most of the cross sections measurements in this work. For simplicity only normalized, and mostly parton level cross sections plots will be shown in this and the following sub-sections. The numeric values for all the measurements, and the plots for rest of the measurements not presented in this chapter are shown in Appendix C.

The correlation between the $p_{\mathrm{T}}(t)$ distribution with respect to the $M(\mathrm{t\bar{t}})$ and $p_{\mathrm{T}}(\mathrm{t\bar{t}})$ kinematic observables of the $\mathrm{t\bar{t}}$ system are studied in Figure 10.3. The $[M(\mathrm{t\bar{t}}),p_{\mathrm{T}}(t)]$ double-differential spectra, can give a hint about the origin of the top p_{T} problem, where most predictions exhibit as a too hard $p_{\mathrm{T}}(t)$ distribution, as was mentioned in Section 6.4. Similar as in the previous analysis [6], the data are poorly described by all the models. 'POW+PYT' and 'FXFX+PYT' predict a harder $p_{\mathrm{T}}(t)$ spectrum than observed in data and this trend grows with increasing $M(\mathrm{t\bar{t}})$. In the two lowest $M(\mathrm{t\bar{t}})$ bins near threshold, the 'POW+HER' model describes the $p_{\mathrm{T}}(t)$ distribution reasonably but in the highest $M(\mathrm{t\bar{t}})$ bin it shows a trend similar to the other models. For the $[p_{\mathrm{T}}(t),p_{\mathrm{T}}(\mathrm{t\bar{t}})]$ comparisons, where the $p_{\mathrm{T}}(\mathrm{t\bar{t}})$ spectrum is shown in different $p_{\mathrm{T}}(t)$ ranges, it is to be noted that larger $p_{\mathrm{T}}(t)$ values can be kinematically correlated with higher $p_{\mathrm{T}}(\mathrm{t\bar{t}})$ values when the $\mathrm{t\bar{t}}$ system is recoiling against extra QCD radiation in the event. In general a non-zero $p_{\mathrm{T}}(\mathrm{t\bar{t}})$ can be an indirect signature of the presence of extra jet radiation in the event, since without additional jets or other particles being produced in addition to the ttbar system, the $p_{\mathrm{T}}(\mathrm{t\bar{t}})$ is expected to be zero due to transverse momentum conservation. For this measurement, the 'FXFX+PYT' model predicts a harder $p_{\mathrm{T}}(\mathrm{t\bar{t}})$ spectrum than observed in the data, which is visible in all $p_{\mathrm{T}}(t)$ ranges. The 'POW+PYT' and 'POW+HER' predictions tend to overestimate the data in the higher $p_{\mathrm{T}}(t)$ ranges in the lower $p_{\mathrm{T}}(\mathrm{t\bar{t}})$ bins.

A complete set of the kinematic variables of the $\mathrm{t\bar{t}}$ systems and their mutual correlation is provided by the $[M(\mathrm{t\bar{t}}),y(\mathrm{t\bar{t}})]$, $[y(\mathrm{t\bar{t}}),p_{\mathrm{T}}(\mathrm{t\bar{t}})]$ and $[M(\mathrm{t\bar{t}}),p_{\mathrm{T}}(\mathrm{t\bar{t}})]$ cross sections (see Figure 10.4), giving important information about the $\mathrm{t\bar{t}}$ system kinematics. The $M(\mathrm{t\bar{t}})$ and $y(\mathrm{t\bar{t}})$ observables are known to be kinematically correlated with the proton momentum fractions [3]. Their combination into the $[M(\mathrm{t\bar{t}}),y(\mathrm{t\bar{t}})]$ cross section is known to provide optimal information for constraining the proton PDFs [180]. For the low and medium $M(\mathrm{t\bar{t}})$ bins, the MC predictions are slightly more central than the data, while in the highest $M(\mathrm{t\bar{t}})$ range the opposite effect is observed. For the $[y(\mathrm{t\bar{t}}),p_{\mathrm{T}}(\mathrm{t\bar{t}})]$ measurement one finds that these two observables are rather uncorrelated and also the quality of the description of the $p_{\mathrm{T}}(\mathrm{t\bar{t}})$ distribution by the models is similar in all $y(\mathrm{t\bar{t}})$ ranges. Since the phase space for QCD radiation, which is strongly correlated with non zero values of the $p_{\mathrm{T}}(\mathrm{t\bar{t}})$ observable, increases with higher $M(\mathrm{t\bar{t}})$ values, the $[M(\mathrm{t\bar{t}}),p_{\mathrm{T}}(\mathrm{t\bar{t}})]$ cross section represent a very interesting observables combination. In this measurement, the 'FXFX+PYT' ('POW+HER') model predicts too hard (soft) $p_{\mathrm{T}}(\mathrm{t\bar{t}})$ distributions and this trend is enhanced in the higher $M(\mathrm{t\bar{t}})$ ranges. The first simultaneous study of all three $\mathrm{t\bar{t}}$ kinematic observables ($M(\mathrm{t\bar{t}})$, $p_{\mathrm{T}}(\mathrm{t\bar{t}})$ and $y(\mathrm{t\bar{t}})$) is shown in Figure 10.5, where 'POW+PYT' provides an overall reasonable description. The

[3] In the leading order $\mathrm{t\bar{t}}$ production, the momentum fractions x_1 and x_2 of the two partons, e.g. two gluons producing the $\mathrm{t\bar{t}}$ pair, are related to these observables by the relations $M(\mathrm{t\bar{t}}) = \mathrm{sqrt}\mathrm{x}_1 \cdot \mathrm{x}_2 \cdot \mathrm{s}$ and $y(\mathrm{t\bar{t}}) = 1/2\ln(\mathrm{x}_1/\mathrm{x}_2)$, as can be easily calculated from momentum conservation in the reaction $gg \to \mathrm{t\bar{t}}$.

'FXFX+PYT' and 'POW+HER' show deficiencies in specific $M(\mathrm{t\bar{t}})$ and $p_{\mathrm{T}}(\mathrm{t\bar{t}})$ bins, with some small dependence on $y(\mathrm{t\bar{t}})$.

The measurements presented in Figure 10.6 are focused on the study of the correlation between $M(\mathrm{t\bar{t}})$ and other kinematic observables by measuring $[M(\mathrm{t\bar{t}}),y(t)]$, $[M(\mathrm{t\bar{t}}),\Delta\eta(t,\bar{t})\,]$ and $[M(\mathrm{t\bar{t}}),\Delta\phi(t,\bar{t})\,]$. For the $[M(\mathrm{t\bar{t}}),y(t)]$ distributions, the predictions exhibit a more central rapidity top quark distribution than the data and this trend slightly increases towards higher $M(\mathrm{t\bar{t}})$ values. The results for the $[M(\mathrm{t\bar{t}}),\Delta\eta(t,\bar{t})\,]$ cross section illustrate that the data show larger rapidity separations than predicted by the models. This effect increases in the higher $M(\mathrm{t\bar{t}})$ bins and 'FXFX+PYT' shows the worst disagreement. It is likely that a relation exist between the deficiencies in the models, predicting harder $p_{\mathrm{T}}(t)$ spectra, and at the same time also smaller $|\Delta\eta(t,\bar{t})|$ distributions, that are found to be enhanced towards higher $M(\mathrm{t\bar{t}})$ values. A hint for this possible relation is that for a given $M(\mathrm{t\bar{t}})$ value, larger $|\Delta\eta(t,\bar{t})|$ are on average correlated with lower $p_{\mathrm{T}}(t)$ values. The measured $[M(\mathrm{t\bar{t}}),\Delta\phi(t,\bar{t})\,]$ cross section illustrate that at low $M(\mathrm{t\bar{t}})$ the data exhibit a slightly more back-to-back distribution of the top quark and the top antiquark compared to the models. In the largest $M(\mathrm{t\bar{t}})$ range this trend seems to reverse at least for the 'FXFX+PYT' and 'POW+PYT' models. In terms of overall description, the 'FXFX+PYT' model provides the best description of this variable combination, especially in the highest $M(\mathrm{t\bar{t}})$ range. It should be noted that deviations of $\Delta\phi(t,\bar{t})$ with a value of π can indicate, like for a non zero $p_{\mathrm{T}}(\mathrm{t\bar{t}})$, the presence of extra jet radiation in the event, since from transverse momentum conservation one expects the top quark and top antiquark to back-to-back in azimuthal angle if no other objects are produced in the hard scattering.

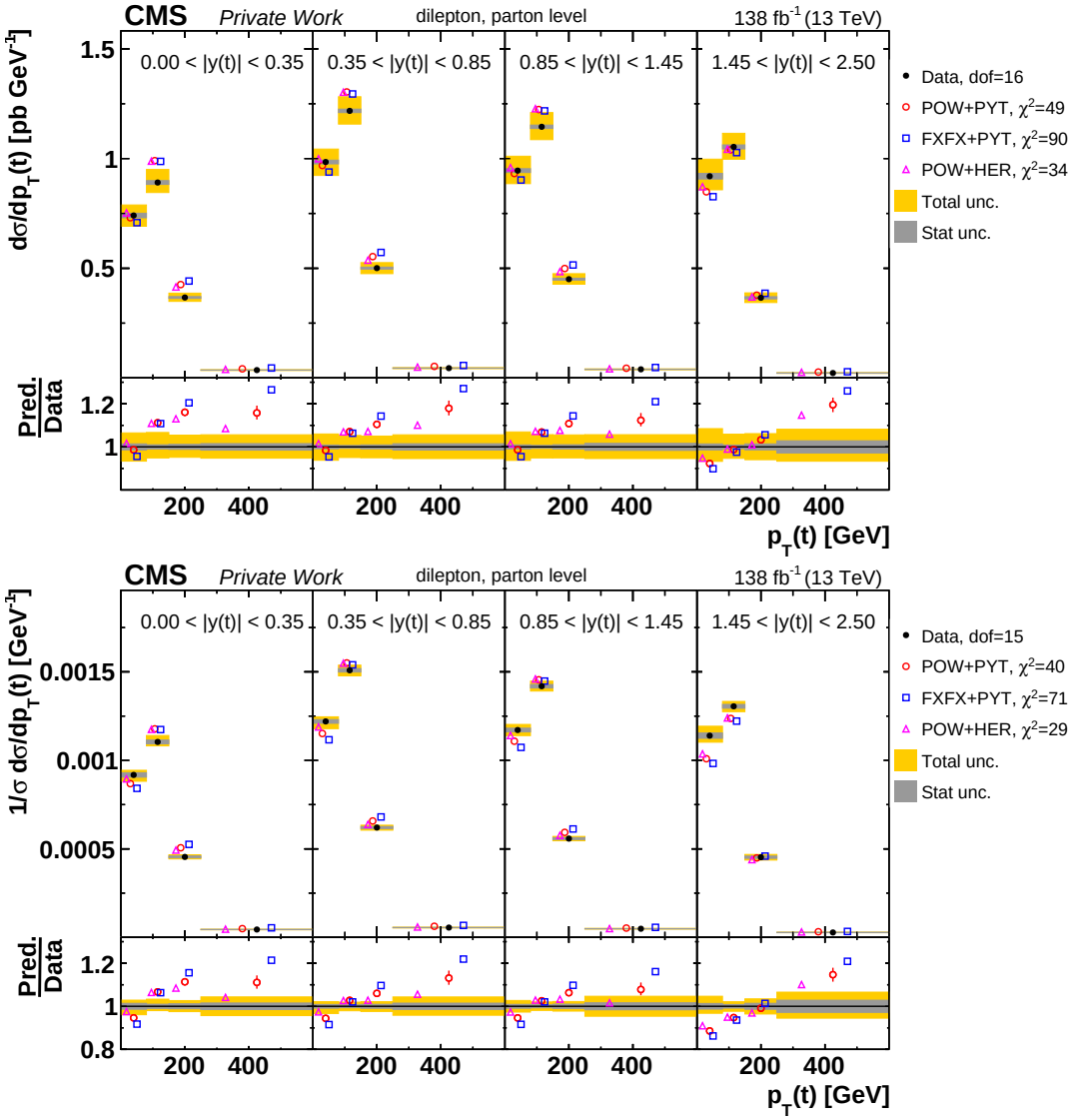

Figure 10.1: Comparison of the measured $[y(t), p_{\mathrm{T}}(t)]$ cross sections to MC predictions calculated using POWHEG + PYTHIA8 ('POW-PYT'), MG5_aMC@NLO(FxFx) + PYTHIA8 ('FXFX-PYT'), and POWHEG + HERWIG7 ('POW-HER'). Absolute (normalized) parton level cross sections are shown in the upper (bottom) plot. The data are shown as filled circles with dark and light bands indicating the statistical and total (sum in quadrature of statistical and systematic) uncertainties, respectively. The other points correspond to the cross sections of the different MC predictions (see the legend). The estimated uncertainties in the 'POW+PYT' simulation are represented by a vertical bar on the corresponding points. For each MC model, a χ^2 value is reported (more details in Section 10.2). In the bottom panel, the ratios for all predictions with respect to the data are shown.

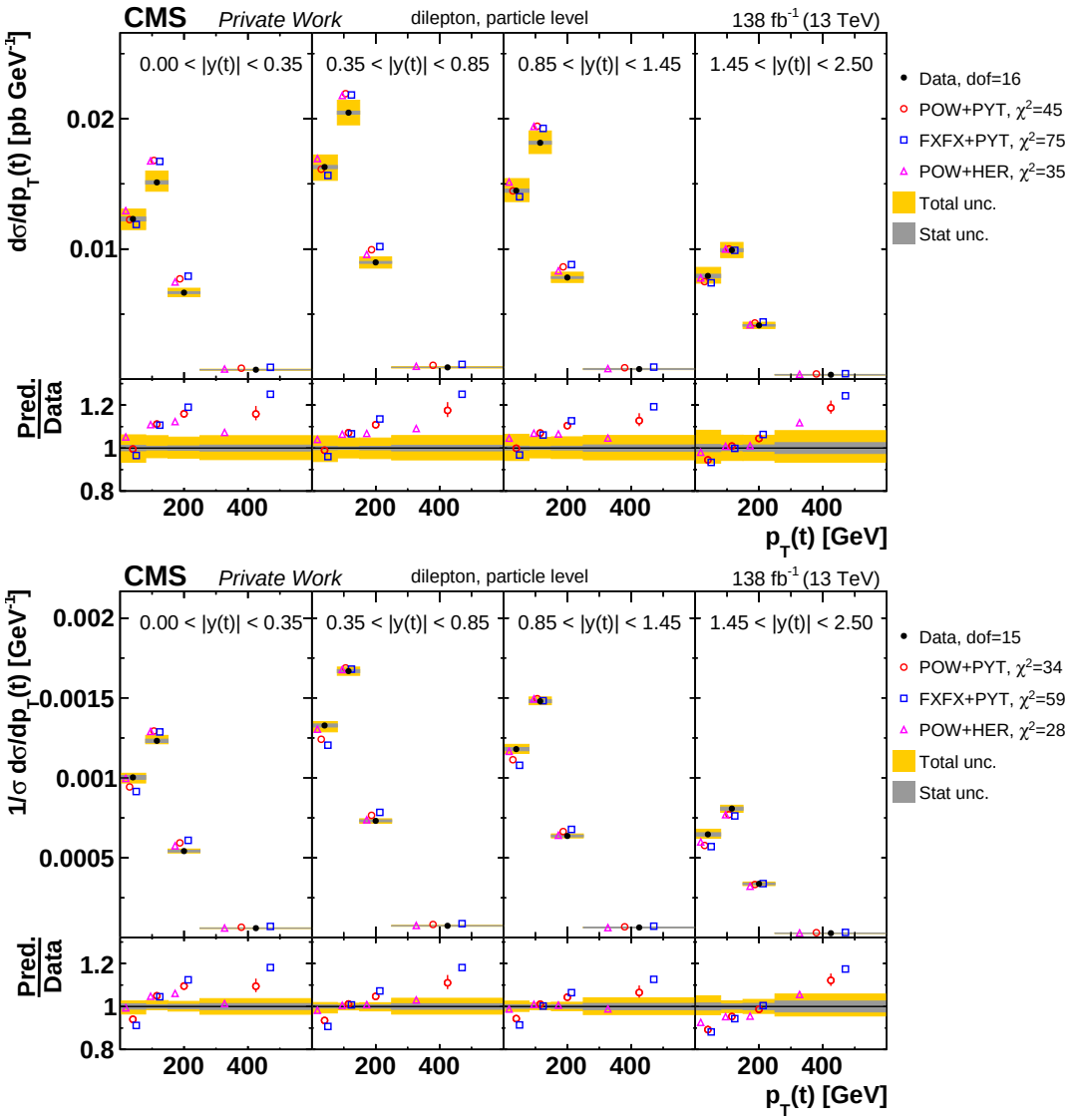

Figure 10.2: Comparison of the measured absolute (top) and normalized (bottom) $[y(t), p_{\mathrm{T}}(t)]$ particle level cross sections to MC predictions (see Fig. 10.1 for further details).

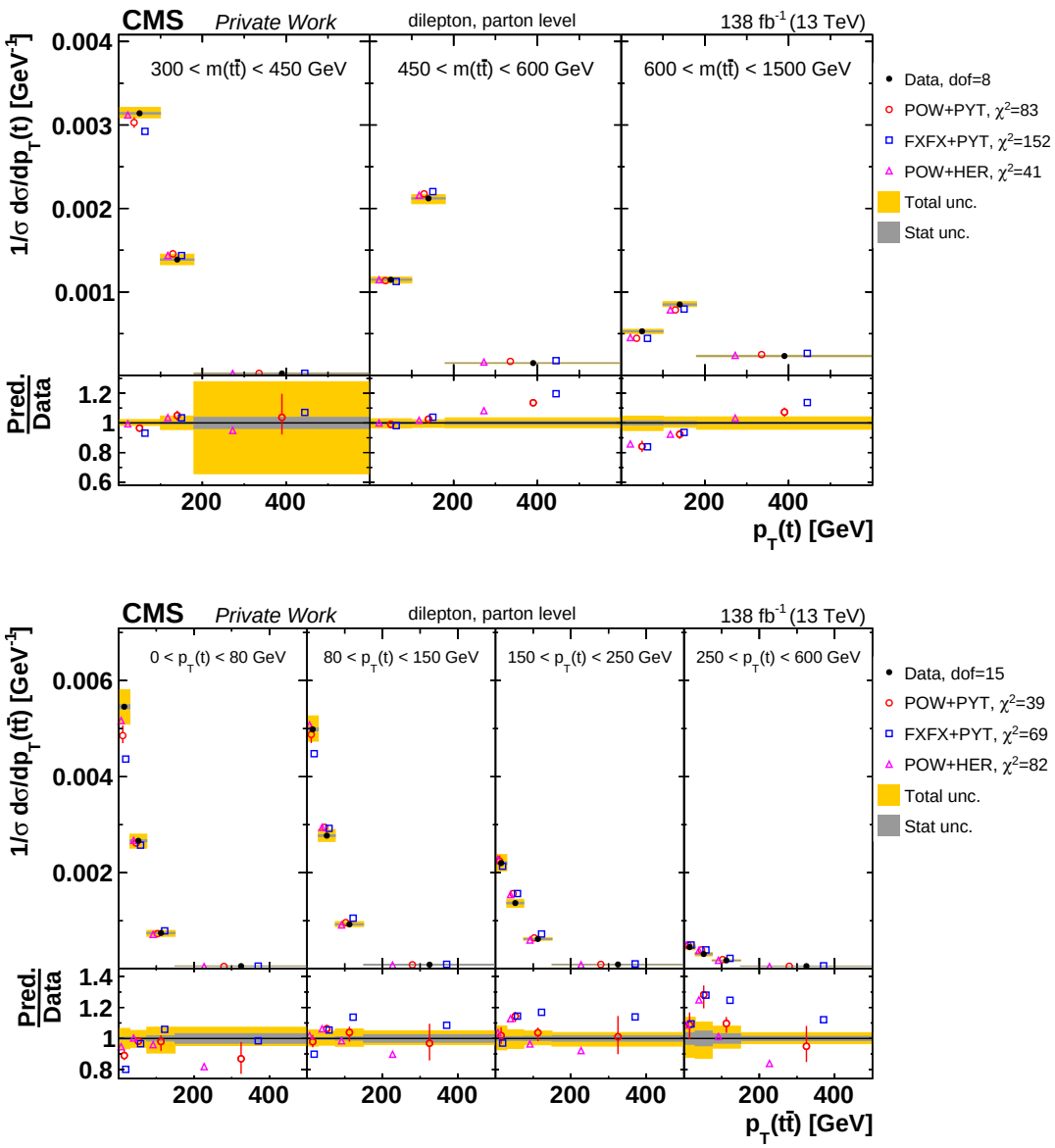

Figure 10.3: Comparison of the measured $[M(\mathrm{t\bar{t}}),p_{\mathrm{T}}(t)]$ (top) and $[p_{\mathrm{T}}(t),p_{\mathrm{T}}(\mathrm{t\bar{t}})]$ (bottom) parton level normalized cross sections to MC predictions (see Fig. 10.1 for further details).

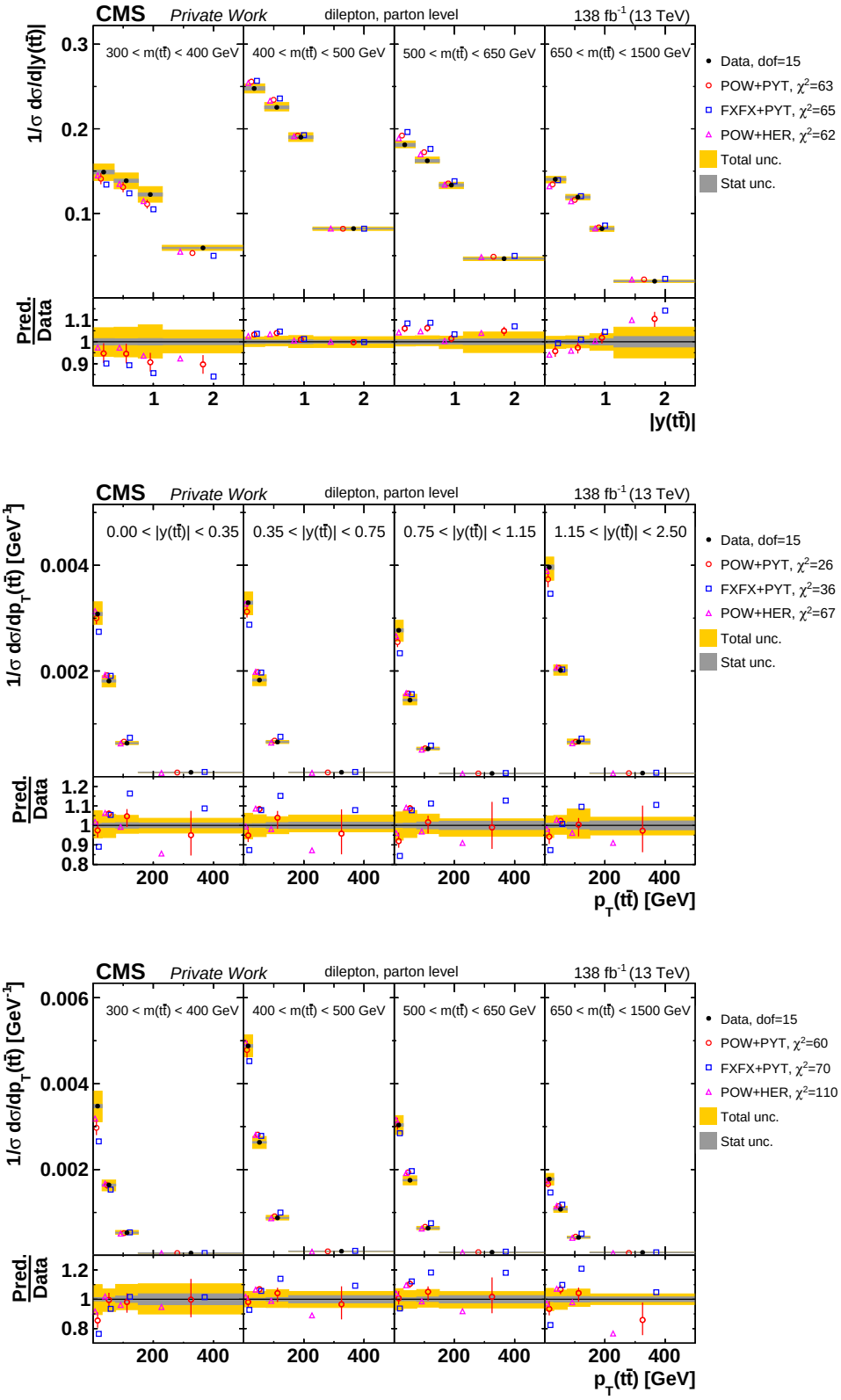

Figure 10.4: Comparison of the measured $[M(\mathrm{t\bar{t}}),y(\mathrm{t\bar{t}})]$ (top), $[y(\mathrm{t\bar{t}}),p_{\mathrm{T}}(\mathrm{t\bar{t}})]$ (middle) and $[M(\mathrm{t\bar{t}}),p_{\mathrm{T}}(\mathrm{t\bar{t}})]$ (bottom) parton level normalized cross sections to MC predictions (see Fig. 10.1 for further details). The *Loose KR* (see Section 7.1.2) is used for $[M(\mathrm{t\bar{t}}),y(\mathrm{t\bar{t}})]$ and $[M(\mathrm{t\bar{t}}),p_{\mathrm{T}}(\mathrm{t\bar{t}})]$.

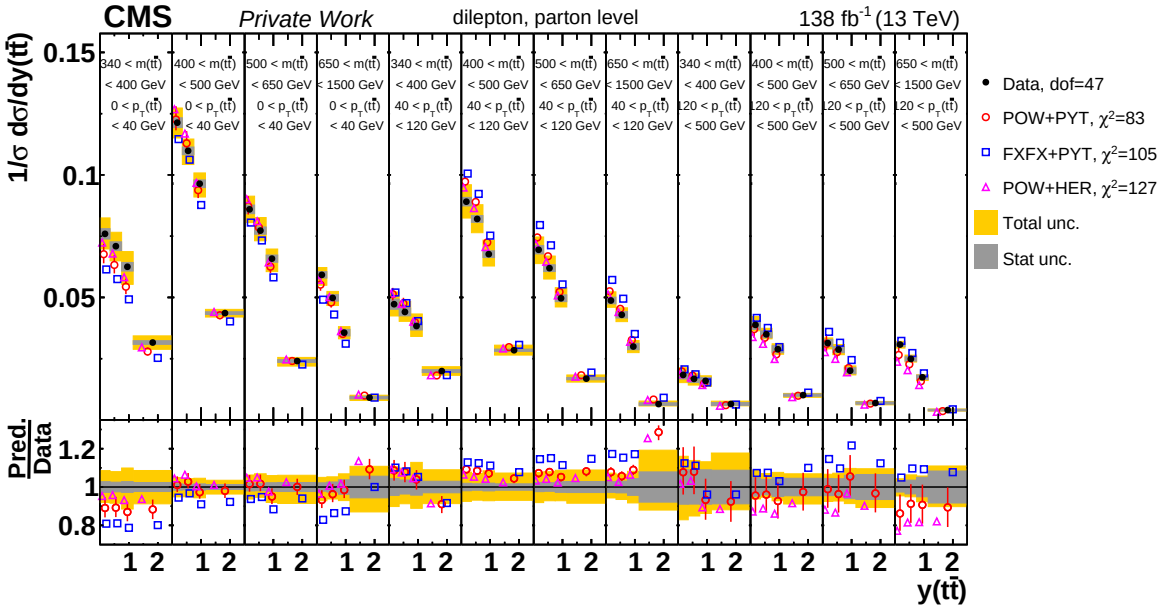

Figure 10.5: Comparison of the measured $[p_{\mathrm{T}}(\mathrm{t\bar{t}}),M(\mathrm{t\bar{t}}),y(\mathrm{t\bar{t}})]$ parton level normalized cross sections to MC predictions (see Fig. 10.1 for further details). The *Loose KR* (see Section 7.1.2) is used for this cross section.

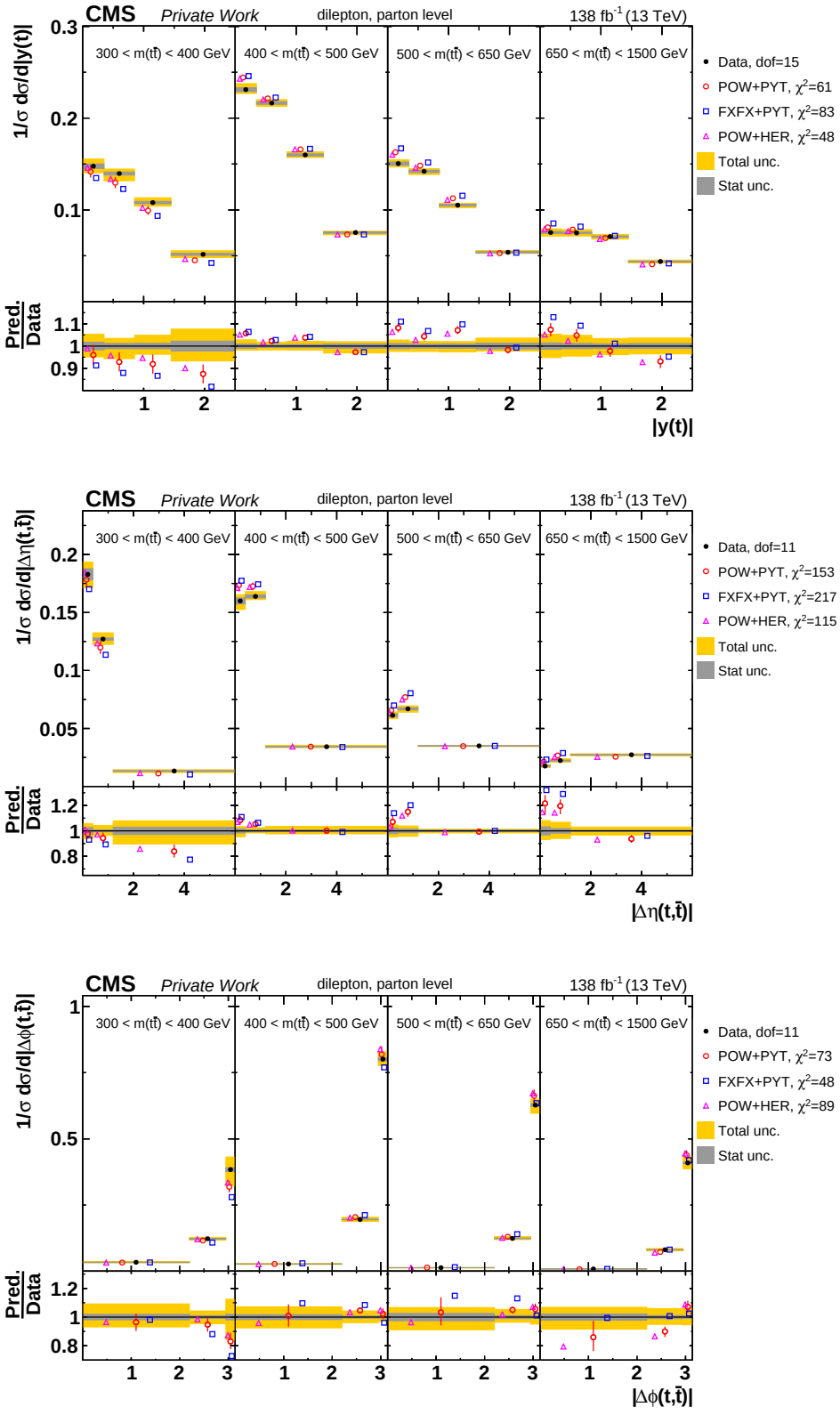

Figure 10.6: Comparison of the measured $[M(\mathrm{t\bar{t}}),y(t)]$ (top), $[M(\mathrm{t\bar{t}}),\Delta\eta(t,\bar{t})\ ]$ (middle) and $[M(\mathrm{t\bar{t}}),\Delta\phi(t,\bar{t})\ ]$ (bottom) parton level normalized cross sections to MC predictions (see Fig. 10.1 for further details).

10.2.2 $t\bar{t}$ production in the presence of additional jets

The correlation of the top and $t\bar{t}$ system observables with the extra jet multiplicity is studied. The additional jets are always measured at particle level, while the top quark and top antiquark are either measured at parton level in the full phase space or at particle level in a fiducial phase space (see Section 8.3.3).

The requirements of a minimum jet p_T ($p_{T\,\mathrm{jet}}^{\mathrm{min}}$) and the minimum separation with respect to the selected b-jets from the top quark and top antiquark decay ($\Delta R_{(b,j)}$) are a key ingredient in the selection of extra jets (see Section 6.2). In Figure 10.7, the extra jet multiplicity (N_{jet}) distributions are shown for minimum extra jet p_T values of 40 and 100 GeV, and also separately for $\Delta R_{(b,j)} = 0.4$ and $\Delta R_{(b,j)} = 0.8$. The distributions correspond to a parton level definition of the top quark and top antiquark. From these measurements one can conclude that the N_{jet} distribution is reasonably well described by the 'POW+PYT' MC for the lower $p_{T\,\mathrm{jet}}^{\mathrm{min}}$ value. At larger jet multiplicities ($N_{\mathrm{jet}} \geqslant 2$), 'POW+PYT' starts to overestimate the data for larger $p_{T\,\mathrm{jet}}^{\mathrm{min}}$ cuts. The 'FXFX+PYT' model exhibits large χ^2 values due to that, nearly independent of the $p_{T\,\mathrm{jet}}^{\mathrm{min}}$ cut, it predicts fewer events with $N_{\mathrm{jet}} = 0$, too many with $N_{\mathrm{jet}} = 1$ and has a reasonable description for other jet multiplicities. Regarding the minimum separation with respect to the selected b-jets, only small changes are observed in the distributions obtained with different $\Delta R_{(b,j)}$ cut values. This is important since in the "predecessor" analysis of this work [6], a $\Delta R_{(b,j)} = 0.4$ cut was used in the extra jets definition while in this work it was decided to increase the separation up to 0.8 in order to reduce the possible contamination coming from gluon radiation emitted by the b-jets from the top quark decays that has the chance of being selected as extra jets. The 'POW+PYT' and 'FXFX+PYT' predictions are consistent for parton and particle level cross sections (see Figure 10.8), while 'POW+HER' predicts too many extra jets for the parton level cross section but describes the data reasonably well at particle level. Even if for both parton and particle level the jet reconstruction is the same, it is not the case for the reconstruction of the top and the top antiquark. Therefore, it might be the case that for the parton level distributions there are larger contributions from extra jets in 'POW+HER' from events that are predominantly outside the particle level fiducial phase space for the top quark and top antiquark.

From now on, for all the presented cross sections, the $p_{T\,\mathrm{jet}}^{\mathrm{min}} > 40\,\mathrm{GeV}$ and $\Delta R_{(b,j)} = 0.8$ cuts are used for the selection of the additional jets. This means that for measurements like $[N_{\mathrm{jet}},M(t\bar{t})]$ and $[N_{\mathrm{jet}},p_T(t)]$, these cuts are used.

In Figure 10.9, the top quark p_T is investigated as a function of N_{jet}. The $[N_{\mathrm{jet}},p_T(t)]$ measurement shows that for 'POW+PYT' the effect of a harder $p_T(t)$ spectrum seems to be mainly present for zero additional jets ($N_{\mathrm{jet}} = 0$) and to to vanish with the increase of N_{jet}. Overall the 'POW+HER' generator provides the best description of the $p_T(t)$ distributions at the particle level, but fails at the parton level where it predicts a clearly too soft $p_T(t)$ spectrum. The results for $[N_{\mathrm{jet}},y(t)]$ and $[N_{\mathrm{jet}},\Delta\eta(t,\bar{t})]$ are presented in Figure 10.10. The distribution of the top quark rapidity as function of the extra jets multiplicity, denoted as $[N_{\mathrm{jet}},y(t)]$, illustrates that the data prefer slightly less central $|y(t)|$ values than the models, with a weak dependence on N_{jet}. The description by the models for the $[N_{\mathrm{jet}},\Delta\eta(t,\bar{t})]$ values is poor, which is also indicated by large χ^2 values. For the $N_{\mathrm{jet}} = 0$ and $N_{\mathrm{jet}} = 1$ bins, there is a clear trend that the models predict too small rapidity separations between top quarks, while in the last bin ($N_{\mathrm{jet}} > 1$) this trend is slightly reversed.

The correlation between the $t\bar{t}$ kinematics and N_{jet} are studied at parton level for the $M(t\bar{t})$, $|y(t\bar{t})|$ and $p_{\text{T}}(t\bar{t})$ observables in Figure 10.11. The 'POW+PYT' model shows a fairly good description of $M(t\bar{t})$ for all N_{jet} ranges, while 'FXFX+PYT' predicts a harder $M(t\bar{t})$ spectra for $N_{\text{jet}} = 1$ and 'POW+HER' presents a considerable deviation with respect to data for $N_{\text{jet}} \leq 1$. In the case of the $[N_{\text{jet}},y(t\bar{t})]$ cross section, the shapes of the distributions are reasonably described by the models irrespectively of the N_{jet} range. It is clear that extra QCD radiation in the event leads to $N_{\text{jet}} \geq 1$, but also causes as well a $p_{\text{T}}(t\bar{t}) \neq 0$. This positive correlation between $p_{\text{T}}(t\bar{t})$ and N_{jet} is evidenced in the $[N_{\text{jet}},p_{\text{T}}(t\bar{t})]$ measurement. The 'POW+PYT' model provides a reasonable description of the measured $p_{\text{T}}(t\bar{t})$ for $N_{\text{jet}} = 0, 1$. This is not the case for higher bin multiplicities ($N_{\text{jet}} > 1$) where this model predicts a too steep rise of the cross section over the first three $p_{\text{T}}(t\bar{t})$ ranges from 0 to 100 GeV. The ratio resulting from the comparison between 'FXFX+PYT' and the data, always exhibits a positive slope over the first three $p_{\text{T}}(t\bar{t})$ ranges, irrespectively of N_{jet}. The prediction from the 'POW+HER' model shows a general trend towards softer $p_{\text{T}}(t\bar{t})$ distributions that is particularly enhanced for $N_{\text{jet}} > 1$.

Triple-differential studies as a function of N_{jet}, $M(t\bar{t})$, and $|y(t\bar{t})|$ are presented in Figures 10.12 and 10.13. The $[N_{\text{jet}}^{0,1+},M(t\bar{t}),y(t\bar{t})]$ and $[N_{\text{jet}}^{0,1,2+},M(t\bar{t}),y(t\bar{t})]$ cross sections[4] were one of the highlights of the analysis [6], where these measurements were used for a simultaneous extraction of the top quark pole mass, the strong coupling α_s and the proton PDFs, with a competitive precision. Besides $[N_{\text{jet}}^{0,1,2+},M(t\bar{t}),y(t\bar{t})]$ and $[N_{\text{jet}}^{0,1,2+},M(t\bar{t}),y(t\bar{t})]$, in this work the measurement of the $[N_{\text{jet}}^{0,1,2,3+},M(t\bar{t}),y(t\bar{t})]$ is presented for the first time, where four bins are used for N_{jet}: $N_{\text{jet}} = 0$, $N_{\text{jet}} = 1$, $N_{\text{jet}} = 2$ and $N_{\text{jet}} \geq 3$. As signaled by the χ^2 values, there is significative increment in the discrepancy between the data and the MC models when going from two, to three and four bins of N_{jet}. Overall, the 'POW+PYT' model provides the best description of the data. The 'FXFX+PYT' predictions exhibit the same normalization problems related to its description of the N_{jet} distribution predicting in particular too many events with $N_{\text{jet}} = 1$ (see Figure 10.7). This model also has a small trend to predict too high cross sections towards large $M(t\bar{t})$, while it seems to describe the $|y(t\bar{t})|$ shapes reasonably well. In Figure 10.12 one observes, that again as a direct consequence from its description of the extra jet multiplicity, the 'POW+HER' model delivers a description at particle level that is comparable to that of 'POW+PYT', but fails at parton level where it overshoots the data for the $N_{\text{jet}} = 2$ and $N_{\text{jet}} > 2$ bins. The new $[N_{\text{jet}}^{0,1,2,3+},M(t\bar{t}),y(t\bar{t})]$ cross sections clearly exhibits the best separation power between the models and the 'POW+PYT' calculations provide the overall best description.

[4] In the cross section names the binning for the extra jet multiplicity is specified. For example, $[N_{\text{jet}}^{0,1,2+},M(t\bar{t}),y(t\bar{t})]$ corresponds to the following binning: $N_{\text{jet}} = 0$, $N_{\text{jet}} = 1$ and $N_{\text{jet}} \geq 2$.

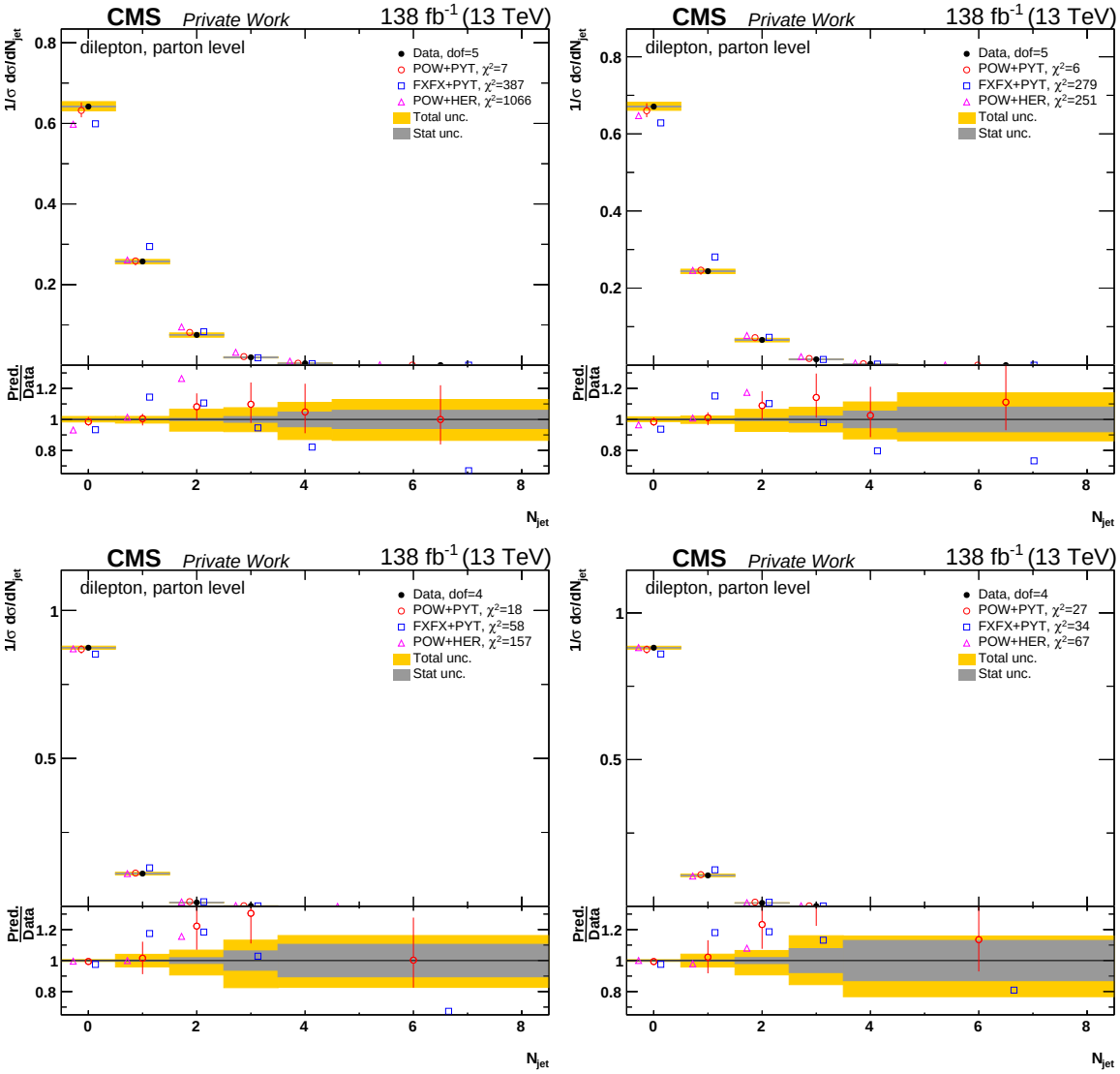

Figure 10.7: Comparison of the measured N_{jet} normalized cross sections to MC predictions (see Fig. 10.1 for further details). The left (right) plots correspond to a selection cut of $\Delta R_{(b,j)} > 0.4$ ($\Delta R_{(b,j)} > 0.8$). The jet p_T cut applied is 40 GeV for the upper plots and 100 GeV for the lower plots. The measurements correspond to the parton level definition of the top quark and top antiquark.

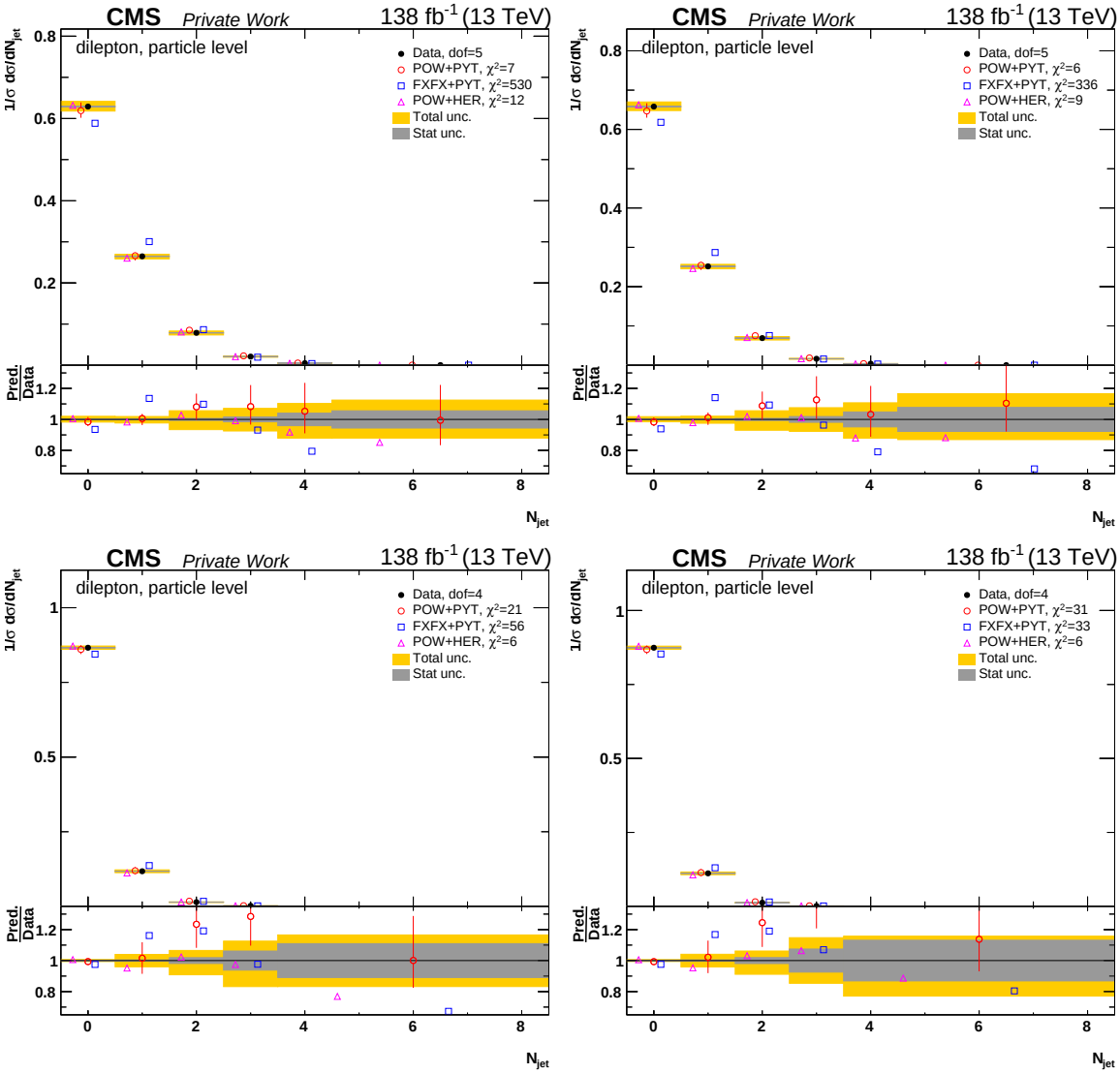

Figure 10.8: Comparison of the measured N_{jet} normalized cross sections to MC predictions (see Fig. 10.1 for further details). The left (right) plots correspond to a $\Delta R_{(b,j)} > 0.4$ ($\Delta R_{(b,j)} > 0.8$). The jet p_T cut has a value of 40 GeV for the top plots and 100 GeV for the bottom plots. The measurements correspond to the particle level definition of the top quark and top antiquark.

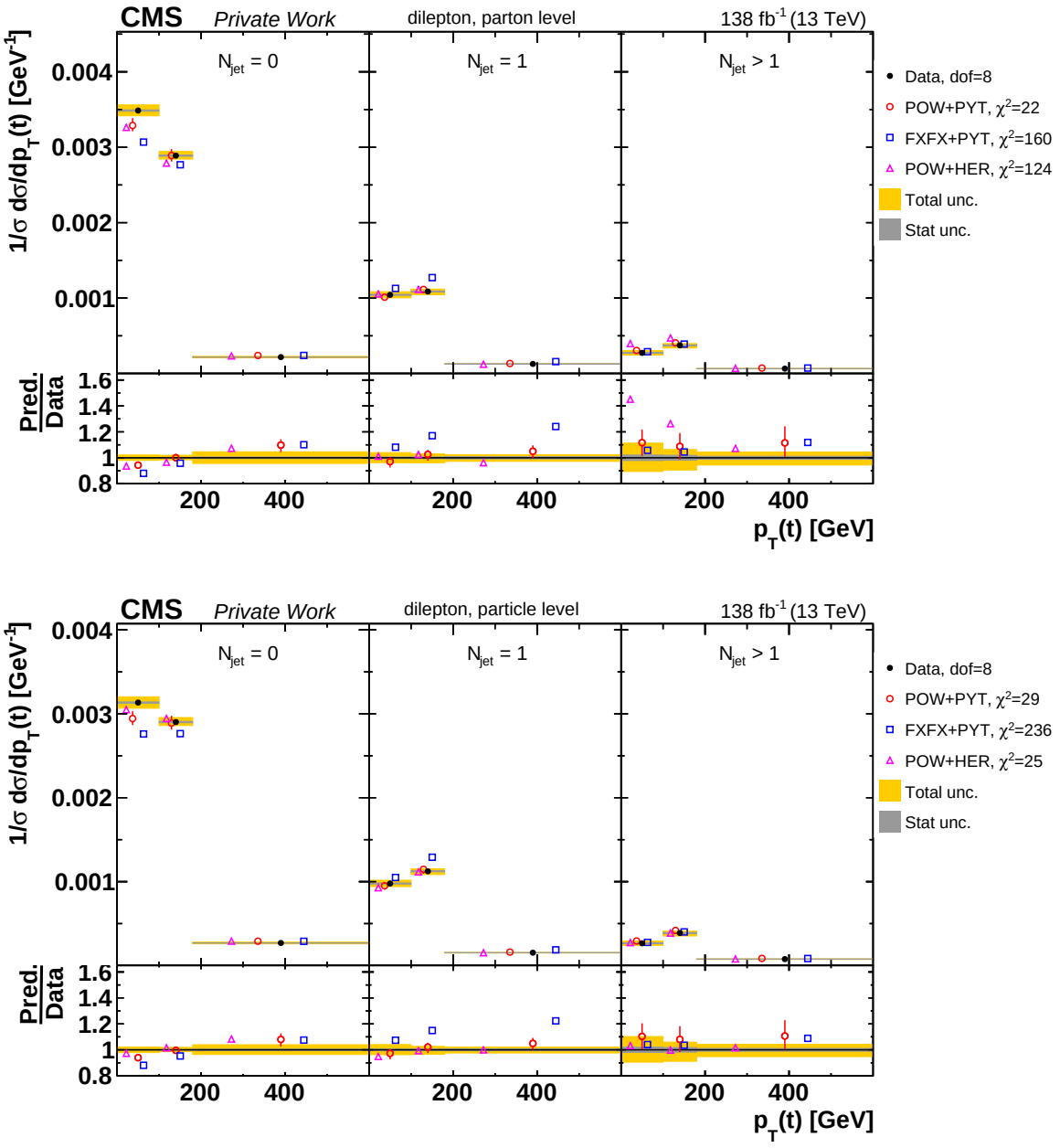

Figure 10.9: Comparison to MC predictions of the measured $[N_{\text{jet}}, p_{\text{T}}(t)]$ normalized cross sections (see Fig. 10.1 for further details). The parton (particle) level measurement is shown in the top (bottom) plot.

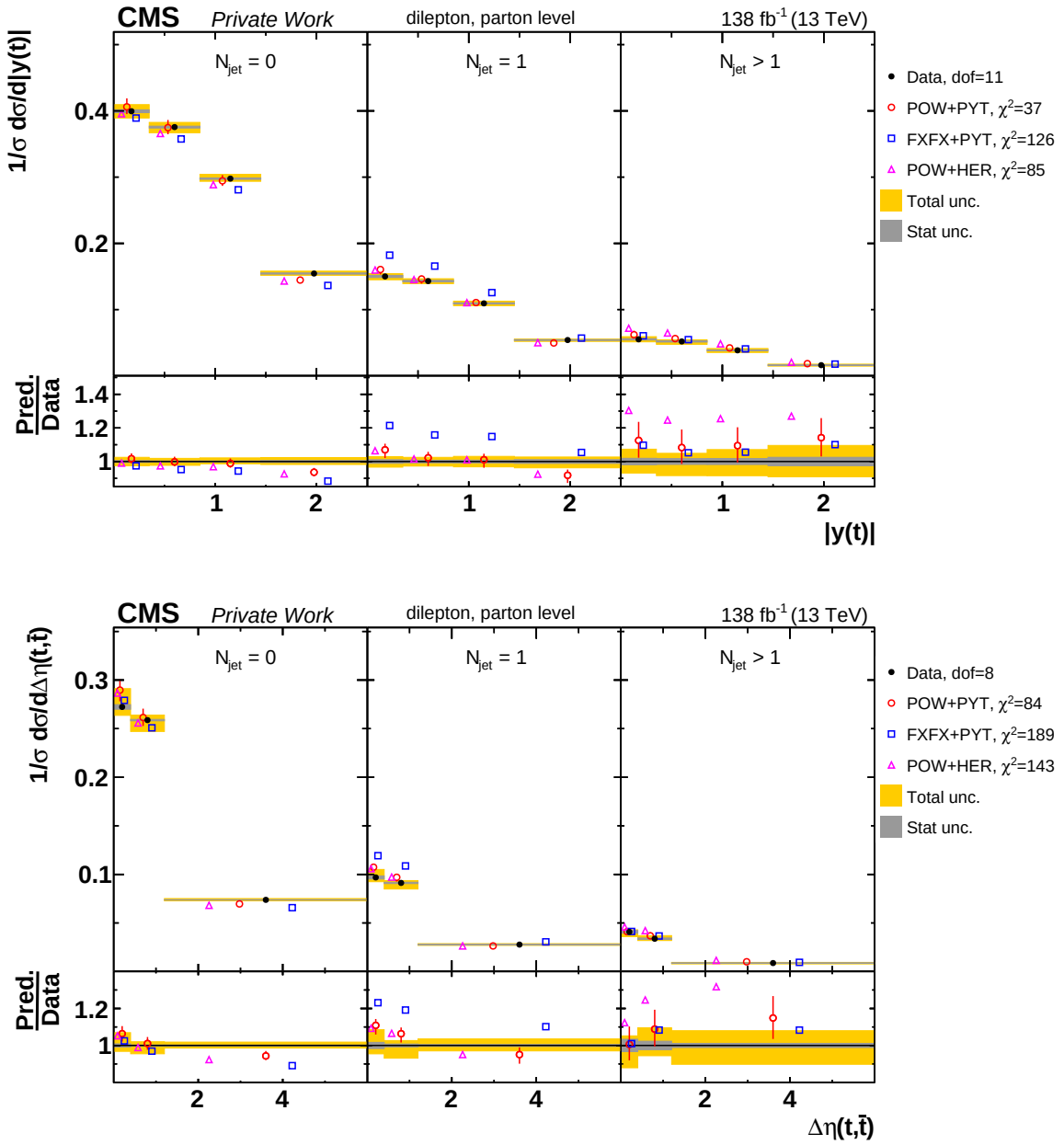

Figure 10.10: Comparison of the measured $[N_{\text{jet}}, y(t)]$ and $[N_{\text{jet}}, \Delta\eta(t,\bar{t})]$ parton level normalized cross sections to MC predictions (see Fig. 10.1 for further details).

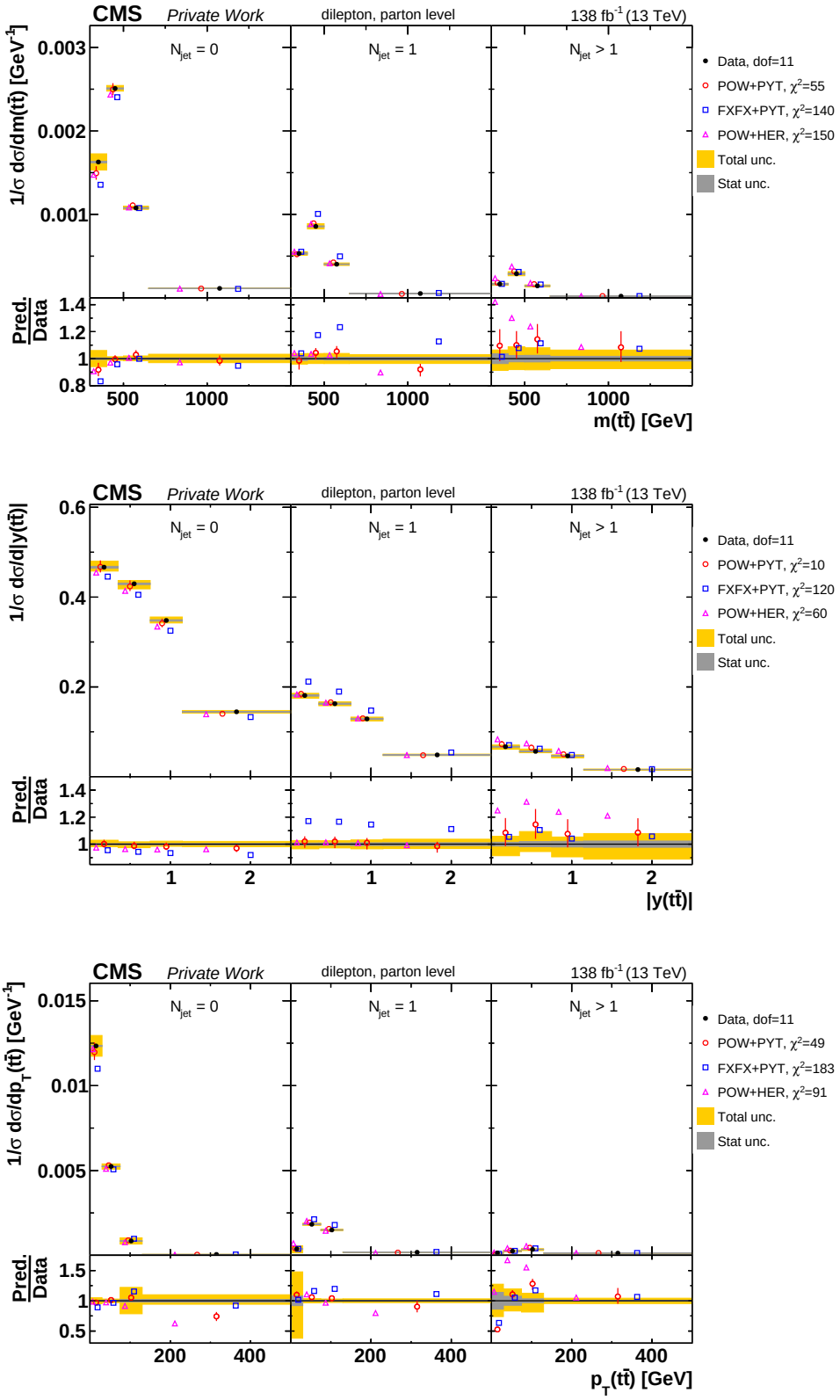

Figure 10.11: Comparison of the measured $[N_{\text{jet}},M(\text{t}\bar{\text{t}})]$ (top), $[N_{\text{jet}},y(\text{t}\bar{\text{t}})]$ (middle) and $[N_{\text{jet}},p_{\text{T}}(\text{t}\bar{\text{t}})]$ (bottom) parton level normalized cross sections to MC predictions (see Fig. 10.1 for further details). The *Loose KR* (see Section 7.1.2) is used for $[N_{\text{jet}},M(\text{t}\bar{\text{t}})]$.

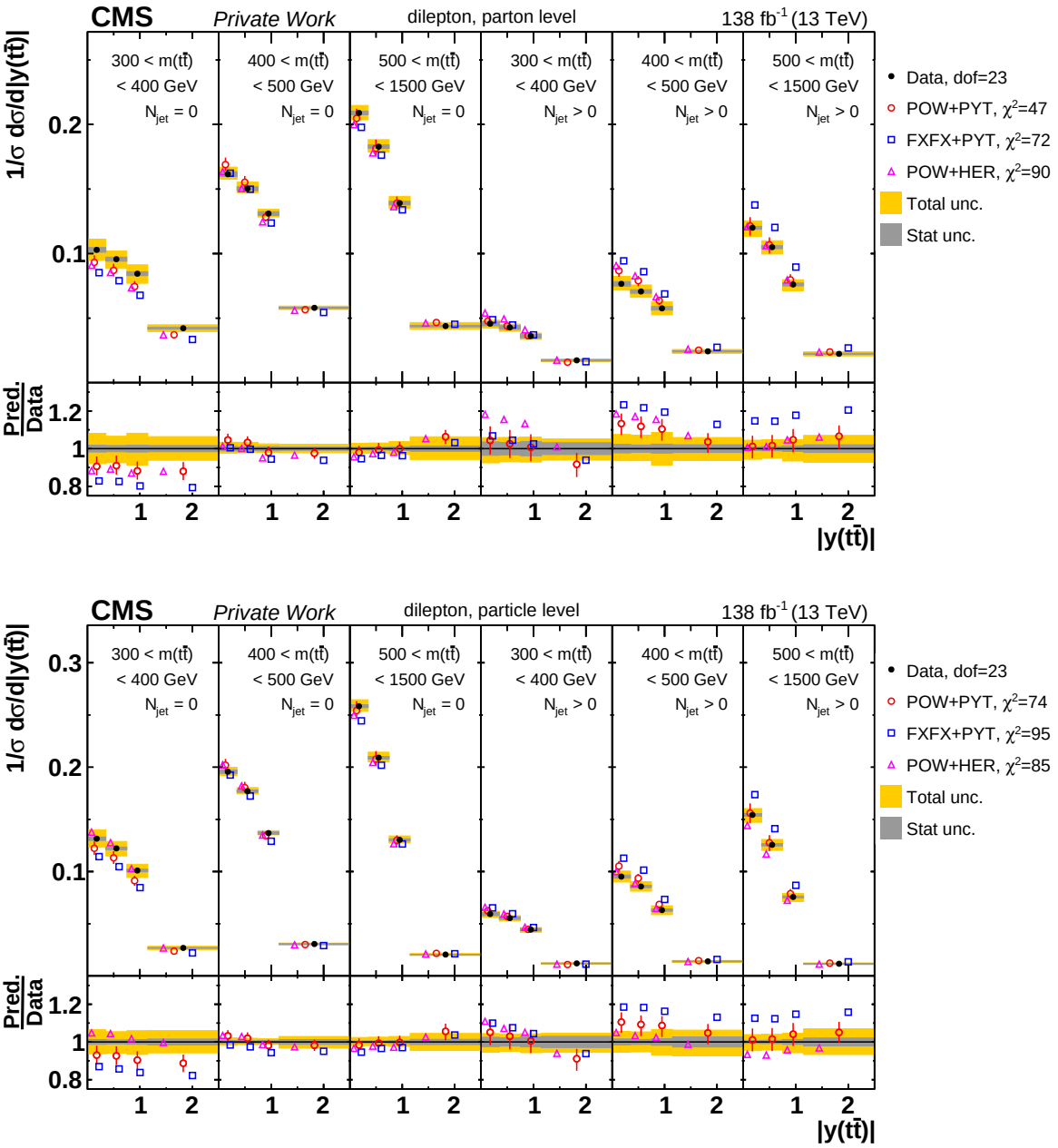

Figure 10.12: Comparison of the measured parton (top) and particle (bottom) level $[N_{\text{jet}}^{0,1+}, M(\text{t}\bar{\text{t}}), y(\text{t}\bar{\text{t}})]$ normalized cross sections to MC predictions (see Fig. 10.1 for further details). The *Loose KR* (see Section 7.1.2) is used for these cross sections.

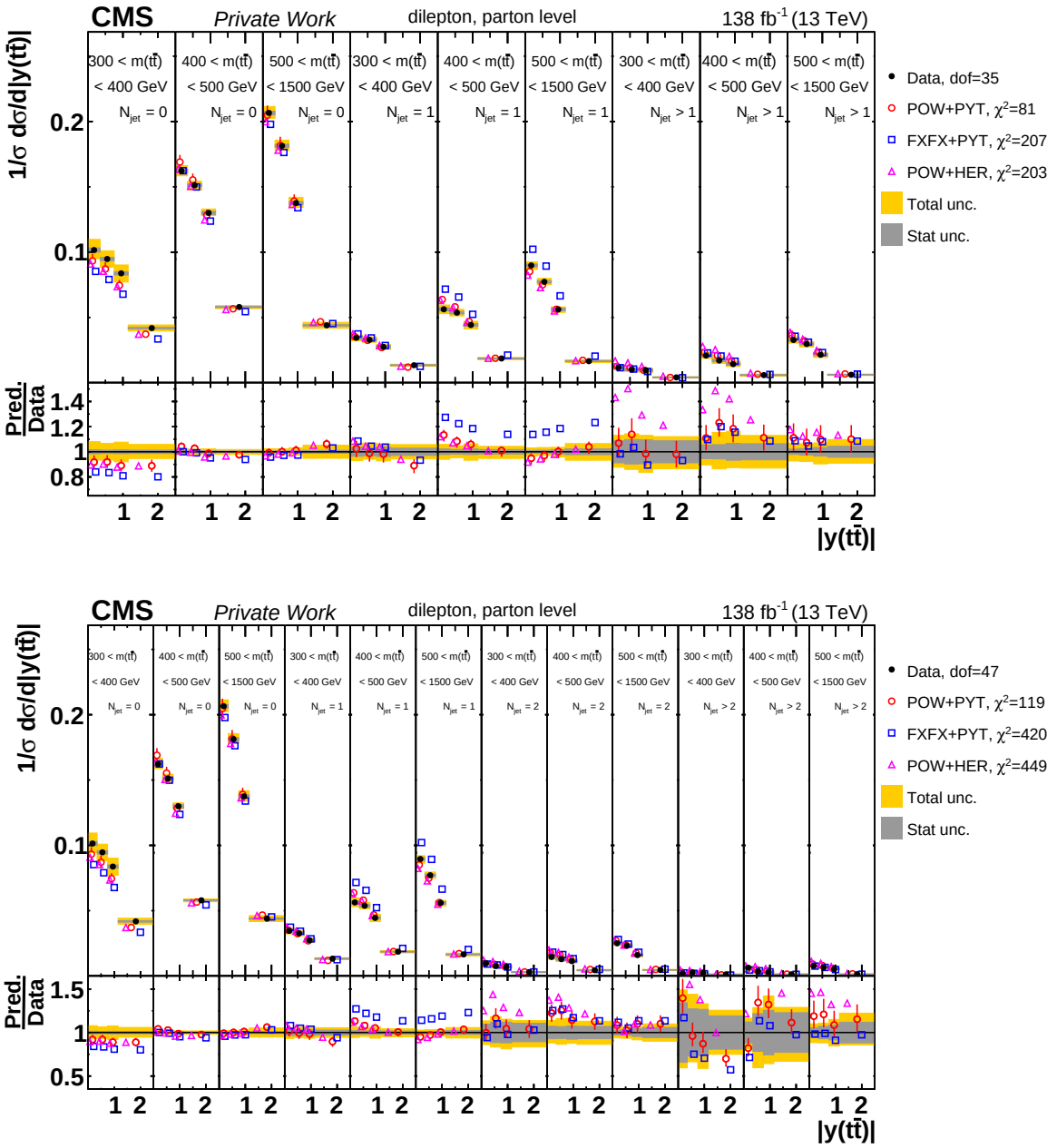

Figure 10.13: Comparison of the measured $[N_{\text{jet}}^{0,1,2+}, M(\text{t}\bar{\text{t}}), y(\text{t}\bar{\text{t}})]$ (top) and $[N_{\text{jet}}^{0,1,2,3+}, M(\text{t}\bar{\text{t}}), y(\text{t}\bar{\text{t}})]$ (bottom) parton level normalized cross sections to MC predictions (see Fig. 10.1 for further details). The *Loose KR* (see Section 7.1.2) is used for these cross sections.

10.2.3 $t\bar{t}$ plus additional jets: studies with leading and sub-leading extra jets

In this section, studies are presented as function of the kinematics of the leading and sub-leading extra jets[5] and the combined $t\bar{t}$ and leading extra jet system[6]. These cross sections are measured only at the $t\bar{t}$ parton level. The p_T and η distributions for the leading (ej_1) and sub-leading ej_2 extra jets are shown in Figure 10.14. These measurements provide a direct probe for our understanding of the jet radiation in $t\bar{t}$ events by the QCD models. The 'POW+PYT' and 'FXFX+PYT' models predict too hard p_T distributions of ej_1 and ej_2. The predictions from 'POW+HER' present in overall the best description of $p_T(ej_1)$ and $p_T(ej_2)$, but shows a significant discrepancy with data in the first and second p_T bins. The $\eta(ej_1)$ and $\eta(ej_2)$ distribution shapes are not well described by the 'POW+HER' model which overestimate the central values and underestimate the tails of the distribution. It is very interesting that 'FXFX+PYT' describes very well the $\eta(ej_2)$ spectrum where the other models show a poorer agreement with the data, predicting more central η distributions. The agreement of the predictions from the 'POW+HER' and 'POW+PYT' MCs with data deteriorates significantly when going from the leading to the sub-leading extra jet by increasing the deviations to the data in the p_T distribution and also predicting too central η values.

In Figure 10.15, the results for the p_T spectra and mass of the $t\bar{t}$+ ej_1 system are presented. The study of $p_T(t\bar{t} + ej_1)$ provides a test of the beyond leading order extra jet production, since non zero values signal the presence of additional jets that leads to a recoiling $t\bar{t}$+ ej_1 system. On the other hand, the $M(t\bar{t} + ej_1)$ observable is known to be highly sensitive to the top quark mass, in particular near the threshold [200]. The best description of the data is provided by 'FXFX+PYT' for $p_T(t\bar{t} + ej_1)$ and 'POW+HER' for $M(t\bar{t} + ej_1)$. In both distributions, 'POW+PYT' highly underestimates the data in the first bin (especially for $M(t\bar{t} + ej_1)$) while overshooting the data in most of the other bins. For the $p_T(t\bar{t} + ej_1)$ distribution, all models seem to exhibit an increasing positive ratio slope.

The measurement of the $p_T(ej_1)/M(t\bar{t})$, $M(t\bar{t} + ej_1)/M(t\bar{t})$ and $\Delta\eta(t, ej_1)/\Delta\eta(t, \bar{t})$ ratio observables are shown in Figure 10.16. None of the MC models shows a good overall description of any of these cross sections, showing in general very similar predictions. The $p_T(ej_1)/M(t\bar{t})$ observable proves the relation of the leading extra jet $p_T(t)$ released in the event to the $t\bar{t}$ invariant mass. The description of the data by the models is similar to what is observed for the $p_T(ej_1)$ distribution (see Figure 10.14). The ratio of the mass of the $t\bar{t}$+ ej_1 system over $M(t\bar{t})$ might be sensitive in the threshold region (i.e. values near 1.0) to soft gluon radiation effects which are addressed in the SM predictions using resummation techniques [201]. In the first bin, representing this threshold region, the data is clearly above the MC predictions. The 'POW+HER' model predicts a particularly bad description for the first and second bins. The $\Delta\eta(t, ej_1)/\Delta\eta(t, \bar{t})$ observable refers to the ratio of the $\Delta\eta$ between the top quark and ej_1 ($\eta_{(t)} - \eta(ej_1)$), over the difference in pseudorapidity of the top and the top antiquark ($\eta_{(t)} - \eta_{(\bar{t})}$). This is a very interesting observable since it is expected to provide information about if the leading extra jet is emitted between or outside the $t\bar{t}$ system. It can be easily deduced that if $0 < \Delta\eta(t, ej_1)/\Delta\eta(t, \bar{t}) < 1$, then the leading extra jet is emitted in between the two top quarks, otherwise, they are emitted outside the two top quarks. All the MC models present a similar overall prediction with 'FXFX+PYT' providing a slightly

[5]The leading (sub-leading) extra jet is the extra jet with the highest (second highest) p_T value.

[6]This system is obtained by adding the Lorentz vectors of the $t\bar{t}$ system and the leading extra jet.

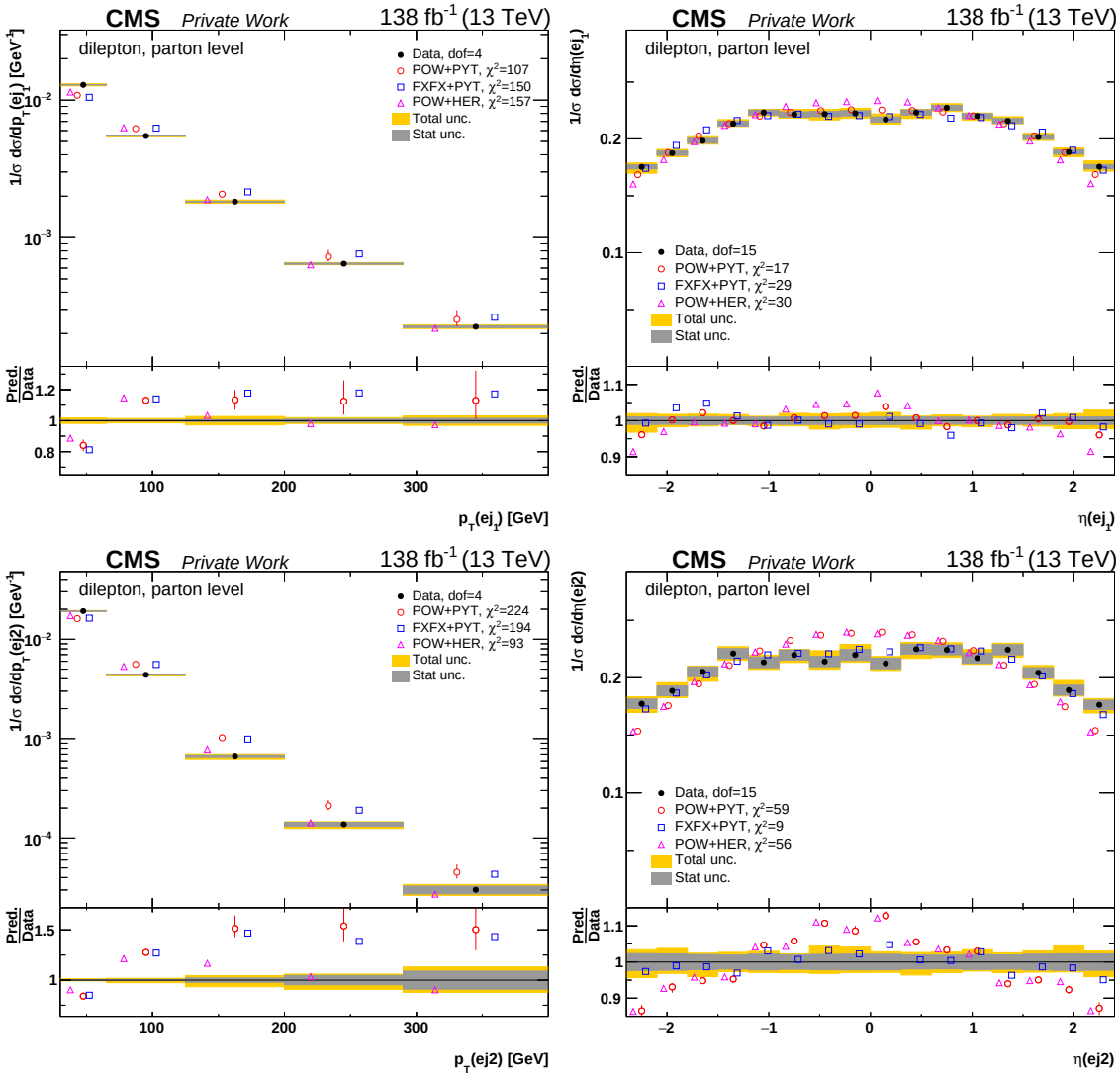

Figure 10.14: Comparison of the normalized p_T (left column) and η (right column) extra jets parton level cross sections for the leading (top row) and sub-leading (bottom row) jet to different MC predictions (see Fig. 10.1 for further details).

better agreement with data. All models clearly predict more leading extra jets coming from in between the two top quarks than seen in data. This gives a hint that there might be a problem in the MC models about the right mixture of extra gluon radiation coming from the NLO matrix element (ME) calculations and the ISR/FSR parton showers; overestimating the ME part.

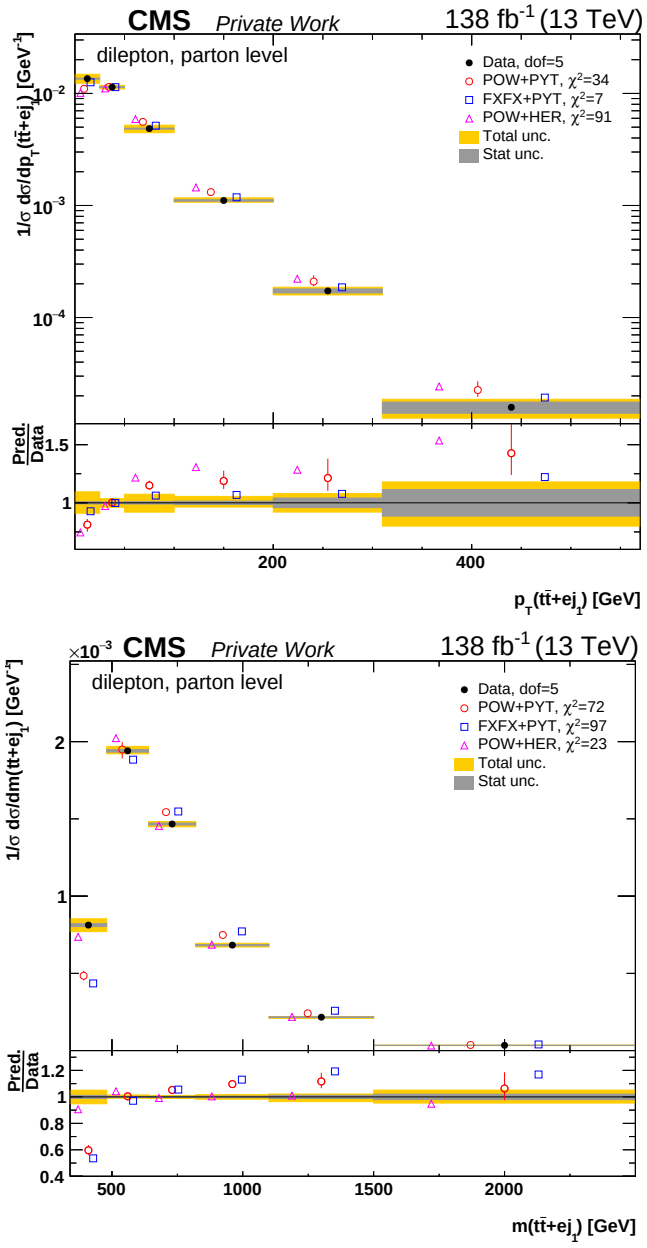

Figure 10.15: Comparison of the measured $p_{\mathrm{T}}(\mathrm{t\bar{t}}+\mathrm{ej}_1)$ (top) and $M(\mathrm{t\bar{t}}+\mathrm{ej}_1)$ (bottom) parton level normalized cross sections to different MC predictions (see Fig. 10.1 for further details).

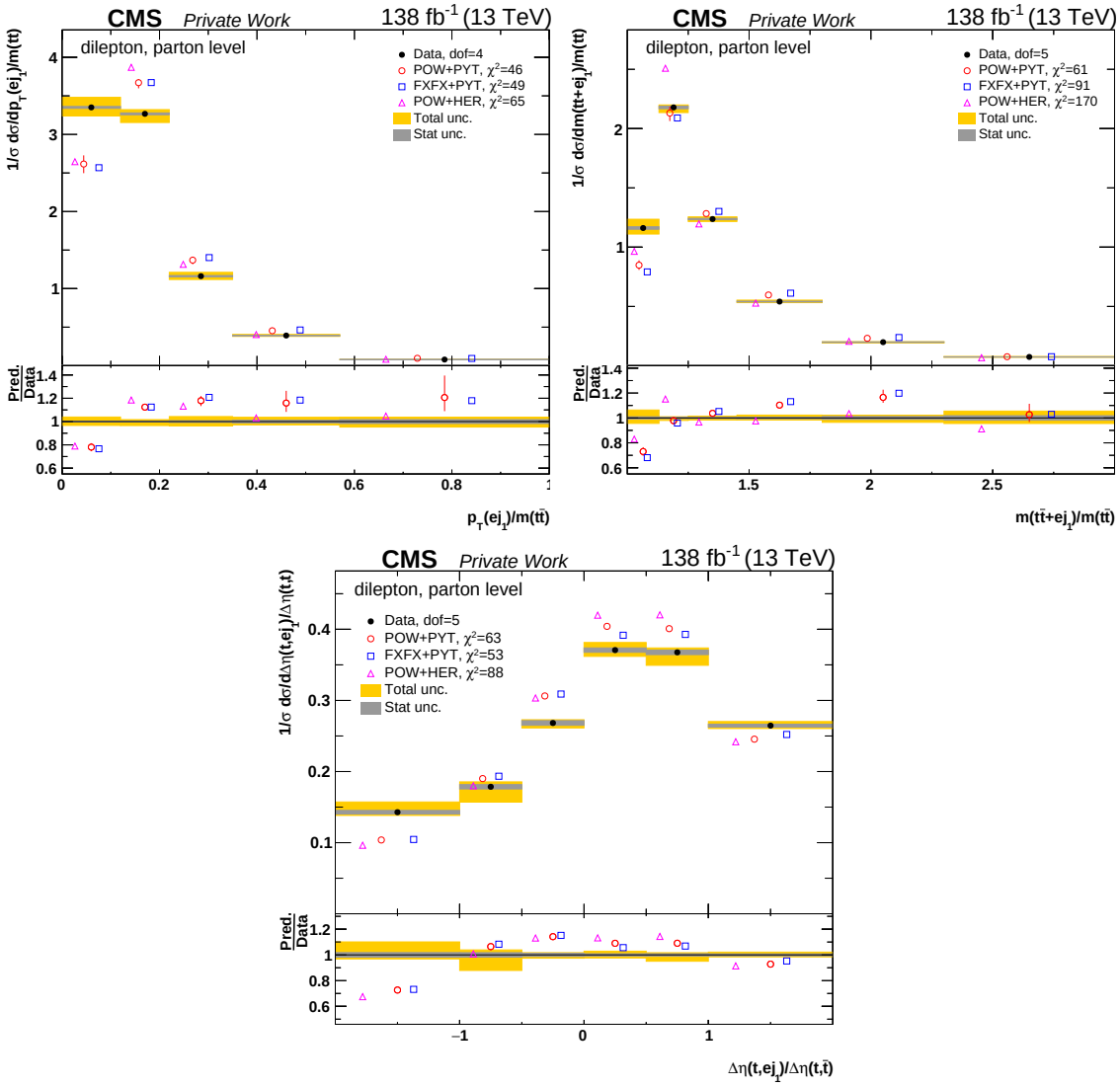

Figure 10.16: Comparison of the measured $p_{\mathrm{T}}(\mathrm{ej}_1)/M(\mathrm{t\bar{t}})$ (top), $M(\mathrm{t\bar{t}}+\mathrm{ej}_1)/\mathrm{M}(\mathrm{t\bar{t}})$ (middle) and $\Delta\eta(t, ej_1)/\Delta\eta(t, \bar{t})$ (bottom) parton level normalized cross sections to different MC predictions (see Fig. 10.1 for further details).

10.3 Comparison of 2D $t\bar{t}$ system cross sections to the latest beyond-NLO fixed order QCD calculations

In this section, the measured normalized parton level cross sections are also compared to the following calculations at beyond-NLO precision:

- $a\mathbf{N^3LO}$: An approximate next-to-NNLO calculation [202] based on the resummation of soft-gluon contributions in the double-differential cross section at NNLL accuracy in the moment-space approach. The renormalization and factorization scales are set to m_T and m_t for the $p_{\mathrm{T}}(t)$ and the $y(t)$ distributions, respectively. This prediction is only available for the $[y(t),p_{\mathrm{T}}(t)]$ cross section.

- **STRIPPER (NNLO)**: A calculation with full NNLO precision in QCD using the STRIPPER framework [203–205]. The dynamic renormalization and factorization scales are set to $m_T/2$ for $p_{\mathrm{T}}(t)$ and $p_{\mathrm{T}}(\bar{t})$ and $H_T/4$ for $y(t)$, $y(\bar{t})$, $p_{\mathrm{T}}(t\bar{t})$, $y(t\bar{t})$, $M(t\bar{t})$, and $|\Delta y(t,\bar{t})|$, where $m_T = \sqrt{m_t^2 + p_{\mathrm{T}}(t)^2}$ and H_T is the sum of the top quark and antiquark m_T values [4, 206].

- **MATRIX (NNLO)**: NNLO QCD accuracy prediction obtained with the MATRIX package [207–214]. The dynamic scales where set to $H_T/4$.

- **MiNNLOPS (NNLOPS)**: NNLOPS predictions computed using POWHEG-BOX-V2 [126]. These calculations are obtained using the MiNNLOPS method [215, 216], which supplements the MiNLO prescription [217, 218] with the missing pieces to reach NNLO accuracy for inclusive observables. The renormalization scale for the two powers of the strong coupling constant is set to $H_T/4$, while the scale of the modified logarithms is set to $0.5\,\mu$. The parton showering is obtained with Pythia 8, and includes the effect of underlying event and hadronization.

In all predictions the top quark mass is set to $m_t = 172.5\,\mathrm{GeV}$ and the NNPDF31(NNLO) [67] PDF set is used.

The comparisons with the described predictions of some top quark and $t\bar{t}$ system multi-differential cross section results are shown in Figures 10.17-10.20. Similarly as for comparison with the MC models, the corresponding χ^2 is shown for the different predictions in each plot and the reference MC ('POW+PYT') is also included to serve as reference for the description by the MC models. The plot style is also similar to the MC to data comparisons discussed earlier in this Chapter and it is explained in the caption of Figure 10.17, where the the $[y(t),p_{\mathrm{T}}(t)]$ cross section is presented. For the MC models it was observed that the positive slope observed in the ratio of the MC and data $p_{\mathrm{T}}(t)$ distributions was present in every range of rapidity, but this is not the case for the theory beyond-NLO predictions which only show such a slope in the ratio in the last rapidity bin. The MiNNLOPS (NNLOPS) prediction shows the best agreement with the data, and in general all the predictions give a better description of the distributions than the MC models.

In Figure 10.18 the comparisons to the $[M(t\bar{t}),p_{\mathrm{T}}(t)]$ and $[M(t\bar{t}),y(t\bar{t})]$ results are shown. The predictions show a very good agreement with data in the $[M(t\bar{t}),p_{\mathrm{T}}(t)]$ cross section, especially in the highest mass values where the MC models experience an enhancement of

the top p_T slope. The best description is provided by the MATRIX (NNLO) calculation for this measurement. For the $[M(t\bar{t}),y(t\bar{t})]$ cross section, all the predictions show similar values to 'POW+PYT', with only a slightly better overall agreement with the data. The beyond-NLO QCD calculations show an improvement with respect to 'POW+PYT' in the second $M(t\bar{t})$ bin but overestimate the data more for the higher values of $|y(t\bar{t})|$ in the last $M(t\bar{t})$ bin.

The weakest point of the the analyzed fixed order predictions is the description of the $p_T(t\bar{t})$ data distribution. This can be deduced from the comparisons in different bins of $p_T(t)$, $y(t\bar{t})$ and $M(t\bar{t})$ in Figure 10.19. Overall, 'POW+PYT' shows a better agreement with data than STRIPPER (NNLO), MATRIX (NNLO) and MiNNLOPS (NNLOPS) for the $[M(t\bar{t}),p_T(t\bar{t})]$, $[y(t\bar{t}),p_T(t\bar{t})]$ and $[p_T(t),p_T(t\bar{t})]$ cross sections. The wiggle effect in the second $p_T(t\bar{t})$ bin of the ratio of prediction and data, that is present in 'POW+PYT' is slightly enhanced for the tested fixed order predictions. The MiNNLOPS (NNLOPS) calculations show small differences with the other predictions, showing a slight reduction of the wiggle effect, but also present bigger disagreements with data in the highest $p_T(t\bar{t})$ bin for all ranges of $p_T(t)$, $y(t\bar{t})$ and $M(t\bar{t})$. It should be noted that since the non-zero $p_T(t\bar{t})$ values are an NLO effect for $t\bar{t}$ production, the NNLO predictions can only provide a NLO accuracy for the distributions of this observable, while for the MC models the parton shower can approximate higher orders.

The comparisons for the $[M(t\bar{t}),y(t)]$ and $[M(t\bar{t}),\Delta\eta(t,\bar{t})\,]$ cross sections are shown in Figure 10.20. In the case of $[M(t\bar{t}),y(t)]$, the predictions show very similar shapes as 'POW+PYT', especially for the first three $M(t\bar{t})$ bins $(300-650$ GeV). The calculations from STRIPPER (NNLO), MATRIX (NNLO) and MiNNLOPS (NNLOPS) provide a slightly better description of the data for the second and last $M(t\bar{t})$ ranges. As shown in Section 10.2.1, all the analyzed MC models have a poor agreement with data for the $[M(t\bar{t}),\Delta\eta(t,\bar{t})\,]$ cross section predicting a too small rapidity separation between the top and top anti-quark. The beyond-NLO QCD predictions show a much better description of the distributions, with the biggest improvement in the second and last $M(t\bar{t})$ bin.

Overall, the tested beyond-NLO theory predictions provide a mostly reasonable description of the data distributions. Major improvements with respect to MC models are the better description of the top p_T distribution and of the $[M(t\bar{t}),\Delta\eta(t,\bar{t})\,]$ cross section. It is also important to remark that the STRIPPER (NNLO) and MATRIX (NNLO) calculations exhibit a not so good $p_T(t\bar{t})$ description that is of similar quality or even worse to the one provided by the MC models.

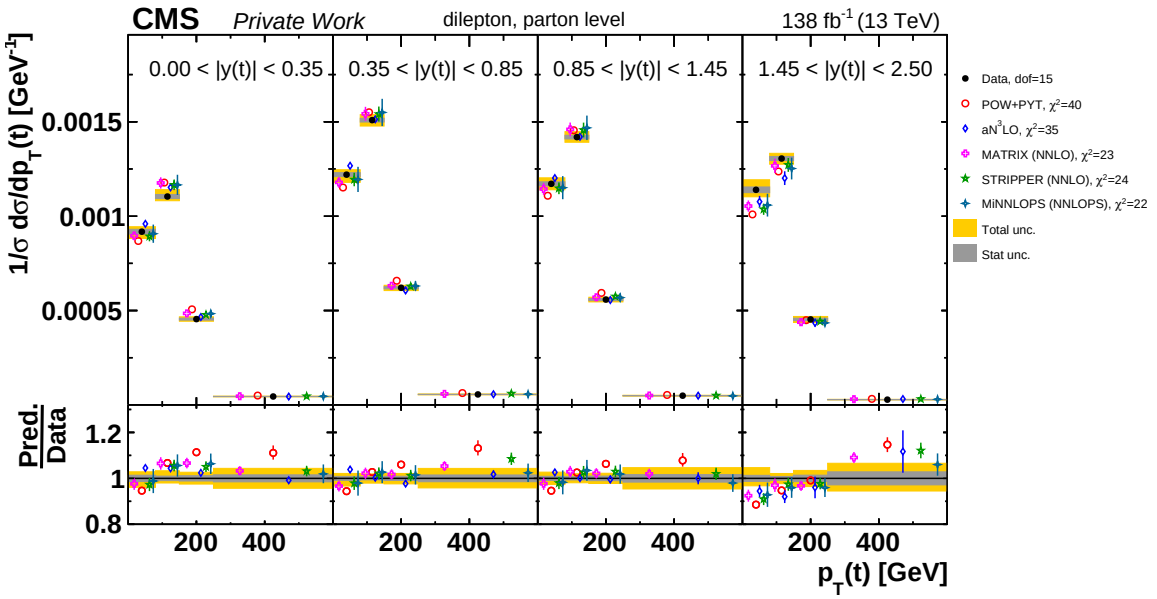

Figure 10.17: Comparison of the measured normalize parton level $[y(t), p_{\mathrm{T}}(t)]$ cross sections to different fixed order predictions: $a\mathrm{N}^3\mathrm{LO}$, MATRIX (NNLO) and STRIPPER (NNLO) (see Section 10.3). The data are shown as filled circles with dark and light bands indicating the statistical and total (sum in quadrature of statistical and systematic) uncertainties, respectively. The other points correspond to the cross sections of the different predictions (see the legend). The error bars represent the total uncertainty for the reference MC prediction ('POW+PYT') and only the scale plus statistical uncertainty for the fixed order predictions. The shown uncertainty for the predictions has been symmetrized. The respective χ^2 value is reported for each prediction (more details in Section 10.2). The bottom panel shows the ratios of predictions and data.

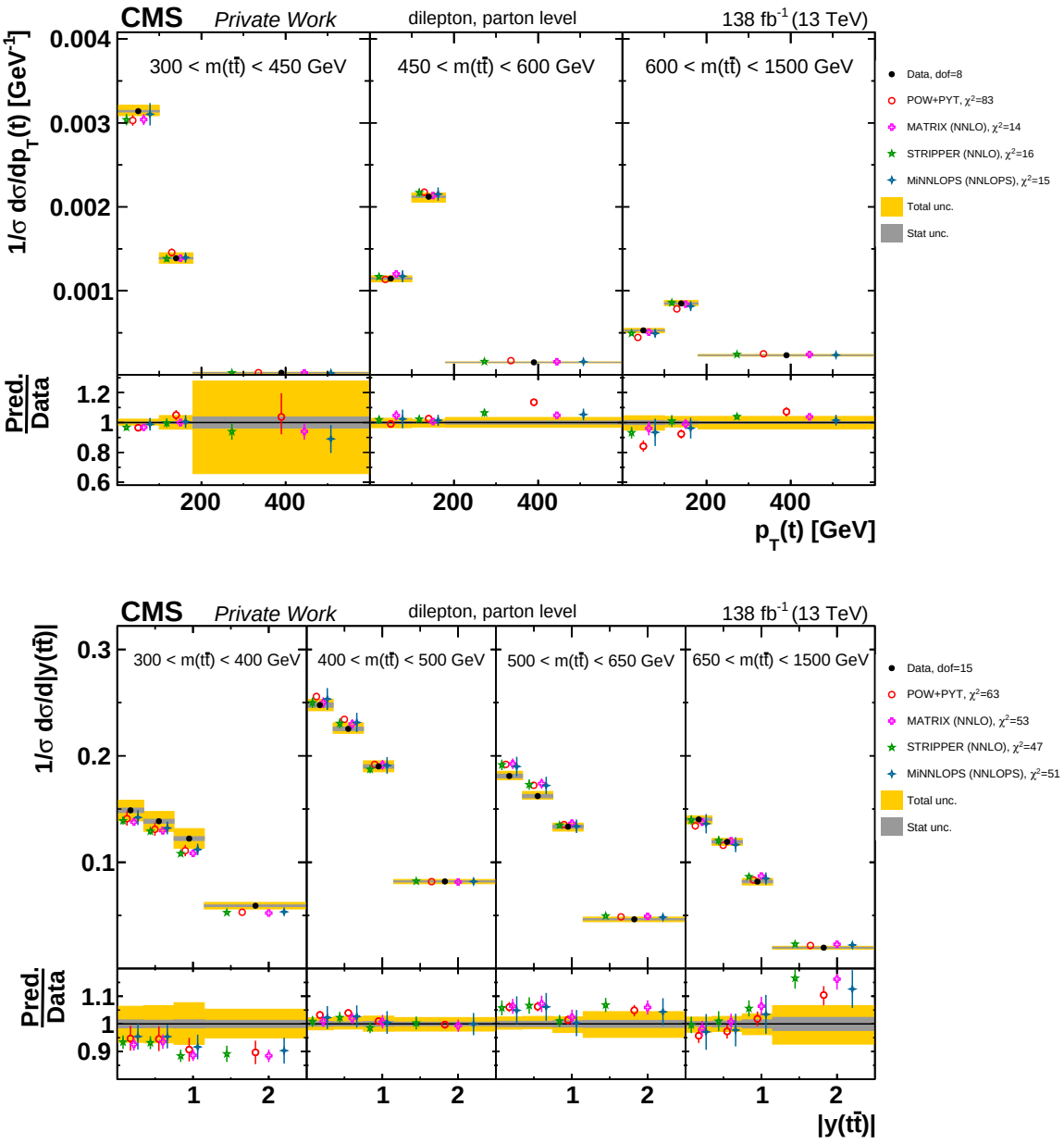

Figure 10.18: Comparison of the measured $[M(t\bar{t}),p_{T}(t)]$ (top) and $[p_{T}(t),p_{T}(t\bar{t})]$ (bottom) parton level normalized cross sections to fixed order predictions (see Fig. 10.17 for further details).

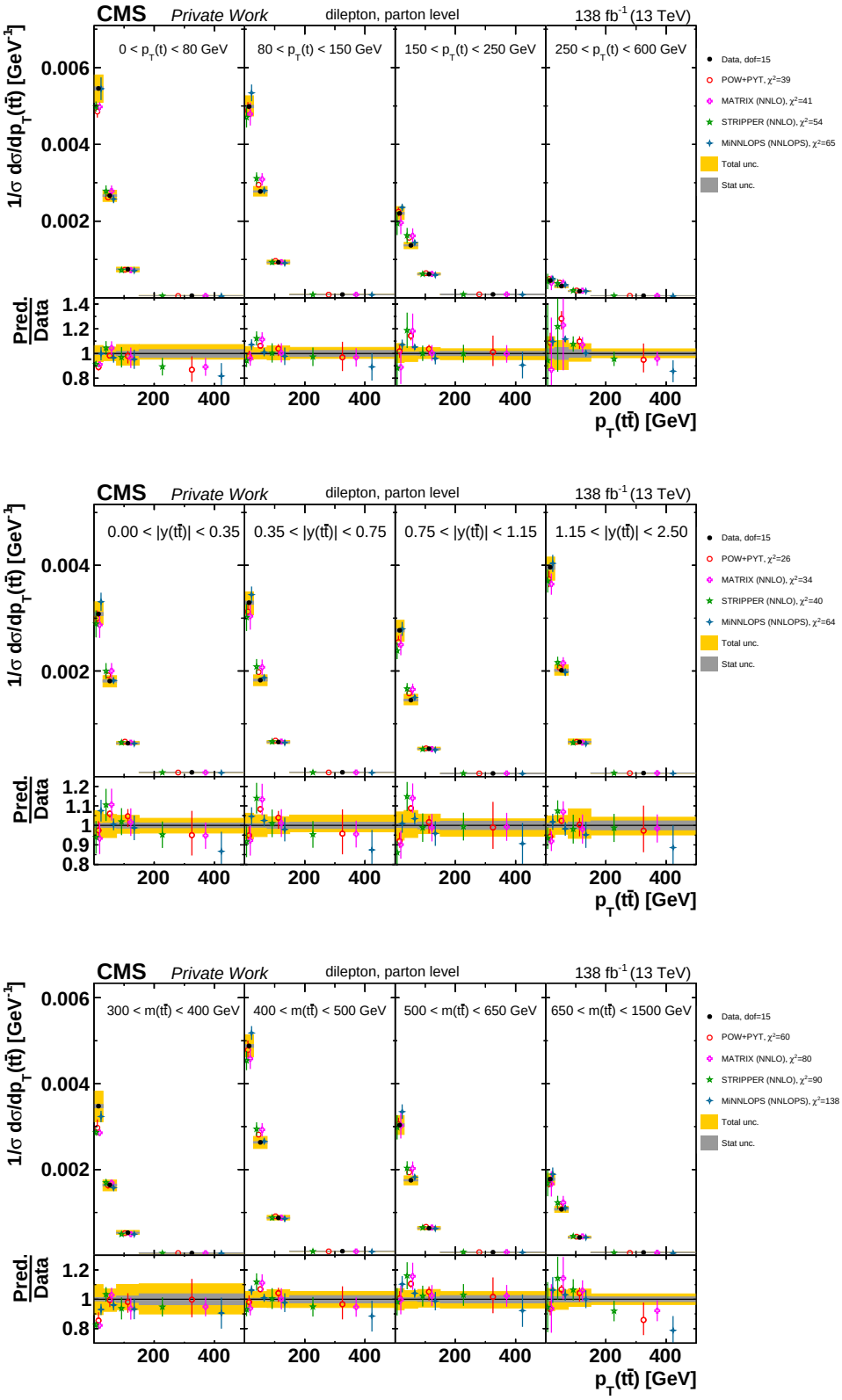

Figure 10.19: Comparison of the measured $[M(\mathrm{t\bar{t}}),y(\mathrm{t\bar{t}})]$ (top), $[y(\mathrm{t\bar{t}}),p_{\mathrm{T}}(\mathrm{t\bar{t}})]$ (middle) and $[M(\mathrm{t\bar{t}}),p_{\mathrm{T}}(\mathrm{t\bar{t}})]$ (bottom) parton level normalized cross sections to fixed order predictions (see Fig. 10.17 for further details). The *Loose KR* (see Section 7.1.2) is used for $[M(\mathrm{t\bar{t}}),y(\mathrm{t\bar{t}})]$ and $[M(\mathrm{t\bar{t}}),p_{\mathrm{T}}(\mathrm{t\bar{t}})]$.

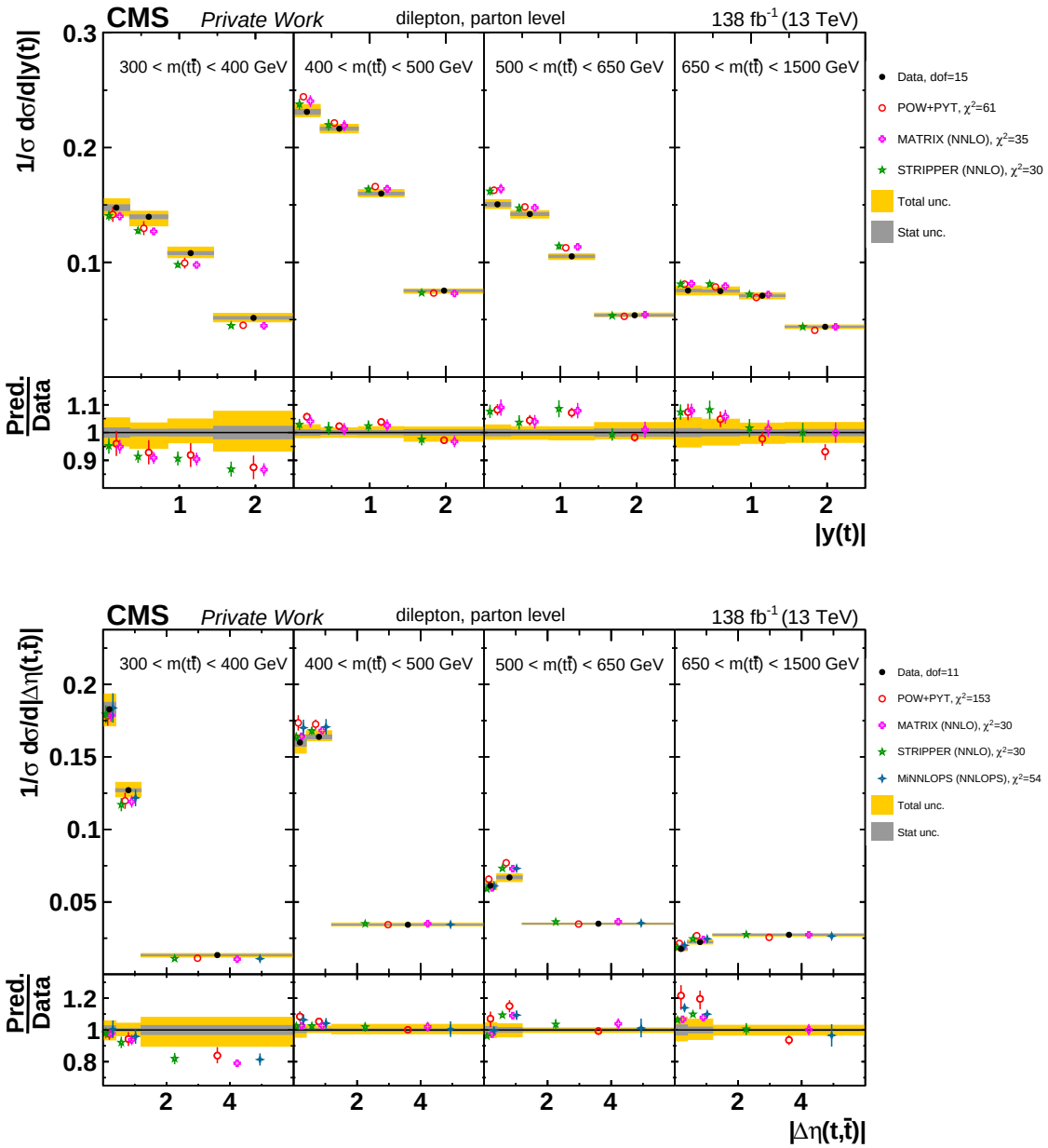

Figure 10.20: Comparison of the measured $[M(t\bar{t}),y(t)]$ (top) and $[M(t\bar{t}),\Delta\eta(t,\bar{t})\ ]$ (bottom) parton level normalized cross sections to fixed order predictions (see Fig. 10.17 for further details).

10.4 Top p_T reweighting at generator level using $[M(\mathrm{t\bar{t}}),p_{\mathrm{T}}(t)]$ unfolded cross section

It was confirmed by different CMS and ATLAS analyses [177,181,219] that the $p_T(t)$ distribution in data is significantly softer than what is predicted by the different MC simulations[7]. Calculations at NNLO+NNLL [220] and approximate N^{3}LO in perturbative QCD [221] have achieved an improved description of top p_T problem. But, as it is seen in Section 10.3 from the comparisons of different beyond-NNLO predictions to data, the issue does not disappear completely. It is still not clear what is the cause of this spectrum effect, but higher order QCD corrections (beyond NNLO+NNLL), electroweak (EWK) corrections and/or non-resonant production of $\mathrm{t\bar{t}}$-like final states (e.g. $gg \to b\bar{b}\mu\nu e\nu$) could have an influence on this effect [222].

The correctness of the top p_{T} spectrum is in particular important for the $\mathrm{t\bar{t}}$ signal simulation when it is used like in the present analysis to correct the data in the cross section unfolding procedure for the effects of the detector acceptance, efficiency and resolution. A mis-modeling affects directly the response matrix used in the unfolding (see Section 8.2) since it varies, in each bin of the matrix, the kinematic distribution of the events at generator level. Procedures have been developed within ATLAS and CMS to treat these effects of the top p_{T} spectrum in the simulation [223].

In this section, a correction is obtained not from a one-dimensional $p_{\mathrm{T}}(t)$ unfolded distribution, but from the two-dimensional $[M(\mathrm{t\bar{t}}),p_{\mathrm{T}}(t)]$ result, and its effects on different observables will be analyzed. The idea is that such a multi-differential correction can provide an improved tuning of the MC to match the data. Figure 10.21 and Table 10.3 present the computed data/MC ratios for different generators. For this purpose, the parton level results of the $[M(\mathrm{t\bar{t}}),p_{\mathrm{T}}(t)]$ normalized cross section were used (see Figure 10.3). Then, these ratios are applied as generator level weights applied in the respective $M(\mathrm{t\bar{t}})$ and $p_{\mathrm{T}}(t)$ bins as shown in Table 10.3. Measurement uncertainties are not considered in this procedure. In Figures 10.22-10.25, cross section results with and without the application of the p_T reweighting are presented allowing the comparison of the effect of this correction for different observables and MC generators. The aim of these comparison plots is to test if the corrections, applied as function of $M(\mathrm{t\bar{t}})$ and $p_{\mathrm{T}}(t)$, lead also to improvements or deterioration in the description of other kinematic spectra. As a sanity check, the resulting $[M(\mathrm{t\bar{t}}),p_{\mathrm{T}}(t)]$ cross section values are shown in the top plot of Figure 10.22, where one can see in the ratio plot and the χ^2 values, that the reweighted distributions perfectly match the data. From the plots in Figure 10.23, where $p_{\mathrm{T}}(t)$ differential cross section values are shown in bins of $y(t)$ (top) and N_{jet} (bottom), one can conclude that the applied reweighting corrects very well the p_T slope problem for all $y(t)$ and N_{jet} values. For 'POW+PYT' and 'FXFX+PYT', the effect of the correction is more evident than for 'POW+HER', where the description doesn't improve so much or it gets a bit worse for some bins. This should be related to the fact that the nominal 'POW+HER' describes much better the p_T slope problem than the nominal 'POW+PYT' and 'FXFX+PYT'.

Changes on the description of different $\mathrm{t\bar{t}}$ observables distributions are a major concern when a reweighting is applied, since the correction could affect them in negative way. In Figures 10.24 and 10.25, the resulting normalized cross section for $[p_{\mathrm{T}}(t),p_{\mathrm{T}}(\mathrm{t\bar{t}})]$, $[M(\mathrm{t\bar{t}}),y(\mathrm{t\bar{t}})]$

[7] simulations based on either LO or NLO matrix elements interfaced with parton showers

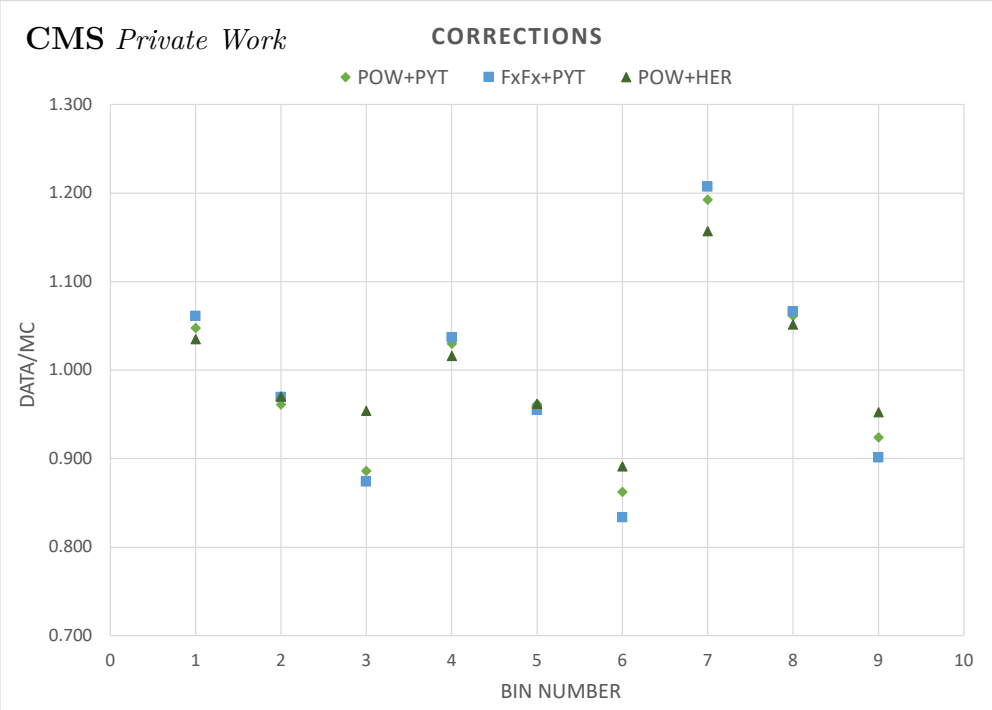

Figure 10.21: The plot shows the values of the data/MC ratios for each bin of the unfolded $[M(t\bar{t}),p_T(t)]$ normalized cross section at parton level. The ratios are shown for different MC generators ('POW+PYT', 'FXFX+PYT' and 'POW+HER'). The exact values and the binning information are shown in Table 10.3.

Bin ID	POW+PYT	FxFx+PYT	POW+HER	$M(t\bar{t})$ [GeV]	$p_T(t)$ [GeV]
1	1.047	1.061	1.035	< 450	< 100
2	0.961	0.969	0.970	< 450	$100 - 180$
3	0.886	0.874	0.954	< 450	> 180
4	1.030	1.037	1.016	$450 - 600$	< 100
5	0.961	0.955	0.962	$450 - 600$	$100 - 180$
6	0.862	0.833	0.891	$450 - 600$	> 180
7	1.192	1.207	1.157	> 600	< 100
8	1.061	1.066	1.051	> 600	$100 - 180$
9	0.924	0.901	0.952	> 600	> 180

Table 10.3: Measured data/MC ratios for the different bins of the $[M(t\bar{t}),p_T(t)]$ normalized cross section at parton level. The values are shown for the 'POW+PYT', 'FXFX+PYT' and 'POW+HER' MC generators. The values of the $M(t\bar{t})$ and $p_T(t)$ ranges in each bin are given in the last two columns.

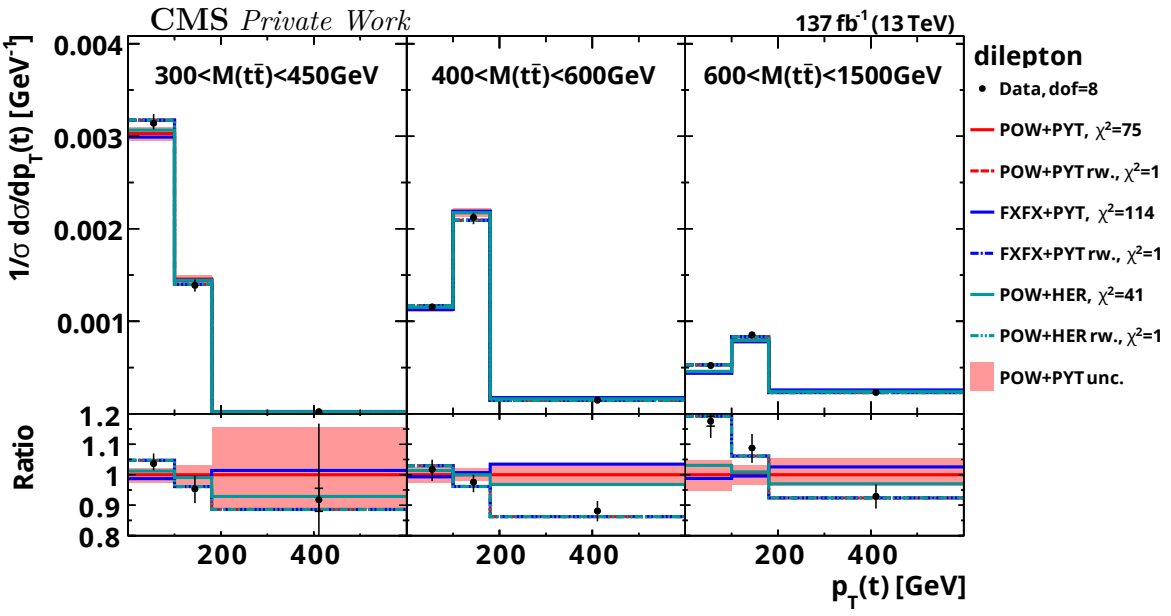

Figure 10.22: The normalized $[M(\mathrm{t\bar{t}}),p_{\mathrm{T}}(t)]$ cross section values at parton level are shown and compared to the predictions from different MC generators with and without reweighting. In the legend, the label **rw.** is added at the end of the generator name if the p_T reweighting is applied. The inner vertical bars on the data points represent the statistical uncertainties and the full bars include also the systematic uncertainties added in quadrature. For each MC model, a χ^2 value is reported. The hatched regions correspond to the estimated uncertainties in 'POW+PYT' (see Chapter 9). In the bottom panel, the ratios of the data and other simulations with respect to the 'POW+PYT' predictions are shown. The same color is used for the same reweighed and non-reweighted generator and a solid (dashed) line style is used for the non-reweighed (reweighed) cases.

and $[p_{\mathrm{T}}(\mathrm{t\bar{t}}),M(\mathrm{t\bar{t}}),y(\mathrm{t\bar{t}})]$ are presented at parton level. For all these cross sections, the reweighted 'FXFX+PYT' shows a better description compared to its nominal prediction. For the case of the $[p_{\mathrm{T}}(t),p_{\mathrm{T}}(\mathrm{t\bar{t}})]$ cross section, a slightly better description is observed for the reweighted 'POW+PYT' only in the last two p_T bins ($150 < p_{\mathrm{T}}(t) < 600\,\mathrm{GeV}$), having almost no effect in the $150 < p_{\mathrm{T}}(t) < 600\,\mathrm{GeV}$ range and making things worse in the first p_T bin ($0 < p_{\mathrm{T}}(t) < 80\,\mathrm{GeV}$). Overall, a somewhat worse description is observed for this cross section for 'POW+PYT' and 'POW+HER' after reweighting. The $[M(\mathrm{t\bar{t}}),y(\mathrm{t\bar{t}})]$ and $[p_{\mathrm{T}}(\mathrm{t\bar{t}}),M(\mathrm{t\bar{t}}),y(\mathrm{t\bar{t}})]$ cross sections, show an improvement in the description for all the reweighted MC generators. The fact that the $[p_{\mathrm{T}}(\mathrm{t\bar{t}}),M(\mathrm{t\bar{t}}),y(\mathrm{t\bar{t}})]$ cross section (Figure 10.25) shows a positive result for the reweighted distributions is very promising since this cross section describes the full kinematic of the $\mathrm{t\bar{t}}$ system. Summarizing, one can conclude that a 2D-reweighting of the $\mathrm{t\bar{t}}$ signal MCs as function of $p_{\mathrm{T}}(t)$ and $M(\mathrm{t\bar{t}})$, might be a good procedure for obtaining overall improved nominal simulations, which could be used in the unfolding procedures or as absolute $\mathrm{t\bar{t}}$ prediction for analyses where this is a background source and the kinematic distributions of the events play an important role.

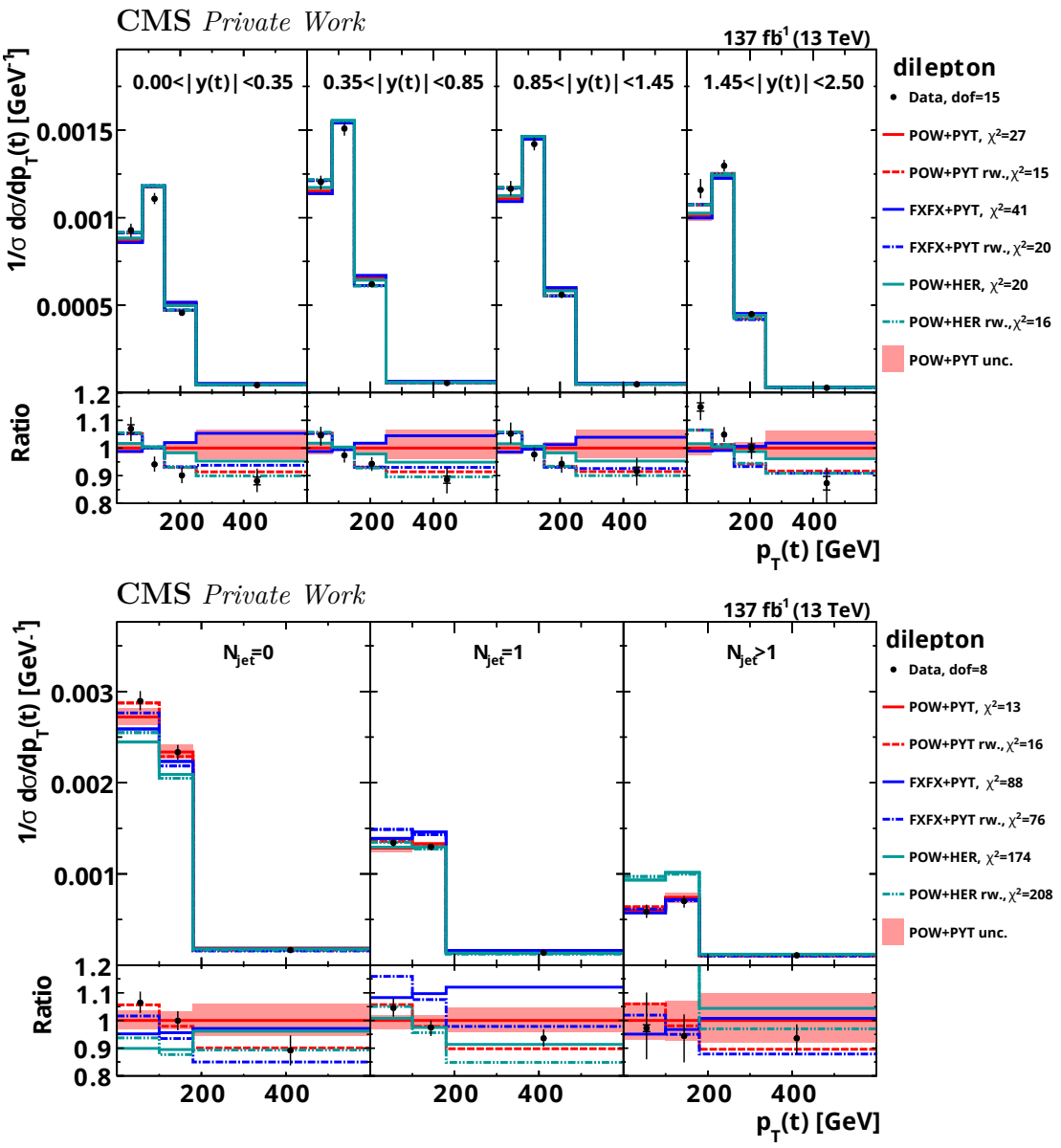

Figure 10.23: The normalized $[y(t),p_T(t)]$ (top) and $[N_{jet},p_T(t)]$ (bottom) cross sections values at parton level are shown and compared to the predictions from different MC generators with and without reweighting. For further details, see Figure 10.22.

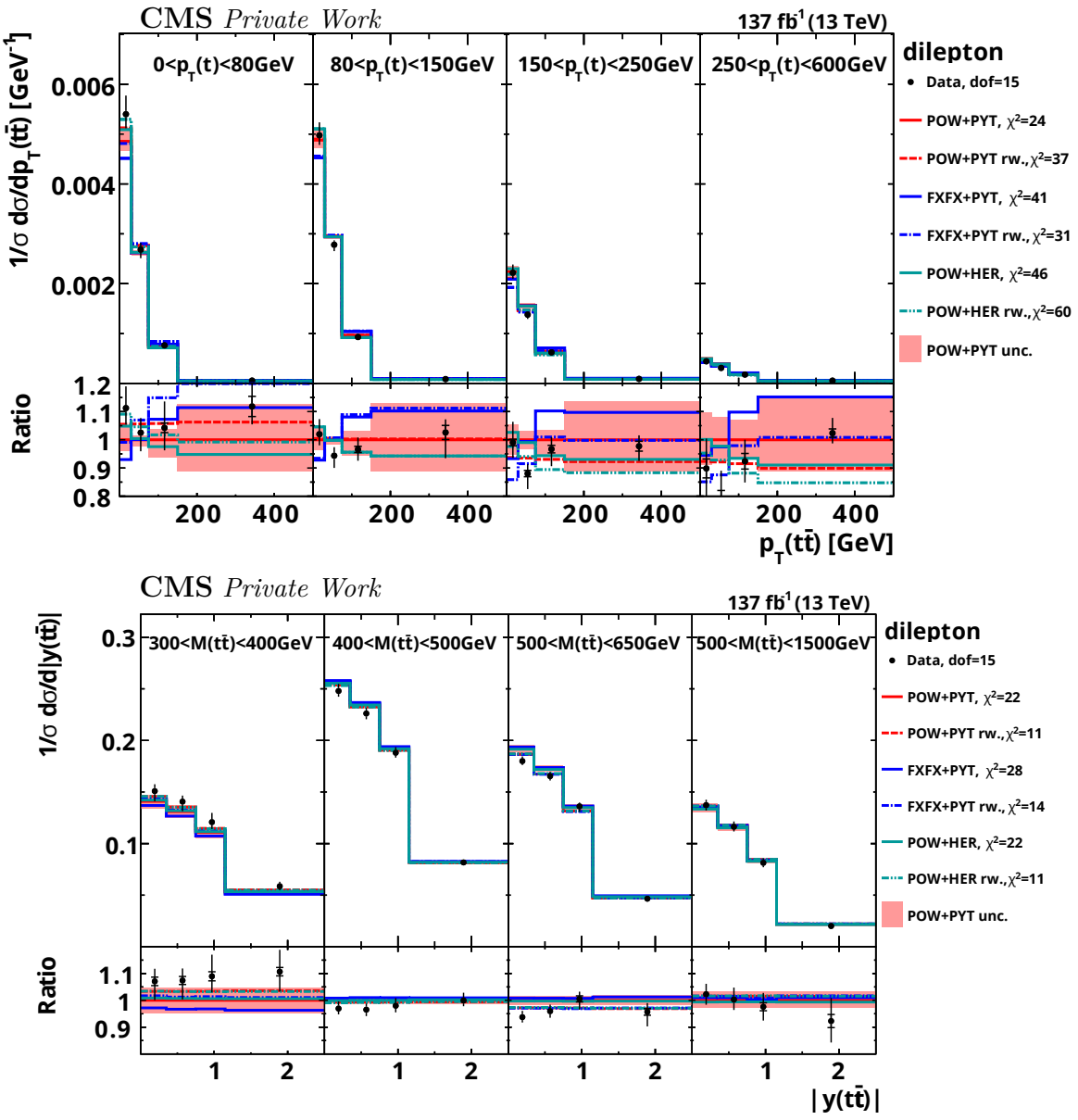

Figure 10.24: The normalized $[p_{\mathrm{T}}(t), p_{\mathrm{T}}(\mathrm{t\bar{t}})]$ (top) and $[M(\mathrm{t\bar{t}}), y(\mathrm{t\bar{t}})]$ (bottom) cross sections values at parton level are shown and compared to the predictions from different MC generators with and without reweighting. For further details, see Figure 10.22.

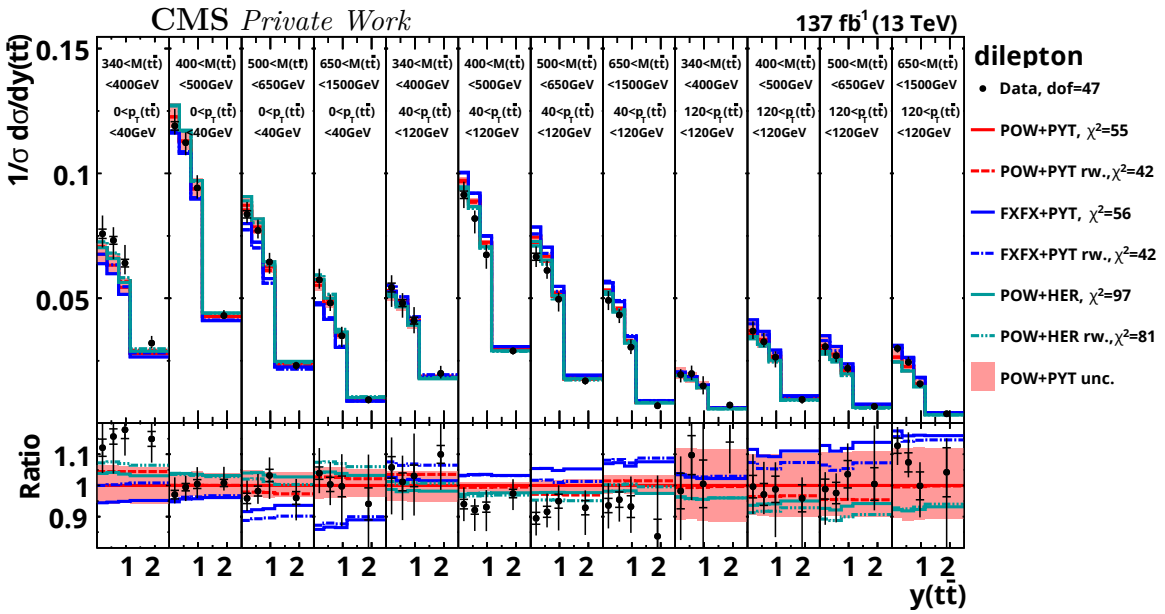

Figure 10.25: The normalized $[p_{\mathrm{T}}(\mathrm{t\bar{t}}),M(\mathrm{t\bar{t}}),y(\mathrm{t\bar{t}})]$ cross section values at parton level are shown and compared to the predictions from different MC generators with and without reweighting. For further details, see Figure 10.22.

10.5 Summary of the results

The measured multi-differential cross sections have been presented in this Chapter and compared to different NLO MC models and also to beyond-NLO QCD calculations. The possible application of the results from $[M(\mathrm{t\bar{t}}),p_{\mathrm{T}}(t)]$ as a way for correcting the top p_{T}-slope issue in MC models was also discussed.

From the χ^2 values (see Tables C.111-C.115) and the visual comparison of the plotted spectra (see Section 10.2), it can be concluded that none of the considered MC generators is able to correctly describe all multi-differential distributions. In general, the best agreement with the data is provided by 'POW+PYT', while 'FXFX+PYT' usually gives the worst description. The spectra of $p_{\mathrm{T}}(t)$ and $p_{\mathrm{T}}(\mathrm{t\bar{t}})$ are in general mildly correlated with rapidity distributions of the same objects. The quality of their description by the MC models is nearly independent of the rapidity. It is also observed that at higher $M(\mathrm{t\bar{t}})$, the trends of the MC models to predict too hard top quark p_{T} spectra is clearly enhanced.

From the studies related to the extra jet multiplicity (see Section 10.2.2) one can conclude that the 'POW+PYT' calculation clearly provides the best description of N_{jet} distribution in $\mathrm{t\bar{t}}$ events. The 'FXFX+PYT' model predicts too many events with $N_{\mathrm{jet}} = 1$ and 'POW+HER' overshoots the data distribution at parton level for $N_{\mathrm{jet}} \geq 2$. There are weak kinematic correlations of the top quark or $\mathrm{t\bar{t}}$ rapidity spectra with N_{jet}. Also the quality of the descriptions of $|y(t)|$ and $|y(\mathrm{t\bar{t}})|$ by the different models is found to be rather independent of the N_{jet} values. As expected, kinematic correlations are observed between the $p_{\mathrm{T}}(t)$, $p_{\mathrm{T}}(\mathrm{t\bar{t}})$ or $M(\mathrm{t\bar{t}})$ and the extra jets multiplicity. These observables show harder spectra for larger N_{jet} and all models exhibit some N_{jet} specific enhanced discrepancies for these spectra. There is an indication that the problem of harder $p_{\mathrm{T}}(t)$ distributions in the models is localized at small jet multiplicities.

The agreement of 'POW+HER' and 'POW+PYT' with data deteriorates significantly for the extra jet p_{T} and η distributions when going from the leading to the sub-leading extra jet, increasing the effect of too hard p_{T} and too central η distribution in the MC models (see Section 10.2.3). For the p_{T} and mass of the $\mathrm{t\bar{t}}+ \mathrm{ej}_1$ system, none of the MC models provides an overall good data description and all of them exhibit in general very similar predictions for these observables. Regarding the $M(\mathrm{t\bar{t}}+\mathrm{ej}_1)/\mathrm{M}(\mathrm{t\bar{t}})$ ratio observable, which might be sensitive to soft gluon resummation effects near the threshold. All MC models, specially 'POW+PYT' and 'FXFX+PYT', predict much too few events in the first bin near the threshold. Also, the analysis of the $\Delta\eta(t, ej_1)/\Delta\eta(t, \bar{t})$ measurement shows that all models clearly predict more leading extra jets coming from the region between the two top quarks than observed in data.

The χ^2 values of the multi-differential $\mathrm{t\bar{t}}$ cross sections in this measurement, are on average, significantly higher than those observed in the corresponding previous measurement [6] based on the 2016 data set only, which can be attributed to a substantially improvement in the precision of the measurements. The observed high χ^2 values for a significant number of cross sections shows a deficiency in the models for predicting the multidimensional process dynamics, which has been also observed in other $\mathrm{t\bar{t}}$ differential cross section papers [199, 224] from the ATLAS and CMS Collaborations. Many of the cross section presented in this chapter are measured for the first time. They can be divided in new multi-differential combinations: $[p_{\mathrm{T}}(t),p_{\mathrm{T}}(\mathrm{t\bar{t}})]$, $[y(\mathrm{t\bar{t}}),p_{\mathrm{T}}(\mathrm{t\bar{t}})]$ and $[p_{\mathrm{T}}(\mathrm{t\bar{t}}),M(\mathrm{t\bar{t}}),y(\mathrm{t\bar{t}})]$ or $[N_{\mathrm{jet}},M(\mathrm{t\bar{t}})]$, and completely new observables like $\Delta\eta(t, ej_1)/\Delta\eta(t, \bar{t})$. The full set of new observables are highlighted in Tables

10.1 and 10.2.

Comparisons with three different beyond-NLO QCD calculations are also performed, as discussed in Section 10.3. In general the predictions show a reasonable agreement with the data. The biggest improvement with respect to the MC models is in the measurements related to the $p_{\mathrm{T}}(t)$ distribution, where the p_{T}-slope issue is drastically reduced. The weakest point of the the analyzed fixed order predictions is the description of the $p_{\mathrm{T}}(\mathrm{t\bar{t}})$ data distribution where pronounced shape effects (wiggle of the ratio of prediction and data) are seen near threshold.

A further study was performed on the possibility of using the $[M(\mathrm{t\bar{t}}),p_{\mathrm{T}}(t)]$ cross section measurement of this analysis as a two-dimensional correction for a top p_T reweighting of the $\mathrm{t\bar{t}}$ signal simulations at generator level. The studies show that the applied reweighting corrects very well the p_T slope problem for all $y(t)$ and N_{jet} ranges, while it doesn't drastically affect the other $\mathrm{t\bar{t}}$ observables. The suggested correction is presented in Table 10.3 for the different MC models.

CHAPTER

11

CONCLUSIONS AND OUTLOOK

11.1 Summary

This work presents measurements of multi-differential top quark pair ($t\bar{t}$) production cross sections in pp collisions at a center-of-mass energy of 13 TeV, using events containing two opposite-sign leptons. The data were collected by the CMS experiment in pp collisions at $\sqrt{s} = 13$ TeV in the years 2016, 2017, and 2018 corresponding to an integrated luminosity of $137\,\text{fb}^{-1}$. After reconstructing the relevant physics objects (e.g., leptons, jets) from the detector information, the kinematics of the top-quark pair is determined by applying two different kinematic reconstruction procedures based on exploiting kinematic constraints. Differential cross-sections are obtained after correcting for backgrounds and detector effects, comprising acceptance, efficiency and resolution, using a regularized unfolding technique.

Differential cross sections are measured as functions of kinematical observables of the $t\bar{t}$ system, the top quark, top antiquark and their decay products, and the total number of additional jets in the event. The measurements are performed simultaneously as functions of two or three kinematic variables. The cross sections are measured at particle-level of the top and top anti-quark in a fiducial phase space close to the detector acceptance and at parton-level in the full phase space. The set of results contains numerous cross sections that are measured for the first time ever, including new multi-differential combinations and completely new observables like the ones related to the $t\bar{t}$ plus leading extra jet system. Overall, the measurements' statistical and systematic uncertainties are improved by a factor of about two compared to the previous analyses [6] which are based on the 2016 data only. To estimate the total uncertainties, the correlation between the different systematic sources among the years were taken into account.

The results are compared to different SM based predictions from NLO QCD plus parton shower MC generators. It is observed that the trend shown by MC calculations predicting a harder $p_{\text{T}}(t)$ spectrum it is pronounced at high $M(t\bar{t})$. It is also revealed that the distribution of the multiplicity of additional jets in the $t\bar{t}$ events shows apparent differences

between the models that are resolved by the data. The studies of the $t\bar{t}$ and top quark and top anti-quark kinematical spectra as a function of the additional jet multiplicity show multiplicity-dependent shape differences between data and models. There is an indication that the problem of harder $p_{\mathrm{T}}(t)$ distributions in the models is localized at small jet multiplicities.

The analysis of the ratio observable of the leading extra jet invariant mass over the mass of the $t\bar{t}$ system, shows an excess of the data near the threshold where there might be some sensitivity to soft gluon effects. Also, from the $\Delta\eta(t, ej_1)/\Delta\eta(t, \bar{t})$ distribution, it is concluded that all models predict more leading extra jets coming from in between the two top quarks than predicted by data. The comparisons to beyond-NLO QCD calculations showed an overall improved agreement with data for all predictions. The major highlight is the improved description of the measurements related to the $p_{\mathrm{T}}(t)$ distribution. The p_{T}-slope issue is drastically reduced with respect to what was observed for the MC models. In the studies about the use of the resulting $[M(t\bar{t}),p_{\mathrm{T}}(t)]$ cross-section measurement as a two-dimensional correction for top p_T reweighting at generator level it is observed that the applied reweighting corrects very well the p_T slope problem for all $y(t)$ and N_{jet} ranges while it doesn't affect the description of the $t\bar{t}$ observables spectra drastically.

11.2 Outlook

The measurements of the differential $t\bar{t}$ production cross sections presented in this work could be extended towards measuring new kinematic observables or new multi-differential combinations of the existent observables. With more statistics, the double-differential cross section in bins of the extra jets multiplicity (e.g., $[N_{\mathrm{jet}},p_{\mathrm{T}}(t)]$) could be extended to at least one more N_{jet} bin, making clearer the observed indications of possible correlations shown in this work.

A further reduction of the systematic uncertainties achieved in the analysis would help identify trends in the distributions more clearly and enhance the sensitivity to effects induced by new-physics phenomena that could modify the known $t\bar{t}$ processes. This could be achieved by improving the reconstruction procedures for the relevant objects or other analysis ingredients like the background estimation, using data in control regions with cuts that be orthogonal to those applied in the nominal event selection

It would also be interesting to use the measured cross sections for the extraction of SM parameters. For example, the same procedure as in [6] could be repeated using the $[N_{\mathrm{jet}},M(t\bar{t}),y(t\bar{t})]$ cross-section to simultaneously extract the top-quark pole mass, the strong coupling α_s and the proton PDFs. Also, the potential of other possibly sensitive cross-sections could be evaluated.

In the coming years new exiting particle physics projects like the High-Luminosity LHC project (HL-LHC) [78, 225] and the possible future colliders CLIC [226], FCC [227], and ILC [228], are ahead. These experiments will increase the potential for discoveries and expand our knowledge about the amazing world of particle physics, where top quarks may play a key role in discovering new physics. One clear example of this promising future for particle physics experiments is that with the upcoming Run 3 of the LHC, it is expected to collect by the CMS experiment $300\,\mathrm{fb}^{-1}$ of data and to reach $\sqrt{s} = 14\,\mathrm{GeV}$; and finally, nearly $3000\,\mathrm{fb}^{-1}$ [29] of data with $\sqrt{s} = 14\,\mathrm{GeV}$ is expected from the High Luminosity LHC runs

starting in 2027.

APPENDIX

A

CONTRIBUTION TO THE MEASUREMENT OF THE INTEGRATED LUMINOSITY IN THE CMS DETECTOR

Contents

A.1 Cross detector stability uncertainty 139
A.1.1 Behavior and stability comparison of luminometers in 2016. 140
A.1.2 Best/second luminometer method. Integrated Luminosity for 2016. . 141
A.1.3 Cross detector stability uncertainty in 2016. 142
A.1.4 Cross detector stability uncertainty in 2015. 142
A.2 Linearity uncertainty 143
A.2.1 Fill-by-fill linearity studies. 144
A.2.2 Linearity uncertainty for 2015 and 2016. 145

A.1 Cross detector stability uncertainty

The luminosity in the CMS detector is measured using more than one luminometer (e.g., PCC, HFOC, RAMSES and PLT), and they report independent luminosity measurements [1]. A brief description of these luminometers was provided in Section 3.2.7. Knowing how well

[1] Some of the detectors, like RAMSES, are cross-calibrated (normalized) to PCC. Still, the intrinsic behavior in time of the detector is not changed by this re-normalization.

these detectors agreed during a data-taking period is essential to ensure a reliable result for the integrated luminosity.

A.1.1 Behavior and stability comparison of luminometers in 2016.

In Figure A.1 a comparison of the luminosity recorded by the PCC, HFOC, PLTZERO, and RAMSES detectors is shown. For this purpose, the ratios between the recorded luminosity of each detector every 50 common lumi-sections[2] (LS) were taken. From this plot, information can be extracted if one detector is not behaving correctly in some specific part of the year. For example, a waving effect of DT is observed. The 50 LS range was chosen, taking into account studies on the histograms using different integration ranges. By taking several LS, statistical effects are mostly suppressed (see Figures A.2 and A.6).

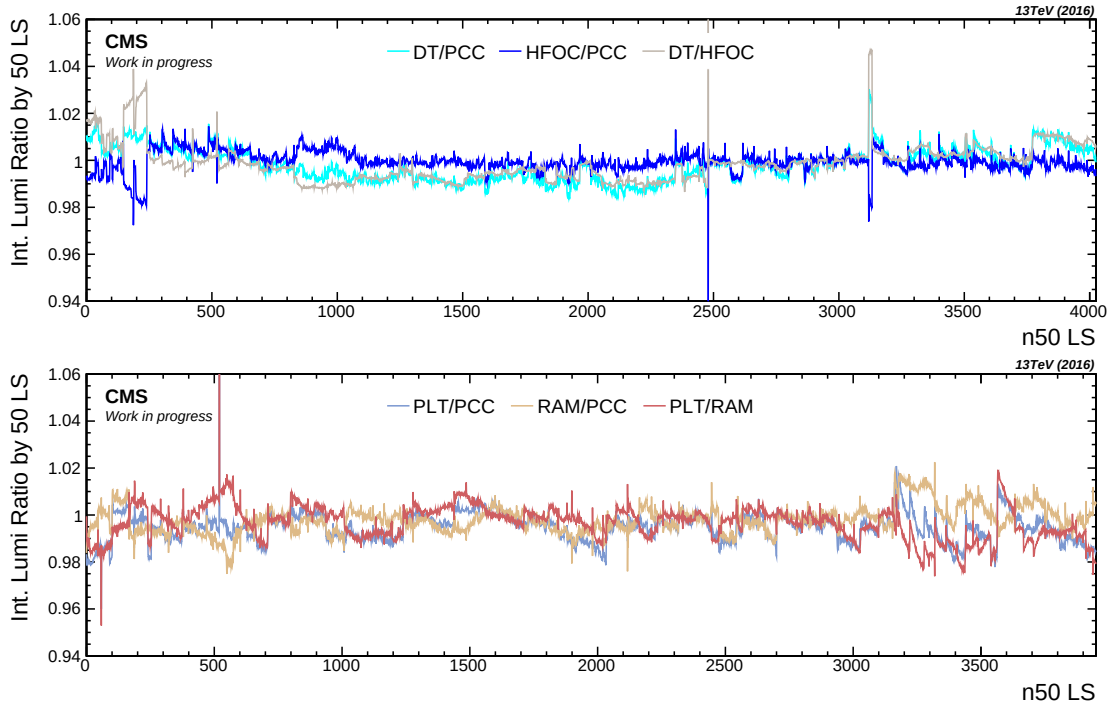

Figure A.1: Best luminometers detector ratios computed using the integrated luminosity of each detector every 50LS.

If two detectors had a good agreement during the year, one expects a mean value of the ratios near unity and a slight standard deviation. The histograms shown in Figure A.3 are the result of the integrated luminosity ratios between a luminometer pair per every 50 LS. Each of these ratios is weighted using the luminosity recorded during this time interval. This weighting approach considers that the points with a low luminosity also have a low impact on the total integrated luminosity. From each of these plots, the standard deviation value can be extracted (Table A.1) and taken as a description of how stable the detector was during the year.

[2]A lumi-section is the common minimum period of time in which the luminometers provide values of the luminosity measurements (1LS = 23.3 s)

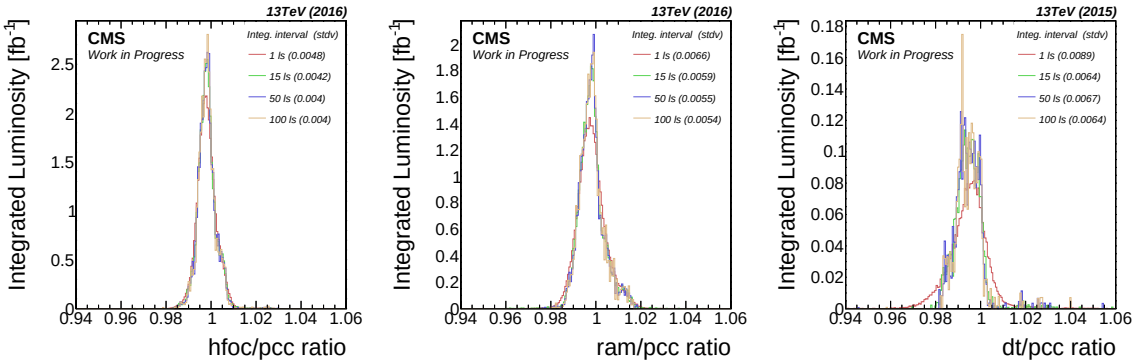

Figure A.2: Integration interval studies.

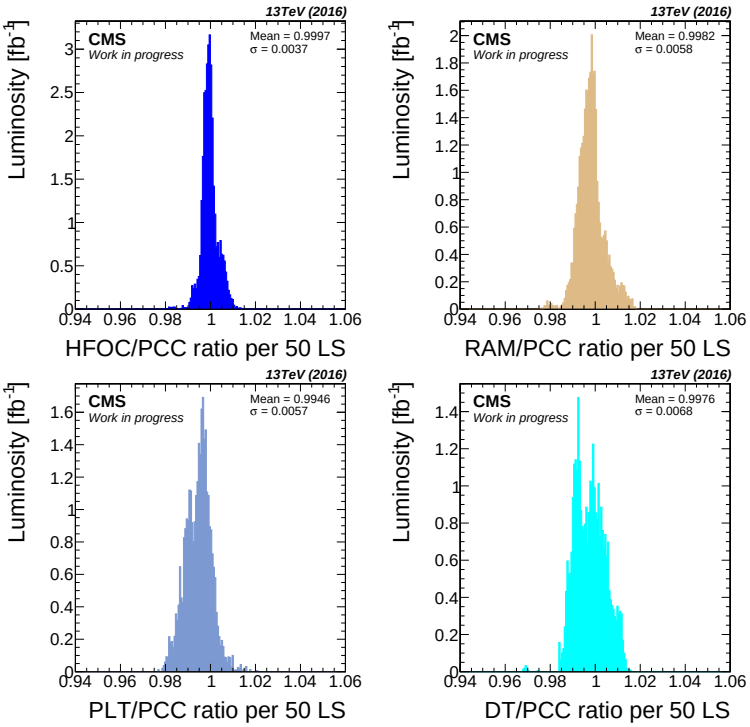

Figure A.3: Histograms of the detector ratios every 50 lumi-sections. Bad zones for the detectors hav been excluded.

A.1.2 Best/second luminometer method. Integrated Luminosity for 2016.

During the 2016 data taking period, the most stable luminosity detectors were PCC, HFOC and RAMSES (from Figure A.3), that is the reason why they were the chosen for measuring the total integrated luminosity. Figure A.4(bottom) shows the detector ratios dependence with the integrated luminosity. In this plot, every point has the same importance in terms of impact on the total integrated luminosity.

The procedure for getting the integrated luminosity is to choose which luminometer to use (best) for each LS and then integrate it all over the year. To get a consistent cross detector stability uncertainty, besides the best it was also chosen the comparison detector using the

Rank	**Luminometer,X**	X/PCC (σ)
1	PCC	n/a
2	HFOC	0.0037
3	RAMSES	0.0058
4	PLT	0.0057
5	DT	0.0068

Table A.1: Standard deviation values for each luminometer/PCC in 2016.

priority sequence: PCC-HFOC-RAMSES (see Table A.1). The selection method is quite simple: if PCC and HFOC have no problems, then they are used as the best and second (comparison) detectors, but if PCC is wrong, then HFOC is the best and RAMSES is the second, and so on. Almost for the entire year, PCC was chosen as the best and HFOC as the second. Just in a few regions, other luminometers were selected to ensure reliable integration and uncertainty determination. The graphic result is shown in Figure A.5 where the ratios between the best and second detector are plotted for each lumisection vs. the accumulated integrated luminosity. The procedure assumes that at least two out of the three luminometers worked fine for any time period, which was the case for the 2016 data.

The ratios distribution achieved with this approach (Figure A.6) behaves much better than those obtained using single detector pairs (Figure A.4). The standard deviation, in this case, is much more stable to the binning choice (this was studied, and σ remains practically constant in this case) and the number of lumisections taken for each ratio point.

Even after selecting the best and second luminometer, some isolated and small cluster points are separated from the expected region. A more exhaustive selection process could improve this, but this is unnecessary because most data points have a meager luminosity contribution. This can be checked in Figure A.7 where the point size and color describe how much luminosity is included.

A.1.3 Cross detector stability uncertainty in 2016.

From Figure A.6 it can be deduced that the correct σ value to take as a description of the cross detector stability uncertainty should be $\sigma \approx 0.005$ which represents a contribution of 0.5% added to the total uncertainty. A visualization of this result is presented in Figure A.8, where it can be confirmed that the majority of the ratios are inside the $\pm 1\sigma$ region.

A.1.4 Cross detector stability uncertainty in 2015.

The same procedure was used for the 2015 stability uncertainty determination. In this case, the main luminometers were PCC, DT, and RAMSES. Compared with 2016, this was a smaller period of time and integrated luminosity. PCC was also the best detector for almost the entire year (Figure A.6 bottom right). The priority sequence used for the best/second

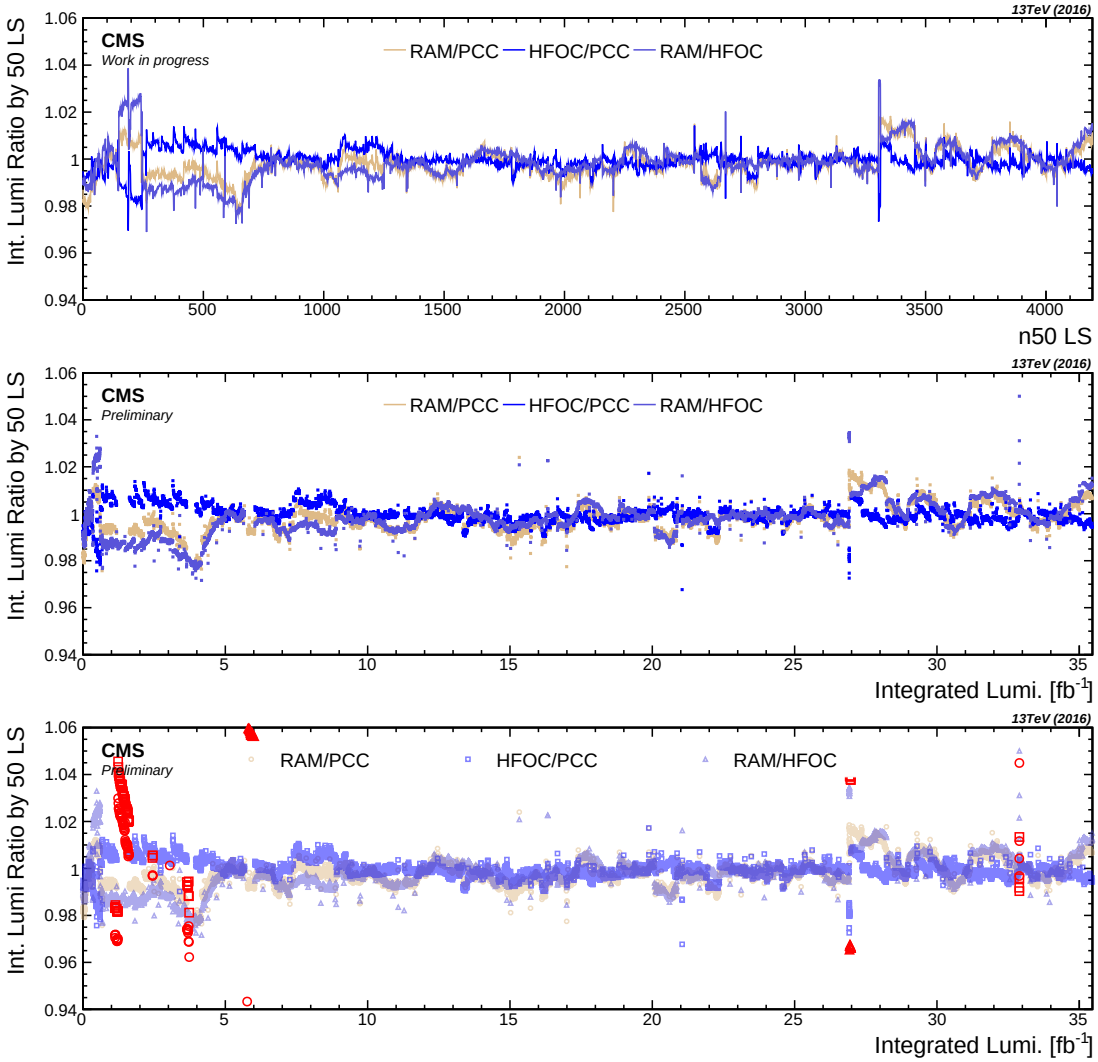

Figure A.4: Best luminometers ratios computed using the integrated luminosity of each detector every 50LS. The stability of the detectors .vs the number of 50LS intervals (plot) and the integrated luminosity (middle) is shown. On the bottom excluded regions can be observed in red.

approach was PCC-DT-RAMSES (Table A.2 and Figure A.10). The obtained distribution was broader compared with 2016 and had more statistical effects, which were removed by taking a sufficient large integration interval as can be seen in Figure A.6 (bottom left). The value for the cross detector stability uncertainty is taken as 0.6% and which was represented in Figure A.8 around the mean ratio value.

A.2 Linearity uncertainty

The PCC luminosity measurements are expected to be linear to the instantaneous luminosity delivered to the detector. Studies were performed to investigate any residual non-linearity behavior and determine the uncertainty induced in the integrated luminosity by this effect.

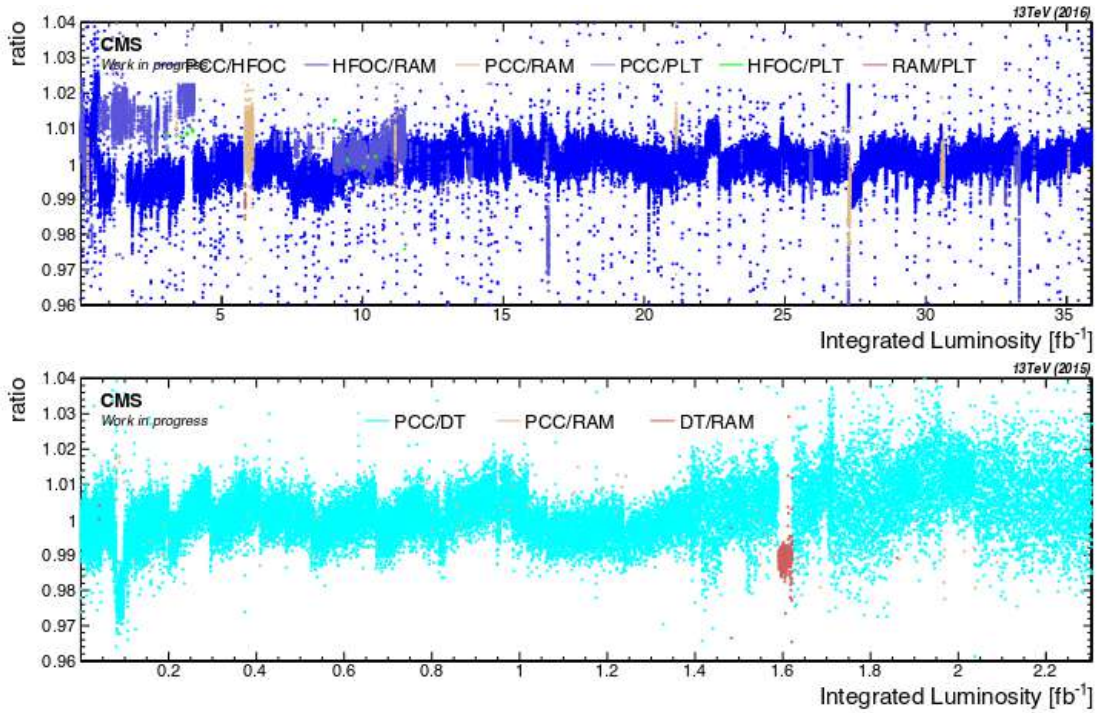

Figure A.5: Instantaneous luminosity ratio between the best and the comparison luminometer for each lumisection.

Rank	**Luminometer,X**	X/PCC (σ)
1	PCC	n/a
2	DT	0.0055
3	RAMSES	0.0083
4	HFOC	0.0093
5	PLT	0.0157

Table A.2: Standard deviation values for each luminometer/PCC in 2015.

For this goal, HFOC and RAMSES[3] were used as main comparison detectors. It is essential to say that these luminometers are not taken as a reference of perfect linearity. On the contrary, not having an ideal reference detector creates uncertainty in the luminosity measurement.

A.2.1 Fill-by-fill linearity studies.

Fill by fill linear fits of the ratios between the detectors vs SBIL (Single Bunch Instantaneous Luminosity) were performed. Statistical effects are clearly present in the data (Figure A.11 **left**), that is why the fitting is performed over the points coming from ratios every 30 LS. The behavior of the fill-by-fill slopes is shown in Figure A.12, where the dependence with

[3]In the plots appears as RAM

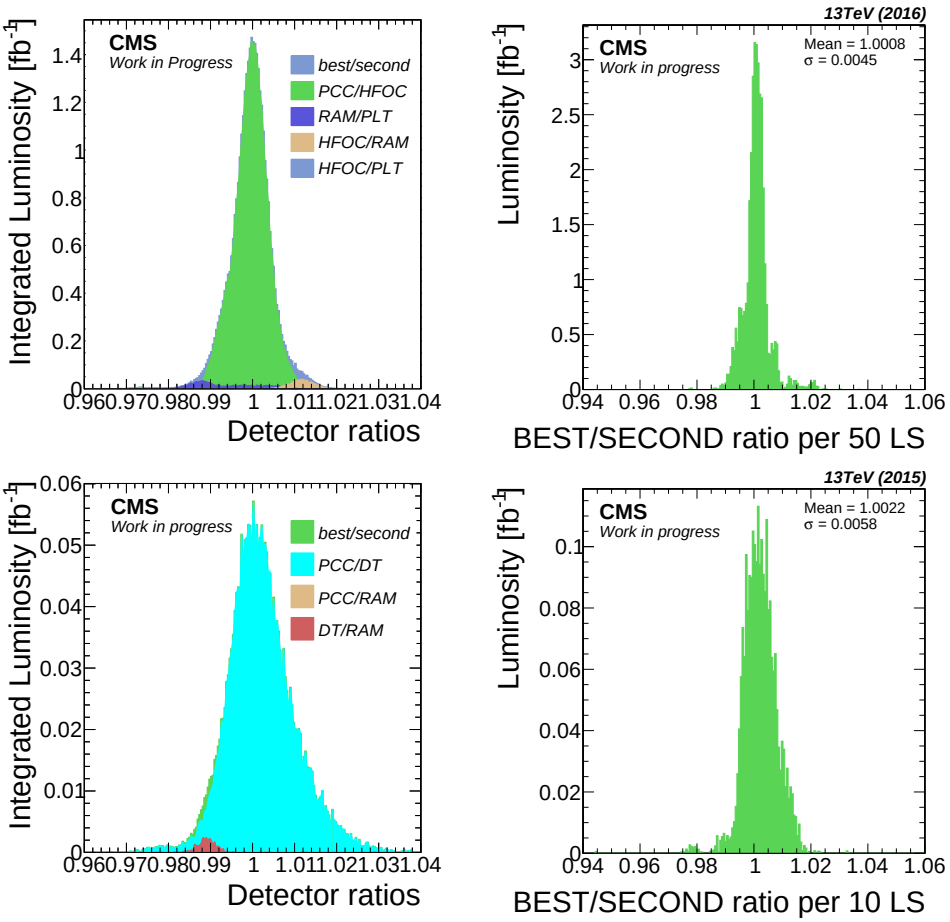

Figure A.6: Best/second ratio histograms. On the **left** the contribution from the best/second combinations. On the **right** the resulting histogram and σ taking 50LS as integration interval for the ratios.

the integrated luminosity is plotted. From the luminosity weighted histogram of the slopes (left Figure A.13), the mean value of the slope can be obtained. To avoid slopes values from bad fitting results, an analysis of the resulting χ^2 for each fill was performed and in addition to a visual rejecting of fills with stability problems. In Figure A.13 (right) slopes with large error can be observed, but its fill have a very low luminosity. This means that they have a minimal impact on the luminosity weighted mean value. The fill-by-fill slopes were also summarized using error-weighted average values in equal integrated luminosity intervals. Figure A.15 shows the resulting plots for HFOC/PCC and RAMSES/PCC. The error bars present in the plots are the statistical error of the averaged points, giving a visual idea about how much spread the slopes were in this region.

A.2.2 Linearity uncertainty for 2015 and 2016.

A summary plot is presented in Figure A.16(left), including the results for PCC compared with HFOC, RAMSES, and DT. All comparisons show reasonable stability for the linearity values over the year. A correction was applied to the data using the computed slopes, and

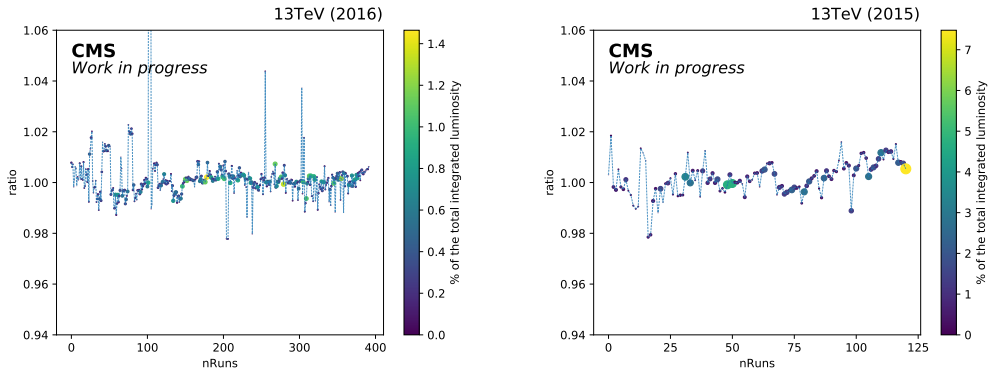

Figure A.7: Integrated luminosity ratio for best/second luminometer for each run vs run number. The color scale and the point size help to describe the significance(%) of the points in term of integrated luminosity.

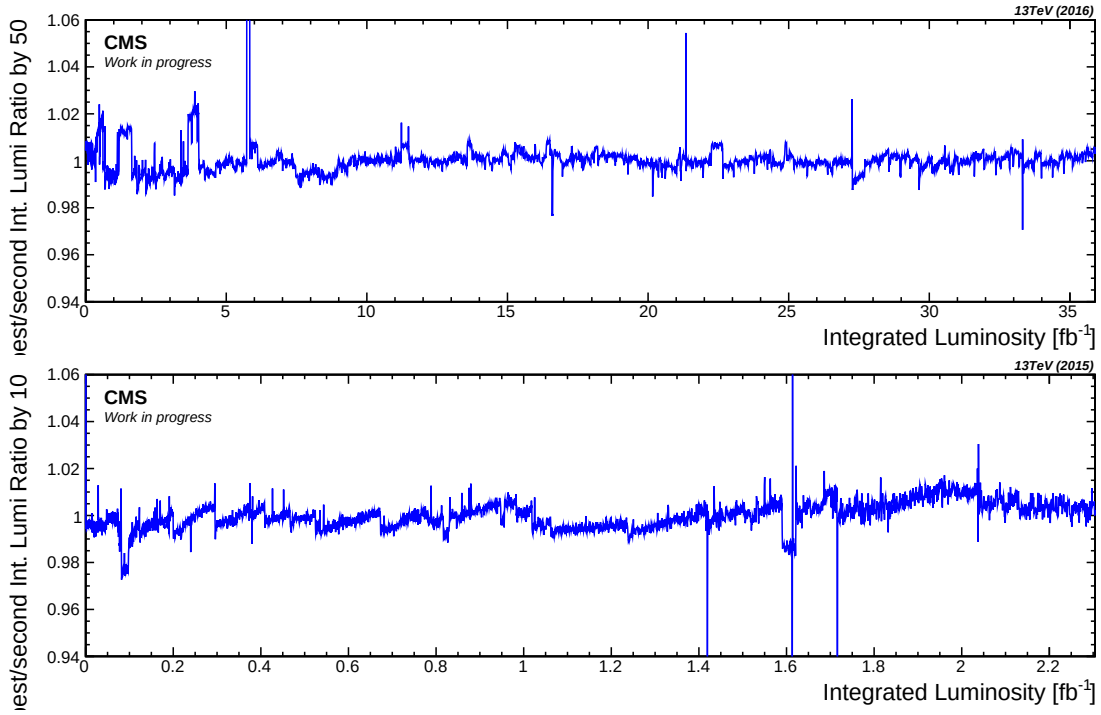

Figure A.8: Integrated luminosity ratio every 50 ls between the best and the comparison detector.

the change on the integrated luminosity was determined. The table in Figure A.16(right) shows the slope values for each detector pair with the respective impact on the integrated luminosity. The most significant value from the impacts on the integrated luminosity was taken as the linearity uncertainty for the 2016 integrated luminosity: 0.3%, corresponding to the non-linearity slope of $0.0008\,(Hz/\mu b)^{-1}$.
For 2015 the same procedure was performed, but only using DT and PCC. Figures A.17 and A.18 show the relevant plots for the 2015 linearity determination. The value of 0.5% is taken as the linearity uncertainty on the 2015 integrated luminosity. This is the impact on the

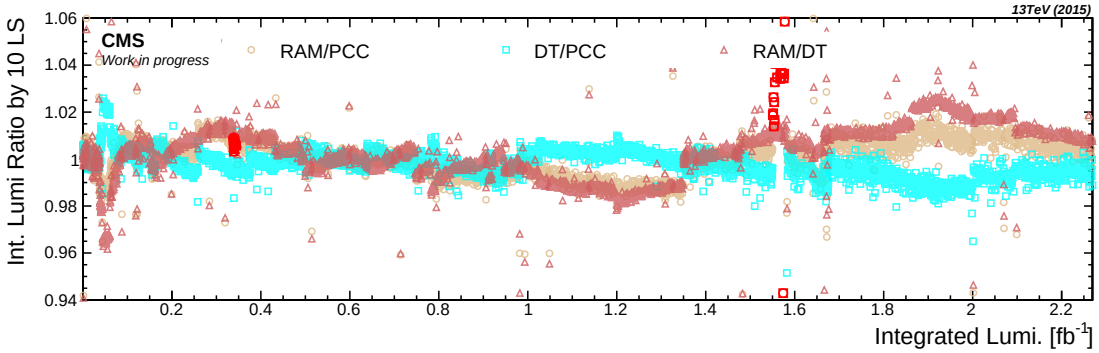

Figure A.9: 2015 Ratios computed using the integrated luminosity of each detector every 50LS. Excluded regions are shown.

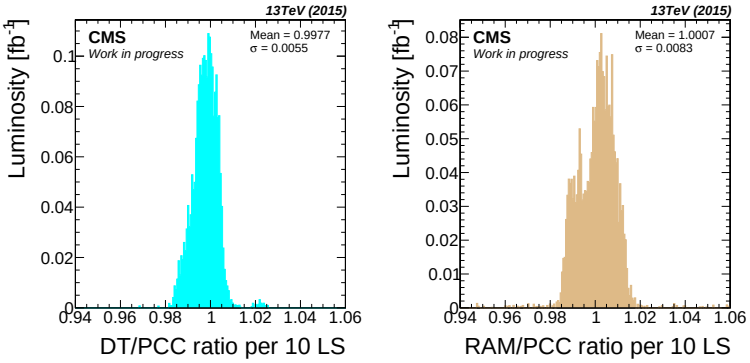

Figure A.10: Histograms of the detector ratios every 50 lumi-sections (2015).

integrated luminosity produced by the $0.0026\,(Hz/\mu b)^{-1}$ non-linearity slope.
The impact of the non-linearity on the integrated luminosity comes from the non-linearity slope value and the SBIL distribution (see Figure A.19). One can estimate the impact, as an

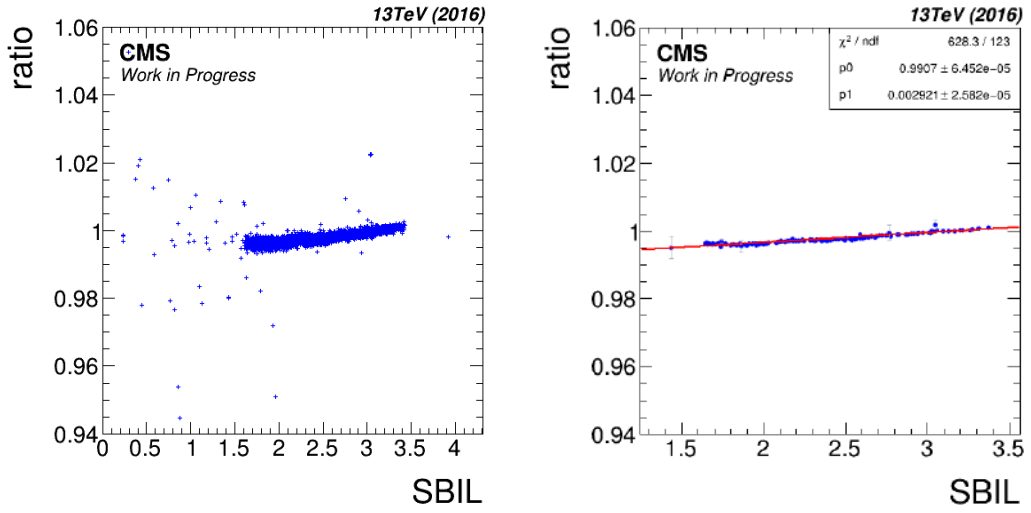

Figure A.11: HFOC/PCC single fill data example. On the **left** original data is shown. The ratio is computed every 30 LS (**rigth**) to reduce statistical effects.

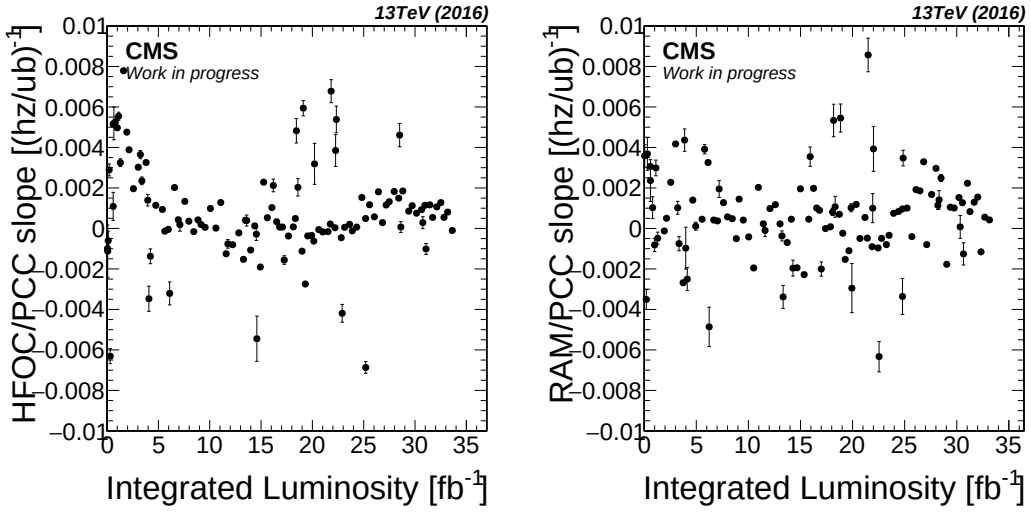

Figure A.12: Fill-by-fill slopes vs the integrated luminosity.

approximation, by multiplying the slope value and the mean value from the SBIL histogram. The given values are computed using the SBIL value in each LS.

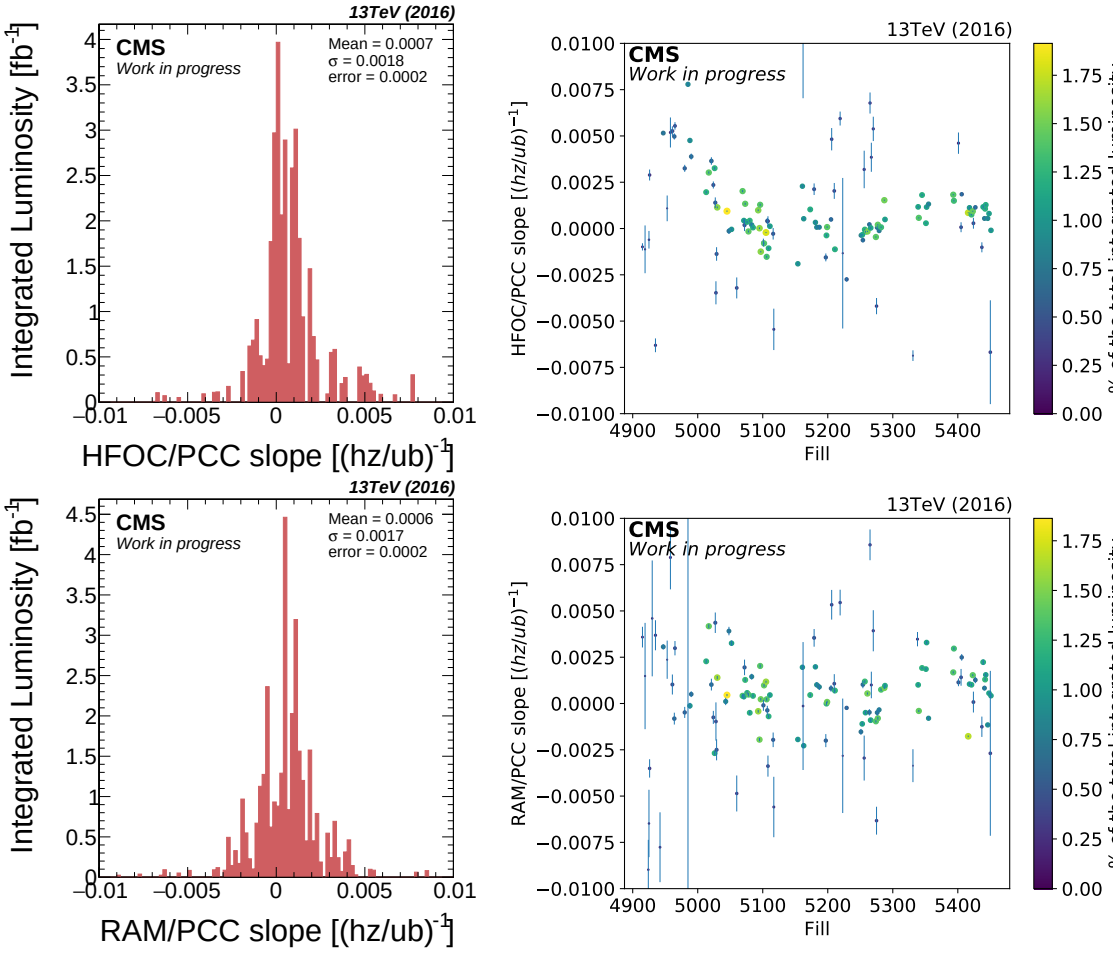

Figure A.13: Luminosity weighted histogram (**left**). Slopes vs fill number where the color bar gives information about the luminosity that each point represent (**right**).

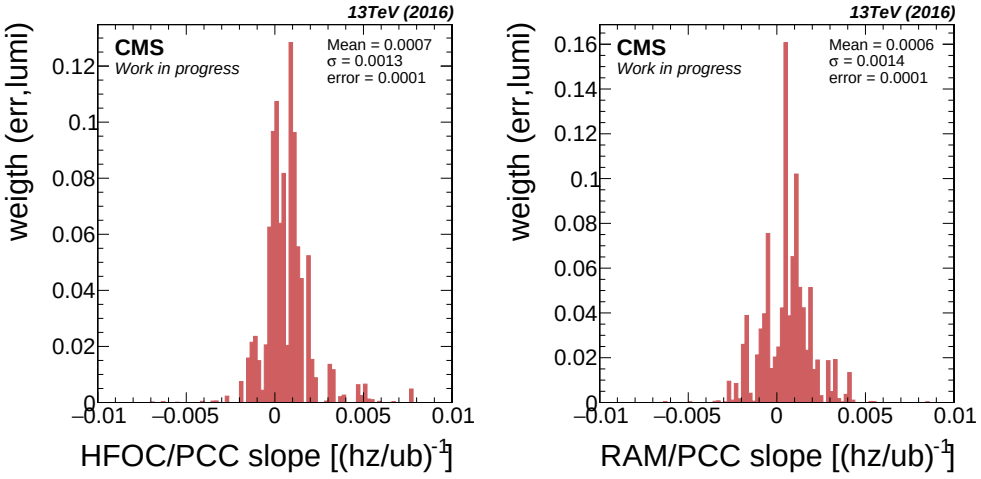

Figure A.14: Luminosity and error weighted histogram.

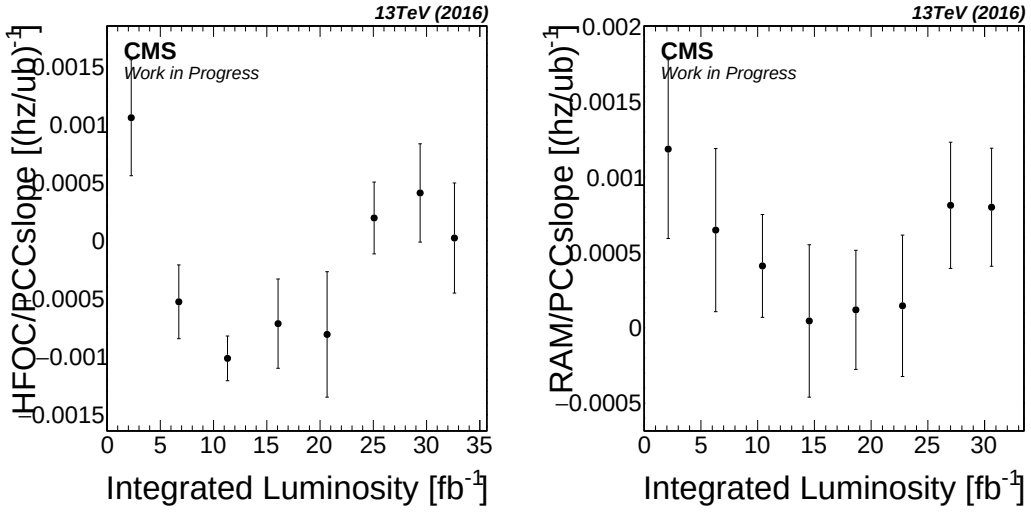

Figure A.15: Error weighted average values of the fill-by-fill slopes in equal integrated luminosity intervals

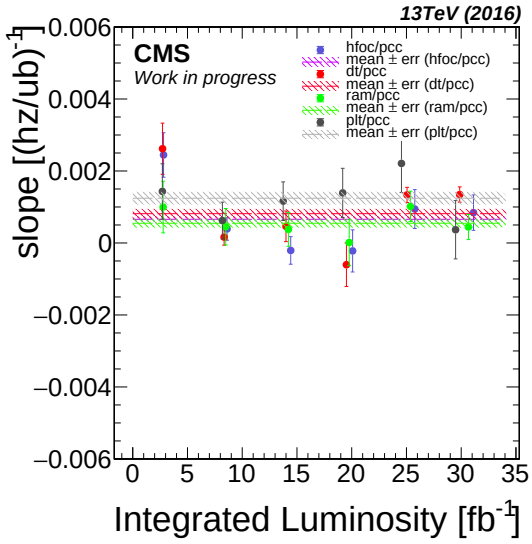

Linearity Summary Table.

detector	slope hist. mean (%)
HFOC-PCC	0.0007 **(0.23)**
RAMSES-PCC	0.0006 **(0.21)**
DT-PCC	0.0008 **(0.27)**
PLT-PCC	0.0012 **(0.43)**

Slopes $[(Hz/\mu b)^{-1}]$ **(uncertainty % on the integrated luminosity. Using values from the luminosity and error weighted histograms.)**

Figure A.16: Linearity summary plot. HFOC, RAMSES and DT combined information for 2016. Two slopes description is plotted for each detector pair: Weighted average values of the fill-by-fill slopes (ratios labels) and the mean value of the fill-by-fill slopes (mean ± error).

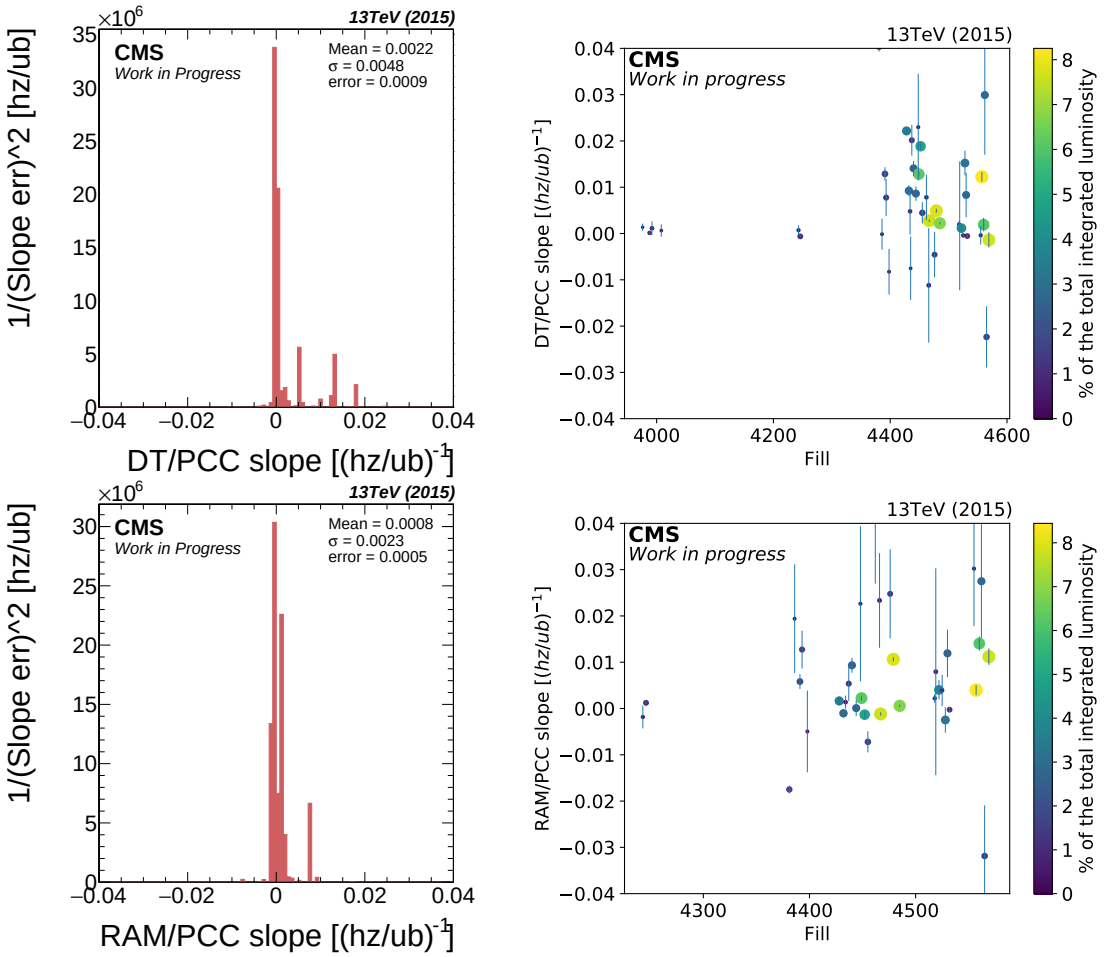

Figure A.17: Slope error weighted histogram (**left**). Slopes vs fill number where the color bar gives information about the luminosity that each point represent (**right**).

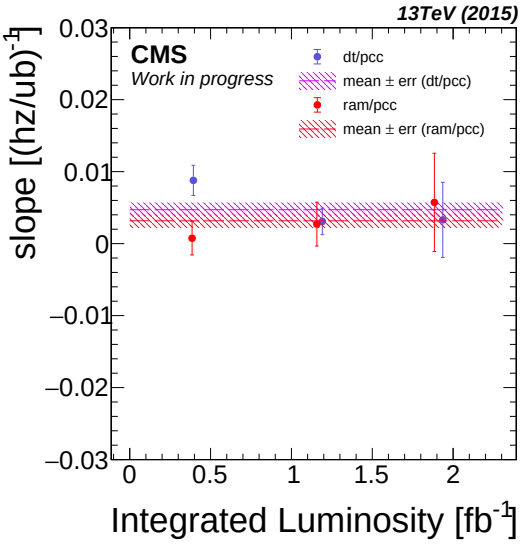

Linearity Summary Table.

detector	slope hist. mean (%)
dt-pcc	0.0026 **(0.48)**
ramses-pcc	0.0012 **(0.20)**

Slopes $[(Hz/\mu b)^{-1}]$ **(uncertainty % on the integrated luminosity)**

Figure A.18: Linearity summary plot for 2015. Two slopes description is plotted for each detector pair: Weighted average values of the fill-by-fill slopes (ratios labels) and the mean value of the fill-by-fill slopes (mean ± error).

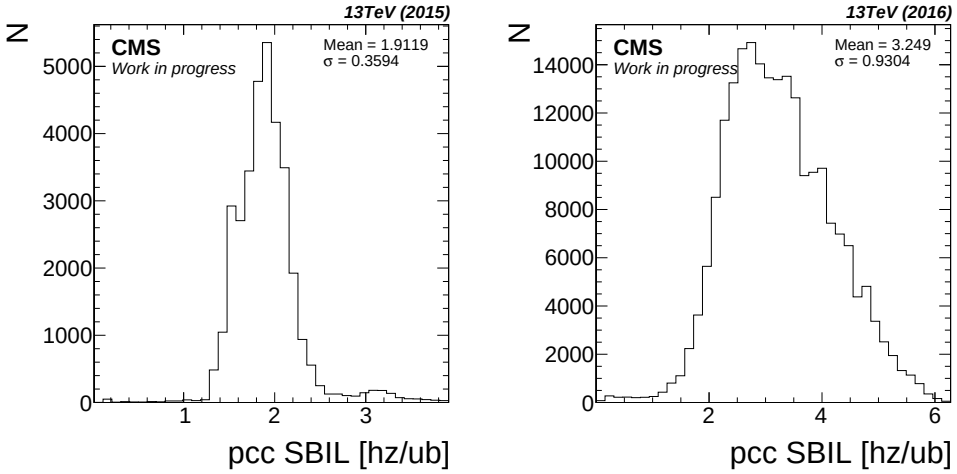

Figure A.19: SBIL distribution for 2015 (left) and 2016 (right) measured by PCC.

APPENDIX

B

CONTROL DISTRIBUTIONS FOR INDIVIDUAL YEARS

Control distributions for the different individual years (2016, 2017 and 2018) are presented in this appendix.

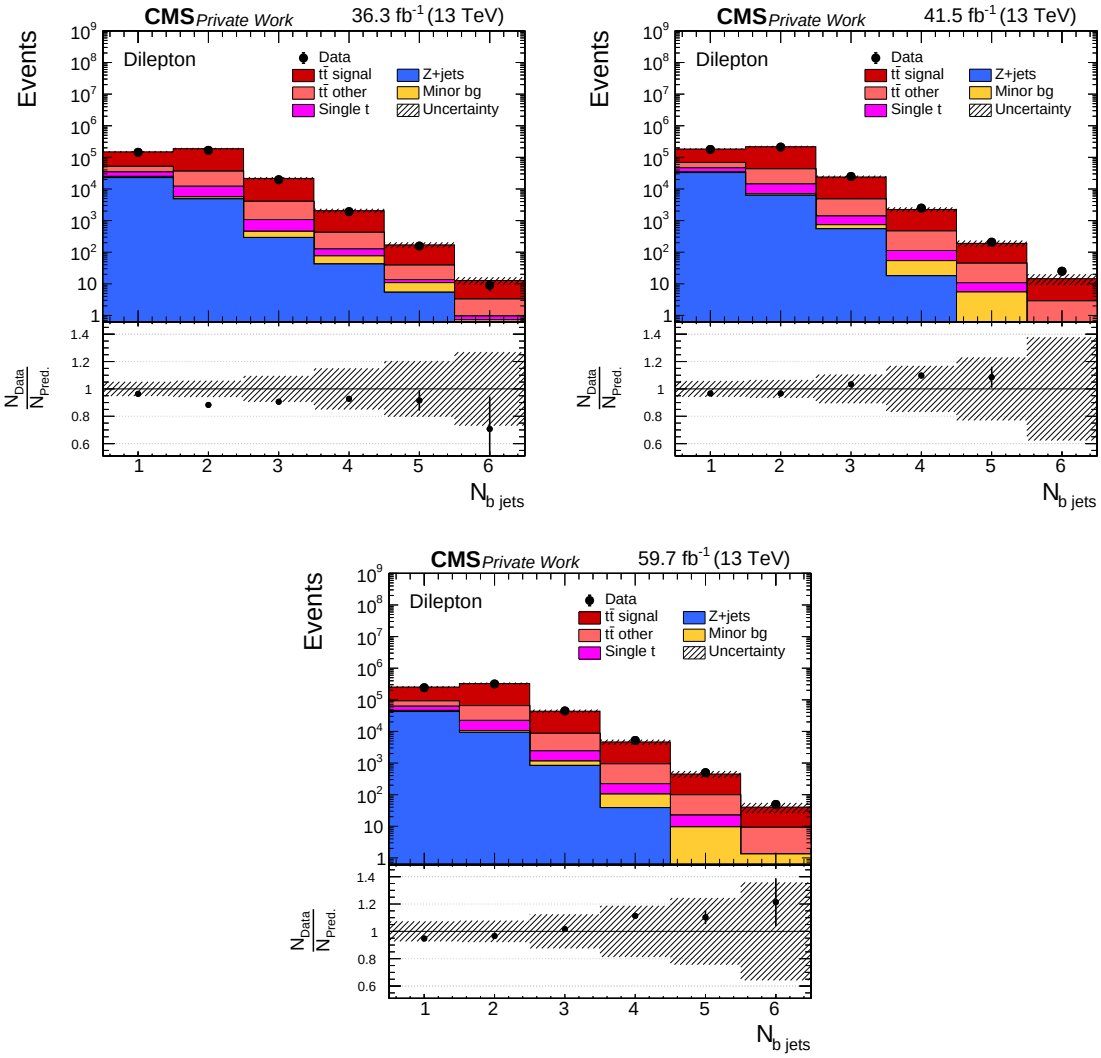

Figure B.1: Multiplicity of b-jets after the requirement of at least one b-tagged jet, including also all previous steps as described in Section 6.2. DY scale factors are applied. The distributions are shown for the different e^+e^- (upper left), $\mu^+\mu^-$ (upper right) and $e^\pm\mu^\mp$ (lower left) channels, and its combination named as Dilepton (lower right). The hatched area represents the shape systematic uncertainties on the $\mathrm{t\bar{t}}$ signal and backgrounds (see Chapter 9). The top plots correspond to the 2016 (left) and 2017 (right) years and the bottom one to the 2018 dataset.

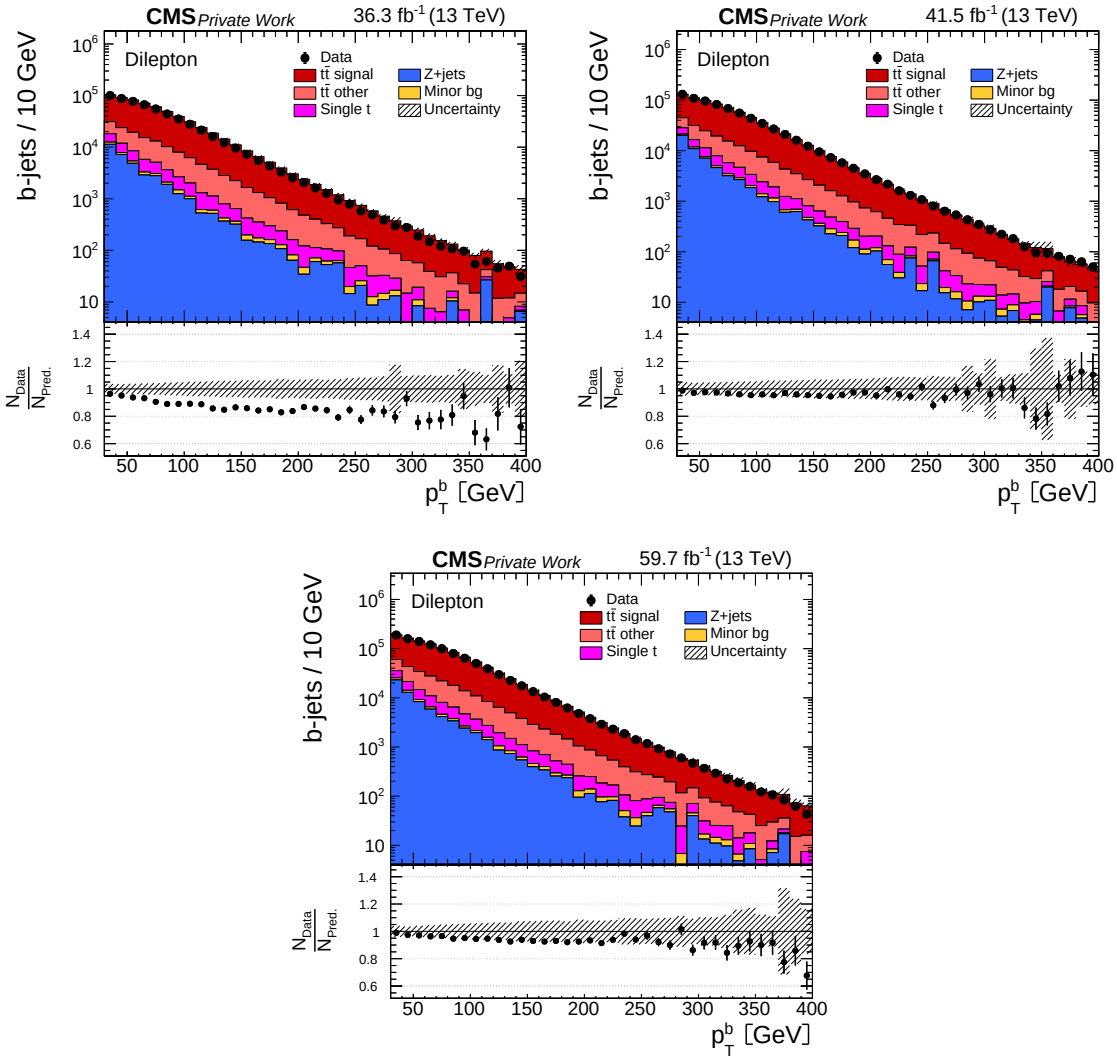

Figure B.2: Transverse momentum of b-jets after the requirement of at least one b-tagged jet, including also all previous steps as described in Section 6.2. DY scale factors are applied. The distributions are shown for the different e^+e^- (upper left), $\mu^+\mu^-$ (upper right) and $e^\pm\mu^\mp$ (lower left) channels, and its combination named as Dilepton (lower right). The hatched area represents the shape systematic uncertainties on the $\mathrm{t\bar{t}}$ signal and backgrounds (see Chapter 9). This distribution is used as an input to the top-quark pair kinematic reconstruction. The top plots correspond to the 2016 (left) and 2017 (right) years and the bottom one to the 2018 dataset.

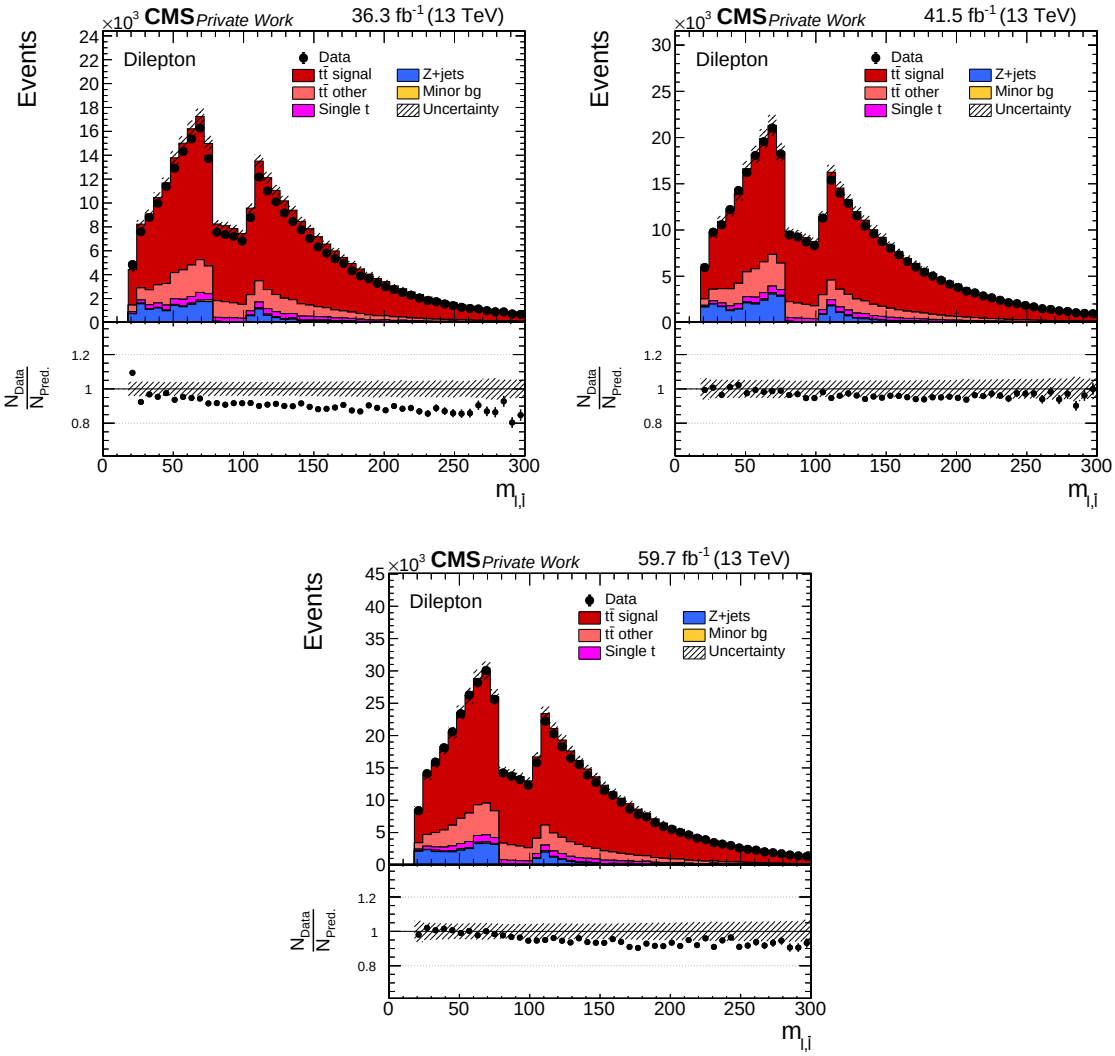

Figure B.3: Invariant mass of the dilepton system after the requirement of at least one b-tagged jet, including also all previous steps as described in Section 6.2. DY scale factors are applied. The distributions are shown for the different e^+e^- (upper left), $\mu^+\mu^-$ (upper right) and $e^\pm\mu^\mp$ (lower left) channels, and its combination named as Dilepton (lower right). The hatched area represents the shape systematic uncertainties on the $\mathrm{t\bar{t}}$ signal and backgrounds (see Chapter 9). The top plots correspond to the 2016 (left) and 2017 (right) years and the bottom one to the 2018 dataset.

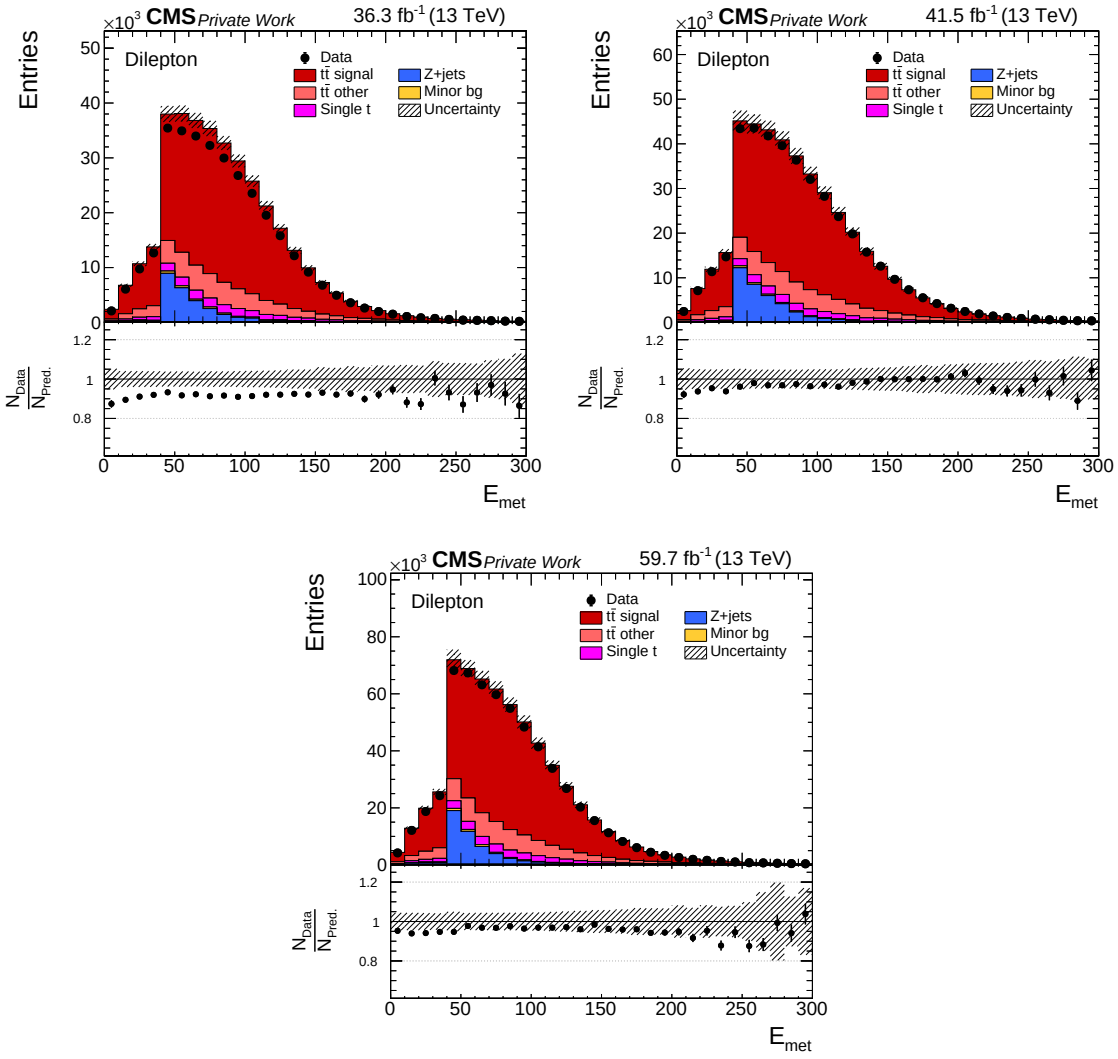

Figure B.4: Missing transverse energy in the event after the requirement of at least one b-tagged jet, including also all previous steps as described in Section 6.2. DY scale factors are applied. The distributions are shown for the different e^+e^- (upper left), $\mu^+\mu^-$ (upper right) and $e^\pm\mu^\mp$ (lower left) channels, and its combination named as Dilepton (lower right). The hatched area represents the shape systematic uncertainties on the $t\bar{t}$ signal and backgrounds (see Chapter 9). This distribution is used as an input to the top-quark pair kinematic reconstruction. The top plots correspond to the 2016 (left) and 2017 (right) years and the bottom one to the 2018 dataset.

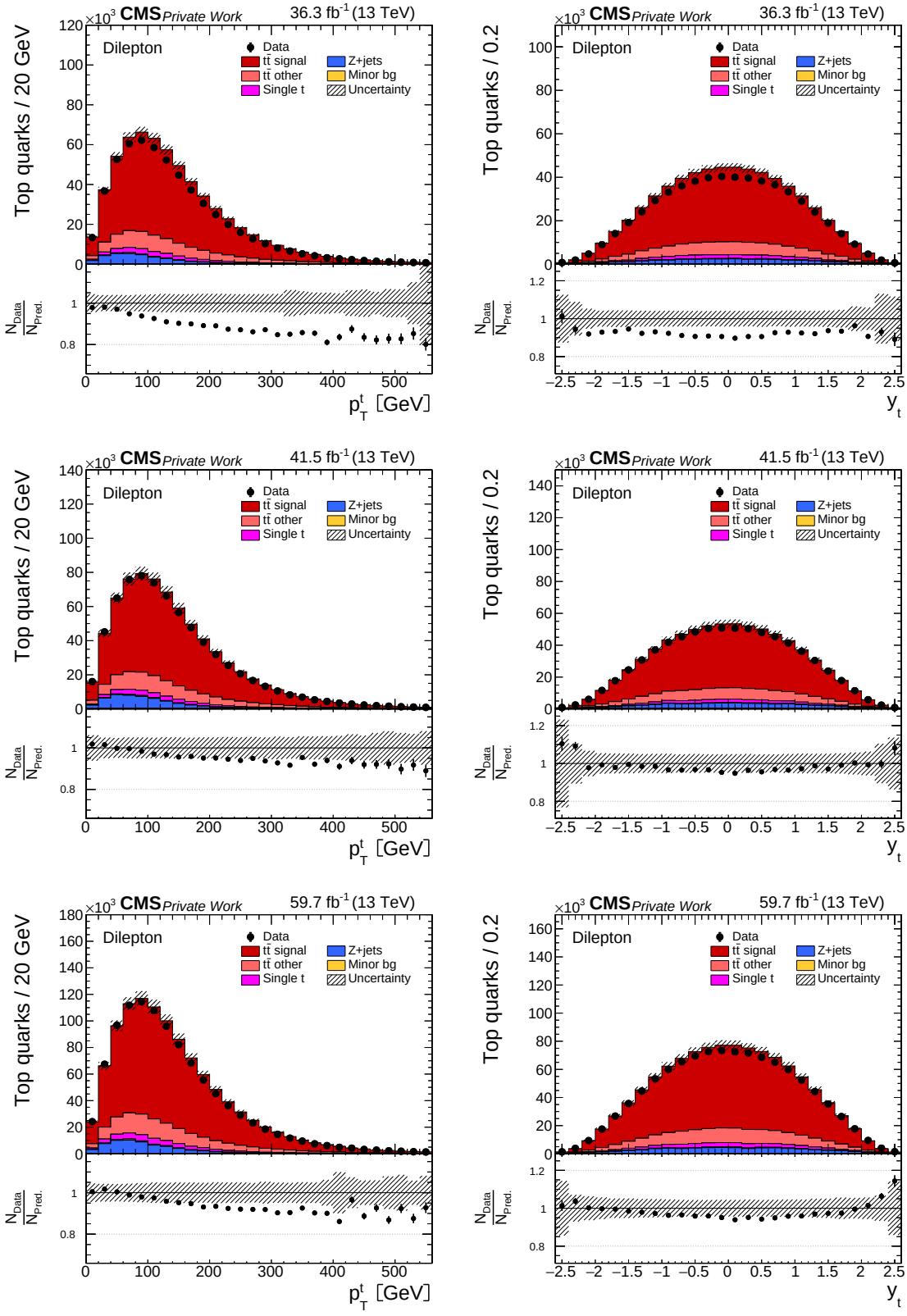

Figure B.5: Transverse momentum (left) and rapidity (right) of the reconstructed top quark and antiquark. Events include all selection requirements described in Section 6.2. The upper, middle and bottom plots correspond to 2016, 2017 and 2018, respectively.

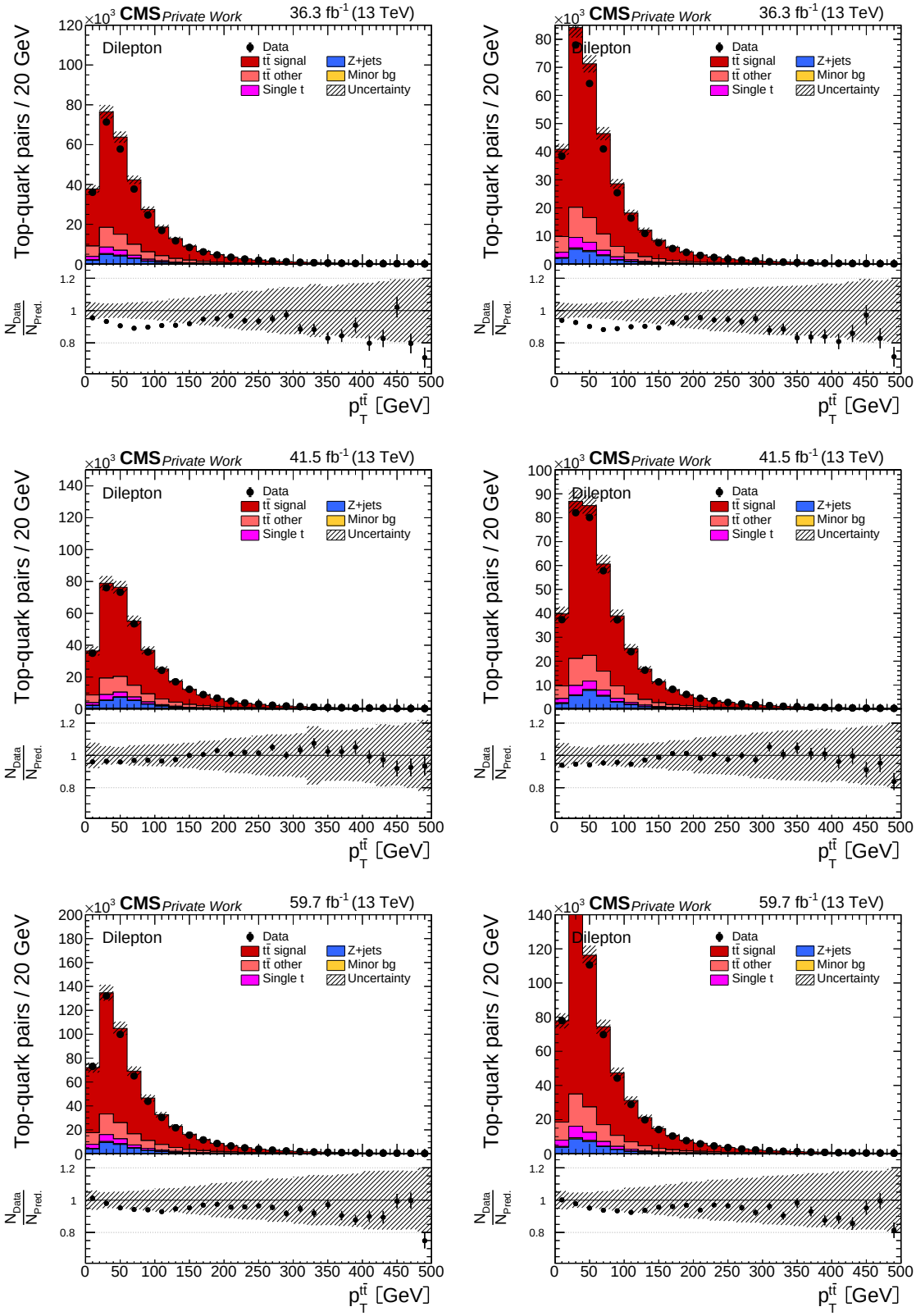

Figure B.6: Transverse momentum of the reconstructed $t\bar{t}$ system using the full (left) and loose (right) kinematic reconstruction methods. Events include all selection requirements described in Section 6.2. The upper, middle and bottom plots correspond to 2016, 2017 and 2018, respectively.

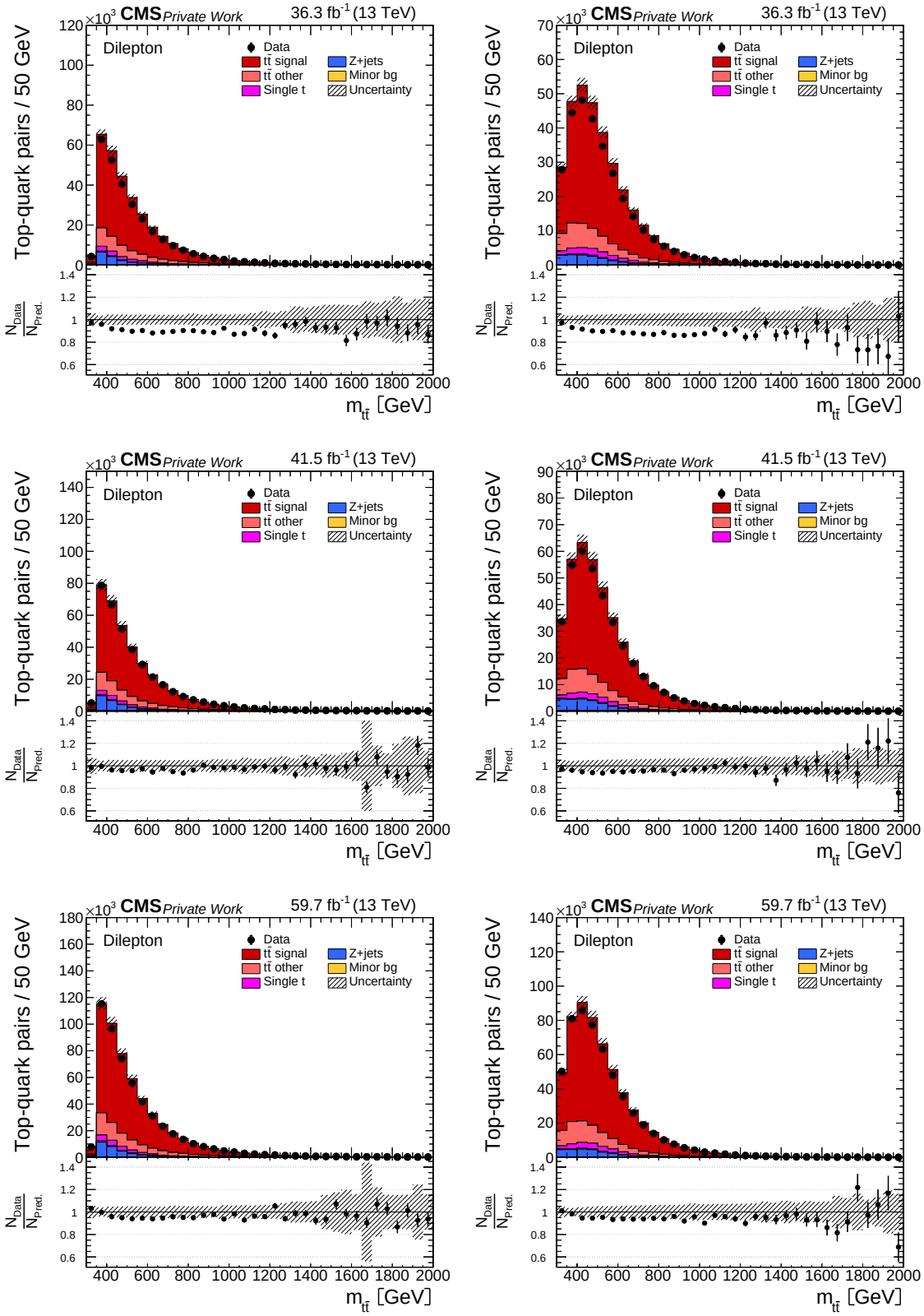

Figure B.7: Invariant mass of the reconstructed $t\bar{t}$ system using the full (left) and loose (right) kinematic reconstruction methods. Events include all selection requirements described in Section 6.2. The upper, middle and bottom plots correspond to 2016, 2017 and 2018, respectively.

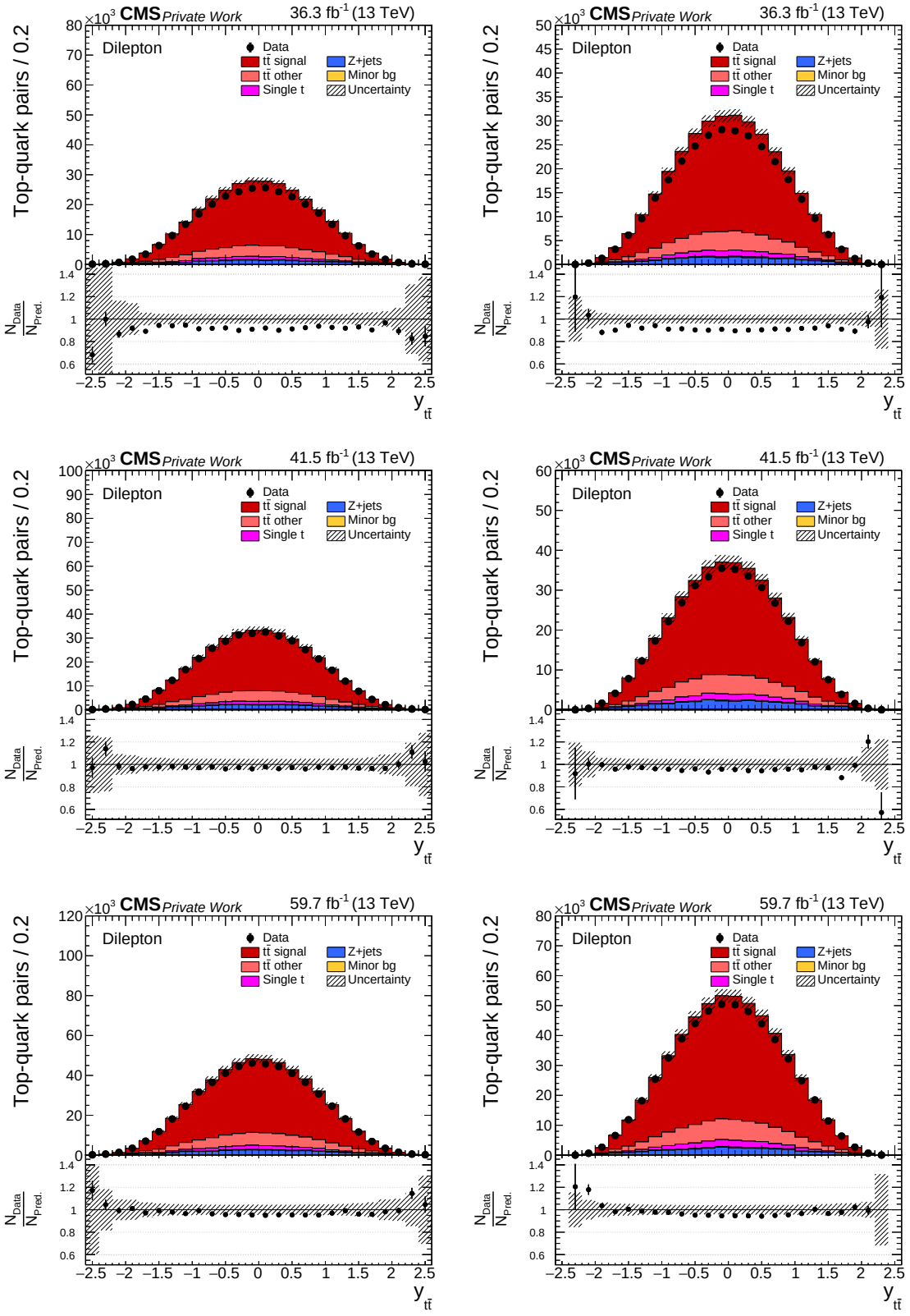

Figure B.8: Rapidity of the reconstructed $t\bar{t}$ system using the full (left) and loose (right) kinematic reconstruction methods. Events include all selection requirements described in Section 6.2. The upper, middle and bottom plots correspond to 2016, 2017 and 2018, respectively.

APPENDIX

C

FULL SET OF CROSS SECTIONS RESULTS

C.1 Cross sections

Here, all absolute and/or particle level "versions" cross section results not present in the results chapter 10 are shown in this appendix. The plots are grouped and presented in the same order as in Chapter 10.

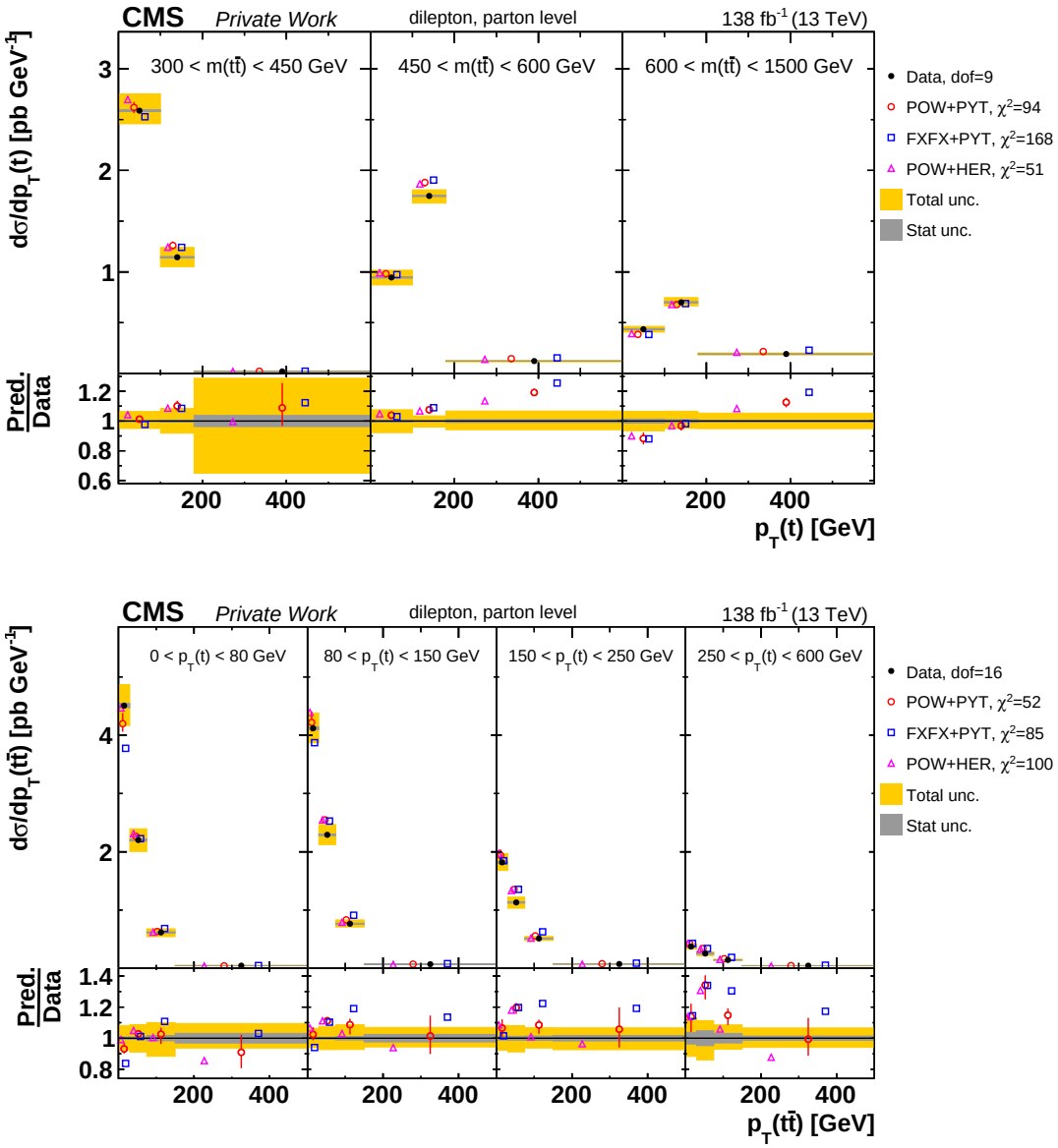

Figure C.1: Comparison of the measured $[M(\mathrm{t\bar{t}}),p_{\mathrm{T}}(t)]$ (top) and $[p_{\mathrm{T}}(t),p_{\mathrm{T}}(\mathrm{t\bar{t}})]$ (bottom) parton level absolute cross sections to MC predictions (see Fig. 10.1 for further details).

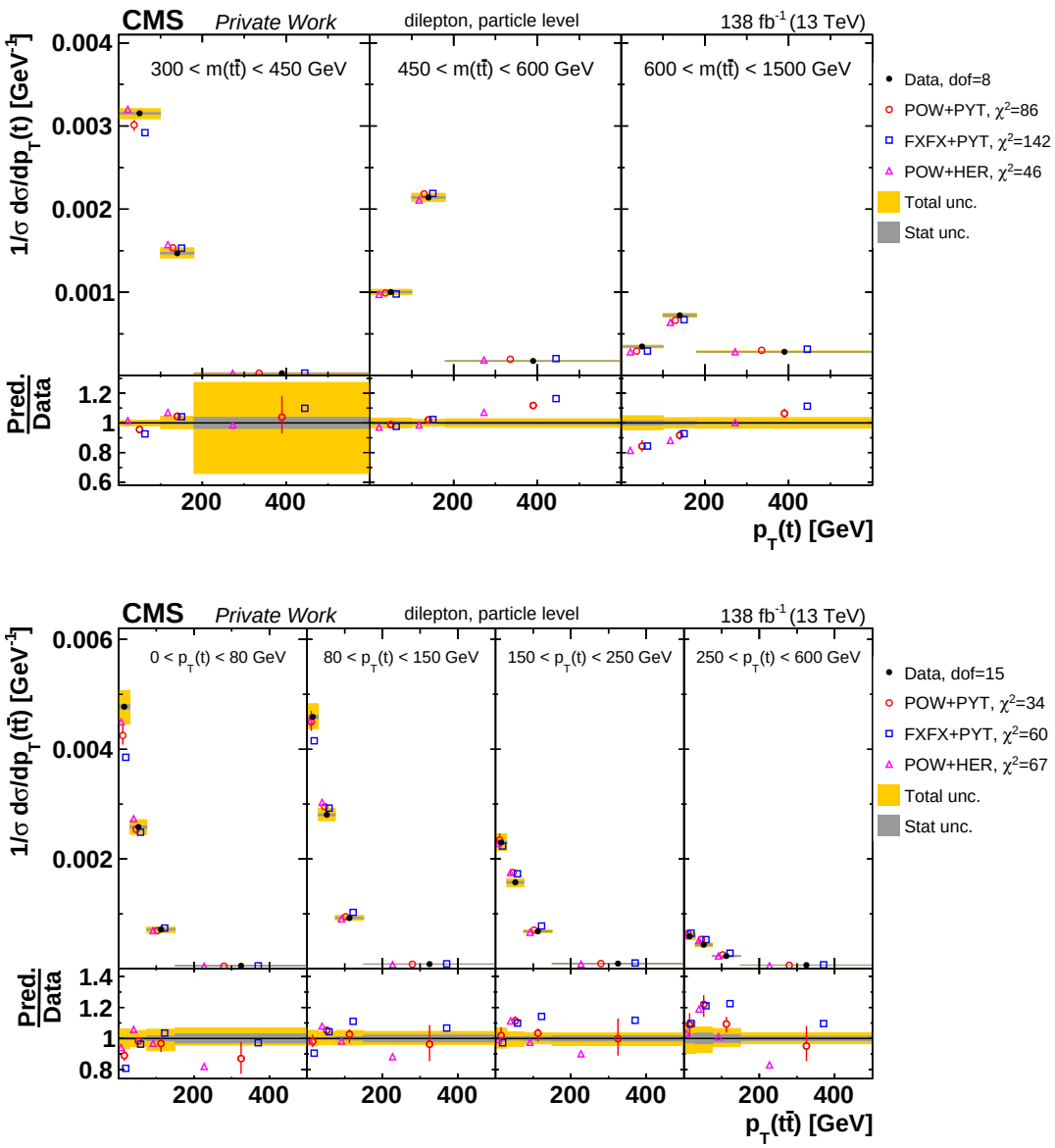

Figure C.2: Comparison of the measured $[M(\mathrm{t\bar{t}}),p_{\mathrm{T}}(t)]$ (top) and $[p_{\mathrm{T}}(t),p_{\mathrm{T}}(\mathrm{t\bar{t}})]$ (bottom) particle level normalized cross sections to MC predictions (see Fig. 10.1 for further details).

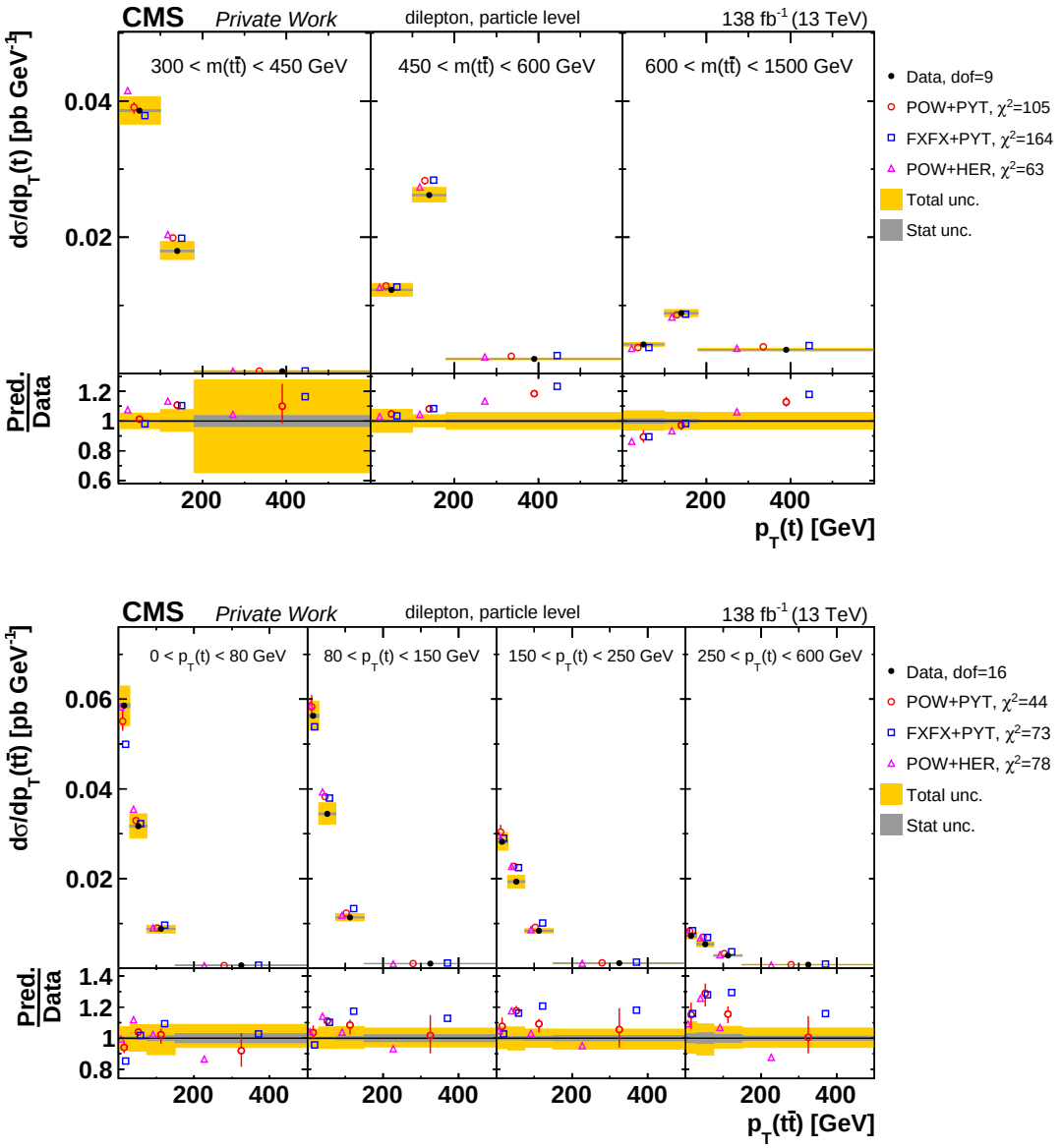

Figure C.3: Comparison of the measured $[M(\mathrm{t\bar{t}}),p_{\mathrm{T}}(t)]$ (top) and $[p_{\mathrm{T}}(t),p_{\mathrm{T}}(\mathrm{t\bar{t}})]$ (bottom) particle level absolute cross sections to MC predictions (see Fig. 10.1 for further details).

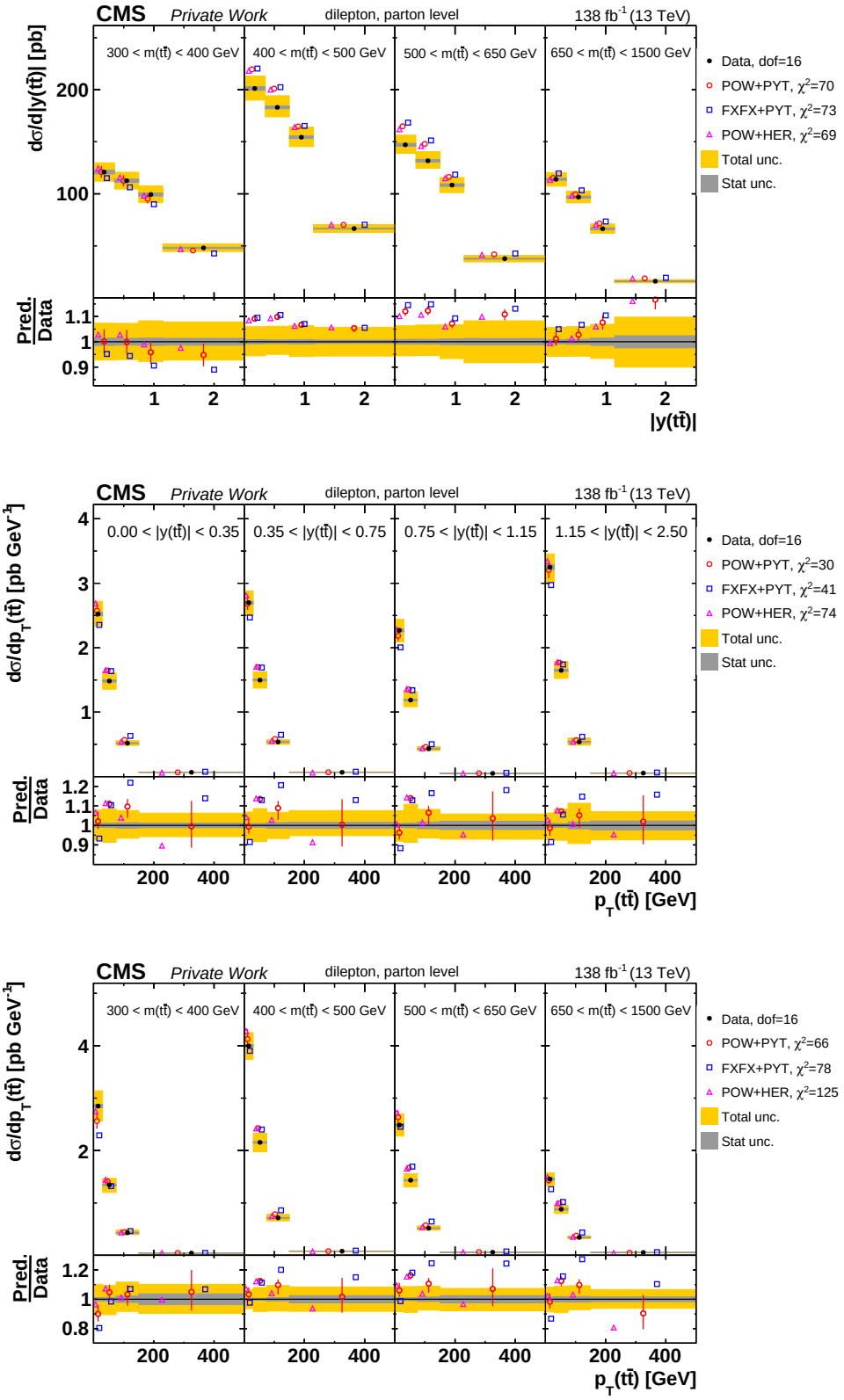

Figure C.4: Comparison of the measured $[M(\mathrm{t\bar{t}}),y(\mathrm{t\bar{t}})]$ (top), $[y(\mathrm{t\bar{t}}),p_{\mathrm{T}}(\mathrm{t\bar{t}})]$ (middle) and $[M(\mathrm{t\bar{t}}),p_{\mathrm{T}}(\mathrm{t\bar{t}})]$ (bottom) parton level absolute cross sections to MC predictions (see Fig. 10.1 for further details). The *Loose KR* (see Section 7.1.2) is used for $[M(\mathrm{t\bar{t}}),y(\mathrm{t\bar{t}})]$ and $[M(\mathrm{t\bar{t}}),p_{\mathrm{T}}(\mathrm{t\bar{t}})]$.

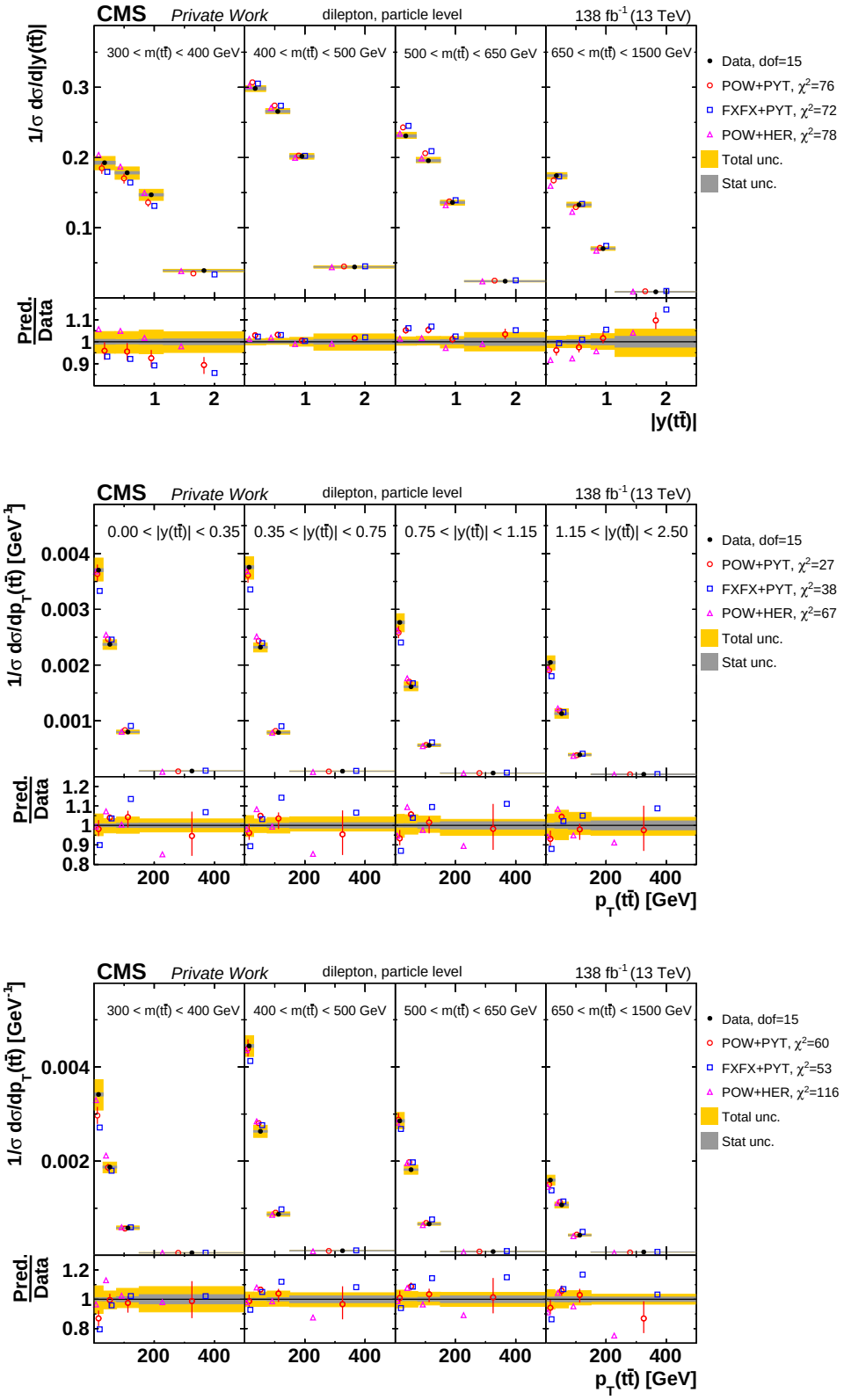

Figure C.5: Comparison of the measured $[M(\mathrm{t\bar{t}}),y(\mathrm{t\bar{t}})]$ (top), $[y(\mathrm{t\bar{t}}),p_{\mathrm{T}}(\mathrm{t\bar{t}})]$ (middle) and $[M(\mathrm{t\bar{t}}),p_{\mathrm{T}}(\mathrm{t\bar{t}})]$ (bottom) particle level normalized cross sections to MC predictions (see Fig. 10.1 for further details). The *Loose KR* (see Section 7.1.2) is used for $[M(\mathrm{t\bar{t}}),y(\mathrm{t\bar{t}})]$ and $[M(\mathrm{t\bar{t}}),p_{\mathrm{T}}(\mathrm{t\bar{t}})]$.

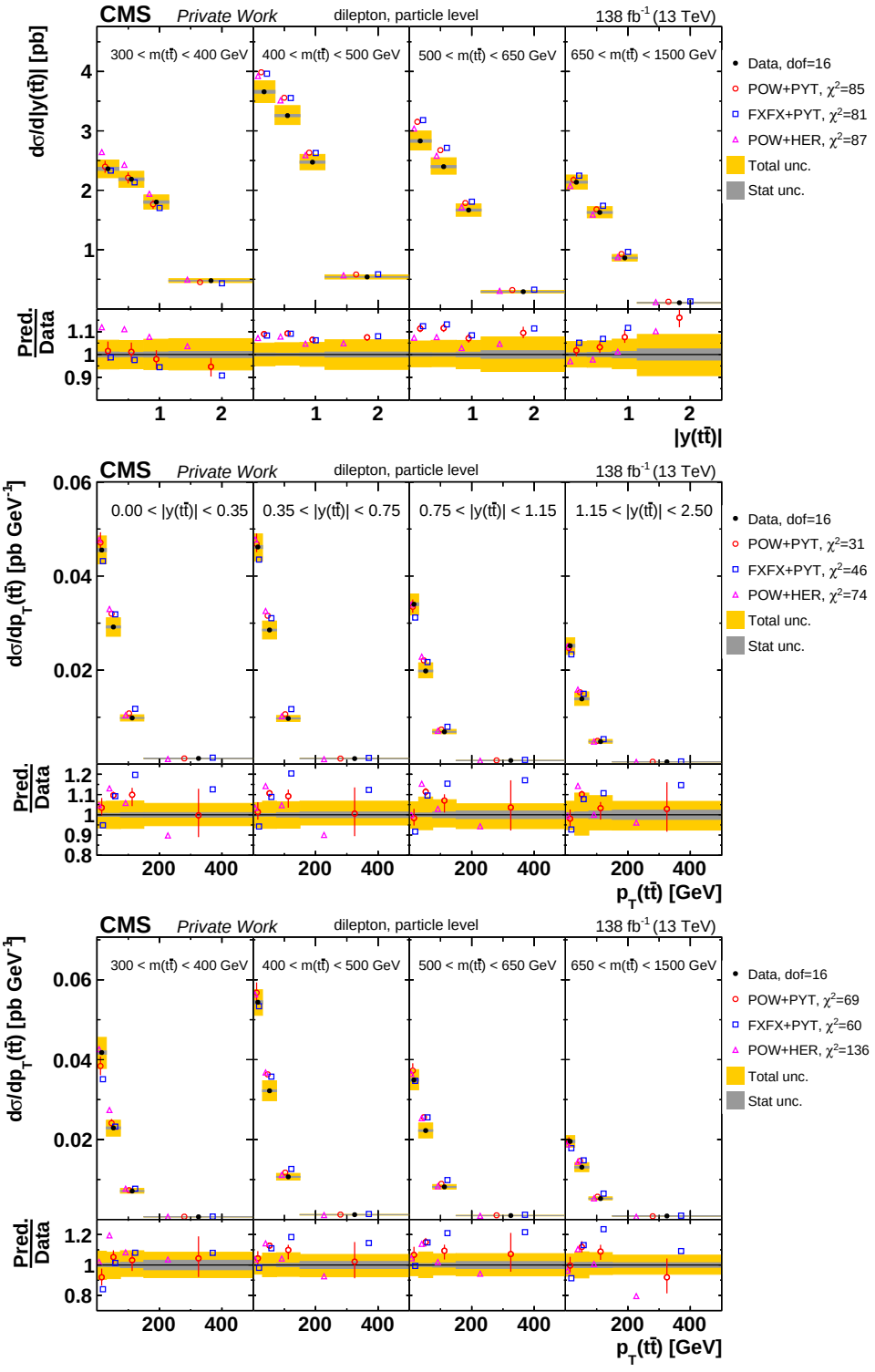

Figure C.6: Comparison of the measured $[M(\mathrm{t\bar{t}}),y(\mathrm{t\bar{t}})]$ (top), $[y(\mathrm{t\bar{t}}),p_{\mathrm{T}}(\mathrm{t\bar{t}})]$ (middle) and $[M(\mathrm{t\bar{t}}),p_{\mathrm{T}}(\mathrm{t\bar{t}})]$ (bottom) particle level absolute cross sections to MC predictions (see Fig. 10.1 for further details). The *Loose KR* (see Section 7.1.2) is used for $[M(\mathrm{t\bar{t}}),y(\mathrm{t\bar{t}})]$ and $[M(\mathrm{t\bar{t}}),p_{\mathrm{T}}(\mathrm{t\bar{t}})]$.

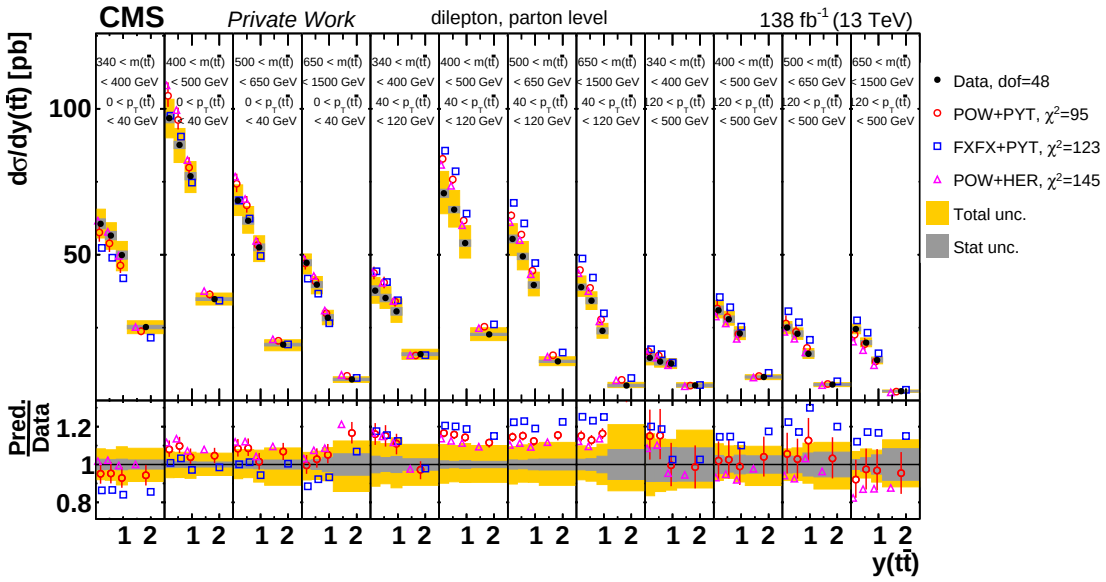

Figure C.7: Comparison of the measured $[p_{\mathrm{T}}(\mathrm{t\bar{t}}),M(\mathrm{t\bar{t}}),y(\mathrm{t\bar{t}})]$ normalized parton level cross section to MC predictions (see Fig. 10.1 for further details). The *Loose KR* (see Section 7.1.2) is used for this cross section.

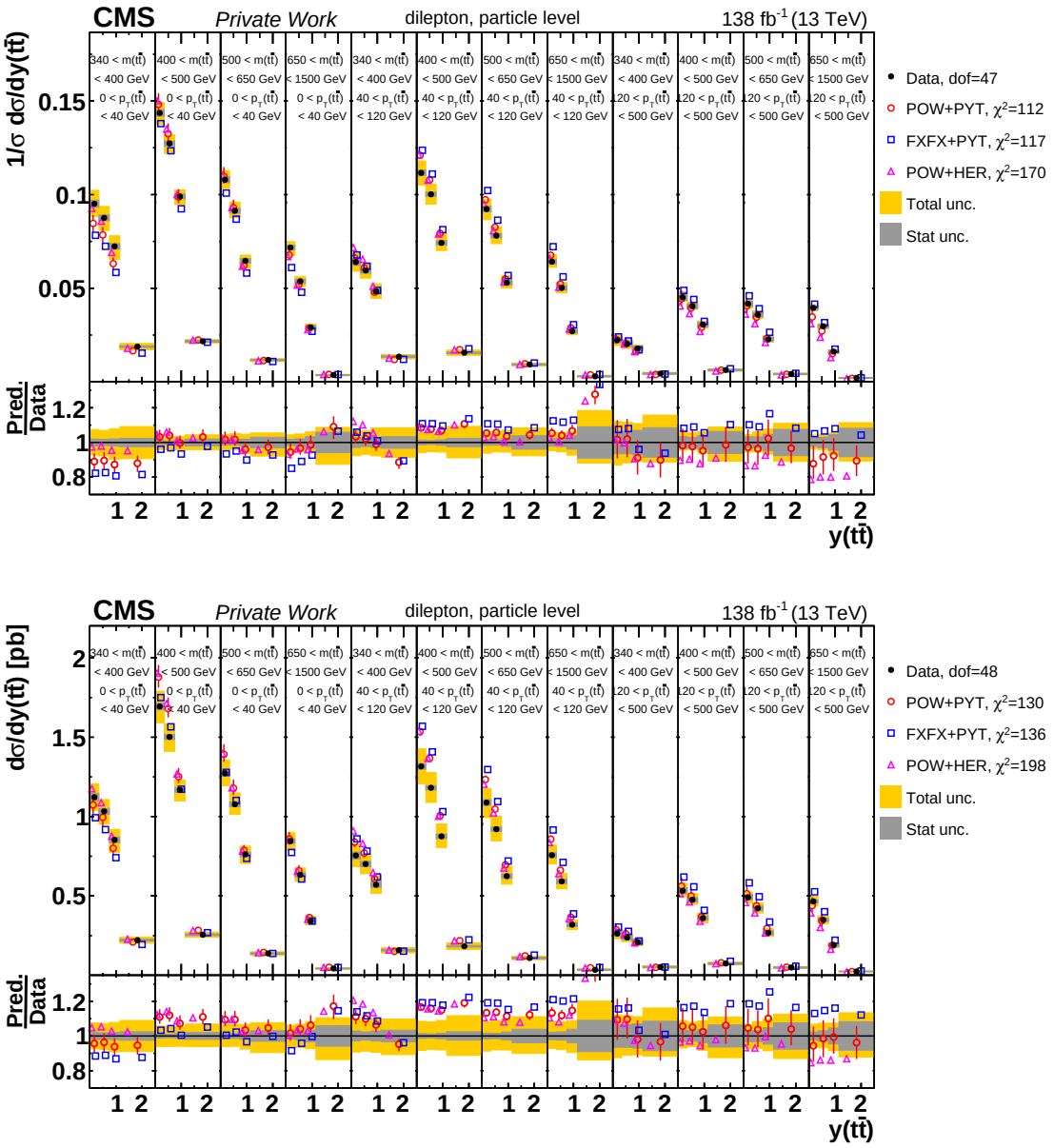

Figure C.8: Comparison of the measured $[p_{\mathrm{T}}(\mathrm{t\bar{t}}), M(\mathrm{t\bar{t}}), y(\mathrm{t\bar{t}})]$ normalized (top) and absolute (bottom) particle level cross sections to MC predictions (see Fig. 10.1 for further details). The *Loose KR* (see Section 7.1.2) is used for this cross section.

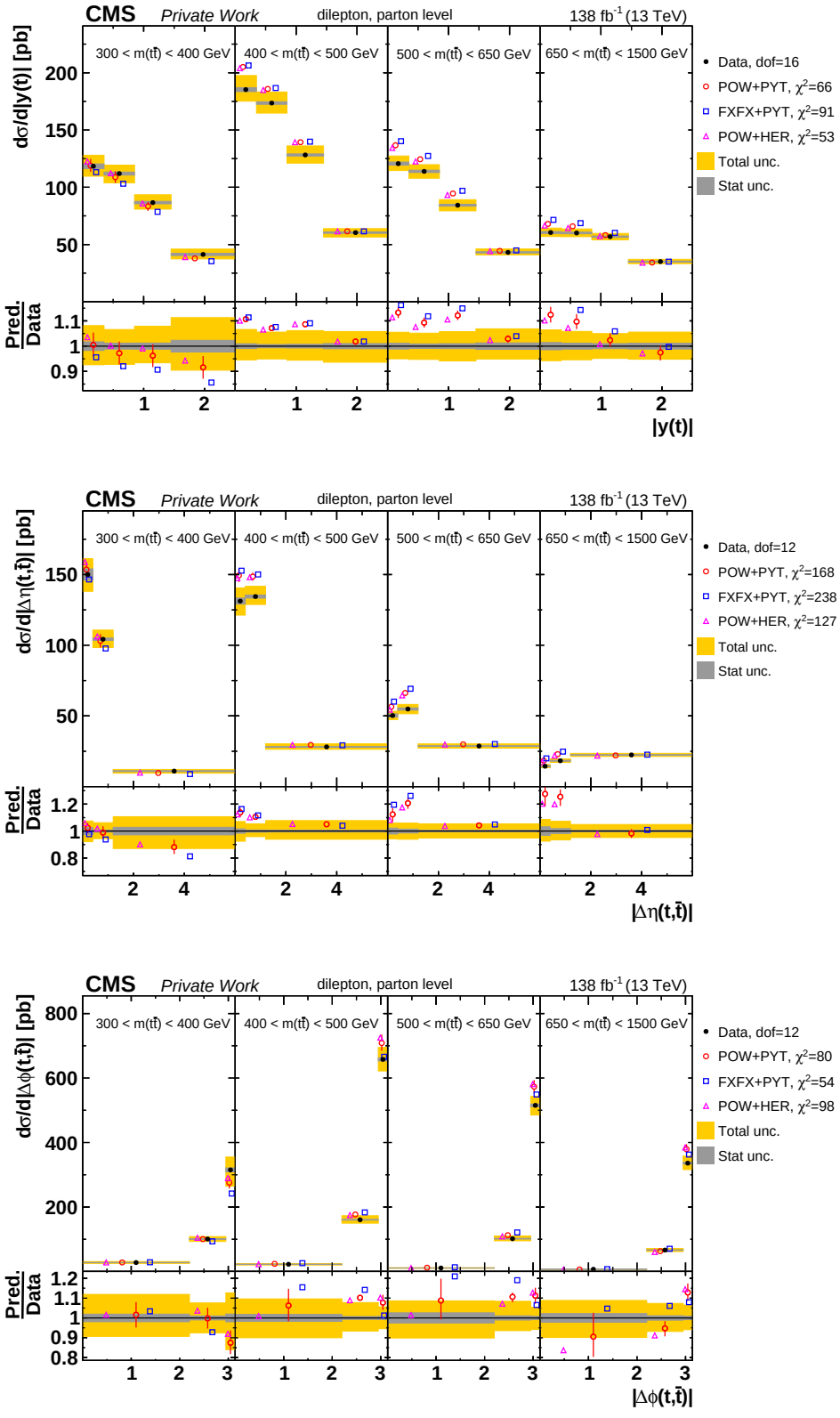

Figure C.9: Comparison of the measured $[M(\mathrm{t\bar{t}}),y(t)]$ (top), $[M(\mathrm{t\bar{t}}),\Delta\eta(t,\bar{t})\ ]$ (middle) and $[M(\mathrm{t\bar{t}}),\Delta\phi(t,\bar{t})\ ]$ (bottom) parton level absolute cross sections to MC predictions (see Fig. 10.1 for further details).

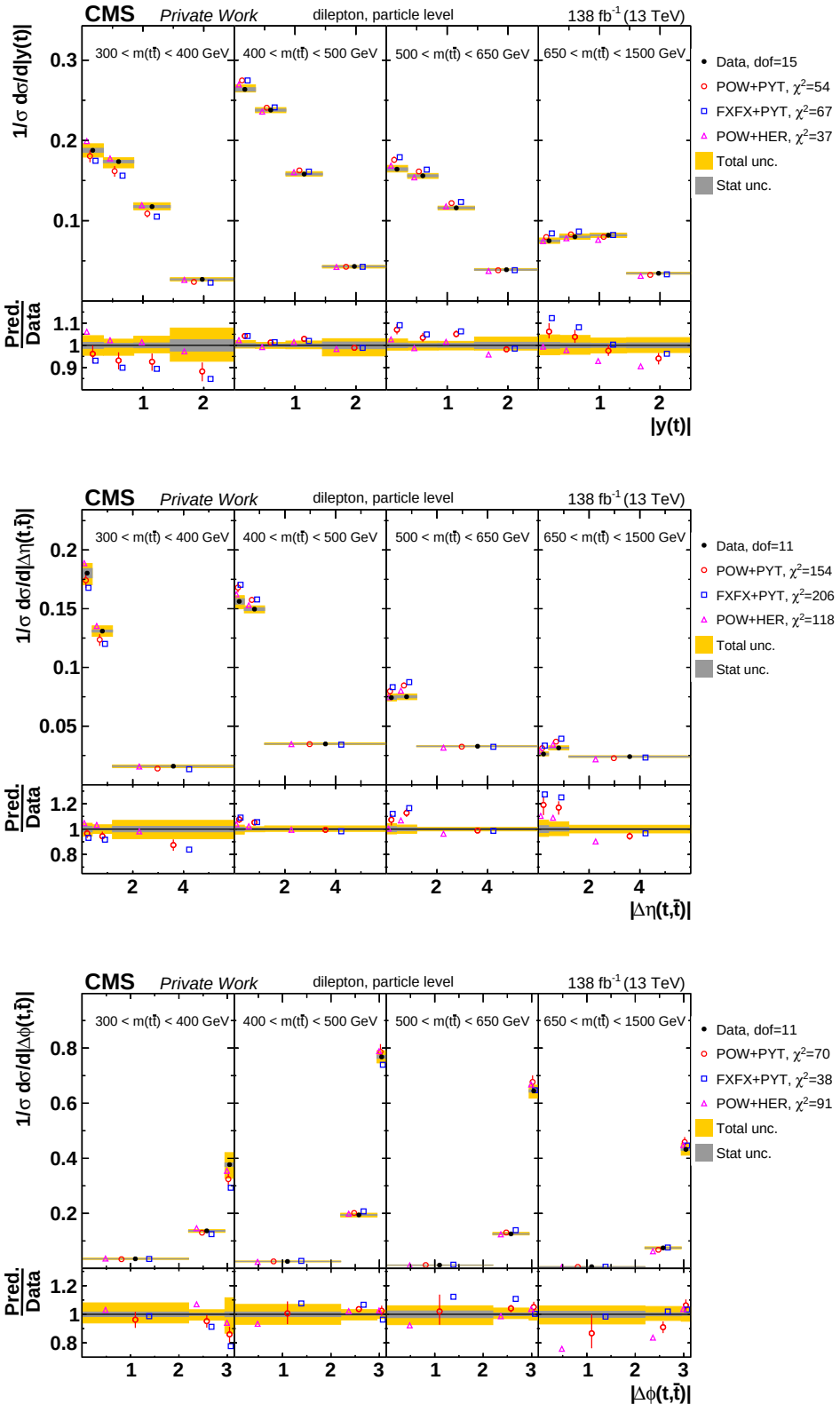

Figure C.10: Comparison of the measured $[M(\mathrm{t\bar{t}}),y(t)]$ (top), $[M(\mathrm{t\bar{t}}),\Delta\eta(t,\bar{t})\ ]$ (middle) and $[M(\mathrm{t\bar{t}}),\Delta\phi(t,\bar{t})\ ]$ (bottom) particle level normalized cross sections to MC predictions (see Fig. 10.1 for further details).

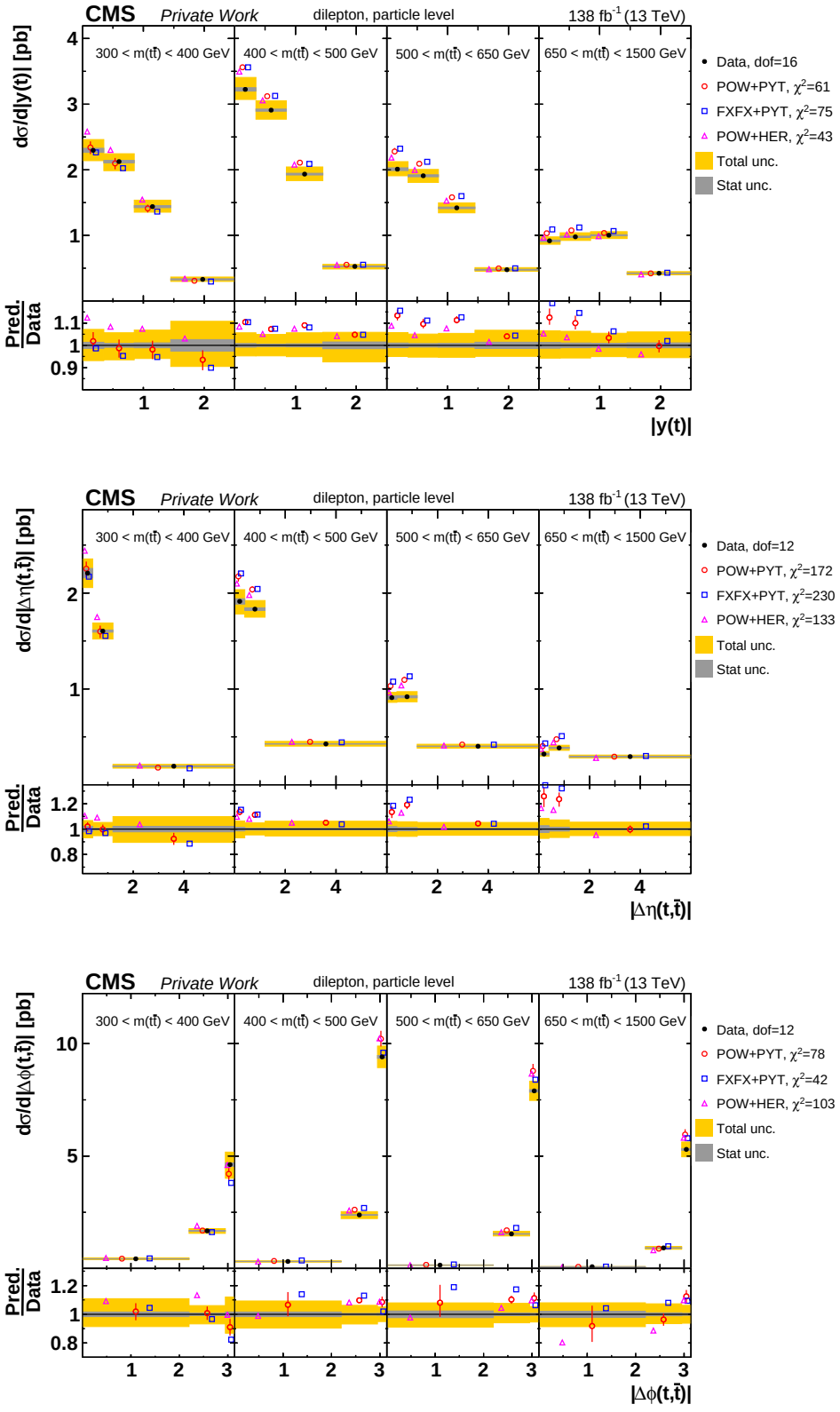

Figure C.11: Comparison of the measured $[M(\mathrm{t\bar{t}}),y(t)]$ (top), $[M(\mathrm{t\bar{t}}),\Delta\eta(t,\bar{t})\ ]$ (middle) and $[M(\mathrm{t\bar{t}}),\Delta\phi(t,\bar{t})\ ]$ (bottom) particle level absolute cross sections to MC predictions (see Fig. 10.1 for further details).

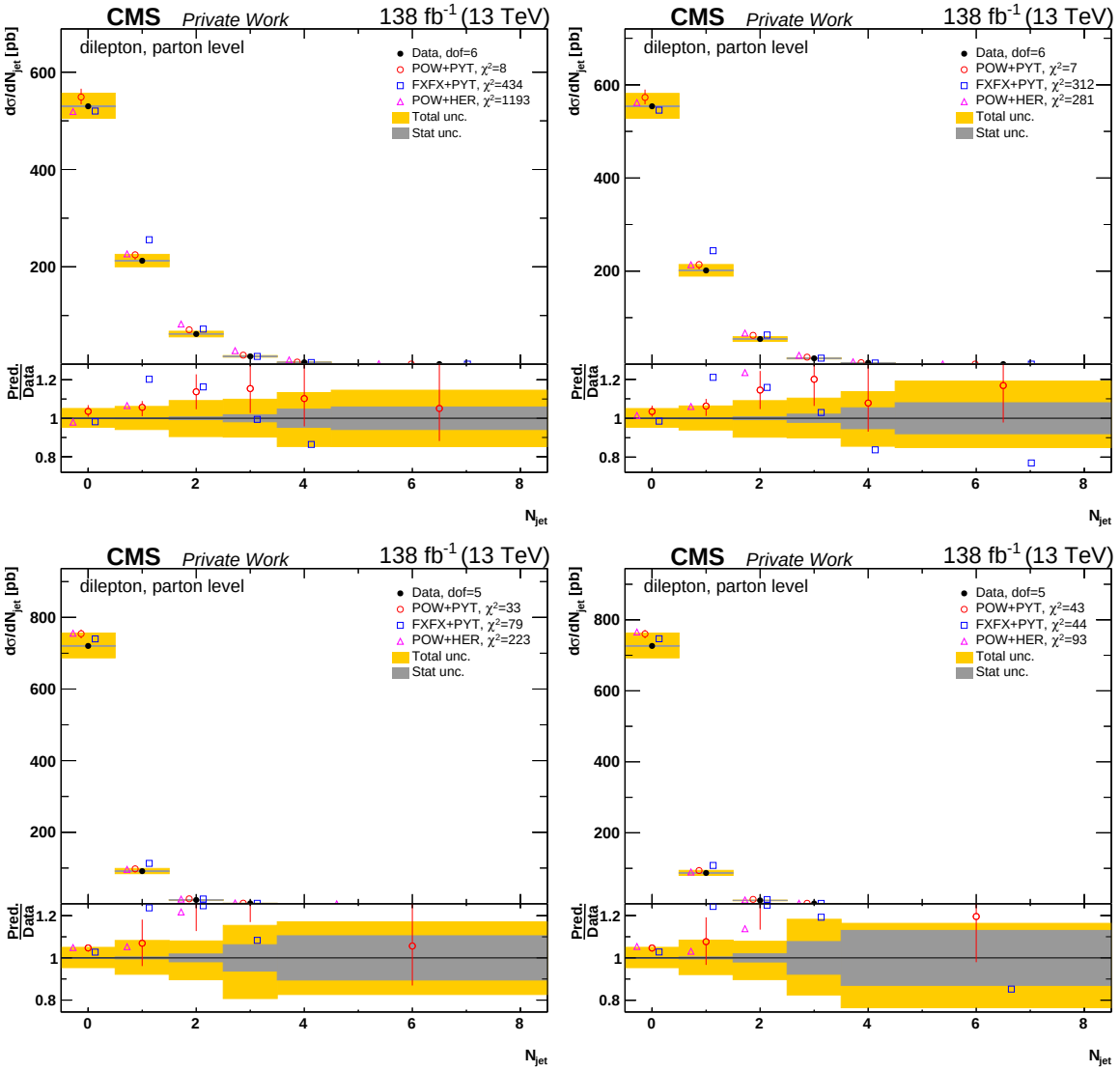

Figure C.12: Comparison of the measured N_{jet} parton level absolute cross sections to MC predictions (see Fig. 10.1 for further details). The left (right) plots correspond to a selection cut of $\Delta R_{(b,j)} > 0.4$ ($\Delta R_{(b,j)} > 0.8$). The jet p_T cut applied is 40 GeV for the upper plots and 100 GeV for the lower plots. This measurement corresponds to the parton level definition of the top quark and top antiquark.

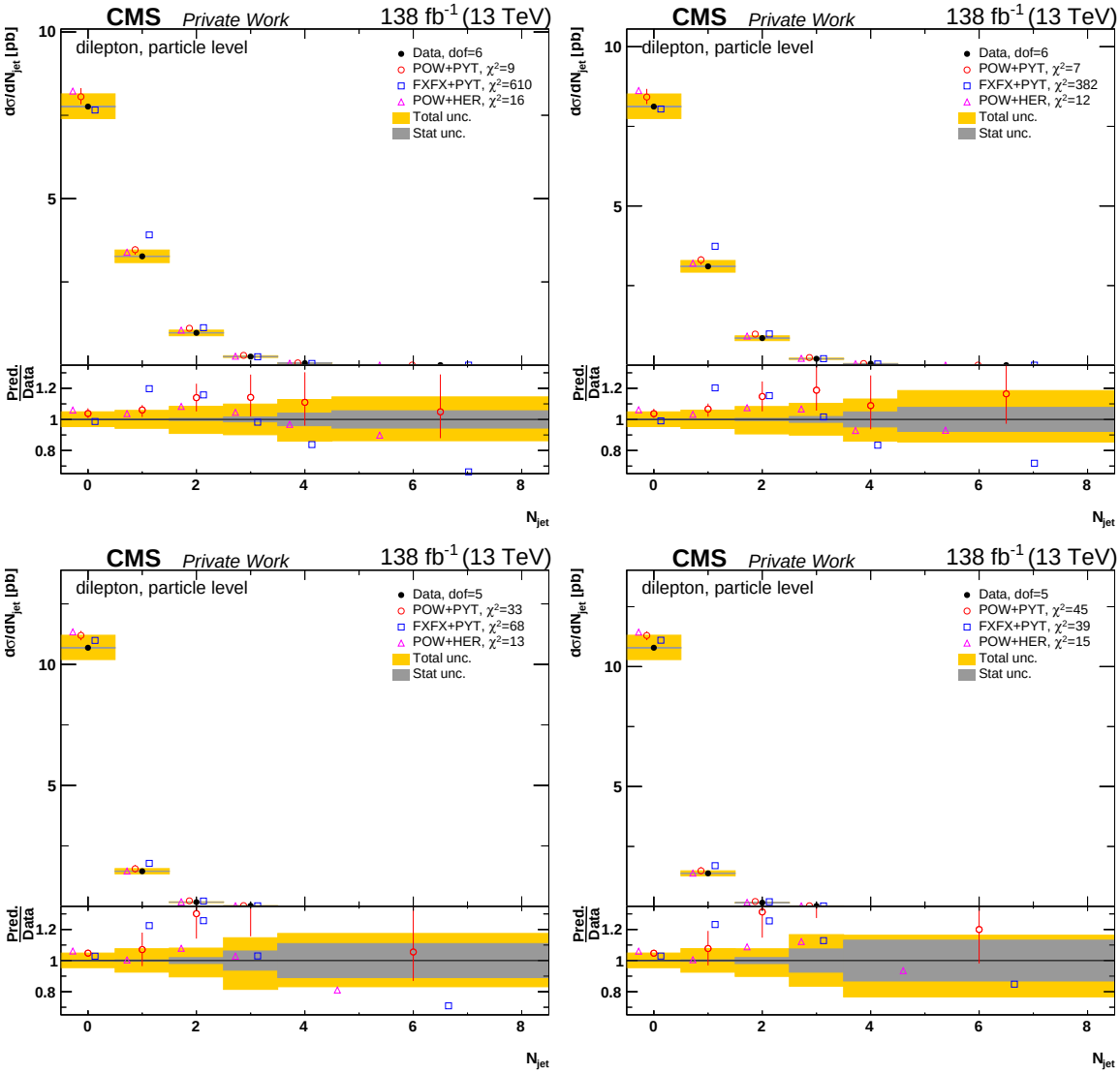

Figure C.13: Comparison of the measured N_{jet} parton level absolute cross sections to MC predictions (see Fig. 10.1 for further details). The left (right) plots correspond to a $\Delta R_{(b,j)} > 0.4$ ($\Delta R_{(b,j)} > 0.8$). The jet p_T cut has a value of 40 GeV for the top plots and 100 GeV for the bottom plots. This measurement corresponds to a particle level definition of the top quark and top antiquark.

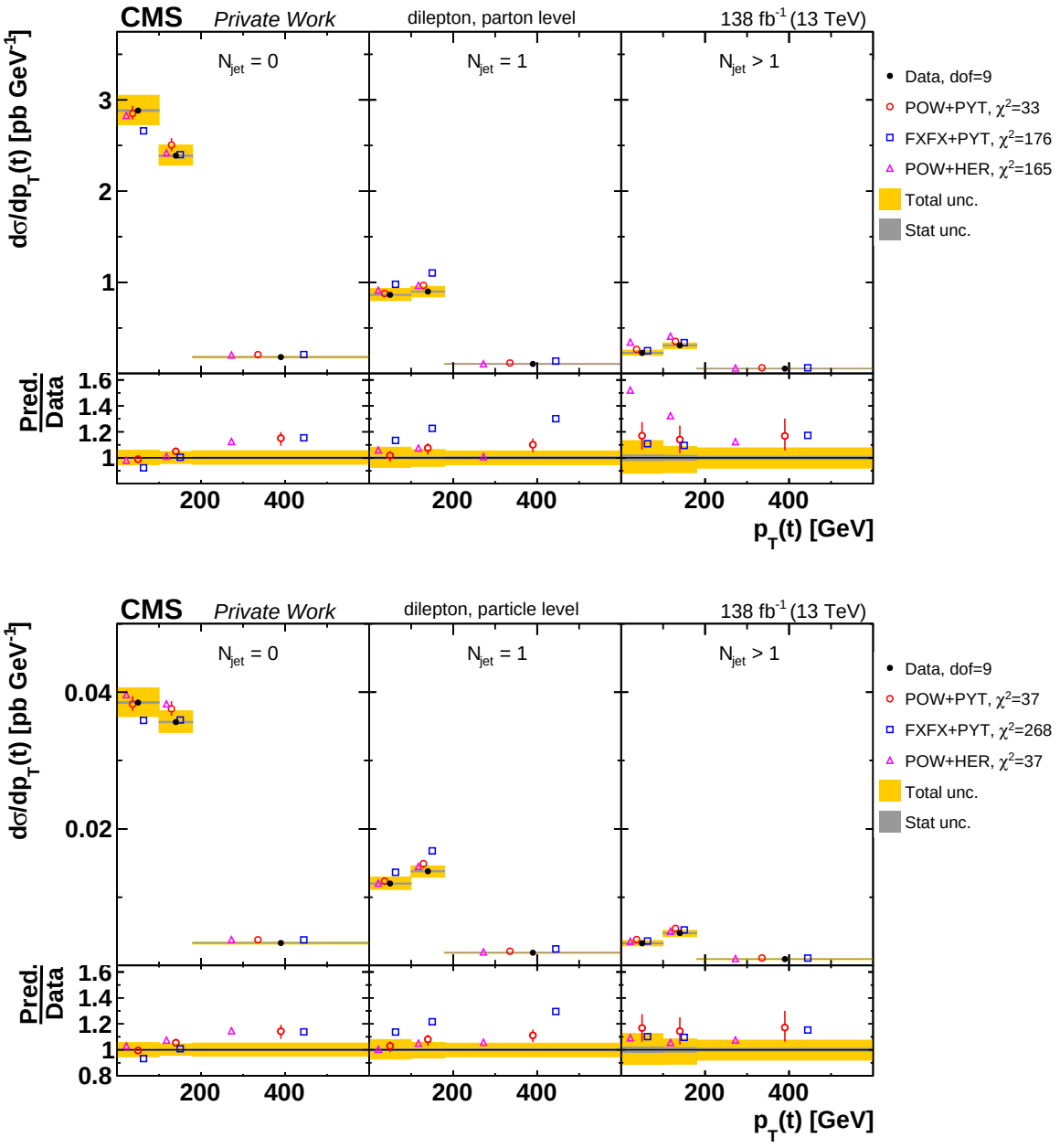

Figure C.14: Comparison of the measured $[N_{\text{jet}},p_{\text{T}}(t)]$ (top: parton level, middle: particle level) and $[N_{\text{jet}},y(t)]$ (bottom: parton level) absolute cross sections to MC predictions (see Fig. 10.1 for further details).

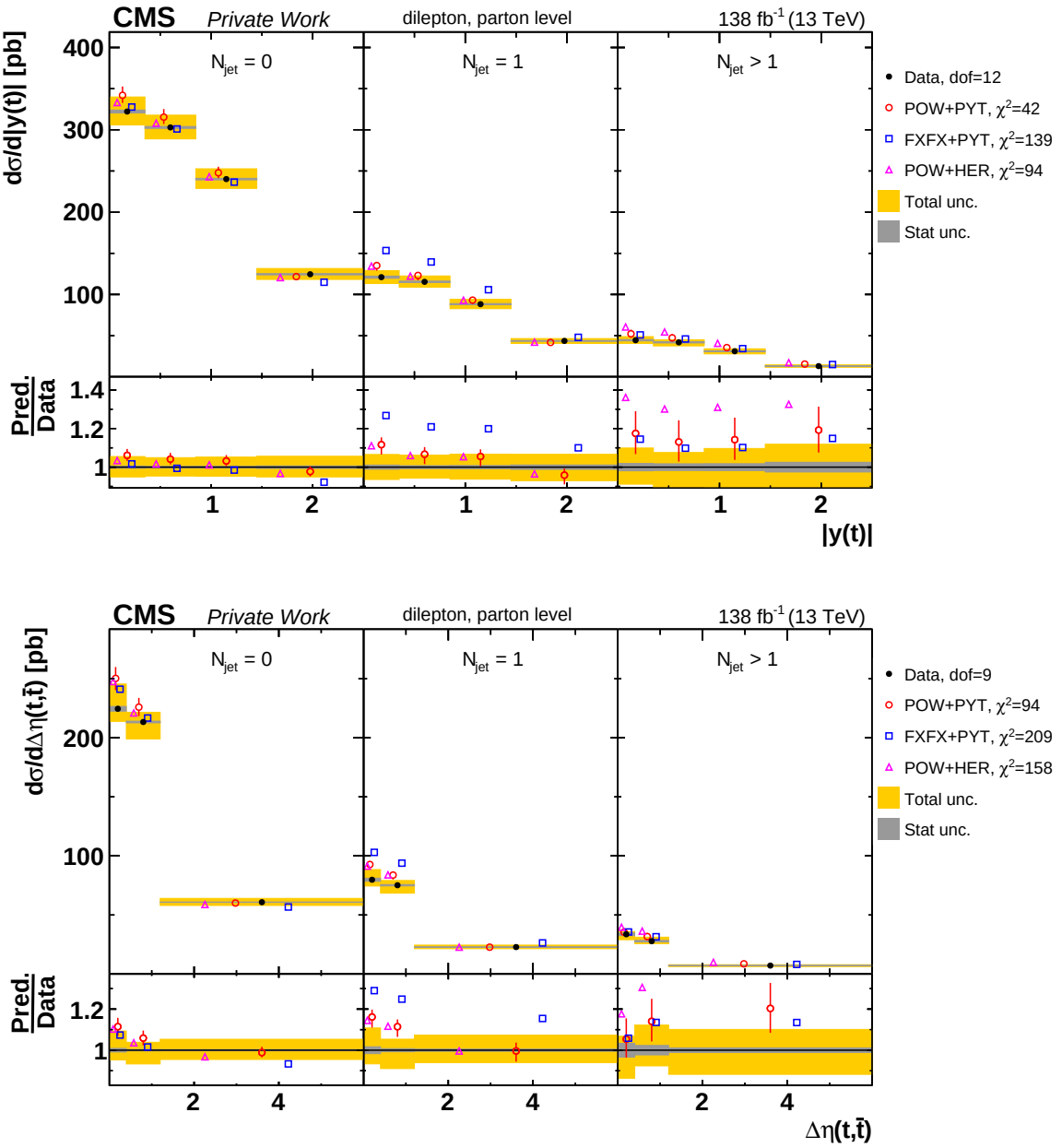

Figure C.15: Comparison of the measured $[N_{\text{jet}}, y(t)]$ and $[N_{\text{jet}}, \Delta\eta(t,\bar{t})]$ parton level absolute cross sections to MC predictions (see Fig. 10.1 for further details).

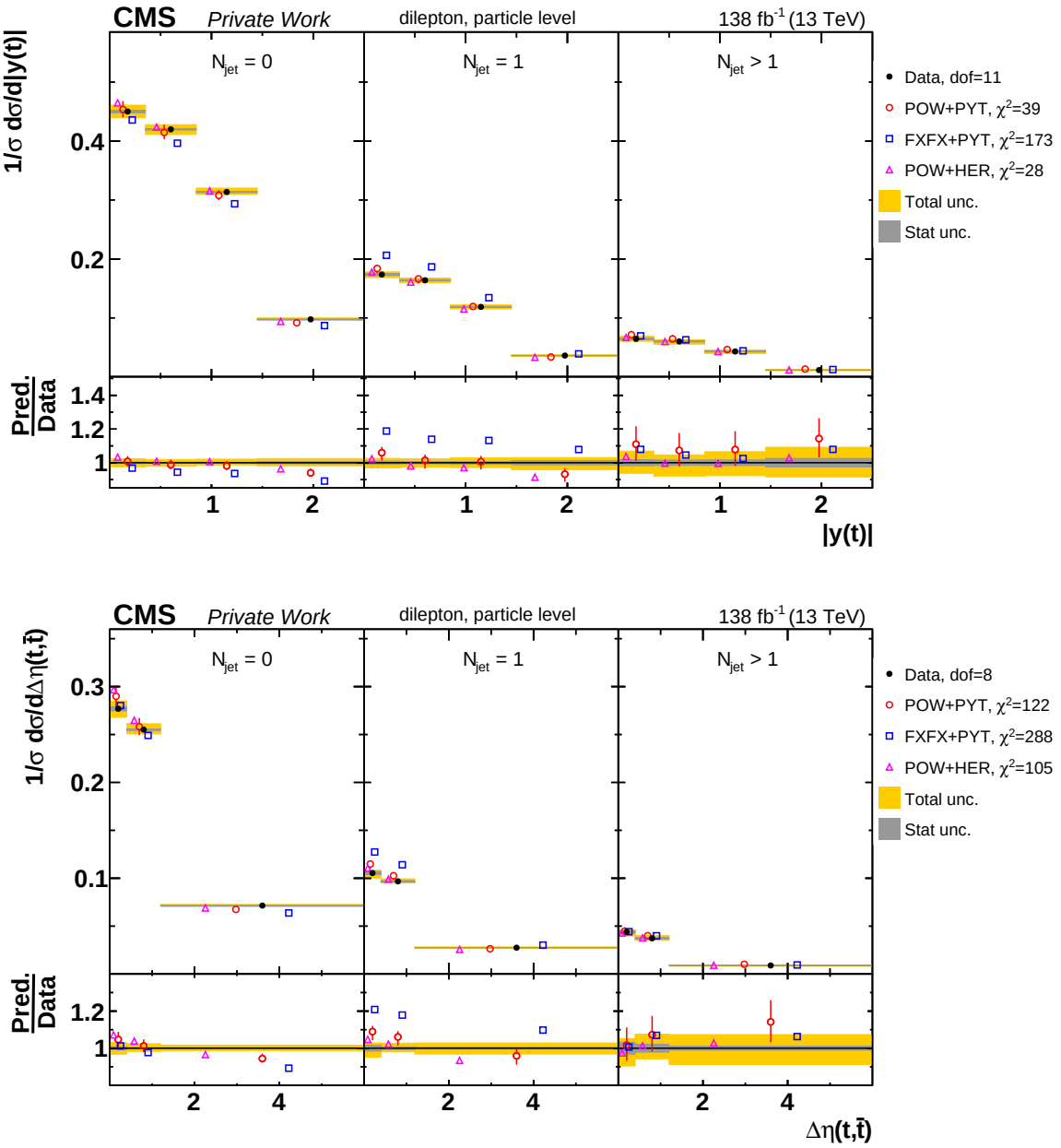

Figure C.16: Comparison of the measured $[N_{\text{jet}}, y(t)]$ and $[N_{\text{jet}}, \Delta\eta(t,\bar{t})]$ particle level normalized cross sections to MC predictions (see Fig. 10.1 for further details).

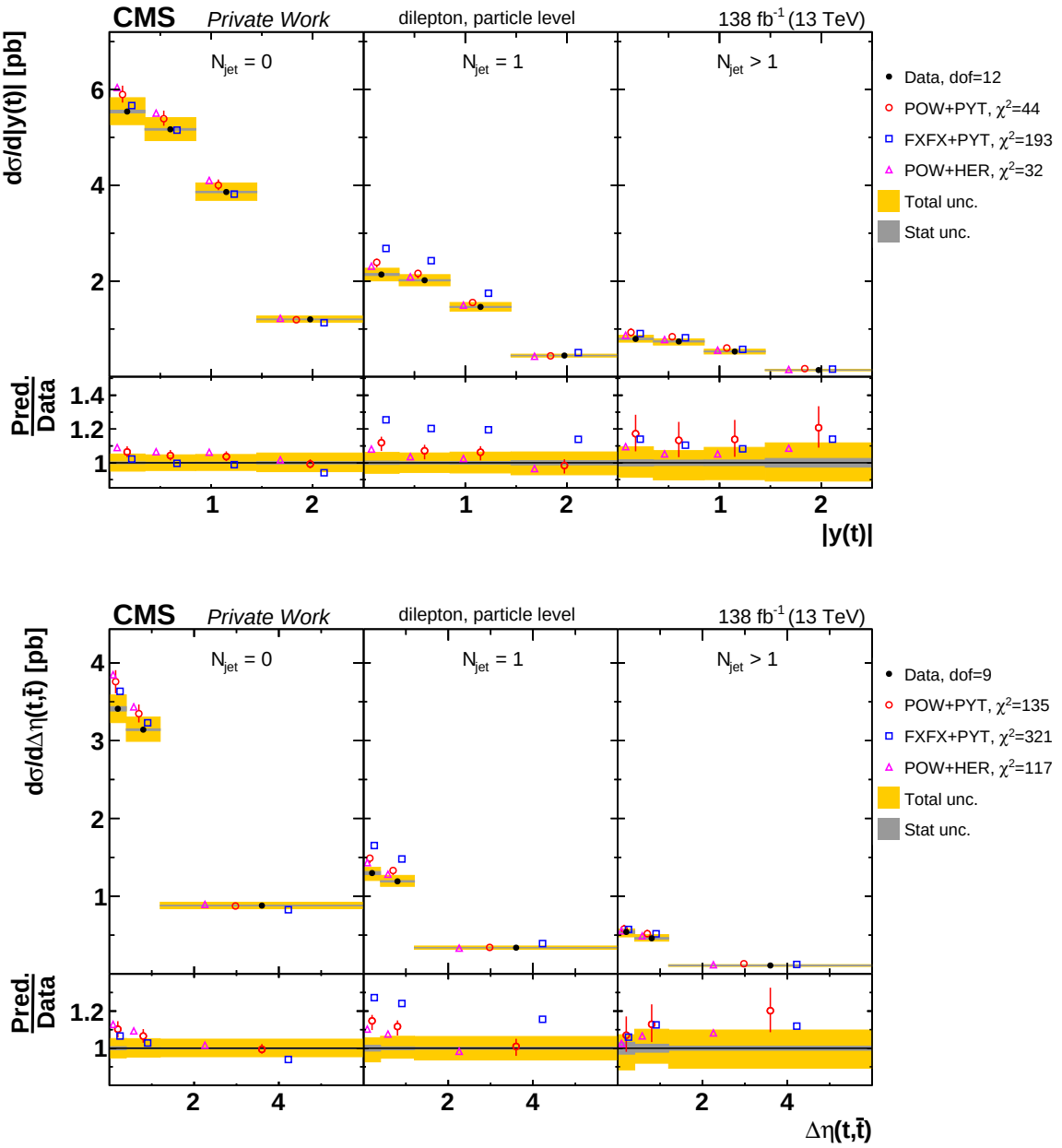

Figure C.17: Comparison of the measured $[N_{\text{jet}}, y(t)]$ and $[N_{\text{jet}}, \Delta\eta(t,\bar{t})]$ particle level absolute cross sections to MC predictions (see Fig. 10.1 for further details).

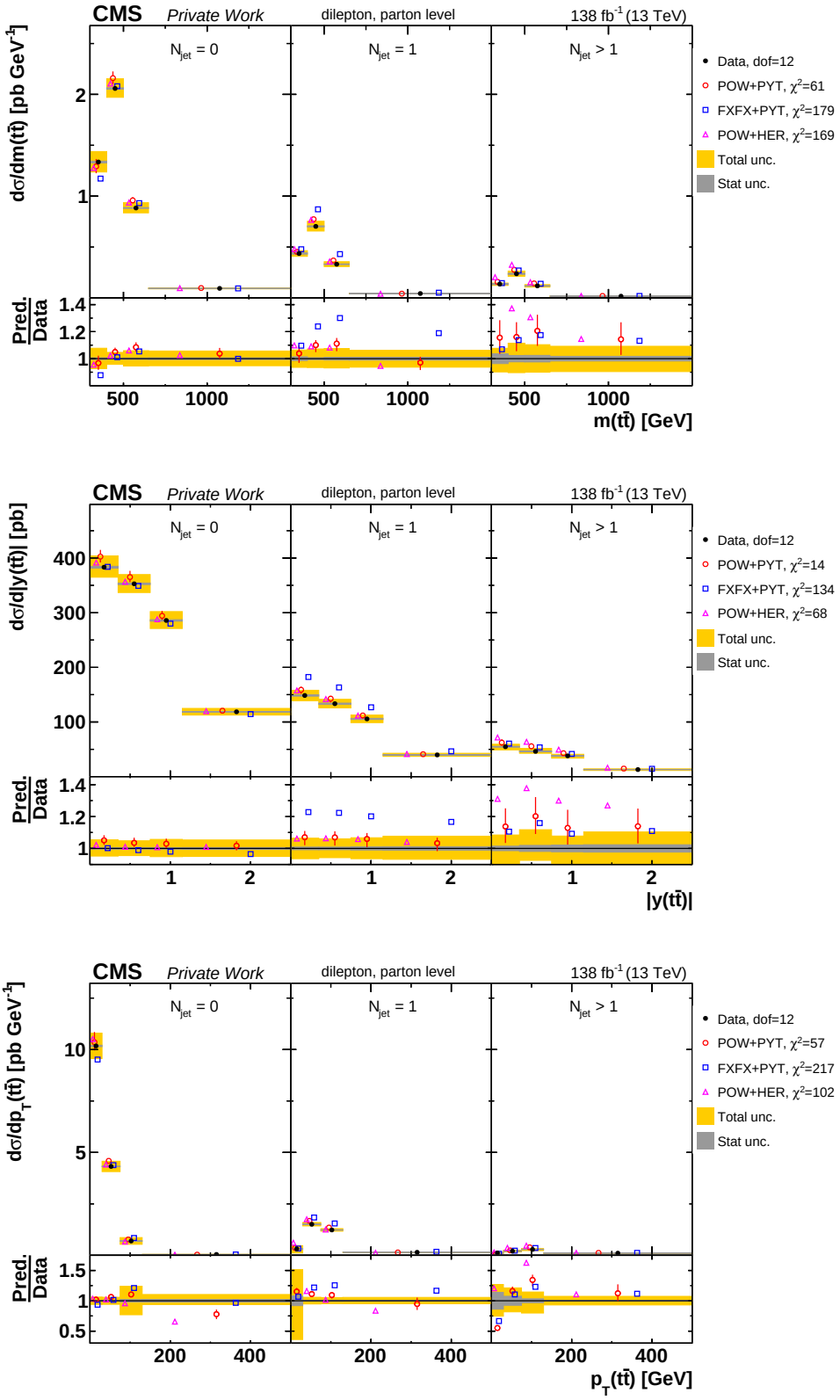

Figure C.18: Comparison of the measured $[N_{\text{jet}},M(\text{t}\bar{\text{t}})]$ (top), $[N_{\text{jet}},y(\text{t}\bar{\text{t}})]$ (middle) and $[N_{\text{jet}},p_{\text{T}}(\text{t}\bar{\text{t}})]$ (bottom) parton level absolute cross sections to MC predictions (see Fig. 10.1 for further details). The *Loose KR* (see Section 7.1.2) is used for $[N_{\text{jet}},M(\text{t}\bar{\text{t}})]$.

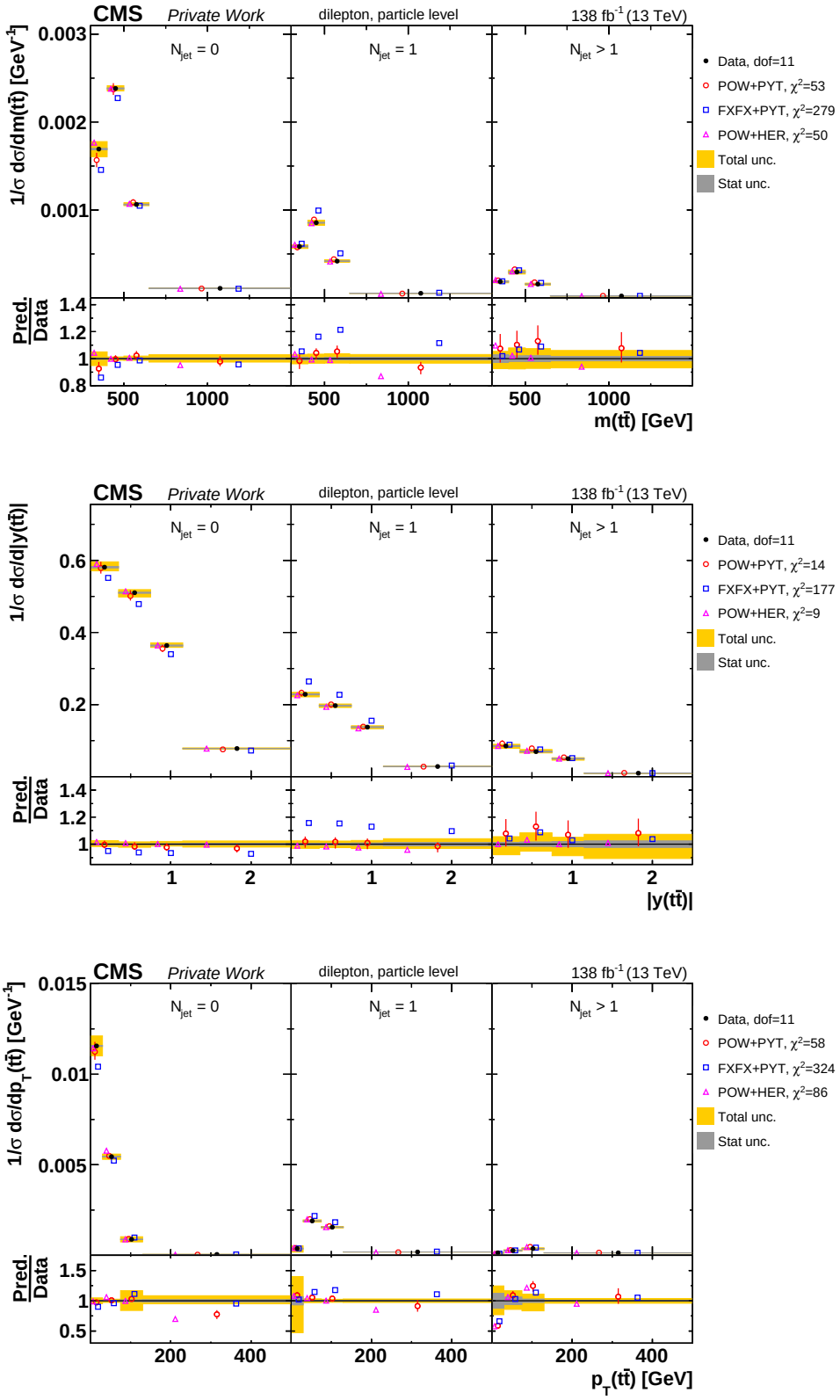

Figure C.19: Comparison of the measured $[N_{\text{jet}},M(\text{t}\bar{\text{t}})]$ (top), $[N_{\text{jet}},y(\text{t}\bar{\text{t}})]$ (middle) and $[N_{\text{jet}},p_{\text{T}}(\text{t}\bar{\text{t}})]$ (bottom) particle level normalized cross sections to MC predictions (see Fig. 10.1 for further details). The *Loose KR* (see Section 7.1.2) is used for $[N_{\text{jet}},M(\text{t}\bar{\text{t}})]$.

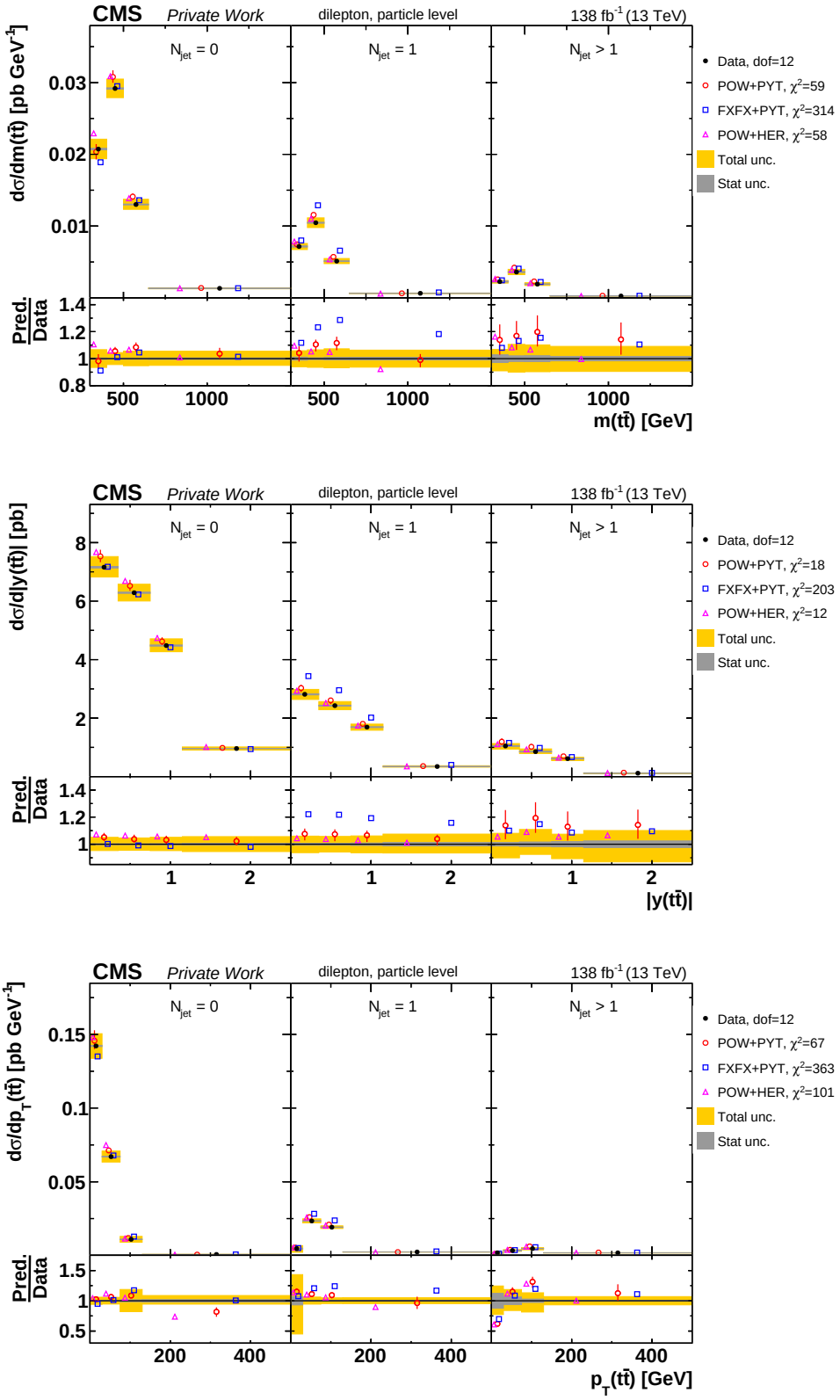

Figure C.20: Comparison of the measured $[N_{\text{jet}},M(\text{t}\bar{\text{t}})]$ (top), $[N_{\text{jet}},y(\text{t}\bar{\text{t}})]$ (middle) and $[N_{\text{jet}},p_{\text{T}}(\text{t}\bar{\text{t}})]$ (bottom) particle level absolute cross sections to MC predictions (see Fig. 10.1 for further details). The *Loose KR* (see Section 7.1.2) is used for $[N_{\text{jet}},M(\text{t}\bar{\text{t}})]$.

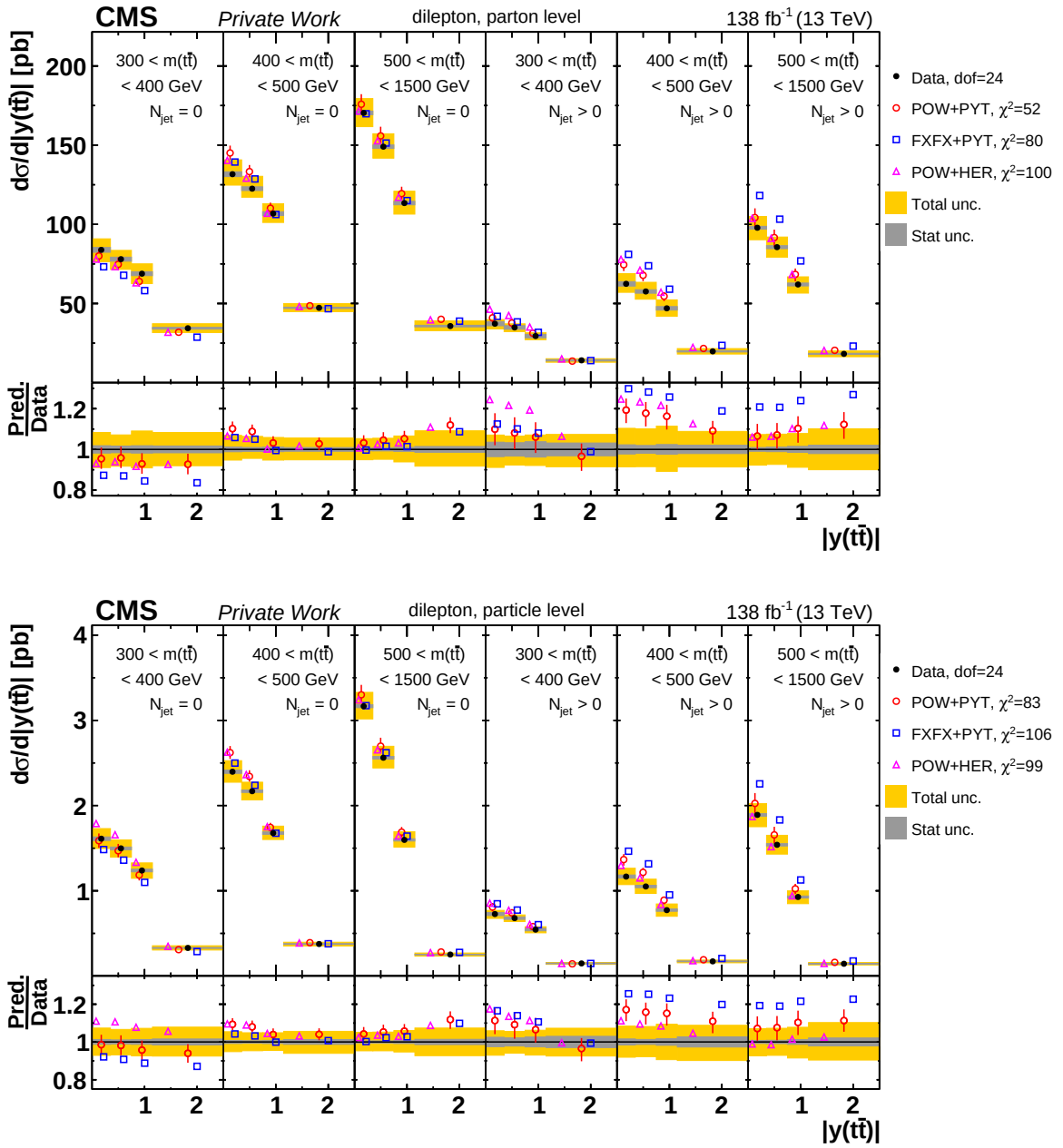

Figure C.21: Comparison of the measured parton (top) and particle (bottom) level $[N_{\text{jet}}^{0,1+}, M(\text{t}\bar{\text{t}}), y(\text{t}\bar{\text{t}})]$ absolute cross sections to MC predictions (see Fig. 10.1 for further details). The *Loose KR* (see Section 7.1.2) is used for these cross sections.

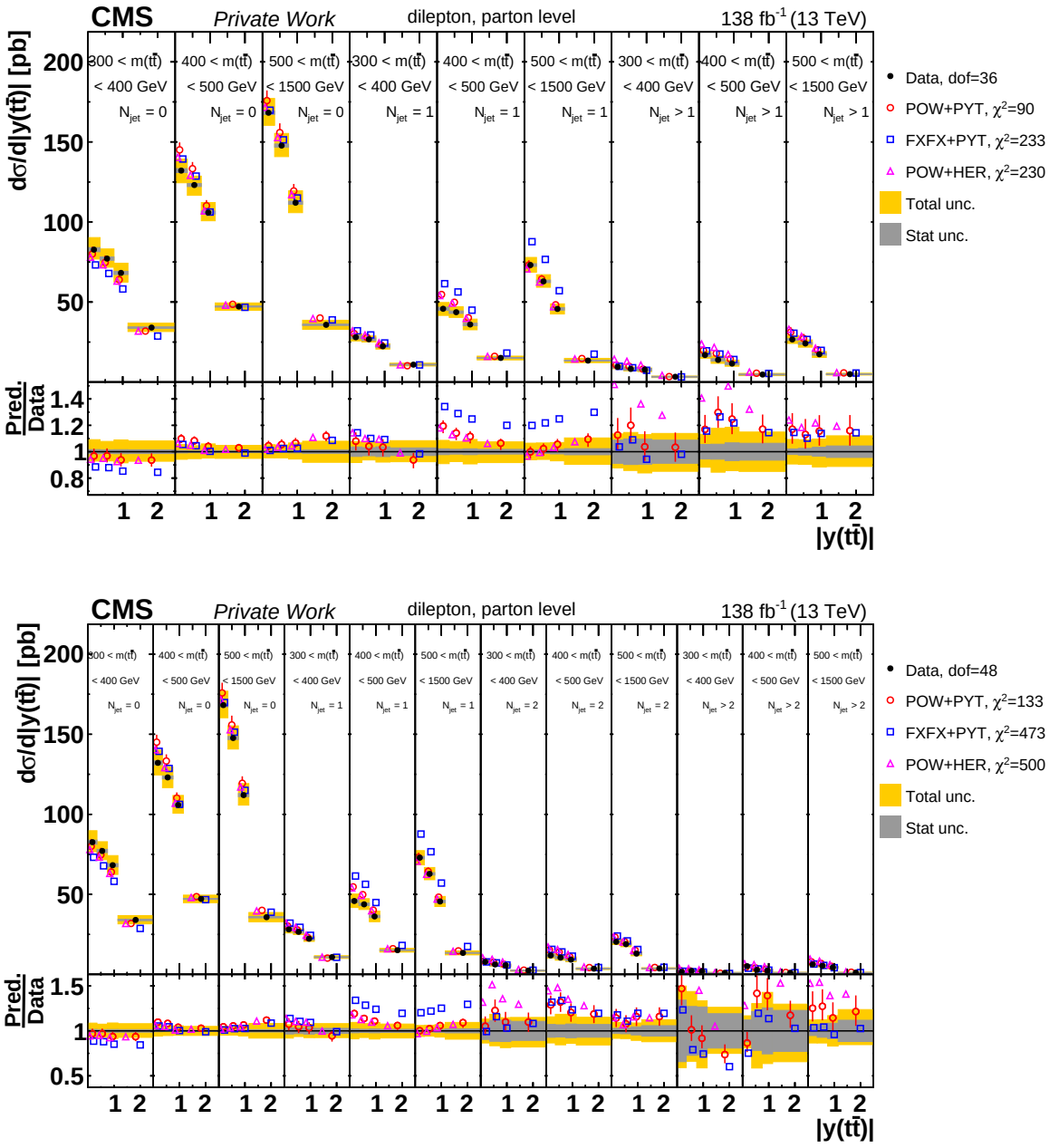

Figure C.22: Comparison of the measured $[N_{\text{jet}}^{0,1,2+}, M(\text{t}\bar{\text{t}}), y(\text{t}\bar{\text{t}})]$ (top) and $[N_{\text{jet}}^{0,1,2,3+}, M(\text{t}\bar{\text{t}}), y(\text{t}\bar{\text{t}})]$ (bottom) parton level absolute cross sections to MC predictions (see Fig. 10.1 for further details). The *Loose KR* (see Section 7.1.2) is used for these cross sections.

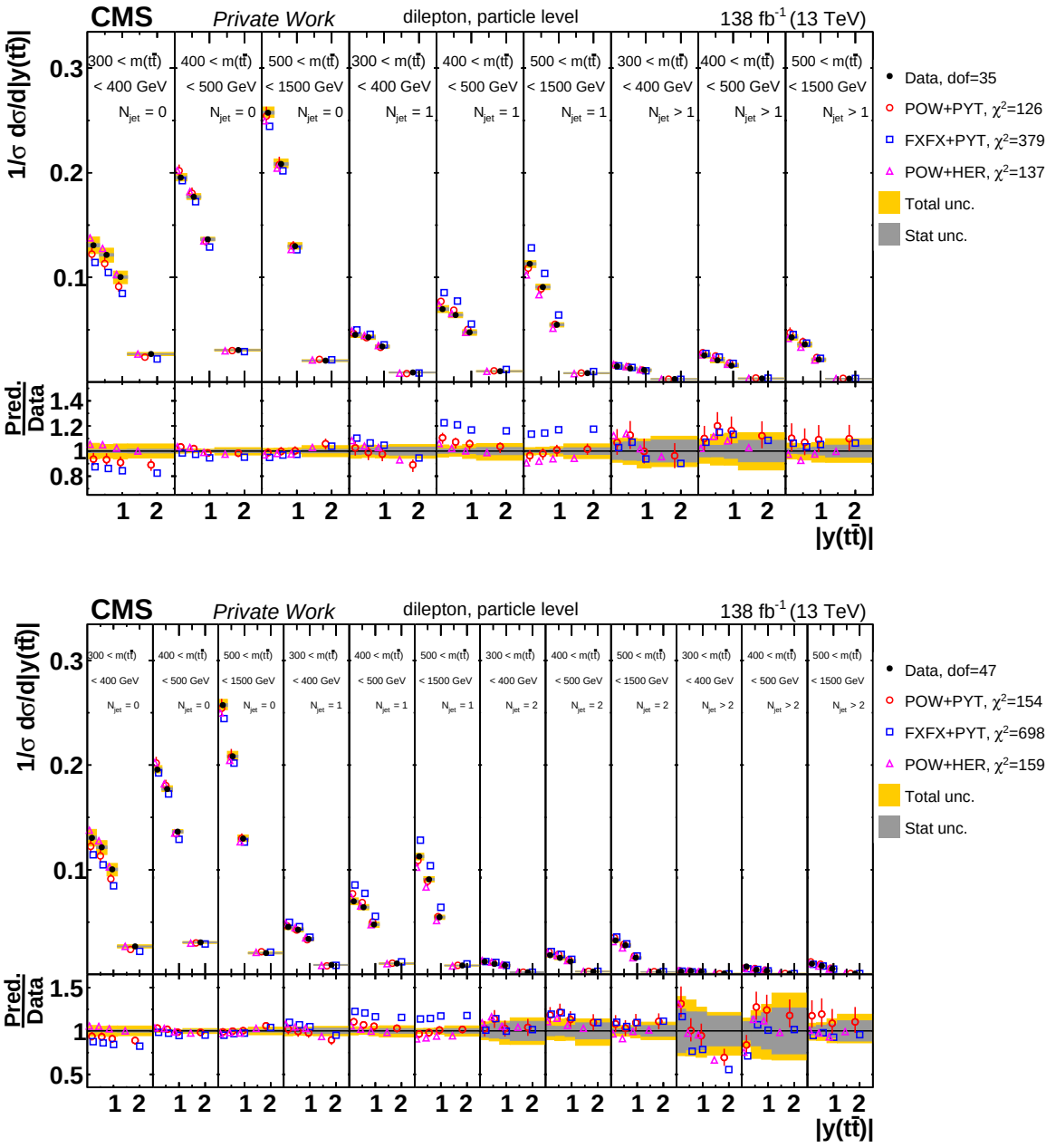

Figure C.23: Comparison of the measured $[N_{\text{jet}}^{0,1,2+}, M(\text{t}\bar{\text{t}}), y(\text{t}\bar{\text{t}})]$ (top) and $[N_{\text{jet}}^{0,1,2,3+}, M(\text{t}\bar{\text{t}}), y(\text{t}\bar{\text{t}})]$ (bottom) particle level normalized cross sections to MC predictions (see Fig. 10.1 for further details). The *Loose KR* (see Section 7.1.2) is used for these cross sections.

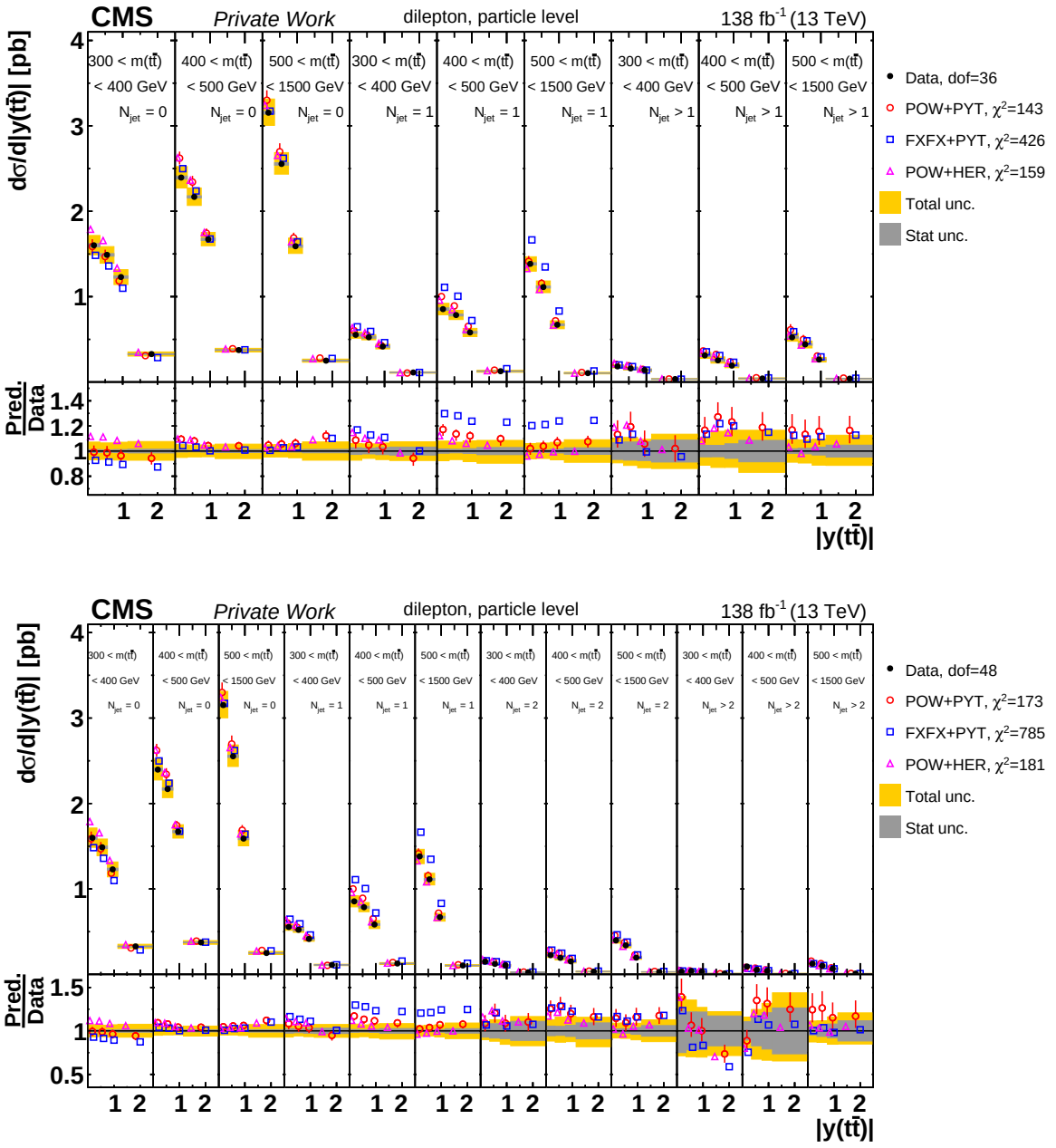

Figure C.24: Comparison of the measured $[N_{\text{jet}}^{0,1,2+}, M(\text{t}\bar{\text{t}}), y(\text{t}\bar{\text{t}})]$ (top) and $[N_{\text{jet}}^{0,1,2,3+}, M(\text{t}\bar{\text{t}}), y(\text{t}\bar{\text{t}})]$ (bottom) particle level absolute cross sections to MC predictions (see Fig. 10.1 for further details). The *Loose KR* (see Section 7.1.2) is used for these cross sections.

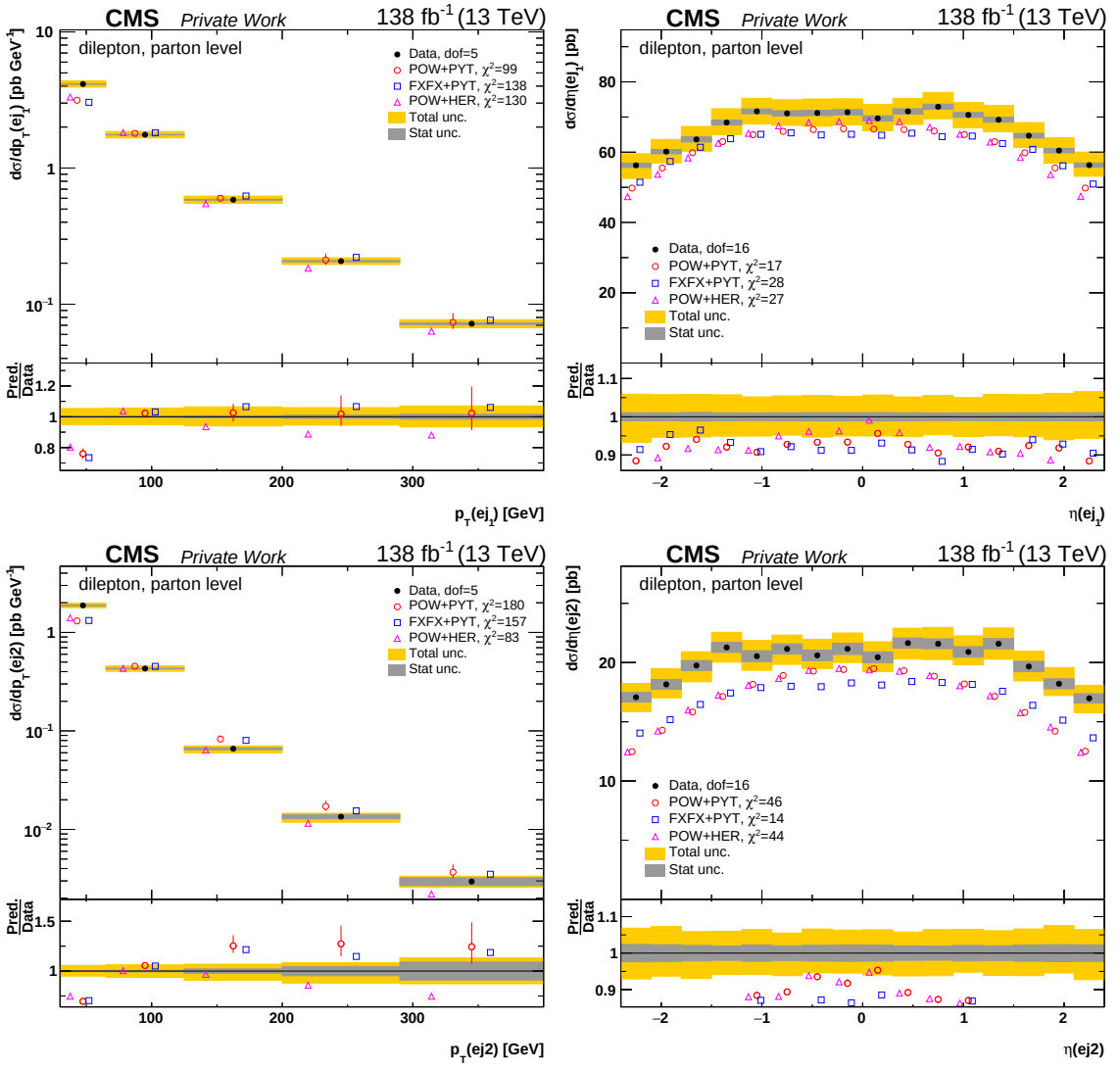

Figure C.25: Comparison of the absolute p_T (left column) and η (right column) for the leading (top row) and sub-leading (bottom row) extra jets parton level cross sections to different MC predictions (see Fig. 10.1 for further details).

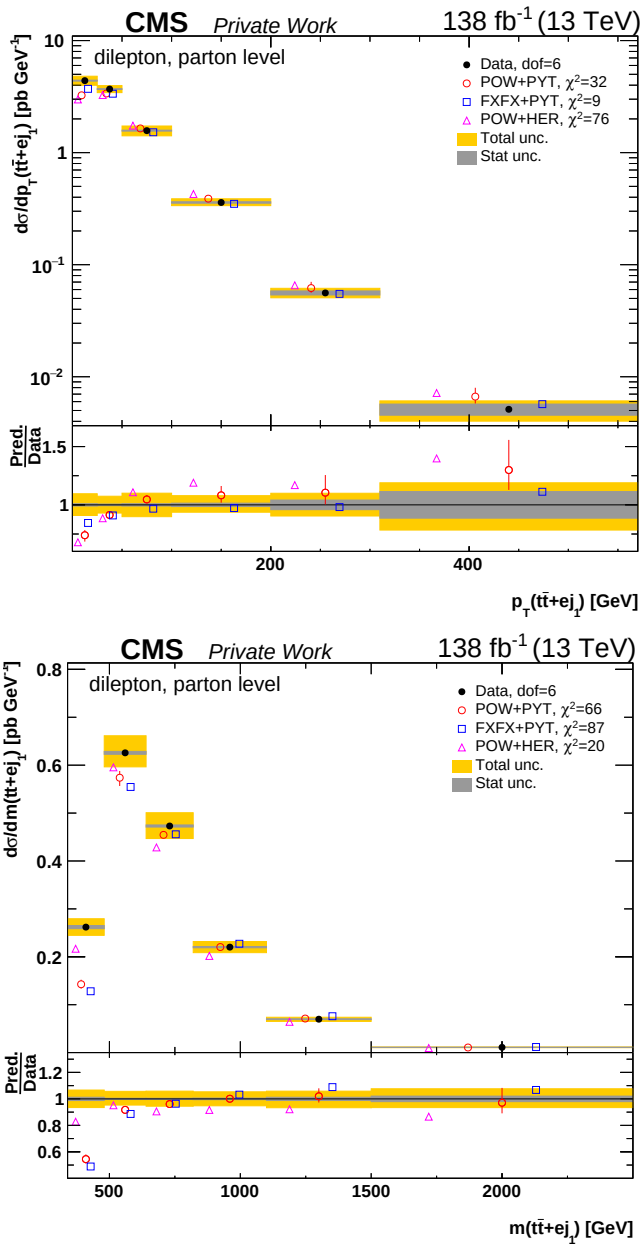

Figure C.26: Comparison of the measured $p_{\mathrm{T}}(\mathrm{t\bar{t}}+\mathrm{ej}_1)$ (top) and $M(\mathrm{t\bar{t}}+\mathrm{ej}_1)$ (bottom) parton level absolute cross sections to different MC predictions (see Fig. 10.1 for further details).

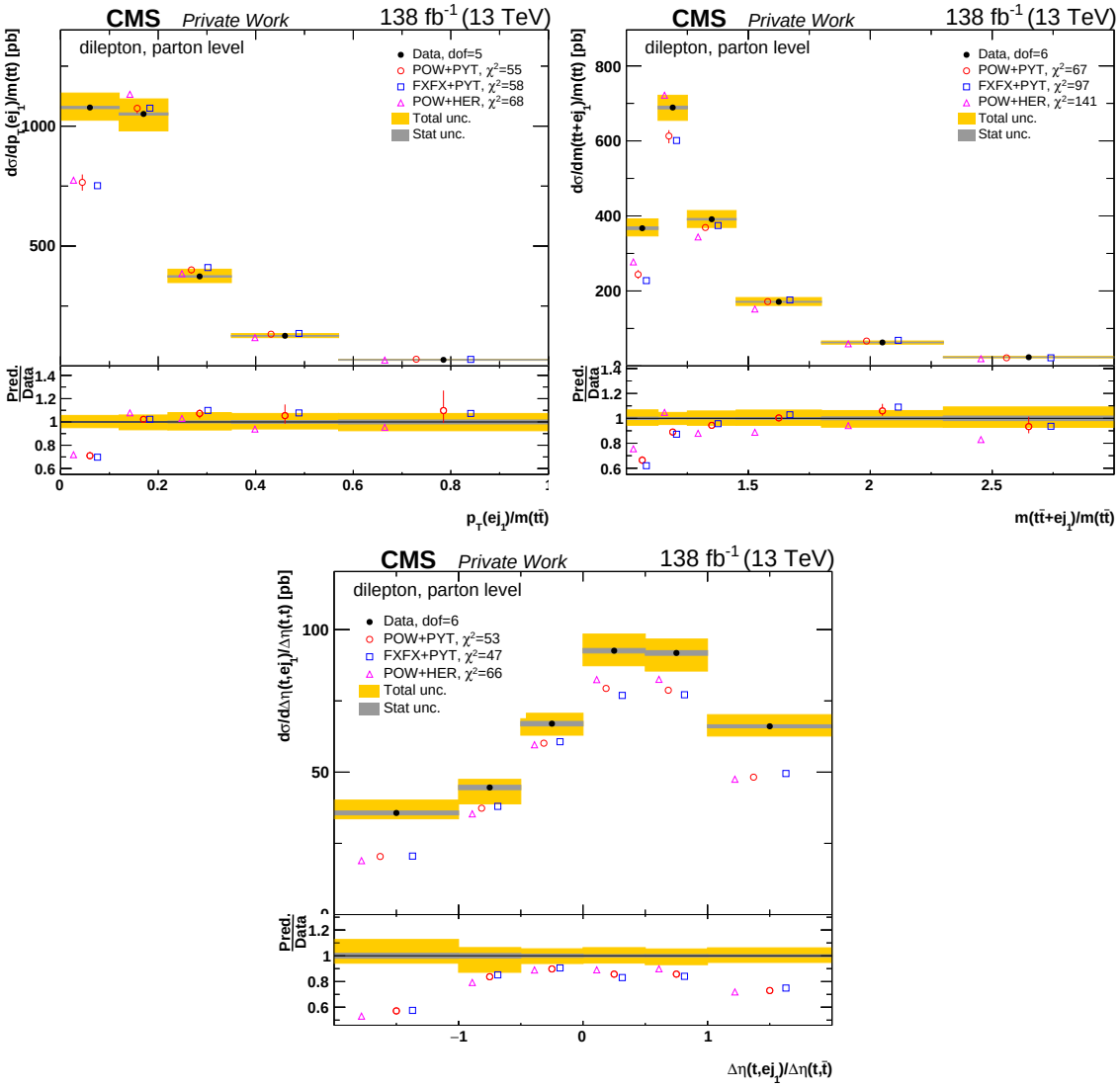

Figure C.27: Comparison of the measured $p_{\mathrm{T}}(\mathrm{ej}_1)/M(\mathrm{t\bar{t}})$ (top), $M(\mathrm{t\bar{t}}+\mathrm{ej}_1)/\mathrm{M}(\mathrm{t\bar{t}})$ (middle) and $\Delta\eta(t, ej_1)/\Delta\eta(t, \bar{t})$ (bottom) parton level absolute cross sections to different MC predictions (see Fig. 10.1 for further details).

C.2 Cross sections values

In this appendix the tables containing the cross sections values for the full set of measurements are presented.

$\lvert y(\mathrm{t})\rvert$	$p_{\mathrm{T}}(\mathrm{t})$ [GeV]	$\frac{1}{\sigma(\mathrm{t\bar{t}})}\frac{\mathrm{d}\sigma}{\mathrm{d}p_{\mathrm{T}}(\mathrm{t})}[\mathrm{GeV}^{-1}]$	stat. [%]	syst. [%]	bin
0.00–0.35	0–80	9.177×10^{-4}	1.4	$^{+2.5}_{-3.7}$	1
0.00–0.35	80–150	1.104×10^{-3}	1.0	$^{+3.2}_{-1.8}$	2
0.00–0.35	150–250	4.546×10^{-4}	1.2	$^{+2.4}_{-2.2}$	3
0.00–0.35	250–600	4.459×10^{-5}	1.5	$^{+4.1}_{-4.0}$	4
0.35–0.85	0–80	1.220×10^{-3}	0.9	$^{+2.0}_{-3.2}$	5
0.35–0.85	80–150	1.509×10^{-3}	0.7	$^{+1.8}_{-2.0}$	6
0.35–0.85	150–250	6.205×10^{-4}	0.9	$^{+1.9}_{-2.2}$	7
0.35–0.85	250–600	5.556×10^{-5}	1.5	$^{+4.1}_{-3.9}$	8
0.85–1.45	0–80	1.171×10^{-3}	0.9	$^{+2.6}_{-2.5}$	9
0.85–1.45	80–150	1.419×10^{-3}	0.7	$^{+1.9}_{-1.8}$	10
0.85–1.45	150–250	5.581×10^{-4}	1.0	$^{+2.0}_{-2.0}$	11
0.85–1.45	250–600	4.891×10^{-5}	1.6	$^{+4.4}_{-4.3}$	12
1.45–2.50	0–80	1.140×10^{-3}	1.3	$^{+4.5}_{-3.0}$	13
1.45–2.50	80–150	1.305×10^{-3}	0.8	$^{+2.0}_{-2.2}$	14
1.45–2.50	150–250	4.530×10^{-4}	1.4	$^{+3.2}_{-3.3}$	15
1.45–2.50	250–600	2.791×10^{-5}	2.8	$^{+5.9}_{-4.7}$	16

Table C.1: Values for each bin of the $[y(t),p_{\mathrm{T}}(t)]$ normalized parton level cross section. The table includes also the binning scheme used in the measurement as well as the values for the statistical and systematic uncertainty.

$\lvert y(\mathrm{t})\rvert$	$p_{\mathrm{T}}(\mathrm{t})$ [GeV]	$\frac{1}{\sigma(\mathrm{t\bar{t}})}\frac{\mathrm{d}\sigma}{\mathrm{d}p_{\mathrm{T}}(\mathrm{t})}$[GeV^{-1}]	stat. [%]	syst. [%]	bin
0.00–0.35	0–80	7.406×10^{-1}	1.4	$^{+6.3}_{-6.5}$	1
0.00–0.35	80–150	8.909×10^{-1}	1.0	$^{+6.6}_{-5.0}$	2
0.00–0.35	150–250	3.669×10^{-1}	1.1	$^{+5.3}_{-4.7}$	3
0.00–0.35	250–600	3.598×10^{-2}	1.5	$^{+5.4}_{-5.0}$	4
0.35–0.85	0–80	9.844×10^{-1}	0.9	$^{+5.9}_{-6.2}$	5
0.35–0.85	80–150	1.218×10^{0}	0.7	$^{+5.3}_{-4.9}$	6
0.35–0.85	150–250	5.008×10^{-1}	0.9	$^{+4.9}_{-5.0}$	7
0.35–0.85	250–600	4.484×10^{-2}	1.5	$^{+5.4}_{-5.2}$	8
0.85–1.45	0–80	9.452×10^{-1}	0.9	$^{+6.9}_{-6.2}$	9
0.85–1.45	80–150	1.145×10^{0}	0.7	$^{+5.6}_{-5.1}$	10
0.85–1.45	150–250	4.504×10^{-1}	1.0	$^{+5.5}_{-5.0}$	11
0.85–1.45	250–600	3.947×10^{-2}	1.6	$^{+5.4}_{-5.2}$	12
1.45–2.50	0–80	9.196×10^{-1}	1.4	$^{+8.4}_{-6.6}$	13
1.45–2.50	80–150	1.053×10^{0}	0.9	$^{+5.8}_{-5.3}$	14
1.45–2.50	150–250	3.655×10^{-1}	1.4	$^{+6.0}_{-5.8}$	15
1.45–2.50	250–600	2.252×10^{-2}	2.8	$^{+7.7}_{-6.0}$	16

Table C.2: Values for each bin of the $[y(t),p_{\mathrm{T}}(t)]$ absolute parton level cross section. The table includes also the binning scheme used in the measurement as well as the values for the statistical and systematic uncertainty.

$\lvert y(\mathrm{t})\rvert$	$p_{\mathrm{T}}(\mathrm{t})$ [GeV]	$\frac{1}{\sigma(\mathrm{t\bar{t}})}\frac{\mathrm{d}\sigma}{\mathrm{d}p_{\mathrm{T}}(\mathrm{t})}[\mathrm{GeV}^{-1}]$	stat. [%]	syst. [%]	bin
0.00–0.35	0–80	1.003×10^{-3}	1.2	$^{+2.3}_{-3.3}$	1
0.00–0.35	80–150	1.232×10^{-3}	0.8	$^{+2.6}_{-1.2}$	2
0.00–0.35	150–250	5.421×10^{-4}	1.0	$^{+2.2}_{-1.9}$	3
0.00–0.35	250–600	5.994×10^{-5}	1.4	$^{+3.4}_{-3.3}$	4
0.35–0.85	0–80	1.328×10^{-3}	0.7	$^{+1.7}_{-2.9}$	5
0.35–0.85	80–150	1.668×10^{-3}	0.6	$^{+1.4}_{-1.5}$	6
0.35–0.85	150–250	7.314×10^{-4}	0.8	$^{+1.6}_{-1.9}$	7
0.35–0.85	250–600	7.460×10^{-5}	1.3	$^{+3.6}_{-3.3}$	8
0.85–1.45	0–80	1.180×10^{-3}	0.9	$^{+2.4}_{-2.1}$	9
0.85–1.45	80–150	1.480×10^{-3}	0.6	$^{+1.7}_{-1.3}$	10
0.85–1.45	150–250	6.368×10^{-4}	0.9	$^{+1.8}_{-1.7}$	11
0.85–1.45	250–600	6.408×10^{-5}	1.4	$^{+3.8}_{-3.4}$	12
1.45–2.50	0–80	6.467×10^{-4}	1.6	$^{+4.7}_{-3.4}$	13
1.45–2.50	80–150	8.080×10^{-4}	1.2	$^{+2.3}_{-2.7}$	14
1.45–2.50	150–250	3.373×10^{-4}	1.5	$^{+3.0}_{-2.9}$	15
1.45–2.50	250–600	2.835×10^{-5}	2.5	$^{+5.2}_{-3.6}$	16

Table C.3: Values for each bin of the $[y(t),p_{\mathrm{T}}(t)]$ normalized particle level cross section. The table includes also the binning scheme used in the measurement as well as the values for the statistical and systematic uncertainty.

$\lvert y(t)\rvert$	$p_T(t)$ [GeV]	$\frac{1}{\sigma(t\bar{t})}\frac{d\sigma}{dp_T(t)}$[GeV^{-1}]	stat. [%]	syst. [%]	bin
0.00–0.35	0–80	1.231×10^{-2}	1.2	$^{+6.0}_{-6.5}$	1
0.00–0.35	80–150	1.511×10^{-2}	0.9	$^{+5.7}_{-4.4}$	2
0.00–0.35	150–250	6.650×10^{-3}	1.0	$^{+5.0}_{-4.6}$	3
0.00–0.35	250–600	7.354×10^{-4}	1.4	$^{+5.6}_{-5.2}$	4
0.35–0.85	0–80	1.629×10^{-2}	0.8	$^{+5.7}_{-6.2}$	5
0.35–0.85	80–150	2.047×10^{-2}	0.6	$^{+4.6}_{-4.5}$	6
0.35–0.85	150–250	8.972×10^{-3}	0.8	$^{+4.6}_{-4.8}$	7
0.35–0.85	250–600	9.152×10^{-4}	1.3	$^{+5.7}_{-5.3}$	8
0.85–1.45	0–80	1.448×10^{-2}	0.9	$^{+6.4}_{-5.7}$	9
0.85–1.45	80–150	1.815×10^{-2}	0.6	$^{+4.9}_{-4.5}$	10
0.85–1.45	150–250	7.813×10^{-3}	0.9	$^{+5.2}_{-4.8}$	11
0.85–1.45	250–600	7.861×10^{-4}	1.4	$^{+5.7}_{-5.3}$	12
1.45–2.50	0–80	7.934×10^{-3}	1.6	$^{+8.1}_{-6.8}$	13
1.45–2.50	80–150	9.912×10^{-3}	1.2	$^{+5.9}_{-5.6}$	14
1.45–2.50	150–250	4.138×10^{-3}	1.5	$^{+5.8}_{-5.6}$	15
1.45–2.50	250–600	3.478×10^{-4}	2.5	$^{+7.7}_{-6.1}$	16

Table C.4: Values for each bin of the $[y(t),p_T(t)]$ absolute particle level cross section. The table includes also the binning scheme used in the measurement as well as the values for the statistical and systematic uncertainty.

$m(\mathrm{t\bar{t}})$ [GeV]	$p_{\mathrm{T}}(\mathrm{t})$ [GeV]	$\frac{1}{\sigma(\mathrm{t\bar{t}})}\frac{\mathrm{d}\sigma}{\mathrm{d}p_{\mathrm{T}}(\mathrm{t})}$[GeV^{-1}]	stat. [%]	syst. [%]	bin
300–450	0–100	3.140×10^{-3}	0.3	$^{+2.2}_{-1.7}$	1
300–450	100–180	1.388×10^{-3}	0.6	$^{+4.6}_{-4.4}$	2
300–450	180–600	2.396×10^{-5}	3.8	$^{+27.5}_{-34.0}$	3
450–600	0–100	1.147×10^{-3}	0.6	$^{+2.7}_{-3.4}$	4
450–600	100–180	2.121×10^{-3}	0.4	$^{+2.1}_{-3.0}$	5
450–600	180–600	1.478×10^{-4}	1.0	$^{+3.3}_{-3.1}$	6
600–1500	0–100	5.285×10^{-4}	1.3	$^{+4.3}_{-4.9}$	7
600–1500	100–180	8.498×10^{-4}	1.0	$^{+3.9}_{-2.8}$	8
600–1500	180–600	2.325×10^{-4}	0.5	$^{+4.0}_{-4.2}$	9

Table C.5: Values for each bin of the $[M(\mathrm{t\bar{t}}),p_{\mathrm{T}}(t)]$ normalized parton level cross section. The table includes also the binning scheme used in the measurement as well as the values for the statistical and systematic uncertainty.

$m(\mathrm{t\bar{t}})$ [GeV]	$p_{\mathrm{T}}(\mathrm{t})$ [GeV]	$\frac{1}{\sigma(\mathrm{t\bar{t}})}\frac{\mathrm{d}\sigma}{\mathrm{d}p_{\mathrm{T}}(\mathrm{t})}$[GeV^{-1}]	stat. [%]	syst. [%]	bin
300–450	0–100	2.588×10^{0}	0.4	$^{+6.4}_{-5.0}$	1
300–450	100–180	1.144×10^{0}	0.7	$^{+8.4}_{-8.1}$	2
300–450	180–600	1.975×10^{-2}	3.8	$^{+28.5}_{-34.8}$	3
450–600	0–100	9.451×10^{-1}	0.7	$^{+7.5}_{-7.8}$	4
450–600	100–180	1.748×10^{0}	0.4	$^{+3.4}_{-4.0}$	5
450–600	180–600	1.218×10^{-1}	1.0	$^{+6.7}_{-5.7}$	6
600–1500	0–100	4.356×10^{-1}	1.4	$^{+6.4}_{-6.4}$	7
600–1500	100–180	7.004×10^{-1}	1.0	$^{+6.5}_{-4.9}$	8
600–1500	180–600	1.916×10^{-1}	0.5	$^{+5.3}_{-5.1}$	9

Table C.6: Values for each bin of the $[M(\mathrm{t\bar{t}}),p_{\mathrm{T}}(t)]$ absolute parton level cross section. The table includes also the binning scheme used in the measurement as well as the values for the statistical and systematic uncertainty.

$m(\mathrm{t\bar{t}})$ [GeV]	$p_{\mathrm{T}}(\mathrm{t})$ [GeV]	$\frac{1}{\sigma(\mathrm{t\bar{t}})}\frac{\mathrm{d}\sigma}{\mathrm{d}p_{\mathrm{T}}(\mathrm{t})}$[GeV^{-1}]	stat. [%]	syst. [%]	bin
300–450	0–100	3.153×10^{-3}	0.3	$^{+1.8}_{-2.1}$	1
300–450	100–180	1.470×10^{-3}	0.6	$^{+4.3}_{-3.8}$	2
300–450	180–600	2.585×10^{-5}	3.7	$^{+27.0}_{-33.9}$	3
450–600	0–100	1.003×10^{-3}	0.7	$^{+3.2}_{-3.2}$	4
450–600	100–180	2.140×10^{-3}	0.4	$^{+2.4}_{-2.3}$	5
450–600	180–600	1.739×10^{-4}	0.9	$^{+2.7}_{-2.8}$	6
600–1500	0–100	3.474×10^{-4}	1.4	$^{+4.6}_{-4.4}$	7
600–1500	100–180	7.232×10^{-4}	1.0	$^{+3.4}_{-3.2}$	8
600–1500	180–600	2.839×10^{-4}	0.5	$^{+3.6}_{-3.5}$	9

Table C.7: Values for each bin of the $[M(\mathrm{t\bar{t}}),p_{\mathrm{T}}(t)]$ normalized particle level cross section. The table includes also the binning scheme used in the measurement as well as the values for the statistical and systematic uncertainty.

$m(\mathrm{t\bar{t}})$ [GeV]	$p_{\mathrm{T}}(\mathrm{t})$ [GeV]	$\frac{1}{\sigma(\mathrm{t\bar{t}})}\frac{\mathrm{d}\sigma}{\mathrm{d}p_{\mathrm{T}}(\mathrm{t})}$[GeV^{-1}]	stat. [%]	syst. [%]	bin
300–450	0–100	3.859×10^{-2}	0.3	$^{+5.3}_{-5.1}$	1
300–450	100–180	1.799×10^{-2}	0.6	$^{+7.6}_{-6.9}$	2
300–450	180–600	3.164×10^{-4}	3.7	$^{+27.4}_{-34.5}$	3
450–600	0–100	1.227×10^{-2}	0.8	$^{+7.7}_{-7.5}$	4
450–600	100–180	2.620×10^{-2}	0.4	$^{+4.2}_{-3.9}$	5
450–600	180–600	2.129×10^{-3}	0.9	$^{+5.6}_{-5.4}$	6
600–1500	0–100	4.252×10^{-3}	1.4	$^{+6.7}_{-5.9}$	7
600–1500	100–180	8.853×10^{-3}	1.0	$^{+5.9}_{-5.5}$	8
600–1500	180–600	3.476×10^{-3}	0.5	$^{+5.8}_{-5.3}$	9

Table C.8: Values for each bin of the $[M(\mathrm{t\bar{t}}),p_{\mathrm{T}}(t)]$ absolute particle level cross section. The table includes also the binning scheme used in the measurement as well as the values for the statistical and systematic uncertainty.

$p_{\mathrm{T}}(\mathrm{t})$ [GeV]	$p_{\mathrm{T}}(\mathrm{t\bar{t}})$ [GeV]	$\frac{1}{\sigma(\mathrm{t\bar{t}})}\frac{\mathrm{d}\sigma}{\mathrm{d}p_{\mathrm{T}}(\mathrm{t\bar{t}})}$[GeV^{-1}]	stat. [%]	syst. [%]	bin
0–80	0–30	5.456×10^{-3}	0.8	$^{+6.4}_{-6.6}$	1
0–80	30–75	2.665×10^{-3}	0.7	$^{+5.1}_{-5.7}$	2
0–80	75–150	7.464×10^{-4}	1.7	$^{+7.1}_{-9.3}$	3
0–80	150–500	5.701×10^{-5}	3.1	$^{+6.5}_{-3.4}$	4
80–150	0–30	4.985×10^{-3}	0.6	$^{+5.6}_{-4.9}$	5
80–150	30–75	2.773×10^{-3}	0.6	$^{+4.6}_{-4.3}$	6
80–150	75–150	9.269×10^{-4}	1.1	$^{+6.0}_{-4.9}$	7
80–150	150–500	8.669×10^{-5}	2.4	$^{+4.3}_{-3.2}$	8
150–250	0–30	2.202×10^{-3}	1.2	$^{+7.9}_{-7.2}$	9
150–250	30–75	1.370×10^{-3}	1.2	$^{+5.5}_{-6.3}$	10
150–250	75–150	6.207×10^{-4}	1.4	$^{+4.6}_{-3.9}$	11
150–250	150–500	9.083×10^{-5}	1.7	$^{+3.4}_{-4.6}$	12
250–600	0–30	4.530×10^{-4}	3.8	$^{+13.1}_{-11.6}$	13
250–600	30–75	3.083×10^{-4}	4.8	$^{+9.4}_{-12.0}$	14
250–600	75–150	1.749×10^{-4}	3.1	$^{+7.3}_{-5.5}$	15
250–600	150–500	5.622×10^{-5}	1.4	$^{+3.5}_{-3.1}$	16

Table C.9: Values for each bin of the $[p_{\mathrm{T}}(t),p_{\mathrm{T}}(\mathrm{t\bar{t}})]$ normalized parton level cross section. The table includes also the binning scheme used in the measurement as well as the values for the statistical and systematic uncertainty.

$p_{\mathrm{T}}(\mathrm{t})$ [GeV]	$p_{\mathrm{T}}(\mathrm{t\bar{t}})$ [GeV]	$\frac{1}{\sigma(\mathrm{t\bar{t}})}\frac{\mathrm{d}\sigma}{\mathrm{d}p_{\mathrm{T}}(\mathrm{t\bar{t}})}$[GeV^{-1}]	stat. [%]	syst. [%]	bin
0–80	0–30	4.508×10^{0}	0.8	$^{+8.0}_{-7.5}$	1
0–80	30–75	2.202×10^{0}	0.8	$^{+8.7}_{-8.9}$	2
0–80	75–150	6.168×10^{-1}	1.7	$^{+9.9}_{-11.5}$	3
0–80	150–500	4.711×10^{-2}	3.1	$^{+8.9}_{-5.6}$	4
80–150	0–30	4.119×10^{0}	0.7	$^{+6.3}_{-6.0}$	5
80–150	30–75	2.291×10^{0}	0.6	$^{+7.6}_{-7.3}$	6
80–150	75–150	7.659×10^{-1}	1.1	$^{+8.6}_{-7.2}$	7
80–150	150–500	7.163×10^{-2}	2.4	$^{+6.5}_{-5.1}$	8
150–250	0–30	1.819×10^{0}	1.2	$^{+8.2}_{-7.6}$	9
150–250	30–75	1.132×10^{0}	1.2	$^{+8.0}_{-8.7}$	10
150–250	75–150	5.129×10^{-1}	1.4	$^{+6.6}_{-6.2}$	11
150–250	150–500	7.506×10^{-2}	1.7	$^{+6.4}_{-7.2}$	12
250–600	0–30	3.743×10^{-1}	3.8	$^{+12.5}_{-11.1}$	13
250–600	30–75	2.548×10^{-1}	4.8	$^{+10.3}_{-13.1}$	14
250–600	75–150	1.445×10^{-1}	3.1	$^{+8.0}_{-6.4}$	15
250–600	150–500	4.645×10^{-2}	1.4	$^{+6.5}_{-5.8}$	16

Table C.10: Values for each bin of the $[p_{\mathrm{T}}(t),p_{\mathrm{T}}(\mathrm{t\bar{t}})]$ absolute parton level cross section. The table includes also the binning scheme used in the measurement as well as the values for the statistical and systematic uncertainty.

$p_{\mathrm{T}}(\mathrm{t})$ [GeV]	$p_{\mathrm{T}}(\mathrm{t\bar{t}})$ [GeV]	$\frac{1}{\sigma(\mathrm{t\bar{t}})}\frac{\mathrm{d}\sigma}{\mathrm{d}p_{\mathrm{T}}(\mathrm{t\bar{t}})}$[GeV^{-1}]	stat. [%]	syst. [%]	bin
0–80	0–30	4.775×10^{-3}	0.7	$^{+6.2}_{-6.5}$	1
0–80	30–75	2.584×10^{-3}	0.7	$^{+5.1}_{-5.2}$	2
0–80	75–150	7.184×10^{-4}	1.5	$^{+5.8}_{-7.8}$	3
0–80	150–500	5.614×10^{-5}	2.9	$^{+6.2}_{-3.2}$	4
80–150	0–30	4.590×10^{-3}	0.6	$^{+5.2}_{-4.6}$	5
80–150	30–75	2.808×10^{-3}	0.6	$^{+4.1}_{-3.8}$	6
80–150	75–150	9.255×10^{-4}	1.1	$^{+5.0}_{-4.0}$	7
80–150	150–500	8.621×10^{-5}	2.2	$^{+4.0}_{-3.2}$	8
150–250	0–30	2.301×10^{-3}	1.0	$^{+6.8}_{-6.1}$	9
150–250	30–75	1.576×10^{-3}	1.0	$^{+4.2}_{-5.0}$	10
150–250	75–150	6.829×10^{-4}	1.2	$^{+3.4}_{-3.2}$	11
150–250	150–500	9.564×10^{-5}	1.6	$^{+3.2}_{-4.2}$	12
250–600	0–30	5.915×10^{-4}	2.9	$^{+10.5}_{-9.2}$	13
250–600	30–75	4.393×10^{-4}	3.4	$^{+6.5}_{-8.4}$	14
250–600	75–150	2.330×10^{-4}	2.5	$^{+5.9}_{-4.5}$	15
250–600	150–500	6.771×10^{-5}	1.3	$^{+3.5}_{-3.1}$	16

Table C.11: Values for each bin of the $[p_{\mathrm{T}}(t),p_{\mathrm{T}}(\mathrm{t\bar{t}})]$ normalized particle level cross section. The table includes also the binning scheme used in the measurement as well as the values for the statistical and systematic uncertainty.

$p_{\mathrm{T}}(\mathrm{t})$ [GeV]	$p_{\mathrm{T}}(\mathrm{t\bar{t}})$ [GeV]	$\frac{1}{\sigma(\mathrm{t\bar{t}})}\frac{\mathrm{d}\sigma}{\mathrm{d}p_{\mathrm{T}}(\mathrm{t\bar{t}})}$[GeV^{-1}]	stat. [%]	syst. [%]	bin
0–80	0–30	5.856×10^{-2}	0.8	$^{+7.4}_{-7.6}$	1
0–80	30–75	3.169×10^{-2}	0.8	$^{+8.7}_{-8.4}$	2
0–80	75–150	8.812×10^{-3}	1.6	$^{+8.7}_{-10.5}$	3
0–80	150–500	6.886×10^{-4}	2.9	$^{+8.4}_{-5.3}$	4
80–150	0–30	5.629×10^{-2}	0.6	$^{+5.8}_{-5.6}$	5
80–150	30–75	3.444×10^{-2}	0.6	$^{+7.2}_{-6.6}$	6
80–150	75–150	1.135×10^{-2}	1.1	$^{+7.4}_{-6.6}$	7
80–150	150–500	1.057×10^{-3}	2.2	$^{+6.1}_{-5.2}$	8
150–250	0–30	2.823×10^{-2}	1.0	$^{+7.1}_{-6.7}$	9
150–250	30–75	1.933×10^{-2}	1.0	$^{+7.2}_{-7.5}$	10
150–250	75–150	8.377×10^{-3}	1.2	$^{+5.7}_{-5.8}$	11
150–250	150–500	1.173×10^{-3}	1.6	$^{+5.6}_{-6.8}$	12
250–600	0–30	7.255×10^{-3}	2.9	$^{+10.3}_{-9.3}$	13
250–600	30–75	5.389×10^{-3}	3.4	$^{+8.6}_{-10.2}$	14
250–600	75–150	2.858×10^{-3}	2.5	$^{+7.2}_{-5.9}$	15
250–600	150–500	8.305×10^{-4}	1.3	$^{+6.4}_{-5.8}$	16

Table C.12: Values for each bin of the [$p_{\mathrm{T}}(t)$,$p_{\mathrm{T}}(\mathrm{t\bar{t}})$] absolute particle level cross section. The table includes also the binning scheme used in the measurement as well as the values for the statistical and systematic uncertainty.

$m(\mathrm{t\bar{t}})$ [GeV]	$\lvert y(\mathrm{t\bar{t}})\rvert$	$\frac{1}{\sigma(\mathrm{t\bar{t}})}\frac{\mathrm{d}\sigma}{\mathrm{d}\lvert y(\mathrm{t\bar{t}})\rvert}$	stat. [%]	syst. [%]	bin
300–400	0.00–0.35	1.488×10^{-1}	1.4	$^{+6.2}_{-6.5}$	1
300–400	0.35–0.75	1.385×10^{-1}	1.3	$^{+6.5}_{-6.7}$	2
300–400	0.75–1.15	1.222×10^{-1}	1.5	$^{+7.5}_{-7.3}$	3
300–400	1.15–2.50	5.910×10^{-2}	1.3	$^{+5.2}_{-4.9}$	4
400–500	0.00–0.35	2.477×10^{-1}	0.8	$^{+2.0}_{-2.0}$	5
400–500	0.35–0.75	2.253×10^{-1}	0.7	$^{+2.4}_{-1.7}$	6
400–500	0.75–1.15	1.900×10^{-1}	0.9	$^{+2.7}_{-2.5}$	7
400–500	1.15–2.50	8.195×10^{-2}	0.7	$^{+2.2}_{-2.5}$	8
500–650	0.00–0.35	1.810×10^{-1}	1.0	$^{+2.3}_{-1.7}$	9
500–650	0.35–0.75	1.622×10^{-1}	1.0	$^{+2.5}_{-1.5}$	10
500–650	0.75–1.15	1.334×10^{-1}	1.1	$^{+2.3}_{-2.9}$	11
500–650	1.15–2.50	4.638×10^{-2}	1.3	$^{+4.3}_{-4.7}$	12
650–1500	0.00–0.35	1.402×10^{-1}	0.8	$^{+2.3}_{-2.9}$	13
650–1500	0.35–0.75	1.192×10^{-1}	1.0	$^{+2.5}_{-2.5}$	14
650–1500	0.75–1.15	8.183×10^{-2}	1.5	$^{+3.4}_{-3.6}$	15
650–1500	1.15–2.50	1.973×10^{-2}	2.4	$^{+6.2}_{-6.9}$	16

Table C.13: Values for each bin of the $[M(\mathrm{t\bar{t}}),y(\mathrm{t\bar{t}})]$ normalized parton level cross section. The table includes also the binning scheme used in the measurement as well as the values for the statistical and systematic uncertainty.

$m(\mathrm{t\bar{t}})$ [GeV]	$\lvert y(\mathrm{t\bar{t}})\rvert$	$\frac{1}{\sigma(\mathrm{t\bar{t}})}\frac{\mathrm{d}\sigma}{\mathrm{d}\lvert y(\mathrm{t\bar{t}})\rvert}$	stat. [%]	syst. [%]	bin
300–400	0.00–0.35	1.209×10^2	1.4	$^{+7.2}_{-7.1}$	1
300–400	0.35–0.75	1.126×10^2	1.3	$^{+7.2}_{-6.9}$	2
300–400	0.75–1.15	9.931×10^1	1.5	$^{+8.2}_{-7.7}$	3
300–400	1.15–2.50	4.802×10^1	1.3	$^{+7.7}_{-7.1}$	4
400–500	0.00–0.35	2.012×10^2	0.8	$^{+5.9}_{-5.5}$	5
400–500	0.35–0.75	1.831×10^2	0.7	$^{+6.1}_{-4.9}$	6
400–500	0.75–1.15	1.544×10^2	0.8	$^{+6.3}_{-5.8}$	7
400–500	1.15–2.50	6.658×10^1	0.7	$^{+5.7}_{-5.6}$	8
500–650	0.00–0.35	1.471×10^2	1.0	$^{+6.3}_{-5.5}$	9
500–650	0.35–0.75	1.317×10^2	1.0	$^{+6.6}_{-5.4}$	10
500–650	0.75–1.15	1.084×10^2	1.1	$^{+6.6}_{-6.6}$	11
500–650	1.15–2.50	3.768×10^1	1.3	$^{+8.2}_{-8.2}$	12
650–1500	0.00–0.35	1.139×10^2	0.8	$^{+5.7}_{-5.7}$	13
650–1500	0.35–0.75	9.682×10^1	1.0	$^{+5.9}_{-5.6}$	14
650–1500	0.75–1.15	6.648×10^1	1.5	$^{+6.8}_{-6.4}$	15
650–1500	1.15–2.50	1.603×10^1	2.4	$^{+9.5}_{-9.8}$	16

Table C.14: Values for each bin of the $[M(\mathrm{t\bar{t}}),y(\mathrm{t\bar{t}})]$ absolute parton level cross section. The table includes also the binning scheme used in the measurement as well as the values for the statistical and systematic uncertainty.

$m(\mathrm{t\bar{t}})$ [GeV]	$\lvert y(\mathrm{t\bar{t}})\rvert$	$\frac{1}{\sigma(\mathrm{t\bar{t}})}\frac{\mathrm{d}\sigma}{\mathrm{d}\lvert y(\mathrm{t\bar{t}})\rvert}$	stat. [%]	syst. [%]	bin
300–400	0.00–0.35	1.925×10^{-1}	1.1	$^{+4.5}_{-5.1}$	1
300–400	0.35–0.75	1.783×10^{-1}	1.0	$^{+4.6}_{-5.1}$	2
300–400	0.75–1.15	1.469×10^{-1}	1.1	$^{+5.2}_{-5.3}$	3
300–400	1.15–2.50	3.894×10^{-2}	1.3	$^{+4.3}_{-4.7}$	4
400–500	0.00–0.35	2.984×10^{-1}	0.6	$^{+1.2}_{-1.3}$	5
400–500	0.35–0.75	2.656×10^{-1}	0.6	$^{+1.5}_{-1.0}$	6
400–500	0.75–1.15	2.017×10^{-1}	0.7	$^{+1.9}_{-1.9}$	7
400–500	1.15–2.50	4.408×10^{-2}	1.1	$^{+3.4}_{-3.7}$	8
500–650	0.00–0.35	2.308×10^{-1}	0.8	$^{+2.1}_{-1.4}$	9
500–650	0.35–0.75	1.955×10^{-1}	0.7	$^{+2.3}_{-1.3}$	10
500–650	0.75–1.15	1.359×10^{-1}	1.0	$^{+2.2}_{-2.6}$	11
500–650	1.15–2.50	2.376×10^{-2}	1.7	$^{+3.9}_{-3.8}$	12
650–1500	0.00–0.35	1.741×10^{-1}	0.7	$^{+2.4}_{-2.6}$	13
650–1500	0.35–0.75	1.326×10^{-1}	0.9	$^{+2.7}_{-2.5}$	14
650–1500	0.75–1.15	7.021×10^{-2}	1.4	$^{+3.4}_{-3.2}$	15
650–1500	1.15–2.50	8.589×10^{-3}	2.4	$^{+5.3}_{-6.3}$	16

Table C.15: Values for each bin of the $[M(\mathrm{t\bar{t}}),y(\mathrm{t\bar{t}})]$ normalized particle level cross section. The table includes also the binning scheme used in the measurement as well as the values for the statistical and systematic uncertainty.

$m(\mathrm{t\bar{t}})$ [GeV]	$\lvert y(\mathrm{t\bar{t}})\rvert$	$\frac{1}{\sigma(\mathrm{t\bar{t}})}\frac{\mathrm{d}\sigma}{\mathrm{d}\lvert y(\mathrm{t\bar{t}})\rvert}$	stat. [%]	syst. [%]	bin
300–400	0.00–0.35	2.361×10^{0}	1.1	$^{+6.2}_{-6.3}$	1
300–400	0.35–0.75	2.186×10^{0}	1.0	$^{+6.1}_{-6.1}$	2
300–400	0.75–1.15	1.801×10^{0}	1.1	$^{+6.6}_{-6.5}$	3
300–400	1.15–2.50	4.775×10^{-1}	1.3	$^{+6.8}_{-6.7}$	4
400–500	0.00–0.35	3.659×10^{0}	0.6	$^{+5.0}_{-4.9}$	5
400–500	0.35–0.75	3.257×10^{0}	0.6	$^{+5.1}_{-4.6}$	6
400–500	0.75–1.15	2.473×10^{0}	0.7	$^{+5.2}_{-5.1}$	7
400–500	1.15–2.50	5.405×10^{-1}	1.1	$^{+6.4}_{-6.4}$	8
500–650	0.00–0.35	2.830×10^{0}	0.8	$^{+5.9}_{-5.3}$	9
500–650	0.35–0.75	2.397×10^{0}	0.8	$^{+6.2}_{-5.3}$	10
500–650	0.75–1.15	1.666×10^{0}	1.0	$^{+6.1}_{-6.2}$	11
500–650	1.15–2.50	2.914×10^{-1}	1.7	$^{+7.5}_{-7.3}$	12
650–1500	0.00–0.35	2.135×10^{0}	0.7	$^{+5.6}_{-5.4}$	13
650–1500	0.35–0.75	1.626×10^{0}	0.9	$^{+5.9}_{-5.5}$	14
650–1500	0.75–1.15	8.608×10^{-1}	1.4	$^{+6.6}_{-6.1}$	15
650–1500	1.15–2.50	1.053×10^{-1}	2.4	$^{+8.5}_{-8.9}$	16

Table C.16: Values for each bin of the $[M(\mathrm{t\bar{t}}),y(\mathrm{t\bar{t}})]$ absolute particle level cross section. The table includes also the binning scheme used in the measurement as well as the values for the statistical and systematic uncertainty.

$\lvert y(\mathrm{t\bar{t}})\rvert$	$p_{\mathrm{T}}(\mathrm{t\bar{t}})$ [GeV]	$\frac{1}{\sigma(\mathrm{t\bar{t}})}\frac{\mathrm{d}\sigma}{\mathrm{d}p_{\mathrm{T}}(\mathrm{t\bar{t}})}$[GeV^{-1}]	stat. [%]	syst. [%]	bin
0.00–0.35	0–30	3.079×10^{-3}	1.0	$^{+7.4}_{-6.4}$	1
0.00–0.35	30–75	1.810×10^{-3}	1.1	$^{+5.5}_{-6.1}$	2
0.00–0.35	75–150	6.332×10^{-4}	1.4	$^{+4.9}_{-3.8}$	3
0.00–0.35	150–500	8.152×10^{-5}	1.2	$^{+3.4}_{-3.7}$	4
0.35–0.75	0–30	3.293×10^{-3}	0.9	$^{+6.1}_{-6.9}$	5
0.35–0.75	30–75	1.828×10^{-3}	0.9	$^{+5.4}_{-5.7}$	6
0.35–0.75	75–150	6.557×10^{-4}	1.4	$^{+4.2}_{-4.0}$	7
0.35–0.75	150–500	8.216×10^{-5}	1.6	$^{+5.0}_{-2.9}$	8
0.75–1.15	0–30	2.770×10^{-3}	1.0	$^{+6.8}_{-7.5}$	9
0.75–1.15	30–75	1.449×10^{-3}	1.2	$^{+7.5}_{-6.1}$	10
0.75–1.15	75–150	5.275×10^{-4}	1.7	$^{+5.5}_{-3.9}$	11
0.75–1.15	150–500	6.053×10^{-5}	2.1	$^{+2.6}_{-5.1}$	12
1.15–2.50	0–30	3.965×10^{-3}	1.0	$^{+4.7}_{-6.1}$	13
1.15–2.50	30–75	2.012×10^{-3}	0.9	$^{+5.0}_{-4.4}$	14
1.15–2.50	75–150	6.566×10^{-4}	1.8	$^{+8.3}_{-6.4}$	15
1.15–2.50	150–500	6.676×10^{-5}	2.3	$^{+3.5}_{-4.3}$	16

Table C.17: Values for each bin of the $[y(\mathrm{t\bar{t}}),p_{\mathrm{T}}(\mathrm{t\bar{t}})]$ normalized parton level cross section. The table includes also the binning scheme used in the measurement as well as the values for the statistical and systematic uncertainty.

$\lvert y(\mathrm{t\bar{t}})\rvert$	$p_{\mathrm{T}}(\mathrm{t\bar{t}})$ [GeV]	$\frac{1}{\sigma(\mathrm{t\bar{t}})}\frac{\mathrm{d}\sigma}{\mathrm{d}p_{\mathrm{T}}(\mathrm{t\bar{t}})}$[GeV^{-1}]	stat. [%]	syst. [%]	bin
0.00–0.35	0–30	2.523×10^{0}	1.0	$^{+7.8}_{-7.3}$	1
0.00–0.35	30–75	1.484×10^{0}	1.1	$^{+8.4}_{-8.6}$	2
0.00–0.35	75–150	5.189×10^{-1}	1.4	$^{+7.5}_{-6.4}$	3
0.00–0.35	150–500	6.681×10^{-2}	1.2	$^{+6.2}_{-5.6}$	4
0.35–0.75	0–30	2.699×10^{0}	0.9	$^{+6.8}_{-7.3}$	5
0.35–0.75	30–75	1.498×10^{0}	0.9	$^{+8.5}_{-8.2}$	6
0.35–0.75	75–150	5.374×10^{-1}	1.4	$^{+6.6}_{-6.6}$	7
0.35–0.75	150–500	6.733×10^{-2}	1.6	$^{+7.4}_{-5.0}$	8
0.75–1.15	0–30	2.270×10^{0}	1.0	$^{+7.4}_{-8.0}$	9
0.75–1.15	30–75	1.188×10^{0}	1.2	$^{+10.7}_{-8.6}$	10
0.75–1.15	75–150	4.323×10^{-1}	1.7	$^{+8.0}_{-6.2}$	11
0.75–1.15	150–500	4.961×10^{-2}	2.1	$^{+5.4}_{-6.7}$	12
1.15–2.50	0–30	3.249×10^{0}	1.1	$^{+6.2}_{-7.2}$	13
1.15–2.50	30–75	1.649×10^{0}	1.0	$^{+8.4}_{-7.6}$	14
1.15–2.50	75–150	5.381×10^{-1}	1.8	$^{+11.2}_{-9.1}$	15
1.15–2.50	150–500	5.471×10^{-2}	2.3	$^{+6.6}_{-7.1}$	16

Table C.18: Values for each bin of the $[y(\mathrm{t\bar{t}}),p_{\mathrm{T}}(\mathrm{t\bar{t}})]$ absolute parton level cross section. The table includes also the binning scheme used in the measurement as well as the values for the statistical and systematic uncertainty.

$\lvert y(\mathrm{t\bar{t}})\rvert$	$p_{\mathrm{T}}(\mathrm{t\bar{t}})$ [GeV]	$\frac{1}{\sigma(\mathrm{t\bar{t}})}\frac{\mathrm{d}\sigma}{\mathrm{d}p_{\mathrm{T}}(\mathrm{t\bar{t}})}$[GeV^{-1}]	stat. [%]	syst. [%]	bin
0.00–0.35	0–30	3.702×10^{-3}	0.7	$^{+5.8}_{-5.2}$	1
0.00–0.35	30–75	2.373×10^{-3}	0.7	$^{+3.4}_{-3.8}$	2
0.00–0.35	75–150	8.002×10^{-4}	1.1	$^{+4.1}_{-3.9}$	3
0.00–0.35	150–500	1.006×10^{-4}	1.1	$^{+3.1}_{-3.2}$	4
0.35–0.75	0–30	3.755×10^{-3}	0.7	$^{+5.0}_{-5.7}$	5
0.35–0.75	30–75	2.320×10^{-3}	0.6	$^{+3.2}_{-3.6}$	6
0.35–0.75	75–150	7.912×10^{-4}	1.1	$^{+3.9}_{-3.8}$	7
0.35–0.75	150–500	9.744×10^{-5}	1.4	$^{+4.2}_{-2.6}$	8
0.75–1.15	0–30	2.766×10^{-3}	0.9	$^{+5.6}_{-6.0}$	9
0.75–1.15	30–75	1.612×10^{-3}	0.9	$^{+5.4}_{-4.4}$	10
0.75–1.15	75–150	5.607×10^{-4}	1.4	$^{+4.6}_{-3.3}$	11
0.75–1.15	150–500	6.447×10^{-5}	1.9	$^{+2.5}_{-4.8}$	12
1.15–2.50	0–30	2.048×10^{-3}	1.2	$^{+5.7}_{-6.6}$	13
1.15–2.50	30–75	1.130×10^{-3}	1.5	$^{+7.6}_{-7.2}$	14
1.15–2.50	75–150	3.915×10^{-4}	1.9	$^{+6.4}_{-4.3}$	15
1.15–2.50	150–500	4.198×10^{-5}	2.3	$^{+3.4}_{-4.5}$	16

Table C.19: Values for each bin of the $[y(\mathrm{t\bar{t}}),p_{\mathrm{T}}(\mathrm{t\bar{t}})]$ normalized particle level cross section. The table includes also the binning scheme used in the measurement as well as the values for the statistical and systematic uncertainty.

$\lvert y(\mathrm{t\bar{t}})\rvert$	$p_{\mathrm{T}}(\mathrm{t\bar{t}})$ [GeV]	$\frac{1}{\sigma(\mathrm{t\bar{t}})}\frac{\mathrm{d}\sigma}{\mathrm{d}p_{\mathrm{T}}(\mathrm{t\bar{t}})}$[GeV^{-1}]	stat. [%]	syst. [%]	bin
0.00–0.35	0–30	4.554×10^{-2}	0.7	$^{+6.5}_{-6.4}$	1
0.00–0.35	30–75	2.918×10^{-2}	0.7	$^{+6.7}_{-6.8}$	2
0.00–0.35	75–150	9.843×10^{-3}	1.1	$^{+6.8}_{-6.6}$	3
0.00–0.35	150–500	1.238×10^{-3}	1.1	$^{+5.5}_{-5.3}$	4
0.35–0.75	0–30	4.619×10^{-2}	0.7	$^{+6.0}_{-6.4}$	5
0.35–0.75	30–75	2.854×10^{-2}	0.6	$^{+6.7}_{-6.7}$	6
0.35–0.75	75–150	9.732×10^{-3}	1.1	$^{+6.4}_{-6.5}$	7
0.35–0.75	150–500	1.199×10^{-3}	1.4	$^{+6.6}_{-4.9}$	8
0.75–1.15	0–30	3.402×10^{-2}	0.9	$^{+6.4}_{-6.6}$	9
0.75–1.15	30–75	1.982×10^{-2}	0.9	$^{+8.7}_{-7.3}$	10
0.75–1.15	75–150	6.896×10^{-3}	1.4	$^{+7.3}_{-5.8}$	11
0.75–1.15	150–500	7.930×10^{-4}	1.9	$^{+5.1}_{-6.6}$	12
1.15–2.50	0–30	2.519×10^{-2}	1.2	$^{+6.6}_{-7.2}$	13
1.15–2.50	30–75	1.389×10^{-2}	1.5	$^{+10.6}_{-9.9}$	14
1.15–2.50	75–150	4.815×10^{-3}	1.9	$^{+9.3}_{-7.2}$	15
1.15–2.50	150–500	5.164×10^{-4}	2.3	$^{+6.2}_{-7.2}$	16

Table C.20: Values for each bin of the $[y(\mathrm{t\bar{t}}),p_{\mathrm{T}}(\mathrm{t\bar{t}})]$ absolute particle level cross section. The table includes also the binning scheme used in the measurement as well as the values for the statistical and systematic uncertainty.

$m(\mathrm{t\bar{t}})$ [GeV]	$p_{\mathrm{T}}(\mathrm{t\bar{t}})$ [GeV]	$\frac{1}{\sigma(\mathrm{t\bar{t}})}\frac{\mathrm{d}\sigma}{\mathrm{d}p_{\mathrm{T}}(\mathrm{t\bar{t}})}$[GeV^{-1}]	stat. [%]	syst. [%]	bin
300–400	0–30	3.477×10^{-3}	1.1	$^{+10.0}_{-10.4}$	1
300–400	30–75	1.640×10^{-3}	1.2	$^{+6.9}_{-8.2}$	2
300–400	75–150	5.274×10^{-4}	2.2	$^{+9.9}_{-6.8}$	3
300–400	150–500	5.350×10^{-5}	3.7	$^{+9.9}_{-9.4}$	4
400–500	0–30	4.878×10^{-3}	0.7	$^{+5.3}_{-5.2}$	5
400–500	30–75	2.633×10^{-3}	0.7	$^{+5.2}_{-5.4}$	6
400–500	75–150	8.740×10^{-4}	1.2	$^{+6.5}_{-5.5}$	7
400–500	150–500	9.643×10^{-5}	2.5	$^{+4.7}_{-5.1}$	8
500–650	0–30	3.036×10^{-3}	1.0	$^{+7.2}_{-7.2}$	9
500–650	30–75	1.750×10^{-3}	1.0	$^{+5.8}_{-6.1}$	10
500–650	75–150	6.330×10^{-4}	1.5	$^{+6.5}_{-5.2}$	11
500–650	150–500	7.294×10^{-5}	2.5	$^{+4.6}_{-5.4}$	12
650–1500	0–30	1.777×10^{-3}	1.6	$^{+7.2}_{-7.6}$	13
650–1500	30–75	1.075×10^{-3}	1.8	$^{+6.0}_{-6.7}$	14
650–1500	75–150	4.180×10^{-4}	1.9	$^{+6.7}_{-4.5}$	15
650–1500	150–500	6.755×10^{-5}	1.6	$^{+3.3}_{-3.2}$	16

Table C.21: Values for each bin of the $[M(\mathrm{t\bar{t}}),p_{\mathrm{T}}(\mathrm{t\bar{t}})]$ normalized parton level cross section. The table includes also the binning scheme used in the measurement as well as the values for the statistical and systematic uncertainty.

$m(\mathrm{t\bar{t}})$ [GeV]	$p_{\mathrm{T}}(\mathrm{t\bar{t}})$ [GeV]	$\frac{1}{\sigma(\mathrm{t\bar{t}})}\frac{\mathrm{d}\sigma}{\mathrm{d}p_{\mathrm{T}}(\mathrm{t\bar{t}})}[\mathrm{GeV}^{-1}]$	stat. [%]	syst. [%]	bin
300–400	0–30	2.848×10^{0}	1.1	$^{+10.2}_{-9.9}$	1
300–400	30–75	1.343×10^{0}	1.2	$^{+9.3}_{-10.4}$	2
300–400	75–150	4.320×10^{-1}	2.2	$^{+11.5}_{-8.0}$	3
300–400	150–500	4.381×10^{-2}	3.7	$^{+9.5}_{-8.9}$	4
400–500	0–30	3.995×10^{0}	0.7	$^{+6.3}_{-6.4}$	5
400–500	30–75	2.156×10^{0}	0.7	$^{+8.0}_{-8.3}$	6
400–500	75–150	7.158×10^{-1}	1.2	$^{+9.3}_{-8.0}$	7
400–500	150–500	7.898×10^{-2}	2.5	$^{+8.0}_{-7.9}$	8
500–650	0–30	2.486×10^{0}	1.0	$^{+8.6}_{-8.3}$	9
500–650	30–75	1.433×10^{0}	1.0	$^{+8.6}_{-8.9}$	10
500–650	75–150	5.184×10^{-1}	1.5	$^{+8.7}_{-7.2}$	11
500–650	150–500	5.974×10^{-2}	2.5	$^{+7.0}_{-7.5}$	12
650–1500	0–30	1.455×10^{0}	1.6	$^{+8.1}_{-8.5}$	13
650–1500	30–75	8.804×10^{-1}	1.8	$^{+8.7}_{-9.0}$	14
650–1500	75–150	3.423×10^{-1}	1.9	$^{+9.0}_{-6.9}$	15
650–1500	150–500	5.532×10^{-2}	1.6	$^{+6.4}_{-6.0}$	16

Table C.22: Values for each bin of the $[M(\mathrm{t\bar{t}}),p_{\mathrm{T}}(\mathrm{t\bar{t}})]$ absolute parton level cross section. The table includes also the binning scheme used in the measurement as well as the values for the statistical and systematic uncertainty.

$m(\mathrm{t\bar{t}})$ [GeV]	$p_{\mathrm{T}}(\mathrm{t\bar{t}})$ [GeV]	$\frac{1}{\sigma(\mathrm{t\bar{t}})}\frac{\mathrm{d}\sigma}{\mathrm{d}p_{\mathrm{T}}(\mathrm{t\bar{t}})}$[GeV^{-1}]	stat. [%]	syst. [%]	bin
300–400	0–30	3.416×10^{-3}	1.0	$^{+9.1}_{-9.7}$	1
300–400	30–75	1.874×10^{-3}	1.0	$^{+5.5}_{-6.4}$	2
300–400	75–150	5.820×10^{-4}	1.7	$^{+7.2}_{-5.4}$	3
300–400	150–500	5.503×10^{-5}	3.1	$^{+8.1}_{-8.1}$	4
400–500	0–30	4.445×10^{-3}	0.7	$^{+4.9}_{-5.0}$	5
400–500	30–75	2.633×10^{-3}	0.6	$^{+4.8}_{-4.9}$	6
400–500	75–150	8.728×10^{-4}	1.1	$^{+5.5}_{-4.6}$	7
400–500	150–500	9.776×10^{-5}	2.3	$^{+3.8}_{-4.6}$	8
500–650	0–30	2.855×10^{-3}	0.9	$^{+6.2}_{-5.8}$	9
500–650	30–75	1.819×10^{-3}	0.9	$^{+5.2}_{-5.3}$	10
500–650	75–150	6.666×10^{-4}	1.4	$^{+4.6}_{-3.6}$	11
500–650	150–500	7.988×10^{-5}	2.3	$^{+4.1}_{-4.4}$	12
650–1500	0–30	1.598×10^{-3}	1.4	$^{+6.3}_{-6.6}$	13
650–1500	30–75	1.070×10^{-3}	1.7	$^{+5.4}_{-5.6}$	14
650–1500	75–150	4.282×10^{-4}	1.7	$^{+5.6}_{-3.5}$	15
650–1500	150–500	7.163×10^{-5}	1.5	$^{+3.1}_{-3.0}$	16

Table C.23: Values for each bin of the $[M(\mathrm{t\bar{t}}),p_{\mathrm{T}}(\mathrm{t\bar{t}})]$ normalized particle level cross section. The table includes also the binning scheme used in the measurement as well as the values for the statistical and systematic uncertainty.

$m(t\bar{t})$ [GeV]	$p_T(t\bar{t})$ [GeV]	$\frac{1}{\sigma(t\bar{t})}\frac{d\sigma}{dp_T(t\bar{t})}$[GeV^{-1}]	stat. [%]	syst. [%]	bin
300–400	0–30	4.178×10^{-2}	1.0	$^{+9.0}_{-9.5}$	1
300–400	30–75	2.293×10^{-2}	1.1	$^{+8.3}_{-8.9}$	2
300–400	75–150	7.118×10^{-3}	1.8	$^{+9.2}_{-7.4}$	3
300–400	150–500	6.731×10^{-4}	3.1	$^{+7.8}_{-7.7}$	4
400–500	0–30	5.437×10^{-2}	0.7	$^{+5.7}_{-6.0}$	5
400–500	30–75	3.221×10^{-2}	0.7	$^{+7.8}_{-7.7}$	6
400–500	75–150	1.068×10^{-2}	1.1	$^{+8.0}_{-7.4}$	7
400–500	150–500	1.196×10^{-3}	2.3	$^{+6.6}_{-7.4}$	8
500–650	0–30	3.492×10^{-2}	0.9	$^{+7.4}_{-7.0}$	9
500–650	30–75	2.225×10^{-2}	0.9	$^{+8.5}_{-8.3}$	10
500–650	75–150	8.153×10^{-3}	1.4	$^{+7.3}_{-6.5}$	11
500–650	150–500	9.771×10^{-4}	2.3	$^{+7.2}_{-6.8}$	12
650–1500	0–30	1.955×10^{-2}	1.4	$^{+7.3}_{-7.3}$	13
650–1500	30–75	1.309×10^{-2}	1.7	$^{+8.5}_{-8.4}$	14
650–1500	75–150	5.238×10^{-3}	1.7	$^{+8.0}_{-6.1}$	15
650–1500	150–500	8.761×10^{-4}	1.5	$^{+6.3}_{-5.9}$	16

Table C.24: Values for each bin of the [$M(t\bar{t})$,$p_T(t\bar{t})$] absolute particle level cross section. The table includes also the binning scheme used in the measurement as well as the values for the statistical and systematic uncertainty.

$p_{\mathrm{T}}(\mathrm{t\bar{t}})$ [GeV]	$m(\mathrm{t\bar{t}})$ [GeV]	$y(\mathrm{t\bar{t}})$	$\frac{1}{\sigma(\mathrm{t\bar{t}})}\frac{\mathrm{d}\sigma}{\mathrm{d}y(\mathrm{t\bar{t}})}$	stat. [%]	syst. [%]	bin
0–40	340–400	0.00–0.35	7.595×10^{-2}	2.8	$^{+8.1}_{-7.6}$	1
0–40	340–400	0.35–0.75	7.091×10^{-2}	2.5	$^{+7.6}_{-8.1}$	2
0–40	340–400	0.75–1.15	6.252×10^{-2}	2.8	$^{+9.5}_{-11.1}$	3
0–40	340–400	1.15–2.50	3.159×10^{-2}	2.4	$^{+8.3}_{-8.5}$	4
0–40	400–500	0.00–0.35	1.213×10^{-1}	1.6	$^{+4.7}_{-4.9}$	5
0–40	400–500	0.35–0.75	1.098×10^{-1}	1.4	$^{+4.2}_{-4.9}$	6
0–40	400–500	0.75–1.15	9.641×10^{-2}	1.6	$^{+4.3}_{-5.4}$	7
0–40	400–500	1.15–2.50	4.359×10^{-2}	1.3	$^{+3.3}_{-3.4}$	8
0–40	500–650	0.00–0.35	8.594×10^{-2}	2.0	$^{+5.9}_{-5.9}$	9
0–40	500–650	0.35–0.75	7.728×10^{-2}	1.9	$^{+6.6}_{-5.0}$	10
0–40	500–650	0.75–1.15	6.583×10^{-2}	2.2	$^{+5.5}_{-7.8}$	11
0–40	500–650	1.15–2.50	2.405×10^{-2}	2.4	$^{+5.7}_{-8.3}$	12
0–40	650–1500	0.00–0.35	5.921×10^{-2}	2.2	$^{+4.5}_{-6.8}$	13
0–40	650–1500	0.35–0.75	4.981×10^{-2}	2.6	$^{+4.6}_{-5.7}$	14
0–40	650–1500	0.75–1.15	3.563×10^{-2}	3.8	$^{+5.8}_{-6.0}$	15
0–40	650–1500	1.15–2.50	9.110×10^{-3}	5.6	$^{+9.2}_{-11.7}$	16
40–120	340–400	0.00–0.35	4.724×10^{-2}	4.4	$^{+9.6}_{-9.2}$	17
40–120	340–400	0.35–0.75	4.408×10^{-2}	3.7	$^{+9.1}_{-7.9}$	18
40–120	340–400	0.75–1.15	3.833×10^{-2}	4.2	$^{+12.1}_{-10.3}$	19
40–120	340–400	1.15–2.50	1.994×10^{-2}	3.0	$^{+8.5}_{-8.1}$	20
40–120	400–500	0.00–0.35	8.908×10^{-2}	2.0	$^{+7.5}_{-7.2}$	21
40–120	400–500	0.35–0.75	8.204×10^{-2}	1.7	$^{+6.9}_{-6.6}$	22
40–120	400–500	0.75–1.15	6.766×10^{-2}	2.0	$^{+8.2}_{-6.9}$	23
40–120	400–500	1.15–2.50	2.845×10^{-2}	1.7	$^{+7.1}_{-6.7}$	24
40–120	500–650	0.00–0.35	6.945×10^{-2}	2.4	$^{+7.1}_{-7.8}$	25
40–120	500–650	0.35–0.75	6.195×10^{-2}	2.2	$^{+7.7}_{-6.8}$	26
40–120	500–650	0.75–1.15	4.966×10^{-2}	2.8	$^{+8.3}_{-6.6}$	27
40–120	500–650	1.15–2.50	1.686×10^{-2}	2.9	$^{+8.4}_{-8.0}$	28
40–120	650–1500	0.00–0.35	4.875×10^{-2}	2.8	$^{+6.7}_{-5.0}$	29
40–120	650–1500	0.35–0.75	4.291×10^{-2}	3.1	$^{+5.9}_{-5.7}$	30
40–120	650–1500	0.75–1.15	2.996×10^{-2}	4.4	$^{+6.9}_{-7.1}$	31
40–120	650–1500	1.15–2.50	6.479×10^{-3}	7.9	$^{+17.5}_{-9.1}$	32
120–500	340–400	0.00–0.35	1.837×10^{-2}	9.0	$^{+13.3}_{-14.6}$	33
120–500	340–400	0.35–0.75	1.676×10^{-2}	8.9	$^{+10.6}_{-12.2}$	34
120–500	340–400	0.75–1.15	1.593×10^{-2}	9.0	$^{+9.7}_{-10.5}$	35
120–500	340–400	1.15–2.50	6.518×10^{-3}	8.8	$^{+15.4}_{-8.0}$	36
120–500	400–500	0.00–0.35	3.879×10^{-2}	4.8	$^{+7.4}_{-4.0}$	37
120–500	400–500	0.35–0.75	3.495×10^{-2}	4.0	$^{+5.8}_{-3.5}$	38
120–500	400–500	0.75–1.15	2.887×10^{-2}	4.9	$^{+5.8}_{-5.2}$	39
120–500	400–500	1.15–2.50	1.014×10^{-2}	4.6	$^{+5.2}_{-7.6}$	40
120–500	500–650	0.00–0.35	3.137×10^{-2}	4.5	$^{+4.9}_{-6.1}$	41
120–500	500–650	0.35–0.75	2.872×10^{-2}	4.3	$^{+5.8}_{-5.9}$	42
120–500	500–650	0.75–1.15	2.010×10^{-2}	6.1	$^{+7.6}_{-6.2}$	43
120–500	500–650	1.15–2.50	6.900×10^{-3}	6.5	$^{+6.9}_{-8.5}$	44
120–500	650–1500	0.00–0.35	3.076×10^{-2}	2.6	$^{+3.4}_{-3.8}$	45
120–500	650–1500	0.35–0.75	2.490×10^{-2}	3.6	$^{+5.2}_{-3.6}$	46
120–500	650–1500	0.75–1.15	1.741×10^{-2}	5.1	$^{+2.7}_{-5.8}$	47
120–500	650–1500	1.15–2.50	4.031×10^{-3}	8.3	$^{+7.1}_{-5.9}$	48

Table C.25: Values for each bin of the $[p_{\mathrm{T}}(\mathrm{t\bar{t}}),M(\mathrm{t\bar{t}}),y(\mathrm{t\bar{t}})]$ normalized parton level cross section. The table includes also the binning scheme used in the measurement as well as the values for the statistical and systematic uncertainty.

$p_T(t\bar{t})$ [GeV]	$m(t\bar{t})$ [GeV]	$y(t\bar{t})$	$\frac{1}{\sigma(t\bar{t})}\frac{d\sigma}{dy(t\bar{t})}$	stat. [%]	syst. [%]	bin
0–40	340–400	0.00–0.35	6.057×10^{1}	2.8	$^{+7.8}_{-7.5}$	1
0–40	340–400	0.35–0.75	5.654×10^{1}	2.5	$^{+7.4}_{-7.9}$	2
0–40	340–400	0.75–1.15	4.986×10^{1}	2.8	$^{+8.9}_{-10.4}$	3
0–40	340–400	1.15–2.50	2.519×10^{1}	2.4	$^{+8.2}_{-8.7}$	4
0–40	400–500	0.00–0.35	9.675×10^{1}	1.6	$^{+6.5}_{-6.8}$	5
0–40	400–500	0.35–0.75	8.759×10^{1}	1.4	$^{+6.3}_{-6.7}$	6
0–40	400–500	0.75–1.15	7.688×10^{1}	1.6	$^{+6.3}_{-7.1}$	7
0–40	400–500	1.15–2.50	3.476×10^{1}	1.3	$^{+5.8}_{-5.6}$	8
0–40	500–650	0.00–0.35	6.853×10^{1}	2.0	$^{+7.6}_{-7.2}$	9
0–40	500–650	0.35–0.75	6.162×10^{1}	1.9	$^{+7.7}_{-6.7}$	10
0–40	500–650	0.75–1.15	5.250×10^{1}	2.2	$^{+7.2}_{-9.0}$	11
0–40	500–650	1.15–2.50	1.918×10^{1}	2.4	$^{+8.4}_{-10.7}$	12
0–40	650–1500	0.00–0.35	4.722×10^{1}	2.2	$^{+6.0}_{-7.9}$	13
0–40	650–1500	0.35–0.75	3.972×10^{1}	2.6	$^{+6.5}_{-7.5}$	14
0–40	650–1500	0.75–1.15	2.841×10^{1}	3.8	$^{+8.1}_{-7.7}$	15
0–40	650–1500	1.15–2.50	7.265×10^{0}	5.7	$^{+11.1}_{-13.1}$	16
40–120	340–400	0.00–0.35	3.767×10^{1}	4.4	$^{+11.2}_{-10.6}$	17
40–120	340–400	0.35–0.75	3.515×10^{1}	3.7	$^{+10.4}_{-9.5}$	18
40–120	340–400	0.75–1.15	3.057×10^{1}	4.2	$^{+13.5}_{-11.5}$	19
40–120	340–400	1.15–2.50	1.590×10^{1}	3.0	$^{+10.2}_{-10.6}$	20
40–120	400–500	0.00–0.35	7.104×10^{1}	2.0	$^{+10.3}_{-9.7}$	21
40–120	400–500	0.35–0.75	6.542×10^{1}	1.7	$^{+9.9}_{-9.0}$	22
40–120	400–500	0.75–1.15	5.396×10^{1}	2.0	$^{+10.9}_{-9.3}$	23
40–120	400–500	1.15–2.50	2.269×10^{1}	1.7	$^{+9.9}_{-9.3}$	24
40–120	500–650	0.00–0.35	5.538×10^{1}	2.4	$^{+9.1}_{-10.0}$	25
40–120	500–650	0.35–0.75	4.940×10^{1}	2.2	$^{+10.1}_{-9.1}$	26
40–120	500–650	0.75–1.15	3.960×10^{1}	2.8	$^{+10.7}_{-9.0}$	27
40–120	500–650	1.15–2.50	1.345×10^{1}	2.9	$^{+11.3}_{-10.6}$	28
40–120	650–1500	0.00–0.35	3.887×10^{1}	2.8	$^{+9.5}_{-7.6}$	29
40–120	650–1500	0.35–0.75	3.422×10^{1}	3.1	$^{+8.4}_{-8.2}$	30
40–120	650–1500	0.75–1.15	2.389×10^{1}	4.4	$^{+9.8}_{-9.6}$	31
40–120	650–1500	1.15–2.50	5.166×10^{0}	7.9	$^{+19.5}_{-11.4}$	32
120–500	340–400	0.00–0.35	1.465×10^{1}	9.0	$^{+13.6}_{-13.8}$	33
120–500	340–400	0.35–0.75	1.337×10^{1}	8.9	$^{+10.1}_{-11.2}$	34
120–500	340–400	0.75–1.15	1.270×10^{1}	9.0	$^{+9.8}_{-10.1}$	35
120–500	340–400	1.15–2.50	5.198×10^{0}	8.8	$^{+15.9}_{-8.7}$	36
120–500	400–500	0.00–0.35	3.093×10^{1}	4.8	$^{+9.9}_{-7.0}$	37
120–500	400–500	0.35–0.75	2.787×10^{1}	4.0	$^{+9.0}_{-6.1}$	38
120–500	400–500	0.75–1.15	2.302×10^{1}	4.9	$^{+8.6}_{-7.8}$	39
120–500	400–500	1.15–2.50	8.083×10^{0}	4.6	$^{+8.5}_{-10.1}$	40
120–500	500–650	0.00–0.35	2.502×10^{1}	4.5	$^{+6.9}_{-7.2}$	41
120–500	500–650	0.35–0.75	2.290×10^{1}	4.3	$^{+7.6}_{-7.2}$	42
120–500	500–650	0.75–1.15	1.603×10^{1}	6.1	$^{+9.5}_{-7.8}$	43
120–500	500–650	1.15–2.50	5.502×10^{0}	6.5	$^{+9.7}_{-11.2}$	44
120–500	650–1500	0.00–0.35	2.453×10^{1}	2.6	$^{+6.4}_{-6.1}$	45
120–500	650–1500	0.35–0.75	1.985×10^{1}	3.6	$^{+7.4}_{-6.2}$	46
120–500	650–1500	0.75–1.15	1.389×10^{1}	5.1	$^{+5.6}_{-7.8}$	47
120–500	650–1500	1.15–2.50	3.214×10^{0}	8.3	$^{+10.0}_{-8.4}$	48

Table C.26: Values for each bin of the $[p_T(t\bar{t}),M(t\bar{t}),y(t\bar{t})]$ absolute parton level cross section. The table includes also the binning scheme used in the measurement as well as the values for the statistical and systematic uncertainty.

$p_{\mathrm{T}}(\mathrm{t\bar{t}})$ [GeV]	$m(\mathrm{t\bar{t}})$ [GeV]	$y(\mathrm{t\bar{t}})$	$\frac{1}{\sigma(\mathrm{tt})}\frac{\mathrm{d}\sigma}{\mathrm{d}y(\mathrm{tt})}$	stat. [%]	syst. [%]	bin
0–40	340–400	0.00–0.35	9.514×10^{-2}	2.0	$^{+7.2}_{-7.0}$	1
0–40	340–400	0.35–0.75	8.759×10^{-2}	1.8	$^{+6.7}_{-7.5}$	2
0–40	340–400	0.75–1.15	7.235×10^{-2}	2.1	$^{+7.5}_{-9.4}$	3
0–40	340–400	1.15–2.50	1.880×10^{-2}	2.4	$^{+8.8}_{-9.0}$	4
0–40	400–500	0.00–0.35	1.436×10^{-1}	1.2	$^{+3.7}_{-4.1}$	5
0–40	400–500	0.35–0.75	1.273×10^{-1}	1.0	$^{+3.4}_{-4.1}$	6
0–40	400–500	0.75–1.15	9.902×10^{-2}	1.3	$^{+3.3}_{-4.2}$	7
0–40	400–500	1.15–2.50	2.165×10^{-2}	2.0	$^{+4.0}_{-3.6}$	8
0–40	500–650	0.00–0.35	1.079×10^{-1}	1.5	$^{+4.3}_{-4.1}$	9
0–40	500–650	0.35–0.75	9.137×10^{-2}	1.4	$^{+4.9}_{-3.8}$	10
0–40	500–650	0.75–1.15	6.463×10^{-2}	1.9	$^{+4.4}_{-5.9}$	11
0–40	500–650	1.15–2.50	1.169×10^{-2}	3.0	$^{+4.6}_{-7.3}$	12
0–40	650–1500	0.00–0.35	7.172×10^{-2}	1.7	$^{+4.1}_{-5.7}$	13
0–40	650–1500	0.35–0.75	5.370×10^{-2}	2.1	$^{+4.5}_{-4.7}$	14
0–40	650–1500	0.75–1.15	2.910×10^{-2}	3.4	$^{+5.2}_{-4.9}$	15
0–40	650–1500	1.15–2.50	3.657×10^{-3}	5.9	$^{+6.4}_{-11.2}$	16
40–120	340–400	0.00–0.35	6.400×10^{-2}	2.9	$^{+7.3}_{-7.1}$	17
40–120	340–400	0.35–0.75	5.946×10^{-2}	2.3	$^{+6.4}_{-6.4}$	18
40–120	340–400	0.75–1.15	4.836×10^{-2}	2.9	$^{+7.8}_{-7.2}$	19
40–120	340–400	1.15–2.50	1.343×10^{-2}	3.3	$^{+7.9}_{-7.8}$	20
40–120	400–500	0.00–0.35	1.116×10^{-1}	1.4	$^{+5.5}_{-5.6}$	21
40–120	400–500	0.35–0.75	1.002×10^{-1}	1.2	$^{+5.2}_{-5.2}$	22
40–120	400–500	0.75–1.15	7.423×10^{-2}	1.6	$^{+6.4}_{-5.3}$	23
40–120	400–500	1.15–2.50	1.551×10^{-2}	2.4	$^{+9.0}_{-8.5}$	24
40–120	500–650	0.00–0.35	9.228×10^{-2}	1.7	$^{+5.4}_{-6.0}$	25
40–120	500–650	0.35–0.75	7.808×10^{-2}	1.5	$^{+6.0}_{-5.3}$	26
40–120	500–650	0.75–1.15	5.297×10^{-2}	2.2	$^{+6.7}_{-5.1}$	27
40–120	500–650	1.15–2.50	9.251×10^{-3}	3.9	$^{+7.5}_{-6.6}$	28
40–120	650–1500	0.00–0.35	6.418×10^{-2}	2.1	$^{+5.4}_{-4.1}$	29
40–120	650–1500	0.35–0.75	5.021×10^{-2}	2.4	$^{+5.2}_{-4.9}$	30
40–120	650–1500	0.75–1.15	2.704×10^{-2}	3.9	$^{+5.0}_{-6.2}$	31
40–120	650–1500	1.15–2.50	2.928×10^{-3}	9.0	$^{+16.1}_{-7.7}$	32
120–500	340–400	0.00–0.35	2.232×10^{-2}	6.5	$^{+10.2}_{-11.3}$	33
120–500	340–400	0.35–0.75	2.022×10^{-2}	6.5	$^{+9.6}_{-9.8}$	34
120–500	340–400	0.75–1.15	1.776×10^{-2}	7.0	$^{+8.4}_{-8.3}$	35
120–500	340–400	1.15–2.50	4.399×10^{-3}	8.5	$^{+13.4}_{-7.5}$	36
120–500	400–500	0.00–0.35	4.515×10^{-2}	3.5	$^{+5.9}_{-2.8}$	37
120–500	400–500	0.35–0.75	4.037×10^{-2}	3.0	$^{+4.7}_{-2.7}$	38
120–500	400–500	0.75–1.15	3.057×10^{-2}	3.9	$^{+5.0}_{-4.8}$	39
120–500	400–500	1.15–2.50	6.321×10^{-3}	6.4	$^{+6.2}_{-8.8}$	40
120–500	500–650	0.00–0.35	4.168×10^{-2}	3.3	$^{+3.1}_{-4.5}$	41
120–500	500–650	0.35–0.75	3.582×10^{-2}	3.2	$^{+5.2}_{-4.2}$	42
120–500	500–650	0.75–1.15	2.271×10^{-2}	4.7	$^{+6.1}_{-4.8}$	43
120–500	500–650	1.15–2.50	4.179×10^{-3}	7.6	$^{+8.0}_{-7.8}$	44
120–500	650–1500	0.00–0.35	3.949×10^{-2}	2.3	$^{+3.6}_{-3.0}$	45
120–500	650–1500	0.35–0.75	2.965×10^{-2}	3.0	$^{+3.8}_{-3.2}$	46
120–500	650–1500	0.75–1.15	1.616×10^{-2}	4.6	$^{+3.0}_{-5.4}$	47
120–500	650–1500	1.15–2.50	2.075×10^{-3}	8.2	$^{+8.0}_{-6.8}$	48

Table C.27: Values for each bin of the $[p_{\mathrm{T}}(\mathrm{t\bar{t}}),M(\mathrm{t\bar{t}}),y(\mathrm{t\bar{t}})]$ normalized particle level cross section. The table includes also the binning scheme used in the measurement as well as the values for the statistical and systematic uncertainty.

$p_{\mathrm{T}}(\mathrm{t\bar{t}})$ [GeV]	$m(\mathrm{t\bar{t}})$ [GeV]	$y(\mathrm{t\bar{t}})$	$\frac{1}{\sigma(\mathrm{t\bar{t}})}\frac{\mathrm{d}\sigma}{\mathrm{d}y(\mathrm{t\bar{t}})}$	stat. [%]	syst. [%]	bin
0–40	340–400	0.00–0.35	1.122×10^{0}	2.0	$^{+7.3}_{-7.2}$	1
0–40	340–400	0.35–0.75	1.033×10^{0}	1.8	$^{+7.0}_{-7.6}$	2
0–40	340–400	0.75–1.15	8.532×10^{-1}	2.1	$^{+7.5}_{-8.9}$	3
0–40	340–400	1.15–2.50	2.217×10^{-1}	2.5	$^{+8.6}_{-8.6}$	4
0–40	400–500	0.00–0.35	1.694×10^{0}	1.2	$^{+5.6}_{-5.9}$	5
0–40	400–500	0.35–0.75	1.502×10^{0}	1.0	$^{+5.4}_{-6.0}$	6
0–40	400–500	0.75–1.15	1.168×10^{0}	1.3	$^{+5.3}_{-5.8}$	7
0–40	400–500	1.15–2.50	2.553×10^{-1}	2.0	$^{+6.6}_{-5.8}$	8
0–40	500–650	0.00–0.35	1.273×10^{0}	1.5	$^{+6.4}_{-6.0}$	9
0–40	500–650	0.35–0.75	1.077×10^{0}	1.4	$^{+6.5}_{-5.8}$	10
0–40	500–650	0.75–1.15	7.622×10^{-1}	1.9	$^{+6.4}_{-7.3}$	11
0–40	500–650	1.15–2.50	1.379×10^{-1}	3.0	$^{+7.0}_{-9.1}$	12
0–40	650–1500	0.00–0.35	8.457×10^{-1}	1.7	$^{+6.0}_{-6.7}$	13
0–40	650–1500	0.35–0.75	6.332×10^{-1}	2.1	$^{+6.4}_{-6.3}$	14
0–40	650–1500	0.75–1.15	3.431×10^{-1}	3.4	$^{+7.6}_{-6.5}$	15
0–40	650–1500	1.15–2.50	4.313×10^{-2}	5.9	$^{+8.7}_{-12.3}$	16
40–120	340–400	0.00–0.35	7.548×10^{-1}	2.9	$^{+9.3}_{-8.8}$	17
40–120	340–400	0.35–0.75	7.012×10^{-1}	2.3	$^{+8.2}_{-8.4}$	18
40–120	340–400	0.75–1.15	5.703×10^{-1}	2.9	$^{+9.6}_{-9.0}$	19
40–120	340–400	1.15–2.50	1.583×10^{-1}	3.3	$^{+9.2}_{-10.2}$	20
40–120	400–500	0.00–0.35	1.316×10^{0}	1.4	$^{+8.3}_{-8.2}$	21
40–120	400–500	0.35–0.75	1.181×10^{0}	1.2	$^{+8.0}_{-7.7}$	22
40–120	400–500	0.75–1.15	8.754×10^{-1}	1.6	$^{+8.8}_{-7.9}$	23
40–120	400–500	1.15–2.50	1.829×10^{-1}	2.4	$^{+11.5}_{-10.9}$	24
40–120	500–650	0.00–0.35	1.088×10^{0}	1.7	$^{+8.0}_{-8.5}$	25
40–120	500–650	0.35–0.75	9.208×10^{-1}	1.5	$^{+8.7}_{-7.9}$	26
40–120	500–650	0.75–1.15	6.246×10^{-1}	2.2	$^{+9.6}_{-7.8}$	27
40–120	500–650	1.15–2.50	1.091×10^{-1}	3.9	$^{+10.5}_{-9.2}$	28
40–120	650–1500	0.00–0.35	7.569×10^{-1}	2.1	$^{+8.1}_{-6.8}$	29
40–120	650–1500	0.35–0.75	5.922×10^{-1}	2.4	$^{+7.9}_{-7.5}$	30
40–120	650–1500	0.75–1.15	3.189×10^{-1}	3.9	$^{+8.0}_{-8.8}$	31
40–120	650–1500	1.15–2.50	3.453×10^{-2}	9.0	$^{+18.0}_{-10.3}$	32
120–500	340–400	0.00–0.35	2.633×10^{-1}	6.5	$^{+10.2}_{-10.7}$	33
120–500	340–400	0.35–0.75	2.384×10^{-1}	6.5	$^{+9.7}_{-9.0}$	34
120–500	340–400	0.75–1.15	2.095×10^{-1}	7.0	$^{+8.7}_{-8.3}$	35
120–500	340–400	1.15–2.50	5.187×10^{-2}	8.5	$^{+13.7}_{-8.0}$	36
120–500	400–500	0.00–0.35	5.325×10^{-1}	3.5	$^{+8.2}_{-6.0}$	37
120–500	400–500	0.35–0.75	4.761×10^{-1}	3.0	$^{+7.3}_{-5.3}$	38
120–500	400–500	0.75–1.15	3.605×10^{-1}	3.9	$^{+7.8}_{-7.3}$	39
120–500	400–500	1.15–2.50	7.454×10^{-2}	6.4	$^{+9.0}_{-10.8}$	40
120–500	500–650	0.00–0.35	4.916×10^{-1}	3.3	$^{+5.8}_{-6.7}$	41
120–500	500–650	0.35–0.75	4.225×10^{-1}	3.2	$^{+7.6}_{-6.3}$	42
120–500	500–650	0.75–1.15	2.678×10^{-1}	4.7	$^{+8.6}_{-7.1}$	43
120–500	500–650	1.15–2.50	4.929×10^{-2}	7.6	$^{+10.0}_{-10.6}$	44
120–500	650–1500	0.00–0.35	4.657×10^{-1}	2.3	$^{+6.4}_{-5.6}$	45
120–500	650–1500	0.35–0.75	3.496×10^{-1}	3.0	$^{+6.7}_{-6.1}$	46
120–500	650–1500	0.75–1.15	1.906×10^{-1}	4.6	$^{+5.8}_{-7.2}$	47
120–500	650–1500	1.15–2.50	2.447×10^{-2}	8.2	$^{+10.6}_{-9.0}$	48

Table C.28: Values for each bin of the $[p_{\mathrm{T}}(\mathrm{t\bar{t}}),M(\mathrm{t\bar{t}}),y(\mathrm{t\bar{t}})]$ absolute particle level cross section. The table includes also the binning scheme used in the measurement as well as the values for the statistical and systematic uncertainty.

$m(\mathrm{t\bar{t}})$ [GeV]	$\lvert y(\mathrm{t})\rvert$	$\frac{1}{\sigma(\mathrm{t\bar{t}})}\frac{\mathrm{d}\sigma}{\mathrm{d}\lvert y(\mathrm{t})\rvert}$	stat. [%]	syst. [%]	bin
300–400	0.00–0.35	1.476×10^{-1}	1.7	$^{+5.0}_{-4.5}$	1
300–400	0.35–0.85	1.396×10^{-1}	1.2	$^{+3.3}_{-5.5}$	2
300–400	0.85–1.45	1.080×10^{-1}	1.2	$^{+4.7}_{-3.5}$	3
300–400	1.45–2.50	5.153×10^{-2}	2.2	$^{+7.3}_{-6.3}$	4
400–500	0.00–0.35	2.311×10^{-1}	0.9	$^{+2.7}_{-1.6}$	5
400–500	0.35–0.85	2.165×10^{-1}	0.7	$^{+1.6}_{-1.6}$	6
400–500	0.85–1.45	1.599×10^{-1}	0.7	$^{+2.0}_{-1.6}$	7
400–500	1.45–2.50	7.528×10^{-2}	1.0	$^{+1.7}_{-3.0}$	8
500–650	0.00–0.35	1.505×10^{-1}	1.2	$^{+2.5}_{-2.1}$	9
500–650	0.35–0.85	1.420×10^{-1}	0.9	$^{+1.9}_{-2.3}$	10
500–650	0.85–1.45	1.051×10^{-1}	1.0	$^{+1.8}_{-2.4}$	11
500–650	1.45–2.50	5.380×10^{-2}	1.3	$^{+3.4}_{-1.8}$	12
650–1500	0.00–0.35	7.538×10^{-2}	1.4	$^{+5.2}_{-5.0}$	13
650–1500	0.35–0.85	7.490×10^{-2}	1.2	$^{+4.7}_{-4.4}$	14
650–1500	0.85–1.45	7.088×10^{-2}	1.0	$^{+3.3}_{-3.8}$	15
650–1500	1.45–2.50	4.374×10^{-2}	1.1	$^{+3.4}_{-3.4}$	16

Table C.29: Values for each bin of the $[M(\mathrm{t\bar{t}}),y(t)]$ normalized parton level cross section. The table includes also the binning scheme used in the measurement as well as the values for the statistical and systematic uncertainty.

$m(\mathrm{t\bar{t}})$ [GeV]	$\lvert y(\mathrm{t})\rvert$	$\frac{1}{\sigma(\mathrm{t\bar{t}})}\frac{\mathrm{d}\sigma}{\mathrm{d}\lvert y(\mathrm{t})\rvert}$	stat. [%]	syst. [%]	bin
300–400	0.00–0.35	1.183×10^2	1.7	$^{+8.0}_{-7.2}$	1
300–400	0.35–0.85	1.119×10^2	1.2	$^{+6.5}_{-7.1}$	2
300–400	0.85–1.45	8.656×10^1	1.2	$^{+7.8}_{-6.5}$	3
300–400	1.45–2.50	4.131×10^1	2.3	$^{+11.1}_{-9.2}$	4
400–500	0.00–0.35	1.853×10^2	1.0	$^{+6.6}_{-5.4}$	5
400–500	0.35–0.85	1.735×10^2	0.7	$^{+5.5}_{-5.0}$	6
400–500	0.85–1.45	1.282×10^2	0.7	$^{+6.1}_{-5.5}$	7
400–500	1.45–2.50	6.035×10^1	1.0	$^{+5.7}_{-6.3}$	8
500–650	0.00–0.35	1.206×10^2	1.2	$^{+5.4}_{-4.9}$	9
500–650	0.35–0.85	1.138×10^2	0.9	$^{+5.1}_{-5.2}$	10
500–650	0.85–1.45	8.428×10^1	1.0	$^{+5.7}_{-5.8}$	11
500–650	1.45–2.50	4.312×10^1	1.3	$^{+6.7}_{-4.9}$	12
650–1500	0.00–0.35	6.043×10^1	1.4	$^{+6.3}_{-5.6}$	13
650–1500	0.35–0.85	6.004×10^1	1.2	$^{+5.7}_{-5.3}$	14
650–1500	0.85–1.45	5.682×10^1	1.0	$^{+4.9}_{-4.8}$	15
650–1500	1.45–2.50	3.506×10^1	1.1	$^{+5.4}_{-5.1}$	16

Table C.30: Values for each bin of the $[M(\mathrm{t\bar{t}}),y(t)]$ absolute parton level cross section. The table includes also the binning scheme used in the measurement as well as the values for the statistical and systematic uncertainty.

$m(\mathrm{t\bar{t}})$ [GeV]	$\lvert y(\mathrm{t})\rvert$	$\frac{1}{\sigma(\mathrm{t\bar{t}})}\frac{\mathrm{d}\sigma}{\mathrm{d}\lvert y(\mathrm{t})\rvert}$	stat. [%]	syst. [%]	bin
300–400	0.00–0.35	1.876×10^{-1}	1.4	$^{+4.2}_{-4.3}$	1
300–400	0.35–0.85	1.736×10^{-1}	0.9	$^{+2.7}_{-4.4}$	2
300–400	0.85–1.45	1.176×10^{-1}	1.1	$^{+4.0}_{-3.2}$	3
300–400	1.45–2.50	2.695×10^{-2}	2.6	$^{+7.4}_{-6.7}$	4
400–500	0.00–0.35	2.635×10^{-1}	0.8	$^{+2.0}_{-0.9}$	5
400–500	0.35–0.85	2.377×10^{-1}	0.5	$^{+1.2}_{-1.2}$	6
400–500	0.85–1.45	1.580×10^{-1}	0.7	$^{+1.8}_{-1.4}$	7
400–500	1.45–2.50	4.308×10^{-2}	1.5	$^{+2.6}_{-4.5}$	8
500–650	0.00–0.35	1.642×10^{-1}	1.0	$^{+2.7}_{-1.9}$	9
500–650	0.35–0.85	1.560×10^{-1}	0.8	$^{+1.7}_{-2.0}$	10
500–650	0.85–1.45	1.160×10^{-1}	0.9	$^{+1.6}_{-1.9}$	11
500–650	1.45–2.50	3.898×10^{-2}	1.4	$^{+3.5}_{-1.6}$	12
650–1500	0.00–0.35	7.497×10^{-2}	1.3	$^{+4.5}_{-4.0}$	13
650–1500	0.35–0.85	7.993×10^{-2}	1.1	$^{+4.3}_{-3.9}$	14
650–1500	0.85–1.45	8.192×10^{-2}	0.9	$^{+3.1}_{-3.3}$	15
650–1500	1.45–2.50	3.452×10^{-2}	1.1	$^{+3.3}_{-3.1}$	16

Table C.31: Values for each bin of the $[M(\mathrm{t\bar{t}}),y(t)]$ normalized particle level cross section. The table includes also the binning scheme used in the measurement as well as the values for the statistical and systematic uncertainty.

$m(\mathrm{t\bar{t}})$ [GeV]	$\lvert y(\mathrm{t})\rvert$	$\frac{1}{\sigma(\mathrm{t\bar{t}})}\frac{\mathrm{d}\sigma}{\mathrm{d}\lvert y(\mathrm{t})\rvert}$	stat. [%]	syst. [%]	bin
300–400	0.00–0.35	2.296×10^{0}	1.4	$^{+7.0}_{-6.7}$	1
300–400	0.35–0.85	2.124×10^{0}	0.9	$^{+5.6}_{-6.5}$	2
300–400	0.85–1.45	1.438×10^{0}	1.1	$^{+6.8}_{-5.8}$	3
300–400	1.45–2.50	3.298×10^{-1}	2.6	$^{+10.5}_{-9.2}$	4
400–500	0.00–0.35	3.225×10^{0}	0.8	$^{+5.6}_{-4.7}$	5
400–500	0.35–0.85	2.909×10^{0}	0.6	$^{+4.9}_{-4.7}$	6
400–500	0.85–1.45	1.934×10^{0}	0.7	$^{+5.6}_{-5.1}$	7
400–500	1.45–2.50	5.271×10^{-1}	1.5	$^{+5.7}_{-7.3}$	8
500–650	0.00–0.35	2.009×10^{0}	1.0	$^{+5.7}_{-4.9}$	9
500–650	0.35–0.85	1.908×10^{0}	0.8	$^{+5.0}_{-5.2}$	10
500–650	0.85–1.45	1.420×10^{0}	0.9	$^{+5.3}_{-5.3}$	11
500–650	1.45–2.50	4.770×10^{-1}	1.4	$^{+6.6}_{-4.8}$	12
650–1500	0.00–0.35	9.174×10^{-1}	1.3	$^{+6.4}_{-5.6}$	13
650–1500	0.35–0.85	9.781×10^{-1}	1.1	$^{+6.3}_{-5.6}$	14
650–1500	0.85–1.45	1.002×10^{0}	0.9	$^{+5.4}_{-5.0}$	15
650–1500	1.45–2.50	4.224×10^{-1}	1.1	$^{+5.9}_{-5.4}$	16

Table C.32: Values for each bin of the $[M(\mathrm{t\bar{t}}),y(t)]$ absolute particle level cross section. The table includes also the binning scheme used in the measurement as well as the values for the statistical and systematic uncertainty.

$m(\mathrm{t\bar{t}})$ [GeV]	$\lvert\Delta\eta(\mathrm{t},\bar{\mathrm{t}})\rvert$	$\frac{1}{\sigma(\mathrm{t\bar{t}})}\frac{\mathrm{d}\sigma}{\mathrm{d}\lvert\Delta\eta(\mathrm{t},\bar{\mathrm{t}})\rvert}$	stat. [%]	syst. [%]	bin
300–400	0.0–0.4	1.828×10^{-1}	2.6	$^{+5.1}_{-5.7}$	1
300–400	0.4–1.2	1.270×10^{-1}	0.8	$^{+4.2}_{-3.5}$	2
300–400	1.2–6.0	1.334×10^{-2}	2.8	$^{+7.4}_{-9.9}$	3
400–500	0.0–0.4	1.599×10^{-1}	1.6	$^{+3.0}_{-4.3}$	4
400–500	0.4–1.2	1.638×10^{-1}	0.8	$^{+2.4}_{-1.5}$	5
400–500	1.2–6.0	3.425×10^{-2}	0.7	$^{+3.5}_{-2.3}$	6
500–650	0.0–0.4	6.128×10^{-2}	2.2	$^{+4.1}_{-4.3}$	7
500–650	0.4–1.2	6.689×10^{-2}	1.4	$^{+3.6}_{-4.1}$	8
500–650	1.2–6.0	3.497×10^{-2}	0.6	$^{+1.2}_{-1.5}$	9
650–1500	0.0–0.4	1.756×10^{-2}	3.2	$^{+7.5}_{-6.1}$	10
650–1500	0.4–1.2	2.230×10^{-2}	1.8	$^{+6.5}_{-5.7}$	11
650–1500	1.2–6.0	2.731×10^{-2}	0.5	$^{+2.9}_{-3.2}$	12

Table C.33: Values for each bin of the [$M(\mathrm{t\bar{t}})$,$\Delta\eta(t,\bar{t})$] normalized parton level cross section. The table includes also the binning scheme used in the measurement as well as the values for the statistical and systematic uncertainty.

$m(\mathrm{t\bar{t}})$ [GeV]	$\lvert\Delta\eta(\mathrm{t},\bar{\mathrm{t}})\rvert$	$\frac{1}{\sigma(\mathrm{t\bar{t}})}\frac{\mathrm{d}\sigma}{\mathrm{d}\lvert\Delta\eta(\mathrm{t},\bar{\mathrm{t}})\rvert}$	stat. [%]	syst. [%]	bin
300–400	0.0–0.4	1.500×10^{2}	2.7	$^{+7.0}_{-7.4}$	1
300–400	0.4–1.2	1.042×10^{2}	0.8	$^{+6.2}_{-5.6}$	2
300–400	1.2–6.0	1.094×10^{1}	2.8	$^{+10.3}_{-12.7}$	3
400–500	0.0–0.4	1.312×10^{2}	1.6	$^{+6.9}_{-7.4}$	4
400–500	0.4–1.2	1.344×10^{2}	0.8	$^{+5.3}_{-4.1}$	5
400–500	1.2–6.0	2.810×10^{1}	0.7	$^{+7.8}_{-6.0}$	6
500–650	0.0–0.4	5.029×10^{1}	2.2	$^{+5.6}_{-5.3}$	7
500–650	0.4–1.2	5.489×10^{1}	1.4	$^{+5.7}_{-5.9}$	8
500–650	1.2–6.0	2.870×10^{1}	0.6	$^{+5.4}_{-5.1}$	9
650–1500	0.0–0.4	1.441×10^{1}	3.2	$^{+8.0}_{-6.8}$	10
650–1500	0.4–1.2	1.830×10^{1}	1.8	$^{+7.0}_{-6.3}$	11
650–1500	1.2–6.0	2.241×10^{1}	0.5	$^{+4.9}_{-4.8}$	12

Table C.34: Values for each bin of the [$M(\mathrm{t\bar{t}})$,$\Delta\eta(t,\bar{t})$] absolute parton level cross section. The table includes also the binning scheme used in the measurement as well as the values for the statistical and systematic uncertainty.

$m(\mathrm{t\bar{t}})$ [GeV]	$\lvert\Delta\eta(\mathrm{t},\bar{\mathrm{t}})\rvert$	$\frac{1}{\sigma(\mathrm{t\bar{t}})}\frac{\mathrm{d}\sigma}{\mathrm{d}\lvert\Delta\eta(\mathrm{t},\bar{\mathrm{t}})\rvert}$	stat. [%]	syst. [%]	bin
300–400	0.0–0.4	1.803×10^{-1}	2.2	$^{+4.0}_{-5.0}$	1
300–400	0.4–1.2	1.309×10^{-1}	0.7	$^{+3.3}_{-3.4}$	2
300–400	1.2–6.0	1.581×10^{-2}	2.1	$^{+6.6}_{-7.3}$	3
400–500	0.0–0.4	1.562×10^{-1}	1.5	$^{+2.8}_{-3.7}$	4
400–500	0.4–1.2	1.496×10^{-1}	0.7	$^{+1.7}_{-2.0}$	5
400–500	1.2–6.0	3.481×10^{-2}	0.6	$^{+2.5}_{-1.7}$	6
500–650	0.0–0.4	7.423×10^{-2}	1.9	$^{+3.9}_{-3.3}$	7
500–650	0.4–1.2	7.501×10^{-2}	1.2	$^{+3.0}_{-3.1}$	8
500–650	1.2–6.0	3.280×10^{-2}	0.6	$^{+1.3}_{-1.3}$	9
650–1500	0.0–0.4	2.618×10^{-2}	2.7	$^{+6.6}_{-5.1}$	10
650–1500	0.4–1.2	3.140×10^{-2}	1.5	$^{+5.6}_{-4.9}$	11
650–1500	1.2–6.0	2.400×10^{-2}	0.5	$^{+3.0}_{-3.0}$	12

Table C.35: Values for each bin of the [$M(\mathrm{t\bar{t}})$,$\Delta\eta(t,\bar{t})$] normalized particle level cross section. The table includes also the binning scheme used in the measurement as well as the values for the statistical and systematic uncertainty.

$m(\mathrm{t\bar{t}})$ [GeV]	$\lvert\Delta\eta(\mathrm{t},\bar{\mathrm{t}})\rvert$	$\frac{1}{\sigma(\mathrm{t\bar{t}})}\frac{\mathrm{d}\sigma}{\mathrm{d}\lvert\Delta\eta(\mathrm{t},\bar{\mathrm{t}})\rvert}$	stat. [%]	syst. [%]	bin
300–400	0.0–0.4	2.207×10^{0}	2.2	$^{+6.4}_{-6.5}$	1
300–400	0.4–1.2	1.603×10^{0}	0.7	$^{+5.2}_{-5.1}$	2
300–400	1.2–6.0	1.936×10^{-1}	2.2	$^{+9.6}_{-10.3}$	3
400–500	0.0–0.4	1.912×10^{0}	1.5	$^{+6.2}_{-6.7}$	4
400–500	0.4–1.2	1.832×10^{0}	0.8	$^{+4.9}_{-4.5}$	5
400–500	1.2–6.0	4.261×10^{-1}	0.6	$^{+6.2}_{-5.4}$	6
500–650	0.0–0.4	9.086×10^{-1}	1.9	$^{+5.8}_{-5.1}$	7
500–650	0.4–1.2	9.181×10^{-1}	1.2	$^{+5.7}_{-5.6}$	8
500–650	1.2–6.0	4.015×10^{-1}	0.6	$^{+5.2}_{-4.9}$	9
650–1500	0.0–0.4	3.204×10^{-1}	2.7	$^{+8.0}_{-6.8}$	10
650–1500	0.4–1.2	3.843×10^{-1}	1.5	$^{+7.1}_{-6.4}$	11
650–1500	1.2–6.0	2.938×10^{-1}	0.5	$^{+5.5}_{-5.1}$	12

Table C.36: Values for each bin of the [$M(\mathrm{t\bar{t}})$,$\Delta\eta(t,\bar{t})$] absolute particle level cross section. The table includes also the binning scheme used in the measurement as well as the values for the statistical and systematic uncertainty.

$m(\mathrm{t\bar{t}})$ [GeV]	$\lvert\Delta\phi(\mathrm{t},\bar{\mathrm{t}})\rvert$	$\frac{1}{\sigma(\mathrm{t\bar{t}})}\frac{\mathrm{d}\sigma}{\mathrm{d}\lvert\Delta\phi(\mathrm{t},\bar{\mathrm{t}})\rvert}$	stat. [%]	syst. [%]	bin
300–400	0.00–2.20	3.377×10^{-2}	1.9	$^{+9.0}_{-6.6}$	1
300–400	2.20–2.95	1.227×10^{-1}	1.0	$^{+4.2}_{-4.5}$	2
300–400	2.95–3.14	3.837×10^{-1}	1.9	$^{+12.3}_{-15.7}$	3
400–500	0.00–2.20	2.730×10^{-2}	1.8	$^{+6.9}_{-7.3}$	4
400–500	2.20–2.95	1.954×10^{-1}	0.7	$^{+4.2}_{-3.8}$	5
400–500	2.95–3.14	8.008×10^{-1}	0.7	$^{+3.3}_{-3.0}$	6
500–650	0.00–2.20	1.325×10^{-2}	2.6	$^{+6.2}_{-8.5}$	7
500–650	2.20–2.95	1.239×10^{-1}	1.1	$^{+5.3}_{-3.5}$	8
500–650	2.95–3.14	6.273×10^{-1}	0.8	$^{+3.5}_{-4.9}$	9
650–1500	0.00–2.20	8.643×10^{-3}	2.2	$^{+6.5}_{-8.1}$	10
650–1500	2.20–2.95	8.093×10^{-2}	1.1	$^{+5.9}_{-5.0}$	11
650–1500	2.95–3.14	4.090×10^{-1}	0.8	$^{+6.0}_{-5.4}$	12

Table C.37: Values for each bin of the [$M(\mathrm{t\bar{t}})$,$\Delta\phi(t,\bar{t})$] normalized parton level cross section. The table includes also the binning scheme used in the measurement as well as the values for the statistical and systematic uncertainty.

$m(\mathrm{t\bar{t}})$ [GeV]	$\lvert\Delta\phi(\mathrm{t},\bar{\mathrm{t}})\rvert$	$\frac{1}{\sigma(\mathrm{t\bar{t}})}\frac{\mathrm{d}\sigma}{\mathrm{d}\lvert\Delta\phi(\mathrm{t},\bar{\mathrm{t}})\rvert}$	stat. [%]	syst. [%]	bin
300–400	0.00–2.20	2.774×10^{1}	1.9	$^{+11.8}_{-9.1}$	1
300–400	2.20–2.95	1.008×10^{2}	1.0	$^{+7.5}_{-7.5}$	2
300–400	2.95–3.14	3.151×10^{2}	2.0	$^{+12.5}_{-15.9}$	3
400–500	0.00–2.20	2.243×10^{1}	1.8	$^{+9.5}_{-9.9}$	4
400–500	2.20–2.95	1.605×10^{2}	0.7	$^{+7.7}_{-6.6}$	5
400–500	2.95–3.14	6.577×10^{2}	0.8	$^{+5.6}_{-5.4}$	6
500–650	0.00–2.20	1.089×10^{1}	2.6	$^{+8.3}_{-9.8}$	7
500–650	2.20–2.95	1.017×10^{2}	1.1	$^{+8.3}_{-6.3}$	8
500–650	2.95–3.14	5.152×10^{2}	0.8	$^{+5.3}_{-5.8}$	9
650–1500	0.00–2.20	7.098×10^{0}	2.2	$^{+8.6}_{-9.6}$	10
650–1500	2.20–2.95	6.647×10^{1}	1.1	$^{+7.3}_{-6.7}$	11
650–1500	2.95–3.14	3.359×10^{2}	0.8	$^{+6.5}_{-5.9}$	12

Table C.38: Values for each bin of the [$M(\mathrm{t\bar{t}})$,$\Delta\phi(t,\bar{t})$] absolute parton level cross section. The table includes also the binning scheme used in the measurement as well as the values for the statistical and systematic uncertainty.

$m(\mathrm{t\bar{t}})$ [GeV]	$\lvert\Delta\phi(\mathrm{t},\bar{\mathrm{t}})\rvert$	$\frac{1}{\sigma(\mathrm{t\bar{t}})}\frac{\mathrm{d}\sigma}{\mathrm{d}\lvert\Delta\phi(\mathrm{t},\bar{\mathrm{t}})\rvert}$	stat. [%]	syst. [%]	bin
300–400	0.00–2.20	3.519×10^{-2}	1.6	$^{+7.8}_{-5.9}$	1
300–400	2.20–2.95	1.367×10^{-1}	0.8	$^{+3.1}_{-4.0}$	2
300–400	2.95–3.14	3.772×10^{-1}	1.7	$^{+11.4}_{-13.1}$	3
400–500	0.00–2.20	2.569×10^{-2}	1.6	$^{+6.7}_{-6.8}$	4
400–500	2.20–2.95	1.945×10^{-1}	0.6	$^{+3.2}_{-3.9}$	5
400–500	2.95–3.14	7.681×10^{-1}	0.7	$^{+2.9}_{-2.8}$	6
500–650	0.00–2.20	1.237×10^{-2}	2.3	$^{+5.5}_{-6.9}$	7
500–650	2.20–2.95	1.256×10^{-1}	0.9	$^{+4.3}_{-2.9}$	8
500–650	2.95–3.14	6.447×10^{-1}	0.7	$^{+3.2}_{-4.0}$	9
650–1500	0.00–2.20	6.601×10^{-3}	2.1	$^{+5.4}_{-6.4}$	10
650–1500	2.20–2.95	7.478×10^{-2}	1.0	$^{+5.4}_{-4.2}$	11
650–1500	2.95–3.14	4.324×10^{-1}	0.7	$^{+5.0}_{-4.8}$	12

Table C.39: Values for each bin of the [$M(\mathrm{t\bar{t}})$,$\Delta\phi(t,\bar{t})$] normalized particle level cross section. The table includes also the binning scheme used in the measurement as well as the values for the statistical and systematic uncertainty.

$m(\mathrm{t\bar{t}})$ [GeV]	$\lvert\Delta\phi(\mathrm{t},\bar{\mathrm{t}})\rvert$	$\frac{1}{\sigma(\mathrm{t\bar{t}})}\frac{\mathrm{d}\sigma}{\mathrm{d}\lvert\Delta\phi(\mathrm{t},\bar{\mathrm{t}})\rvert}$	stat. [%]	syst. [%]	bin
300–400	0.00–2.20	4.310×10^{-1}	1.6	$^{+10.8}_{-8.4}$	1
300–400	2.20–2.95	1.675×10^{0}	0.8	$^{+6.0}_{-6.6}$	2
300–400	2.95–3.14	4.621×10^{0}	1.7	$^{+11.9}_{-13.1}$	3
400–500	0.00–2.20	3.147×10^{-1}	1.6	$^{+9.1}_{-9.4}$	4
400–500	2.20–2.95	2.383×10^{0}	0.6	$^{+6.2}_{-6.7}$	5
400–500	2.95–3.14	9.410×10^{0}	0.7	$^{+5.1}_{-5.0}$	6
500–650	0.00–2.20	1.516×10^{-1}	2.3	$^{+7.6}_{-8.6}$	7
500–650	2.20–2.95	1.539×10^{0}	0.9	$^{+7.6}_{-5.8}$	8
500–650	2.95–3.14	7.898×10^{0}	0.7	$^{+5.4}_{-5.3}$	9
650–1500	0.00–2.20	8.086×10^{-2}	2.1	$^{+7.7}_{-8.4}$	10
650–1500	2.20–2.95	9.161×10^{-1}	1.0	$^{+7.2}_{-6.4}$	11
650–1500	2.95–3.14	5.297×10^{0}	0.7	$^{+6.2}_{-6.2}$	12

Table C.40: Values for each bin of the [$M(\mathrm{t\bar{t}})$,$\Delta\phi(t,\bar{t})$] absolute particle level cross section. The table includes also the binning scheme used in the measurement as well as the values for the statistical and systematic uncertainty.

N_{jet}	$\frac{1}{\sigma(\text{t}\bar{\text{t}})}\frac{\text{d}\sigma}{\text{d}N_{\text{jet}}}$	stat. [%]	syst. [%]	bin
0	6.417×10^{-1}	0.1	$^{+1.9}_{-1.6}$	1
1	2.575×10^{-1}	0.2	$^{+1.9}_{-2.4}$	2
2	7.517×10^{-2}	0.7	$^{+6.6}_{-7.5}$	3
2.5–3.5	1.952×10^{-2}	1.8	$^{+7.3}_{-7.7}$	4
3.5–4.5	4.791×10^{-3}	4.8	$^{+9.9}_{-12.1}$	5
4.5–8.5	3.432×10^{-4}	5.9	$^{+11.4}_{-12.2}$	6

Table C.41: Values for each bin of the N_{jet} normalized parton level cross section with $\Delta R_{(b,j)} > 0.4$ and $p_{\text{T}}^{\text{min}}_{\text{jet}} > 40\,\text{GeV}$. The table includes also the binning scheme used in the measurement as well as the values for the statistical and systematic uncertainty.

N_{jet}	$\frac{1}{\sigma(\text{t}\bar{\text{t}})}\frac{\text{d}\sigma}{\text{d}N_{\text{jet}}}$	stat. [%]	syst. [%]	bin
0	5.299×10^{2}	0.2	$^{+5.1}_{-4.7}$	1
1	2.126×10^{2}	0.3	$^{+6.1}_{-5.9}$	2
2	6.207×10^{1}	0.7	$^{+9.2}_{-9.5}$	3
2.5–3.5	1.612×10^{1}	1.8	$^{+9.7}_{-9.6}$	4
3.5–4.5	3.956×10^{0}	4.8	$^{+12.5}_{-13.9}$	5
4.5–8.5	2.834×10^{-1}	5.9	$^{+13.3}_{-13.5}$	6

Table C.42: Values for each bin of the N_{jet} absolute parton level cross section with $\Delta R_{(b,j)} > 0.4$ and $p_{\text{T}}^{\text{min}}_{\text{jet}} > 40\,\text{GeV}$. The table includes also the binning scheme used in the measurement as well as the values for the statistical and systematic uncertainty.

N_{jet}	$\frac{1}{\sigma(\text{t}\bar{\text{t}})}\frac{\text{d}\sigma}{\text{d}N_{\text{jet}}}$	stat. [%]	syst. [%]	bin
0	6.289×10^{-1}	0.1	$^{+2.0}_{-1.7}$	1
1	2.647×10^{-1}	0.2	$^{+1.9}_{-2.3}$	2
2	7.879×10^{-2}	0.6	$^{+5.6}_{-6.6}$	3
2.5–3.5	2.099×10^{-2}	1.6	$^{+7.0}_{-7.3}$	4
3.5–4.5	5.123×10^{-3}	4.1	$^{+9.5}_{-11.4}$	5
4.5–8.5	3.671×10^{-4}	5.6	$^{+11.2}_{-10.7}$	6

Table C.43: Values for each bin of the N_{jet} normalized particle level cross section with $\Delta R_{(b,j)} > 0.4$ and $p_{\text{T}}^{\text{min}}_{\text{jet}} > 40\,\text{GeV}$. The table includes also the binning scheme used in the measurement as well as the values for the statistical and systematic uncertainty.

N_{jet}	$\frac{1}{\sigma(\text{t}\bar{\text{t}})}\frac{\text{d}\sigma}{\text{d}N_{\text{jet}}}$	stat. [%]	syst. [%]	bin
0	7.761×10^{0}	0.2	$^{+4.9}_{-4.6}$	1
1	3.267×10^{0}	0.3	$^{+5.8}_{-5.7}$	2
2	9.723×10^{-1}	0.6	$^{+8.4}_{-9.0}$	3
2.5–3.5	2.590×10^{-1}	1.6	$^{+9.8}_{-9.7}$	4
3.5–4.5	6.322×10^{-2}	4.1	$^{+12.2}_{-13.4}$	5
4.5–8.5	4.530×10^{-3}	5.6	$^{+13.4}_{-12.5}$	6

Table C.44: Values for each bin of the N_{jet} absolute particle level cross section with $\Delta R_{(b,j)} > 0.4$ and $p_{\text{T}}^{\text{min}}_{\text{jet}} > 40\,\text{GeV}$. The table includes also the binning scheme used in the measurement as well as the values for the statistical and systematic uncertainty.

N_{jet}	$\frac{1}{\sigma(\text{t}\bar{\text{t}})}\frac{\text{d}\sigma}{\text{d}N_{\text{jet}}}$	stat. [%]	syst. [%]	bin
0	6.707×10^{-1}	0.1	$^{+1.7}_{-1.5}$	1
1	2.438×10^{-1}	0.2	$^{+2.1}_{-2.5}$	2
2	6.560×10^{-2}	0.7	$^{+6.4}_{-7.7}$	3
2.5–3.5	1.527×10^{-2}	2.1	$^{+7.6}_{-7.8}$	4
3.5–4.5	3.708×10^{-3}	5.4	$^{+9.9}_{-11.4}$	5
4.5–8.5	2.139×10^{-4}	8.0	$^{+15.2}_{-11.3}$	6

Table C.45: Values for each bin of the N_{jet} normalized parton level cross section with $\Delta R_{(b,j)} > 0.8$ and $p_{\text{T}}^{\text{min}}_{\text{jet}} > 40\,\text{GeV}$. The table includes also the binning scheme used in the measurement as well as the values for the statistical and systematic uncertainty.

N_{jet}	$\frac{1}{\sigma(\text{t}\bar{\text{t}})}\frac{\text{d}\sigma}{\text{d}N_{\text{jet}}}$	stat. [%]	syst. [%]	bin
0	5.539×10^{2}	0.2	$^{+5.0}_{-4.6}$	1
1	2.014×10^{2}	0.3	$^{+6.3}_{-6.0}$	2
2	5.418×10^{1}	0.7	$^{+9.0}_{-9.7}$	3
2.5–3.5	1.261×10^{1}	2.1	$^{+10.1}_{-9.9}$	4
3.5–4.5	3.062×10^{0}	5.4	$^{+12.6}_{-13.3}$	5
4.5–8.5	1.767×10^{-1}	8.0	$^{+17.4}_{-12.8}$	6

Table C.46: Values for each bin of the N_{jet} absolute parton level cross section with $\Delta R_{(b,j)} > 0.8$ and $p_{\text{T}}^{\text{min}}_{\text{jet}} > 40\,\text{GeV}$. The table includes also the binning scheme used in the measurement as well as the values for the statistical and systematic uncertainty.

N_{jet}	$\frac{1}{\sigma(\text{t}\bar{\text{t}})}\frac{\text{d}\sigma}{\text{d}N_{\text{jet}}}$	stat. [%]	syst. [%]	bin
0	6.581×10^{-1}	0.1	$^{+1.8}_{-1.5}$	1
1	2.515×10^{-1}	0.2	$^{+2.1}_{-2.5}$	2
2	6.906×10^{-2}	0.7	$^{+5.6}_{-7.0}$	3
2.5–3.5	1.643×10^{-2}	1.9	$^{+7.3}_{-7.5}$	4
3.5–4.5	3.938×10^{-3}	4.8	$^{+9.6}_{-11.1}$	5
4.5–8.5	2.276×10^{-4}	7.8	$^{+14.7}_{-10.5}$	6

Table C.47: Values for each bin of the N_{jet} normalized particle level cross section with $\Delta R_{(b,j)} > 0.8$ and $p_{\text{T}}^{\text{min}}_{\text{jet}} > 40\,\text{GeV}$. The table includes also the binning scheme used in the measurement as well as the values for the statistical and systematic uncertainty.

N_{jet}	$\frac{1}{\sigma(\text{t}\bar{\text{t}})}\frac{\text{d}\sigma}{\text{d}N_{\text{jet}}}$	stat. [%]	syst. [%]	bin
0	8.120×10^{0}	0.2	$^{+4.9}_{-4.6}$	1
1	3.103×10^{0}	0.3	$^{+6.0}_{-5.9}$	2
2	8.521×10^{-1}	0.7	$^{+8.3}_{-9.3}$	3
2.5–3.5	2.028×10^{-1}	1.9	$^{+10.2}_{-9.9}$	4
3.5–4.5	4.859×10^{-2}	4.8	$^{+12.2}_{-13.2}$	5
4.5–8.5	2.808×10^{-3}	7.8	$^{+16.9}_{-12.3}$	6

Table C.48: Values for each bin of the N_{jet} absolute particle level cross section with $\Delta R_{(b,j)} > 0.8$ and $p_{\text{T}}^{\text{min}}_{\text{jet}} > 40\,\text{GeV}$. The table includes also the binning scheme used in the measurement as well as the values for the statistical and systematic uncertainty.

N_{jet}	$\frac{1}{\sigma(\text{t}\bar{\text{t}})}\frac{\text{d}\sigma}{\text{d}N_{\text{jet}}}$	stat. [%]	syst. [%]	bin
0	8.741×10^{-1}	0.1	$^{+0.6}_{-0.6}$	1
1	1.108×10^{-1}	0.4	$^{+4.0}_{-4.0}$	2
2	1.314×10^{-2}	1.9	$^{+6.5}_{-9.1}$	3
2.5–3.5	1.653×10^{-3}	6.2	$^{+11.6}_{-16.3}$	4
3.5–8.5	6.052×10^{-5}	10.5	$^{+12.3}_{-13.8}$	5

Table C.49: Values for each bin of the N_{jet} normalized parton level cross section with $\Delta R_{(b,j)} > 0.4$ and $p_{\text{T}}^{\text{min}}_{\text{jet}} > 100\,\text{GeV}$. The table includes also the binning scheme used in the measurement as well as the values for the statistical and systematic uncertainty.

N_{jet}	$\frac{1}{\sigma(\text{t}\bar{\text{t}})}\frac{\text{d}\sigma}{\text{d}N_{\text{jet}}}$	stat. [%]	syst. [%]	bin
0	7.204×10^{2}	0.1	$^{+5.0}_{-4.6}$	1
1	9.136×10^{1}	0.4	$^{+8.2}_{-7.8}$	2
2	1.083×10^{1}	1.9	$^{+7.8}_{-10.2}$	3
2.5–3.5	1.362×10^{0}	6.2	$^{+14.1}_{-18.2}$	4
3.5–8.5	4.988×10^{-2}	10.5	$^{+13.5}_{-13.8}$	5

Table C.50: Values for each bin of the N_{jet} absolute parton level cross section with $\Delta R_{(b,j)} > 0.4$ and $p_{\text{T}}^{\text{min}}_{\text{jet}} > 100\,\text{GeV}$. The table includes also the binning scheme used in the measurement as well as the values for the statistical and systematic uncertainty.

N_{jet}	$\frac{1}{\sigma(\text{t}\bar{\text{t}})}\frac{\text{d}\sigma}{\text{d}N_{\text{jet}}}$	stat. [%]	syst. [%]	bin
0	8.660×10^{-1}	0.1	$^{+0.7}_{-0.6}$	1
1	1.176×10^{-1}	0.4	$^{+4.0}_{-4.0}$	2
2	1.420×10^{-2}	1.9	$^{+6.3}_{-9.0}$	3
2.5–3.5	1.853×10^{-3}	6.2	$^{+10.9}_{-15.6}$	4
3.5–8.5	6.644×10^{-5}	10.9	$^{+12.4}_{-12.7}$	5

Table C.51: Values for each bin of the N_{jet} normalized particle level cross section with $\Delta R_{(b,j)} > 0.4$ and $p_{\text{T}}^{\text{min}}_{\text{jet}} > 100\,\text{GeV}$. The table includes also the binning scheme used in the measurement as well as the values for the statistical and systematic uncertainty.

N_{jet}	$\frac{1}{\sigma(\text{t}\bar{\text{t}})}\frac{\text{d}\sigma}{\text{d}N_{\text{jet}}}$	stat. [%]	syst. [%]	bin
0	1.069×10^{1}	0.1	$^{+4.8}_{-4.6}$	1
1	1.452×10^{0}	0.5	$^{+7.6}_{-7.4}$	2
2	1.753×10^{-1}	1.9	$^{+7.8}_{-10.3}$	3
2.5–3.5	2.287×10^{-2}	6.2	$^{+13.3}_{-17.5}$	4
3.5–8.5	8.200×10^{-4}	10.9	$^{+13.6}_{-12.8}$	5

Table C.52: Values for each bin of the N_{jet} absolute particle level cross section with $\Delta R_{(b,j)} > 0.4$ and $p_{\text{T jet}}^{\text{min}} > 100\,\text{GeV}$. The table includes also the binning scheme used in the measurement as well as the values for the statistical and systematic uncertainty.

N_{jet}	$\frac{1}{\sigma(\text{t}\bar{\text{t}})}\frac{\text{d}\sigma}{\text{d}N_{\text{jet}}}$	stat. [%]	syst. [%]	bin
0	8.813×10^{-1}	0.1	$^{+0.6}_{-0.5}$	1
1	1.056×10^{-1}	0.4	$^{+4.1}_{-4.1}$	2
2	1.172×10^{-2}	1.9	$^{+6.2}_{-9.1}$	3
2.5–3.5	1.256×10^{-3}	7.7	$^{+14.1}_{-13.5}$	4
3.5–8.5	4.151×10^{-5}	13.0	$^{+9.1}_{-19.3}$	5

Table C.53: Values for each bin of the N_{jet} normalized parton level cross section with $\Delta R_{(b,j)} > 0.8$ and $p_{\text{T}}^{\text{min}}_{\text{jet}} > 100\,\text{GeV}$. The table includes also the binning scheme used in the measurement as well as the values for the statistical and systematic uncertainty.

N_{jet}	$\frac{1}{\sigma(\text{t}\bar{\text{t}})}\frac{\text{d}\sigma}{\text{d}N_{\text{jet}}}$	stat. [%]	syst. [%]	bin
0	7.263×10^{2}	0.1	$^{+5.0}_{-4.6}$	1
1	8.699×10^{1}	0.5	$^{+8.4}_{-7.9}$	2
2	9.661×10^{0}	1.9	$^{+7.6}_{-10.1}$	3
2.5–3.5	1.035×10^{0}	7.7	$^{+16.5}_{-15.7}$	4
3.5–8.5	3.421×10^{-2}	13.0	$^{+9.9}_{-19.6}$	5

Table C.54: Values for each bin of the N_{jet} absolute parton level cross section with $\Delta R_{(b,j)} > 0.8$ and $p_{\text{T}}^{\text{min}}_{\text{jet}} > 100\,\text{GeV}$. The table includes also the binning scheme used in the measurement as well as the values for the statistical and systematic uncertainty.

N_{jet}	$\frac{1}{\sigma(\text{t}\bar{\text{t}})}\frac{\text{d}\sigma}{\text{d}N_{\text{jet}}}$	stat. [%]	syst. [%]	bin
0	8.742×10^{-1}	0.1	$^{+0.6}_{-0.6}$	1
1	1.117×10^{-1}	0.4	$^{+4.1}_{-4.1}$	2
2	1.254×10^{-2}	1.9	$^{+5.9}_{-8.6}$	3
2.5–3.5	1.379×10^{-3}	7.4	$^{+12.8}_{-12.6}$	4
3.5–8.5	4.377×10^{-5}	13.1	$^{+8.7}_{-18.8}$	5

Table C.55: Values for each bin of the N_{jet} normalized particle level cross section with $\Delta R_{(b,j)} > 0.8$ and $p_{\text{T}}^{\text{min}}_{\text{jet}} > 100\,\text{GeV}$. The table includes also the binning scheme used in the measurement as well as the values for the statistical and systematic uncertainty.

N_{jet}	$\frac{1}{\sigma(\text{t}\bar{\text{t}})}\frac{\text{d}\sigma}{\text{d}N_{\text{jet}}}$	stat. [%]	syst. [%]	bin
0	1.079×10^{1}	0.1	$^{+4.8}_{-4.6}$	1
1	1.378×10^{0}	0.5	$^{+7.7}_{-7.5}$	2
2	1.548×10^{-1}	1.9	$^{+7.3}_{-10.0}$	3
2.5–3.5	1.702×10^{-2}	7.5	$^{+14.9}_{-14.7}$	4
3.5–8.5	5.402×10^{-4}	13.1	$^{+9.7}_{-19.3}$	5

Table C.56: Values for each bin of the N_{jet} absolute particle level cross section with $\Delta R_{(b,j)} > 0.8$ and $p_{\text{T jet}}^{\text{min}} > 100\,\text{GeV}$. The table includes also the binning scheme used in the measurement as well as the values for the statistical and systematic uncertainty.

N_{jet}	p_{T}(t) [GeV]	$\frac{1}{\sigma(\text{t}\bar{\text{t}})}\frac{\text{d}\sigma}{\text{d}p_{\text{T}}(\text{t})}$[GeV^{-1}]	stat. [%]	syst. [%]	bin
0	0–100	3.486×10^{-3}	0.2	$^{+2.1}_{-2.0}$	1
0	100–180	2.888×10^{-3}	0.3	$^{+1.9}_{-1.5}$	2
0	180–600	2.176×10^{-4}	0.6	$^{+4.6}_{-4.3}$	3
1	0–100	1.043×10^{-3}	0.6	$^{+4.0}_{-3.7}$	4
1	100–180	1.087×10^{-3}	0.7	$^{+2.9}_{-3.8}$	5
1	180–600	1.268×10^{-4}	0.8	$^{+2.2}_{-2.6}$	6
≥ 2	0–100	2.734×10^{-4}	2.1	$^{+11.1}_{-10.4}$	7
≥ 2	100–180	3.732×10^{-4}	1.9	$^{+6.1}_{-9.3}$	8
≥ 2	180–600	6.476×10^{-5}	1.1	$^{+4.3}_{-5.4}$	9

Table C.57: Values for each bin of the [N_{jet},$p_{\text{T}}(t)$] normalized parton level cross section. The table includes also the binning scheme used in the measurement as well as the values for the statistical and systematic uncertainty.

N_{jet}	p_{T}(t) [GeV]	$\frac{1}{\sigma(\text{t}\bar{\text{t}})}\frac{\text{d}\sigma}{\text{d}p_{\text{T}}(\text{t})}$[GeV^{-1}]	stat. [%]	syst. [%]	bin
0	0–100	2.884×10^{0}	0.3	$^{+5.8}_{-5.4}$	1
0	100–180	2.389×10^{0}	0.3	$^{+4.9}_{-4.4}$	2
0	180–600	1.800×10^{-1}	0.6	$^{+5.5}_{-4.9}$	3
1	0–100	8.627×10^{-1}	0.7	$^{+8.1}_{-7.4}$	4
1	100–180	8.988×10^{-1}	0.7	$^{+6.3}_{-6.5}$	5
1	180–600	1.049×10^{-1}	0.8	$^{+5.3}_{-5.2}$	6
≥ 2	0–100	2.261×10^{-1}	2.1	$^{+13.1}_{-11.7}$	7
≥ 2	100–180	3.087×10^{-1}	1.9	$^{+8.7}_{-11.3}$	8
≥ 2	180–600	5.357×10^{-2}	1.1	$^{+7.5}_{-7.9}$	9

Table C.58: Values for each bin of the [N_{jet},$p_{\text{T}}(t)$] absolute parton level cross section. The table includes also the binning scheme used in the measurement as well as the values for the statistical and systematic uncertainty.

N_{jet}	$p_{\text{T}}(\text{t})$ [GeV]	$\frac{1}{\sigma(\text{t}\bar{\text{t}})}\frac{\text{d}\sigma}{\text{d}p_{\text{T}}(\text{t})}$[GeV^{-1}]	stat. [%]	syst. [%]	bin
0	0–100	3.134×10^{-3}	0.3	$^{+2.2}_{-2.1}$	1
0	100–180	2.902×10^{-3}	0.3	$^{+1.9}_{-1.4}$	2
0	180–600	2.687×10^{-4}	0.5	$^{+3.9}_{-3.6}$	3
1	0–100	9.773×10^{-4}	0.6	$^{+4.0}_{-3.7}$	4
1	100–180	1.123×10^{-3}	0.6	$^{+2.6}_{-3.5}$	5
1	180–600	1.530×10^{-4}	0.7	$^{+2.0}_{-2.4}$	6
≥ 2	0–100	2.650×10^{-4}	2.0	$^{+10.1}_{-9.3}$	7
≥ 2	100–180	3.870×10^{-4}	1.8	$^{+5.7}_{-8.7}$	8
≥ 2	180–600	7.688×10^{-5}	1.1	$^{+4.1}_{-5.1}$	9

Table C.59: Values for each bin of the [N_{jet},$p_{\text{T}}(t)$] normalized particle level cross section. The table includes also the binning scheme used in the measurement as well as the values for the statistical and systematic uncertainty.

N_{jet}	$p_{\text{T}}(\text{t})$ [GeV]	$\frac{1}{\sigma(\text{t}\bar{\text{t}})}\frac{\text{d}\sigma}{\text{d}p_{\text{T}}(\text{t})}$[GeV^{-1}]	stat. [%]	syst. [%]	bin
0	0–100	3.848×10^{-2}	0.3	$^{+5.6}_{-5.3}$	1
0	100–180	3.563×10^{-2}	0.3	$^{+4.6}_{-4.2}$	2
0	180–600	3.300×10^{-3}	0.5	$^{+5.2}_{-4.8}$	3
1	0–100	1.200×10^{-2}	0.7	$^{+7.9}_{-7.1}$	4
1	100–180	1.380×10^{-2}	0.6	$^{+5.7}_{-6.3}$	5
1	180–600	1.879×10^{-3}	0.7	$^{+5.1}_{-5.3}$	6
≥ 2	0–100	3.255×10^{-3}	2.1	$^{+12.3}_{-11.2}$	7
≥ 2	100–180	4.752×10^{-3}	1.8	$^{+8.1}_{-10.9}$	8
≥ 2	180–600	9.440×10^{-4}	1.1	$^{+7.4}_{-7.9}$	9

Table C.60: Values for each bin of the [N_{jet},$p_{\text{T}}(t)$] absolute particle level cross section. The table includes also the binning scheme used in the measurement as well as the values for the statistical and systematic uncertainty.

N_{jet}	$\lvert y(\text{t})\rvert$	$\frac{1}{\sigma(\text{t}\bar{\text{t}})}\frac{\text{d}\sigma}{\text{d}\lvert y(\text{t})\rvert}$	stat. [%]	syst. [%]	bin
0	0.00–0.35	3.995×10^{-1}	0.5	$^{+2.4}_{-2.5}$	1
0	0.35–0.85	3.755×10^{-1}	0.4	$^{+1.9}_{-2.2}$	2
0	0.85–1.45	2.977×10^{-1}	0.4	$^{+2.1}_{-1.3}$	3
0	1.45–2.50	1.544×10^{-1}	0.6	$^{+2.3}_{-1.7}$	4
1	0.00–0.35	1.500×10^{-1}	1.1	$^{+2.7}_{-3.2}$	5
1	0.35–0.85	1.430×10^{-1}	0.8	$^{+2.4}_{-2.6}$	6
1	0.85–1.45	1.094×10^{-1}	0.8	$^{+3.0}_{-3.1}$	7
1	1.45–2.50	5.404×10^{-2}	1.1	$^{+2.4}_{-3.6}$	8
≥ 2	0.00–0.35	5.509×10^{-2}	1.9	$^{+7.1}_{-6.6}$	9
≥ 2	0.35–0.85	5.190×10^{-2}	1.7	$^{+4.6}_{-8.2}$	10
≥ 2	0.85–1.45	3.850×10^{-2}	1.8	$^{+6.9}_{-8.3}$	11
≥ 2	1.45–2.50	1.610×10^{-2}	2.5	$^{+9.2}_{-8.7}$	12

Table C.61: Values for each bin of the [N_{jet},$y(t)$] normalized parton level cross section. The table includes also the binning scheme used in the measurement as well as the values for the statistical and systematic uncertainty.

N_{jet}	$\lvert y(\text{t})\rvert$	$\frac{1}{\sigma(\text{t}\bar{\text{t}})}\frac{\text{d}\sigma}{\text{d}\lvert y(\text{t})\rvert}$	stat. [%]	syst. [%]	bin
0	0.00–0.35	3.222×10^{2}	0.6	$^{+5.5}_{-5.0}$	1
0	0.35–0.85	3.029×10^{2}	0.4	$^{+4.9}_{-4.6}$	2
0	0.85–1.45	2.402×10^{2}	0.4	$^{+5.2}_{-4.7}$	3
0	1.45–2.50	1.246×10^{2}	0.6	$^{+5.6}_{-5.0}$	4
1	0.00–0.35	1.210×10^{2}	1.1	$^{+6.5}_{-6.3}$	5
1	0.35–0.85	1.154×10^{2}	0.8	$^{+6.2}_{-5.7}$	6
1	0.85–1.45	8.824×10^{1}	0.8	$^{+6.6}_{-6.2}$	7
1	1.45–2.50	4.359×10^{1}	1.2	$^{+6.6}_{-6.9}$	8
≥ 2	0.00–0.35	4.444×10^{1}	1.9	$^{+9.7}_{-8.6}$	9
≥ 2	0.35–0.85	4.186×10^{1}	1.7	$^{+7.4}_{-10.2}$	10
≥ 2	0.85–1.45	3.106×10^{1}	1.8	$^{+9.5}_{-10.2}$	11
≥ 2	1.45–2.50	1.298×10^{1}	2.5	$^{+11.6}_{-10.7}$	12

Table C.62: Values for each bin of the [N_{jet},$y(t)$] absolute parton level cross section. The table includes also the binning scheme used in the measurement as well as the values for the statistical and systematic uncertainty.

N_{jet}	$\lvert y(\text{t})\rvert$	$\frac{1}{\sigma(\text{t}\bar{\text{t}})}\frac{\text{d}\sigma}{\text{d}\lvert y(\text{t})\rvert}$	stat. [%]	syst. [%]	bin
0	0.00–0.35	4.501×10^{-1}	0.5	$^{+2.4}_{-2.3}$	1
0	0.35–0.85	4.199×10^{-1}	0.3	$^{+1.8}_{-2.1}$	2
0	0.85–1.45	3.136×10^{-1}	0.3	$^{+2.1}_{-1.3}$	3
0	1.45–2.50	9.750×10^{-2}	0.6	$^{+2.4}_{-1.8}$	4
1	0.00–0.35	1.736×10^{-1}	1.0	$^{+2.4}_{-2.9}$	5
1	0.35–0.85	1.638×10^{-1}	0.7	$^{+2.2}_{-2.6}$	6
1	0.85–1.45	1.186×10^{-1}	0.8	$^{+2.8}_{-2.8}$	7
1	1.45–2.50	3.608×10^{-2}	1.2	$^{+2.8}_{-3.9}$	8
≥ 2	0.00–0.35	6.434×10^{-2}	1.8	$^{+6.7}_{-6.0}$	9
≥ 2	0.35–0.85	6.002×10^{-2}	1.6	$^{+4.4}_{-7.7}$	10
≥ 2	0.85–1.45	4.297×10^{-2}	1.7	$^{+6.3}_{-7.5}$	11
≥ 2	1.45–2.50	1.143×10^{-2}	2.6	$^{+8.8}_{-8.0}$	12

Table C.63: Values for each bin of the $[N_{\text{jet}},y(t)]$ normalized particle level cross section. The table includes also the binning scheme used in the measurement as well as the values for the statistical and systematic uncertainty.

N_{jet}	$\lvert y(\text{t})\rvert$	$\frac{1}{\sigma(\text{t}\bar{\text{t}})}\frac{\text{d}\sigma}{\text{d}\lvert y(\text{t})\rvert}$	stat. [%]	syst. [%]	bin
0	0.00–0.35	5.541×10^{0}	0.5	$^{+5.2}_{-4.9}$	1
0	0.35–0.85	5.169×10^{0}	0.3	$^{+4.7}_{-4.6}$	2
0	0.85–1.45	3.860×10^{0}	0.4	$^{+4.9}_{-4.5}$	3
0	1.45–2.50	1.200×10^{0}	0.7	$^{+5.8}_{-5.2}$	4
1	0.00–0.35	2.137×10^{0}	1.0	$^{+6.1}_{-6.2}$	5
1	0.35–0.85	2.016×10^{0}	0.7	$^{+5.8}_{-5.7}$	6
1	0.85–1.45	1.460×10^{0}	0.8	$^{+6.3}_{-6.0}$	7
1	1.45–2.50	4.442×10^{-1}	1.2	$^{+6.3}_{-7.0}$	8
≥ 2	0.00–0.35	7.920×10^{-1}	1.8	$^{+9.3}_{-8.4}$	9
≥ 2	0.35–0.85	7.389×10^{-1}	1.6	$^{+7.1}_{-10.0}$	10
≥ 2	0.85–1.45	5.290×10^{-1}	1.7	$^{+9.0}_{-9.8}$	11
≥ 2	1.45–2.50	1.407×10^{-1}	2.6	$^{+11.5}_{-10.5}$	12

Table C.64: Values for each bin of the $[N_{\text{jet}},y(t)]$ absolute particle level cross section. The table includes also the binning scheme used in the measurement as well as the values for the statistical and systematic uncertainty.

N_{jet}	$\Delta\eta(\text{t},\bar{\text{t}})$	$\frac{1}{\sigma(\text{t}\bar{\text{t}})}\frac{\text{d}\sigma}{\text{d}\Delta\eta(\text{t},\bar{\text{t}})}$	stat. [%]	syst. [%]	bin
0	0.0–0.4	2.723×10^{-1}	0.9	$^{+6.9}_{-3.1}$	1
0	0.4–1.2	2.588×10^{-1}	0.3	$^{+2.0}_{-4.5}$	2
0	1.2–6.0	7.378×10^{-2}	0.3	$^{+1.8}_{-1.4}$	3
1	0.0–0.4	9.684×10^{-2}	1.7	$^{+8.3}_{-4.2}$	4
1	0.4–1.2	9.120×10^{-2}	0.8	$^{+2.6}_{-6.9}$	5
1	1.2–6.0	2.771×10^{-2}	0.5	$^{+3.5}_{-2.9}$	6
≥ 2	0.0–0.4	4.083×10^{-2}	3.4	$^{+4.0}_{-11.6}$	7
≥ 2	0.4–1.2	3.376×10^{-2}	2.3	$^{+9.3}_{-5.1}$	8
≥ 2	1.2–6.0	8.725×10^{-3}	1.1	$^{+7.9}_{-10.1}$	9

Table C.65: Values for each bin of the $[N_{\text{jet}},\Delta\eta(t,\bar{t})]$ normalized parton level cross section. The table includes also the binning scheme used in the measurement as well as the values for the statistical and systematic uncertainty.

N_{jet}	$\Delta\eta(\text{t},\bar{\text{t}})$	$\frac{1}{\sigma(\text{t}\bar{\text{t}})}\frac{\text{d}\sigma}{\text{d}\Delta\eta(\text{t},\bar{\text{t}})}$	stat. [%]	syst. [%]	bin
0	0.0–0.4	2.245×10^{2}	0.9	$^{+9.3}_{-4.7}$	1
0	0.4–1.2	2.133×10^{2}	0.3	$^{+3.8}_{-6.7}$	2
0	1.2–6.0	6.082×10^{1}	0.3	$^{+5.3}_{-4.5}$	3
1	0.0–0.4	7.982×10^{1}	1.7	$^{+10.7}_{-6.5}$	4
1	0.4–1.2	7.518×10^{1}	0.8	$^{+5.3}_{-8.9}$	5
1	1.2–6.0	2.284×10^{1}	0.5	$^{+7.3}_{-6.1}$	6
≥ 2	0.0–0.4	3.365×10^{1}	3.4	$^{+5.9}_{-13.2}$	7
≥ 2	0.4–1.2	2.783×10^{1}	2.3	$^{+12.0}_{-7.3}$	8
≥ 2	1.2–6.0	7.192×10^{0}	1.1	$^{+10.1}_{-11.7}$	9

Table C.66: Values for each bin of the $[N_{\text{jet}},\Delta\eta(t,\bar{t})]$ absolute parton level cross section. The table includes also the binning scheme used in the measurement as well as the values for the statistical and systematic uncertainty.

N_{jet}	$\Delta\eta(\text{t},\bar{\text{t}})$	$\frac{1}{\sigma(\text{t}\bar{\text{t}})}\frac{\text{d}\sigma}{\text{d}\Delta\eta(\text{t},\bar{\text{t}})}$	stat. [%]	syst. [%]	bin
0	0.0–0.4	2.768×10^{-1}	0.8	$^{+2.9}_{-3.1}$	1
0	0.4–1.2	2.550×10^{-1}	0.3	$^{+2.4}_{-1.7}$	2
0	1.2–6.0	7.147×10^{-2}	0.3	$^{+1.6}_{-1.5}$	3
1	0.0–0.4	1.054×10^{-1}	1.5	$^{+2.4}_{-4.7}$	4
1	0.4–1.2	9.677×10^{-2}	0.7	$^{+2.6}_{-1.7}$	5
1	1.2–6.0	2.754×10^{-2}	0.5	$^{+2.8}_{-3.1}$	6
≥ 2	0.0–0.4	4.393×10^{-2}	3.2	$^{+4.1}_{-9.1}$	7
≥ 2	0.4–1.2	3.733×10^{-2}	2.1	$^{+7.3}_{-5.4}$	8
≥ 2	1.2–6.0	8.955×10^{-3}	1.1	$^{+7.2}_{-8.7}$	9

Table C.67: Values for each bin of the $[N_{\text{jet}},\Delta\eta(t,\bar{t})]$ normalized particle level cross section. The table includes also the binning scheme used in the measurement as well as the values for the statistical and systematic uncertainty.

N_{jet}	$\Delta\eta(\text{t},\bar{\text{t}})$	$\frac{1}{\sigma(\text{t}\bar{\text{t}})}\frac{\text{d}\sigma}{\text{d}\Delta\eta(\text{t},\bar{\text{t}})}$	stat. [%]	syst. [%]	bin
0	0.0–0.4	3.409×10^{0}	0.8	$^{+5.2}_{-5.2}$	1
0	0.4–1.2	3.141×10^{0}	0.4	$^{+5.2}_{-4.8}$	2
0	1.2–6.0	8.803×10^{-1}	0.3	$^{+4.9}_{-4.6}$	3
1	0.0–0.4	1.298×10^{0}	1.5	$^{+5.4}_{-7.2}$	4
1	0.4–1.2	1.192×10^{0}	0.8	$^{+6.4}_{-5.4}$	5
1	1.2–6.0	3.392×10^{-1}	0.5	$^{+6.3}_{-6.3}$	6
≥ 2	0.0–0.4	5.411×10^{-1}	3.2	$^{+6.5}_{-11.2}$	7
≥ 2	0.4–1.2	4.598×10^{-1}	2.1	$^{+10.0}_{-7.8}$	8
≥ 2	1.2–6.0	1.103×10^{-1}	1.1	$^{+9.8}_{-10.7}$	9

Table C.68: Values for each bin of the $[N_{\text{jet}},\Delta\eta(t,\bar{t})]$ absolute particle level cross section. The table includes also the binning scheme used in the measurement as well as the values for the statistical and systematic uncertainty.

N_{jet}	$m(\text{t}\bar{\text{t}})$ [GeV]	$\frac{1}{\sigma(\text{t}\bar{\text{t}})}\frac{\text{d}\sigma}{\text{d}m(\text{t}\bar{\text{t}})}$[GeV^{-1}]	stat. [%]	syst. [%]	bin
0	300–400	1.628×10^{-3}	0.6	$^{+6.0}_{-5.9}$	1
0	400–500	2.509×10^{-3}	0.3	$^{+1.4}_{-1.2}$	2
0	500–650	1.077×10^{-3}	0.5	$^{+2.0}_{-1.4}$	3
0	650–1500	1.138×10^{-4}	0.6	$^{+3.2}_{-2.9}$	4
1	300–400	5.315×10^{-4}	1.4	$^{+3.5}_{-3.8}$	5
1	400–500	8.566×10^{-4}	0.7	$^{+3.7}_{-3.5}$	6
1	500–650	4.033×10^{-4}	1.0	$^{+3.7}_{-3.5}$	7
1	650–1500	5.226×10^{-5}	1.1	$^{+2.8}_{-3.4}$	8
≥ 2	300–400	1.655×10^{-4}	3.7	$^{+5.3}_{-7.9}$	9
≥ 2	400–500	2.887×10^{-4}	2.4	$^{+8.4}_{-7.8}$	10
≥ 2	500–650	1.439×10^{-4}	2.4	$^{+7.7}_{-7.9}$	11
≥ 2	650–1500	2.044×10^{-5}	1.7	$^{+6.1}_{-7.2}$	12

Table C.69: Values for each bin of the $[N_{\text{jet}},M(\text{t}\bar{\text{t}})]$ normalized parton level cross section. The table includes also the binning scheme used in the measurement as well as the values for the statistical and systematic uncertainty.

N_{jet}	$m(\text{t}\bar{\text{t}})$ [GeV]	$\frac{1}{\sigma(\text{t}\bar{\text{t}})}\frac{\text{d}\sigma}{\text{d}m(\text{t}\bar{\text{t}})}$[GeV^{-1}]	stat. [%]	syst. [%]	bin
0	300–400	1.336×10^{0}	0.7	$^{+7.7}_{-7.3}$	1
0	400–500	2.058×10^{0}	0.3	$^{+4.6}_{-4.2}$	2
0	500–650	8.838×10^{-1}	0.5	$^{+5.9}_{-5.4}$	3
0	650–1500	9.336×10^{-2}	0.6	$^{+5.7}_{-5.2}$	4
1	300–400	4.361×10^{-1}	1.4	$^{+6.3}_{-6.3}$	5
1	400–500	7.028×10^{-1}	0.7	$^{+7.2}_{-6.5}$	6
1	500–650	3.309×10^{-1}	1.0	$^{+7.4}_{-6.8}$	7
1	650–1500	4.288×10^{-2}	1.1	$^{+6.1}_{-6.2}$	8
≥ 2	300–400	1.358×10^{-1}	3.7	$^{+6.8}_{-9.1}$	9
≥ 2	400–500	2.369×10^{-1}	2.4	$^{+11.2}_{-10.1}$	10
≥ 2	500–650	1.181×10^{-1}	2.4	$^{+10.1}_{-9.7}$	11
≥ 2	650–1500	1.677×10^{-2}	1.7	$^{+9.0}_{-9.4}$	12

Table C.70: Values for each bin of the $[N_{\text{jet}},M(\text{t}\bar{\text{t}})]$ absolute parton level cross section. The table includes also the binning scheme used in the measurement as well as the values for the statistical and systematic uncertainty.

N_{jet}	$m(\text{t}\bar{\text{t}})$ [GeV]	$\frac{1}{\sigma(\text{t}\bar{\text{t}})}\frac{\text{d}\sigma}{\text{d}m(\text{t}\bar{\text{t}})}$[GeV^{-1}]	stat. [%]	syst. [%]	bin
0	300–400	1.693×10^{-3}	0.5	$^{+5.0}_{-5.1}$	1
0	400–500	2.382×10^{-3}	0.3	$^{+1.3}_{-1.1}$	2
0	500–650	1.063×10^{-3}	0.4	$^{+1.9}_{-1.2}$	3
0	650–1500	1.086×10^{-4}	0.5	$^{+2.9}_{-2.5}$	4
1	300–400	5.848×10^{-4}	1.1	$^{+3.0}_{-3.7}$	5
1	400–500	8.547×10^{-4}	0.7	$^{+3.3}_{-3.4}$	6
1	500–650	4.179×10^{-4}	0.9	$^{+3.6}_{-3.2}$	7
1	650–1500	5.233×10^{-5}	0.9	$^{+2.9}_{-3.2}$	8
≥ 2	300–400	1.851×10^{-4}	2.9	$^{+4.6}_{-6.8}$	9
≥ 2	400–500	2.940×10^{-4}	2.1	$^{+7.7}_{-7.3}$	10
≥ 2	500–650	1.564×10^{-4}	2.2	$^{+7.1}_{-6.9}$	11
≥ 2	650–1500	2.149×10^{-5}	1.6	$^{+5.8}_{-6.6}$	12

Table C.71: Values for each bin of the $[N_{\text{jet}},M(\text{t}\bar{\text{t}})]$ normalized particle level cross section. The table includes also the binning scheme used in the measurement as well as the values for the statistical and systematic uncertainty.

N_{jet}	$m(\text{t}\bar{\text{t}})$ [GeV]	$\frac{1}{\sigma(\text{t}\bar{\text{t}})}\frac{\text{d}\sigma}{\text{d}m(\text{t}\bar{\text{t}})}$[GeV^{-1}]	stat. [%]	syst. [%]	bin
0	300–400	2.073×10^{-2}	0.5	$^{+6.6}_{-6.5}$	1
0	400–500	2.918×10^{-2}	0.3	$^{+4.5}_{-4.4}$	2
0	500–650	1.301×10^{-2}	0.4	$^{+5.6}_{-5.2}$	3
0	650–1500	1.331×10^{-3}	0.5	$^{+5.5}_{-5.0}$	4
1	300–400	7.163×10^{-3}	1.1	$^{+5.8}_{-5.9}$	5
1	400–500	1.047×10^{-2}	0.7	$^{+6.5}_{-6.4}$	6
1	500–650	5.118×10^{-3}	0.9	$^{+7.2}_{-6.7}$	7
1	650–1500	6.409×10^{-4}	1.0	$^{+6.2}_{-6.2}$	8
≥ 2	300–400	2.267×10^{-3}	2.9	$^{+6.2}_{-8.6}$	9
≥ 2	400–500	3.601×10^{-3}	2.1	$^{+10.4}_{-9.7}$	10
≥ 2	500–650	1.915×10^{-3}	2.2	$^{+10.0}_{-9.4}$	11
≥ 2	650–1500	2.632×10^{-4}	1.6	$^{+8.9}_{-9.3}$	12

Table C.72: Values for each bin of the $[N_{\text{jet}},M(\text{t}\bar{\text{t}})]$ absolute particle level cross section. The table includes also the binning scheme used in the measurement as well as the values for the statistical and systematic uncertainty.

N_{jet}	$\lvert y(\text{t}\bar{\text{t}})\rvert$	$\frac{1}{\sigma(\text{t}\bar{\text{t}})}\frac{\text{d}\sigma}{\text{d}\lvert y(\text{t}\bar{\text{t}})\rvert}$	stat. [%]	syst. [%]	bin
0	0.00–0.35	4.666×10^{-1}	0.4	$^{+2.9}_{-1.8}$	1
0	0.35–0.75	4.296×10^{-1}	0.4	$^{+1.7}_{-2.6}$	2
0	0.75–1.15	3.480×10^{-1}	0.5	$^{+2.2}_{-1.6}$	3
0	1.15–2.50	1.444×10^{-1}	0.5	$^{+2.0}_{-1.8}$	4
1	0.00–0.35	1.808×10^{-1}	0.8	$^{+2.5}_{-3.4}$	5
1	0.35–0.75	1.625×10^{-1}	0.8	$^{+2.4}_{-2.7}$	6
1	0.75–1.15	1.286×10^{-1}	1.0	$^{+3.0}_{-3.3}$	7
1	1.15–2.50	4.839×10^{-2}	1.0	$^{+3.5}_{-3.1}$	8
≥ 2	0.00–0.35	6.660×10^{-2}	1.4	$^{+5.6}_{-8.5}$	9
≥ 2	0.35–0.75	5.627×10^{-2}	1.9	$^{+9.1}_{-5.2}$	10
≥ 2	0.75–1.15	4.626×10^{-2}	2.1	$^{+4.9}_{-9.2}$	11
≥ 2	1.15–2.50	1.574×10^{-2}	2.3	$^{+7.5}_{-10.8}$	12

Table C.73: Values for each bin of the $[N_{\text{jet}},y(\text{t}\bar{\text{t}})]$ normalized parton level cross section. The table includes also the binning scheme used in the measurement as well as the values for the statistical and systematic uncertainty.

N_{jet}	$\lvert y(\text{t}\bar{\text{t}})\rvert$	$\frac{1}{\sigma(\text{t}\bar{\text{t}})}\frac{\text{d}\sigma}{\text{d}\lvert y(\text{t}\bar{\text{t}})\rvert}$	stat. [%]	syst. [%]	bin
0	0.00–0.35	3.832×10^{2}	0.4	$^{+5.4}_{-4.8}$	1
0	0.35–0.75	3.528×10^{2}	0.4	$^{+4.8}_{-4.5}$	2
0	0.75–1.15	2.858×10^{2}	0.5	$^{+5.7}_{-5.1}$	3
0	1.15–2.50	1.186×10^{2}	0.6	$^{+5.3}_{-5.0}$	4
1	0.00–0.35	1.485×10^{2}	0.8	$^{+6.4}_{-6.4}$	5
1	0.35–0.75	1.335×10^{2}	0.8	$^{+6.0}_{-5.8}$	6
1	0.75–1.15	1.056×10^{2}	1.0	$^{+6.6}_{-6.4}$	7
1	1.15–2.50	3.974×10^{1}	1.1	$^{+7.6}_{-6.7}$	8
≥ 2	0.00–0.35	5.469×10^{1}	1.4	$^{+8.3}_{-10.4}$	9
≥ 2	0.35–0.75	4.621×10^{1}	1.9	$^{+11.6}_{-7.2}$	10
≥ 2	0.75–1.15	3.799×10^{1}	2.1	$^{+7.5}_{-11.0}$	11
≥ 2	1.15–2.50	1.293×10^{1}	2.3	$^{+10.1}_{-12.9}$	12

Table C.74: Values for each bin of the $[N_{\text{jet}},y(\text{t}\bar{\text{t}})]$ absolute parton level cross section. The table includes also the binning scheme used in the measurement as well as the values for the statistical and systematic uncertainty.

N_{jet}	$\lvert y(\text{t}\bar{\text{t}})\rvert$	$\frac{1}{\sigma(\text{t}\bar{\text{t}})}\frac{\text{d}\sigma}{\text{d}\lvert y(\text{t}\bar{\text{t}})\rvert}$	stat. [%]	syst. [%]	bin
0	0.00–0.35	5.810×10^{-1}	0.3	$^{+2.6}_{-1.7}$	1
0	0.35–0.75	5.101×10^{-1}	0.3	$^{+1.7}_{-2.3}$	2
0	0.75–1.15	3.637×10^{-1}	0.4	$^{+2.0}_{-1.4}$	3
0	1.15–2.50	7.797×10^{-2}	0.6	$^{+2.3}_{-2.1}$	4
1	0.00–0.35	2.283×10^{-1}	0.7	$^{+2.3}_{-3.0}$	5
1	0.35–0.75	1.970×10^{-1}	0.7	$^{+2.2}_{-2.5}$	6
1	0.75–1.15	1.373×10^{-1}	0.9	$^{+2.6}_{-3.1}$	7
1	1.15–2.50	2.807×10^{-2}	1.2	$^{+3.8}_{-2.9}$	8
≥ 2	0.00–0.35	8.499×10^{-2}	1.3	$^{+5.4}_{-7.7}$	9
≥ 2	0.35–0.75	6.934×10^{-2}	1.7	$^{+8.2}_{-4.9}$	10
≥ 2	0.75–1.15	4.991×10^{-2}	1.9	$^{+4.7}_{-8.4}$	11
≥ 2	1.15–2.50	9.539×10^{-3}	2.4	$^{+6.9}_{-10.3}$	12

Table C.75: Values for each bin of the $[N_{\text{jet}},y(\text{t}\bar{\text{t}})]$ normalized particle level cross section. The table includes also the binning scheme used in the measurement as well as the values for the statistical and systematic uncertainty.

N_{jet}	$\lvert y(\text{t}\bar{\text{t}})\rvert$	$\frac{1}{\sigma(\text{t}\bar{\text{t}})}\frac{\text{d}\sigma}{\text{d}\lvert y(\text{t}\bar{\text{t}})\rvert}$	stat. [%]	syst. [%]	bin
0	0.00–0.35	7.160×10^{0}	0.4	$^{+5.1}_{-4.7}$	1
0	0.35–0.75	6.287×10^{0}	0.3	$^{+4.6}_{-4.5}$	2
0	0.75–1.15	4.482×10^{0}	0.4	$^{+5.1}_{-4.7}$	3
0	1.15–2.50	9.610×10^{-1}	0.6	$^{+5.6}_{-5.4}$	4
1	0.00–0.35	2.814×10^{0}	0.7	$^{+5.9}_{-6.2}$	5
1	0.35–0.75	2.428×10^{0}	0.7	$^{+5.7}_{-5.7}$	6
1	0.75–1.15	1.693×10^{0}	0.9	$^{+6.1}_{-6.2}$	7
1	1.15–2.50	3.460×10^{-1}	1.3	$^{+7.4}_{-6.4}$	8
≥ 2	0.00–0.35	1.048×10^{0}	1.3	$^{+8.0}_{-10.0}$	9
≥ 2	0.35–0.75	8.546×10^{-1}	1.7	$^{+10.8}_{-7.3}$	10
≥ 2	0.75–1.15	6.151×10^{-1}	1.9	$^{+7.2}_{-10.5}$	11
≥ 2	1.15–2.50	1.176×10^{-1}	2.4	$^{+9.8}_{-12.8}$	12

Table C.76: Values for each bin of the $[N_{\text{jet}},y(\text{t}\bar{\text{t}})]$ absolute particle level cross section. The table includes also the binning scheme used in the measurement as well as the values for the statistical and systematic uncertainty.

N_{jet}	$p_{\text{T}}(\text{t}\bar{\text{t}})$ [GeV]	$\frac{1}{\sigma(\text{t}\bar{\text{t}})}\frac{\text{d}\sigma}{\text{d}p_{\text{T}}(\text{t}\bar{\text{t}})}$[GeV^{-1}]	stat. [%]	syst. [%]	bin
0	0–30	1.234×10^{-2}	0.3	$^{+5.0}_{-4.9}$	1
0	30–75	5.241×10^{-3}	0.3	$^{+2.8}_{-3.1}$	2
0	75–130	8.470×10^{-4}	1.9	$^{+22.0}_{-21.4}$	3
0	130–500	5.531×10^{-5}	2.1	$^{+9.7}_{-5.4}$	4
1	0–30	3.797×10^{-4}	8.1	$^{+47.1}_{-61.4}$	5
1	30–75	1.831×10^{-3}	0.9	$^{+3.4}_{-3.3}$	6
1	75–130	1.498×10^{-3}	0.9	$^{+2.8}_{-2.7}$	7
1	130–500	1.818×10^{-4}	0.8	$^{+3.1}_{-2.9}$	8
≥ 2	0–30	1.438×10^{-4}	13.9	$^{+23.7}_{-22.2}$	9
≥ 2	30–75	2.524×10^{-4}	7.5	$^{+18.0}_{-15.2}$	10
≥ 2	75–130	3.520×10^{-4}	3.2	$^{+12.0}_{-18.4}$	11
≥ 2	130–500	1.313×10^{-4}	0.8	$^{+4.2}_{-4.5}$	12

Table C.77: Values for each bin of the [N_{jet},$p_{\text{T}}(\text{t}\bar{\text{t}})$] normalized parton level cross section. The table includes also the binning scheme used in the measurement as well as the values for the statistical and systematic uncertainty.

N_{jet}	$p_{\text{T}}(\text{t}\bar{\text{t}})$ [GeV]	$\frac{1}{\sigma(\text{t}\bar{\text{t}})}\frac{\text{d}\sigma}{\text{d}p_{\text{T}}(\text{t}\bar{\text{t}})}$[GeV^{-1}]	stat. [%]	syst. [%]	bin
0	0–30	1.017×10^{1}	0.3	$^{+6.1}_{-6.0}$	1
0	30–75	4.322×10^{0}	0.4	$^{+5.8}_{-5.8}$	2
0	75–130	6.985×10^{-1}	1.9	$^{+23.8}_{-23.0}$	3
0	130–500	4.561×10^{-2}	2.1	$^{+10.1}_{-5.9}$	4
1	0–30	3.131×10^{-1}	8.1	$^{+50.7}_{-63.4}$	5
1	30–75	1.510×10^{0}	0.8	$^{+5.8}_{-5.2}$	6
1	75–130	1.235×10^{0}	0.9	$^{+5.2}_{-4.7}$	7
1	130–500	1.499×10^{-1}	0.8	$^{+5.5}_{-4.8}$	8
≥ 2	0–30	1.186×10^{-1}	13.8	$^{+23.1}_{-21.3}$	9
≥ 2	30–75	2.081×10^{-1}	7.5	$^{+19.9}_{-16.7}$	10
≥ 2	75–130	2.903×10^{-1}	3.2	$^{+14.1}_{-20.0}$	11
≥ 2	130–500	1.083×10^{-1}	0.8	$^{+7.3}_{-6.9}$	12

Table C.78: Values for each bin of the [N_{jet},$p_{\text{T}}(\text{t}\bar{\text{t}})$] absolute parton level cross section. The table includes also the binning scheme used in the measurement as well as the values for the statistical and systematic uncertainty.

N_{jet}	$p_{\text{T}}(\text{t}\bar{\text{t}})$ [GeV]	$\frac{1}{\sigma(\text{t}\bar{\text{t}})}\frac{\text{d}\sigma}{\text{d}p_{\text{T}}(\text{t}\bar{\text{t}})}$[GeV^{-1}]	stat. [%]	syst. [%]	bin
0	0–30	1.156×10^{-2}	0.3	$^{+4.8}_{-4.7}$	1
0	30–75	5.449×10^{-3}	0.3	$^{+2.6}_{-2.7}$	2
0	75–130	8.837×10^{-4}	1.5	$^{+16.6}_{-16.0}$	3
0	130–500	5.179×10^{-5}	1.8	$^{+8.2}_{-4.7}$	4
1	0–30	3.756×10^{-4}	6.9	$^{+39.5}_{-52.3}$	5
1	30–75	1.900×10^{-3}	0.8	$^{+3.1}_{-3.0}$	6
1	75–130	1.555×10^{-3}	0.8	$^{+2.4}_{-2.5}$	7
1	130–500	1.873×10^{-4}	0.8	$^{+2.9}_{-2.7}$	8
≥ 2	0–30	1.416×10^{-4}	12.3	$^{+21.2}_{-19.5}$	9
≥ 2	30–75	2.671×10^{-4}	6.2	$^{+15.4}_{-12.8}$	10
≥ 2	75–130	3.763×10^{-4}	2.8	$^{+10.6}_{-16.5}$	11
≥ 2	130–500	1.399×10^{-4}	0.8	$^{+3.7}_{-4.0}$	12

Table C.79: Values for each bin of the [N_{jet},$p_{\text{T}}(\text{t}\bar{\text{t}})$] normalized particle level cross section. The table includes also the binning scheme used in the measurement as well as the values for the statistical and systematic uncertainty.

N_{jet}	$p_{\text{T}}(\text{t}\bar{\text{t}})$ [GeV]	$\frac{1}{\sigma(\text{t}\bar{\text{t}})}\frac{\text{d}\sigma}{\text{d}p_{\text{T}}(\text{t}\bar{\text{t}})}$[GeV^{-1}]	stat. [%]	syst. [%]	bin
0	0–30	1.422×10^{-1}	0.3	$^{+5.8}_{-5.9}$	1
0	30–75	6.703×10^{-2}	0.3	$^{+5.7}_{-5.5}$	2
0	75–130	1.087×10^{-2}	1.5	$^{+18.6}_{-18.0}$	3
0	130–500	6.372×10^{-4}	1.8	$^{+8.5}_{-5.3}$	4
1	0–30	4.620×10^{-3}	6.9	$^{+42.7}_{-54.4}$	5
1	30–75	2.337×10^{-2}	0.8	$^{+6.1}_{-5.5}$	6
1	75–130	1.913×10^{-2}	0.8	$^{+4.8}_{-4.5}$	7
1	130–500	2.304×10^{-3}	0.8	$^{+5.0}_{-4.6}$	8
≥ 2	0–30	1.742×10^{-3}	12.3	$^{+21.1}_{-19.0}$	9
≥ 2	30–75	3.286×10^{-3}	6.2	$^{+17.5}_{-14.8}$	10
≥ 2	75–130	4.629×10^{-3}	2.8	$^{+12.9}_{-18.4}$	11
≥ 2	130–500	1.721×10^{-3}	0.8	$^{+6.9}_{-6.7}$	12

Table C.80: Values for each bin of the [N_{jet},$p_{\text{T}}(\text{t}\bar{\text{t}})$] absolute particle level cross section. The table includes also the binning scheme used in the measurement as well as the values for the statistical and systematic uncertainty.

N_{jet}	$m(\text{t}\bar{\text{t}})$ [GeV]	$\lvert y(\text{t}\bar{\text{t}})\rvert$	$\frac{1}{\sigma(\text{t}\bar{\text{t}})}\frac{\text{d}\sigma}{\text{d}\lvert y(\text{t}\bar{\text{t}})\rvert}$	stat. [%]	syst. [%]	bin
0	300–400	0.00–0.35	1.029×10^{-1}	1.8	$^{+7.9}_{-7.7}$	1
0	300–400	0.35–0.75	9.569×10^{-2}	1.6	$^{+6.4}_{-7.3}$	2
0	300–400	0.75–1.15	8.445×10^{-2}	1.8	$^{+7.9}_{-8.6}$	3
0	300–400	1.15–2.50	4.218×10^{-2}	1.6	$^{+6.2}_{-5.9}$	4
0	400–500	0.00–0.35	1.615×10^{-1}	1.2	$^{+3.2}_{-2.1}$	5
0	400–500	0.35–0.75	1.503×10^{-1}	1.0	$^{+3.2}_{-1.8}$	6
0	400–500	0.75–1.15	1.310×10^{-1}	1.1	$^{+2.2}_{-1.7}$	7
0	400–500	1.15–2.50	5.799×10^{-2}	0.9	$^{+2.2}_{-2.0}$	8
0	500–1500	0.00–0.35	2.090×10^{-1}	0.7	$^{+2.7}_{-2.5}$	9
0	500–1500	0.35–0.75	1.828×10^{-1}	0.8	$^{+2.9}_{-2.2}$	10
0	500–1500	0.75–1.15	1.392×10^{-1}	1.0	$^{+3.6}_{-2.9}$	11
0	500–1500	1.15–2.50	4.387×10^{-2}	1.4	$^{+6.1}_{-5.6}$	12
≥ 1	300–400	0.00–0.35	4.570×10^{-2}	3.6	$^{+4.7}_{-6.7}$	13
≥ 1	300–400	0.35–0.75	4.280×10^{-2}	3.3	$^{+5.0}_{-6.1}$	14
≥ 1	300–400	0.75–1.15	3.613×10^{-2}	3.8	$^{+4.8}_{-6.0}$	15
≥ 1	300–400	1.15–2.50	1.733×10^{-2}	3.2	$^{+4.1}_{-5.2}$	16
≥ 1	400–500	0.00–0.35	7.658×10^{-2}	2.3	$^{+7.2}_{-6.0}$	17
≥ 1	400–500	0.35–0.75	7.066×10^{-2}	1.9	$^{+6.9}_{-6.1}$	18
≥ 1	400–500	0.75–1.15	5.761×10^{-2}	2.4	$^{+8.3}_{-8.4}$	19
≥ 1	400–500	1.15–2.50	2.429×10^{-2}	2.1	$^{+5.5}_{-6.0}$	20
≥ 1	500–1500	0.00–0.35	1.200×10^{-1}	0.9	$^{+4.4}_{-5.6}$	21
≥ 1	500–1500	0.35–0.75	1.050×10^{-1}	1.1	$^{+4.6}_{-5.0}$	22
≥ 1	500–1500	0.75–1.15	7.609×10^{-2}	1.5	$^{+4.6}_{-6.4}$	23
≥ 1	500–1500	1.15–2.50	2.234×10^{-2}	2.1	$^{+6.7}_{-6.9}$	24

Table C.81: Values for each bin of the $[N_{\text{jet}}^{0,1+}, M(\text{t}\bar{\text{t}}), y(\text{t}\bar{\text{t}})]$ normalized parton level cross section. The table includes also the binning scheme used in the measurement as well as the values for the statistical and systematic uncertainty.

N_{jet}	$m(\text{t}\bar{\text{t}})$ [GeV]	$\lvert y(\text{t}\bar{\text{t}})\rvert$	$\frac{1}{\sigma(\text{t}\bar{\text{t}})}\frac{\text{d}\sigma}{\text{d}\lvert y(\text{t}\bar{\text{t}})\rvert}$	stat. [%]	syst. [%]	bin
0	300–400	0.00–0.35	8.386×10^{1}	1.8	$^{+8.1}_{-8.7}$	1
0	300–400	0.35–0.75	7.799×10^{1}	1.7	$^{+6.9}_{-8.1}$	2
0	300–400	0.75–1.15	6.883×10^{1}	1.8	$^{+8.9}_{-8.9}$	3
0	300–400	1.15–2.50	3.438×10^{1}	1.7	$^{+8.1}_{-7.9}$	4
0	400–500	0.00–0.35	1.317×10^{2}	1.2	$^{+6.8}_{-5.1}$	5
0	400–500	0.35–0.75	1.225×10^{2}	1.0	$^{+6.3}_{-4.3}$	6
0	400–500	0.75–1.15	1.068×10^{2}	1.1	$^{+5.8}_{-5.1}$	7
0	400–500	1.15–2.50	4.727×10^{1}	0.9	$^{+5.5}_{-5.1}$	8
0	500–1500	0.00–0.35	1.703×10^{2}	0.7	$^{+5.3}_{-5.1}$	9
0	500–1500	0.35–0.75	1.490×10^{2}	0.7	$^{+5.4}_{-4.8}$	10
0	500–1500	0.75–1.15	1.134×10^{2}	1.0	$^{+6.5}_{-6.1}$	11
0	500–1500	1.15–2.50	3.576×10^{1}	1.4	$^{+9.0}_{-8.1}$	12
≥ 1	300–400	0.00–0.35	3.725×10^{1}	3.6	$^{+6.1}_{-8.1}$	13
≥ 1	300–400	0.35–0.75	3.489×10^{1}	3.3	$^{+5.7}_{-6.9}$	14
≥ 1	300–400	0.75–1.15	2.944×10^{1}	3.8	$^{+6.0}_{-7.0}$	15
≥ 1	300–400	1.15–2.50	1.412×10^{1}	3.2	$^{+6.6}_{-7.9}$	16
≥ 1	400–500	0.00–0.35	6.242×10^{1}	2.3	$^{+10.1}_{-8.3}$	17
≥ 1	400–500	0.35–0.75	5.759×10^{1}	1.9	$^{+9.9}_{-8.3}$	18
≥ 1	400–500	0.75–1.15	4.695×10^{1}	2.4	$^{+11.2}_{-10.5}$	19
≥ 1	400–500	1.15–2.50	1.980×10^{1}	2.1	$^{+8.6}_{-8.4}$	20
≥ 1	500–1500	0.00–0.35	9.783×10^{1}	0.9	$^{+7.2}_{-7.7}$	21
≥ 1	500–1500	0.35–0.75	8.557×10^{1}	1.1	$^{+7.4}_{-7.3}$	22
≥ 1	500–1500	0.75–1.15	6.201×10^{1}	1.5	$^{+7.7}_{-8.7}$	23
≥ 1	500–1500	1.15–2.50	1.821×10^{1}	2.1	$^{+9.9}_{-9.8}$	24

Table C.82: Values for each bin of the $[N_{\text{jet}}^{0,1+}, M(\text{t}\bar{\text{t}}), y(\text{t}\bar{\text{t}})]$ absolute parton level cross section. The table includes also the binning scheme used in the measurement as well as the values for the statistical and systematic uncertainty.

N_{jet}	$m(\text{t}\bar{\text{t}})$ [GeV]	$\lvert y(\text{t}\bar{\text{t}})\rvert$	$\frac{1}{\sigma(\text{t}\bar{\text{t}})}\frac{\text{d}\sigma}{\text{d}\lvert y(\text{t}\bar{\text{t}})\rvert}$	stat. [%]	syst. [%]	bin
0	300–400	0.00–0.35	1.315×10^{-1}	1.3	$^{+6.3}_{-6.1}$	1
0	300–400	0.35–0.75	1.222×10^{-1}	1.1	$^{+5.3}_{-5.9}$	2
0	300–400	0.75–1.15	1.010×10^{-1}	1.3	$^{+5.8}_{-6.5}$	3
0	300–400	1.15–2.50	2.687×10^{-2}	1.6	$^{+5.8}_{-5.6}$	4
0	400–500	0.00–0.35	1.956×10^{-1}	0.8	$^{+2.0}_{-1.6}$	5
0	400–500	0.35–0.75	1.770×10^{-1}	0.7	$^{+1.9}_{-1.3}$	6
0	400–500	0.75–1.15	1.369×10^{-1}	0.8	$^{+1.5}_{-0.9}$	7
0	400–500	1.15–2.50	3.064×10^{-2}	1.3	$^{+2.6}_{-3.0}$	8
0	500–1500	0.00–0.35	2.584×10^{-1}	0.6	$^{+2.3}_{-1.8}$	9
0	500–1500	0.35–0.75	2.091×10^{-1}	0.6	$^{+2.5}_{-1.8}$	10
0	500–1500	0.75–1.15	1.304×10^{-1}	0.8	$^{+2.8}_{-2.1}$	11
0	500–1500	1.15–2.50	2.054×10^{-2}	1.4	$^{+4.3}_{-4.3}$	12
≥ 1	300–400	0.00–0.35	5.934×10^{-2}	2.5	$^{+3.7}_{-4.9}$	13
≥ 1	300–400	0.35–0.75	5.542×10^{-2}	2.2	$^{+3.6}_{-4.5}$	14
≥ 1	300–400	0.75–1.15	4.442×10^{-2}	2.6	$^{+3.4}_{-5.1}$	15
≥ 1	300–400	1.15–2.50	1.206×10^{-2}	3.0	$^{+3.5}_{-4.7}$	16
≥ 1	400–500	0.00–0.35	9.521×10^{-2}	1.6	$^{+5.4}_{-5.2}$	17
≥ 1	400–500	0.35–0.75	8.573×10^{-2}	1.3	$^{+5.2}_{-5.1}$	18
≥ 1	400–500	0.75–1.15	6.308×10^{-2}	1.8	$^{+6.4}_{-6.8}$	19
≥ 1	400–500	1.15–2.50	1.401×10^{-2}	2.7	$^{+5.7}_{-6.8}$	20
≥ 1	500–1500	0.00–0.35	1.543×10^{-1}	0.8	$^{+3.8}_{-4.5}$	21
≥ 1	500–1500	0.35–0.75	1.256×10^{-1}	0.9	$^{+4.0}_{-4.2}$	22
≥ 1	500–1500	0.75–1.15	7.567×10^{-2}	1.3	$^{+4.4}_{-5.6}$	23
≥ 1	500–1500	1.15–2.50	1.172×10^{-2}	2.1	$^{+6.7}_{-6.3}$	24

Table C.83: Values for each bin of the $[N_{\text{jet}}^{0,1+}, M(\text{t}\bar{\text{t}}), y(\text{t}\bar{\text{t}})]$ normalized particle level cross section. The table includes also the binning scheme used in the measurement as well as the values for the statistical and systematic uncertainty.

N_{jet}	$m(\text{t}\bar{\text{t}})$ [GeV]	$\lvert y(\text{t}\bar{\text{t}})\rvert$	$\frac{1}{\sigma(\text{t}\bar{\text{t}})}\frac{\text{d}\sigma}{\text{d}\lvert y(\text{t}\bar{\text{t}})\rvert}$	stat. [%]	syst. [%]	bin
0	300–400	0.00–0.35	1.611×10^{0}	1.3	$^{+7.3}_{-7.0}$	1
0	300–400	0.35–0.75	1.497×10^{0}	1.1	$^{+6.6}_{-6.7}$	2
0	300–400	0.75–1.15	1.238×10^{0}	1.3	$^{+7.1}_{-7.3}$	3
0	300–400	1.15–2.50	3.292×10^{-1}	1.6	$^{+7.7}_{-7.3}$	4
0	400–500	0.00–0.35	2.397×10^{0}	0.8	$^{+5.4}_{-5.1}$	5
0	400–500	0.35–0.75	2.168×10^{0}	0.7	$^{+4.8}_{-4.6}$	6
0	400–500	0.75–1.15	1.677×10^{0}	0.9	$^{+4.8}_{-4.4}$	7
0	400–500	1.15–2.50	3.754×10^{-1}	1.3	$^{+5.5}_{-5.9}$	8
0	500–1500	0.00–0.35	3.166×10^{0}	0.6	$^{+5.1}_{-4.7}$	9
0	500–1500	0.35–0.75	2.561×10^{0}	0.6	$^{+5.2}_{-4.7}$	10
0	500–1500	0.75–1.15	1.597×10^{0}	0.8	$^{+6.0}_{-5.2}$	11
0	500–1500	1.15–2.50	2.517×10^{-1}	1.4	$^{+7.2}_{-7.1}$	12
≥ 1	300–400	0.00–0.35	7.270×10^{-1}	2.5	$^{+5.4}_{-6.6}$	13
≥ 1	300–400	0.35–0.75	6.790×10^{-1}	2.2	$^{+5.1}_{-5.6}$	14
≥ 1	300–400	0.75–1.15	5.443×10^{-1}	2.6	$^{+5.6}_{-6.5}$	15
≥ 1	300–400	1.15–2.50	1.477×10^{-1}	3.0	$^{+6.6}_{-6.8}$	16
≥ 1	400–500	0.00–0.35	1.166×10^{0}	1.6	$^{+8.3}_{-7.9}$	17
≥ 1	400–500	0.35–0.75	1.050×10^{0}	1.3	$^{+8.1}_{-7.7}$	18
≥ 1	400–500	0.75–1.15	7.728×10^{-1}	1.8	$^{+9.2}_{-9.2}$	19
≥ 1	400–500	1.15–2.50	1.717×10^{-1}	2.7	$^{+8.4}_{-9.5}$	20
≥ 1	500–1500	0.00–0.35	1.890×10^{0}	0.8	$^{+7.0}_{-7.3}$	21
≥ 1	500–1500	0.35–0.75	1.539×10^{0}	0.9	$^{+7.2}_{-7.0}$	22
≥ 1	500–1500	0.75–1.15	9.271×10^{-1}	1.3	$^{+7.7}_{-8.4}$	23
≥ 1	500–1500	1.15–2.50	1.436×10^{-1}	2.1	$^{+10.1}_{-9.3}$	24

Table C.84: Values for each bin of the $[N_{\text{jet}}^{0,1+}, M(\text{t}\bar{\text{t}}), y(\text{t}\bar{\text{t}})]$ absolute particle level cross section. The table includes also the binning scheme used in the measurement as well as the values for the statistical and systematic uncertainty.

N_{jet}	$m(\text{t}\bar{\text{t}})$ [GeV]	$\lvert y(\text{t}\bar{\text{t}})\rvert$	$\frac{1}{\sigma(\text{t}\bar{\text{t}})}\frac{\text{d}\sigma}{\text{d}\lvert y(\text{t}\bar{\text{t}})\rvert}$	stat. [%]	syst. [%]	bin
0	300–400	0.00–0.35	1.015×10^{-1}	1.6	$^{+7.9}_{-6.3}$	1
0	300–400	0.35–0.75	9.470×10^{-2}	1.4	$^{+6.5}_{-6.5}$	2
0	300–400	0.75–1.15	8.372×10^{-2}	1.5	$^{+7.5}_{-7.8}$	3
0	300–400	1.15–2.50	4.179×10^{-2}	1.4	$^{+5.7}_{-5.2}$	4
0	400–500	0.00–0.35	1.622×10^{-1}	0.9	$^{+2.3}_{-2.1}$	5
0	400–500	0.35–0.75	1.511×10^{-1}	0.8	$^{+1.9}_{-2.2}$	6
0	400–500	0.75–1.15	1.300×10^{-1}	0.9	$^{+2.1}_{-1.3}$	7
0	400–500	1.15–2.50	5.794×10^{-2}	0.7	$^{+1.7}_{-2.0}$	8
0	500–1500	0.00–0.35	2.065×10^{-1}	0.6	$^{+2.3}_{-1.9}$	9
0	500–1500	0.35–0.75	1.814×10^{-1}	0.7	$^{+2.3}_{-1.8}$	10
0	500–1500	0.75–1.15	1.375×10^{-1}	0.9	$^{+3.1}_{-2.3}$	11
0	500–1500	1.15–2.50	4.393×10^{-2}	1.2	$^{+5.1}_{-5.0}$	12
1	300–400	0.00–0.35	3.440×10^{-2}	3.6	$^{+4.6}_{-6.0}$	13
1	300–400	0.35–0.75	3.284×10^{-2}	3.1	$^{+6.2}_{-5.0}$	14
1	300–400	0.75–1.15	2.745×10^{-2}	3.7	$^{+5.1}_{-6.2}$	15
1	300–400	1.15–2.50	1.337×10^{-2}	2.9	$^{+4.9}_{-4.8}$	16
1	400–500	0.00–0.35	5.622×10^{-2}	2.2	$^{+5.5}_{-5.5}$	17
1	400–500	0.35–0.75	5.360×10^{-2}	1.8	$^{+4.4}_{-4.3}$	18
1	400–500	0.75–1.15	4.419×10^{-2}	2.2	$^{+5.9}_{-6.3}$	19
1	400–500	1.15–2.50	1.854×10^{-2}	1.8	$^{+3.9}_{-5.0}$	20
1	500–1500	0.00–0.35	8.977×10^{-2}	1.2	$^{+2.9}_{-3.2}$	21
1	500–1500	0.35–0.75	7.722×10^{-2}	1.3	$^{+3.2}_{-2.6}$	22
1	500–1500	0.75–1.15	5.610×10^{-2}	1.7	$^{+3.1}_{-3.7}$	23
1	500–1500	1.15–2.50	1.649×10^{-2}	2.3	$^{+6.1}_{-6.3}$	24
≥ 2	300–400	0.00–0.35	1.166×10^{-2}	8.8	$^{+9.7}_{-8.6}$	25
≥ 2	300–400	0.35–0.75	1.009×10^{-2}	9.7	$^{+10.5}_{-10.1}$	26
≥ 2	300–400	0.75–1.15	9.598×10^{-3}	9.5	$^{+9.0}_{-13.4}$	27
≥ 2	300–400	1.15–2.50	4.072×10^{-3}	8.8	$^{+8.3}_{-10.3}$	28
≥ 2	400–500	0.00–0.35	2.076×10^{-2}	5.5	$^{+9.7}_{-8.8}$	29
≥ 2	400–500	0.35–0.75	1.701×10^{-2}	5.7	$^{+14.3}_{-12.3}$	30
≥ 2	400–500	0.75–1.15	1.421×10^{-2}	6.7	$^{+14.9}_{-10.7}$	31
≥ 2	400–500	1.15–2.50	5.802×10^{-3}	6.4	$^{+11.3}_{-11.3}$	32
≥ 2	500–1500	0.00–0.35	3.269×10^{-2}	2.1	$^{+6.5}_{-7.0}$	33
≥ 2	500–1500	0.35–0.75	2.964×10^{-2}	2.6	$^{+5.9}_{-7.3}$	34
≥ 2	500–1500	0.75–1.15	2.137×10^{-2}	3.4	$^{+6.3}_{-9.0}$	35
≥ 2	500–1500	1.15–2.50	6.077×10^{-3}	4.4	$^{+8.7}_{-8.0}$	36

Table C.85: Values for each bin of the $[N_{\text{jet}}^{0,1,2+}, M(\text{t}\bar{\text{t}}), y(\text{t}\bar{\text{t}})]$ normalized parton level cross section. The table includes also the binning scheme used in the measurement as well as the values for the statistical and systematic uncertainty.

N_{jet}	$m(\text{t}\bar{\text{t}})$ [GeV]	$\lvert y(\text{t}\bar{\text{t}})\rvert$	$\frac{1}{\sigma(\text{t}\bar{\text{t}})}\frac{\text{d}\sigma}{\text{d}\lvert y(\text{t}\bar{\text{t}})\rvert}$	stat. [%]	syst. [%]	bin
0	300–400	0.00–0.35	8.271×10^{1}	1.6	$^{+9.0}_{-6.9}$	1
0	300–400	0.35–0.75	7.714×10^{1}	1.4	$^{+7.7}_{-6.9}$	2
0	300–400	0.75–1.15	6.819×10^{1}	1.5	$^{+8.8}_{-8.3}$	3
0	300–400	1.15–2.50	3.404×10^{1}	1.4	$^{+8.1}_{-7.1}$	4
0	400–500	0.00–0.35	1.321×10^{2}	0.9	$^{+5.3}_{-5.7}$	5
0	400–500	0.35–0.75	1.231×10^{2}	0.8	$^{+4.5}_{-5.2}$	6
0	400–500	0.75–1.15	1.059×10^{2}	0.9	$^{+5.9}_{-4.8}$	7
0	400–500	1.15–2.50	4.719×10^{1}	0.7	$^{+4.8}_{-5.0}$	8
0	500–1500	0.00–0.35	1.682×10^{2}	0.6	$^{+5.3}_{-4.6}$	9
0	500–1500	0.35–0.75	1.477×10^{2}	0.7	$^{+5.1}_{-4.6}$	10
0	500–1500	0.75–1.15	1.120×10^{2}	0.9	$^{+6.6}_{-5.5}$	11
0	500–1500	1.15–2.50	3.578×10^{1}	1.2	$^{+7.9}_{-7.9}$	12
1	300–400	0.00–0.35	2.802×10^{1}	3.6	$^{+6.7}_{-7.4}$	13
1	300–400	0.35–0.75	2.675×10^{1}	3.1	$^{+7.1}_{-5.4}$	14
1	300–400	0.75–1.15	2.236×10^{1}	3.7	$^{+6.0}_{-7.0}$	15
1	300–400	1.15–2.50	1.089×10^{1}	2.9	$^{+7.9}_{-7.0}$	16
1	400–500	0.00–0.35	4.579×10^{1}	2.2	$^{+8.3}_{-8.8}$	17
1	400–500	0.35–0.75	4.366×10^{1}	1.8	$^{+7.6}_{-7.3}$	18
1	400–500	0.75–1.15	3.599×10^{1}	2.2	$^{+9.0}_{-9.0}$	19
1	400–500	1.15–2.50	1.511×10^{1}	1.8	$^{+7.3}_{-8.1}$	20
1	500–1500	0.00–0.35	7.312×10^{1}	1.1	$^{+6.4}_{-6.0}$	21
1	500–1500	0.35–0.75	6.290×10^{1}	1.3	$^{+6.5}_{-5.7}$	22
1	500–1500	0.75–1.15	4.570×10^{1}	1.7	$^{+6.8}_{-6.7}$	23
1	500–1500	1.15–2.50	1.343×10^{1}	2.3	$^{+10.2}_{-9.3}$	24
≥ 2	300–400	0.00–0.35	9.494×10^{0}	8.8	$^{+10.3}_{-8.6}$	25
≥ 2	300–400	0.35–0.75	8.216×10^{0}	9.7	$^{+10.9}_{-10.4}$	26
≥ 2	300–400	0.75–1.15	7.819×10^{0}	9.5	$^{+8.9}_{-13.0}$	27
≥ 2	300–400	1.15–2.50	3.317×10^{0}	8.8	$^{+10.7}_{-12.0}$	28
≥ 2	400–500	0.00–0.35	1.691×10^{1}	5.5	$^{+12.0}_{-10.4}$	29
≥ 2	400–500	0.35–0.75	1.385×10^{1}	5.7	$^{+16.8}_{-14.5}$	30
≥ 2	400–500	0.75–1.15	1.158×10^{1}	6.7	$^{+17.3}_{-12.7}$	31
≥ 2	400–500	1.15–2.50	4.726×10^{0}	6.4	$^{+13.5}_{-13.5}$	32
≥ 2	500–1500	0.00–0.35	2.663×10^{1}	2.1	$^{+9.1}_{-9.1}$	33
≥ 2	500–1500	0.35–0.75	2.414×10^{1}	2.6	$^{+8.7}_{-9.3}$	34
≥ 2	500–1500	0.75–1.15	1.740×10^{1}	3.4	$^{+9.0}_{-11.1}$	35
≥ 2	500–1500	1.15–2.50	4.950×10^{0}	4.4	$^{+11.3}_{-10.3}$	36

Table C.86: Values for each bin of the $[N_{\text{jet}}^{0,1,2+}, M(\text{t}\bar{\text{t}}), y(\text{t}\bar{\text{t}})]$ absolute parton level cross section. The table includes also the binning scheme used in the measurement as well as the values for the statistical and systematic uncertainty.

N_{jet}	$m(\text{t}\bar{\text{t}})$ [GeV]	$\lvert y(\text{t}\bar{\text{t}})\rvert$	$\frac{1}{\sigma(\text{t}\bar{\text{t}})}\frac{\text{d}\sigma}{\text{d}\lvert y(\text{t}\bar{\text{t}})\rvert}$	stat. [%]	syst. [%]	bin
0	300–400	0.00–0.35	1.307×10^{-1}	1.2	$^{+6.1}_{-5.9}$	1
0	300–400	0.35–0.75	1.216×10^{-1}	1.0	$^{+5.2}_{-5.6}$	2
0	300–400	0.75–1.15	1.004×10^{-1}	1.2	$^{+5.5}_{-6.2}$	3
0	300–400	1.15–2.50	2.679×10^{-2}	1.5	$^{+5.5}_{-5.4}$	4
0	400–500	0.00–0.35	1.955×10^{-1}	0.7	$^{+1.8}_{-1.5}$	5
0	400–500	0.35–0.75	1.770×10^{-1}	0.6	$^{+1.6}_{-1.3}$	6
0	400–500	0.75–1.15	1.364×10^{-1}	0.8	$^{+1.2}_{-0.8}$	7
0	400–500	1.15–2.50	3.061×10^{-2}	1.2	$^{+2.5}_{-2.9}$	8
0	500–1500	0.00–0.35	2.574×10^{-1}	0.5	$^{+2.1}_{-1.7}$	9
0	500–1500	0.35–0.75	2.085×10^{-1}	0.5	$^{+2.2}_{-1.7}$	10
0	500–1500	0.75–1.15	1.298×10^{-1}	0.8	$^{+2.5}_{-2.0}$	11
0	500–1500	1.15–2.50	2.050×10^{-2}	1.4	$^{+4.1}_{-4.2}$	12
1	300–400	0.00–0.35	4.517×10^{-2}	2.7	$^{+3.2}_{-5.0}$	13
1	300–400	0.35–0.75	4.287×10^{-2}	2.3	$^{+4.2}_{-4.5}$	14
1	300–400	0.75–1.15	3.400×10^{-2}	2.8	$^{+3.6}_{-4.6}$	15
1	300–400	1.15–2.50	9.181×10^{-3}	3.2	$^{+4.1}_{-4.8}$	16
1	400–500	0.00–0.35	6.974×10^{-2}	1.7	$^{+4.6}_{-4.4}$	17
1	400–500	0.35–0.75	6.407×10^{-2}	1.4	$^{+3.9}_{-3.8}$	18
1	400–500	0.75–1.15	4.748×10^{-2}	1.9	$^{+5.0}_{-5.5}$	19
1	400–500	1.15–2.50	1.040×10^{-2}	2.9	$^{+5.3}_{-6.7}$	20
1	500–1500	0.00–0.35	1.130×10^{-1}	1.0	$^{+2.6}_{-2.9}$	21
1	500–1500	0.35–0.75	9.082×10^{-2}	1.0	$^{+2.8}_{-2.5}$	22
1	500–1500	0.75–1.15	5.480×10^{-2}	1.6	$^{+3.2}_{-3.7}$	23
1	500–1500	1.15–2.50	8.578×10^{-3}	2.6	$^{+5.1}_{-5.4}$	24
≥ 2	300–400	0.00–0.35	1.500×10^{-2}	6.7	$^{+7.7}_{-5.9}$	25
≥ 2	300–400	0.35–0.75	1.304×10^{-2}	7.2	$^{+7.1}_{-7.8}$	26
≥ 2	300–400	0.75–1.15	1.152×10^{-2}	7.5	$^{+6.0}_{-11.1}$	27
≥ 2	300–400	1.15–2.50	2.925×10^{-3}	8.7	$^{+8.0}_{-8.8}$	28
≥ 2	400–500	0.00–0.35	2.553×10^{-2}	4.6	$^{+8.2}_{-8.5}$	29
≥ 2	400–500	0.35–0.75	2.080×10^{-2}	4.5	$^{+12.5}_{-10.1}$	30
≥ 2	400–500	0.75–1.15	1.576×10^{-2}	5.8	$^{+13.0}_{-9.5}$	31
≥ 2	400–500	1.15–2.50	3.480×10^{-3}	8.5	$^{+11.9}_{-12.4}$	32
≥ 2	500–1500	0.00–0.35	4.278×10^{-2}	1.9	$^{+6.0}_{-6.0}$	33
≥ 2	500–1500	0.35–0.75	3.603×10^{-2}	2.2	$^{+5.5}_{-6.7}$	34
≥ 2	500–1500	0.75–1.15	2.157×10^{-2}	3.1	$^{+6.1}_{-8.2}$	35
≥ 2	500–1500	1.15–2.50	3.281×10^{-3}	4.7	$^{+8.6}_{-7.6}$	36

Table C.87: Values for each bin of the $[N_{\text{jet}}^{0,1,2+}, M(\text{t}\bar{\text{t}}), y(\text{t}\bar{\text{t}})]$ normalized particle level cross section. The table includes also the binning scheme used in the measurement as well as the values for the statistical and systematic uncertainty.

N_{jet}	$m(\text{t}\bar{\text{t}})$ [GeV]	$\lvert y(\text{t}\bar{\text{t}})\rvert$	$\frac{1}{\sigma(\text{t}\bar{\text{t}})}\frac{\text{d}\sigma}{\text{d}\lvert y(\text{t}\bar{\text{t}})\rvert}$	stat. [%]	syst. [%]	bin
0	300–400	0.00–0.35	1.601×10^{0}	1.2	$^{+7.1}_{-6.8}$	1
0	300–400	0.35–0.75	1.489×10^{0}	1.0	$^{+6.4}_{-6.5}$	2
0	300–400	0.75–1.15	1.230×10^{0}	1.2	$^{+7.0}_{-7.1}$	3
0	300–400	1.15–2.50	3.282×10^{-1}	1.5	$^{+7.5}_{-7.2}$	4
0	400–500	0.00–0.35	2.394×10^{0}	0.8	$^{+5.3}_{-5.0}$	5
0	400–500	0.35–0.75	2.168×10^{0}	0.6	$^{+4.8}_{-4.6}$	6
0	400–500	0.75–1.15	1.671×10^{0}	0.8	$^{+4.8}_{-4.4}$	7
0	400–500	1.15–2.50	3.750×10^{-1}	1.2	$^{+5.4}_{-5.8}$	8
0	500–1500	0.00–0.35	3.153×10^{0}	0.5	$^{+5.1}_{-4.7}$	9
0	500–1500	0.35–0.75	2.554×10^{0}	0.5	$^{+5.2}_{-4.6}$	10
0	500–1500	0.75–1.15	1.590×10^{0}	0.8	$^{+5.9}_{-5.3}$	11
0	500–1500	1.15–2.50	2.511×10^{-1}	1.4	$^{+7.2}_{-7.1}$	12
1	300–400	0.00–0.35	5.534×10^{-1}	2.7	$^{+5.4}_{-6.8}$	13
1	300–400	0.35–0.75	5.251×10^{-1}	2.3	$^{+5.3}_{-5.4}$	14
1	300–400	0.75–1.15	4.165×10^{-1}	2.8	$^{+5.8}_{-6.2}$	15
1	300–400	1.15–2.50	1.125×10^{-1}	3.2	$^{+6.7}_{-6.8}$	16
1	400–500	0.00–0.35	8.543×10^{-1}	1.7	$^{+7.8}_{-7.5}$	17
1	400–500	0.35–0.75	7.849×10^{-1}	1.4	$^{+6.9}_{-6.6}$	18
1	400–500	0.75–1.15	5.817×10^{-1}	1.9	$^{+7.9}_{-8.2}$	19
1	400–500	1.15–2.50	1.273×10^{-1}	2.9	$^{+8.0}_{-9.2}$	20
1	500–1500	0.00–0.35	1.384×10^{0}	1.0	$^{+5.9}_{-6.1}$	21
1	500–1500	0.35–0.75	1.113×10^{0}	1.0	$^{+6.3}_{-5.8}$	22
1	500–1500	0.75–1.15	6.714×10^{-1}	1.6	$^{+6.8}_{-6.8}$	23
1	500–1500	1.15–2.50	1.051×10^{-1}	2.6	$^{+8.7}_{-8.5}$	24
≥ 2	300–400	0.00–0.35	1.838×10^{-1}	6.7	$^{+7.9}_{-6.6}$	25
≥ 2	300–400	0.35–0.75	1.597×10^{-1}	7.2	$^{+8.1}_{-8.9}$	26
≥ 2	300–400	0.75–1.15	1.412×10^{-1}	7.5	$^{+5.6}_{-10.9}$	27
≥ 2	300–400	1.15–2.50	3.583×10^{-2}	8.7	$^{+10.3}_{-10.8}$	28
≥ 2	400–500	0.00–0.35	3.128×10^{-1}	4.6	$^{+10.2}_{-10.3}$	29
≥ 2	400–500	0.35–0.75	2.549×10^{-1}	4.5	$^{+15.1}_{-12.2}$	30
≥ 2	400–500	0.75–1.15	1.931×10^{-1}	5.8	$^{+15.5}_{-11.6}$	31
≥ 2	400–500	1.15–2.50	4.263×10^{-2}	8.5	$^{+14.2}_{-14.6}$	32
≥ 2	500–1500	0.00–0.35	5.241×10^{-1}	1.9	$^{+8.9}_{-8.6}$	33
≥ 2	500–1500	0.35–0.75	4.414×10^{-1}	2.2	$^{+8.6}_{-9.2}$	34
≥ 2	500–1500	0.75–1.15	2.643×10^{-1}	3.1	$^{+8.9}_{-10.7}$	35
≥ 2	500–1500	1.15–2.50	4.019×10^{-2}	4.7	$^{+11.7}_{-10.4}$	36

Table C.88: Values for each bin of the $[N_{\text{jet}}^{0,1,2+}, M(\text{t}\bar{\text{t}}), y(\text{t}\bar{\text{t}})]$ absolute particle level cross section. The table includes also the binning scheme used in the measurement as well as the values for the statistical and systematic uncertainty.

N_{jet}	$m(\text{t}\bar{\text{t}})$ [GeV]	$\lvert y(\text{t}\bar{\text{t}})\rvert$	$\frac{1}{\sigma(\text{t}\bar{\text{t}})}\frac{\text{d}\sigma}{\text{d}\lvert y(\text{t}\bar{\text{t}})\rvert}$	stat. [%]	syst. [%]	bin
0	300–400	0.00–0.35	1.014×10^{-1}	1.6	$^{+7.7}_{-6.7}$	1
0	300–400	0.35–0.75	9.467×10^{-2}	1.4	$^{+6.5}_{-6.7}$	2
0	300–400	0.75–1.15	8.376×10^{-2}	1.5	$^{+7.5}_{-7.8}$	3
0	300–400	1.15–2.50	4.180×10^{-2}	1.4	$^{+5.7}_{-5.2}$	4
0	400–500	0.00–0.35	1.622×10^{-1}	0.9	$^{+2.4}_{-2.0}$	5
0	400–500	0.35–0.75	1.511×10^{-1}	0.8	$^{+2.1}_{-1.8}$	6
0	400–500	0.75–1.15	1.299×10^{-1}	0.9	$^{+1.8}_{-1.3}$	7
0	400–500	1.15–2.50	5.793×10^{-2}	0.7	$^{+1.7}_{-1.9}$	8
0	500–1500	0.00–0.35	2.065×10^{-1}	0.6	$^{+2.3}_{-1.9}$	9
0	500–1500	0.35–0.75	1.813×10^{-1}	0.7	$^{+2.3}_{-1.8}$	10
0	500–1500	0.75–1.15	1.375×10^{-1}	0.9	$^{+3.0}_{-2.3}$	11
0	500–1500	1.15–2.50	4.390×10^{-2}	1.2	$^{+5.1}_{-5.1}$	12
1	300–400	0.00–0.35	3.456×10^{-2}	3.5	$^{+4.3}_{-5.9}$	13
1	300–400	0.35–0.75	3.268×10^{-2}	3.0	$^{+5.9}_{-5.1}$	14
1	300–400	0.75–1.15	2.742×10^{-2}	3.6	$^{+5.0}_{-5.5}$	15
1	300–400	1.15–2.50	1.328×10^{-2}	2.8	$^{+4.8}_{-4.8}$	16
1	400–500	0.00–0.35	5.631×10^{-2}	2.1	$^{+5.9}_{-5.3}$	17
1	400–500	0.35–0.75	5.375×10^{-2}	1.8	$^{+4.6}_{-4.2}$	18
1	400–500	0.75–1.15	4.447×10^{-2}	2.1	$^{+5.8}_{-6.1}$	19
1	400–500	1.15–2.50	1.861×10^{-2}	1.7	$^{+3.9}_{-4.6}$	20
1	500–1500	0.00–0.35	8.954×10^{-2}	1.1	$^{+2.6}_{-3.3}$	21
1	500–1500	0.35–0.75	7.712×10^{-2}	1.2	$^{+3.0}_{-2.6}$	22
1	500–1500	0.75–1.15	5.595×10^{-2}	1.7	$^{+3.1}_{-3.7}$	23
1	500–1500	1.15–2.50	1.654×10^{-2}	2.2	$^{+5.3}_{-6.0}$	24
2	300–400	0.00–0.35	9.682×10^{-3}	9.6	$^{+9.4}_{-10.1}$	25
2	300–400	0.35–0.75	7.661×10^{-3}	11.6	$^{+14.0}_{-11.9}$	26
2	300–400	0.75–1.15	7.021×10^{-3}	11.9	$^{+9.6}_{-14.6}$	27
2	300–400	1.15–2.50	2.985×10^{-3}	10.6	$^{+8.7}_{-12.8}$	28
2	400–500	0.00–0.35	1.457×10^{-2}	7.2	$^{+11.7}_{-9.6}$	29
2	400–500	0.35–0.75	1.291×10^{-2}	6.8	$^{+14.7}_{-11.7}$	30
2	400–500	0.75–1.15	1.137×10^{-2}	7.6	$^{+14.5}_{-9.8}$	31
2	400–500	1.15–2.50	4.439×10^{-3}	7.1	$^{+10.9}_{-11.6}$	32
2	500–1500	0.00–0.35	2.503×10^{-2}	2.9	$^{+6.0}_{-5.5}$	33
2	500–1500	0.35–0.75	2.324×10^{-2}	3.2	$^{+5.9}_{-5.7}$	34
2	500–1500	0.75–1.15	1.600×10^{-2}	4.5	$^{+4.1}_{-7.1}$	35
2	500–1500	1.15–2.50	4.608×10^{-3}	5.8	$^{+8.0}_{-8.1}$	36
≥ 3	300–400	0.00–0.35	2.003×10^{-3}	34.3	$^{+35.0}_{-21.7}$	37
≥ 3	300–400	0.35–0.75	2.675×10^{-3}	27.2	$^{+34.5}_{-19.8}$	38
≥ 3	300–400	0.75–1.15	2.439×10^{-3}	26.6	$^{+19.6}_{-31.5}$	39
≥ 3	300–400	1.15–2.50	1.263×10^{-3}	19.1	$^{+17.0}_{-16.2}$	40
≥ 3	400–500	0.00–0.35	6.350×10^{-3}	12.1	$^{+11.1}_{-13.8}$	41
≥ 3	400–500	0.35–0.75	3.532×10^{-3}	21.7	$^{+18.5}_{-34.1}$	42
≥ 3	400–500	0.75–1.15	2.896×10^{-3}	25.6	$^{+33.4}_{-25.0}$	43
≥ 3	400–500	1.15–2.50	1.298×10^{-3}	22.8	$^{+17.8}_{-24.0}$	44
≥ 3	500–1500	0.00–0.35	7.719×10^{-3}	5.2	$^{+8.5}_{-10.4}$	45
≥ 3	500–1500	0.35–0.75	6.644×10^{-3}	7.2	$^{+8.2}_{-9.5}$	46
≥ 3	500–1500	0.75–1.15	5.404×10^{-3}	8.5	$^{+12.3}_{-13.1}$	47
≥ 3	500–1500	1.15–2.50	1.402×10^{-3}	11.9	$^{+18.9}_{-7.8}$	48

Table C.89: Values for each bin of the $[N_{\text{jet}}^{0,1,2,3+}, M(\text{t}\bar{\text{t}}), y(\text{t}\bar{\text{t}})]$ normalized parton level cross section. The table includes also the binning scheme used in the measurement as well as the values for the statistical and systematic uncertainty.

N_{jet}	$m(\text{t}\bar{\text{t}})$ [GeV]	$\lvert y(\text{t}\bar{\text{t}})\rvert$	$\frac{1}{\sigma(\text{t}\bar{\text{t}})}\frac{\text{d}\sigma}{\text{d}\lvert y(\text{t}\bar{\text{t}})\rvert}$	stat. [%]	syst. [%]	bin
0	300–400	0.00–0.35	8.261×10^{1}	1.6	$^{+8.5}_{-7.0}$	1
0	300–400	0.35–0.75	7.712×10^{1}	1.4	$^{+7.4}_{-7.0}$	2
0	300–400	0.75–1.15	6.823×10^{1}	1.5	$^{+8.7}_{-8.3}$	3
0	300–400	1.15–2.50	3.405×10^{1}	1.4	$^{+7.9}_{-7.1}$	4
0	400–500	0.00–0.35	1.322×10^{2}	0.9	$^{+5.9}_{-5.7}$	5
0	400–500	0.35–0.75	1.231×10^{2}	0.8	$^{+5.3}_{-5.1}$	6
0	400–500	0.75–1.15	1.058×10^{2}	0.9	$^{+5.6}_{-4.8}$	7
0	400–500	1.15–2.50	4.719×10^{1}	0.7	$^{+5.0}_{-5.0}$	8
0	500–1500	0.00–0.35	1.682×10^{2}	0.6	$^{+5.1}_{-4.7}$	9
0	500–1500	0.35–0.75	1.477×10^{2}	0.7	$^{+5.1}_{-4.6}$	10
0	500–1500	0.75–1.15	1.120×10^{2}	0.9	$^{+6.4}_{-5.5}$	11
0	500–1500	1.15–2.50	3.576×10^{1}	1.2	$^{+8.1}_{-8.0}$	12
1	300–400	0.00–0.35	2.815×10^{1}	3.5	$^{+6.0}_{-7.3}$	13
1	300–400	0.35–0.75	2.662×10^{1}	3.0	$^{+6.2}_{-5.5}$	14
1	300–400	0.75–1.15	2.233×10^{1}	3.6	$^{+6.4}_{-6.6}$	15
1	300–400	1.15–2.50	1.081×10^{1}	2.8	$^{+7.6}_{-7.0}$	16
1	400–500	0.00–0.35	4.587×10^{1}	2.1	$^{+9.2}_{-8.6}$	17
1	400–500	0.35–0.75	4.378×10^{1}	1.8	$^{+7.9}_{-7.2}$	18
1	400–500	0.75–1.15	3.622×10^{1}	2.1	$^{+9.0}_{-8.8}$	19
1	400–500	1.15–2.50	1.516×10^{1}	1.8	$^{+7.4}_{-7.7}$	20
1	500–1500	0.00–0.35	7.294×10^{1}	1.1	$^{+5.9}_{-6.1}$	21
1	500–1500	0.35–0.75	6.282×10^{1}	1.2	$^{+6.2}_{-5.7}$	22
1	500–1500	0.75–1.15	4.558×10^{1}	1.7	$^{+6.7}_{-6.7}$	23
1	500–1500	1.15–2.50	1.347×10^{1}	2.2	$^{+9.2}_{-9.0}$	24
2	300–400	0.00–0.35	7.887×10^{0}	9.6	$^{+9.1}_{-9.5}$	25
2	300–400	0.35–0.75	6.241×10^{0}	11.6	$^{+14.3}_{-11.8}$	26
2	300–400	0.75–1.15	5.720×10^{0}	11.9	$^{+8.7}_{-14.4}$	27
2	300–400	1.15–2.50	2.432×10^{0}	10.6	$^{+10.6}_{-14.4}$	28
2	400–500	0.00–0.35	1.187×10^{1}	7.2	$^{+13.9}_{-11.4}$	29
2	400–500	0.35–0.75	1.052×10^{1}	6.8	$^{+17.2}_{-13.9}$	30
2	400–500	0.75–1.15	9.261×10^{0}	7.6	$^{+16.8}_{-11.6}$	31
2	400–500	1.15–2.50	3.616×10^{0}	7.1	$^{+13.4}_{-14.0}$	32
2	500–1500	0.00–0.35	2.039×10^{1}	2.9	$^{+8.9}_{-7.8}$	33
2	500–1500	0.35–0.75	1.893×10^{1}	3.2	$^{+8.8}_{-8.0}$	34
2	500–1500	0.75–1.15	1.303×10^{1}	4.5	$^{+7.6}_{-9.6}$	35
2	500–1500	1.15–2.50	3.753×10^{0}	5.8	$^{+10.9}_{-10.6}$	36
≥ 3	300–400	0.00–0.35	1.631×10^{0}	34.3	$^{+36.3}_{-22.4}$	37
≥ 3	300–400	0.35–0.75	2.179×10^{0}	27.2	$^{+34.4}_{-20.2}$	38
≥ 3	300–400	0.75–1.15	1.987×10^{0}	26.6	$^{+20.3}_{-31.4}$	39
≥ 3	300–400	1.15–2.50	1.029×10^{0}	19.1	$^{+17.9}_{-16.2}$	40
≥ 3	400–500	0.00–0.35	5.172×10^{0}	12.1	$^{+11.6}_{-14.6}$	41
≥ 3	400–500	0.35–0.75	2.877×10^{0}	21.7	$^{+21.3}_{-35.2}$	42
≥ 3	400–500	0.75–1.15	2.359×10^{0}	25.6	$^{+34.4}_{-25.9}$	43
≥ 3	400–500	1.15–2.50	1.058×10^{0}	22.8	$^{+19.1}_{-25.7}$	44
≥ 3	500–1500	0.00–0.35	6.288×10^{0}	5.2	$^{+11.0}_{-12.4}$	45
≥ 3	500–1500	0.35–0.75	5.412×10^{0}	7.2	$^{+10.2}_{-11.4}$	46
≥ 3	500–1500	0.75–1.15	4.402×10^{0}	8.5	$^{+14.7}_{-14.6}$	47
≥ 3	500–1500	1.15–2.50	1.142×10^{0}	11.9	$^{+20.5}_{-9.7}$	48

Table C.90: Values for each bin of the $[N_{\text{jet}}^{0,1,2,3+}, M(\text{t}\bar{\text{t}}), y(\text{t}\bar{\text{t}})]$ absolute parton level cross section. The table includes also the binning scheme used in the measurement as well as the values for the statistical and systematic uncertainty.

N_{jet}	$m(\text{t}\bar{\text{t}})$ [GeV]	$\lvert y(\text{t}\bar{\text{t}})\rvert$	$\frac{1}{\sigma(\text{t}\bar{\text{t}})}\frac{\text{d}\sigma}{\text{d}\lvert y(\text{t}\bar{\text{t}})\rvert}$	stat. [%]	syst. [%]	bin
0	300–400	0.00–0.35	1.305×10^{-1}	1.2	$^{+6.1}_{-5.9}$	1
0	300–400	0.35–0.75	1.215×10^{-1}	1.0	$^{+5.2}_{-5.6}$	2
0	300–400	0.75–1.15	1.004×10^{-1}	1.2	$^{+5.5}_{-6.2}$	3
0	300–400	1.15–2.50	2.679×10^{-2}	1.4	$^{+5.5}_{-5.3}$	4
0	400–500	0.00–0.35	1.957×10^{-1}	0.7	$^{+1.8}_{-1.5}$	5
0	400–500	0.35–0.75	1.771×10^{-1}	0.6	$^{+1.6}_{-1.2}$	6
0	400–500	0.75–1.15	1.364×10^{-1}	0.8	$^{+1.2}_{-0.8}$	7
0	400–500	1.15–2.50	3.061×10^{-2}	1.2	$^{+2.4}_{-2.8}$	8
0	500–1500	0.00–0.35	2.573×10^{-1}	0.5	$^{+2.1}_{-1.6}$	9
0	500–1500	0.35–0.75	2.084×10^{-1}	0.5	$^{+2.2}_{-1.7}$	10
0	500–1500	0.75–1.15	1.298×10^{-1}	0.8	$^{+2.5}_{-2.0}$	11
0	500–1500	1.15–2.50	2.049×10^{-2}	1.3	$^{+4.1}_{-4.3}$	12
1	300–400	0.00–0.35	4.536×10^{-2}	2.5	$^{+3.1}_{-5.0}$	13
1	300–400	0.35–0.75	4.267×10^{-2}	2.2	$^{+4.1}_{-4.4}$	14
1	300–400	0.75–1.15	3.394×10^{-2}	2.7	$^{+3.5}_{-4.5}$	15
1	300–400	1.15–2.50	9.126×10^{-3}	3.1	$^{+4.1}_{-4.7}$	16
1	400–500	0.00–0.35	6.982×10^{-2}	1.6	$^{+4.5}_{-4.3}$	17
1	400–500	0.35–0.75	6.422×10^{-2}	1.4	$^{+3.8}_{-3.7}$	18
1	400–500	0.75–1.15	4.771×10^{-2}	1.8	$^{+4.8}_{-5.3}$	19
1	400–500	1.15–2.50	1.045×10^{-2}	2.7	$^{+5.2}_{-6.4}$	20
1	500–1500	0.00–0.35	1.128×10^{-1}	0.9	$^{+2.5}_{-2.9}$	21
1	500–1500	0.35–0.75	9.084×10^{-2}	1.0	$^{+2.7}_{-2.5}$	22
1	500–1500	0.75–1.15	5.472×10^{-2}	1.5	$^{+3.2}_{-3.7}$	23
1	500–1500	1.15–2.50	8.565×10^{-3}	2.6	$^{+5.1}_{-5.4}$	24
2	300–400	0.00–0.35	1.222×10^{-2}	7.2	$^{+7.3}_{-7.0}$	25
2	300–400	0.35–0.75	1.008×10^{-2}	8.3	$^{+8.7}_{-8.1}$	26
2	300–400	0.75–1.15	8.720×10^{-3}	8.9	$^{+6.7}_{-12.7}$	27
2	300–400	1.15–2.50	2.103×10^{-3}	11.0	$^{+10.3}_{-11.1}$	28
2	400–500	0.00–0.35	1.839×10^{-2}	5.6	$^{+9.6}_{-8.5}$	29
2	400–500	0.35–0.75	1.586×10^{-2}	5.2	$^{+12.7}_{-10.0}$	30
2	400–500	0.75–1.15	1.249×10^{-2}	6.4	$^{+13.1}_{-8.7}$	31
2	400–500	1.15–2.50	2.741×10^{-3}	9.2	$^{+10.4}_{-13.9}$	32
2	500–1500	0.00–0.35	3.251×10^{-2}	2.4	$^{+5.7}_{-5.2}$	33
2	500–1500	0.35–0.75	2.783×10^{-2}	2.7	$^{+5.6}_{-5.6}$	34
2	500–1500	0.75–1.15	1.608×10^{-2}	4.0	$^{+4.7}_{-6.9}$	35
2	500–1500	1.15–2.50	2.437×10^{-3}	6.1	$^{+8.0}_{-8.0}$	36
≥ 3	300–400	0.00–0.35	2.660×10^{-3}	25.0	$^{+30.7}_{-13.6}$	37
≥ 3	300–400	0.35–0.75	3.204×10^{-3}	21.8	$^{+28.0}_{-18.8}$	38
≥ 3	300–400	0.75–1.15	2.686×10^{-3}	21.7	$^{+16.5}_{-21.3}$	39
≥ 3	300–400	1.15–2.50	9.067×10^{-4}	17.2	$^{+12.5}_{-22.0}$	40
≥ 3	400–500	0.00–0.35	7.601×10^{-3}	10.6	$^{+10.4}_{-15.2}$	41
≥ 3	400–500	0.35–0.75	4.453×10^{-3}	17.1	$^{+15.7}_{-26.6}$	42
≥ 3	400–500	0.75–1.15	3.386×10^{-3}	20.9	$^{+22.3}_{-25.1}$	43
≥ 3	400–500	1.15–2.50	7.637×10^{-4}	26.4	$^{+34.6}_{-20.6}$	44
≥ 3	500–1500	0.00–0.35	1.025×10^{-2}	4.7	$^{+7.5}_{-9.6}$	45
≥ 3	500–1500	0.35–0.75	8.220×10^{-3}	6.4	$^{+6.9}_{-9.0}$	46
≥ 3	500–1500	0.75–1.15	5.487×10^{-3}	7.9	$^{+11.5}_{-11.1}$	47
≥ 3	500–1500	1.15–2.50	8.167×10^{-4}	11.7	$^{+15.2}_{-7.4}$	48

Table C.91: Values for each bin of the $[N_{\text{jet}}^{0,1,2,3+}, M(\text{t}\bar{\text{t}}), y(\text{t}\bar{\text{t}})]$ normalized particle level cross section. The table includes also the binning scheme used in the measurement as well as the values for the statistical and systematic uncertainty.

N_{jet}	$m(\text{t}\bar{\text{t}})$ [GeV]	$\lvert y(\text{t}\bar{\text{t}})\rvert$	$\frac{1}{\sigma(\text{t}\bar{\text{t}})}\frac{\text{d}\sigma}{\text{d}\lvert y(\text{t}\bar{\text{t}})\rvert}$	stat. [%]	syst. [%]	bin
0	300–400	0.00–0.35	1.599×10^{0}	1.2	$^{+7.1}_{-6.8}$	1
0	300–400	0.35–0.75	1.488×10^{0}	1.0	$^{+6.4}_{-6.5}$	2
0	300–400	0.75–1.15	1.230×10^{0}	1.2	$^{+7.0}_{-7.1}$	3
0	300–400	1.15–2.50	3.282×10^{-1}	1.5	$^{+7.5}_{-7.1}$	4
0	400–500	0.00–0.35	2.397×10^{0}	0.7	$^{+5.3}_{-5.0}$	5
0	400–500	0.35–0.75	2.170×10^{0}	0.6	$^{+4.8}_{-4.6}$	6
0	400–500	0.75–1.15	1.671×10^{0}	0.8	$^{+4.8}_{-4.4}$	7
0	400–500	1.15–2.50	3.749×10^{-1}	1.2	$^{+5.4}_{-5.8}$	8
0	500–1500	0.00–0.35	3.152×10^{0}	0.5	$^{+5.1}_{-4.7}$	9
0	500–1500	0.35–0.75	2.553×10^{0}	0.5	$^{+5.2}_{-4.6}$	10
0	500–1500	0.75–1.15	1.590×10^{0}	0.8	$^{+6.0}_{-5.3}$	11
0	500–1500	1.15–2.50	2.511×10^{-1}	1.4	$^{+7.2}_{-7.2}$	12
1	300–400	0.00–0.35	5.556×10^{-1}	2.6	$^{+5.3}_{-6.7}$	13
1	300–400	0.35–0.75	5.227×10^{-1}	2.2	$^{+5.3}_{-5.4}$	14
1	300–400	0.75–1.15	4.157×10^{-1}	2.7	$^{+5.7}_{-6.1}$	15
1	300–400	1.15–2.50	1.118×10^{-1}	3.1	$^{+6.7}_{-6.8}$	16
1	400–500	0.00–0.35	8.553×10^{-1}	1.6	$^{+7.7}_{-7.4}$	17
1	400–500	0.35–0.75	7.867×10^{-1}	1.4	$^{+6.9}_{-6.5}$	18
1	400–500	0.75–1.15	5.845×10^{-1}	1.8	$^{+7.7}_{-8.0}$	19
1	400–500	1.15–2.50	1.281×10^{-1}	2.7	$^{+8.0}_{-9.0}$	20
1	500–1500	0.00–0.35	1.382×10^{0}	0.9	$^{+5.9}_{-6.1}$	21
1	500–1500	0.35–0.75	1.113×10^{0}	1.0	$^{+6.3}_{-5.8}$	22
1	500–1500	0.75–1.15	6.703×10^{-1}	1.5	$^{+6.8}_{-6.8}$	23
1	500–1500	1.15–2.50	1.049×10^{-1}	2.6	$^{+8.7}_{-8.6}$	24
2	300–400	0.00–0.35	1.497×10^{-1}	7.2	$^{+7.4}_{-7.1}$	25
2	300–400	0.35–0.75	1.235×10^{-1}	8.3	$^{+9.7}_{-8.6}$	26
2	300–400	0.75–1.15	1.068×10^{-1}	8.9	$^{+6.2}_{-12.6}$	27
2	300–400	1.15–2.50	2.576×10^{-2}	11.0	$^{+12.3}_{-13.1}$	28
2	400–500	0.00–0.35	2.252×10^{-1}	5.6	$^{+11.6}_{-10.3}$	29
2	400–500	0.35–0.75	1.942×10^{-1}	5.2	$^{+15.2}_{-12.0}$	30
2	400–500	0.75–1.15	1.530×10^{-1}	6.4	$^{+15.4}_{-10.6}$	31
2	400–500	1.15–2.50	3.358×10^{-2}	9.2	$^{+12.7}_{-15.7}$	32
2	500–1500	0.00–0.35	3.983×10^{-1}	2.4	$^{+8.6}_{-7.8}$	33
2	500–1500	0.35–0.75	3.409×10^{-1}	2.7	$^{+8.6}_{-8.2}$	34
2	500–1500	0.75–1.15	1.969×10^{-1}	4.0	$^{+7.9}_{-9.5}$	35
2	500–1500	1.15–2.50	2.986×10^{-2}	6.1	$^{+11.2}_{-10.8}$	36
≥ 3	300–400	0.00–0.35	3.258×10^{-2}	25.0	$^{+30.7}_{-14.1}$	37
≥ 3	300–400	0.35–0.75	3.925×10^{-2}	21.8	$^{+28.0}_{-20.3}$	38
≥ 3	300–400	0.75–1.15	3.290×10^{-2}	21.7	$^{+16.1}_{-21.0}$	39
≥ 3	300–400	1.15–2.50	1.111×10^{-2}	17.2	$^{+13.9}_{-22.6}$	40
≥ 3	400–500	0.00–0.35	9.312×10^{-2}	10.6	$^{+11.9}_{-16.6}$	41
≥ 3	400–500	0.35–0.75	5.455×10^{-2}	17.1	$^{+17.7}_{-27.7}$	42
≥ 3	400–500	0.75–1.15	4.148×10^{-2}	20.9	$^{+23.7}_{-26.5}$	43
≥ 3	400–500	1.15–2.50	9.355×10^{-3}	26.4	$^{+35.0}_{-22.4}$	44
≥ 3	500–1500	0.00–0.35	1.256×10^{-1}	4.7	$^{+10.4}_{-11.9}$	45
≥ 3	500–1500	0.35–0.75	1.007×10^{-1}	6.4	$^{+9.8}_{-11.6}$	46
≥ 3	500–1500	0.75–1.15	6.722×10^{-2}	7.9	$^{+14.0}_{-13.2}$	47
≥ 3	500–1500	1.15–2.50	1.000×10^{-2}	11.7	$^{+17.2}_{-9.6}$	48

Table C.92: Values for each bin of the $[N_{\text{jet}}^{0,1,2,3+}, M(\text{t}\bar{\text{t}}), y(\text{t}\bar{\text{t}})]$ absolute particle level cross section. The table includes also the binning scheme used in the measurement as well as the values for the statistical and systematic uncertainty.

$p_{\mathrm{T}}(ej_1)$ [GeV]	$\frac{1}{\sigma(\mathrm{t\bar{t}})}\frac{\mathrm{d}\sigma}{\mathrm{d}p_{\mathrm{T}}(ej_1)}$[GeV^{-1}]	stat. [%]	syst. [%]	bin
30–65	1.291×10^{-2}	0.3	$^{+1.8}_{-1.8}$	1
65–125	5.478×10^{-3}	0.3	$^{+1.3}_{-1.4}$	2
125–200	1.824×10^{-3}	0.6	$^{+2.6}_{-2.7}$	3
200–290	6.454×10^{-4}	1.0	$^{+1.7}_{-1.5}$	4
290–400	2.242×10^{-4}	1.5	$^{+2.6}_{-2.6}$	5

Table C.93: Values for each bin of the $p_{\mathrm{T}}(\mathrm{ej}_1)$ normalized parton level cross section. The table includes also the binning scheme used in the measurement as well as the values for the statistical and systematic uncertainty.

$p_{\mathrm{T}}(ej_1)$ [GeV]	$\frac{1}{\sigma(\mathrm{t\bar{t}})}\frac{\mathrm{d}\sigma}{\mathrm{d}p_{\mathrm{T}}(ej_1)}$[GeV^{-1}]	stat. [%]	syst. [%]	bin
30–65	4.141×10^{0}	0.4	$^{+5.4}_{-5.1}$	1
65–125	1.758×10^{0}	0.4	$^{+5.7}_{-5.2}$	2
125–200	5.853×10^{-1}	0.7	$^{+6.4}_{-5.9}$	3
200–290	2.071×10^{-1}	1.0	$^{+5.8}_{-5.3}$	4
290–400	7.192×10^{-2}	1.6	$^{+6.9}_{-6.5}$	5

Table C.94: Values for each bin of the $p_{\mathrm{T}}(\mathrm{ej}_1)$ absolute parton level cross section. The table includes also the binning scheme used in the measurement as well as the values for the statistical and systematic uncertainty.

$p_{\mathrm{T}}(ej2)$ [GeV]	$\frac{1}{\sigma(\mathrm{t\bar{t}})}\frac{\mathrm{d}\sigma}{\mathrm{d}p_{\mathrm{T}}(ej2)}$[GeV^{-1}]	stat. [%]	syst. [%]	bin
30–65	1.917×10^{-2}	0.3	$^{+1.3}_{-0.8}$	1
65–125	4.384×10^{-3}	0.6	$^{+1.7}_{-2.5}$	2
125–200	6.725×10^{-4}	2.1	$^{+4.0}_{-6.2}$	3
200–290	1.372×10^{-4}	4.7	$^{+3.8}_{-8.0}$	4
290–400	3.013×10^{-5}	9.0	$^{+9.6}_{-8.2}$	5

Table C.95: Values for each bin of the $p_{\mathrm{T}}(\mathrm{ej}_2)$ normalized parton level cross section. The table includes also the binning scheme used in the measurement as well as the values for the statistical and systematic uncertainty.

$p_{\mathrm{T}}(ej2)$ [GeV]	$\frac{1}{\sigma(\mathrm{t\bar{t}})}\frac{\mathrm{d}\sigma}{\mathrm{d}p_{\mathrm{T}}(ej2)}$[GeV^{-1}]	stat. [%]	syst. [%]	bin
30–65	1.880×10^{0}	0.5	$^{+5.7}_{-5.0}$	1
65–125	4.300×10^{-1}	0.7	$^{+6.3}_{-6.2}$	2
125–200	6.596×10^{-2}	2.2	$^{+6.6}_{-8.9}$	3
200–290	1.346×10^{-2}	4.7	$^{+7.1}_{-11.1}$	4
290–400	2.956×10^{-3}	9.0	$^{+10.0}_{-9.0}$	5

Table C.96: Values for each bin of the $p_{\mathrm{T}}(\mathrm{ej}_2)$ absolute parton level cross section. The table includes also the binning scheme used in the measurement as well as the values for the statistical and systematic uncertainty.

$\eta(ej_1)$	$\frac{1}{\sigma(\mathrm{t\bar{t}})}\frac{\mathrm{d}\sigma}{\mathrm{d}\eta(ej_1)}$	stat. [%]	syst. [%]	bin
−2.4–−2.1	1.754×10^{-1}	1.0	$^{+1.7}_{-3.0}$	1
−2.1–−1.8	1.876×10^{-1}	1.0	$^{+1.4}_{-1.4}$	2
−1.8–−1.5	1.984×10^{-1}	1.1	$^{+1.4}_{-1.0}$	3
−1.5–−1.2	2.134×10^{-1}	1.0	$^{+1.4}_{-0.6}$	4
−1.2–−0.9	2.233×10^{-1}	1.0	$^{+0.7}_{-1.0}$	5
−0.9–−0.6	2.215×10^{-1}	1.0	$^{+1.7}_{-1.0}$	6
−0.6–−0.3	2.219×10^{-1}	1.1	$^{+1.5}_{-2.1}$	7
−0.3–0.0	2.225×10^{-1}	1.0	$^{+1.7}_{-1.7}$	8
0.0–0.3	2.170×10^{-1}	1.1	$^{+2.0}_{-1.5}$	9
0.3–0.6	2.232×10^{-1}	1.0	$^{+0.7}_{-2.1}$	10
0.6–0.9	2.274×10^{-1}	1.0	$^{+1.3}_{-1.1}$	11
0.9–1.2	2.201×10^{-1}	1.0	$^{+0.7}_{-1.4}$	12
1.2–1.5	2.158×10^{-1}	1.0	$^{+1.4}_{-0.6}$	13
1.5–1.8	2.017×10^{-1}	1.0	$^{+1.3}_{-1.1}$	14
1.8–2.1	1.885×10^{-1}	1.0	$^{+1.6}_{-2.0}$	15
2.1–2.4	1.756×10^{-1}	1.1	$^{+2.7}_{-2.0}$	16

Table C.97: Values for each bin of the $\eta(\mathrm{ej_1})$ normalized parton level cross section. The table includes also the binning scheme used in the measurement as well as the values for the statistical and systematic uncertainty.

$\eta(ej_1)$	$\frac{1}{\sigma(t\bar{t})}\frac{d\sigma}{d\eta(ej_1)}$	stat. [%]	syst. [%]	bin
−2.4–−2.1	5.625×10^1	1.1	$^{+5.8}_{-6.6}$	1
−2.1–−1.8	6.015×10^1	1.0	$^{+5.7}_{-5.3}$	2
−1.8–−1.5	6.362×10^1	1.1	$^{+5.7}_{-5.2}$	3
−1.5–−1.2	6.843×10^1	1.0	$^{+5.7}_{-5.0}$	4
−1.2–−0.9	7.160×10^1	1.0	$^{+5.1}_{-5.0}$	5
−0.9–−0.6	7.104×10^1	1.1	$^{+5.3}_{-4.7}$	6
−0.6–−0.3	7.115×10^1	1.1	$^{+5.5}_{-5.2}$	7
−0.3–0.0	7.135×10^1	1.1	$^{+5.2}_{-4.9}$	8
0.0–0.3	6.960×10^1	1.1	$^{+5.6}_{-4.9}$	9
0.3–0.6	7.159×10^1	1.1	$^{+5.1}_{-5.1}$	10
0.6–0.9	7.292×10^1	1.0	$^{+5.5}_{-4.6}$	11
0.9–1.2	7.059×10^1	1.0	$^{+4.9}_{-5.1}$	12
1.2–1.5	6.922×10^1	1.0	$^{+5.8}_{-4.8}$	13
1.5–1.8	6.469×10^1	1.0	$^{+5.7}_{-5.1}$	14
1.8–2.1	6.044×10^1	1.1	$^{+6.0}_{-5.9}$	15
2.1–2.4	5.632×10^1	1.1	$^{+6.5}_{-5.5}$	16

Table C.98: Values for each bin of the $\eta(\mathrm{ej}_1)$ absolute parton level cross section. The table includes also the binning scheme used in the measurement as well as the values for the statistical and systematic uncertainty.

$\eta(ej2)$	$\frac{1}{\sigma(\mathrm{t\bar{t}})}\frac{\mathrm{d}\sigma}{\mathrm{d}\eta(ej2)}$	stat. [%]	syst. [%]	bin
−2.4–−2.1	1.774×10^{-1}	2.3	$^{+2.5}_{-3.6}$	1
−2.1–−1.8	1.887×10^{-1}	2.3	$^{+3.0}_{-2.2}$	2
−1.8–−1.5	2.052×10^{-1}	2.1	$^{+1.3}_{-3.5}$	3
−1.5–−1.2	2.212×10^{-1}	2.0	$^{+1.9}_{-1.8}$	4
−1.2–−0.9	2.135×10^{-1}	2.2	$^{+2.0}_{-1.9}$	5
−0.9–−0.6	2.198×10^{-1}	2.0	$^{+1.1}_{-2.2}$	6
−0.6–−0.3	2.141×10^{-1}	2.1	$^{+3.9}_{-2.3}$	7
−0.3–0.0	2.199×10^{-1}	2.2	$^{+3.5}_{-1.9}$	8
0.0–0.3	2.125×10^{-1}	2.2	$^{+1.8}_{-1.9}$	9
0.3–0.6	2.249×10^{-1}	2.0	$^{+1.8}_{-3.0}$	10
0.6–0.9	2.243×10^{-1}	1.9	$^{+2.0}_{-2.2}$	11
0.9–1.2	2.172×10^{-1}	2.1	$^{+2.7}_{-1.4}$	12
1.2–1.5	2.244×10^{-1}	2.0	$^{+1.6}_{-2.2}$	13
1.5–1.8	2.044×10^{-1}	2.2	$^{+2.2}_{-1.7}$	14
1.8–2.1	1.893×10^{-1}	2.3	$^{+3.8}_{-1.5}$	15
2.1–2.4	1.765×10^{-1}	2.3	$^{+2.1}_{-3.4}$	16

Table C.99: Values for each bin of the $\eta(\mathrm{ej_2})$ normalized parton level cross section. The table includes also the binning scheme used in the measurement as well as the values for the statistical and systematic uncertainty.

$\eta(ej2)$	$\frac{1}{\sigma(\mathrm{t\bar{t}})}\frac{\mathrm{d}\sigma}{\mathrm{d}\eta(ej2)}$	stat. [%]	syst. [%]	bin
−2.4–−2.1	1.707×10^{1}	2.4	$^{+6.4}_{-6.6}$	1
−2.1–−1.8	1.816×10^{1}	2.3	$^{+6.9}_{-5.9}$	2
−1.8–−1.5	1.975×10^{1}	2.1	$^{+5.5}_{-6.6}$	3
−1.5–−1.2	2.128×10^{1}	2.0	$^{+5.6}_{-5.5}$	4
−1.2–−0.9	2.054×10^{1}	2.2	$^{+6.1}_{-5.4}$	5
−0.9–−0.6	2.115×10^{1}	2.0	$^{+5.1}_{-5.8}$	6
−0.6–−0.3	2.061×10^{1}	2.2	$^{+6.2}_{-4.9}$	7
−0.3–0.0	2.116×10^{1}	2.2	$^{+5.9}_{-5.0}$	8
0.0–0.3	2.045×10^{1}	2.2	$^{+6.0}_{-5.5}$	9
0.3–0.6	2.164×10^{1}	2.0	$^{+5.5}_{-5.9}$	10
0.6–0.9	2.159×10^{1}	1.9	$^{+6.1}_{-5.9}$	11
0.9–1.2	2.090×10^{1}	2.1	$^{+6.1}_{-4.8}$	12
1.2–1.5	2.159×10^{1}	2.0	$^{+5.8}_{-5.8}$	13
1.5–1.8	1.966×10^{1}	2.2	$^{+6.2}_{-5.8}$	14
1.8–2.1	1.821×10^{1}	2.3	$^{+7.2}_{-4.9}$	15
2.1–2.4	1.698×10^{1}	2.3	$^{+6.0}_{-6.9}$	16

Table C.100: Values for each bin of the $\eta(\mathrm{ej_2})$ absolute parton level cross section. The table includes also the binning scheme used in the measurement as well as the values for the statistical and systematic uncertainty.

$p_{\mathrm{T}}(\mathrm{t\bar{t}} + ej_1)$ [GeV]	$\frac{1}{\sigma(\mathrm{t\bar{t}})} \frac{\mathrm{d}\sigma}{\mathrm{d}p_{\mathrm{T}}(\mathrm{t\bar{t}}+ej_1)}$[GeV^{-1}]	stat. [%]	syst. [%]	bin
0–25	1.355×10^{-2}	0.9	$^{+9.4}_{-8.9}$	1
25–50	1.139×10^{-2}	0.7	$^{+3.5}_{-3.7}$	2
50–100	4.850×10^{-3}	1.0	$^{+7.3}_{-7.9}$	3
100–200	1.108×10^{-3}	1.4	$^{+5.3}_{-3.3}$	4
200–310	1.728×10^{-4}	4.1	$^{+6.8}_{-6.8}$	5
310–570	1.580×10^{-5}	11.4	$^{+13.9}_{-16.5}$	6

Table C.101: Values for each bin of the $p_{\mathrm{T}}(\mathrm{t\bar{t}} + \mathrm{ej_1})$ normalized parton level cross section. The table includes also the binning scheme used in the measurement as well as the values for the statistical and systematic uncertainty.

$p_{\mathrm{T}}(\mathrm{t\bar{t}} + ej_1)$ [GeV]	$\frac{1}{\sigma(\mathrm{t\bar{t}})} \frac{\mathrm{d}\sigma}{\mathrm{d}p_{\mathrm{T}}(\mathrm{t\bar{t}}+ej_1)}$[GeV^{-1}]	stat. [%]	syst. [%]	bin
0–25	4.392×10^{0}	1.0	$^{+9.5}_{-9.1}$	1
25–50	3.692×10^{0}	0.7	$^{+7.4}_{-7.0}$	2
50–100	1.572×10^{0}	1.0	$^{+10.0}_{-10.1}$	3
100–200	3.592×10^{-1}	1.5	$^{+7.8}_{-6.2}$	4
200–310	5.600×10^{-2}	4.1	$^{+9.1}_{-8.6}$	5
310–570	5.122×10^{-3}	11.4	$^{+15.1}_{-18.4}$	6

Table C.102: Values for each bin of the $p_{\mathrm{T}}(\mathrm{t\bar{t}} + \mathrm{ej_1})$ absolute parton level cross section. The table includes also the binning scheme used in the measurement as well as the values for the statistical and systematic uncertainty.

$m(\mathrm{t\bar{t}} + ej_1)$ [GeV]	$\frac{1}{\sigma(\mathrm{t\bar{t}})}\frac{\mathrm{d}\sigma}{\mathrm{d}m(\mathrm{t\bar{t}}+ej_1)}$[GeV^{-1}]	stat. [%]	syst. [%]	bin
340.0–480.0	8.123×10^{-4}	1.2	$^{+4.9}_{-5.1}$	1
480.0–640.0	1.940×10^{-3}	0.4	$^{+1.4}_{-0.9}$	2
640.0–820.0	1.467×10^{-3}	0.4	$^{+1.0}_{-1.1}$	3
820.0–1100.0	6.827×10^{-4}	0.6	$^{+1.6}_{-1.6}$	4
1100.0–1500.0	2.163×10^{-4}	1.2	$^{+1.8}_{-3.4}$	5
1500.0–2500.0	3.413×10^{-5}	2.1	$^{+4.7}_{-4.2}$	6

Table C.103: Values for each bin of the $M(\mathrm{t\bar{t}} + \mathrm{ej_1})$ normalized parton level cross section. The table includes also the binning scheme used in the measurement as well as the values for the statistical and systematic uncertainty.

$m(\mathrm{t\bar{t}} + ej_1)$ [GeV]	$\frac{1}{\sigma(\mathrm{t\bar{t}})}\frac{\mathrm{d}\sigma}{\mathrm{d}m(\mathrm{t\bar{t}}+ej_1)}$[GeV^{-1}]	stat. [%]	syst. [%]	bin
340.0–480.0	2.620×10^{-1}	1.3	$^{+6.6}_{-6.4}$	1
480.0–640.0	6.257×10^{-1}	0.5	$^{+5.7}_{-4.7}$	2
640.0–820.0	4.730×10^{-1}	0.5	$^{+5.8}_{-5.5}$	3
820.0–1100.0	2.202×10^{-1}	0.6	$^{+5.3}_{-5.2}$	4
1100.0–1500.0	6.976×10^{-2}	1.2	$^{+5.7}_{-6.6}$	5
1500.0–2500.0	1.101×10^{-2}	2.1	$^{+7.4}_{-6.3}$	6

Table C.104: Values for each bin of the $M(\mathrm{t\bar{t}} + \mathrm{ej_1})$ absolute parton level cross section. The table includes also the binning scheme used in the measurement as well as the values for the statistical and systematic uncertainty.

$p_{\mathrm{T}}(ej_1)/m(\mathrm{t\bar{t}})$	$\frac{1}{\sigma(\mathrm{t\bar{t}})}\frac{\mathrm{d}\sigma}{\mathrm{d}p_{\mathrm{T}}(ej_1)}m(\mathrm{t\bar{t}})$	stat. [%]	syst. [%]	bin
0.0–0.1	3.350×10^{0}	0.4	$^{+3.9}_{-3.3}$	1
0.1–0.2	3.267×10^{0}	0.4	$^{+1.6}_{-3.4}$	2
0.2–0.3	1.161×10^{0}	0.7	$^{+4.2}_{-3.7}$	3
0.3–0.6	3.912×10^{-1}	1.1	$^{+3.5}_{-2.6}$	4
0.6–1.0	7.976×10^{-2}	1.7	$^{+3.4}_{-4.4}$	5

Table C.105: Values for each bin of the $p_{\mathrm{T}}(\mathrm{ej_1})/M(\mathrm{t\bar{t}})$ normalized parton level cross section. The table includes also the binning scheme used in the measurement as well as the values for the statistical and systematic uncertainty.

$p_{\mathrm{T}}(ej_1)/m(\mathrm{t\bar{t}})$	$\frac{1}{\sigma(\mathrm{t\bar{t}})}\frac{\mathrm{d}\sigma}{\mathrm{d}p_{\mathrm{T}}(ej_1)}m(\mathrm{t\bar{t}})$	stat. [%]	syst. [%]	bin
0.0–0.1	1.077×10^{3}	0.4	$^{+5.6}_{-4.9}$	1
0.1–0.2	1.051×10^{3}	0.4	$^{+6.0}_{-6.7}$	2
0.2–0.3	3.735×10^{2}	0.8	$^{+8.0}_{-6.8}$	3
0.3–0.6	1.258×10^{2}	1.1	$^{+7.2}_{-5.9}$	4
0.6–1.0	2.565×10^{1}	1.7	$^{+7.1}_{-7.3}$	5

Table C.106: Values for each bin of the $p_{\mathrm{T}}(\mathrm{ej_1})/M(\mathrm{t\bar{t}})$ absolute parton level cross section. The table includes also the binning scheme used in the measurement as well as the values for the statistical and systematic uncertainty.

$m(\mathrm{t\bar{t}}+ej_1)/m(\mathrm{t\bar{t}})$	$\frac{1}{\sigma(\mathrm{t\bar{t}})}\frac{\mathrm{d}\sigma}{\mathrm{d}m(\mathrm{t\bar{t}}+ej_1)}m(\mathrm{t\bar{t}})$	stat. [%]	syst. [%]	bin
1.0–1.1	1.161×10^{0}	0.9	$^{+6.3}_{-4.3}$	1
1.1–1.2	2.179×10^{0}	0.5	$^{+0.8}_{-1.9}$	2
1.2–1.4	1.237×10^{0}	0.5	$^{+1.4}_{-1.6}$	3
1.4–1.8	5.408×10^{-1}	0.6	$^{+2.2}_{-1.6}$	4
1.8–2.3	1.984×10^{-1}	1.1	$^{+1.9}_{-3.4}$	5
2.3–3.0	7.382×10^{-2}	1.8	$^{+5.2}_{-4.1}$	6

Table C.107: Values for each bin of the $M(\mathrm{t\bar{t}} + \mathrm{ej_1})/\mathrm{M}(\mathrm{t\bar{t}})$ normalized parton level cross section. The table includes also the binning scheme used in the measurement as well as the values for the statistical and systematic uncertainty.

$m(\mathrm{t\bar{t}}+ej_1)/m(\mathrm{t\bar{t}})$	$\frac{1}{\sigma(\mathrm{t\bar{t}})}\frac{\mathrm{d}\sigma}{\mathrm{d}m(\mathrm{t\bar{t}}+ej_1)}m(\mathrm{t\bar{t}})$	stat. [%]	syst. [%]	bin
1.0–1.1	3.672×10^{2}	0.9	$^{+6.7}_{-5.5}$	1
1.1–1.2	6.889×10^{2}	0.5	$^{+4.7}_{-4.9}$	2
1.2–1.4	3.912×10^{2}	0.5	$^{+5.9}_{-5.6}$	3
1.4–1.8	1.710×10^{2}	0.7	$^{+6.6}_{-5.6}$	4
1.8–2.3	6.275×10^{1}	1.2	$^{+6.1}_{-7.0}$	5
2.3–3.0	2.334×10^{1}	1.8	$^{+9.0}_{-7.0}$	6

Table C.108: Values for each bin of the $M(\mathrm{t\bar{t}}+\mathrm{ej_1})/\mathrm{M}(\mathrm{t\bar{t}})$ absolute parton level cross section. The table includes also the binning scheme used in the measurement as well as the values for the statistical and systematic uncertainty.

$\Delta\eta(t, ej_1)/\Delta\eta(\mathrm{t}, \bar{\mathrm{t}})$	$\frac{1}{\sigma(\mathrm{t\bar{t}})} \frac{\mathrm{d}\sigma}{\mathrm{d}\Delta\eta(t,ej_1)} \Delta\eta(\mathrm{t}, \bar{\mathrm{t}})$	stat. [%]	syst. [%]	bin
−2.0–−1.0	1.428×10^{-1}	1.8	$^{+9.9}_{-2.6}$	1
−1.0–−0.5	1.786×10^{-1}	1.7	$^{+3.5}_{-12.0}$	2
−0.5–0.0	2.683×10^{-1}	1.2	$^{+1.2}_{-2.3}$	3
0.0–0.5	3.708×10^{-1}	0.8	$^{+2.8}_{-2.2}$	4
0.5–1.0	3.676×10^{-1}	0.9	$^{+1.4}_{-4.9}$	5
1.0–2.0	2.646×10^{-1}	0.8	$^{+2.0}_{-1.3}$	6

Table C.109: Values for each bin of the $\Delta\eta(t, ej_1)/\Delta\eta(t, \bar{t})$ normalized parton level cross section. The table includes also the binning scheme used in the measurement as well as the values for the statistical and systematic uncertainty.

$\Delta\eta(t, ej_1)/\Delta\eta(\mathrm{t}, \bar{\mathrm{t}})$	$\frac{1}{\sigma(\mathrm{t\bar{t}})} \frac{\mathrm{d}\sigma}{\mathrm{d}\Delta\eta(t,ej_1)} \Delta\eta(\mathrm{t}, \bar{\mathrm{t}})$	stat. [%]	syst. [%]	bin
−2.0–−1.0	3.567×10^{1}	1.9	$^{+12.5}_{-5.5}$	1
−1.0–−0.5	4.461×10^{1}	1.7	$^{+6.1}_{-12.8}$	2
−0.5–0.0	6.701×10^{1}	1.2	$^{+5.3}_{-5.9}$	3
0.0–0.5	9.261×10^{1}	0.9	$^{+6.3}_{-5.6}$	4
0.5–1.0	9.182×10^{1}	0.9	$^{+5.2}_{-6.9}$	5
1.0–2.0	6.609×10^{1}	0.8	$^{+6.1}_{-5.1}$	6

Table C.110: Values for each bin of the $\Delta\eta(t, ej_1)/\Delta\eta(t, \bar{t})$ absolute parton level cross section. The table includes also the binning scheme used in the measurement as well as the values for the statistical and systematic uncertainty.

C.3 Tables with χ^2 values for the comparison of results with MC models.

In this section the χ^2 values for the comparison of all cross sections with different MC models are presented. The tables include the χ^2 values for parton and particle level, as well as for the two possible kinematic reconstruction algorithms wherever is possible.

Table C.111: The χ^2 values (taking into account data uncertainties only) and dof of the measured normalized parton level cross sections with respect to various MC predictions.

Cross section variables	dof	χ^2		
		POW-PYT	POW-HER	FXFX-PYT
$[y(t), p_{\mathrm{T}}(t)]$	15	39	29	70
$[p_{\mathrm{T}}(t), p_{\mathrm{T}}(\mathrm{t\bar{t}})]$	15	38	82	68
$[M(\mathrm{t\bar{t}}), y(\mathrm{t\bar{t}})]$	15	34	27	47
$[M(\mathrm{t\bar{t}}), y(\mathrm{t\bar{t}})]$ (loose kin. reco.)	15	62	61	65
$[y(\mathrm{t\bar{t}}), p_{\mathrm{T}}(\mathrm{t\bar{t}})]$	15	26	66	35
$[M(\mathrm{t\bar{t}}), p_{\mathrm{T}}(\mathrm{t\bar{t}})]$	15	64	120	46
$[M(\mathrm{t\bar{t}}), p_{\mathrm{T}}(\mathrm{t\bar{t}})]$ (loose kin. reco.)	15	59	109	69
$[M(\mathrm{t\bar{t}}), p_{\mathrm{T}}(t)]$	8	83	41	151
$[M(\mathrm{t\bar{t}}), y(t)]$	15	60	47	82
$[M(\mathrm{t\bar{t}}), \Delta\eta(t, \bar{t})\ ]$	11	153	115	216
$[M(\mathrm{t\bar{t}}), \Delta\phi(t, \bar{t})\ ]$	11	72	88	48
$[p_{\mathrm{T}}(\mathrm{t\bar{t}}), M(\mathrm{t\bar{t}}), y(\mathrm{t\bar{t}})]$	47	132	207	100
$[p_{\mathrm{T}}(\mathrm{t\bar{t}}), M(\mathrm{t\bar{t}}), y(\mathrm{t\bar{t}})]$ (loose kin. reco.)	47	83	126	105
$N_{\mathrm{jet}}(p_{\mathrm{T}} > 30\,\mathrm{GeV})$ $(\Delta R_{iso} = 0.4)$	5	26	653	457
$N_{\mathrm{jet}}(p_{\mathrm{T}} > 50\,\mathrm{GeV})$ $(\Delta R_{iso} = 0.4)$	5	9	871	240
$N_{\mathrm{jet}}(p_{\mathrm{T}} > 100\,\mathrm{GeV})$ $(\Delta R_{iso} = 0.4)$	4	18	156	57
$N_{\mathrm{jet}}(p_{\mathrm{T}} > 30\,\mathrm{GeV})$ $(\Delta R_{iso} = 0.8)$	5	22	200	469
$N_{\mathrm{jet}}(p_{\mathrm{T}} > 40\,\mathrm{GeV})$ $(\Delta R_{iso} = 0.8)$	5	5	250	278
$N_{\mathrm{jet}}(p_{\mathrm{T}} > 50\,\mathrm{GeV})$ $(\Delta R_{iso} = 0.8)$	5	11	253	158
$N_{\mathrm{jet}}(p_{\mathrm{T}} > 100\,\mathrm{GeV})$ $(\Delta R_{iso} = 0.8)$	4	26	67	33
$[N_{\mathrm{jet}}, p_{\mathrm{T}}(t)]$	8	21	123	159
$[N_{\mathrm{jet}}, y(t)]$	11	37	84	126
$[N_{\mathrm{jet}}, M(\mathrm{t\bar{t}})]$	11	42	118	102
$[N_{\mathrm{jet}}, M(\mathrm{t\bar{t}})]$ (loose kin. reco.)	11	55	150	139
$[N_{\mathrm{jet}}, y(\mathrm{t\bar{t}})]$	11	10	59	120
$[N_{\mathrm{jet}}, p_{\mathrm{T}}(\mathrm{t\bar{t}})]$	11	49	91	183
$[N_{\mathrm{jet}}, \Delta\eta(t, \bar{t})]$	8	84	142	188
$[N_{\mathrm{jet}}^{0,1+}, M(\mathrm{t\bar{t}}), y(\mathrm{t\bar{t}})]$	23	23	44	54
$[N_{\mathrm{jet}}^{0,1+}, M(\mathrm{t\bar{t}}), y(\mathrm{t\bar{t}})]$ (loose kin. reco.)	23	46	89	72
$[N_{\mathrm{jet}}^{0,1,2+}, M(\mathrm{t\bar{t}}), y(\mathrm{t\bar{t}})]$	35	42	118	165
$[N_{\mathrm{jet}}^{0,1,2+}, M(\mathrm{t\bar{t}}), y(\mathrm{t\bar{t}})]$ (loose kin. reco.)	35	80	202	207
$[N_{\mathrm{jet}}^{0,1,2,3+}, M(\mathrm{t\bar{t}}), y(\mathrm{t\bar{t}})]$	47	78	280	283
$[N_{\mathrm{jet}}^{0,1,2,3+}, M(\mathrm{t\bar{t}}), y(\mathrm{t\bar{t}})]$ (loose kin. reco.)	47	118	449	420

Table C.112: The χ^2 values (taking into account data uncertainties only) and dof of the measured absolute parton level cross sections with respect to various MC predictions.

Cross section variables	dof	χ^2		
		POW-PYT	POW-HER	FXFX-PYT
$[y(t),p_{\mathrm{T}}(t)]$	16	49	34	89
$[p_{\mathrm{T}}(t),p_{\mathrm{T}}(\mathrm{t\bar{t}})]$	16	52	100	84
$[M(\mathrm{t\bar{t}}),y(\mathrm{t\bar{t}})]$	16	38	30	52
$[M(\mathrm{t\bar{t}}),y(\mathrm{t\bar{t}})]$ (loose kin. reco.)	16	69	68	72
$[y(\mathrm{t\bar{t}}),p_{\mathrm{T}}(\mathrm{t\bar{t}})]$	16	29	73	41
$[M(\mathrm{t\bar{t}}),p_{\mathrm{T}}(\mathrm{t\bar{t}})]$	16	71	133	52
$[M(\mathrm{t\bar{t}}),p_{\mathrm{T}}(\mathrm{t\bar{t}})]$ (loose kin. reco.)	16	66	124	77
$[M(\mathrm{t\bar{t}}),p_{\mathrm{T}}(t)]$	9	93	51	167
$[M(\mathrm{t\bar{t}}),y(t)]$	16	66	52	90
$[M(\mathrm{t\bar{t}}),\Delta\eta(t,\bar{t})\ ]$	12	168	127	238
$[M(\mathrm{t\bar{t}}),\Delta\phi(t,\bar{t})\ ]$	12	80	98	53
$[p_{\mathrm{T}}(\mathrm{t\bar{t}}),M(\mathrm{t\bar{t}}),y(\mathrm{t\bar{t}})]$	48	147	230	110
$[p_{\mathrm{T}}(\mathrm{t\bar{t}}),M(\mathrm{t\bar{t}}),y(\mathrm{t\bar{t}})]$ (loose kin. reco.)	48	95	144	123
$N_{\mathrm{jet}}(p_{\mathrm{T}} > 30\,\mathrm{GeV})$ $(\Delta R_{iso} = 0.4)$	6	29	725	505
$N_{\mathrm{jet}}(p_{\mathrm{T}} > 50\,\mathrm{GeV})$ $(\Delta R_{iso} = 0.4)$	6	12	997	279
$N_{\mathrm{jet}}(p_{\mathrm{T}} > 100\,\mathrm{GeV})$ $(\Delta R_{iso} = 0.4)$	5	32	222	79
$N_{\mathrm{jet}}(p_{\mathrm{T}} > 30\,\mathrm{GeV})$ $(\Delta R_{iso} = 0.8)$	6	25	223	518
$N_{\mathrm{jet}}(p_{\mathrm{T}} > 40\,\mathrm{GeV})$ $(\Delta R_{iso} = 0.8)$	6	7	281	312
$N_{\mathrm{jet}}(p_{\mathrm{T}} > 50\,\mathrm{GeV})$ $(\Delta R_{iso} = 0.8)$	6	14	283	180
$N_{\mathrm{jet}}(p_{\mathrm{T}} > 100\,\mathrm{GeV})$ $(\Delta R_{iso} = 0.8)$	5	42	92	43
$[N_{\mathrm{jet}},p_{\mathrm{T}}(t)]$	9	33	165	175
$[N_{\mathrm{jet}},y(t)]$	12	41	93	138
$[N_{\mathrm{jet}},M(\mathrm{t\bar{t}})]$	12	46	131	113
$[N_{\mathrm{jet}},M(\mathrm{t\bar{t}})]$ (loose kin. reco.)	12	61	169	179
$[N_{\mathrm{jet}},y(\mathrm{t\bar{t}})]$	12	13	67	133
$[N_{\mathrm{jet}},p_{\mathrm{T}}(\mathrm{t\bar{t}})]$	12	57	102	216
$[N_{\mathrm{jet}},\Delta\eta(t,\bar{t})]$	9	93	157	208
$[N_{\mathrm{jet}}^{0,1+},M(\mathrm{t\bar{t}}),y(\mathrm{t\bar{t}})]$	24	29	59	60
$[N_{\mathrm{jet}}^{0,1+},M(\mathrm{t\bar{t}}),y(\mathrm{t\bar{t}})]$ (loose kin. reco.)	24	52	99	80
$[N_{\mathrm{jet}}^{0,1,2+},M(\mathrm{t\bar{t}}),y(\mathrm{t\bar{t}})]$	36	51	154	182
$[N_{\mathrm{jet}}^{0,1,2+},M(\mathrm{t\bar{t}}),y(\mathrm{t\bar{t}})]$ (loose kin. reco.)	36	90	229	232
$[N_{\mathrm{jet}}^{0,1,2,3+},M(\mathrm{t\bar{t}}),y(\mathrm{t\bar{t}})]$	48	88	333	313
$[N_{\mathrm{jet}}^{0,1,2,3+},M(\mathrm{t\bar{t}}),y(\mathrm{t\bar{t}})]$ (loose kin. reco.)	48	132	499	473

Table C.113: The χ^2 values (taking into account data uncertainties only) and dof of the measured normalized particle level cross sections with respect to various MC predictions.

Cross section variables	dof	χ^2		
		POW-PYT	POW-HER	FXFX-PYT
$[y(t), p_{\mathrm{T}}(t)]$	15	33	28	58
$[p_{\mathrm{T}}(t), p_{\mathrm{T}}(\mathrm{t\bar{t}})]$	15	34	66	59
$[M(\mathrm{t\bar{t}}), y(\mathrm{t\bar{t}})]$ (loose kin. reco.)	15	75	77	71
$[y(\mathrm{t\bar{t}}), p_{\mathrm{T}}(\mathrm{t\bar{t}})]$	15	26	66	38
$[M(\mathrm{t\bar{t}}), p_{\mathrm{T}}(\mathrm{t\bar{t}})]$	15	55	96	36
$[M(\mathrm{t\bar{t}}), p_{\mathrm{T}}(\mathrm{t\bar{t}})]$ (loose kin. reco.)	15	59	116	53
$[M(\mathrm{t\bar{t}}), p_{\mathrm{T}}(t)]$	8	85	45	141
$[M(\mathrm{t\bar{t}}), y(t)]$	15	53	37	66
$[M(\mathrm{t\bar{t}}), \Delta\eta(t, \bar{t})\ ]$	11	153	118	206
$[M(\mathrm{t\bar{t}}), \Delta\phi(t, \bar{t})\ ]$	11	69	90	37
$[p_{\mathrm{T}}(\mathrm{t\bar{t}}), M(\mathrm{t\bar{t}}), y(\mathrm{t\bar{t}})]$	47	155	207	127
$[p_{\mathrm{T}}(\mathrm{t\bar{t}}), M(\mathrm{t\bar{t}}), y(\mathrm{t\bar{t}})]$ (loose kin. reco.)	47	112	170	116
$N_{\mathrm{jet}}(p_{\mathrm{T}} > 30\,\mathrm{GeV})$ $(\Delta R_{iso} = 0.4)$	5	29	34	642
$N_{\mathrm{jet}}(p_{\mathrm{T}} > 50\,\mathrm{GeV})$ $(\Delta R_{iso} = 0.4)$	5	10	8	304
$N_{\mathrm{jet}}(p_{\mathrm{T}} > 100\,\mathrm{GeV})$ $(\Delta R_{iso} = 0.4)$	4	20	5	55
$N_{\mathrm{jet}}(p_{\mathrm{T}} > 30\,\mathrm{GeV})$ $(\Delta R_{iso} = 0.8)$	5	22	26	563
$N_{\mathrm{jet}}(p_{\mathrm{T}} > 40\,\mathrm{GeV})$ $(\Delta R_{iso} = 0.8)$	5	6	8	335
$N_{\mathrm{jet}}(p_{\mathrm{T}} > 50\,\mathrm{GeV})$ $(\Delta R_{iso} = 0.8)$	5	13	6	200
$N_{\mathrm{jet}}(p_{\mathrm{T}} > 100\,\mathrm{GeV})$ $(\Delta R_{iso} = 0.8)$	4	30	6	33
$[N_{\mathrm{jet}}, p_{\mathrm{T}}(t)]$	8	29	25	236
$[N_{\mathrm{jet}}, y(t)]$	11	38	27	172
$[N_{\mathrm{jet}}, M(\mathrm{t\bar{t}})]$	11	42	27	176
$[N_{\mathrm{jet}}, M(\mathrm{t\bar{t}})]$ (loose kin. reco.)	11	52	50	279
$[N_{\mathrm{jet}}, y(\mathrm{t\bar{t}})]$	11	14	8	177
$[N_{\mathrm{jet}}, p_{\mathrm{T}}(\mathrm{t\bar{t}})]$	11	57	86	323
$[N_{\mathrm{jet}}, \Delta\eta(t, \bar{t})]$	8	122	105	288
$[N_{\mathrm{jet}}^{0,1+}, M(\mathrm{t\bar{t}}), y(\mathrm{t\bar{t}})]$	23	28	22	54
$[N_{\mathrm{jet}}^{0,1+}, M(\mathrm{t\bar{t}}), y(\mathrm{t\bar{t}})]$ (loose kin. reco.)	23	73	84	94
$[N_{\mathrm{jet}}^{0,1,2+}, M(\mathrm{t\bar{t}}), y(\mathrm{t\bar{t}})]$	35	59	39	229
$[N_{\mathrm{jet}}^{0,1,2+}, M(\mathrm{t\bar{t}}), y(\mathrm{t\bar{t}})]$ (loose kin. reco.)	35	125	136	378
$[N_{\mathrm{jet}}^{0,1,2,3+}, M(\mathrm{t\bar{t}}), y(\mathrm{t\bar{t}})]$	47	80	51	377
$[N_{\mathrm{jet}}^{0,1,2,3+}, M(\mathrm{t\bar{t}}), y(\mathrm{t\bar{t}})]$ (loose kin. reco.)	47	153	158	698

Table C.114: The χ^2 values (taking into account data uncertainties only) and dof of the measured absolute particle level cross sections with respect to various MC predictions.

Cross section variables	dof	χ^2		
		POW-PYT	POW-HER	FXFX-PYT
$[y(t),p_{\mathrm{T}}(t)]$	16	44	34	74
$[p_{\mathrm{T}}(t),p_{\mathrm{T}}(\mathrm{t\bar{t}})]$	16	43	78	72
$[M(\mathrm{t\bar{t}}),y(\mathrm{t\bar{t}})]$ (loose kin. reco.)	16	84	87	80
$[y(\mathrm{t\bar{t}}),p_{\mathrm{T}}(\mathrm{t\bar{t}})]$	16	31	74	46
$[M(\mathrm{t\bar{t}}),p_{\mathrm{T}}(\mathrm{t\bar{t}})]$	16	64	108	45
$[M(\mathrm{t\bar{t}}),p_{\mathrm{T}}(\mathrm{t\bar{t}})]$ (loose kin. reco.)	16	69	136	59
$[M(\mathrm{t\bar{t}}),p_{\mathrm{T}}(t)]$	9	104	63	163
$[M(\mathrm{t\bar{t}}),y(t)]$	16	60	42	75
$[M(\mathrm{t\bar{t}}),\Delta\eta(t,\bar{t})\ ]$	12	171	132	230
$[M(\mathrm{t\bar{t}}),\Delta\phi(t,\bar{t})\ ]$	12	78	103	42
$[p_{\mathrm{T}}(\mathrm{t\bar{t}}),M(\mathrm{t\bar{t}}),y(\mathrm{t\bar{t}})]$	48	171	227	139
$[p_{\mathrm{T}}(\mathrm{t\bar{t}}),M(\mathrm{t\bar{t}}),y(\mathrm{t\bar{t}})]$ (loose kin. reco.)	48	130	197	135
$N_{\mathrm{jet}}(p_{\mathrm{T}} > 30\,\mathrm{GeV})$ $(\Delta R_{iso} = 0.4)$	6	35	41	757
$N_{\mathrm{jet}}(p_{\mathrm{T}} > 50\,\mathrm{GeV})$ $(\Delta R_{iso} = 0.4)$	6	12	11	338
$N_{\mathrm{jet}}(p_{\mathrm{T}} > 100\,\mathrm{GeV})$ $(\Delta R_{iso} = 0.4)$	5	32	12	68
$N_{\mathrm{jet}}(p_{\mathrm{T}} > 30\,\mathrm{GeV})$ $(\Delta R_{iso} = 0.8)$	6	29	34	664
$N_{\mathrm{jet}}(p_{\mathrm{T}} > 40\,\mathrm{GeV})$ $(\Delta R_{iso} = 0.8)$	6	7	11	381
$N_{\mathrm{jet}}(p_{\mathrm{T}} > 50\,\mathrm{GeV})$ $(\Delta R_{iso} = 0.8)$	6	15	9	221
$N_{\mathrm{jet}}(p_{\mathrm{T}} > 100\,\mathrm{GeV})$ $(\Delta R_{iso} = 0.8)$	5	45	14	39
$[N_{\mathrm{jet}},p_{\mathrm{T}}(t)]$	9	37	36	267
$[N_{\mathrm{jet}},y(t)]$	12	43	31	193
$[N_{\mathrm{jet}},M(\mathrm{t\bar{t}})]$	12	47	31	206
$[N_{\mathrm{jet}},M(\mathrm{t\bar{t}})]$ (loose kin. reco.)	12	59	58	313
$[N_{\mathrm{jet}},y(\mathrm{t\bar{t}})]$	12	17	11	202
$[N_{\mathrm{jet}},p_{\mathrm{T}}(\mathrm{t\bar{t}})]$	12	66	101	363
$[N_{\mathrm{jet}},\Delta\eta(t,\bar{t})]$	9	135	116	321
$[N_{\mathrm{jet}}^{0,1+},M(\mathrm{t\bar{t}}),y(\mathrm{t\bar{t}})]$	24	34	30	61
$[N_{\mathrm{jet}}^{0,1+},M(\mathrm{t\bar{t}}),y(\mathrm{t\bar{t}})]$ (loose kin. reco.)	24	83	98	106
$[N_{\mathrm{jet}}^{0,1,2+},M(\mathrm{t\bar{t}}),y(\mathrm{t\bar{t}})]$	36	68	48	260
$[N_{\mathrm{jet}}^{0,1,2+},M(\mathrm{t\bar{t}}),y(\mathrm{t\bar{t}})]$ (loose kin. reco.)	36	142	158	425
$[N_{\mathrm{jet}}^{0,1,2,3+},M(\mathrm{t\bar{t}}),y(\mathrm{t\bar{t}})]$	48	90	60	435
$[N_{\mathrm{jet}}^{0,1,2,3+},M(\mathrm{t\bar{t}}),y(\mathrm{t\bar{t}})]$ (loose kin. reco.)	48	172	181	785

Table C.115: The χ^2 values (taking into account data uncertainties only) and dof of the measured normalized $t\bar{t}$ plus extra jets cross sections at parton level with respect to various MC predictions.

Cross section variables	dof	χ^2		
		POW-PYT	POW-HER	FXFX-PYT
$\eta(ej_1)$	15	16	29	28
$\eta(ej_2)$	15	59	56	8
$p_T(ej_1)$	4	107	156	149
$p_T(ej_2)$	4	224	92	193
$M(t\bar{t}+ej_1)$	5	72	22	97
$p_T(t\bar{t}+ej_1)$	5	34	91	6
$M(t\bar{t}+ej_1)/M(t\bar{t})$	5	61	170	90
$p_T(ej_1)/M(t\bar{t})$	4	46	65	48
$\Delta\eta(t,ej_1)/\Delta\eta(t,\bar{t})$	5	62	87	53

BIBLIOGRAPHY

[1] CDF Collaboration, "Observation of top quark production in $\bar{p}p$ collisions", *Phys. Rev. Lett.* **74** (1995) 2626–2631, doi:10.1103/PhysRevLett.74.2626, arXiv:hep-ex/9503002. 1, 10

[2] M. Diehl, "Theory Uncertainties", ch. 9, pp. 297–328. John Wiley and Sons, Ltd, 2013. arXiv:https://onlinelibrary.wiley.com/doi/pdf/10.1002/9783527653416.ch9. doi:https://doi.org/10.1002/9783527653416.ch9. 2, 14

[3] I. Korol, "Measurement of Double Differential $\mathrm{t\bar{t}}$ Production Cross Sections with the CMS Detector". PhD thesis, Hamburg U., 2016. doi:10.3204/DESY-THESIS-2016-011. 2, 16, 42, 66, 67, 70, 82

[4] CMS Collaboration, "Measurements of $\mathrm{t\bar{t}}$ differential cross sections in proton-proton collisions at $\sqrt{s} = 13$ TeV using events containing two leptons", *JHEP* **02** (2019) 149, doi:10.1007/JHEP02(2019)149, arXiv:1811.06625. 2, 35, 48, 66, 70, 79, 84, 86, 120

[5] M. Savitskyi, "Measurements of differential cross sections for $t\bar{t}$ production in proton-proton collisions at $\sqrt{s} = 13$ TeV using events containing two leptons with the CMS experiment". PhD thesis, Hamburg U., Hamburg, 2018. doi:10.3204/PUBDB-2018-02408. 2, 13, 14, 15, 42, 79, 82, 84, 86

[6] CMS Collaboration, "Measurement of $\mathrm{t\bar{t}}$ normalised multi-differential cross sections in pp collisions at $\sqrt{s} = 13$ TeV, and simultaneous determination of the strong coupling strength, top quark pole mass, and parton distribution functions", *Eur. Phys. J. C* **80** (2020), no. 7, 658, doi:10.1140/epjc/s10052-020-7917-7, arXiv:1904.05237. 2, 35, 42, 48, 66, 68, 69, 70, 79, 81, 84, 86, 91, 99, 107, 108, 132, 135, 136

[7] B. Pullman and A. Reisinger, "The Atom in the History of Human Thought". Oxford University Press, 2001. 3

[8] S. L. Glashow, "Partial Symmetries of Weak Interactions", *Nucl. Phys.* **22** (1961) 579–588, doi:10.1016/0029-5582(61)90469-2. 4, 9

[9] M. Gell-Mann, "The Eightfold Way: A Theory of strong interaction symmetry", doi:10.2172/4008239. 4

[10] P. W. Higgs, "Broken symmetries, massless particles and gauge fields", *Phys. Lett.* **12** (1964) 132–133, doi:10.1016/0031-9163(64)91136-9. 4

[11] P. W. Higgs, "Broken Symmetries and the Masses of Gauge Bosons", *Phys. Rev. Lett.* **13** (1964) 508–509, doi:10.1103/PhysRevLett.13.508. 4

[12] F. Englert and R. Brout, "Broken Symmetry and the Mass of Gauge Vector Mesons", *Phys. Rev. Lett.* **13** (1964) 321–323, doi:10.1103/PhysRevLett.13.321. 4

[13] G. S. Guralnik, C. R. Hagen, and T. W. B. Kibble, "Global Conservation Laws and Massless Particles", *Phys. Rev. Lett.* **13** (1964) 585–587, doi:10.1103/PhysRevLett.13.585. 4

[14] S. Weinberg, "A Model of Leptons", *Phys. Rev. Lett.* **19** (1967) 1264–1266, doi:10.1103/PhysRevLett.19.1264. 4, 9

[15] A. Salam, "Weak and Electromagnetic Interactions", *Conf. Proc. C* **680519** (1968) 367–377, doi:10.1142/9789812795915_0034. 4, 9

[16] G. ALTARELLI, "The Standard model of particle physics", arXiv:hep-ph/0510281. 4

[17] M. E. Peskin and D. V. Schroeder, "An Introduction to quantum field theory". Addison-Wesley, Reading, USA, 1995. 4, 10

[18] "100 incredible years of physics – particle physics". https://www.iop.org/about/iop-history/100th-anniversary/100-incredible-years. Accessed: 2021-07-30. 4

[19] S. Weinberg, "The Making of the standard model", *Eur. Phys. J. C* **34** (2004) 5–13, doi:10.1140/epjc/s2004-01761-1, arXiv:hep-ph/0401010. 4

[20] A. Pich, "Quantum chromodynamics", in *1994 European School of High-energy Physics*. 5, 1995. arXiv:hep-ph/9505231. 4, 6

[21] H. Leutwyler, "On the history of the strong interaction", *Mod. Phys. Lett. A* **29** (2014) 1430023, doi:10.1142/S0217732314300237, arXiv:1211.6777. 4

[22] J. J. Thomson, "Cathode rays", *Phil. Mag. Ser. 5* **44** (1897) 293–316, doi:10.1080/14786449708621070. 4

[23] J.-P. Luminet, "The Dark Matter Enigma", arXiv:2101.10127. 4

[24] "A new map of all the particles and forces". https://www.quantamagazine.org/a-new-map-of-the-standard-model-of-particle-physics-20201022/. Accessed: 2021-07-30. 5

[25] A. Plotnitsky, "A Matter of Principle: The Principles of Quantum Theory, Dirac's Equation, and Quantum Information", *Found. Phys.* **45** (2015), no. 10, 1222–1268, doi:10.1007/s10701-015-9928-z, arXiv:1503.02229. 4

[26] Super-Kamiokande Collaboration, "Evidence for oscillation of atmospheric neutrinos", *Phys. Rev. Lett.* **81** (1998) 1562–1567, doi:10.1103/PhysRevLett.81.1562, arXiv:hep-ex/9807003. 5, 10

[27] ALEPH, DELPHI, L3, OPAL, SLD, LEP Electroweak Working Group, SLD Electroweak Group, SLD Heavy Flavour Group Collaboration, "Precision electroweak measurements on the Z resonance", *Phys. Rept.* **427** (2006) 257–454, doi:10.1016/j.physrep.2005.12.006, arXiv:hep-ex/0509008. 6

[28] TASSO Collaboration, "Evidence for Planar Events in e+ e- Annihilation at High-Energies", *Phys. Lett. B* **86** (1979) 243–249, doi:10.1016/0370-2693(79)90830-X. 6

[29] J. Knolle, "Measuring luminosity and the $\mathrm{t\bar{t}Z}$ production cross section with the CMS experiment". PhD thesis, Hamburg U., Hamburg, 2020. doi:10.3204/PUBDB-2020-03187. 6, 8, 9, 25, 27, 136

[30] Particle Data Group Collaboration, "Review of Particle Physics", *PTEP* **2020** (2020), no. 8, 083C01, doi:10.1093/ptep/ptaa104. 7, 9, 10, 11, 12, 13, 22, 52, 66, 87, 88

[31] D. J. Gross and F. Wilczek, "Ultraviolet Behavior of Nonabelian Gauge Theories", *Phys. Rev. Lett.* **30** (1973) 1343–1346, doi:10.1103/PhysRevLett.30.1343. 7

[32] H. Bohr and H. B. Nielsen, "Hadron Production from a Boiling Quark Soup", *Nucl. Phys. B* **128** (1977) 275–293, doi:10.1016/0550-3213(77)90032-3. 7

[33] R. P. Feynman, "QED: The Strange Theory of Light and Matter". 1986. 7

[34] P. A. M. Dirac, "Quantum theory of emission and absorption of radiation", *Proc. Roy. Soc. Lond. A* **114** (1927) 243, doi:10.1098/rspa.1927.0039. 7

[35] N. Cabibbo, "Unitary Symmetry and Leptonic Decays", *Phys. Rev. Lett.* **10** (1963) 531–533, doi:10.1103/PhysRevLett.10.531. 8

[36] S. L. Glashow, J. Iliopoulos, and L. Maiani, "Weak Interactions with Lepton-Hadron Symmetry", *Phys. Rev. D* **2** (1970) 1285–1292, doi:10.1103/PhysRevD.2.1285. 8

[37] M. Kobayashi and T. Maskawa, "CP Violation in the Renormalizable Theory of Weak Interaction", *Prog. Theor. Phys.* **49** (1973) 652–657, doi:10.1143/PTP.49.652. 8

[38] I. J. R. Aitchison and A. J. G. Hey, "Gauge theories in particle physics: A practical introduction. Vol. 1: From relativistic quantum mechanics to QED". CRC Press, 2012. 8

[39] A. Maas, "Brout-Englert-Higgs physics: From foundations to phenomenology", *Prog. Part. Nucl. Phys.* **106** (2019) 132–209, doi:10.1016/j.ppnp.2019.02.003, arXiv:1712.04721. 9

[40] A. Santamaria, "Masses, mixings, Yukawa couplings and their symmetries", *Phys. Lett. B* **305** (Feb, 1993) 90–97. 14 p, doi:10.1016/0370-2693(93)91110-9. 9

[41] R. M. Wald, "General Relativity". Chicago Univ. Pr., Chicago, USA, 1984. 9

[42] T. Sauer, "Albert Einstein's 1916 review article on general relativity", arXiv:physics/0405066. 9

[43] H. Nicolai, "Quantum Gravity: the view from particle physics", *Fundam. Theor. Phys.* **177** (2014) 369–387, doi:10.1007/978-3-319-06349-2_18, arXiv:1301.5481. 9

[44] C. Kiefer, "Quantum gravity: General introduction and recent developments", *Annalen Phys.* **15** (2005) 129–148, doi:10.1002/andp.200510175, arXiv:gr-qc/0508120. 9, 10

[45] G. Ross, "Grand Unified Theories (Frontiers in Physics)". Westview Press, 2003. 10

[46] H. Georgi and S. L. Glashow, "Unity of All Elementary-Particle Forces", *Phys. Rev. Lett.* **32** (Feb, 1974) 438–441, doi:10.1103/PhysRevLett.32.438. 10

[47] S. William, "Theory of Everything: The Origin and Fate of the Universe". Motilal Books UK, 2007. 10

[48] L. Baudis, "The Search for Dark Matter", doi:10.1017/S1062798717000783, arXiv:1801.08128. 10

[49] J. Einasto, "Dark Matter", 2010. 10

[50] L. Amendola and S. Tsujikawa, "Dark Energy: Theory and Observations". Cambridge University Press, 2010. 10

[51] G. Bertone, D. Hooper, and J. Silk, "Particle dark matter: Evidence, candidates and constraints", *Phys. Rept.* **405** (2005) 279–390, doi:10.1016/j.physrep.2004.08.031, arXiv:hep-ph/0404175. 10

[52] W. Bernreuther, "CP violation and baryogenesis", *Lect. Notes Phys.* **591** (2002) 237–293, arXiv:hep-ph/0205279. 10

[53] SNO Collaboration, "Measurement of the rate of $\nu_e + d \to p + p + e^-$ interactions produced by ^{8}B solar neutrinos at the Sudbury Neutrino Observatory", *Phys. Rev. Lett.* **87** (2001) 071301, doi:10.1103/PhysRevLett.87.071301, arXiv:nucl-ex/0106015. 10

[54] Planck Collaboration, "Planck 2018 results. VI. Cosmological parameters", *Astron. Astrophys.* **641** (2020) A6, doi:10.1051/0004-6361/201833910, arXiv:1807.06209. [Erratum: Astron.Astrophys. 652, C4 (2021)]. 10

[55] I. J. R. Aitchison, "Supersymmetry in Particle Physics. An Elementary Introduction". Cambridge University Press, Cambridge, 2007. 10

[56] H. Baer and X. Tata, "The Minimal Supersymmetric Standard Model", p. 127–189. Cambridge University Press, 2006. doi:10.1017/CBO9780511617270.009. 10

[57] S. Weinberg, "Effective Gauge Theories", *Phys. Lett. B* **91** (1980) 51–55, doi:10.1016/0370-2693(80)90660-7. 10

[58] W. Buchmuller and D. Wyler, "Effective Lagrangian Analysis of New Interactions and Flavor Conservation", *Nucl. Phys. B* **268** (1986) 621–653, doi:10.1016/0550-3213(86)90262-2. 10

[59] J. Polchinski, "String theory. Vol. 1: An introduction to the bosonic string". Cambridge Monographs on Mathematical Physics. Cambridge University Press, 12, 2007. 10

[60] O. Alvarez, "Theory of Strings with Boundaries: Fluctuations, Topology, and Quantum Geometry", *Nucl. Phys. B* **216** (1983) 125–184, doi:10.1016/0550-3213(83)90490-X. 10

[61] D0 Collaboration, "Observation of the top quark", *Phys. Rev. Lett.* **74** (1995) 2632–2637, doi:10.1103/PhysRevLett.74.2632, arXiv:hep-ex/9503003. 10

[62] ATLAS Collaboration, T. Barillari, "Top-quark mass and top-quark pole mass measurements with the ATLAS detector", 10, 2017. arXiv:1710.06019. 10

[63] V. Shiltsev, "Achievements and Lessons from Tevatron", *Conf. Proc. C* **110904** (2011) 903–907, arXiv:1205.0536. 11

[64] on behalf of the ATLAS Collaboration, CDF Collaboration, CMS Collaboration and D0 Collaboration Collaboration, "Production of single top quark - results from the Tevatron and the LHC", technical report, Oct, 2014. arXiv:1410.3045, Comments: 5 pages, 4 figures, for the ATLAS, CDF, CMS and D0 collaborations, Presented at 26th Rencontres de Blois, Particle Physics and Cosmology, May 18-23, 2014. 11

[65] H1, ZEUS Collaboration, "Combination of measurements of inclusive deep inelastic $e^{\pm}p$ scattering cross sections and QCD analysis of HERA data", *Eur. Phys. J. C* **75** (2015), no. 12, 580, doi:10.1140/epjc/s10052-015-3710-4, arXiv:1506.06042. 12

[66] NNPDF Collaboration, "Parton distributions from high-precision collider data", *Eur. Phys. J. C* **77** (2017), no. 10, 663, doi:10.1140/epjc/s10052-017-5199-5, arXiv:1706.00428. 12

[67] NNPDF Collaboration, "Parton distributions from high-precision collider data", *Eur. Phys. J. C* **77** (2017), no. 10, 663, doi:10.1140/epjc/s10052-017-5199-5, arXiv:1706.00428. 12, 34, 86, 120

[68] M. M. Defranchis, "First measurement of the running of the top quark mass". PhD thesis, Hamburg U., Hamburg, 2020. doi:10.3204/PUBDB-2020-02655. 12

[69] J. B. Kogut and L. Susskind, "Parton models and asymptotic freedom", *Phys. Rev. D* **9** (1974) 3391–3399, doi:10.1103/PhysRevD.9.3391. 12

[70] CMS Collaboration, "Measurement of the ratio $\mathcal{B}(t \to Wb)/\mathcal{B}(t \to Wq)$ in pp collisions at $\sqrt{s} = 8$ TeV", *Phys. Lett. B* **736** (2014) 33–57, doi:10.1016/j.physletb.2014.06.076, arXiv:1404.2292. 13

[71] A. Ali and G. Kramer, "Jets and QCD: A Historical Review of the Discovery of the Quark and Gluon Jets and its Impact on QCD", *Eur. Phys. J. H* **36** (2011) 245–326, doi:10.1140/epjh/e2011-10047-1, arXiv:1012.2288. 14

[72] L. Evans and P. Bryant, "LHC Machine", *Journal of Instrumentation* **3** (aug, 2008) S08001–S08001, doi:10.1088/1748-0221/3/08/s08001. 17

[73] The CMS Collaboration, "The CMS experiment at the CERN LHC", *Journal of Instrumentation* **3** (aug, 2008) S08004–S08004, doi:10.1088/1748-0221/3/08/s08004. 17

[74] The ALICE Collaboration, "The ALICE experiment at the CERN LHC", *Journal of Instrumentation* **3** (aug, 2008) S08002–S08002, doi:10.1088/1748-0221/3/08/s08002. 17

[75] The ATLAS Collaboration, "The ATLAS Experiment at the CERN Large Hadron Collider", *Journal of Instrumentation* **3** (aug, 2008) S08003–S08003, doi:10.1088/1748-0221/3/08/s08003. 17, 19

[76] The LHCb Collaboration, "The LHCb Detector at the LHC", *Journal of Instrumentation* **3** (aug, 2008) S08005–S08005, doi:10.1088/1748-0221/3/08/s08005. 17

[77] "The CERN accelerator complex. Complexe des acclrateurs du CERN.", Technical Report CERN-DI-0812015, CERN, Geneva, 2008. 18

[78] A. G. et al., "High-Luminosity Large Hadron Collider (HL-LHC): Technical Design Report V. 0.1". CERN Yellow Reports: Monographs. CERN, Geneva, 2017. 18, 136

[79] A. Dainese et al., "Report on the Physics at the HL-LHC, and Perspectives for the HE-LHC", Technical Report CERN-2019-007, Geneva, Switzerland, 2019. doi:10.23731/CYRM-2019-007. 18

[80] T. Sakuma and T. McCauley, "Detector and Event Visualization with SketchUp at the CMS Experiment", *Journal of Physics: Conference Series* **513** (Jun, 2014) 022032, doi:10.1088/1742-6596/513/2/022032. 20

[81] A. Sirunyan et al., "Particle-flow reconstruction and global event description with the CMS detector", *Journal of Instrumentation* **12** (Oct, 2017) P10003–P10003, doi:10.1088/1748-0221/12/10/p10003. 20, 40

[82] CMS Collaboration, "Alignment of the CMS silicon tracker during commissioning with cosmic rays", *Journal of Instrumentation* **5** (Mar, 2010) T03009–T03009, doi:10.1088/1748-0221/5/03/t03009. 22

[83] A. Dominguez et al., "CMS Technical Design Report for the Pixel Detector Upgrade", Technical Report CERN-LHCC-2012-016. CMS-TDR-11, Sep, 2012. Additional contacts: Jeffrey Spalding, Fermilab, Jeffrey.Spalding@cern.ch Didier Contardo, Universite Claude Bernard-Lyon I, didier.claude.contardo@cern.ch. 21

[84] CMS Collaboration, "The Phase-1 Upgrade of the CMS Pixel Detector", Technical Report CMS-CR-2017-135. 06, CERN, Geneva, May, 2017. doi:10.1088/1748-0221/12/07/C07009. 21

[85] A. Benaglia, "The CMS ECAL performance with examples", *Journal of Instrumentation* **9** (feb, 2014) C02008–C02008, doi:10.1088/1748-0221/9/02/c02008. 22, 23

[86] *Journal of Instrumentation* **8** (Sep, 2013) P09009–P09009, doi:10.1088/1748-0221/8/09/p09009. 22

[87] S. Abdullin et al., "Design, performance, and calibration of CMS forward calorimeter wedges", *The European Physical Journal C* **53** (2008) 103–116, doi:10.1140/epjc/s10052-007-0459-4. 23

[88] CMS Collaboration, "CMS Physics: Technical Design Report Volume 1: Detector Performance and Software". Technical design report. CMS. CERN, Geneva, 2006. There is an error on cover due to a technical problem for some items. 23, 24, 25

[89] CMS Collaboration, "Performance of CMS hadron calorimeter timing and synchronization using test beam, cosmic ray, and LHC beam data", *Journal of Instrumentation* **5** (Mar, 2010) T03013–T03013, doi:10.1088/1748-0221/5/03/t03013. 24

[90] V. Khachatryan et al., "The CMS trigger system", *Journal of Instrumentation* **12** (Jan, 2017) P01020–P01020, doi:10.1088/1748-0221/12/01/p01020. 24

[91] CMS Collaboration, "Precision luminosity measurement in proton-proton collisions at $\sqrt{s} = 13$ TeV in 2015 and 2016 at CMS", *Eur. Phys. J. C* **81** (2021), no. 9, 800, doi:10.1140/epjc/s10052-021-09538-2, arXiv:2104.01927. 25, 26, 27

[92] O. Karacheban, "Luminosity measurement at CMS", 2017. Presented 05 Jan 2017. 25, 26

[93] S. van der Meer, "Calibration of the effective beam height in the ISR", technical report, CERN, Geneva, 1968. 25

[94] U. Amaldi et al., "Precision Measurement of Proton Proton Total Cross-section at the CERN Intersecting Storage Rings", *Nucl. Phys. B* **145** (1978) 367–401, doi:10.1016/0550-3213(78)90090-1. 27

[95] CMS Collaboration, "Public CMS luminosity information". https://cmslumi.web.cern.ch/publicplots/, 2021. 27, 39, 40

[96] N. Metropolis and S. Ulam, "The Monte Carlo Method", *Journal of the American Statistical Association* **44** (1949), no. 247, 335–341, doi:10.1080/01621459.1949.10483310, arXiv:https://www.tandfonline.com/doi/pdf/10.1080/01621459.1949.10483310. PMID: 18139350. 29, 35

[97] N. Bartosik. http://bartosik.pp.ua, 2016. 30

[98] T. Sjöstrand and P. Z. Skands, "Transverse-momentum-ordered showers and interleaved multiple interactions", *The European Physical Journal C* **39** (Feb, 2005) 129–154, doi:10.1140/epjc/s2004-02084-y. 31

[99] T. Sjöstrand et al., "An introduction to PYTHIA 8.2", *Computer Physics Communications* **191** (2015) 159–177, doi:https://doi.org/10.1016/j.cpc.2015.01.024. 31

[100] Bähr, Manuel et al., "Herwig++ physics and manual", *Eur. Phys. J. C* **58** (2008), no. 4, 639–707, doi:10.1140/epjc/s10052-008-0798-9. 31

[101] X. Artru and G. Mennessier, "String model and multiproduction", *Nucl. Phys. B* **70** (1974) 93–115, doi:10.1016/0550-3213(74)90360-5. 31

[102] B. Andersson, G. Gustafson, G. Ingelman, and T. Sjöstrand, "Parton fragmentation and string dynamics", *Physics Reports* **97** (1983), no. 2, 31–145, doi:https://doi.org/10.1016/0370-1573(83)90080-7. 31

[103] T. Sjöstrand, S. Mrenna, and P. Skands, "PYTHIA 6.4 physics and manual", *Journal of High Energy Physics* **2006** (may, 2006) 026–026, doi:10.1088/1126-6708/2006/05/026. 31

[104] A. Buckley et al., "General-purpose event generators for LHC physics", *Physics Reports* **504** (Jul, 2011) 145–233, doi:10.1016/j.physrep.2011.03.005. 32

[105] D. Amati and G. Veneziano, "Preconfinement as a Property of Perturbative QCD", *Phys. Lett. B* **83** (1979) 87–92, doi:10.1016/0370-2693(79)90896-7. 32

[106] B. R. Webber, "Fragmentation and hadronization", *Int. J. Mod. Phys. A* **15S1** (2000) 577–606, doi:10.1142/S0217751X00005334, arXiv:hep-ph/9912292. 33

[107] P. Nason, "A New Method for Combining NLO QCD with Shower Monte Carlo Algorithms", *Journal of High Energy Physics* **2004** (Nov, 2004) 040–040, doi:10.1088/1126-6708/2004/11/040. 32

[108] S. Frixione, P. Nason, and C. Oleari, "Matching NLO QCD computations with parton shower simulations: the POWHEG method", *Journal of High Energy Physics* **2007** (nov, 2007) 070–070, doi:10.1088/1126-6708/2007/11/070. 32

[109] T. Ježo, J. M. Lindert, N. Moretti, and S. Pozzorini, "New NLOPS predictions for $t\bar{t} + b$ -jet production at the LHC", *Eur. Phys. J. C* **78** (2018), no. 6, 502, doi:10.1140/epjc/s10052-018-5956-0, arXiv:1802.00426. 33

[110] P. Skands, S. Carrazza, and J. Rojo, "Tuning PYTHIA 8.1: the Monash 2013 Tune", *Eur. Phys. J. C* **74** (2014), no. 8, 3024, doi:10.1140/epjc/s10052-014-3024-y, arXiv:1404.5630. 33

[111] R. Frederix and S. Frixione, "Merging meets matching in MC@NLO", *Journal of High Energy Physics* **2012** (Dec, 2012) doi:10.1007/jhep12(2012)061. 33

[112] CMS Collaboration, "Event generator tunes obtained from underlying event and multiparton scattering measurements", *Eur. Phys. J. C* **76** (2016), no. 3, 155, doi:10.1140/epjc/s10052-016-3988-x, arXiv:1512.00815. 33

[113] A. Buckley et al., "General-purpose event generators for LHC physics", *Physics Reports* **504** (2011), no. 5, 145–233, doi:https://doi.org/10.1016/j.physrep.2011.03.005. 34

[114] "Color reconnection implementations in Pythia8". http://home.thep.lu.se/Pythia/pythia82html/ColourReconnection.html. 34

[115] S. Gieseke, C. Rohr, and A. Siodmok, "Colour reconnections in Herwig++", *Eur. Phys. J. C* **72** (2012) 2225, doi:10.1140/epjc/s10052-012-2225-5, arXiv:1206.0041. 34

[116] "Color reconnection in $t\bar{t}$ final states". https://indico.cern.ch/event/340357/contributions/1733545/attachments/667577/917604/ColorReconnection.pdf. 34

[117] "Unbiased global determination of parton distributions and their uncertainties at NNLO and at LO", *Nuclear Physics B* **855** (2012), no. 2, 153–221, doi:https://doi.org/10.1016/j.nuclphysb.2011.09.024. 34

[118] A. Buckley et al., "General-purpose event generators for LHC physics", *Phys. Rept.* **504** (2011) 145–233, doi:10.1016/j.physrep.2011.03.005, arXiv:1101.2599. 35

[119] T. Sjöstrand et al., "An introduction to PYTHIA 8.2", *Comput. Phys. Commun.* **191** (2015) 159–177, doi:10.1016/j.cpc.2015.01.024, arXiv:1410.3012. 35

[120] CMS Collaboration, "Extraction and validation of a new set of CMS PYTHIA8 tunes from underlying-event measurements", *Eur. Phys. J. C* **80** (2020), no. 1, 4, doi:10.1140/epjc/s10052-019-7499-4, arXiv:1903.12179. 35, 87

[121] J. Bellm et al., "Herwig 7.0/Herwig++ 3.0 release note", *Eur. Phys. J. C* **76** (2016), no. 4, 196, doi:10.1140/epjc/s10052-016-4018-8, arXiv:1512.01178. 35

[122] CMS Collaboration, "Development and validation of HERWIG 7 tunes from CMS underlying-event measurements", *Eur. Phys. J. C* **81** (2021), no. 4, 312, doi:10.1140/epjc/s10052-021-08949-5, arXiv:2011.03422. 35

[123] J. Alwall et al., "The automated computation of tree-level and next-to-leading order differential cross sections, and their matching to parton shower simulations", *JHEP* **07** (2014) 079, doi:10.1007/JHEP07(2014)079, arXiv:1405.0301. 35

[124] R. Frederix et al., "A study of multi-jet production in association with an electroweak vector boson", *JHEP* **02** (2016) 131, doi:10.1007/JHEP02(2016)131, arXiv:1511.00847. 35

[125] P. Artoisenet, R. Frederix, O. Mattelaer, and R. Rietkerk, "Automatic spin-entangled decays of heavy resonances in Monte Carlo simulations", *JHEP* **03** (2013) 015, doi:10.1007/JHEP03(2013)015, arXiv:1212.3460. 35

[126] S. Alioli, P. Nason, C. Oleari, and E. Re, "A general framework for implementing NLO calculations in shower Monte Carlo programs: the POWHEG BOX", *JHEP* **06** (2010) 043, doi:10.1007/JHEP06(2010)043, arXiv:1002.2581. 35, 120

[127] S. Frixione, P. Nason, and G. Ridolfi, "A Positive-weight next-to-leading-order Monte Carlo for heavy flavour hadroproduction", *JHEP* **09** (2007) 126, doi:10.1088/1126-6708/2007/09/126, arXiv:0707.3088. 35

[128] O. Latunde-Dada, S. Gieseke, and B. Webber, "A Positive-Weight Next-to-Leading-Order Monte Carlo for e+ e- Annihilation to Hadrons", *JHEP* **02** (2007) 051, doi:10.1088/1126-6708/2007/02/051, arXiv:hep-ph/0612281. 35

[129] O. Latunde-Dada, "Applying the POWHEG method to top pair production and decays at the ILC", *Eur. Phys. J. C* **58** (2008) 543–554, doi:10.1140/epjc/s10052-008-0785-1, arXiv:0806.4560. 35

[130] S. Alioli, P. Nason, C. Oleari, and E. Re, "NLO single-top production matched with shower in POWHEG: s- and t-channel contributions", *JHEP* **09** (2009) 111, doi:10.1088/1126-6708/2009/09/111, arXiv:0907.4076. [Erratum: JHEP 02, 011 (2010)]. 35

[131] M. Czakon and A. Mitov, "Top++: A Program for the Calculation of the Top-Pair Cross-Section at Hadron Colliders", *Comput. Phys. Commun.* **185** (2014) 2930, doi:10.1016/j.cpc.2014.06.021, arXiv:1112.5675. 36

[132] M. Cacciari et al., "Top-pair production at hadron colliders with next-to-next-to-leading logarithmic soft-gluon resummation", *Phys. Lett. B* **710** (2012) 612–622, doi:10.1016/j.physletb.2012.03.013, arXiv:1111.5869. 36

[133] P. Bärnreuther, M. Czakon, and A. Mitov, "Percent Level Precision Physics at the Tevatron: First Genuine NNLO QCD Corrections to $q\bar{q} \to t\bar{t} + X$", *Phys. Rev. Lett.* **109** (2012) 132001, doi:10.1103/PhysRevLett.109.132001, arXiv:1204.5201. 36

[134] M. Czakon and A. Mitov, "NNLO corrections to top-pair production at hadron colliders: the all-fermionic scattering channels", *JHEP* **12** (2012) 054, doi:10.1007/JHEP12(2012)054, arXiv:1207.0236. 36

[135] M. Czakon and A. Mitov, "NNLO corrections to top pair production at hadron colliders: the quark-gluon reaction", *JHEP* **01** (2013) 080, doi:10.1007/JHEP01(2013)080, arXiv:1210.6832. 36

[136] M. Beneke, P. Falgari, S. Klein, and C. Schwinn, "Hadronic top-quark pair production with NNLL threshold resummation", *Nucl. Phys. B* **855** (2012) 695–741, doi:10.1016/j.nuclphysb.2011.10.021, arXiv:1109.1536. 36

[137] M. Czakon, P. Fiedler, and A. Mitov, "Total Top-Quark Pair-Production Cross Section at Hadron Colliders Through $O(\alpha_S^4)$", *Phys. Rev. Lett.* **110** (2013) 252004, doi:10.1103/PhysRevLett.110.252004, arXiv:1303.6254. 36

[138] S. Agostinelli et al., "Geant4—a simulation toolkit", *Nuclear Instruments and Methods in Physics Research Section A: Accelerators, Spectrometers, Detectors and Associated Equipment* **506** (2003), no. 3, 250–303, doi:https://doi.org/10.1016/S0168-9002(03)01368-8. 36

[139] CMS Collaboration and T. Mc Cauley, "Collisions recorded by the CMS detector on 14 Oct 2016 during the high pile-up fill", (Nov, 2016). CMS Collection. 38

[140] CMS Collaboration, "Alignment of the CMS silicon tracker during commissioning with cosmic rays", *Journal of Instrumentation* **5** (mar, 2010) T03009–T03009, doi:10.1088/1748-0221/5/03/t03009. 38

[141] CMS Collaboration, "Description and performance of track and primary-vertex reconstruction with the CMS tracker", *Journal of Instrumentation* **9** (Oct, 2014) P10009–P10009, doi:10.1088/1748-0221/9/10/p10009. 38, 39, 40

[142] P. Billoir and S. Qian, "Simultaneous pattern recognition and track fitting by the Kalman filtering method", *Nuclear Instruments and Methods in Physics Research Section A: Accelerators, Spectrometers, Detectors and Associated Equipment* **294** (1990), no. 1, 219–228, doi:https://doi.org/10.1016/0168-9002(90)91835-Y. 39

[143] K. Rose, "Deterministic annealing for clustering, compression, classification, regression, and related optimization problems", *Proceedings of the IEEE* **86** (1998), no. 11, 2210–2239, doi:10.1109/5.726788. 39

[144] W. Waltenberger, R. Frühwirth, and P. Vanlaer, "Adaptive vertex fitting", *Journal of Physics G: Nuclear and Particle Physics* **34** (nov, 2007) N343–N356, doi:10.1088/0954-3899/34/12/n01. 39

[145] CMS Collaboration, "Particle-Flow Event Reconstruction in CMS and Performance for Jets, Taus, and MET", Technical Report CMS-PAS-PFT-09-001, CERN, Geneva, Apr, 2009. 40

[146] N. Bartosik, "PF concept in CMS". http://bartosik.pp.ua/hep_sketches/cms_particle_flow, 2016. 41

[147] CMS Collaboration, "Muon Identification and Isolation efficiency on full 2016 dataset",. 41

[148] CMS Collaboration, "Measurement of the $t\bar{t}$ production cross section using events in the eμ final state in pp collisions at $\sqrt{s} = 13$ TeV", *Eur. Phys. J. C* **77** (2017) 172, doi:10.1140/epjc/s10052-017-4718-8, arXiv:1611.04040. 41, 42, 43

[149] S. Chatrchyan et al., "Measurement of the inclusive W and Z production cross sections in pp collisions at $\sqrt{s} = 7$ TeV with the CMS experiment", *Journal of High Energy Physics* **2011** (Oct, 2011) doi:10.1007/jhep10(2011)132. 41

[150] W. Adam, R. Frühwirth, A. Strandlie, and T. Todor, "Reconstruction of Electrons with the Gaussian-Sum Filter in the CMS Tracker at the LHC", Technical Report CMS-NOTE-2005-001, CERN, Geneva, Jan, 2005. 42

[151] CMS Collaboration, "Commissioning of the Particle-flow Event Reconstruction with the first LHC collisions recorded in the CMS detector",. 42

[152] F. F. S. Baffioni, C. Charlot, "Electron reconstruction in CMS", *The European Physical Journal C* **49** (2007) doi:10.1140/epjc/s10052-006-0175-5. 42

[153] CMS Collaboration, "Measurement of the Top Quark Pair Production Cross Section in Proton-Proton Collisions at $\sqrt{s} = 13$ TeV", *Phys. Rev. Lett.* **116** (Feb, 2016) 052002, doi:10.1103/PhysRevLett.116.052002. 42

[154] M. Cacciari, G. P. Salam, and G. Soyez, "The anti-ktjet clustering algorithm", *Journal of High Energy Physics* **2008** (Apr, 2008) 063–063, doi:10.1088/1126-6708/2008/04/063. 43

[155] CMS Collaboration Collaboration, "Jet algorithms performance in 13 TeV data", Technical Report CMS-PAS-JME-16-003, CERN, Geneva, 2017. 43

[156] CMS Collaboration, "A Deep Neural Network for Simultaneous Estimation of b Jet Energy and Resolution", *Comput. Softw. Big Sci.* **4** (2020), no. 1, 10, doi:10.1007/s41781-020-00041-z, arXiv:1912.06046. 43

[157] A. Sirunyan et al., "Identification of heavy-flavour jets with the CMS detector in pp collisions at 13 TeV", *Journal of Instrumentation* **13** (May, 2018) P05011–P05011, doi:10.1088/1748-0221/13/05/p05011. 44, 45, 85

[158] D. Guest et al., "Jet flavor classification in high-energy physics with deep neural networks", *Physical Review D* **94** (Dec, 2016) doi:10.1103/physrevd.94.112002. 44

[159] T. Sakuma for the CMS Collaboration, "CMS-doc-12312-v1: Missing ET Schematic Diagram". https://cms-docdb.cern.ch/cgi-bin/PublicDocDB/ShowDocument?docid=12312, 2014. 45

[160] CMS Collaboration, "Pileup mitigation at CMS in 13 TeV data", *JINST* **15** (2020), no. 09, P09018, doi:10.1088/1748-0221/15/09/P09018, arXiv:2003.00503. 45

[161] CMS Collaboration Collaboration, "Performance of missing energy reconstruction in 13 TeV pp collision data using the CMS detector", Technical Report CMS-PAS-JME-16-004, CERN, Geneva, 2016. 45

[162] T. C. collaboration, "Performance of the CMS missing transverse momentum reconstruction in pp data at $\sqrt{s} = 8$ TeV", *Journal of Instrumentation* **10** (feb, 2015) P02006–P02006, doi:10.1088/1748-0221/10/02/p02006. 45

[163] "CMS Luminosity Physics Object Group (Lumi POG)". `https://twiki.cern.ch/twiki/bin/view/CMS/TWikiLUM`. 48

[164] CMS Collaboration, "Precision luminosity measurement in proton-proton collisions at $\sqrt{s} = 13$ TeV in 2015 and 2016 at CMS", technical report, CERN, Geneva, Apr, 2021. `arXiv:2104.01927`, Submitted to EPJC. All figures and tables can be found at http://cms-results.web.cern.ch/cms-results/public-results/publications/LUM-17-003 (CMS Public Pages). 48

[165] CMS Collaboration Collaboration, "CMS luminosity measurement for the 2017 data-taking period at $\sqrt{s} = 13$ TeV", technical report, CERN, Geneva, 2018. 48

[166] CMS Collaboration Collaboration, "CMS luminosity measurement for the 2018 data-taking period at $\sqrt{s} = 13$ TeV", technical report, CERN, Geneva, 2019. 48

[167] M. Rovere, "The Data Quality Monitoring Software for the CMS experiment at the LHC", *Journal of Physics: Conference Series* **664** (dec, 2015) 072039, `doi:10.1088/1742-6596/664/7/072039`. 48

[168] N. Kidonakis, "Top Quark Production", in *Helmholtz International Summer School on Physics of Heavy Quarks and Hadrons*. 11, 2013. `arXiv:1311.0283`. `doi:10.3204/DESY-PROC-2013-03/Kidonakis`. 50

[169] N. Kidonakis, "Two-loop soft anomalous dimensions for single top quark associated production with a W^- or H^-", *Phys. Rev. D* **82** (Sep, 2010) 054018, `doi:10.1103/PhysRevD.82.054018`. 50

[170] J. M. Campbell and R. K. Ellis, "MCFM for the Tevatron and the LHC", *Nucl. Phys. B Proc. Suppl.* **205-206** (2010) 10–15, `doi:10.1016/j.nuclphysbps.2010.08.011`, `arXiv:1007.3492`. 50

[171] T. Gehrmann et al., "Jet cross sections and transverse momentum distributions with NNLOJET", *PoS* **RADCOR2017** (2018) 074, `doi:10.22323/1.290.0074`, `arXiv:1801.06415`. 50

[172] R. Gavin, Y. Li, F. Petriello, and S. Quackenbush, "FEWZ 2.0: A code for hadronic Z production at next-to-next-to-leading order", *Comput. Phys. Commun.* **182** (2011) 2388–2403, `doi:10.1016/j.cpc.2011.06.008`, `arXiv:1011.3540`. 50, 51

[173] R. Gavin, Y. Li, F. Petriello, and S. Quackenbush, "W Physics at the LHC with FEWZ 2.1", *Comput. Phys. Commun.* **184** (2013) 208–214, `doi:10.1016/j.cpc.2012.09.005`, `arXiv:1201.5896`. 50, 51

[174] Y. Li and F. Petriello, "Combining QCD and electroweak corrections to dilepton production in the framework of the FEWZ simulation code", *Phys. Rev. D* **86** (Nov, 2012) 094034, `doi:10.1103/PhysRevD.86.094034`. 50, 51

[175] I. Antcheva et al., "ROOT — A C++ framework for petabyte data storage, statistical analysis and visualization", *Comput. Phys. Commun.* **182** (2011) 1384–1385, `doi:10.1016/j.cpc.2011.02.008`. 51

[176] R. J. Barlow and C. Beeston, "Fitting using finite Monte Carlo samples", *Comput. Phys. Commun.* **77** (1993) 219–228, doi:10.1016/0010-4655(93)90005-W. 51

[177] CMS Collaboration, "Measurement of the differential cross section for top quark pair production in pp collisions at $\sqrt{s} = 8$ TeV", *Eur. Phys. J. C* **75** (2015), no. 11, 542, doi:10.1140/epjc/s10052-015-3709-x, arXiv:1505.04480. 66, 126

[178] B. A. Betchart, R. Demina, and A. Harel, "Analytic solutions for neutrino momenta in decay of top quarks", *Nucl. Instrum. Meth. A* **736** (2014) 169–178, doi:10.1016/j.nima.2013.10.039, arXiv:1305.1878. 66

[179] L. Sonnenschein, "Analytical solution of ttbar dilepton equations", *Phys. Rev. D* **73** (2006) 054015, doi:10.1103/PhysRevD.78.079902, arXiv:hep-ph/0603011. [Erratum: Phys.Rev.D 78, 079902 (2008)]. 66, 67

[180] CMS Collaboration, "Measurement of double-differential cross sections for top quark pair production in pp collisions at $\sqrt{s} = 8$ TeV and impact on parton distribution functions", *Eur. Phys. J. C* **77** (2017), no. 7, 459, doi:10.1140/epjc/s10052-017-4984-5, arXiv:1703.01630. 66, 99

[181] CMS Collaboration, "Measurement of Differential Top-Quark Pair Production Cross Sections in *pp* collisions at $\sqrt{s} = 7$ TeV", *Eur. Phys. J. C* **73** (2013), no. 3, 2339, doi:10.1140/epjc/s10052-013-2339-4, arXiv:1211.2220. 70, 126

[182] CMS Collaboration, "Measurement of normalized differential $\mathrm{t\bar{t}}$ cross sections in the dilepton channel from pp collisions at $\sqrt{s} = 13$ TeV", *JHEP* **04** (2018) 060, doi:10.1007/JHEP04(2018)060, arXiv:1708.07638. 70

[183] N. Kidonakis, "Top-quark double-differential distributions at approximate $\mathrm{N^3LO}$", *Phys. Rev. D* **101** (2020), no. 7, 074006, doi:10.1103/PhysRevD.101.074006, arXiv:1912.10362. 70

[184] S. Schmitt, "Data Unfolding Methods in High Energy Physics", *EPJ Web Conf.* **137** (2017) 11008, doi:10.1051/epjconf/201713711008, arXiv:1611.01927. 74, 76

[185] "Unfolding in High Energy Physics". https://indico.desy.de/event/9288/contributions/89070/attachments/59802/72532/UnfoldStatSchool2014.pdf. Accessed: 2021-05-26. 75

[186] S. Schmitt, "TUnfold: an algorithm for correcting migration effects in high energy physics", *JINST* **7** (2012) T10003, doi:10.1088/1748-0221/7/10/T10003, arXiv:1205.6201. 75, 90

[187] A. N. Tikhonov, "Solution of incorrectly formulated problems and the regularization method", *Soviet Math. Dokl.* **4** (1963) 1035–1038. 75

[188] "PYTHIA event generator, Particle Properties". http://home.thep.lu.se/~torbjorn/pythia81html/ParticleProperties.html. Accessed: 2021-05-30. 79

[189] "LHCTopWG - LHC Top Physics Working Group". `https://twiki.cern.ch/twiki/bin/view/LHCPhysics/LHCTopWG`. Accessed: 2021-05-30. 79

[190] CMS Collaboration Collaboration, "Object definitions for top quark analyses at the particle level", technical report, CERN, Geneva, Jun, 2017. 79

[191] M. Cacciari and G. P. Salam, "Pileup subtraction using jet areas", *Phys. Lett. B* **659** (2008) 119–126, `doi:10.1016/j.physletb.2007.09.077`, `arXiv:0707.1378`. 80

[192] E. Bols et al., "Jet Flavour Classification Using DeepJet", *JINST* **15** (2020), no. 12, P12012, `doi:10.1088/1748-0221/15/12/P12012`, `arXiv:2008.10519`. 80

[193] V. Khachatryan et al., "Jet energy scale and resolution in the CMS experiment in pp collisions at 8 TeV", *Journal of Instrumentation* **12** (Feb, 2017) P02014–P02014, `doi:10.1088/1748-0221/12/02/p02014`. 84

[194] ATLAS Collaboration, "Measurement of the Inelastic Proton-Proton Cross Section at $\sqrt{s} = 13$ TeV with the ATLAS Detector at the LHC", *Phys. Rev. Lett.* **117** (2016), no. 18, 182002, `doi:10.1103/PhysRevLett.117.182002`, `arXiv:1606.02625`. 85

[195] S. Argyropoulos and T. Sjöstrand, "Effects of color reconnection on $t\bar{t}$ final states at the LHC", *JHEP* **11** (2014) 043, `doi:10.1007/JHEP11(2014)043`, `arXiv:1407.6653`. 87

[196] E. Ben-Haim, "The b Quark Fragmentation Function, From LEP to TeVatron". PhD thesis, Paris U., VI-VII, 2004. `doi:10.2172/15011748`. 87

[197] CMS Collaboration, "Investigations of the impact of the parton shower tuning in Pythia 8 in the modelling of $\mathrm{t\bar{t}}$ at $\sqrt{s} = 8$ and 13 TeV", technical report, CERN, Geneva, 2016. 87

[198] C. Peterson, D. Schlatter, I. Schmitt, and P. M. Zerwas, "Scaling Violations in Inclusive e+ e- Annihilation Spectra", *Phys. Rev. D* **27** (1983) 105, `doi:10.1103/PhysRevD.27.105`. 87

[199] CMS Collaboration, "Measurement of differential cross sections for the production of top quark pairs and of additional jets in lepton+jets events from pp collisions at $\sqrt{s} =$ 13 TeV", *Phys. Rev. D* **97** (2018), no. 11, 112003, `doi:10.1103/PhysRevD.97.112003`, `arXiv:1803.08856`. 97, 132

[200] ATLAS Collaboration, "Measurement of the top-quark mass in $t\bar{t} + 1$-jet events collected with the ATLAS detector in pp collisions at $\sqrt{s} = 8$ TeV", *JHEP* **11** (2019) 150, `doi:10.1007/JHEP11(2019)150`, `arXiv:1905.02302`. 116

[201] M. L. Czakon et al., "Top quark pair production at complete NLO accuracy with NNLO+NNLL' corrections in QCD", *Chin. Phys. C* **44** (2020), no. 8, 083104, `doi:10.1088/1674-1137/44/8/083104`, `arXiv:1901.08281`. 116

[202] N. Kidonakis, "NNNLO soft-gluon corrections for the top-quark p_T and rapidity distributions", *Phys. Rev. D* **91** (2015), no. 3, 031501, `doi:10.1103/PhysRevD.91.031501`, `arXiv:1411.2633`. 120

[203] M. Czakon, "A novel subtraction scheme for double-real radiation at NNLO", *Phys. Lett. B* **693** (2010) 259–268, doi:10.1016/j.physletb.2010.08.036, arXiv:1005.0274. 120

[204] M. Czakon and D. Heymes, "Four-dimensional formulation of the sector-improved residue subtraction scheme", *Nucl. Phys. B* **890** (2014) 152–227, doi:10.1016/j.nuclphysb.2014.11.006, arXiv:1408.2500. 120

[205] M. Czakon, "Double-real radiation in hadronic top quark pair production as a proof of a certain concept", *Nucl. Phys. B* **849** (2011) 250–295, doi:10.1016/j.nuclphysb.2011.03.020, arXiv:1101.0642. 120

[206] M. Czakon et al., "Top-pair production at the LHC through NNLO QCD and NLO EW", *JHEP* **10** (2017) 186, doi:10.1007/JHEP10(2017)186, arXiv:1705.04105. 120

[207] M. Grazzini, S. Kallweit, and M. Wiesemann, "Fully differential NNLO computations with MATRIX", arXiv:1711.06631. 120

[208] S. Catani et al., "Top-quark pair production at the LHC: Fully differential QCD predictions at NNLO", *JHEP* **07** (2019) 100, doi:10.1007/JHEP07(2019)100, arXiv:1906.06535. 120

[209] S. Catani et al., "Top-quark pair hadroproduction at next-to-next-to-leading order in QCD", *Phys. Rev.* **D99** (2019), no. 5, 051501, doi:10.1103/PhysRevD.99.051501, arXiv:1901.04005. 120

[210] F. Buccioni et al., "OpenLoops 2", arXiv:1907.13071. 120

[211] F. Cascioli, P. Maierhofer, and S. Pozzorini, "Scattering Amplitudes with Open Loops", *Phys. Rev. Lett.* **108** (2012) 111601, doi:10.1103/PhysRevLett.108.111601, arXiv:1111.5206. 120

[212] A. Denner, S. Dittmaier, and L. Hofer, "Collier: a fortran-based Complex One-Loop LIbrary in Extended Regularizations", *Comput. Phys. Commun.* **212** (2017) 220–238, doi:10.1016/j.cpc.2016.10.013, arXiv:1604.06792. 120

[213] S. Catani et al., "Vector boson production at hadron colliders: hard-collinear coefficients at the NNLO", *Eur. Phys. J.* **C72** (2012) 2195, doi:10.1140/epjc/s10052-012-2195-7, arXiv:1209.0158. 120

[214] S. Catani and M. Grazzini, "An NNLO subtraction formalism in hadron collisions and its application to Higgs boson production at the LHC", *Phys. Rev. Lett.* **98** (2007) 222002, doi:10.1103/PhysRevLett.98.222002, arXiv:hep-ph/0703012. 120

[215] P. F. Monni et al., "MiNNLO$_{PS}$: a new method to match NNLO QCD to parton showers", *JHEP* **05** (2020) 143, doi:10.1007/JHEP05(2020)143, arXiv:1908.06987. 120

[216] P. F. Monni, E. Re, and M. Wiesemann, "MiNNLO$_{\rm PS}$: optimizing $2 \to 1$ hadronic processes", *Eur. Phys. J. C* **80** (2020), no. 11, 1075, doi:10.1140/epjc/s10052-020-08658-5, arXiv:2006.04133. 120

[217] K. Hamilton, P. Nason, and G. Zanderighi, "MINLO: Multi-Scale Improved NLO", *JHEP* **10** (2012) 155, doi:10.1007/JHEP10(2012)155, arXiv:1206.3572. 120

[218] K. Hamilton, P. Nason, C. Oleari, and G. Zanderighi, "Merging H/W/Z + 0 and 1 jet at NLO with no merging scale: a path to parton shower + NNLO matching", *JHEP* **05** (2013) 082, doi:10.1007/JHEP05(2013)082, arXiv:1212.4504. 120

[219] ATLAS Collaboration, "Measurements of differential cross sections of top quark pair production in association with jets in pp collisions at $\sqrt{s} = 13$ TeV using the ATLAS detector", *JHEP* **10** (2018) 159, doi:10.1007/JHEP10(2018)159, arXiv:1802.06572. 126

[220] M. Czakon, D. Heymes, and A. Mitov, "High-precision differential predictions for top-quark pairs at the LHC", *Phys. Rev. Lett.* **116** (2016), no. 8, 082003, doi:10.1103/PhysRevLett.116.082003, arXiv:1511.00549. 126

[221] N. Kidonakis, "NNLL threshold resummation for top-pair and single-top production", *Phys. Part. Nucl.* **45** (2014), no. 4, 714–722, doi:10.1134/S1063779614040091, arXiv:1210.7813. 126

[222] "The reweighting of pt(top-quark) in MC". https://twiki.cern.ch/twiki/bin/view/Sandbox/JamesKeaveneySandbox. Accessed: 2021-06-14. 126

[223] ATLAS Collaboration Collaboration, "Treatment of top-quark backgrounds in extreme phase spaces: the "top p_T reweighting" and novel data-driven estimations in ATLAS and CMS", technical report, CERN, Geneva, Apr, 2021. arXiv:2105.03977, Proceeding for 13th International Workshop on Top Quark Physics. 126

[224] ATLAS Collaboration, "Measurements of top-quark pair differential and double-differential cross-sections in the ℓ+jets channel with pp collisions at $\sqrt{s} = 13$ TeV using the ATLAS detector", *Eur. Phys. J. C* **79** (2019), no. 12, 1028, doi:10.1140/epjc/s10052-019-7525-6, arXiv:1908.07305. [Erratum: Eur.Phys.J.C 80, 1092 (2020)]. 132

[225] G. Apollinari et al., "High-Luminosity Large Hadron Collider (HL-LHC): Preliminary Design Report". CERN Yellow Reports: Monographs. CERN, Geneva, 2015. 136

[226] CLIC and C. Collaborations, "Updated baseline for a staged Compact Linear Collider". CERN Yellow Reports: Monographs. CERN, Geneva, 2016. 136

[227] M. Mangano and M. Mangano, "Physics at the FCC-hh, a 100 TeV pp collider". CERN Yellow Reports: Monographs. CERN, Geneva, Oct, 2017. 136

[228] "The International Linear Collider Technical Design Report - Volume 2: Physics", arXiv:1306.6352. 136

ACKNOWLEDGMENTS

Esta tesis ha sido un capítulo de mi vida de mucho esfuerzo y horas de trabajo. Tanto el apoyo científico, moral como sentimental de muchas personas han sido pilares importantísimos para su culminación. Le agradezco a mi familia, a esos que están y también a los que ha dolido dejar ir. Gracias a mi madre, que incluso desde tantos kilómetros de distancia, no ha dejado de darme amor y comprensión. Gracias a mi esposa que ha estado a mi lado y que me ha apoyado desde el primer momento en que decidí viajar tan lejos para seguir mis sueños. Gracias a todos mis amigos que durante este tiempo he llegado a conocer mejor y que me han ayudado en innumerables ocasiones. Gracias a mi tutor por su inmenso apoyo y por todo lo que me ha enseñado. Gracias al DESY por la oportunidad de ser parte de tan prestigioso centro y a todos los compañeros de trabajo que de una forma u otra me han ayudado y han contribuido a mi crecimiento profesional.

Gracias a todos por su apoyo.